

Active Galactic Nuclei throughout the Spectrum: M 87, PKS 2052–47, and the MOJAVE sample

Inaugural-Dissertation

zur

Erlangung des Doktorgrades

der Mathematisch-Naturwissenschaftlichen Fakultät

der Universität Köln

vorgelegt von

Chin-Shin Chang

aus Taipei, Taiwan, ROC

Berichterstatter: Prof. Dr. Andreas Eckart
Prof. Dr. Anton Zensus

Tag der mündlichen Prüfung: 25. Oktober 2010

獻給我最親愛的父親母親與妹妹

To my beloved father, mother, and sister

Contents

Summary	7
Zusammenfassung	9
Summary (Chinese)	11
1 Introduction	13
1.1 AGN Classification and the Unified Model	14
1.1.1 AGN Class	14
1.1.2 The Unified Model	16
1.2 Radiation Processes	17
1.2.1 Thermal Emission	17
1.2.2 Synchrotron Emission	18
1.2.3 Inverse Compton Scattering	20
1.2.4 X-ray Emission of AGN	22
1.3 Very Long Baseline Interferometry	23
1.3.1 Fundamentals of Radio Interferometry	23
1.3.2 Synthesis Imaging	26
1.4 The Study of Blazars	26
1.4.1 The Emission of Blazars	26
1.4.2 The Spectral Energy Distribution of Blazars	28
1.4.3 Parsec-scale Jets: Intrinsic and Observed Properties	29
1.4.4 The AGN Study in This Thesis	30
2 A multi-band flare of the HST-1 feature in the M 87 jet	33
2.1 Introduction	33
2.2 VLBI Observations and Data Analysis	35
2.2.1 Very Long Baseline Array	35
2.2.2 Observations and Data Analysis	36
2.3 Results	38
2.3.1 Imaging of the inner jet of M 87	41
2.3.2 Imaging of the HST-1 region	42
2.3.3 Spectral properties of HST-1	42
2.3.4 HST-1 kinematics	44
2.4 Discussion	47
2.4.1 Variability timescale and HST-1 flaring region at parsec-scales	47

2.4.2	Speeds of HST-1	49
2.4.3	Detection limits	49
2.4.4	HST-1 parsec-scale spectrum	49
2.4.5	A blazar nature of HST-1	51
2.5	Summary and Future Work	51
3	Blazar Flare: a Multiwavelength Study of the Flat Spectrum Radio Quasar	
	PKS 2052–47	53
3.1	Introduction	53
3.2	Data Acquisition	56
3.2.1	The Multiwavelength Campaign	58
3.3	Data Analysis	59
3.4	Results	60
3.4.1	The Multiband Properties of PKS 2052–47	60
3.4.2	The Broadband SED of PKS 2052–47	62
3.5	Discussion	62
3.6	Summary	64
4	The Broadband Spectral Energy Distribution of the MOJAVE Sample	67
4.1	The MOJAVE Sample	67
4.1.1	Parsec-scale Jet Properties and High Energy Emission	69
4.2	The Project	70
4.3	Data Acquisition	70
4.3.1	University of Michigan Radio Astronomy Observatory	71
4.3.2	<i>Fermi</i> -GST AGN Multi-frequency Monitoring Alliance	72
4.3.3	The <i>Swift</i> Gamma-Ray Burst Mission	73
4.3.4	<i>Fermi</i> Gamma-ray Space Telescope	76
4.4	Data Analysis	78
4.4.1	<i>Swift</i> /XRT Data Reduction	82
4.4.2	<i>Swift</i> /UVOT Data Reduction	91
4.4.3	Extinction Correction	92
4.4.4	<i>Fermi</i> /LAT data	94
4.5	The Broadband SED of the MOJAVE sources	95
4.6	Statistical Properties of the MOJAVE Sample	133
4.6.1	Histograms	133
4.6.2	Dispersion Relation	138
4.7	Summary	141
A	The X-ray Spectra of the MOJAVE Sample	147
B	The Broadband SED of the MOJAVE Sample	171
C	Previously Published Broadband SED of the MOJAVE Sources	189
D	Glossary of Acronyms	221
	Bibliography	223

Acknowledgements	273
Acknowledgements (Chinese)	275
Erklärung	277
Curriculum Vitae	279

Summary

Active galactic nuclei (AGN) are one of the many mysteries in the Universe. AGN hosts a super massive black hole (SMBH) in its center surrounded by a rotating accretion disk, and a powerful jet is ejected along the pole directions of the accretion disk. The powerful jet is definitely the highlight of AGN. Those extragalactic jets appears to have superluminal motions up to $60c$, and they are very luminous and variable across the electromagnetic spectrum. The jets can be highly polarized, which indicates the existence of strong magnetic fields; they can have a highly bended morphology due to reasons we do not completely understand. Astronomers have been studying AGN jets for the past decades by performing observations from the radio to the γ -ray band, applying physical jet models to the observed properties, and trying to put the pieces into the whole picture. We now understand many aspects of the AGN phenomena, but a significant part is still missing.

The aim of this thesis is to study the extragalactic jets by using different approaches. We investigate: (i) a bright feature in the jet of the radio galaxy M 87 as observed using high-resolution VLBI technique; (ii) a multiband flare of the blazar PKS 2052–47 by conducting a multifrequency campaign; (iii) the broadband spectral energy distribution (SED) of a radio-selected, statistically-complete sample of the most conspicuous AGN in the Northern sky: the **M**onitoring **O**f **J**ets in **A**ctive galactic nuclei with **V**LBA **E**xperiments (MOJAVE) sample.

Very long baseline interferometry (VLBI) is a powerful technique that can resolve distant AGN to parsec-scales by combining global radio antennas to perform together as a giant telescope with a radius of the earth. With the VLBI technique, we are able to trace bright features being ejected from the center moving along the jet. In this thesis, we use the VLBI technique to detect a bright knot 80 pc from the center of the radio galaxy M 87. It was suggested that the HST-1 knot was the site where a TeV flare of M 87 was generated from. By analyzing the VLBI data at 15 GHz from 2000 to 2009, we detected HST-1 during 2003 and 2007. We studied the apparent speed, the flux variability, and the spectral properties of HST-1. Although we found that the light curve of the compact HST-1 region at VLBA 15 GHz peaked in 2005, we saw that the HST-1 region was very extended and had a steep spectrum; the projected apparent speed of HST-1 was subluminal. Therefore, our results do not completely support the hypothesis.

Studying multiband flares is one of the best ways to distinguish different mechanisms taken place in AGN. Current jet models suggest that time delays between multiband flares have different features while the emission mechanism differs. In this thesis, we studied the flat spectrum radio quasar PKS 2052–47, which experienced an optical flare followed by a γ -ray flare in July 2009. We arranged a multiwavelength campaign from radio to γ -ray after the blazar's flare. In the campaign, VLBI observations by the **T**racking **A**ctive **G**alactic **N**uclei with **A**ustral **M**illiarcsecond **I**nterferometry (TANAMI) program are in-

cluded in order to trace any change of jet morphology, if any; the millimeter radio flux density was measured by the **A**tacama **P**athfinder **E**Xperiment (APEX); the optical and the X-ray band observations were obtained by the *Swift* UV/Optical telescope (UVOT) and X-ray telescope (XRT); the γ -ray observations were obtained by the *Fermi* Large Area Telescope (LAT). We do not see significant change in the X-ray photon indices and fluxes during the 5-day *Swift* monitoring of the source.

The broadband spectral energy distribution reflects the emission properties of AGN, and it shows the energy output in different wavebands. By simulating physical jet models and reconstructing the broadband SED, one can probe the emission mechanism, the jet composition, the magnetic field, the bulk velocity in jet, and the structure of AGN. In this thesis, we study the broadband SED from the radio to the γ -ray band of a radio-selected sample. The MOJAVE program has been monitoring 135 radio-bright, statistically-complete sample of AGN using the Very Long Baseline Array (VLBA) at 15 GHz for a decade, and the MOJAVE sample is consisted of mostly blazars, which are AGN as seen jet-on. The typical broadband SED of a blazar has a double-hump profile. It is believed that the lower-energy hump is caused by the synchrotron emission from the AGN jet, and the higher-energy hump is produced by the inverse-Compton (IC) up-scattering of the seed photons from the jet or other external sources. We constructed a broadband SED catalog of the MOJAVE sample, and we applied polynomial fits to the observed data at the low and the high energy humps of the SED as a first approach to understand the properties of the sources. The peak positions of the two humps can be derived from the polynomial fit for many of the MOJAVE sources except for some sources having deviated SED profiles.

In this thesis, we try to understand the AGN puzzles by using different approaches. We contributed in understanding the emission nature of AGN with novel techniques and instruments, and our efforts help to make a step forward to reveal the whole picture.

Keywords: VLBI, radio, X-ray, γ -ray, SED, broadband, multifrequency, M 87, PKS 2052–47, MOJAVE.

Zusammenfassung

Aktive Galaktische Kerne sind eines der Mysterien des Universums. AGN beherbergen ein supermassives schwarzes Loch, werden von einer rotierenden Akkretionsscheibe umkreist und stoßen energiereiche Jets entlang der Polachse der Akkretionsscheibe aus. Die Jets sind zweifellos das Highlight der AGNs. Diese extragalaktischen Jets weisen Überlichtgeschwindigkeiten bis zum 60-fachen der Lichtgeschwindigkeit auf, sind sehr leuchtstark und veränderlich entlang des elektromagnetischen Spektrums. Die Jets können stark polarisiert sein, was auf die Existenz von starken Magnetfeldern schließen lässt. Aus noch nicht verstandenen Gründen können sie eine stark gekrümmte Struktur (Erscheinungsbild) aufweisen. Seit Jahrzehnten studieren Astronomen AGNs mittels Beobachtungen vom Radio- bis zum Gammastrahlenbereich, wenden physikalische Jetmodelle auf die beobachteten Eigenschaften an und versuchen die einzelnen Fragmente zu einem Ganzen zusammenzusetzen. Heute verstehen wir einige Aspekte des AGN-Phänomens, aber ein erheblicher Teil ist noch nicht bekannt.

Das Ziel dieser Arbeit ist es, extragalaktischen Jets aus unterschiedlichen Betrachtungsweisen zu studieren. Wir erforschen: i) einen hellen Bereich im Jet der Radiogalaxie M 87 beobachtet mit hochauflösender VLBI-Technik; ii) einen Anstieg der Helligkeit über mehrere Frequenzbereiche im Blazar PKS 2052–47 mittels einer dirigierten multifrequenz Beoberkungskampagne; iii) die spektrale Energieverteilung (SED) eines mittels Radiobeobachtungen ausgewählten, statistisch vollständigen Stichproben der auffälligsten AGN in der nördlichen Hemisphäre: die MOJAVE Durchmusterung (Beobachtung der Jets in Aktiven Galaktischen Kernen mittels VLBA Experimenten, engl. **Monitoring Of Jets in Active Galactic Nuclei with VLBA Experiments**).

Interferometrie mit langen Basislinien (engl. Very Long Baseline Interferometry, VLBI) ist eine leistungsfähige Technologie, die entfernte AGN bis auf Parsec-Skala auflösen kann, mittels der Kombination von weltweiten Radioteleskopen zu einem riesigen Teleskop mit dem Durchmesser der Erde. Mittels der VLBI-Technik konnten wir einen hellen Knoten, der sich 80 pc vom Zentrum der Radiogalaxie M 87 entfernt befindet, zu detektieren. Es wurde vermutet, dass der HST-1 Knoten der Ursprung eines TeV Flares (Ausbruches) von M 87 war. Während der Auswertung der 15 GHz VLBI Daten zwischen 2000 und 2009 konnten wir HST-1 zwischen 2003 und 2007 detektieren. Obgleich wir feststellten, dass die 15 GHz VLBI Lichtkurve der kompakten HST-1 Region ihren Maximalwert in 2005 hatte, sahen wir, dass die HST-1 Region sehr ausgedehnt war, ein steiles Spektrum besitzt und die projizierte scheinbare Geschwindigkeit nicht relativistisch ist. Folglich befürworten unsere Ergebnisse diese Vermutung nicht vollständig.

Das Studium von Helligkeitsausbrüchen in unterschiedlichen Frequenzbereichen ist

eine der besten Methoden um verschiedenen, in AGN stattfindenden Vorgänge, zu unterscheiden. Die gegenwärtigen Jetmodelle legen nahe, dass die Zeitverzögerungen zwischen den Ausbrüchen unterschiedlicher Frequenz unterschiedliche Merkmale haben, während sich die Strahlungsprozesse ändern. In der vorliegenden Arbeit untersuchen wir den Radioquasar PKS 2052–47, der ein flaches Spektrum aufweist und in welchem sich an einem Helligkeitsausbruch im optischen im Juli 2005 ein Ausbruch im Gammastrahlenbereich anreichte. Wir leiteten eine multi-frequenz Beobachtungskampagne vom Radio bis zum Gammastrahlenbereich nach dem Ausbruch des Blazars ein. Innerhalb der Kampagne wurden VLBI Beobachtungen mit dem TANAMI (Tracking Active Galactic Nuclei with Austral Milliarcsecond Interferometry) Programm verwendet um, falls vorhanden Änderungen im Jeterscheinungsbild zu verfolgen, die Radioflussdichte im Millimeterbereich wurde vom APEX (Atacama Pathfinder EXperiment) gemessen, die Beobachtungen Röntgenstrahlenbereich wurden vom *Swift* UV/Optical Teleskop (UVOT) und vom X-ray Teleskop (XRT) und die Gammastrahlenbeobachtung vom *Fermi* Large Area Telescope (LAT) durchgeführt. Wir sehen keine wesentlichen Änderungen im Photonenindex und Flussdichte der Röntgenstrahlen während der 5-Tage Beobachtung mit *Swift*.

Die spektrale Energieverteilung spiegelt die Strahlungseigenschaften der AGN wieder und zeigt den Energieausstoss in unterschiedlichen Wellenlängenbereichen. Durch die Simulation von physikalischen Jetmodellen und der Rekonstruktion der SED kann man die Strahlungsprozesse, die Jetzusammensetzung, das Magnetfeld, Flussgeschwindigkeit im Jet und die Struktur des Jets untersuchen. In der vorliegenden Arbeit untersuchen wir die SED vom Radio bis zum Gammastrahlenbereich eines mittels Radiobeobachtungen ausgewählten Ensemble. Das MOJAVE Programm beobachtet seit 15 Jahren eine statistisch vollständige Auswahl von 135 radiolauten AGN bei 15 GHz mittels dem Very Long Baseline Array (VLBA). Die MOJAVE Auswahl besteht zum grössten Teil aus Blazaren, AGN deren Jet zum Beobachter zeigt. Die typische SED eines Blazars besitzt zwei Höcker. Man nimmt an, dass der niederenergetische Höcker durch Synchrotronstrahlung des AGN Jets und hochenergetische durch inverse Comptonstreuung der Keimphotonen des Jets oder externer Quellen erzeugt wird. Wir erstellten einen SED Katalog des MOJAVE Ensembles und passten Polynome, als erste Näherung an den nieder- und hochenergetischen Buckel der SED an, um die Eigenschaften der Quellen zu verstehen. Die Position des Scheitelpunkts der beiden Hügel kann für viele Quellen des MOJAVE Programms aus den Polynomanpassungen abgeleitet werden, ausser für einige Quellen die ein abweichendes Profil aufweisen.

In dieser Arbeit versuchen wir das AGN Puzzle zu verstehen indem wir unterschiedliche Ansätze verwenden. Zum Verständnis der Strahlungsmechanismen in AGN mit neuartigen Techniken und Instrumenten trugen wir bei und unser Anstrengungen helfen eine Schritt in Richtung der Enthüllung des ganzen Bildes zu machen.

摘要

活躍星系核是宇宙的眾多謎團之一，在一個活躍星系核的系統中心是一個超巨大質量的黑洞，其周圍環繞著旋轉的吸積盤，含有強大能量的噴流隨旋轉軸的方向由吸積盤中心射出。這強大的噴射流讓天文學家十分著迷，由電波天文觀測結果顯示，這些銀河系外的噴流以將近60倍光速的投射速度向外噴發，而且展現出十分強與多變的光度，佔據了整個電磁波波段。系外噴流有時具有高度偏振性，這是強大磁場存在的證據；它們也可以是複雜彎曲的，但科學家們並不瞭解其成因。過去數十年間，為了解系外噴流的原理與成因，天文學家們致力於研究其由電波至伽瑪射線波段的性質。雖然目前我們已經有基本的理論可以解釋這個現象，但所知的仍然有限。

在這篇博士論文裡，我們用不同的方式來研究系外噴流。一、用甚長基線干涉測量（VLBI）技術，高度解析一個在電波星系M87噴流裡的亮結。二、運用多波段觀測，研究類星體PKS2052-47在光學及伽瑪射線波段的光度突增現象。三、研究一個在統計上完整的電波活躍星系核樣本（MOJAVE），其能量光譜在寬頻電磁波段的分布。

電波甚長基線干涉測量（VLBI）是目前解析度最高的天文觀測技術，這需動用分布在世界各地的電波望遠鏡觀測同一個天體，之後結合各地的觀測資料，運用電腦計算，模擬出的結果相當於一座有地球直徑大小的望遠鏡。這項技術可以解析系外的活躍星系核至秒差距的大小。在本論文裡，我們在波長兩公分的範圍用VLBI技術觀測電波星系M87，並解析偵測到其噴流內距核中心80秒差距的一個亮結HST-1。之前的研究報告指出，M87在2005年被偵測到TeV能量的射線，此為宇宙中最高能量的射線，有些研究則推測HST-1可能是發出此TeV射線的源頭。我們分析了由2000至2009年用VLBI技術對M87的觀測資料，結果我們首次於2003至2007年間用VLBI兩公分波段偵測到了HST-1。我們分析了HST-1的視速度、光度變化、及光譜性質。我們發現HST-1的光度曲線在2005年達到了最大值，但是HST-1區域的光度分散且光譜陡峭，加上視速度並未達到光速，因此，我們的研究結果並不支持之前的假說。

研究多波段的光度突增現象可以分辨活躍星系核的不同物理機制，觀測結果顯示，對於同一個活躍星系核，不同波段的光度突增有些許的時間差，研究此時間上的延誤可以瞭解系外噴流的發射光線機制。在2009年，類星體PKS2052-47被發現在可見光及伽瑪射線波段有光度突增現象。在這不久之後，我們安排了對PKS2052-47的同時多波段觀測。參與的研究機構包含了南半球的VLBI聯盟：TANAMI計畫，位於智利的APEX電波望遠鏡（電波毫米波段），太空望遠鏡Swift涵蓋了X射線及光學波段的觀測，以及太空望遠鏡Fermi涵蓋伽瑪射線的觀測。我們的研究結果顯示，在五天Swift的監測中，PKS2052-46的X射線光譜性質並沒有明顯的改變。

能量光譜在寬頻電磁波段的分布像是活躍星系的指紋，可以反映其產生電磁波的機制，透過電腦模擬系外噴流的結構及物理模型，可以計算出噴流產生的寬頻電磁波在各個波段的強度，進而了解噴流的結構、周圍磁場、噴流速度、以及活躍星系核的結構。在此論文中，我們研究一個含有135個活躍星系核的樣本（MOJAVE），其在統計學上是完整的採樣，且所有樣本皆有強的電波亮度。過去的十年裡，MOJAVE計畫在2公分波段用VLBI技術監測這135個活躍星系核。通常它們寬頻的能量光譜看起來像雙駝峰，根據目前的瞭解，在低頻

波段的高峰是透過同步輻射的機制由活躍星系核的電波噴流產生，而高頻波段的高峰則是透過逆康普頓機制，將低頻的光子轉化為高能光子而產生。我們收集了MOJAVE樣本由電波至伽瑪射線波段的數據，集結了135個活躍星系核的寬頻能量光譜。我們用數學多項式的模型擬合能量光譜上的數據，估計雙峰的峰頂位置。在MOJAVE樣本裡，此多項式模型可擬合大部份的活躍星系核能量光譜，但是有些活躍星系核的能量光譜並沒有一般的雙駝峰形狀，因此無法估計峰頂位置。

在本博士論文裡，我們試著用不同的方法探討活躍星系核。我們運用最先進的觀測技術研究這個宇宙中具有強大能量的天體，希望這些研究可以對瞭解其物理機制有所貢獻。

1 Introduction

Active galactic nuclei (AGN) are the most energetic objects in the Universe. AGN dominate the high-energy sky in the extragalactic regime, and since its first discovery (Seyfert 1943), different types of AGN are observed with various behaviors (see Section 1.1.1). After decades of study, we believe that we are able to unify the AGN phenomenon in a common scheme (see Section 1.1.2). A super-massive black hole (SMBH) located in the center of an AGN is fueling the whole system with matter accreting around the central engine. Strong magnetic fields are dragged along by the rotating accretion disk, adopting a cone-shaped morphology with a warped structure (see Figure 1.1). An energetic plasma jet is launched in the vicinity of the SMBH following the magnetic field lines along the pole direction of the accretion disk. There is an enormous amount of energy released from AGN and observed by us across the whole electromagnetic spectrum from the radio to the TeV band.

To find out the exact mechanisms at work in AGN systems is one of the main efforts for astronomers. After decades of effort, we have a better understanding in different branches of AGN research (accretion disk, jet, broad/narrow line region, etc.) from various studies at different wavelengths. However, most of the major problems still remain open: How is the jet launched from the central engine? What is its composition? Where does the very-high-energy (VHE) emission come from? How does emission of different wavebands relate to each other? Why are there emitting components from the central engine transmitting outwards? How do they work?

Right now, it is probably the best time to have a chance to peek at the mystery of AGN. Current astronomical facilities span from radio to TeV bands, providing the best wavelength coverage ever. Also, much improved networking connects teams of different wavelengths to collaborate and react to a single activity of a given AGN, enables us to dig deeper to different states of the object.

In this chapter, I will give a brief overview of the AGN picture. In Section 1.1, I will describe AGN classes and the unified scheme. In Section 1.2, I will introduce the emission mechanisms involved in AGN. I especially discuss about the X-ray emission processes in Section 1.2.4. In Section 1.4.1, I summarize current understandings of the location of AGN emission at different wavelength. In Section 1.3, I will introduce the very long baseline interferometry (VLBI) technique, which is an important tool to study AGN outflows. Finally, I attach a table of current major astronomical facilities at different wavelengths that are contributing to AGN studies in Section 1.4.4.

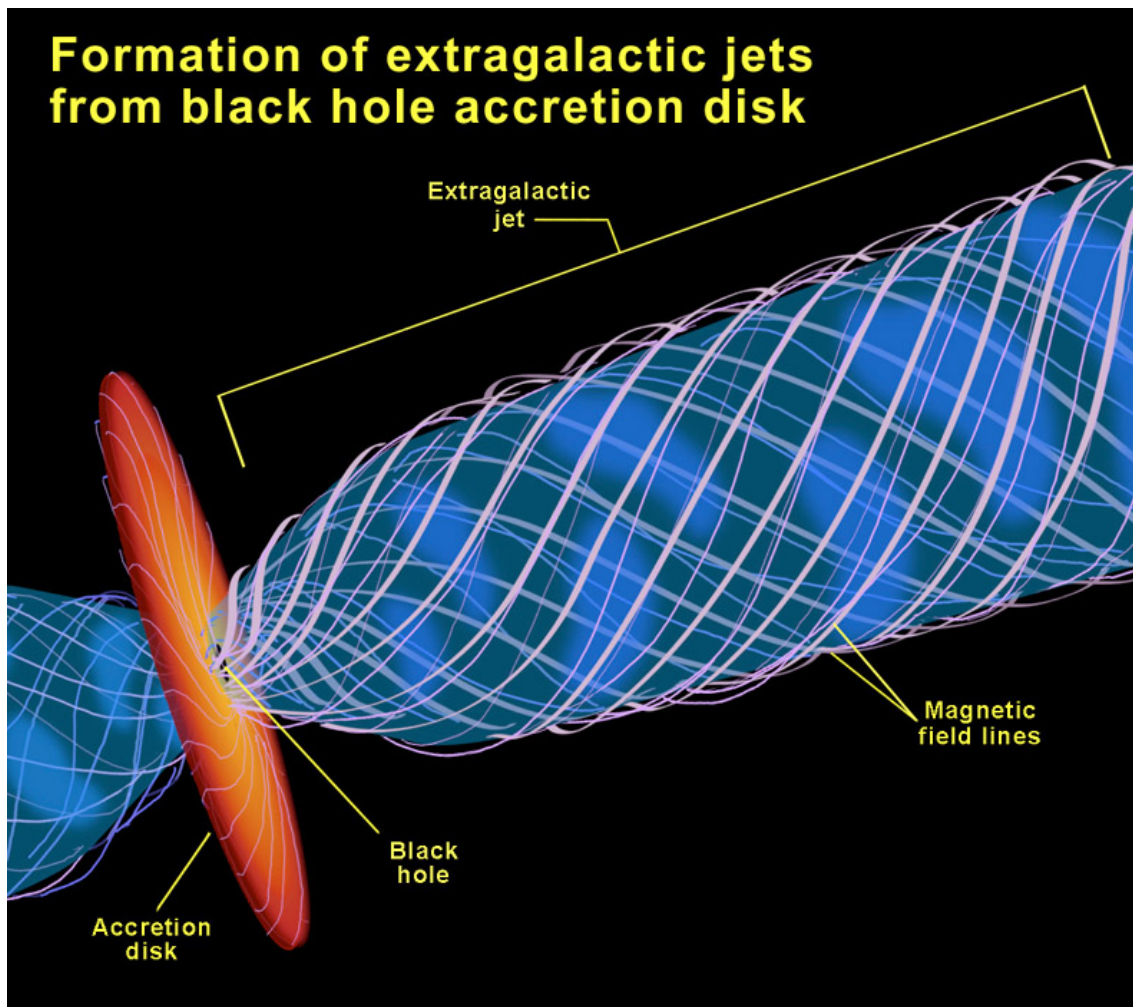


Figure 1.1: Artistic illustration of an AGN system. White curves represent magnetic field lines warped in a cone shape. In the center of the galaxy, there is a super massive black hole (image credit: NASA and Ann Field, Space Telescope Science Institute).

1.1 AGN Classification and the Unified Model

1.1.1 AGN Class

AGN are categorized into various classes based on the properties as observed in different wavebands. Figure 1.2 illustrates the relations between different types of AGN based on the characteristics of radio emission, nuclear luminosity, and optical line properties. Here I briefly introduce the AGN classification, for more details about this topic, please see Krolik (1999).

Quasar When quasars were discovered (Hazard et al. 1963), the term “quasi-stellar object” was used to refer to these strange objects which appeared to be stellar-like but were indeed very distant and luminous, as it was seen from their strongly redshifted optical spectra. Quasars have strong optical and X-ray continuum emission, as well as broad and narrow optical emission lines. The huge power output from quasars extend across the

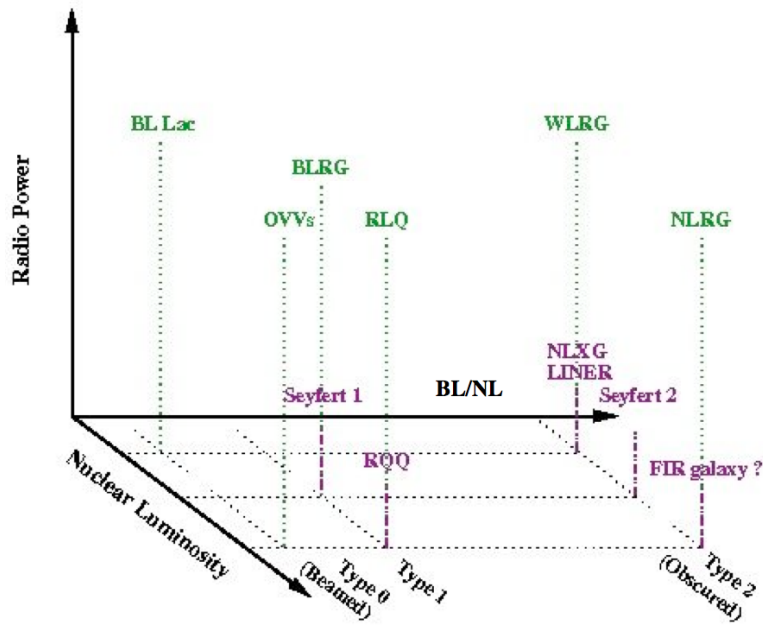


Figure 1.2: Relations between different types of AGN (Image credit: C. Tadhunter). For abbreviations: BLRG - broad line radio galaxies, RLQ - radio loud quasars, OVV - optically violent variable quasar, WLRG - weak emission-line radio galaxy, narrow emission-line radio galaxy, RQQ - radio quiet quasars, NLXG - narrow line X-ray galaxy, FIR galaxy - far infrared radio galaxy, BL - broad line, NL - narrow line.

whole electromagnetic spectrum. Quasars with a strong nuclear and jet radio emission are categorized as radio-loud quasars, otherwise they belong to radio-quiet quasars. Radio-loud quasars showing strong optical variability are called optically violent variable (OVV) quasars; quasars with flat radio spectrum and strong broad emission lines are called flat-spectrum radio quasars (FSRQ).

BL Lac Object BL Lac objects are categorized by their rapid and large amplitude flux variability and significant optical polarization. As for the spectral properties, they have a featureless non-thermal continuum. Very often we use the term **blazars**¹ to refer to BL Lac objects and FSRQ. Blazars have high radio brightness and flat radio spectra; in the optical band, they have high optical polarization, as well as strong optical variability. Padovani and Giommi (1995) divide BL Lac objects into three categories by the peak frequency of the synchrotron bump (ν_s) in their spectral energy distribution (SED; see Section 1.4.2): sources with $\nu_s < 10^{14.5}$ Hz are low energy peaked BL Lac objects (LBL), those with $10^{14.5} < \nu_s < 10^{16.5}$ Hz are intermediate BL Lac objects (IBL), and those with $\nu_s < 10^{16.5}$ Hz are classified as high energy peaked BL Lac objects (HBL).

Radio Galaxy This type of AGN shows strong radio emission in the core and extended jet, and sometimes they display narrow and broad emission lines. Fanaroff and Riley (1974) discovered that there is a transition of radio luminosity occurring at $P_{178\text{MHz}} \approx$

¹The term blazar (blazing quasi-stellar object) was firstly used by Edward Spiegel in 1978 to refer to OVV quasars and BL Lac objects.

$10^{25} \text{W Hz}^{-1} \text{sr}^{-1}$, and they divided radio sources into two classes, which were later called Fanaroff and Riley Class I (FRI) and Class II (FRII). FRI has smooth jets emanating from the nucleus and lobes, where the surface brightness decreases toward the edges. FRII are more powerful radio galaxies having faint jets and edge-brightened lobes. There are two approaches of models that explain the FRI/FRII transition. The morphological difference can be explained by deceleration of jets caused by the environment, and the dichotomy of transition can be modeled by differences in fundamental parameters such as black hole spin, accretion mode, and jet composition (see Gopal-Krishna and Wiita 2000 for a summary).

Seyfert galaxies This class of AGN was identified by Seyfert (1943). They have luminous nuclei and bright emission lines. The Seyfert galaxies are divided into Type 1 and Type 2 based on their spectroscopic properties at the optical band. Type 1 Seyfert galaxies show both narrow and broad emission lines, and Type 2 show only narrow lines. The spectral line emission from the Seyfert galaxies is produced from highly ionized gas, which contains hydrogen, helium, nitrogen, and oxygen, and the emission lines display Doppler broadening. The Seyfert galaxies are quite luminous across the broadband spectrum, and only $\sim 5\%$ of Seyfert galaxies are found to be radio-loud. As indicated in Figure 1.3, the Seyfert galaxies are mostly radio quiet quasars, which are seen edge-on. For this reason, they are ideal objects for us to study the dusty torus, the accretion disk, and the broad line region.

1.1.2 The Unified Model

It is widely accepted that the discrepant properties we observed in AGN are caused by orientation effects (Antonucci 1993, Urry and Padovani 1995). Figure 1.3 illustrates the unified scheme of AGN. The SMBH is located in the center and is surrounded by an accretion disk, further out there is a donut-shape, dusty torus. Close to the SMBH, there is a broad line region, which is a very compact region of gas where broad emission lines are formed (Popovic 2006, Osterbrock 1989). Farther away from the central engine, there is an extended region of interstellar gas ionized and heated by the AGN (Groves 2007), which is denoted as the narrow line region. A relativistic jet is launched from the vicinity of the SMBH and travels in the space passing through those regions mentioned previously and interact with each other.

Based on this model, if an AGN is seen edge-on, the broad line region is blocked by the dusty torus along the line-of-sight, and only the narrow line region can be seen from the observer, thus it would appear to be a narrow line radio galaxy (radio-loud) or a Type 2 Seyfert galaxy (radio-quiet). When an observer sees an AGN with an angle between edge-on and pole-on, the broad line region starts to become visible along the line of sight, and this is the case for broad-line radio galaxies (radio-loud) and Type 1 Seyfert galaxies (radio-quiet). If an AGN is seen pole-on, the source would appear to be highly variable and luminous, because the jet is emitting towards us, this is the case of blazars (radio-loud) and radio-quiet quasars. The unified scheme is supported by many observational evidences (Antonucci and Miller 1985, Miller and Goodrich 1990, Klöckner et al. 2003, Greenhill et al. 2003).

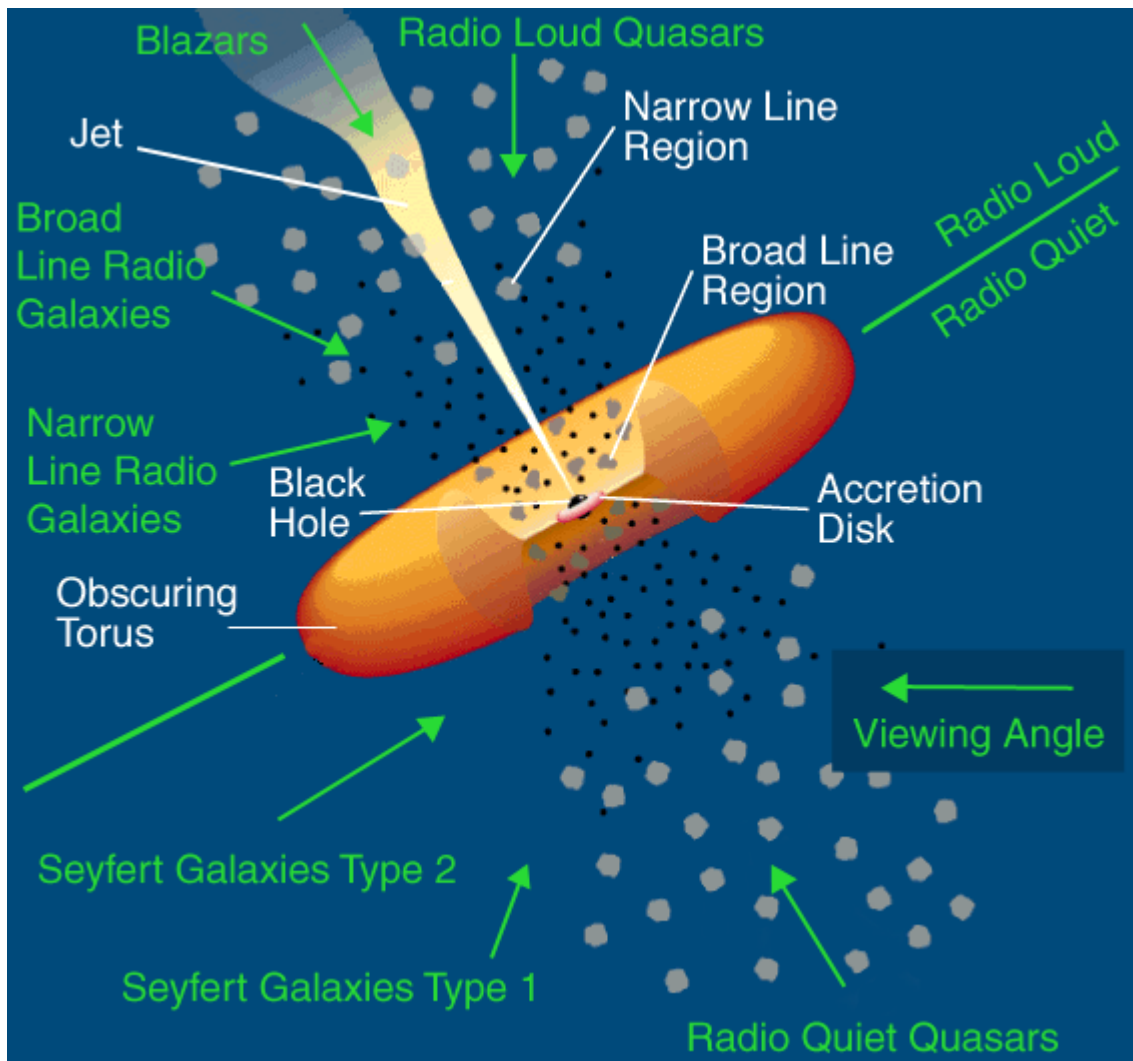


Figure 1.3: The unified model of AGN (Urry and Padovani 1995). The green arrows illustrate the viewing angles responsible for different categories of AGN. The upper part shows the unification for radio-loud sources, whereas the lower part describes the radio-quiet ones.

1.2 Radiation Processes

1.2.1 Thermal Emission

Thermal emission is the black-body emission. A system emits blackbody radiation when it reaches thermal equilibrium, and its emission can be described by the Planck law:

$$B_{\nu}(T) = \frac{2h\nu^3}{c^2} \frac{1}{e^{\frac{h\nu}{kT}} - 1},$$

where $B_{\nu}(T)$ is the intensity function, k is the Boltzmann's constant, h is the Planck constant, T is the temperature of the system, ν is the frequency of emission, and c denotes the speed of light. A very good example in astronomical schemes of thermal emission is

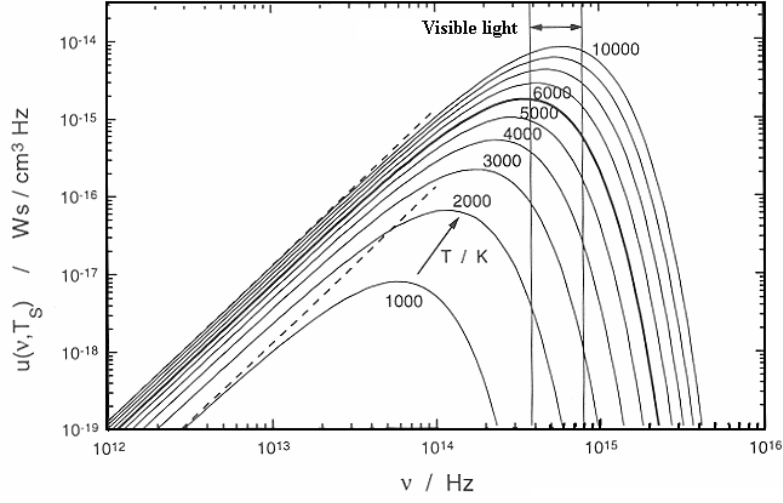


Figure 1.4: Planck radiation (image credit: H. Föll). As the equilibrium temperature gets higher, the peak of the emission intensity shifts to higher frequency.

the cosmic microwave background radiation (Penzias and Wilson 1965), which shows a black body spectrum of 2.725 K. Also, the optical emission of stars are dominated by the black body radiation, and non-thermal spectral lines are observed as well.

1.2.2 Synchrotron Emission

The dominant mechanism for radio emission in blazars is the synchrotron radiation. When charged particles move in a region with a magnetic field, they encounter a Lorentz force that leads them travel along a curved path. The observed spectrum is clearly diverges from Planck’s spectrum, and therefore is called “non-thermal”. In AGN systems, charged particles moving in the relativistic jets are the main source of synchrotron radiation.

When a charged particle moves in a magnetic field, it experiences a Lorentz force

$$\mathbf{F}_L = q(\mathbf{E} + \boldsymbol{\beta} \times \mathbf{B}),$$

where $\boldsymbol{\beta} = v/c$ is the velocity of the moving particle in units of the speed of light, q denotes the charge of the particle, and \mathbf{E} and \mathbf{B} are the electric and magnetic fields. For the case that the magnetic field dominates, and the magnetic field has only one direction, it results in a helical motion of the charged particle with the frequency

$$\omega_L = \frac{qB}{\gamma mc},$$

where ω_L is the Larmor frequency, $\gamma = 1/\sqrt{1 - \beta^2}$, and m is the mass of the particle. It can be shown that the synchrotron spectrum of a single electron can be described as:

$$P_\nu = \frac{4}{3} \sin^2 \theta \gamma^2 \frac{\sigma_{TC}}{\nu_c} \frac{B^2}{8\pi} F_s \left(\frac{\nu}{\nu_c} \right),$$

where θ is the angle between the direction of the charged particle and the magnetic field line, and ν_c is the critical frequency:

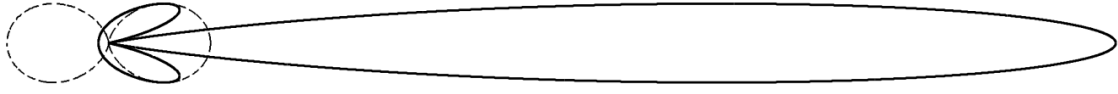


Figure 1.5: Relativistic beaming transforms the dipole pattern of Larmor radiation (dotted curve) into a narrow beam in the observer's frame. The solid curve illustrates the effect when $\gamma = 5$ (image credit: NRAO).

$$\nu_c = \frac{3}{2}\gamma^2 \sin\theta \frac{eB}{2\pi m_e c},$$

and σ_T is the Thomson cross section (Billings 1966):

$$\sigma_T \equiv \frac{8\pi}{3} \left(\frac{e^2}{m_e c^2} \right) \approx 6.65 \times 10^{-25} \text{ cm}^2.$$

When a charged particle moves with a relativistic speed, the emission is beamed sharply in the direction of motion as v approaches c . It can be shown that:

$$\sin\theta = \frac{\sin\theta'}{\gamma(1 + \beta\cos\theta')},$$

where θ denotes the viewing angle of the observer's frame, and θ' denotes the local frame of the moving electron. The Doppler factor is defined by

$$\delta = \frac{1}{\gamma(1 - \beta_{\parallel}\cos\theta)},$$

where β_{\parallel} is the longitudinal velocity component relative to the observer. The observed flux density S_{ν} then has a relation with the flux density in the co-moving frame S'_{ν} :

$$S_{\nu} = \delta^3 S'_{\nu}.$$

This is called the relativistic Doppler effect. Figure 1.5 illustrates the relativistic beaming effect.

In general, what we observe from astronomical sources is the synchrotron radiation emitted by a group of charged particles. Assuming a group of electrons with power law energy distribution

$$N(E)dE = K E^{-a} dE,$$

where $N(E)dE$ is the number of electrons per unit volume in the range of E and $E+dE$, and a is a parameter describing the distribution. Approximately each electron radiates the power of

$$P = -\frac{dE}{dt} = \frac{4}{3}\sigma_T \beta^2 \gamma^2 c U_B,$$

where U_B is the magnetic field density. It can be shown that

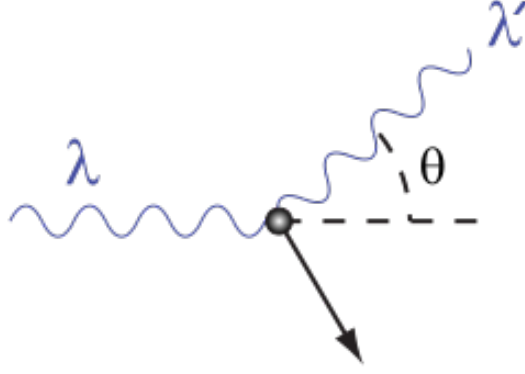


Figure 1.6: A photon of wavelength λ incidents and collide with a particle, producing a photon of wavelength λ' . Compton scattering: $\lambda > \lambda'$; inverse-Compton scattering: $\lambda < \lambda'$ (image credit: J. Wok).

$$S \propto \nu^{+\alpha},$$

where $\alpha = \frac{1-a}{2}$ denotes the spectral index.

1.2.3 Inverse Compton Scattering

Compton scattering is important in astronomical processes. Seed photons with wavelength λ interact with electrons, and photons with wavelength λ' are produced (see Figure 1.6). If $\lambda' > \lambda$, photons are scattered to higher energy, this is so-called inverse Compton (IC) scattering. IC scattering is believed to be a major mechanism taken place in relativistic flows. High-energy emission of AGN are non-thermal, and IC is a major mechanism to generate X-ray, γ -ray, and TeV photons.

For a single electron, the Poynting flux of a plane wave incident on the electron is

$$S = \frac{c}{4\pi} |E|^2,$$

and the scattered radiation of the electron has a power of

$$P = |S| \sigma_{\text{T}} = \sigma_{\text{T}} c U_{\text{rad}},$$

where $U_{\text{rad}} = |\mathbf{S}|/c$, the energy density of the incident wave. Now if we consider scattering by a relativistic electron, the equation in the local frame of the electron is

$$P' = \sigma_{\text{T}} c U_{\text{rad}}.$$

It can be shown that the total power in the radiation field after IC scattering is

$$P = \frac{4}{3} \sigma_{\text{T}} c U_{\text{rad}} \left(\gamma^2 - \frac{1}{4} \right),$$

thus the net power added due to IC scattering is

$$P_{\text{IC}} = \frac{4}{3} \sigma_{\text{T}} c U_{\text{rad}} \left(\gamma^2 - \frac{1}{4} \right) - \sigma_{\text{T}} c U_{\text{rad}} = \frac{4}{3} \sigma_{\text{T}} c \beta^2 \gamma^2 U_{\text{rad}}.$$

The power of synchrotron field is

$$P_{\text{sync}} = \frac{4}{3} \sigma_{\text{T}} c \beta^2 \gamma^2 U_{\text{B}}.$$

The relation of the power of IC and synchrotron is

$$\frac{P_{\text{IC}}}{P_{\text{sync}}} = \frac{U_{\text{rad}}}{U_{\text{B}}}.$$

Therefore, the power of IC scattering depends only on the photon field of the synchrotron region U_{rad} , and the magnetic field energy density U_{B} . It can be shown that, when $\beta \rightarrow 1$, the maximum frequency of the IC scattering radiation is

$$\frac{\nu}{\nu_0} \approx 4\gamma^2.$$

According to different sources of seed photons, there are several typical processes at work in AGN systems. **Synchrotron self-Compton (SSC)** emission refers to that synchrotron photons are up-scattered by the group of relativistic electrons which produce them. Usually this happens in relativistic jets, where strong synchrotron radiation is observed, and relativistic electrons move along jets. In the case of SSC, the IC mechanism cools relativistic electrons efficiently when the brightness temperature exceeds 10^{12} K, which is the upper-limit indicator of the SSC mechanism. Readhead (1994) derived a lower-limit of brightness temperature $T_{\text{b}} \sim 10^{11}$ using the equipartition method. In the case of **external radiation Compton (ERC)**, seed photons can come from various sources, such as a molecular torus, an accretion disk, and emission-line clouds.

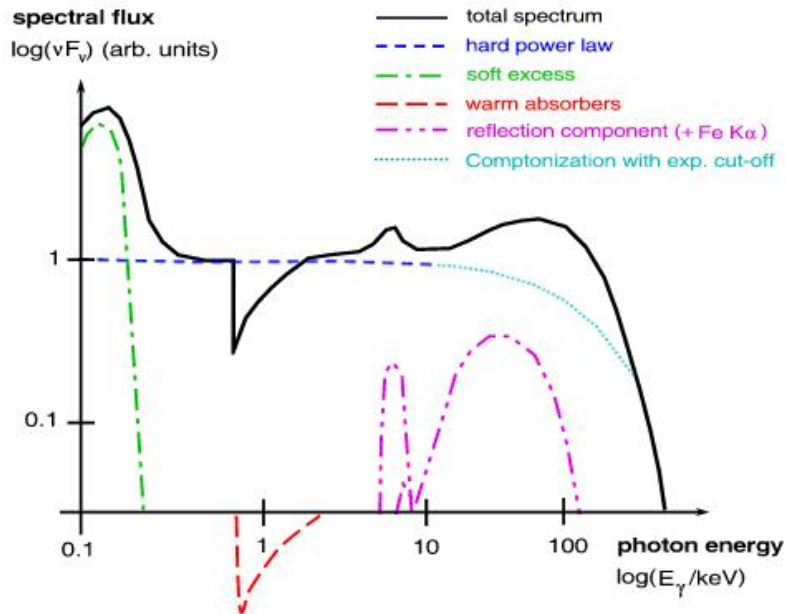


Figure 1.7: X-ray spectrum of a type-1 AGN (Müller and Camenzind 2004).

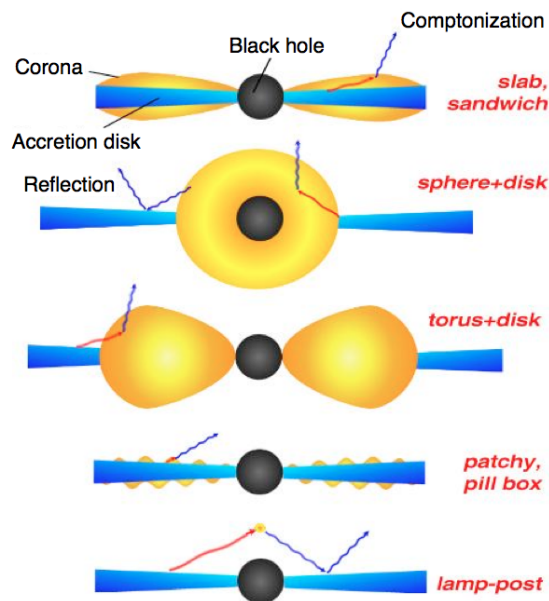


Figure 1.8: Different schemes of coronal distribution in the nucleus region of AGN. The red path represents the trajectory of seed photons from blackbody accretion disk, and the blue path represents the IC photons which are observed in X-ray spectra. (Image source: http://www.wissenschaft-online.de/astrowissen/lexdt_k05.html)

1.2.4 X-ray Emission of AGN

The observed X-ray properties of AGN are different based on their viewing angles. For radio-quiet AGN, we can see the X-ray emission coming from the accretion disk and the dusty torus. For radio-loud AGN, the IC up-scattered X-ray emission from relativistic jets dominates the spectrum. In the following paragraphs, I will discuss about the X-ray emission mechanisms observed in AGN.

Radio-quiet AGN

Figure 1.7 illustrates the X-ray spectrum of a radio-quiet AGN (Müller and Camenzind 2004), in which one peers directly into the central region of the AGN nucleus. As shown, the spectrum is dominated by a continuum emission produced by the IC process. Below 1 keV, there is a soft excess emission. Around 1 keV, there is an absorption dip originated from warm absorbers surrounding the black hole. We see the reflection component from the accretion disk at higher energy. The origin of the power-law profile of the spectrum is believed to be the IC of seed photons from blackbody accretion disk by hot electrons (in corona, temperature ~ 200 keV) above the surface of the accretion disk. Figure 1.8 illustrates different models of this scheme. The corona could be distributed above the accretion disk (sandwich) or around the black hole (sphere+disk); it can be torus-like next to the black hole (torus+disk), or spread unevenly above the black hole (patchy); its morphology can appear as clumps above the black hole (lamp-post). Usually one sees those features of X-ray spectra in objects like Seyfert 1 galaxies, broadline radio galaxies, and type-1 quasars. The X-ray studies of radio-quiet AGN can probe the structure in the vicinity of black holes.

Radio-loud AGN

Unlike radio-quiet AGN, the X-ray emission in radio-loud AGN is dominated by synchrotron/IC processes from relativistic jets, especially for blazars. If an AGN is highly energetic, the X-ray emission can be generated from solely the synchrotron process in relativistic outflows (e.g., HBLs). The X-ray emission can also be generated by SSC or ERC mechanisms (see Section 1.2.3), depending on the surrounding environment of jets (see Section 1.4.2 for further discussions).

1.3 Very Long Baseline Interferometry

Very long baseline interferometry (VLBI) is one of the best techniques for studying extragalactic jets. With its parsec-scale resolution at cosmological distances, VLBI enables us to trace the ejection of bright features from the jet base. In this section, I will give a brief summary of the VLBI technique. For detailed information about radio interferometry and VLBI, please see Thompson (1999).

1.3.1 Fundamentals of Radio Interferometry

The resolving power of a telescope r is determined by the wavelength of incoming electromagnetic wave and the diameter of the telescope $r \propto \lambda/D$. The idea of VLBI is based on the principle of the Michelson interferometer, that is, to use two or multiple telescopes to observe a source, correlate the data collected by each telescope, and reconstruct the image of the source region by Fourier deconvolution. Figure 1.9 shows the principle of a double-slit interference and the VLBI technique. We learn from the Young's double slit experiment that the wavefront passing through the two slits generates Huygens waves that produce interference fringes. When the path difference is an integer number of the wavelength, we see constructive interference. By analogy, VLBI works with the same principle. As seen in Figure 1.9, the two radio telescopes work as two slits, and if we imagine the sky as the screen in the double slit experiment, regions which would cause constructive and destructive interference can be considered as stripes in the sky. If the source is bigger than the smallest spacing of the stripes, the source is unresolved, otherwise it is resolved. This can be seen as a contrast of the fringes, or "visibility". The larger the distance between two telescopes, the higher resolution the interferometer has.

The incoming wavefront from the source is collected by radio antennas, and the signals are transmitted through waveguides to the amplifier. The signals are then amplified and the intensities are detected by the receiver, producing voltage signals $V_1(t)$ and $V_2(t)$ at the backend of two antennas. The voltage signal is sent to a correlator for data correlation (see Figure 1.10). Before obtaining the voltage signal, one needs to correct for the geometrical delay τ_g , which is caused by the arrival time difference of the wavefront due to the geometric distribution of the two telescopes:

$$\tau_g = \frac{\mathbf{b} \cdot \mathbf{s}}{c},$$

where \mathbf{b} is the baseline vector, \mathbf{s} is the unit vector towards the source, and c is the speed of light. Note that τ_g changes slightly with time as the Earth rotates. When the corrected

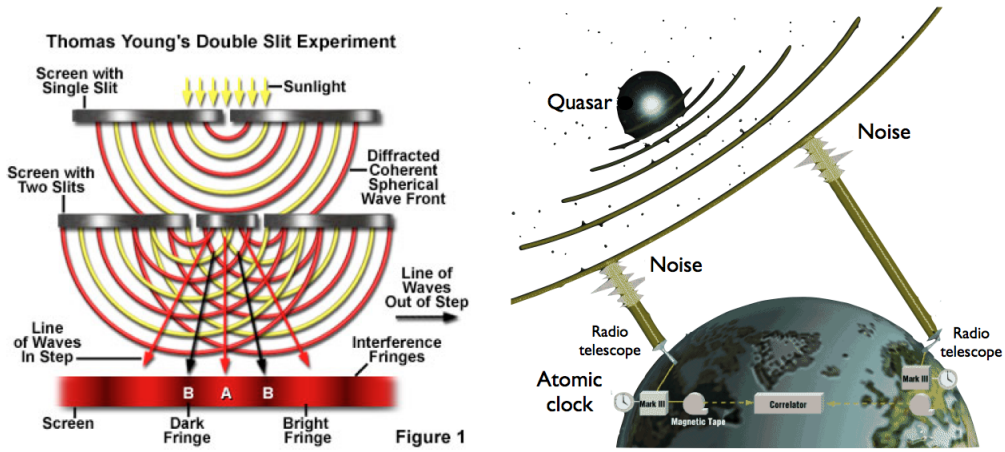


Figure 1.9: Analogy of double-slit interferometer and VLBI technique. The left panel shows the Young's double slit experiment, and the right panel is the global VLBI illustration. Image credit: left – M. J. Parry-Hill and M. W. Davidson; right – taken from <http://www.haystack.mit.edu/tech/vlbi/evlbi/index.html>.

voltage signal enters the correlator, where the signals are combined, it has a form like this

$$V_1 = v_1 \cos 2\pi\nu(t - \tau_g)$$

$$V_2 = v_2 \cos 2\pi\nu(t).$$

The output of the correlator is

$$r(\tau_g) = \langle V_1(t)V_2(t) \rangle = v_1 v_2 \cos 2\pi\nu\tau_g.$$

The correlator output is an oscillating signal representing the motion of the source through the interferometer fringe pattern on the sky. Next, we want to express the output by the integrated brightness over the sky. We use $I(\mathbf{s})$ to denote the brightness in the direction \mathbf{s} at frequency ν . The power of the signal from a small area of the source $d\Omega$ received in bandwidth $\Delta\nu$ can be expressed as $A(\mathbf{s})I(\mathbf{s})\Delta\nu d\Omega$, where $A(\mathbf{s})$ represents the sampling function of the antenna in the direction of \mathbf{s} . Combining those, one could express the correlator output as

$$dr = A(\mathbf{s})I(\mathbf{s})\Delta\nu \cos 2\pi\nu\tau_g d\Omega,$$

which leads to

$$r = \Delta\nu \int_S A(\mathbf{s})I(\mathbf{s}) \cos \left(\frac{2\pi\nu \mathbf{b} \cdot \mathbf{s}}{c} \right) d\Omega$$

for an extended source. Note that this relation is only valid when the source locates in the far field, from where the signal becomes a plane wave when it reaches the Earth. If a source is extended and resolved, the contributed incoming signal would be from a composition of slightly different directions, instead of one direction \mathbf{s} . To represent this scenario, we choose a direction towards the source as phase center \mathbf{s}_0 , and we define $\mathbf{s} = \mathbf{s}_0 + \boldsymbol{\sigma}$. Therefore

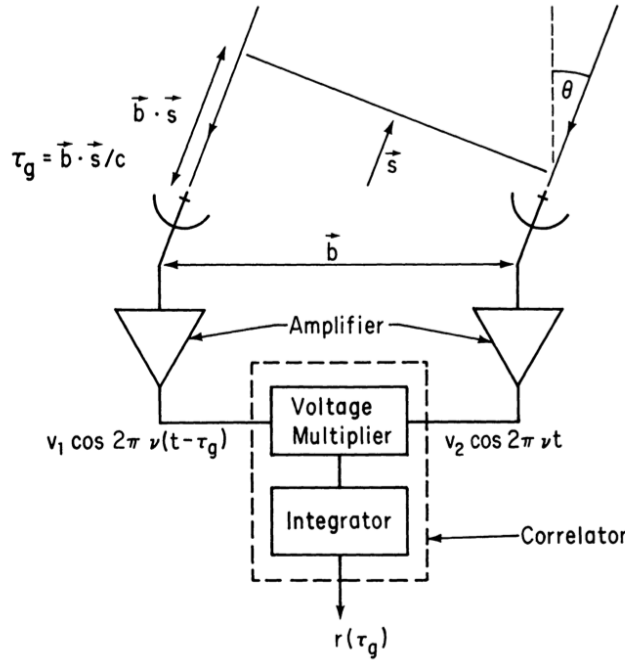


Figure 1.10: A simplified diagram of a two-antenna interferometer, image taken from Thompson (1999).

$$r = \Delta\nu \cos\left(\frac{2\pi\nu\mathbf{b}\cdot\mathbf{s}_0}{c}\right) \int_S A(\boldsymbol{\sigma})I(\boldsymbol{\sigma})\cos\left(\frac{2\pi\nu\mathbf{b}\cdot\boldsymbol{\sigma}}{c}\right) d\Omega$$

$$- \Delta\nu \sin\left(\frac{2\pi\nu\mathbf{b}\cdot\mathbf{s}_0}{c}\right) \int_S A(\boldsymbol{\sigma})I(\boldsymbol{\sigma})\sin\left(\frac{2\pi\nu\mathbf{b}\cdot\boldsymbol{\sigma}}{c}\right) d\Omega.$$

Next, we introduce the term visibility V :

$$V = |V|e^{i\phi_V} = \int_S A_n(\boldsymbol{\sigma})I(\boldsymbol{\sigma})e^{-\frac{2\pi\nu\mathbf{b}\cdot\boldsymbol{\sigma}}{c}},$$

where A_n is the normalized antenna reception pattern. As shown, visibility is a function of the source structure, the baseline length and the orientation of the interferometer. Each observation with two telescopes at a given time in an array measures one value of the visibility. Combining all measured visibilities, we could know the source brightness and reconstruct its structure. To express the exponential function of the visibility as a complex term:

$$e^{-i\left(\frac{2\pi\nu\mathbf{b}\cdot\boldsymbol{\sigma}}{c}\right)} = \cos\left(\frac{2\pi\nu\mathbf{b}\cdot\boldsymbol{\sigma}}{c}\right) - i \sin\left(\frac{2\pi\nu\mathbf{b}\cdot\boldsymbol{\sigma}}{c}\right).$$

If we separate the real and imaginary parts of visibility, we obtain

$$A_0|V|\cos\phi_V = \int_S A(\boldsymbol{\sigma})I(\boldsymbol{\sigma})\cos\left(\frac{2\pi\nu\mathbf{b}\cdot\boldsymbol{\sigma}}{c}\right) d\Omega$$

$$A_0|V|\sin\phi_V = - \int_S A(\boldsymbol{\sigma})I(\boldsymbol{\sigma})\sin\left(\frac{2\pi\nu\mathbf{b}\cdot\boldsymbol{\sigma}}{c}\right) d\Omega.$$

Substituting these equations into previous one, we get

$$r = A_0 \Delta \nu |V| \cos \left(\frac{2\pi \nu \mathbf{b} \cdot \mathbf{s}_0}{c} - \phi_V \right).$$

As shown, one can obtain the amplitude and phase of the visibility after data calibration. Once this is known, we apply synthesis imaging method to reconstruct the sky brightness of the source region (see Briggs et al. 1999).

1.3.2 Synthesis Imaging

To reconstruct the image of the source region, we need to measure $|V|$ and ϕ_V with different baselines. We express the distribution of baseline coverage in terms of a two-dimensional (u, v) plane, which has a east-west/north-south coordinate. The measured visibility is a function of u and v , because different positions on the (u, v) plane measures different part of the sources with different orientations. To obtain a good image, the sampling of the (u, v) plane has to be frequent enough to be able to perform Fourier transform between the visibility plane $V(u, v)$ and the image plane $I(l, m)$ taking into account the primary beam pattern $A(l, m)$, where l and m denotes the coordinates of the observed projected sky. The relation of the visibility plane and the sky plane can be expressed as:

$$A(l, m)I(l, m) = \iint_{-\infty}^{\infty} V(u, v) e^{2\pi i(ul+vm)} du dv,$$

which is a two-dimensional Fourier transform. Using Fourier deconvolution methods, one could produce maps of sky brightness.

1.4 The Study of Blazars

In this section, we will introduce the emission properties and parsec-scale jet study of blazars, as well as the current astronomy facilities that are often used in AGN research.

1.4.1 The Emission of Blazars

So far we have introduced the unified model and emission mechanisms involved in AGN. To relate observational properties and the actual structures of AGN, I will discuss the emitting regions at different bands in this section. Based on current knowledge, we can illustrate the structure of AGN and the emitting regions at different wavebands in Figure 1.11, which shows the scales of structures like SMBH, accretion disk, dusty torus, relativistic jet (confined by a helical magnetic field), as well as the broad and narrow line regions.

Radio Radio emission mainly generates from the relativistic outflows originated nearby the SMBH. Hot plasma flows along the jet, in which charged particle interacts with magnetic field and produce synchrotron radiation. Typically, the scale of radio jets in AGN are observed at scales from pc to kpc. Usually we see one-sided radio jets due to Doppler boosting effect, which amplifies the jet approaching towards the observer. From VLBI

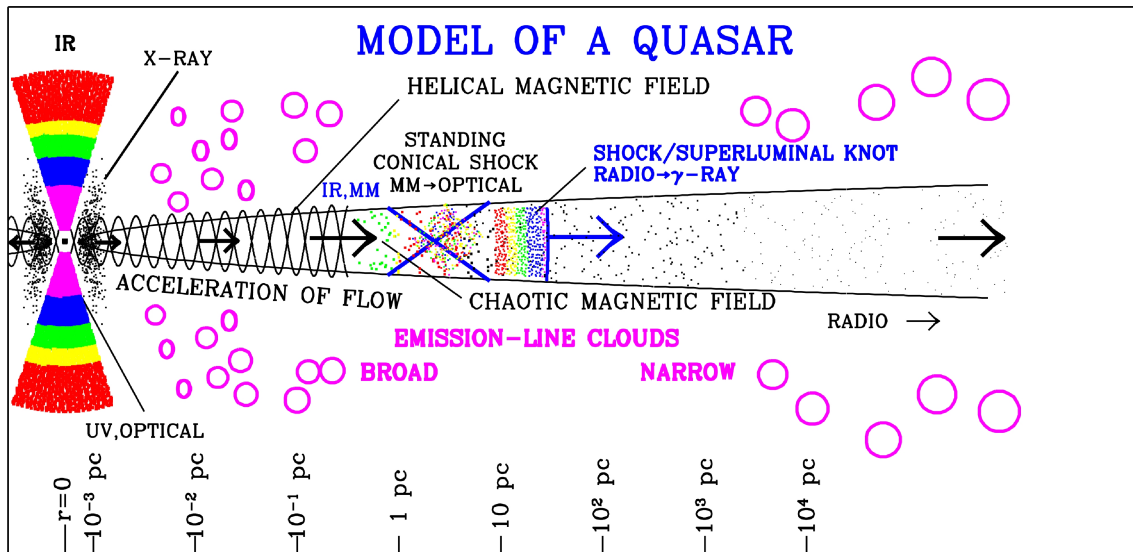


Figure 1.11: Illustration of the structure of AGN and the locations correspond to different bands of emission (Image credit: A. Marscher).

observations (see Section 1.3), even superluminal knots along radio jets with apparent speed up to $50c$ are detected (Lister et al. 2009b).

Infrared In radio-loud AGN, such as blazars, infrared emission is mainly dominated by non-thermal synchrotron process. For radio-quiet AGN, the emission from the near-infrared through sub-millimeter bands correspond to thermal dust emission close to the nucleus region (Sanders 1999).

Optical and Ultra Violet The jet synchrotron process extends to the optical and UV bands. The accretion disk surrounding the nucleus is also expected to peak at the UV-optical band, and this corresponds to thermal emission. Optical and UV thermal photons from accretion disk might serve as seed photons and be upscattered to higher-energy photons, such as X-rays (see Section 1.2.4)

X-rays In blazars, X-rays can be generated in shocks and superluminal knots in jets by the IC process. As mentioned in previous paragraph, X-ray photons can be produced by ERC process, in which the seed photons are from the accretion disk and upscattered by obscuring torus in surrounding environment.

γ -rays through TeV Due to the resolution limitation in very-high-energy (VHE) observatories, it is not possible to locate γ -ray and TeV emission in AGN. In current theoretical models, it is believed that VHE photons can be generated from shocks in relativistic jets (Dermer and Schlickeiser 1993, 1994), and one of the mechanisms is through synchrotron process (leptonic). Other possible scenarios include proton-proton process (hadronic), and leptonic-hadronic, etc.

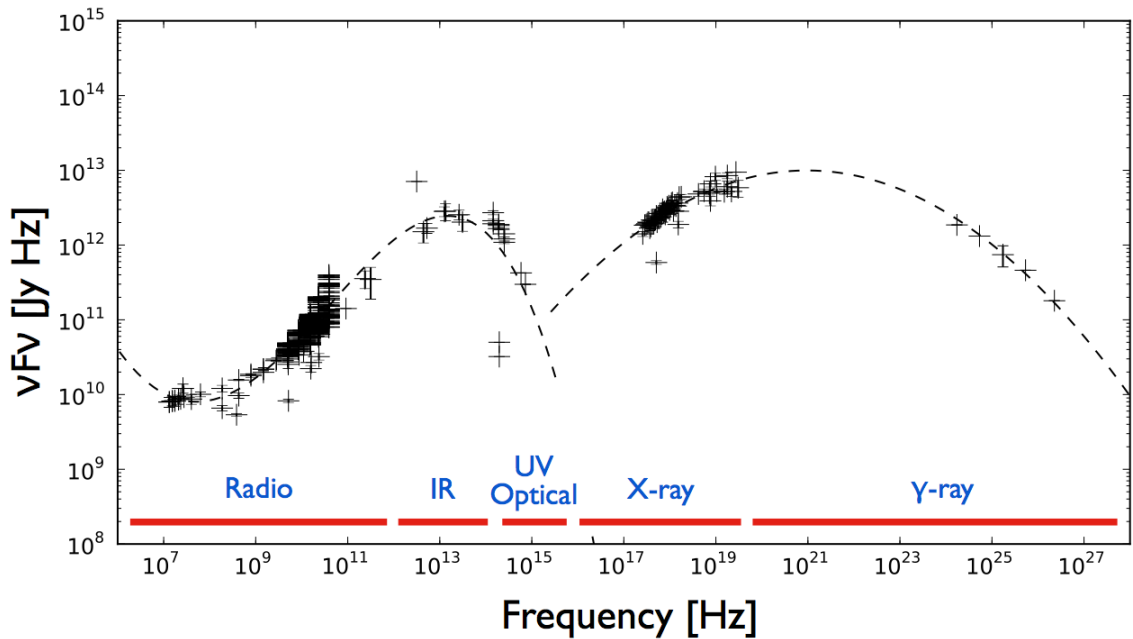


Figure 1.12: The broadband SED of the broad-line FR II radio galaxy 3C 111 (see Chapter 4; Chang et al. in preparation). At the bottom of the figure, red bars mark the range of different band of emission in Hz.

1.4.2 The Spectral Energy Distribution of Blazars

Typically, the broadband SED of blazars have a double-hump profile spanning from radio to VHE band (e.g., Dermer and Schlickeiser 1993), as shown in Figure 1.12. The double-peak shape of blazar broadband SED can be explained by current models of non-thermal emission. As illustrated in Figure 1.13, the lower energy hump can be modeled by synchrotron emission from blazar jets, and depending on the energy output of the jet, the emission could cover from radio to UV/X-rays. As for the higher energy hump, there are several possible mechanisms which can generate high energy photons: SSC (Jones et al. 1974, Ghisellini and Maraschi 1989), ERC (Sikora et al. 1994, Dermer and Schlickeiser 2002). In the SSC scheme, IC seed photons are produced locally as the same group of synchrotron photons in blazar jets. In the ERC scheme, seed photons can come from several sources such as a molecular torus (Błażejowski et al. 2000), an accretion disk (Dermer and Schlickeiser 1993), and emission-line clouds (Sikora et al. 1994). Moreover, the seed photons produced by local synchrotron emission may be scattered by nearby clouds surrounding the jet and enter the IC region again (mirror Compton; Ghisellini and Madau 1996).

The physical processes involved in the SED study are complex, and the fact that we cannot distinguish different emission regions from a target source makes broadband SED modeling challenging. For example, the SED study of 48 *Fermi* bright blazars (Abdo et al. 2010a) shows that a homogeneous one-zone model with SSC mechanism cannot explain most of their results, and more complex models involving external Compton radiation or multiple SSC components are needed to model the blazar SEDs. One of the main problems of modeling broadband SED is to reproduce the radio emission. Current available SED models are able to fit the high energy band well, however, the synchrotron emis-

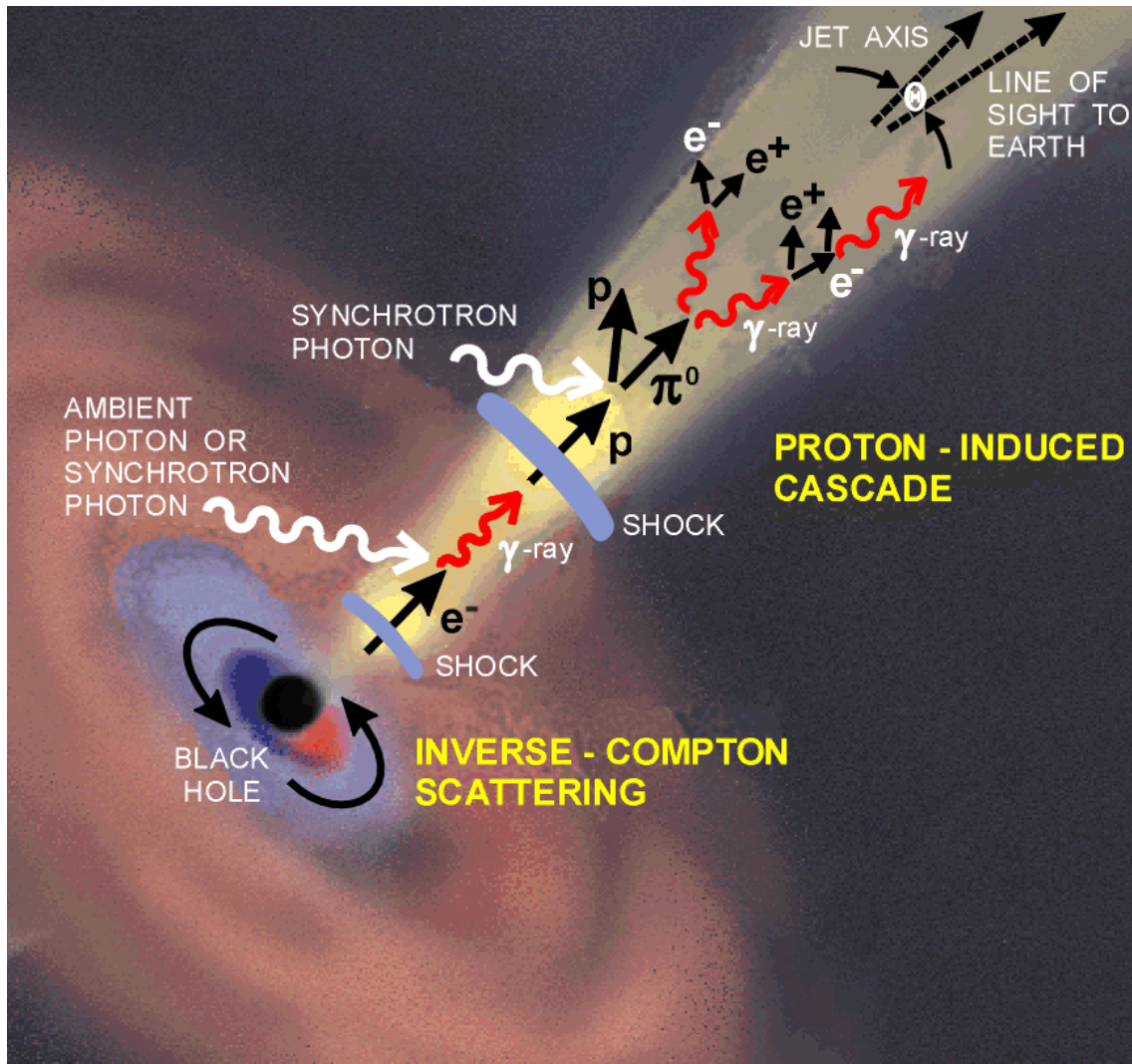


Figure 1.13: Artistic illustration of the emission mechanisms in AGN jet (image source: <http://www.mpifr-bonn.mpg.de/bonn04/>).

sion from the radio jet in AGN is usually underestimated (e.g., Finke and Dermer 2010, and Abdo et al. 2010d). The radio emission is believed to be generated via synchrotron process in the extended jet region, yet in the SED models, the high energy emission is reconstructed from a rather compact region, which cannot reproduce the radio emission well.

1.4.3 Parsec-scale Jets: Intrinsic and Observed Properties

In AGN studies, it is important to be aware of what are the intrinsic parameters of AGN and what are the observed ones. The main indicators of jet flow are the intrinsic Lorentz factor ($\gamma = (1 - \beta^2)^{1/2}$, where β is the speed of relativistic flow in the unit of c), the intrinsic luminosity L_0 , and the intrinsic brightness temperature T_0 . However, in real life we can only observe the apparent jet speeds β_{app} , luminosities L_{app} , and brightness temperatures T_{app} which are dependent on parameters like the Doppler factor δ , the Lorentz

factor γ , and the jet viewing angle θ w.r.t observer. β_{app} , L_{app} , T_{app} and δ can be derived from γ , θ , and L_0 . Here I list the relations between the parameters:

$$\begin{aligned}\beta_{\text{app}} &= \frac{\beta \sin \theta}{1 - \beta \cos \theta}, \\ L_{\text{app}} &= L_0 \delta^n, \\ \delta &= \gamma^{-1} (1 - \beta \cos \theta)^{-1}, \\ T_{\text{app}} &= \delta T_0, \\ \gamma &= (1 - \beta^2)^{-1/2},\end{aligned}$$

where n depends on the geometry and spectral index. Typically, mathematical n needed is in the range between 2 and 3, depending on the geometry and spectral index of jet. Very often the apparent speeds of AGN jet β_{app} can appear to be superluminal, which is due to the illusion caused by viewing effect (Rees 1966). Currently, the observed apparent projected speeds of AGN can be up to $\sim 60 c$ (e.g., Lister et al. 2009b).

1.4.4 The AGN Study in This Thesis

In the following Chapters, we will present our studies of AGN with different approaches. In Chapter 2, we study a bright feature in the powerful jet of the radio galaxy M 87 with the VBI technique. In Chapter 3, we study a multiband flare of the Southern blazar PKS 2052–47 by performing multiwavelength observations. In Chapter 4, we study the emission properties of a statistically-complete radio-selected blazar sample by constructing a broadband SED catalog of the 135 sources. The study of AGN in this thesis covers the whole electromagnetic spectrum, and we used ground base telescopes, radio interferometric arrays, as well as space observatories to perform our study. Table 1.1 lists current astronomical facilities that are in operation which are often used in AGN studies, and we marked the facilities that were used to perform the study in this thesis. We hope our efforts will push us a step forward in understanding the physical mechanisms of AGN jets.

Table 1.1: Current observatories in operation that are used in AGN studies.

Facility	Band	Observing range	Operation time	Location
Arecibo 300 m	Radio	300 MHz – 10 GHz	1963	Puerto Rico
*UMRAO 26 m	Radio	4.8, 8, 14.5 GHz	1958	Michigan, USA
*CHI ^a	Radio/array	6.6 GHz		Australia
EVN	Radio/VLBI	1.6 – 22 GHz	1980	Europe
*LBA ^a	Radio/VLBI	8.4 & 22 GHz	-	Australia/South Africa
MERLIN	Radio/array	151 MHz – 24 GHz	1980	The United Kingdom
*VLBA	Radio/VLBI	0.3 – 43 GHz	1993	USA
VLA	Radio/array	1 – 50 GHz	1980	New Mexico, USA
*Effelsberg 100 m	Radio	408 MHz – 86 GHz	1972	NRW, Germany
GBT 100 m	Radio	290 MHz – 90 GHz	2000	Virginia, USA
IRAM-PdBI	Radio/array	100 GHz	1988	Grenoble, France
*APEX	Radio	345 GHz	2007	Atacama, Chile
*IRAM 30 m	Radio	100 – 380 GHz	1984	Pico Veleta, Spain
ALMA	Radio	84 – 720 GHz	2011	Atacama, Chile
<i>Planck</i>	Microwave	30 – 70, 100 – 857 GHz	2009	Space observatory
<i>Herschel</i>	Far-infrared	60 – 670 μ m	2009	Space observatory
<i>HST</i>	Optical/UV/IR		1990	Space observatory
* <i>Swift</i> /UVOT	Optical	170 – 650 nm	2004	Space observatory
* <i>Swift</i> /XRT	X-ray	0.2 – 10 keV	2004	Space observatory
* <i>Swift</i> /BAT	Hard X-ray	15 – 150 keV	2004	Space observatory
<i>Chandra</i>	X-ray	0.1 – 10 keV	1999	Space observatory
<i>XMM-Newton</i> /EPIC	X-ray	0.2 – 12 keV	1999	Space observatory
<i>RXTE</i>	X-ray	1.5 – 250 keV	1995	Space observatory
<i>Suzaku</i>	X- to γ -ray	0.3 – 600 keV	2005	Space observatory
<i>INTEGRAL</i> /IBIS	Hard X-ray	15 keV – 1 MeV	2002	Space observatory
<i>INTEGRAL</i> /SPI	Hard X-ray	20 keV – 8 MeV	2002	Space observatory
<i>CGRO</i> /EGRET	γ -ray	20 MeV – 30 GeV	1991	Space observatory
* <i>Fermi</i> /LAT	γ -ray	30 MeV – 300 GeV	2008	Space observatory
HESS	γ -ray	100 GeV – TeV	2003	Namibia

* Relevant to this thesis.

^a The TANAMI project; see Section 3.2.

2 A multi-band flare of the HST-1 feature in the M 87 jet

As mentioned in the previous chapter, the VLBI technique allows us to trace motions in AGN outflows with very high resolution. Thus, it becomes a powerful tool that can be used for probing outburst events in parsec scale jets of AGN. In this chapter, we use the VLBI wide-field imaging technique to investigate a bright flaring feature HST-1 in the jet of the radio galaxy M 87. This multi-band flare in 2005 caught the attention of the community mainly for its possible relation with a TeV flare from M 87 observed around the same time. By applying wide-field imaging to the VLBA 2 cm Survey/MOJAVE data from 2000 to 2009, we imaged the HST-1 region with the highest resolution ever obtained. We examined the VLBI properties of HST-1, and compared with other bands. This chapter describes the details of this work, which has been published in A&A 515, 328 (2010).

2.1 Introduction

One of the most studied AGN is M 87 (also known as Virgo A), a nearby elliptical galaxy located in the Virgo cluster. It hosts a very powerful one-sided jet emerging from the central region, and was also the first extragalactic jet to be discovered (Curtis 1918). The synchrotron-emitting nature of the M 87 jet was suggested by Baade (1956). Observations show that M 87 contains $2.4 \times 10^9 M_{\odot}$ within a $0.25''$ radius (Sargent et al. 1978, Young et al. 1978), which suggests the presence of a SMBH in its nucleus (Harms et al. 1994). Due to its proximity (16.4 Mpc, $z=0.00436$, $1 \text{ mas} = 0.08 \text{ pc}$, $1 \text{ mas yr}^{-1} = 0.26 c$, Jordán et al. 2005), M 87 is an ideal candidate for studying AGN phenomena, and has been monitored at many different wavelengths over the last several decades. In the observed one-sided jet of M 87 (Shklovsky 1964), superluminal motion was reported from *Hubble Space Telescope* (HST) observations within the innermost $6''$ of the jet with apparent speeds of $4 c$ to $6 c$ (Biretta et al. 1999). Discrepant speeds were reported from VLBA observations at 7 mm with values between $0.25 c$ to $0.4 c$ (Ly et al. 2007), and a value of $2 c$ or even larger (Acciari et al. 2009). VLBA $\lambda 2 \text{ cm}$ observations showed apparent speeds $< 0.05 c$ from 1994 to 2007 (Kovalev et al. 2007, Lister et al. 2009b). Therefore, the kinematical properties of the jet in M 87 remain an important topic of discussion.

In 1999 HST observations revealed a bright knot in the jet located $1''$ (projected distance of 0.08 kpc) away from the core. This feature, named HST-1, is active in the radio, optical, and X-ray regimes. VLBA $\lambda 20 \text{ cm}$ observations showed that HST-1 has sub-structure and appears to contain superluminal components moving at speeds up to $4 c$

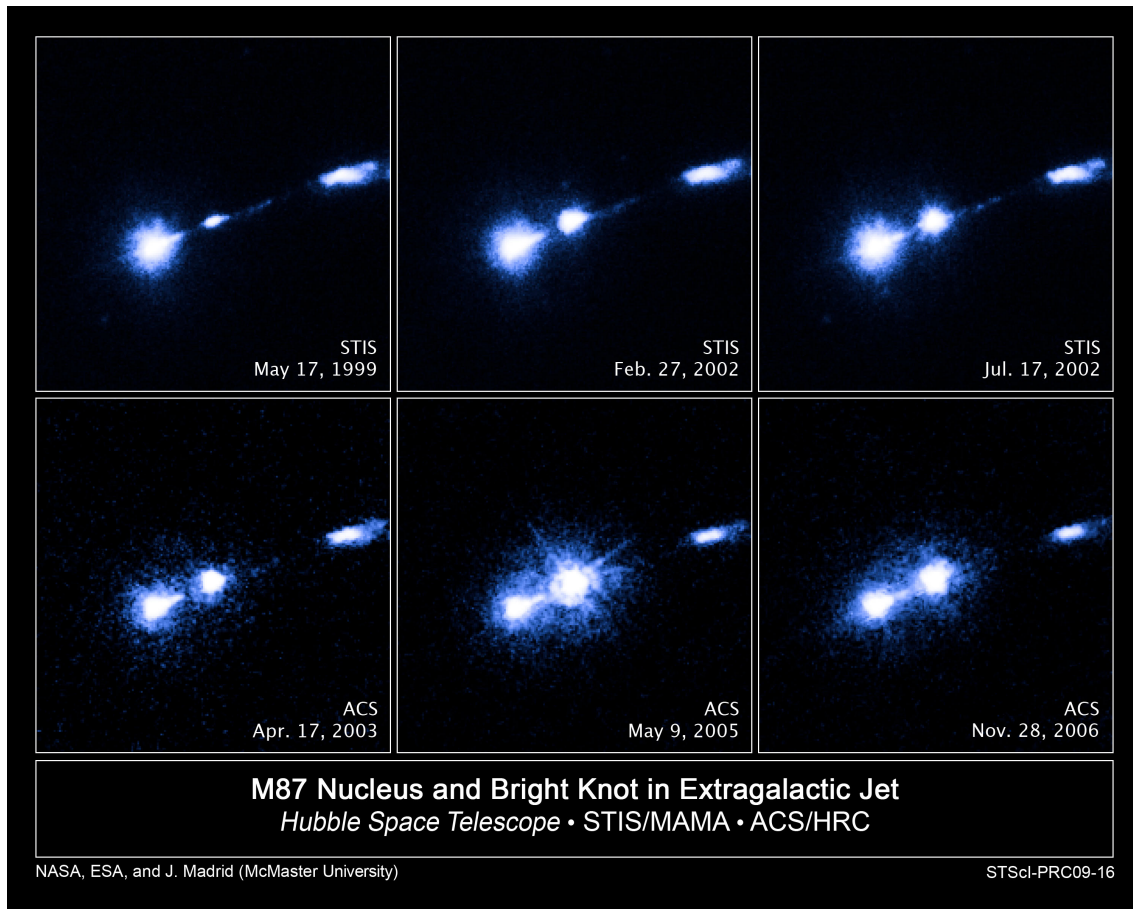


Figure 2.1: The 2005 outburst of HST-1 observed by *HST* in the near-UV band. Image credit: NASA, ESA, and J. Madrid (McMaster University).

(Cheung et al. 2007). These observations suggest that HST-1 is a collimated shock in the AGN jet. Furthermore, recent multi-wavelength observations were used to show that HST-1 could be related to the origin of the TeV emission observed in M 87 in 2005 by the HESS telescope (Aharonian et al. 2006). Comparing data taken in the soft X-rays (*Chandra*), near ultraviolet by Madrid (2009), and VLA $\lambda 2$ cm observations (Cheung et al. 2007, Harris et al. 2006), the light curves of HST-1 reached a maximum in 2005, while the resolved core showed no correlation with the TeV flare (see Figure 2.1 and 2.2). Therefore, the TeV emission from M 87 was suggested to originate in HST-1 (Harris et al. 2008). Based on those findings, Harris et al. (2008) suggest that HST-1 has a blazar nature. However, Acciari et al. (2009) reported rapid TeV flares from M 87 in February 2008, which may have originated in the core, instead of HST-1, which remained in a low state during the flares in 2008. Recently, the *Fermi* Large Area Telescope (LAT) team reported the detection of M 87 at gamma-ray energies (Abdo et al. 2009c).

The AGN standard model considers the blazar behavior to originate at the vicinity of the SMBH. However, HST-1 is 80 pc away from the core. If the HST-1 blazar hypothesis is true, this would pose a challenge to current AGN models. In this chapter, we examine this hypothesis with $\lambda 2$ cm VLBI wide-field imaging of the HST-1 feature. In Section 2.2, I will introduce the Very Long Baseline Array (VLBA) in detail, and describe our VLBI

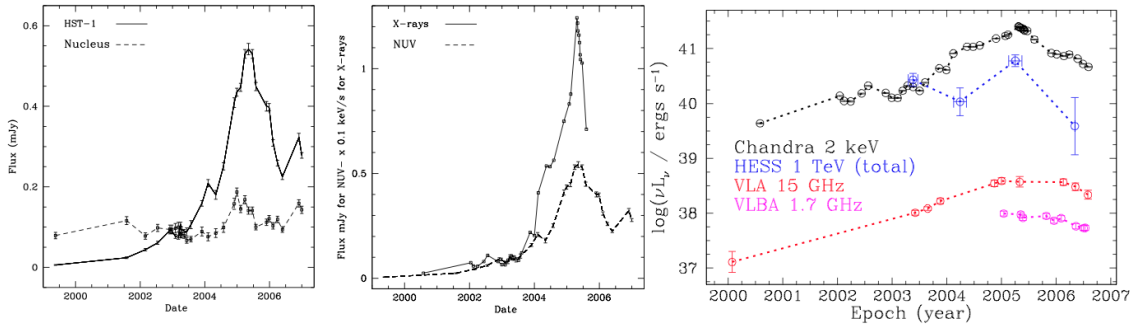


Figure 2.2: The light curves of HST-1 and M87 core. Left: NUV light curves of HST-1 and the M87 nucleus, center: NUV and X-ray light curves of HST-1 (Madrid 2009), and right: light curves of the TeV emission from M87 (Aharonian et al. 2006) and the X-ray and radio emission from HST-1 (Cheung et al. 2007).

observations and the corresponding data reduction. Next, I will present the results in Section 2.3, followed by a discussion in Section 2.4. Finally, I will give a short summary in Section 2.5. Throughout this chapter, we use the term “core” as the apparent origin of AGN jets that commonly appears as the brightest feature in VLBI radio images of blazars (Lobanov 1998, Marscher 2008). We use a cosmology with $\Omega_m = 0.27$, $\Omega_\Lambda = 0.73$, and $H_0 = 71 \text{ km s}^{-1} \text{ Mpc}^{-1}$ (Komatsu et al. 2009).

2.2 VLBI Observations and Data Analysis

2.2.1 Very Long Baseline Array

The Very Long Baseline Array (VLBA) consist of 10 stations, and each is a 25 m antenna of the same design. The construction began in February 1986, and finished in May 1993. The first light of the array was taken in May 29, 1993. In Figure 2.3, one can see the geometrical distribution of VLBA. The baseline lengths range from 236 km to 8611 km,

Table 2.1: List of VLBA stations and High-Sensitivity Array.

Antenna	Location	Latitude	Longitude
MK	Mauna Kea, Hawaii	19°48′04.97″ N	155°27′19.81″ W
BR	Brewster, Washington	48°07′52.42″ N	119°40′59.80″ W
OV	Owens Valley	37°13′53.95″ N	118°16′37.37″ W
KP	Kitt Peak	31°57′22.70″ N	111°36′44.72″ W
PT	Pie Town, New Mexico	34°18′03.61″ N	108°07′09.06″ W
VLA*	New Mexico	34°04′43.75″ N	107°37′05.91″ W
LA	Los Alamos, New Mexico	35°46′30.45″ N	106°14′44.15″ W
FD	Fort Davis, Texas	30°38′06.11″ N	103°56′41.34″ W
NL	North Liberty, Iowa	41°46′17.13″ N	91°34′26.88″ W
GBT*	Green Bank, West Virginia	38°25′59.24″ N	79°50′23.41″ W
HN	Hancock, New Hampshire	42°56′00.99″ N	71°59′11.69″ W
Arecibo*	Puerto Rico	18°20′36.60″ N	66°45′11.10″ W
SC	St. Croix, United States Virgin Islands	17°45′23.68″ N	64°35′01.07″ W
Effelsberg*	NRW, Germany	50°31′30.00″ N	6°53′00.30″ W

* Antenna added to VLBA to form the High-Sensitivity Array

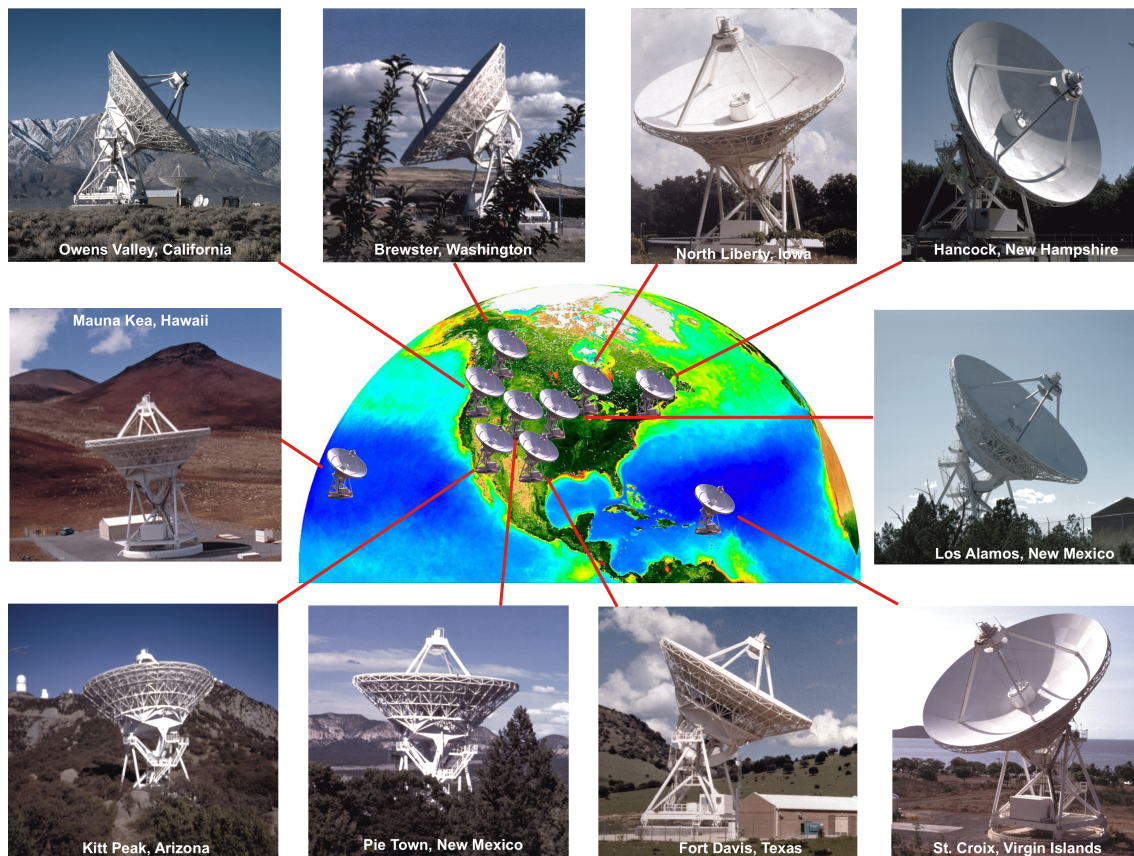


Figure 2.3: Sketch of the 10 VLBA antennas (Image credit: NRAO/AUI, SeaWiFSProject NASA/GSFC and ORBIMAGE).

providing excellent resolutions.

By adding the Arecibo 300 m dish, the Green Bank Telescope (GBT), the Very Large Array (VLA), and the Effelsberg 100 m telescope to the VLBA, the resulting interferometric network is called the High-Sensitivity Array, which provide higher sensitivity. In this study of M 87, three of the observing epochs in 2000 were obtained by VLBA plus one VLA antenna, which is part of the High-Sensitivity Array.

2.2.2 Observations and Data Analysis

M 87 has been monitored at $\lambda 2$ cm with the VLBA since 1994 by the 2 cm Survey/MOJAVE programs¹ (Kellermann et al. 2004, Lister et al. 2009a). We re-analyzed 12 epochs of data from these monitoring program obtained after late 2001, together with three observing sets of targeted observations on M 87 in 2000 (see Table 2.2). The 2 cm Survey/MOJAVE epochs from 2001 to 2009 were snapshot observations with a total integration time from 20 minutes to one hour, and were broken up into about six-minute-long scans in order to have a better (u, v) coverage; the three epochs in 2000 were full-track observations with eight-hour integration time and included a single VLA antenna (Y1).

The VLBA data were processed by following the standard procedures as described in

¹<http://www.physics.purdue.edu/MOJAVE/>

Table 2.2: Journal of VLBA $\lambda 2$ cm observations of M 87^a.

Epoch	Exp. Code	t_{int}^b [min]	N_{ant}	Beam ^c		$S_{\text{total}}^{\text{VLBA,M87}}$ [Jy]	$S_{\text{peak,A}}^{\text{M87}}$ [Jy beam ⁻¹]	$S_{\text{total}}^{\text{HST-1}}$ [mJy]	$S_{\text{peak,A}}^{\text{HST-1}}$ [mJy beam ⁻¹]	$S_{\text{peak,B}}^{\text{HST-1}}$ [mJy beam ⁻¹]	rms_A^d [$\mu\text{Jy beam}^{-1}$]	rms_B^d [$\mu\text{Jy beam}^{-1}$]
				size[mas]	ϕ [degree]							
2000.06	BK073A ^{e,i}	476	11	2.07×1.35	-7	2.26	1.24	<1.36	<0.26	<0.23	79	68
2000.35	BK073B ^{e,f}	476	11	1.88×1.31	-13	2.33	1.29	<1.42	<0.20	<0.21	70	71
2000.99	BK073C ^{e,f}	476	10 ^j	2.12×1.52	-3	2.46	1.33	<1.84	<0.25	<0.33	100	92
2001.99	BR077D ^{g,h}	68	10	1.74×1.09	-8	2.74	1.42	<5.24	<0.66	<0.70	212	262
2002.25	BR077J ^{g,h}	57	10	1.77×1.13	-6	2.54	1.40	<5.84	<0.80	<0.81	300	292
2003.09	BL111E ^g	54	10	1.85×1.30	-8	2.85	1.57	3.98	1.01	2.13	218	206
2004.61	BL111N ^g	63	10	1.88×1.16	-11	2.32	1.27	22.03	4.14	8.76	198	210
2004.92	BL111O ^g	64	10	1.95×1.23	-14	2.41	1.39	23.59	2.70	9.97	223	295
2005.30	BL123E ^g	63	9 ^k	2.06×1.37	-16	2.35	1.37	19.72	2.57	7.03	237	226
2005.85	BL123P ^g	63	10	2.11×1.25	-17	2.39	1.31	19.93	3.67	9.53	188	208
2006.45	BL137F ^g	22	10	1.85×1.22	-10	2.51	1.51	<6.96	<1.02	<1.44	295	348
2007.10	BL137N ^g	42	10	1.95×1.23	-13	2.67	1.53	10.49	1.14	2.94	201	255
2007.42	BL149AA ^g	45	10	1.78×1.25	-8	2.69	1.46	<7.70	<0.81	<1.13	272	385
2008.33	BL149AO ^e	41	9 ^j	1.77×1.10	-7	3.24	1.79	<3.22	<0.54	<0.75	193	161
2009.10	BL149BG ⁱ	50	9 ^l	2.25×1.52	-12	1.99	1.13	<5.26	<0.36	<0.49	223	263

^a Observations are in dual-polarization mode, except as indicated

^b Total scheduled VLBI on-source time

^c Beam A: natural weighting and tapering of Gaussian full-width half maximum 0.3 at 200 M λ

^d Root-mean-square image noise using natural weighting and tapering with a Gaussian factor of 0.3 at a radius of 200 M λ

^e Recording rate: 256 Mbit s⁻¹, 2 bits per sample

^f Dedicated full-track experiment on M 87 (see Kovalev et al. 2007); the array included a single VLA antenna (Y1)

^g Recording rate: 128 Mbit s⁻¹, 1 bit per sample

^h Single polarization hand (LL) observations only

ⁱ Recording rate: 512 Mbit s⁻¹, 2 bits per sample

^j Antenna NL missing

^k Antenna SC missing

^l Antenna HN missing

detail by Kovalev et al. (2007), Lister et al. (2009a). The data were fringe-fitted before the imaging process. The data from the MOJAVE project epochs after 2007.61 were processed using the pulse calibration signals to align the phases instead of fringe fitting, because the positions of the sources and the VLBA antennas are well determined (Petrov et al. 2008, 2009), and the station clocks are known to be stable. However, for our wide-field imaging purposes, fringe fitting was necessary for a better determination of the phase and rate across the observed band, and therefore to better image the extended jet of M 87. Moreover, it ensures the homogeneity of all the datasets.

In order to accurately image HST-1 with VLBI, there are two issues that need to be considered. First, HST-1 lies $\sim 800 \lambda 2$ cm beamwidths away from the brightest feature (the VLBA core). For this reason, time or frequency data averaging would produce time and bandwidth smearing in the HST-1 region. Second, based on earlier VLBA $\lambda 20$ cm and VLA $\lambda 2$ cm observations of HST-1 (Cheung et al. 2007), we expect the total 2 cm flux density to be at the milli-Jansky level, which is much weaker than the total flux density of the inner jet (~ 2.5 Jy). To detect HST-1, we need to image the inner jet region with its extended structure (over tens of milliarcseconds); otherwise, the sidelobes from the core would cover the HST-1 emission. To reach this goal, we applied natural weighting and (u, v) -tapering on the whole dataset.

First, we averaged the data 16-sec in time and averaged all channels in each IF in frequency, and obtained the inner jet initial model by applying phase and amplitude self-calibration using DIFMAP. The time-smearing effect of 16 seconds begins to be relevant at a distance of 200 mas from the field center, which is beyond the inner jet scale, and did not affect our data analysis at this stage. When the inner jet model was reasonably good, we applied the obtained CLEAN-components to the un-averaged data for the first

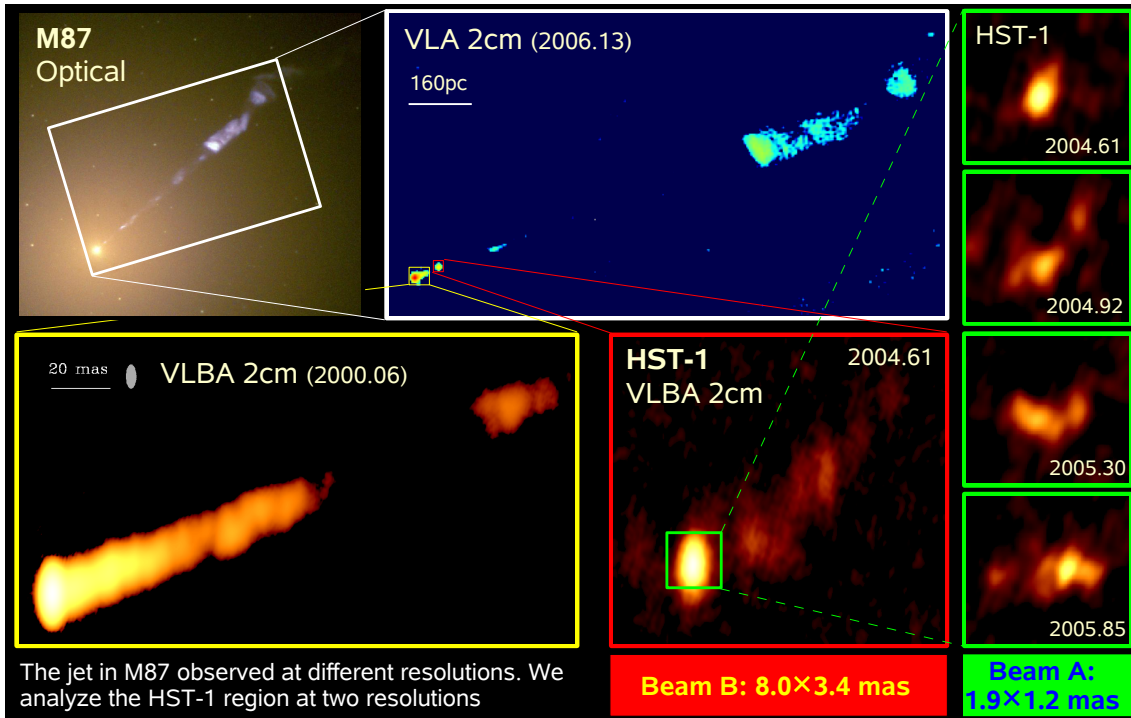


Figure 2.4: M 87 and HST-1 observed in different bands. This figure illustrates the size scale of M 87 and HST-1 observed in different wavelengths. The panels in yellow, red, and green show the results of our observations.

amplitude-and-phase self-calibration using AIPS. Natural weighting and tapering with a Gaussian factor of 0.3 at a radius of $200 M\lambda$ in the (u, v) -plane was applied to the whole dataset, and the resultant beam sizes are shown in Table 2.2. If we remove tapering and apply uniform weighting, the inner jet is better resolved but less flux density is recovered. In this case, the image noise level is too high to detect the HST-1 feature.

To better identify the extended component, and since full-resolution, uniform weighting imaging did not produce detections of this feature, we chose the approach of tapering and natural weighting. Furthermore, we downgraded the resolution to a larger beam size of 8×3.4 mas in P.A. 0° . This beam size was chosen specifically for comparison with the VLBA $\lambda 20$ cm observations of (Cheung et al. 2007). In the following Sections, we label the smaller beams as **beam A**, noting that the beam sizes are slightly different in each epoch. These are listed in Table 2.2. **Beam B** refers to the beam size of 8×3.4 mas. Figure 2.4 shows multi-band image of M 87 and HST-1, and illustrates the image scales of beam A and beam B.

2.3 Results

We completed the wide-field imaging of 15 epochs of M 87 VLBA $\lambda 2$ cm obtained between 2000 and 2009. Each epoch was imaged using beam A and beam B (see Section 2.2), and for each beam size, we applied two image cleaning fields, one for the M 87 inner jet region, and another for the HST-1 region, which was phase-shifted as -788.5 mas

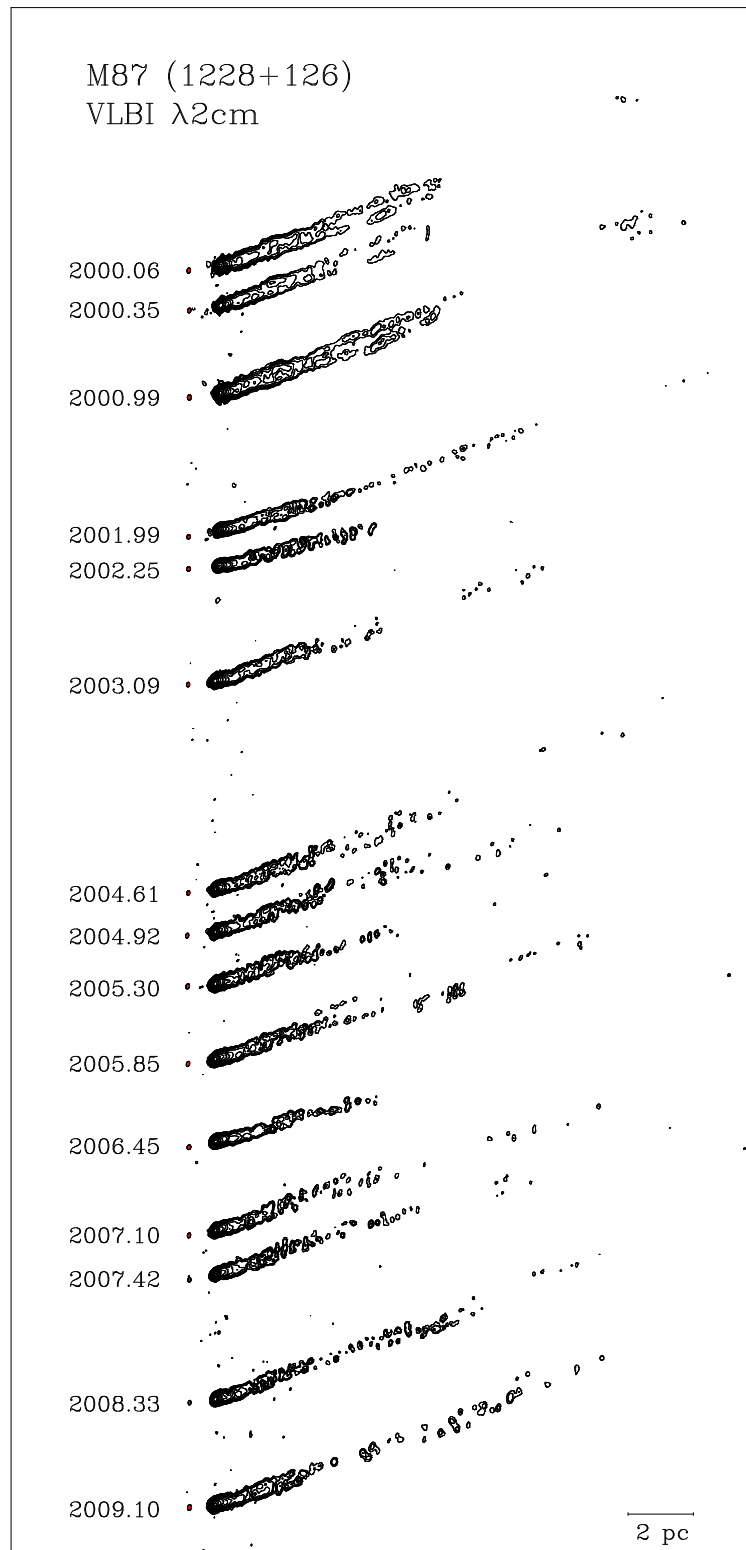


Figure 2.5: Images of the central 220 mas (17.6 pc in projection) of the M87 jet (beam A, resulting from a (u, v) -taper of Gaussian 0.3 at 200 M λ and natural weighting), spaced by their relative time intervals. The images are plotted with the same size scale. The contour levels all increase by factors of $\sqrt{2}$, and the lowest contours are (from 2000.06 to 2008.33): 0.5, 0.7, 0.5, 1.1, 1.3, 0.9, 0.9, 0.9, 0.9, 0.9, 1.1, 1.0, 1.2, 0.9, 0.9 mJy beam $^{-1}$, respectively. The restoring beams and brightness peak values are given in Table 2.2. 39

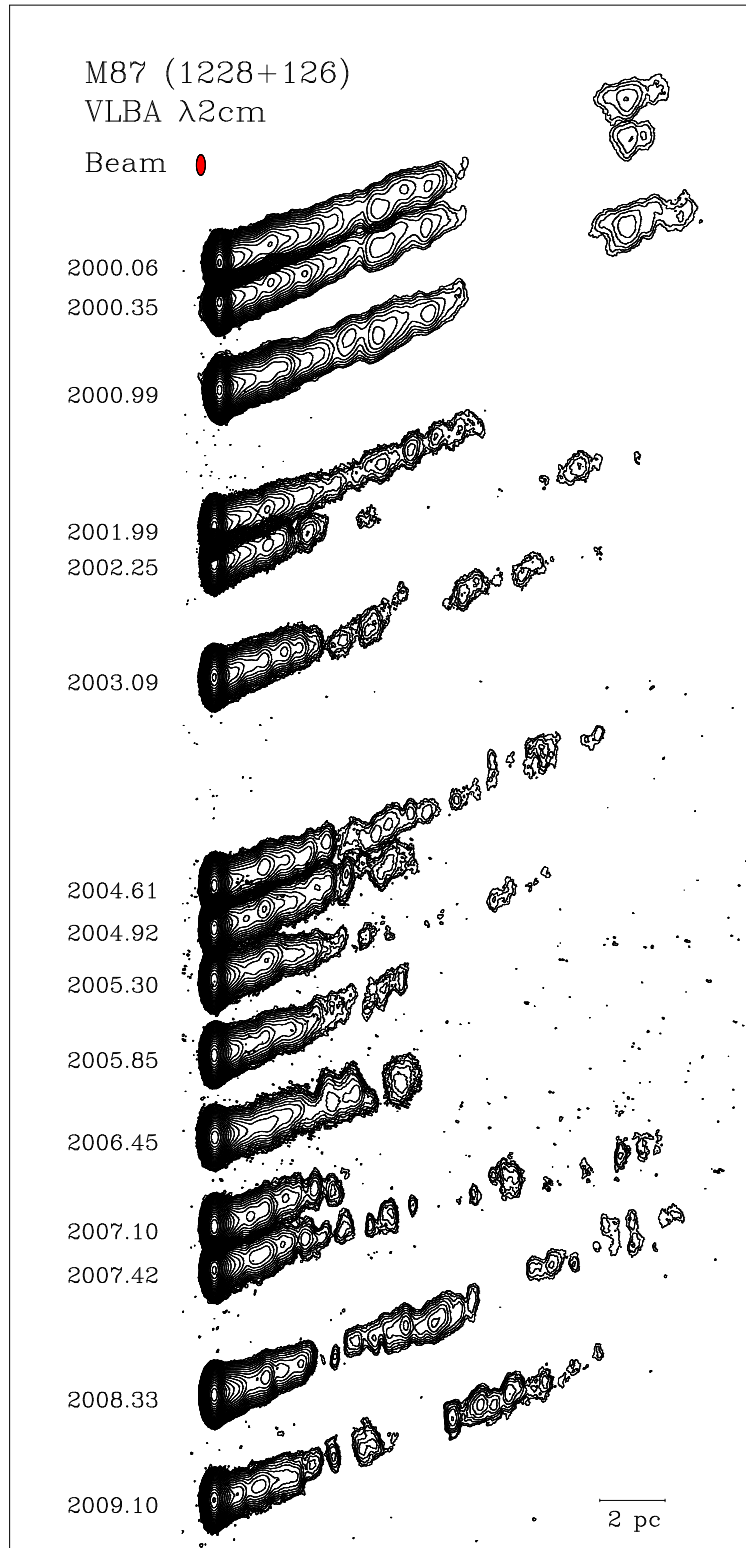


Figure 2.6: Downgraded resolution images of the central 220 mas of the M 87 jet with beam B (8×3.4 mas in P.A. 0°), spaced by their relative time intervals. The contour levels all increase by factors of $\sqrt{2}$, and the lowest contours are (from 2000.06 to 2008.33): 0.5, 0.7, 0.5, 1.1, 1.3, 0.9, 0.9, 0.9, 0.9, 0.9, 1.1, 1.0, 1.2, 0.9, 0.9 mJy beam^{-1} , respectively.

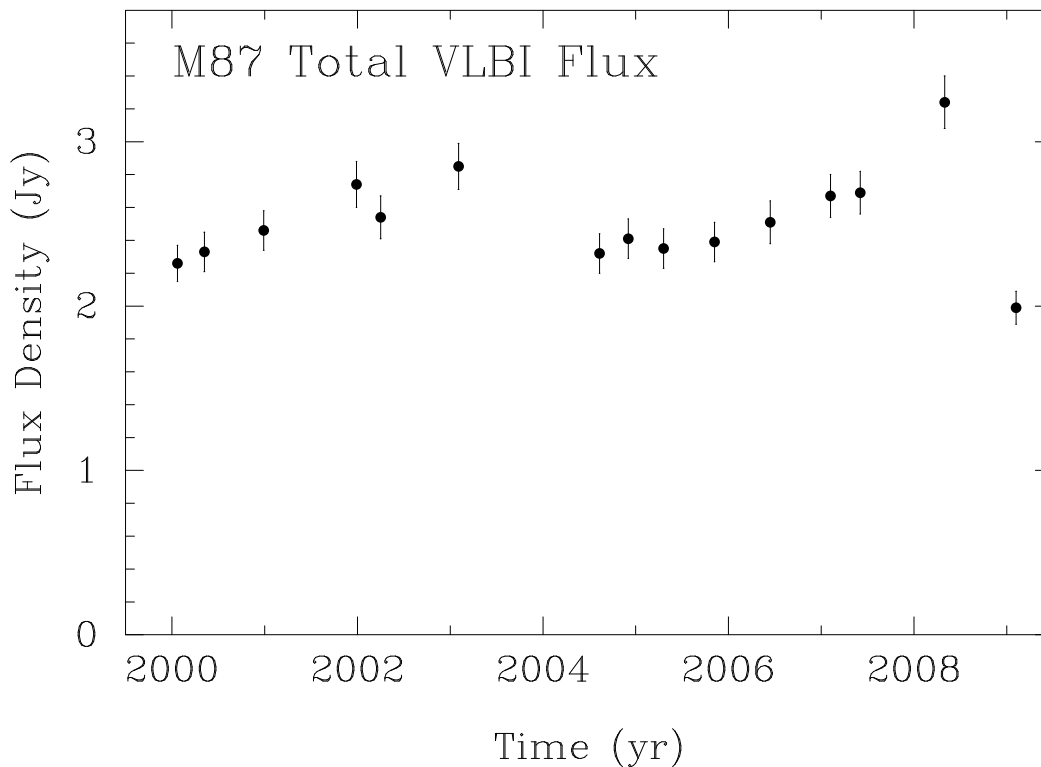


Figure 2.7: Total VLBA flux density of M87 at $\lambda 2$ cm versus time.

in right ascension and 348.9 mas in declination. We performed deep cleaning iterations until the image rms reached the expected thermal noise value. The rms values of the final images are listed in Table 2.2. Three epochs in the year 2000 are full-track observations with an on-source time of 476 minutes, and have the lowest rms.

2.3.1 Imaging of the inner jet of M 87

With tapering and natural weighting of the data, the extended inner jet was imaged over a region 100-200 mas in size, which varied according to the different sensitivity of each epoch. The inner jet images are shown in Figure 2.5 (beam A) and Figure 2.6 (beam B). The inner jet structure has an average total flux density of ~ 2.5 Jy, with overall flux density changes up to 1 Jy during 2000 to 2009, as shown in Figure 2.7. We estimate the error in flux densities to be 5%, based on the typical amplitude calibration accuracy of the VLBA (Kovalev et al. 2005 and Ulvestad and Wrobel 2009). In February 2008, multiple very high energy flares were detected by the multi-wavelength campaign of HESS, MAGIC, VERITAS; meanwhile, VLBA $\lambda 7$ mm observations detected a flare in the VLBA core simultaneously (Acciari et al. 2009, 2010). We have also seen the 2008 flare from the core in our VLBA $\lambda 2$ cm data, and therefore confirmed this result (see Figure 2.7).

The inner jet showed structural changes during the period of our observations. However, the study of the inner jet is beyond the scope of this thesis (see e.g., Kovalev et al. 2007, Walker et al. 2008, and Lister et al. 2009b for a detailed discussion of the structure

and kinematics of the inner jet).

2.3.2 Imaging of the HST-1 region

HST-1 was detected in six of the 15 epochs we analyzed from 2003 to early 2007 (detection limit: 5σ). As discussed in Section 2.4, this feature was too faint in most epochs, and the image noise was too high to allow us to detect it. Figure 2.8 shows hybrid maps of this region. The HST-1 images produced using beam A show that the brightest component has a size of ~ 10 mas down to the lowest contours, while the images produced using beam B reveal an extended structure ~ 50 mas in size, which is comparable with VLBA $\lambda 20$ cm observations (Cheung et al. 2007). We estimated the total flux density of HST-1 by summing all the clean components of the final image in the HST-1 region. We obtained the maximum surface brightness of HST-1 by using the task `IMSTAT` in AIPS. The feature has a total flux density that varies between 4 and 24 mJy (Figure 2.9). The peak surface brightness varies from 1 to 4 mJy beam $^{-1}$ (beam A) and 2 to 10 mJy beam $^{-1}$ (beam B), as shown in Figure 2.10. Epochs which have no detection are marked as upper limits (inverted triangles) in Figs. 2.9 and 2.10.

In 2003.09, HST-1 is marginally detected with both beam sizes; the brightness peak is ~ 1 mJy beam $^{-1}$, and the total flux density is 3.7 mJy. During 2004.61–2005.85, 4 epochs show significant detections of HST-1 with beam A and beam B, where the peak component remains dominant, and the total flux density fluctuation is $\sim 30\%$. In 2007, the structure of HST-1 becomes more extended and complex, reaching a total flux density of 10 mJy and developing two distinct peaks (peak **a** and peak **b** in Figure 2.8).

For the epochs with no detections, we derived an upper limit on the total VLBI flux density of HST-1. These were estimated based on the rms noise values of each epoch. The maximum amount of flux density hidden below the noise would be the rms value times the size of the HST-1 emission region (in units of beam size). Based on our HST-1 detection, we assume that the size of the HST-1 emission region is about 20 times the beam size, and we derived the upper limit on each epoch accordingly. We also derived the upper limit of the brightness temperature in this region as 9×10^6 K at $\lambda 2$ cm.

2.3.3 Spectral properties of HST-1

Figure 2.11 illustrates two overlaid images of HST-1 at $\lambda 20$ cm (Cheung et al. 2007 and Cheung, priv. comm.) and $\lambda 2$ cm (beam A) of two adjacent epochs. The images were co-aligned using the peak of the inner jet as a common reference point. This figure shows

Table 2.3: HST-1 $\lambda 20$ – $\lambda 2$ cm spectral index^a

Epoch		S_ν [mJy]		α
$\lambda 2$ cm	$\lambda 20$ cm	$\lambda 2$ cm	$\lambda 20$ cm	
2005.30	2005.35	19.7 ± 1.0	111 ± 6^b	-0.75 ± 0.03
2005.85	2005.82	19.9 ± 1.0	126 ± 6^b	-0.80 ± 0.02

^a The spectral index and its errors are formal, see section 2.4.4

^b 5% error assumed for VLBI observations

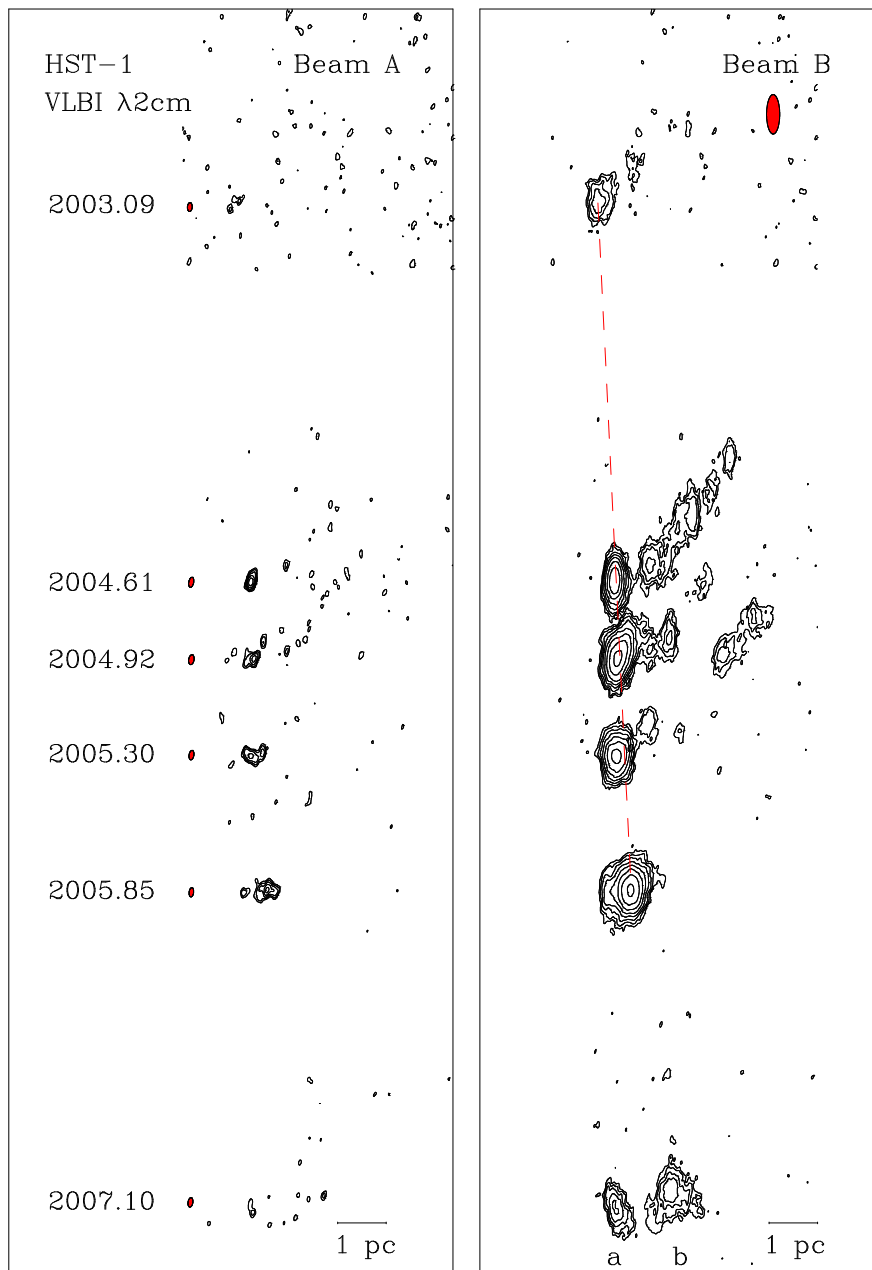


Figure 2.8: Images of the HST-1 region restored with beam A (left panel) and beam B (right panel). The distance between epochs is proportional to their relative time intervals, and the images are plotted with the same size scale. The contour levels increase by successive factors of $\sqrt{2}$, and the lowest contours for both images are (2003.09 to 2007.10): 0.6, 0.8, 0.8, 0.8, 0.8, 0.7 mJy beam^{-1} , respectively. The beam sizes of the beam A images are plotted to the right of each epoch label, while the beam size of the beam B images is shown in the upper-right corner. The HST-1 field is phase-shifted -788.5 mas in right ascension (RA) and 348.9 mas in declination (DEC). These images were obtained after performing self-calibration in the imaging process. In the right panel, **a** and **b** represent the two peaks of HST-1 in epoch 2007.10. The red dashed line illustrates the linear fit yielding HST-1's projected apparent speed (see Figure 2.13).

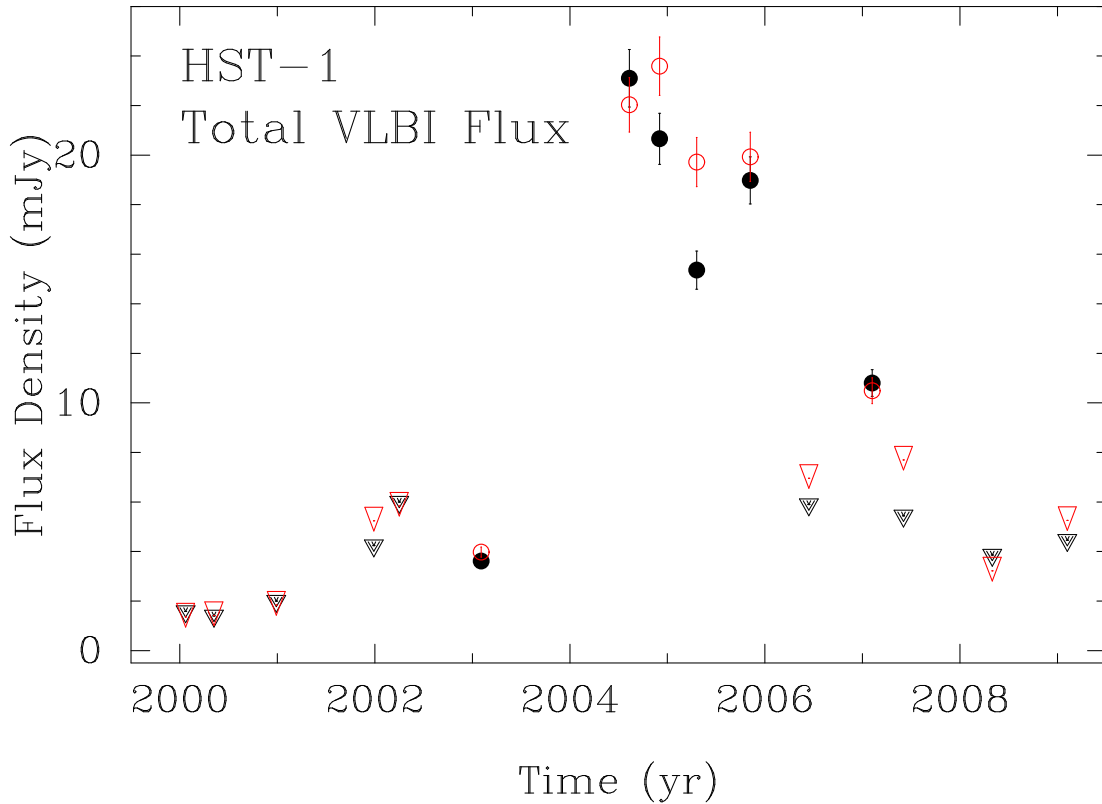


Figure 2.9: Total VLBI $\lambda 2$ cm flux density of the HST-1 region versus time. The values for epochs with no confident detection (inverted triangles) are upper limits, whereas the epochs with a detection are marked as dots. The results of using beam A are in black closed circles/triangles, while the results of using beam B are in red open circles/triangles.

that our observations are resolving the HST-1 peak component. We use those epochs to derive the HST-1 spectral properties by producing a rendition of the $\lambda 2$ cm image using the same restoring beam as the $\lambda 20$ cm image, namely, 8×3.4 mas at a position angle of 0° (beam B; Figure 2.8, right panel). Table 2.3 lists the epochs of $\lambda 20$ cm and $\lambda 2$ cm observations and the corresponding spectral index α , where $S_\nu \propto \nu^{+\alpha}$. The uncertainties of the spectral indices are formal errors, and are estimated using standard error propagation methods. The spectral index maps are shown in Figure 2.12. When interpreting these values, one needs to keep in mind that the resolution of $\lambda 20$ cm and $\lambda 2$ cm are very different. First, the frequency is different by one order of magnitude, which results in small formal error bars of the spectral index. Second, the incomplete (u, v) coverage on short VLBA baselines caused the missing flux effect in the HST-1 region at $\lambda 2$ cm (see Section 2.4.4 for a discussion). The average value of the derived spectral index is $\alpha \sim -0.78$.

2.3.4 HST-1 kinematics

To study the kinematics of HST-1, we fitted the peak of HST-1 and the M 87 core in the image plane with a Gaussian component using `IMFIT` in `AIPS`. As shown in Figure 2.8, it is difficult to identify moving components in this region, because the detections are

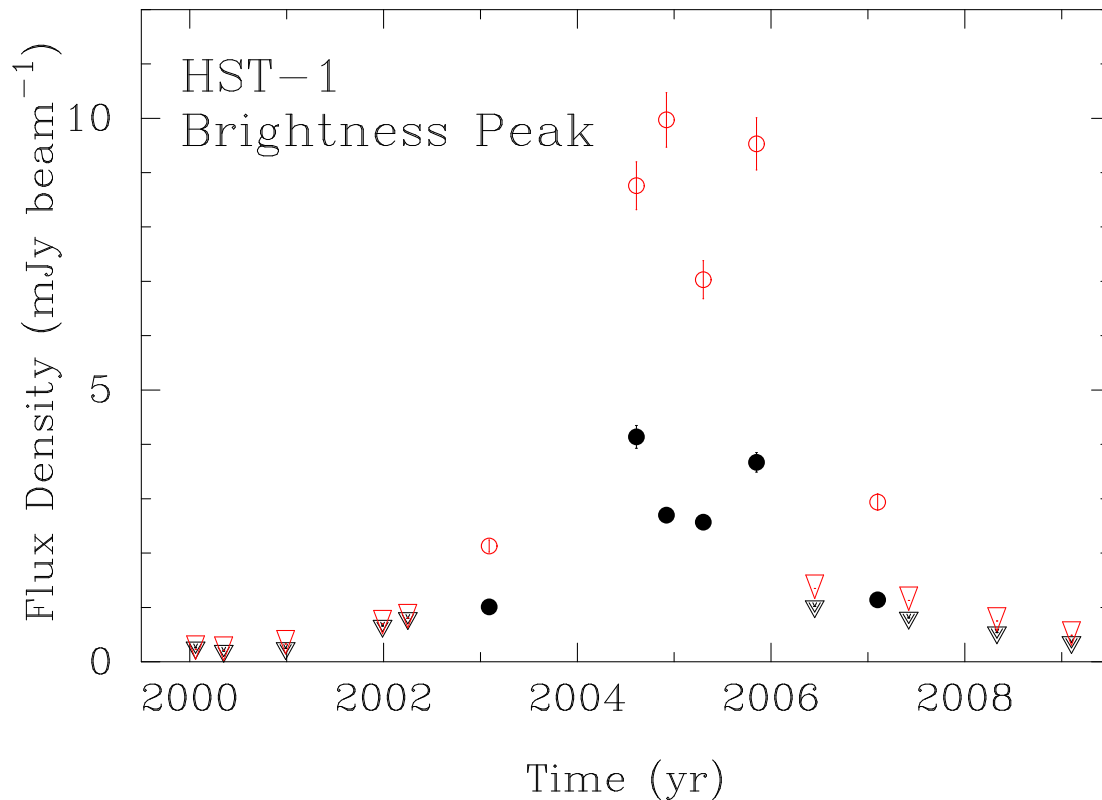


Figure 2.10: Brightness peak value at VLBI $\lambda 2$ cm of the HST-1 region versus time. The values for epochs with no confident detection (inverted triangles) are upper limits, whereas the epochs with a detection are marked as dots. The results of using beam A are in black closed circles/triangles, while the results of using beam B are in red open circles/triangles.

weak. Therefore, it is difficult to derive an accurate apparent speed for the HST-1 sub-components. For this reason, we use the relative position between the peak of HST-1 and the M 87 core to estimate the apparent speed of HST-1. Moreover, among the 6 epochs of detection, HST-1 was almost resolved out in epoch 2007.10, and appeared to have a double-peak morphology in the beam B image (Figure 2.8). By considering that the HST-1 detection in 2007.10 was weak, and the double-peak structure might be due to the effect of convolution, we excluded this epoch from the kinematic analysis (see Section 2.4.2 for a discussion). As shown in Figure 2.13, we plotted the peak positions of HST-1 with respect to the M 87 core against time, and we estimated the position errors as the FWHM of the fitted Gaussian component. By applying a linear regression to the peak positions, we obtained a value for the projected apparent speed of the HST-1 feature of 2.36 ± 1.19 mas yr⁻¹, which correspond to $\beta_{\text{app}} = 0.61 \pm 0.31$.

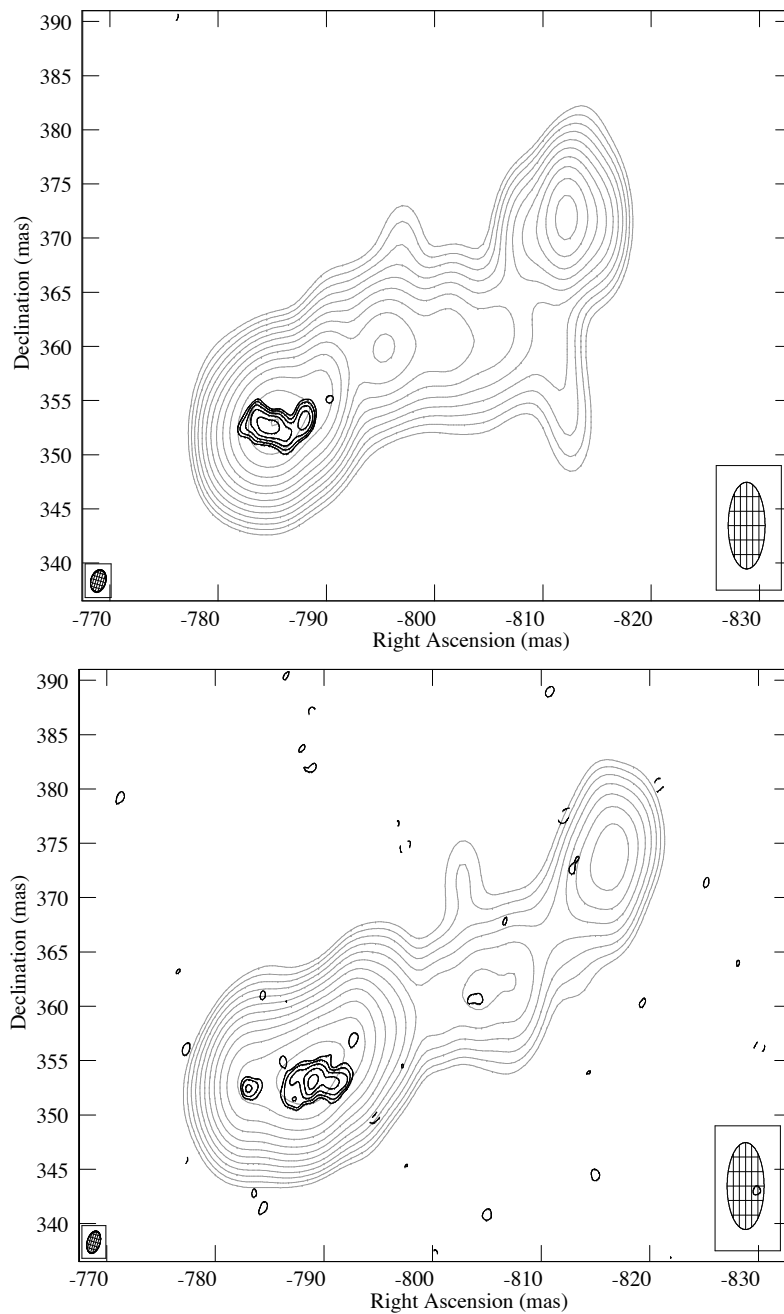


Figure 2.11: VLBA images of the HST-1 region in M87 at $\lambda 2$ cm (this thesis: black contour, beam size at half power level = 2×1 mas, P.A. = -16° , plotted bottom left) and $\lambda 20$ cm (Cheung et al. (2007): gray contour, beam size = 8×3.4 mas, P.A. = 0° , plotted bottom right). Upper panel: epoch 2005.30 ($\lambda 2$ cm, peak surface brightness: $3.4 \text{ mJy beam}^{-1}$) and 2005.35 ($\lambda 20$ cm, peak: 45 mJy beam^{-1}); lower panel: epoch 2005.85 ($\lambda 2$ cm, peak: $3.3 \text{ mJy beam}^{-1}$) and 2005.82 ($\lambda 20$ cm, peak: 42 mJy beam^{-1}). The lowest contour is $0.7 \text{ mJy beam}^{-1}$, and the contour levels are separated by a factor of $\sqrt{2}$. The images of two frequencies were registered using the peak of the inner jet of HST-1 as a common reference point.

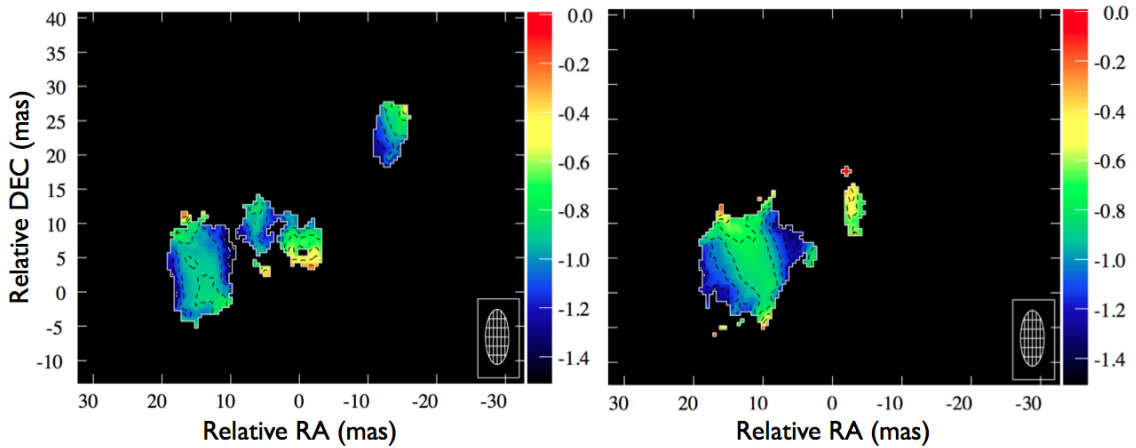


Figure 2.12: Spectral index maps of the HST-1 region. The map on the left-hand side was produced by overlaying the images of λ 2 cm (epoch 2005.30, beam B) and λ 20 cm (epoch 2005.35), while as the map on the right-hand side was from the images of λ 2 cm (epoch 2005.85, beam B) and λ 20 cm (epoch 2005.82).

2.4 Discussion

2.4.1 Variability timescale and HST-1 flaring region at parsec-scales

We derived the variability timescale of the 2005 flare from HST-1 assuming that a single flare would produce a logarithmic rise and fall in the light curve. By fitting the available light curves from VLBI and VLA measurements before and after the maximum flux density during the flare, we derived corresponding variability timescales and the upper limit of the characteristic size where the flare was produced. We define the logarithmic variability timescale as $\tau_{\text{var}} = dt/d[\ln(S)]$, where S is the flux density, t is the time interval between observations in units of years (Burbidge et al. 1974). Next, we estimate the upper limit of the characteristic size of the emission region from light-travel time: $\theta_{\text{char}} \approx 0.13(1+z)D^{-1}\tau_{\text{var}}\delta$, where z is the redshift, D is the luminosity distance in Gpc, and δ is the Doppler factor (Marscher et al. 1979). Table 2.4 shows the result of the derived characteristic size of the 2005 flare in HST-1.

Harris et al. (2003) estimated the Doppler factor δ of HST-1 to have a value between 2 and 5, based on decay timescales of *Chandra* observations. In the same context, Wang and

Table 2.4: HST-1 variability timescale and characteristic size during the rise and fall of the 2005 flare.

Wavelength	τ_{rise} [yr]	τ_{fall} [yr]	θ_{rise} [mas]	θ_{fall} [mas]
VLA λ 2 cm	1.5	4.9	$8.7 \delta^{\text{a}}$	28δ
VLBA λ 2 cm (beam A)	1.0	4.2	5.6δ	24δ
VLBA λ 2 cm (beam B)	1.0	2.7	5.7δ	15δ

^aThe characteristic size is related to the Doppler factor δ .

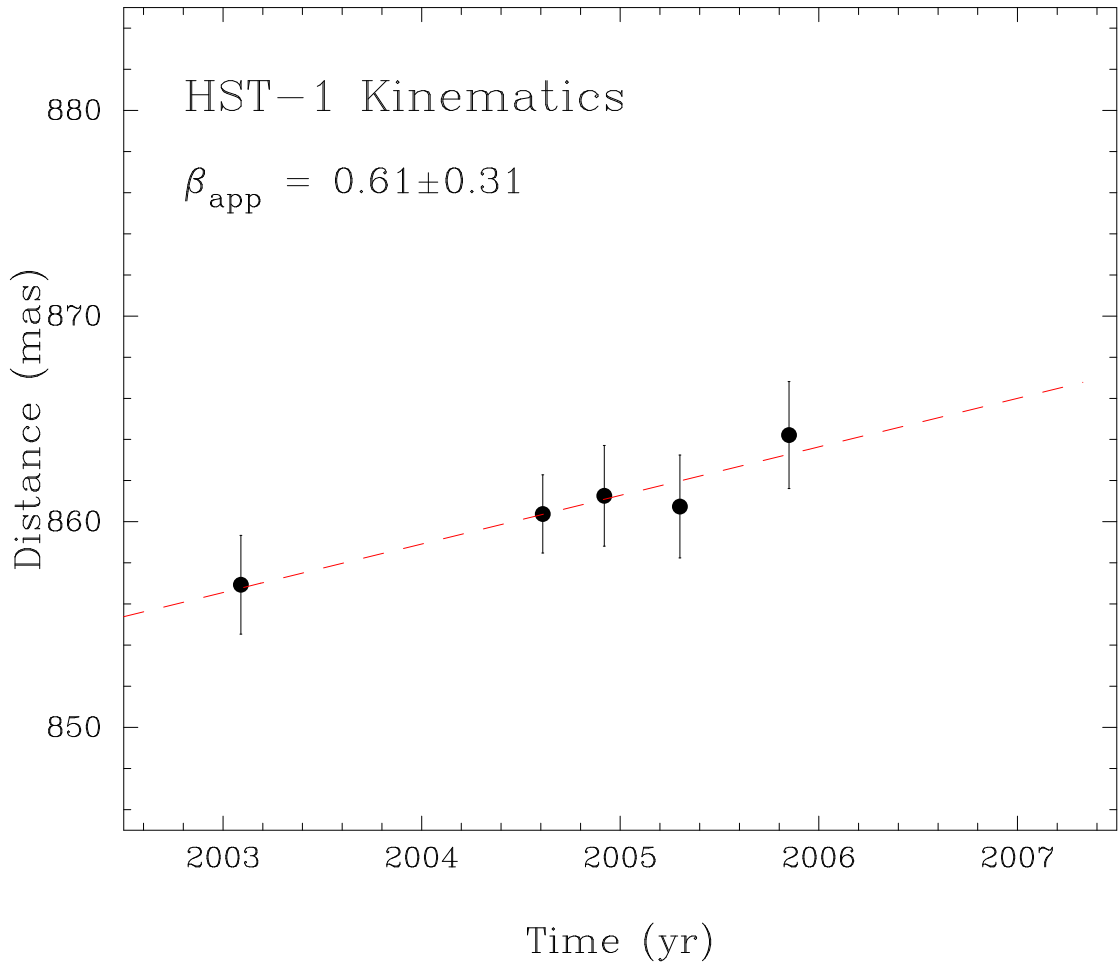


Figure 2.13: The linear fit of HST-1 proper motion shown as the red dashed line. This plot illustrates the position of HST-1 component peaks with respect to the M 87 core component as a function of time from 2003.09 to 2005.85. The fitted projected apparent speed of HST-1 β_{app} is shown at the upper-left corner of the plot.

Zhou (2009) estimated the Doppler factor of HST-1 to be 3.57 ± 0.51 by fitting the non-simultaneous spectral energy distribution of M87 using a synchrotron spectrum model. Simulations incorporating MHD models for the M 87 jet have suggested that the recollimation shock formed close to the HST-1 position had a relatively low Doppler factor $\sim 1-2$ (Gracia et al. 2009). If we use $\delta=3.57$, the derived characteristic sizes of HST-1 emission region during its flaring time are $20\text{mas} < \theta_{\text{rise}} < 31\text{mas}$ and $54\text{mas} < \theta_{\text{fall}} < 100\text{mas}$. The size scale of structural changes of HST-1 (see Figure 2.8) is between 20–50 mas (1 pc = 12.5 mas), which is within the derived characteristic size scale. However, if $\delta < 3.5$, θ_{rise} derived from VLBA $\lambda 2$ cm is smaller than 20 mas, which would create a causality problem, since the largest structural change of HST-1 cannot be bigger than the upper limit of the information propagation time. Therefore, $\delta > 3.5$ is needed based on the causality argument.

If δ is less than 3.5 in the HST-1 region, we could explain the causality problem by the self-calibration procedure that we used while imaging HST-1. We applied self-calibration

to the inner jet and HST-1 for all of the epochs with detections in beam A and beam B. Self-calibration works better with stronger objects, in our case, the marginal detection in epoch 2003.09 might not provide a satisfactory result in recovering extended emissions, comparing with stronger detections between 2004.61 and 2005.85, in which after self-calibration, we were able to recover more extended emission.

2.4.2 Speeds of HST-1

We used the peak position and fitted Gaussian errors to estimate the projected apparent speed of HST-1 $\beta_{\text{app}} = 0.61 \pm 0.31$ (see Figure 2.13), which is sub-luminal. In the kinematic analysis, we excluded epoch 2007.10 for obtaining a robust kinematic result. However, to make our results more solid, we estimated the upper and lower limit of HST-1 apparent speed by including epoch 2007.10 as a test. The derived possible range of the apparent speed is $0.23 < \beta_{\text{app}} < 1.2$, which is still consistent with a mildly relativistic jet motion.

To compare our kinematic results with previous findings, we show the positional evolution on the sky of the HST-1 peak at VLBA $\lambda 2$ cm with both beam A and beam B (see Figure 2.14), and components C1 and C2 at VLBA $\lambda 20$ cm (Cheung et al. 2007 and priv. comm.). As illustrated, our derived apparent speed range and structural evolution in time at $\lambda 2$ cm are consistent with the $\lambda 20$ cm results. However, our sub-luminal speed measurements of HST-1 are inconsistent with the high apparent superluminal motions reported in Cheung et al. (2007) from VLBA $\lambda 20$ cm observations and with the *HST* (Biretta et al. 1999). Nevertheless, in the VLBA $\lambda 20$ cm observations (Cheung et al. 2007), lower speeds were derived from some components in HST-1: c2 has $\beta_{\text{app}} = 0.47 \pm 0.39$, and HST-1d has $\beta_{\text{app}} = 1.14 \pm 0.14$. Our results are consistent with these findings.

2.4.3 Detection limits

HST-1 was not detected in epoch 2006.45. This epoch had only 22 minute integration time and the sampling rate was 128 Mbit s^{-1} . Therefore, the rms level ($0.35 \text{ mJy beam}^{-1}$) was not low enough to detect HST-1, which was also fading according to our light curve (Figure 2.9).

The total flux density of HST-1 measured by the VLA at $\lambda 2$ cm reached its maximum value of $\sim 123 \text{ mJy}$ in 2005 (Harris et al. 2006). Our VLBA $\lambda 2$ cm results recovered a HST-1 total flux density of $\sim 23 \text{ mJy}$, which is only 19% of the VLA measurement. We conclude that the innermost region of HST-1 was resolved out with the long baselines of the VLBA. The low measured flux density suggests that HST-1 is very extended.

2.4.4 HST-1 parsec-scale spectrum

We derived the spectral index of the HST-1 region based on VLBA $\lambda 2$ cm and $\lambda 20$ cm data (Table 2.3). However, one should be cautious with these values. First, the two datasets have a frequency difference of a factor of 10, which results in small formal error bars of the derived spectral index. One should be aware that the spectral index here could provide us with a trend in the spectrum of HST-1 and the physical condition of the region, but not the absolute value. Second, we have found that the incomplete (u, v) coverage on short

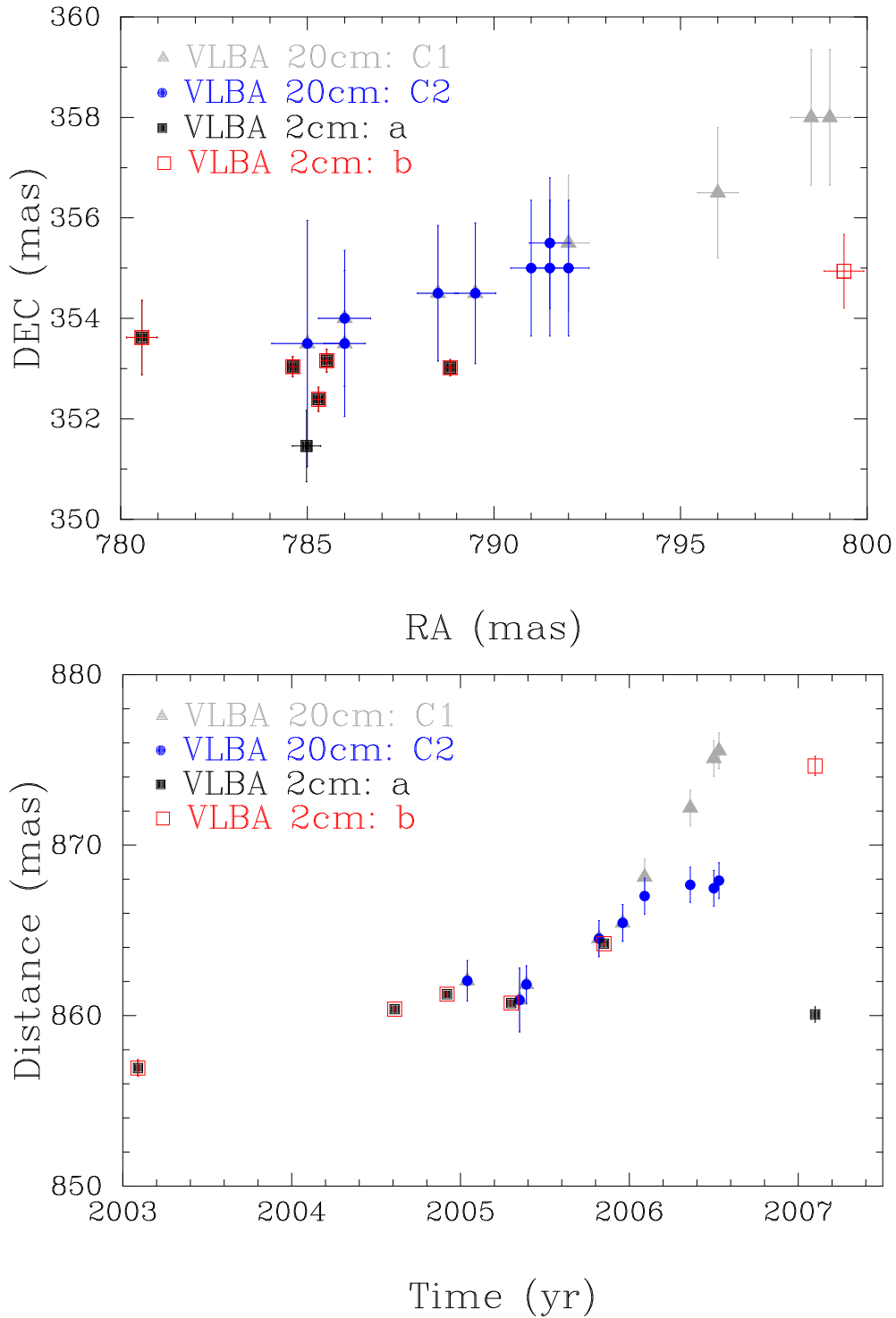


Figure 2.14: HST-1 sky positions (upper panel) and radial distance as a function of time relative to the M 87 core (lower panel). VLBA $\lambda 20$ cm (Cheung et al. 2007 priv. comm.): time range of components C1 and C2 is from 2005.04 to 2006.53; VLBA $\lambda 2$ cm (beam B): time range of components **a** and **b** is from 2003.09 to 2007.10; components **a** and **b** are shown in Figure 2.8.

VLBA baselines has resulted in missing flux in the HST-1 region at $\lambda 2$ cm. Therefore, the spectral index value of the HST-1 region is a lower limit, and the results suggest that HST-1 was optically thin during the flare in 2005. If assuming that HST-1 was a flat-spectrum source, there would have been ~ 90 mJy missing flux in this region in our 2 cm VLBA measurements.

2.4.5 A blazar nature of HST-1

The intensity of HST-1 reached a maximum in different wavebands in 2005, and the light curves from the VLA $\lambda 2$ cm, VLBA $\lambda 20$ cm, NUV, and X-ray observations all show the same tendency (Harris et al. 2009, Madrid 2009). Our light curve of HST-1 at VLBA $\lambda 2$ cm (Figure 2.9) is consistent with the other observations. Although this trend could be taken as evidence that HST-1 is the source of the HESS-detected TeV flare in 2005 (Aharonian et al. 2006), its VLBA radio properties that we have derived do not support it. These include (i) a very low compactness of the dominant emission, (ii) low brightness temperature, (iii) sub-luminal motion, and (iv) possibly low optical depth across the feature at parsec-scales. Those are in contrast to the typical blazar core features, which tend to have flat or inverted spectral indices in cm-wave VLBA images. We observed that HST-1 has radio properties consistent with those commonly seen in jet components. TeV observatories cannot resolve the M 87 core and HST-1 separately. To probe the origin of TeV emission, correlating variability between different bands is a powerful tool. Recent examples of this approach were successfully shown for a sample of blazars by Kovalev et al. (2009), and for M 87 by Acciari et al. (2009). Another approach is to apply physical models to multiwavelength observations to probe the TeV origin. There are models that suggest radio-TeV connections. For example, high energy flares could be generated from parsec-scale radio jets by inverse-Compton scattering of the photons and particles emitting from the core, and Stawarz et al. (2006) used this approach to explain the TeV flare from M87 in 2005. However, Acciari et al. (2009) reported about the VHE flare of M87 in 2008, and suggested that there might be correlations with the radio flare observed by VLBA at 43 GHz from the core. From our results, although we cannot fully discount, however, that HST-1 was the source of the TeV flare in 2005 based on our results alone, we do not favor the blazar nature for HST-1 suggested by Harris et al. (2008).

2.5 Summary and Future Work

With our VLBA $\lambda 2$ cm data from 2000.06 to 2009.10, we have detected HST-1 during 2003.09–2007.10, which covered the multi-band flaring period of HST-1. The total flux density of HST-1 varied from 4–24 mJy in our detections; by comparing the images of VLBA $\lambda 2$ cm and $\lambda 20$ cm, we saw a steep spectrum with $\alpha > -0.8$ in this region. The projected apparent speed of HST-1 derived from the brightness peak position is $0.61 \pm 0.31c$, which suggests a sub-luminal nature at VLBA $\lambda 2$ cm.

Our results showed that HST-1 is extremely extended at parsec-scales, and has a steep spectrum. No compact feature with a brightness temperature higher than 9×10^6 K is present in the $\lambda 2$ cm VLBA observations of this region of the M 87 jet, which implies that HST-1 does not have the properties of a standard blazar core. Combining our findings, we

do not find evidence of a blazar nature for HST-1 in the jet of M 87.

To investigate the ongoing physical mechanisms of HST-1, it is very important to trace its spectral evolution, especially when during a flare. Using the existing telescopes (see Table 4.2 in Chapter 1) under proper coordination, one can obtain several epochs of simultaneous observations, and study the spectral property of HST-1 during a flare. Additionally, tracing multiband light curves of HST-1 is a useful tool to study the correlations between different bands. To further resolve the HST-1 feature, one can use European VLBI Network (EVN) observations (due to its high sensitivity) and combine with the observatories in other bands, such as *HST* and *Chandra*. Combining the broadband data, one can construct the SED and investigate further the nature of HST-1. This is an advantage of studying the M 87 jet, which is so close to us that we can resolve the bright knots. Those are the possible future works to be done in order to understand the physical mechanisms taken place in the HST-1 feature.

3 Blazar Flare: a Multiwavelength Study of the Flat Spectrum Radio Quasar PKS 2052–47

One of the best way to distinguish different mechanisms taken place in blazars is to study their behavior at different wavebands during an outburst. Sokolov et al. (2004) showed that blazar flares dominated by SSC mechanism display frequency-dependent time delays. Cross-correlation analysis of long-term variability in low- and high- energy emission suggests that both synchrotron emission and IC emission are originated at the same location in the blazar jets (McHardy et al. 1999, Marscher et al. 2004). The time-delay between multi-frequency flares has different features while the IC mechanism is ERC-dominant. The time delay between radio and γ -ray flares was investigated by Pushkarev et al. (2010a) and Pushkarev et al. (2010b). The broadband SED model by Sokolov and Marscher (2005) shows that the spectral index of the ERC emission must be positive for at least half of the duration of the flare to cause a time-delay, whileas of the SSC emission, the spectral index remains negative at all times.

In July 2009, the flat-spectrum radio quasar PKS 2052–47 experienced an optical flare, which was followed by a γ -ray flare in August. We took this chance and arranged a multiwavelength campaign together with VLBI observations after the blazar’s flare, and hope to dig deeper into the nature of jet emission.

3.1 Introduction

PKS 2052–47 is a flat-spectrum radio quasar with a redshift of 1.489 (Jauncey et al. 1984). Earlier Australia Telescope Compact Array¹ (ATCA) and *Chandra* X-ray observations showed that the source has a two-sided jet at kiloparsec scales in the radio band, with no extended emission in X-rays (see Figure 3.1; Marshall et al. 2005). PKS 2052–47 is one of the identified γ -ray blazars, it has an EGRET counterpart 3EG 2055–4716 (Thompson et al. 1995, Hartman et al. 1999), and is associated with the *Fermi* source 1FGL J2056.3–4714 (Abdo et al. 2010b). Nolan et al. (2003) studied the γ -ray variabilities of the Southern sources using the *CGRO*/EGRET data, and they found that PKS 2052–47 was highly variable. Based on the 9-year *CGRO*/EGRET observations, Nandikotkur et al. (2007) derived the γ -ray photon index of PKS 2052–47 at 30 MeV–10 GeV to be $\Gamma_\gamma = 1.85 \pm 0.26$, and the flux at the energy range of >100 MeV to be $F_\gamma =$

¹<http://www.narrabri.atnf.csiro.au/>

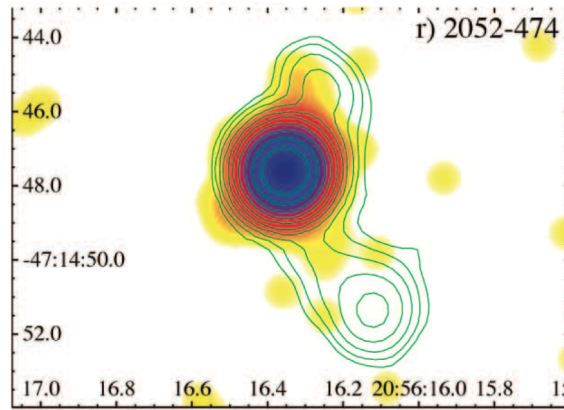


Figure 3.1: X-ray images obtained with *Chandra*, overlaid by contours of radio emission obtained at the Australia Telescope Compact Array (Marshall et al. 2005).

$2.14 \pm 0.58 \times 10^{-9}$ photon $\text{cm}^{-2} \text{s}^{-1}$. The submillimeter flux density of PKS 2052–47 was measured in May 1996 by the Swedish-ESO² Submillimetre Telescope continuum survey at 2 and 3 mm wavelength, and they obtained $S_{2\text{mm}} = 0.63 \pm 0.09$ Jy and $S_{3\text{mm}} = 1.19 \pm 0.12$ Jy (Beasley et al. 1997). The central black hole mass of PKS 2052–47 was estimated by Liang and Liu (2003) based on its γ -ray emission using the relation derived by Dermer and Gehrels (1995), and they obtained a black hole mass of $10^{9.6} M_{\odot}$. Massardi et al. (2008) reported results from the ATCA monitoring on this source during 2002 and 2007, and they suggested that after October 2004, the source went through a declining stage of a flaring phase, and its radio flux changed rapidly. The averaged spectral indices of PKS 2052–47 between 1.4, 2.4, 4.8, and 8.6 GHz obtained by ATCA in 1994 were reported by Kedziora-Chudczer et al. (2001), and they found the values were between -0.10 and -0.31 . The polarization properties at 18.5 GHz of this source were reported by Ricci et al. (2004) using ATCA, and they found its fractional polarization to be $1.7 \pm 0.4\%$, which indicates the source is weakly polarized. VLBI observations by TANAMI³ (Tracking Active Galactic Nuclei with Austral Milliarcsecond Interferometry; see Section 3.2) show that the parsec-scale structure of PKS 2052–47 is very compact, with a relatively high brightness-temperature core of 2×10^{12} K and a size of 0.3×0.1 mas at 8.4 GHz, together with a very faint jet to the west. At 22 GHz the source is unresolved with a restoring beam of 1.9×1.3 mas (see Figure 3.2). Ojha et al. (2004) presented a VLBI image of PKS 2052–47 using the Australian Long Baseline Array (LBA) together with the telescopes in South Africa and Hawaii at 8.4 GHz, and they presented two epochs of observations in July and November 2002. Celotti and Ghisellini (2008) studied the broadband SED of this source by using the archival data. They applied a jet model based on an one-zone leptonic synchrotron and IC emission taking into account of the seed photons originated in the jet and from external source, as shown in Figure 3.3.

From July 2009, the Automatic Telescope for Optical Monitoring (ATOM) team reported a steady increase of flux density from PKS 2052-47, which reached its high state and flared in the optical band in August (Hauser et al. 2009). The ATOM team reported that the source was fainter than 18 magnitude in the R band in the second half

²European Southern Observatory

³<http://pulsar.sternwarte.uni-erlangen.de/tanami/>

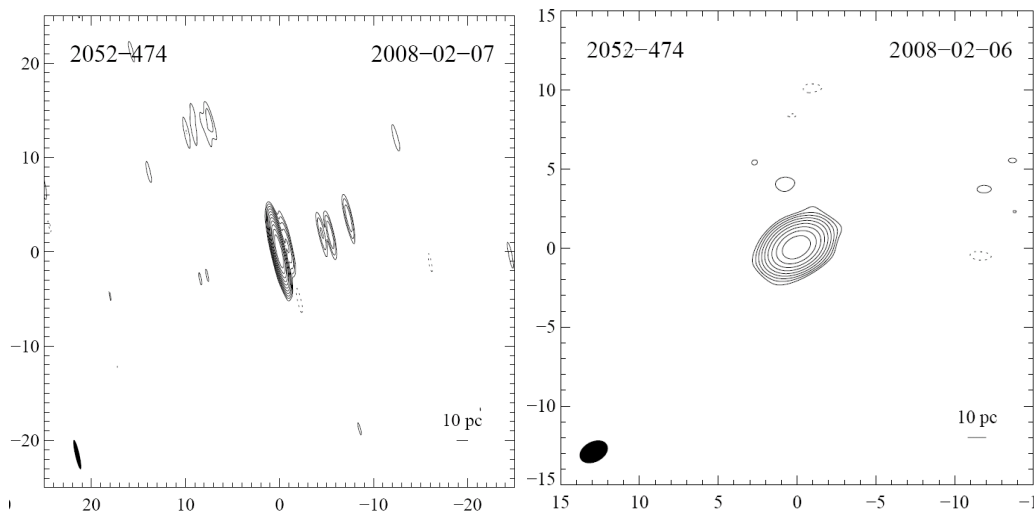


Figure 3.2: The TANAMI VLBI images of PKS 2052–47 at 8 GHz (left, February 7, 2008) and 22 GHz (right, February 6, 2008). The axes are relative right ascension (RA) and declination (DEC) in milli-arcsecond (mas). On the bottom right, the scale of 10 parsec is shown. The scales are different in both images.

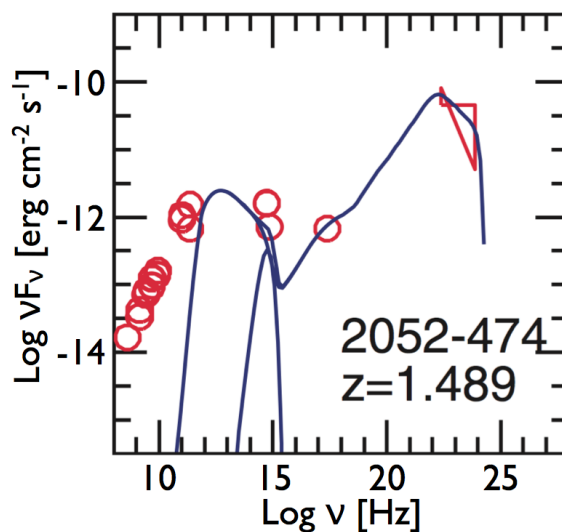


Figure 3.3: Previously published broadband SED of PKS 2052-47 by Celotti and Ghisellini (2008). The red circles denote the archival data, and the solid line is the SED model, which is based on an one-zone leptonic synchrotron and IC mechanism, taking into account of the seed photons originated both in the jet and from external source.

of 2008, and it gradually increased its brightness to 17.5 magnitude until May 2009. The source had two small flares in June and July 2009, and since July 21, the flux started to increase up to 15.6 magnitude until August 12, 2009. Right after this, the *Fermi* Large Area Telescope (LAT) reported a γ -ray flare from this source (Chang 2009). On August 9, 2009, PKS 2052–47 reached its high state in the γ -ray band with a flux of $F_\gamma = (8.7 \pm 1.6) \times 10^{-7}$ photon $\text{cm}^{-2} \text{s}^{-1}$ (one-day integration time), which was four-time brighter than the average level observed in the previous week (July 29 – August

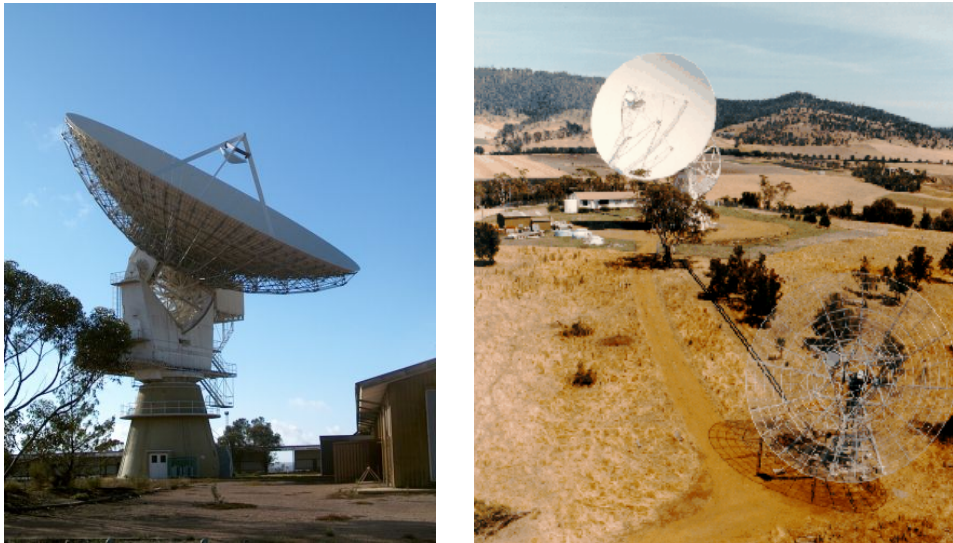


Figure 3.4: The 30 m dish at the Ceduna Observatory (left) and the 26 m dish at the Hobart Observatory (right). Image source: <http://www-ra.phys.utas.edu.au/wiki/>.

4, 2009). Following the flaring events, Baily and Muir (2009) reported the continuing outbursts in the optical band observed by the SMARTS 1 m telescope⁴. They found that PKS 2052–47 had mean optical magnitudes of 15.40 (R band) and 16.54 (B band), and its variability up to 0.05 magnitudes in less than 1 hour.

In order to study the flat spectrum radio quasar PKS 2052–47 at its active phase, we arranged a multiwavelength campaign from the radio to the γ -ray band in early September 2009. In the next sections, we will introduce the facilities that participated in the campaign (Section 3.2), the procedures of data analysis (Section 3.3), and the multiwavelength results (Section 3.4).

3.2 Data Acquisition

The multifrequency observation campaign of PKS 2052–47 covers the frequency range from the radio to the γ -ray band. In this section, we will introduce the facilities that contributed to the campaign.

The Ceduna-Hobart Interferometer The Ceduna-Hobart Interferometer (CHI) is an interferometer located in Australia which consists of a 30 m dish in the Ceduna Observatory and a 26 m dish in the Hobart Observatory⁵, and both of the observatories are operated by the University of Tasmania (see Figure 3.4). The interferometer has a observing frequency of 6.6 GHz.

The TANAMI program The Tracking Active Galactic Nuclei with Austral Milliarcsecond Interferometry (TANAMI) program⁶ is a parsec-scale radio monitoring program target-

⁴<http://www.astro.yale.edu/smarts/smarts1.0m.html>

⁵<http://www-ra.phys.utas.edu.au/wiki/>

⁶<http://pulsar.sternwarte.uni-erlangen.de/tanami/>

Table 3.1: Participating facilities of the TANAMI program (Ojha et al. 2010b).

Facility	Telescopes	Latitude	Longitude	Location
Parkes Observatory	64 m	32°59'54"S	148°15'49"E	Parkes, Australia
ATCA	5×22 m	30°18'46"S	149°33'01"E	Narrabri, Australia
Hobart Observatory	26 m	42°48'18"S	147°26'21"E	Hobart, Australia
Ceduna Observatory	30 m			Ceduna, Australia
Hartebeesthoek	26 m	25°53'14"S	27°41'05"E	Hartebeesthoek, South Africa
DSS43 ^a	70 m	35°24'09"S	148°58'53"E	ACT, Australia
DSS45 ^a	34 m	35°23'54"S	148°58'40"E	ACT, Australia
O'Higgins ^b	9 m			Antarctica
TIGO ^b	6 m			Concepción, Chile

^a Operated by the Deep Space Network of the National Aeronautics and Space Administration, USA.

^b Operated by the German Bundesamt für Kartographie und Geodäsie.

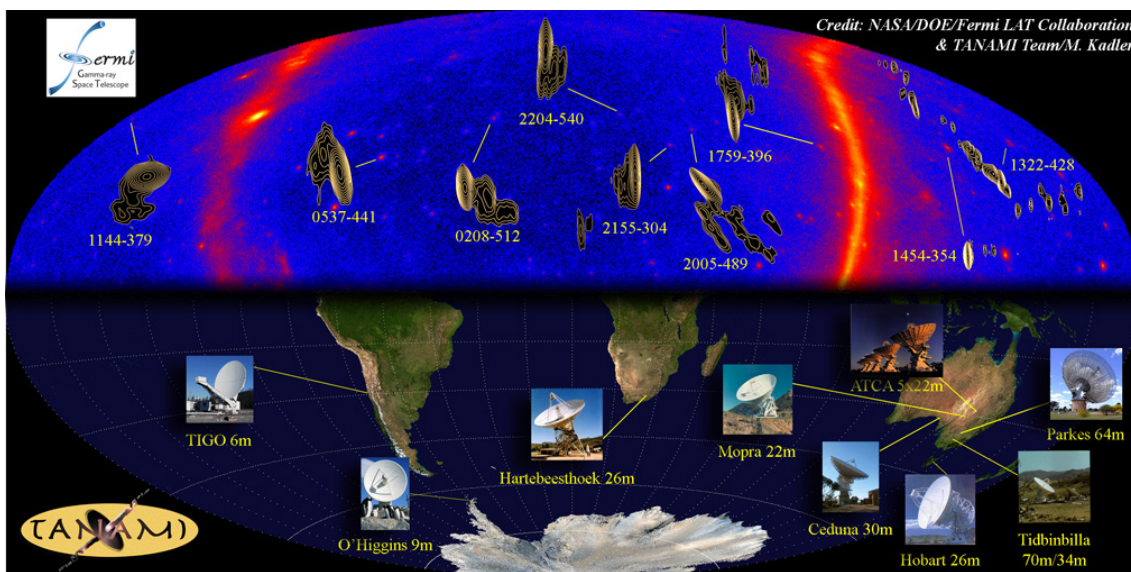


Figure 3.5: Cartoon for the TANAMI program. Upper panel: the Southern γ -ray sky as seen by *Fermi*/LAT (color-scale map) and the AGN structures resolved by the LBA of the TANAMI program (contour maps). Lower panel: the locations of the LBA in the TANAMI program at the Southern hemisphere. Image credit: NASA/DOE/*Fermi*/LAT Collaboration & TANAMI Team/M. Kadler.

ing extragalactic jets south of -30° declination (Ojha et al. 2010a,b), and it monitors an initial sample of 43 sources since November 2007. The TANAMI observations are made with the Australian/South-African Long Baseline Array, and the joint facilities are listed in Table 3.1; Figure 3.5 illustrates the locations of the stations in the Southern hemisphere. The observing frequencies are 8.4 GHz and 22 GHz. PKS 2052–47 is one of the TANAMI sources, and the observation was scheduled on September 5th–6th in 2009 with two available frequencies.

APEX/LABOCA The Large Apex **B**olometer **C**amera⁷ (LABOCA; Siringo et al. 2009; see Figure 3.6) is a multi-channel bolometer array designed and built at the MPIfR, and

⁷<http://www.apex-telescope.org/bolometer/laboca/>

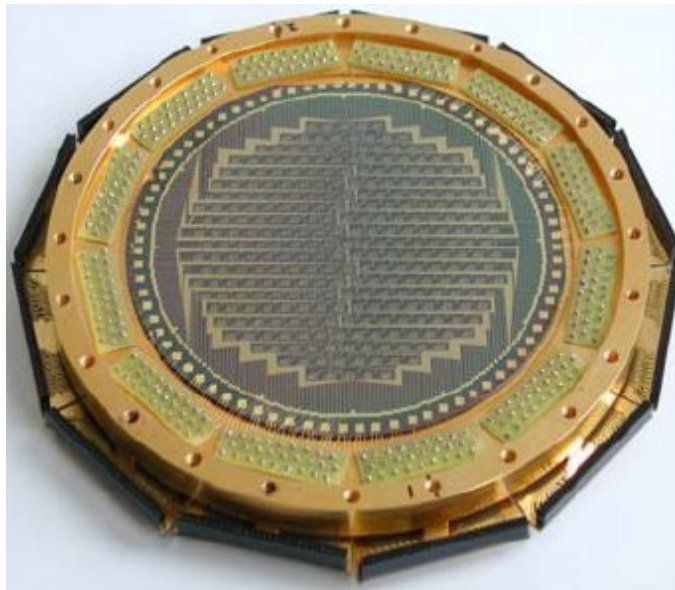


Figure 3.6: The LABOCA array, which is currently mounted on APEX telescope in Chile (image source: <http://www.apex-telescope.org/bolometer/laboca/>).

is mounted on the APEX telescope in Chile (see Section 4.3). LABOCA operates at 345 GHz with a bandwidth of 60 GHz. As a bolometer, it is designed to operate for continuum observations. It has an angular resolution of $18.6''$ with a field of view of $11.4'$.

The *Swift* Space Telescope The UV/Optical telescope (UVOT) and the X-ray telescope (XRT) onboard *Swift* were used in the multiwavelength observation of PKS 2052–47. For a detail introduction of the *Swift* mission, please see Section 4.3.3.

***Fermi* Large Area Telescope** The *Fermi*/LAT has been monitoring the whole sky since its operation in August 2008, and we used the LAT data in the multiwavelength analysis. For a detailed introduction of the *Fermi* mission, please see Section 4.3.4.

3.2.1 The Multiwavelength Campaign

The multiwavelength campaign of PKS 2052–47 was arranged simultaneously with the scheduled southern VLBI observations of TANAMI in 5–6 September 2009. The observation log is reported in Table 3.2. As mentioned in the previous section, the participating facilities include: the CHI, the LABOCA mounted on APEX, the UVOT and XRT onboard *Swift*, and the *Fermi*/LAT. We have an one-epoch observation from the CHI, and two-epoch VLBI observations by the LBA at two frequencies (8 and 22 GHz). PKS 2052–47 was monitored by the Ceduna Observatory since after its flare from August to November in 2009. With APEX, we have two epochs of flux measurement on September 2 and 6, 2009. We obtained the *Swift* observations through Target of Opportunity (ToO) request, and the observations covered five days from September 4 to 8 (see Table 3.3). The *Fermi*/LAT data is available in all time for that it is under an all-sky survey mode.

Table 3.2: The multiwavelength campaign observation of PKS 2052–47.

Start date	End date	Facility	Band	Comments
2009-09-05	2009-09-06	CHI	6.6 GHz	Single epoch
2009-08-17	2009-11-05	Ceduna Observatory	-	Monitoring
2009-09-05	2009-09-06	LBA	8 & 22 GHz	One epoch per frequency
2009-09-02	2009-09-06	APEX	345 GHz	Two epochs
2009-09-04	2009-09-08	<i>Swift</i> /UVOT	2000–3500 Å	~2 ks per day
2009-09-04	2009-09-08	<i>Swift</i> /XRT	0.3–10 keV	~2 ks per day
2008-06-11	present	<i>Fermi</i> /LAT	100 MeV–300 GeV	All-sky survey

3.3 Data Analysis

TANAMI

The TANAMI correlated data were analyzed following a standard procedure using the National Radio Astronomy Observatory’s Astronomical Image Processing System (AIPS) software (Greisen 1998). Observations of known sources with $\geq 90\%$ of their correlated flux in a compact core were used to improve overall amplitude calibration. For each antenna, a single amplitude gain correction factor was derived based on fitting a simple Gaussian source model to the visibility data of the respective compact source after applying the initial calibration based on the measured system temperatures and gain curves. Based on the differences between the observed and model visibilities, gain correction factors were calculated and the resulting set of amplitude gain correction factors was applied to the visibility data of the target source. The accuracy of the absolute amplitude calibration is conservatively estimated to be 20%.

After data calibration using AIPS, Difmap (Shepherd 1997) was used to image the source. The data were averaged into 30-second bins, and imaged using the CLEAN algorithm using natural weighting and phase self-calibration. The model was improved using time-dependent gain factor with decreasing time intervals (180, 60, 20, 5, 2, 1 minutes). The TANAMI data analysis is performed by our collaborators R. Ojha and M. Kadler.

Swift XRT and UVOT

We analyzed the data of UVOT and XRT using HEASOFT version 6.8⁸. For UVOT data, we extracted the source flux with an aperture size of 5". For XRT data, we extract the spectrum of the source with a circle of 20-pixel radius. We fit the X-ray spectrum using XSPEC version 12.5.1 with an absorbed power law model. While applying the power law model, we set a lower-limit of the neutral hydrogen column density as $2.79 \times 10^{20} \text{ cm}^{-2}$, which is the galactic neutral hydrogen abundance from the LAB survey⁹ (Kalberla et al. 2005). We corrected for the Galactic and intrinsic extinction in the optical and the X-ray band based on the derived N_{H} value (see Table 3.3). For the detailed description of the XRT and UVOT data reduction, please see Section 4.4.1 and 4.4.2. In Table 3.3, we list the results of the X-ray spectral analysis for the six *Swift* observing epochs. Column (1) is the observation date, column (2) is the *Swift* observation ID, column (3) is the exposure

⁸<http://heasarc.nasa.gov/lheasoft>

⁹<http://www.astro.uni-bonn.de/webaiub/english/tools-labsurvey.php>

time of the *Swift*/XRT, column (4) is the *Swift*/UVOT exposure time, column (5) is the UVOT filter used in the observation, column (6) is the derived intrinsic neutral hydrogen column density, column (7) is the uncertainty of the derived neutral hydrogen column density, column (8) and (9) is the X-ray photon index and flux at the energy range 2–10 keV, column (10) is the reduced χ^2 of the fitting result, and column (11) is the degree of freedom, which is simply the energy bins subtracted by the number of free parameters in the fitting function. For an absorbed power law function, the number of free parameters is three.

***Fermi*/LAT**

In the broadband SED of PKS 2052–47, we included the γ -ray spectrum of the 11-month *Fermi*/LAT results reported by Abdo et al. (2010b). Based on their findings, PKS 2052–47 has a photon index of $\Gamma_\gamma=2.54\pm 0.05$, which was derived at the energy range of 100 MeV to 100 GeV.

3.4 Results

As of August 2010, the data collected include: *Swift* UVOT and XRT, *Fermi*/LAT, and the preliminary results from APEX/LABOCA and Ceduna Observatory. We have analyzed the *Swift* data, and we collected all the available data to construct the broadband SED of PKS 2052–47.

3.4.1 The Multiband Properties of PKS 2052–47

APEX/LABOCA The preliminary APEX flux density presented here was provided by S. Larsson on behalf of the F-GAMMA team, and the final data calibration is in process. There were three epochs of measurement by the APEX/LABOCA at 345 GHz. The preliminary flux densities obtained on September 2 is 374 ± 16 mJy, and on September 6 are 740 ± 24 mJy and 710 ± 22 mJy.

TANAMI The TANAMI datasets have been correlated, and is in the data calibration process. The final result will be delivered by M. Kadler and R. Ojha on behalf of the TANAMI team. To illustrate the radio morphology at parsec-scales, we show two TANAMI VLBI images of PKS 2052–47 obtained in February 2008 at 8 and 22 GHz (Ojha et al., submitted to A&A, and Kadler et al. in preparation) in Figure 3.2. Notice that the image resolution of the 8 GHz map is higher than that at 22 GHz, due to the inclusion of a telescope in Chile, equipped only with a receiver at 8 GHz, providing longer baselines to better resolve the source.

Ceduna Observatory As mentioned in the previous section, PKS 2052–47 was monitored by the Ceduna Observatory since its flare in August 2009. The monitoring observations started right after the multiband flare in the optical and the γ -ray band. In Figure 3.7

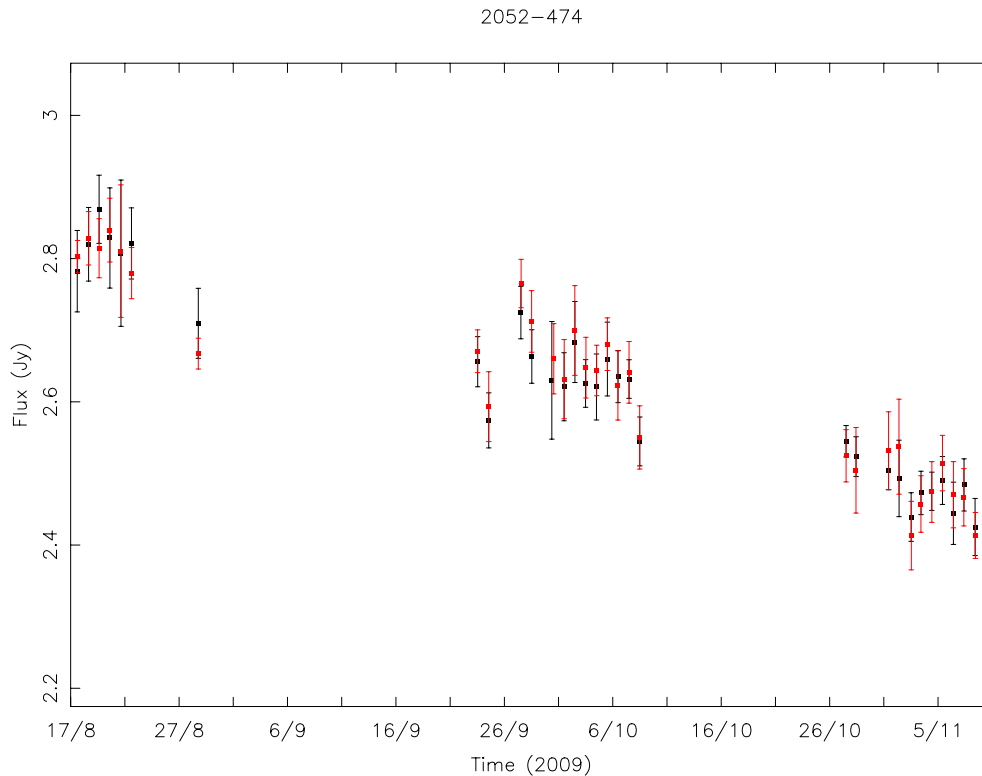


Figure 3.7: The radio flux density variation of PKS 2052–47 monitored by the Ceduna Observatory from August 17 to November 5, 2009. The source displayed a decreasing brightness in the radio band (Image credit: J. Blanchard).

one can find the preliminary light curve of PKS 2052–47 during August 17 and November 10 in 2009 (J. Blanchard priv. comm.). We see a steady decay of the flux density in the three months after the flare, from 2.8 Jy to 2.4 Jy.

The *Swift* UVOT and XRT We analyzed all the six epochs of *Swift* observations on PKS 2052–47, and we derived the intrinsic neutral hydrogen column density, the photon index, and the X-ray flux, as listed in Table 3.3. Figure 3.8 shows the X-ray spectra of PKS 2052–47, as presented, we applied an absorbed power law model to fit the spectra. We obtained a range of photon index Γ_X between 1.4 ± 0.3 and 1.9 ± 0.3 , however, by considering the uncertainties in these values, the variation is not significant, as shown in Figure 3.9. The intrinsic N_H that we derived is very low; in three epochs, the N_H value is zero. The flux we derived has values between 1.76×10^{-12} and 3.63×10^{-12} ergs cm $^{-2}$ s $^{-1}$. One epoch with the shortest integration time obtained in August 5 (Obs. ID 00038412001) has very low counts; after data grouping, the X-ray spectrum has only two energy bins, which are less than the free parameters to be fitted. In order to estimate the source flux, we assumed a photon index of $\Gamma_X=1.7$ according to the values of Γ_X obtained in the other epochs, and we fixed the N_H value to be 2.79×10^{20} cm $^{-2}$.

Table 3.3: The *Swift* observation epochs of PKS 2052–47 and the corresponding derived parameters in the X-ray band.

<i>Swift</i>				— N_{H} [10^{22} cm^{-2}] —		Γ_{X}	F_{X}	χ_{red}^2	d.o.f.	
Obs. date	Obs. ID	T_{XRT} [s]	T_{UVOT} [s]	Filter	Intrinsic	Uncertainty	(8)	(9)	(10)	(11)
(1)	(2)	(3)	(4)	(5)	(6)	(7)	(8)	(9)	(10)	(11)
2009-08-05 ^a	00038412001	1192	1192	U	-	-	1.7 ^b	1.76	-	-
2009-09-04	00038412002	1799	1799	UM2	0.0	0.3	1.4±0.3	3.63	0.38	4
2009-09-05	00038412003	1588	1587	UW1	0.0	-	1.7±0.2	2.56	1.78	3
2009-09-06	00038412004	2452	2452	U	0.2	0.1	1.8±0.3	2.55	0.20	6
2009-09-07	00038412005	2105	2333	UW2	0.0	0.3	1.5±0.4	2.87	0.34	3
2009-09-08	00038412006	2217	2215	UM2	0.2	0.1	1.9±0.3	2.53	0.84	5

Column note: (1) *Swift* observation date; (2) *Swift* observation ID; (3) *Swift*/XRT exposure time; (4) *Swift*/UVOT exposure time; (5) UVOT filter; (6) Derived intrinsic neutral hydrogen column density; (7) the uncertainty of neutral hydrogen column density (Galactic+intrinsic); (8) Photon index; (9) Model flux at the energy range of 2–10 keV in an unit of $10^{-12} \text{ ergs cm}^{-2} \text{ s}^{-1}$; (10) Reduced χ^2 value; (11) Degree of freedom of the fit.

^a The X-ray spectrum has only two energy bins after data grouping. We fix the N_{H} and F_{X} in order to estimate the flux.

^b Fix parameter while fitting.

3.4.2 The Broadband SED of PKS 2052–47

After our *Swift* analysis and additional available data from the multi-band campaign, we have compiled six broadband SED plots of PKS 2052–47, presented in Figure 3.10. The non-*Swift* data are common for all six plots. We corrected for the Galactic and intrinsic extinction in the optical and the X-ray band (see Section 4.4.3). As shown, the IC hump of the SED has a much higher energy peak than the synchrotron hump. Table 3.4 lists the peak values of the synchrotron and the IC hump that we derived. The IC energy peak is almost two orders of magnitude higher than the synchrotron hump. We obtained a synchrotron peak frequency of $3.5 \times 10^{13} \text{ Hz} \leq \nu_{\text{peak}}^{\text{sync}} \leq 8.9 \times 10^{13} \text{ Hz}$; according to the classification by Abdo et al. (2010a), PKS 2052–47 is a low synchrotron peaked blazar. Additionally, we see a possible decreasing trend with time in the values of $\nu_{\text{peak}}^{\text{sync}}$, $\nu F_{\nu}^{\text{sync}}$, and νF_{ν}^{IC} (see Table 3.4).

Comparing our broadband SED results with the work by Celotti and Ghisellini (2008), they derived a synchrotron peak frequency of $\nu_{\text{peak}}^{\text{sync}} \sim 10^{13.5} \text{ Hz}$ (see Figure 3.3), which is consistent with our results. The IC hump that they derived is two orders of magnitude higher than the synchrotron hump, which is also very similar to our findings.

3.5 Discussion

From our X-ray data analysis, we derived the X-ray photon index which ranges from 1.4 ± 0.3 to 1.9 ± 0.3 (see Table 3.3). The results show that the X-ray spectrum of PKS 2052–47 did not have significant changes during our multiwavelength campaign performed in September 2009, as illustrated in Figure 3.9.

We constructed the broadband SED of PKS 2052–47 during the six days of *Swift* observations, and the six SED plots share common data except for the *Swift* observations in the optical and the X-ray band. Therefore, the variations of the SED profile are caused by the differences of the *Swift* UVOT and XRT results. We derived the peak positions of the synchrotron and the IC hump of the SED (see Table 3.4). The peak position of the IC hump do not show a clear trend, however, we see a possible decreasing trend for the

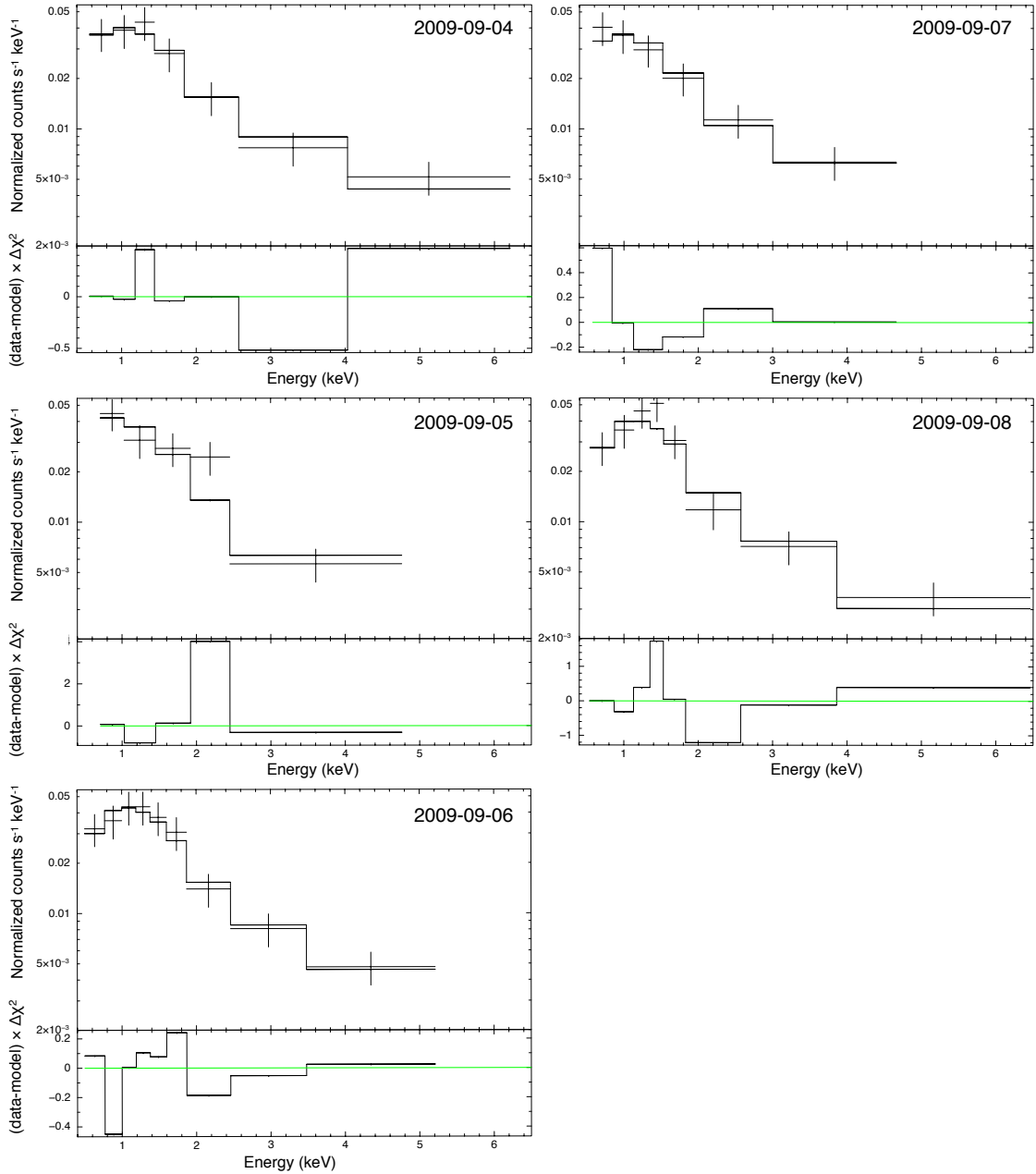


Figure 3.8: X-ray spectra of PKS 2052-47 measured by *Swift*/XRT, and the observing date is marked on the upper-right corner of each plot. An absorbed power-law model is applied to each of the spectrum. We do not show the X-ray spectrum measured on August 5, 2009 due to the poor quality of the spectrum (one energy bin after data grouping).

peak frequency and energy peak of the SED synchrotron hump. During the multiwavelength campaign, the value of synchrotron peak frequency dropped from 8.9×10^{13} Hz to 3.9×10^{13} Hz, and the value of synchrotron peak energy dropped from 6.6×10^{11} Hz Jy to 5.1×10^{11} Hz Jy. This variation of the synchrotron hump in the SED is mainly caused by the *Swift*/UVOT measurement, therefore, further examination is needed to see if this trend is significant. By adding the upcoming results from CHI measurements during the multiwavelength campaign, we will be able to constrain the SED profile better. Furthermore, the TANAMI measurements of PKS 2052-47 will be delivered, and with the upcom-

Table 3.4: The estimated peak values of the synchrotron and the IC hump in the broadband SED of PKS 2052–47 (see Figure 3.10).

Obs. ID	$\nu_{\text{peak}}^{\text{sync}}$ [10^{13} Hz]	$\nu F_{\nu}^{\text{sync}}$ [10^{11} Hz Jy]	$\nu_{\text{peak}}^{\text{IC}}$ [10^{22} Hz]	νF_{ν}^{IC} [10^{13} Hz Jy]
(1)	(2)	(3)	(4)	(5)
00038412001	8.3	6.7	2.2	1.8
00038412002	8.9	6.6	2.3	1.5
00038412003	4.3	5.3	2.3	1.5
00038412004	5.6	5.9	2.5	1.2
00038412005	3.5	4.9	2.4	1.5
00038412006	3.9	5.1	2.5	1.2

ing VLBI results, we will be able to check the parsec-scale map of this source and to search for possible morphology changes by comparing the TANAMI observation during the campaign with previous VLBI maps.

3.6 Summary

We arranged a multiwavelength observation on PKS 2052–47 from the radio to the γ -ray band after its flaring phase. Preliminary results were presented in Chang et al. (2009). Currently, the optical and the X-ray data analysis have been completed; the flux density measurements and the VLBI observations in the radio band are in the process of data reduction, and the results will be presented in a future publication. We use the preliminary

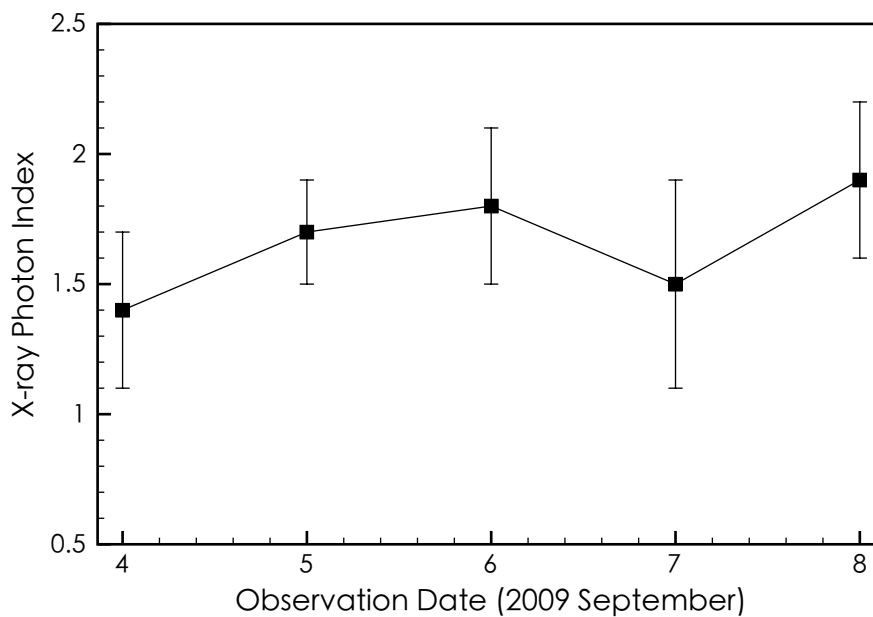


Figure 3.9: The variation of the photon index measured by *Swift*/XRT during the 5-day multiwavelength campaign.

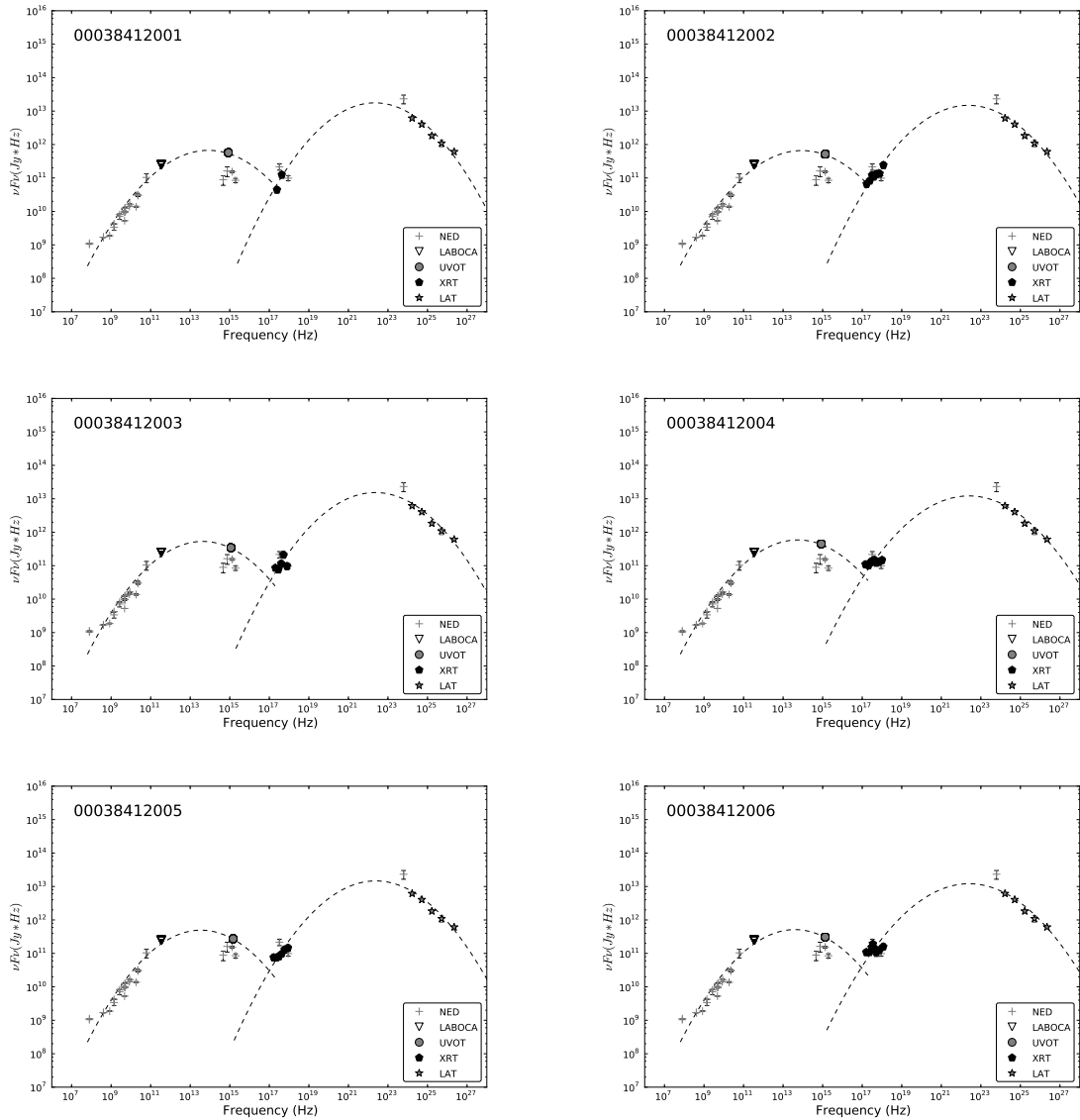


Figure 3.10: The broadband SED of PKS 2052–47 from the radio to the γ -ray band. As indicated in the lower-right corner of each plot, different symbols distinguish the data sources. The NED archival data, the LABOCA data, and the LAT data are the same for all of the six plots; only the *Swift* UVOT and XRT data are different. On the upper-left corner, the *Swift* observation ID of PKS 2052–47 is marked in each plot.

results of APEX/LABOCA, together with the available *Swift* UVOT/XRT and *Fermi*/LAT data to construct the broadband SED of PKS 2052–47. We obtained the SED for all the six epochs of *Swift* observation, and we derived the peak values of the synchrotron and the IC humps in the SED. We see a possible decreasing trend with time in the values of $\nu_{\text{peak}}^{\text{sync}}$, $\nu F_{\nu}^{\text{sync}}$, and νF_{ν}^{IC} .

To further understand the physical mechanism of PKS 2052–47, we plan to apply physical model to the broadband SED of this source. With the good frequency coverage of data, we will be able to constrain the physical parameters in the jet of PKS 2052–47. The values from modeling should help us to better understand the physics at work and emission mechanisms of this flaring blazar.

4 The Broadband Spectral Energy Distribution of the MOJAVE Sample

The study of the broadband SEDs can provide a big amount of information to understand the emission mechanisms of extragalactic jets (see Section 1.4.2). With the presence of the *Swift* (launched in 2004) and *Fermi* (launched in 2008) missions, together with ground-based instruments (e.g., Table 1.1), this is possible with unprecedented data quality covering from radio to very-high-energy bands. Given simultaneous observations in different bands, SEDs can be constructed, and physical models for the jet emission can be applied to the observational data.

In this chapter, I will present our broadband SED study on a radio-selected AGN sample. We constructed a simultaneous SED catalog for 135 sources, and to get an estimate of the brightness peak and the peak frequency of the synchrotron and the IC humps, we applied polynomial fits in the $\log \nu - \log \nu F_\nu$ plane. In Section 4.1, I will introduce the statistically-complete sample. The data collection and astronomical facilities involved will be described in Section 4.3. In Section 4.4, the procedures of data analysis will be described. The broadband SED of the MOJAVE sources will be presented in Section 4.5, and a discussion of the relationship between the properties derived in X-rays and in the broadband SED will be presented in Section 4.6.

4.1 The MOJAVE Sample

The Monitoring Of Jets in Active galactic nuclei with VLBA Experiments¹ (MOJAVE) program has been studying a statistically-complete sample of radio-loud AGN using the VLBA at 15 GHz (Lister et al. 2009a). The MOJAVE project is a continuation of the VLBA 2 cm Survey (Kellermann et al. 1998; Zensus et al. 2002; Kellermann et al. 2004; Kovalev et al. 2005), which studied the parsec-scale jets of 170 AGNs monitored from 1994 to 2002 (see Table 4.1). Based on the knowledge obtained from the VLBA 2 cm Survey, the MOJAVE program started to monitor a complete sample of AGNs in 2002, with the selection criteria listed below:

1. J2000.0 declination $\geq -20^\circ$.
2. Galactic latitude $|b| \geq 2.5^\circ$.
3. Total 15 GHz VLBA flux density ≥ 1.5 Jy (2 Jy for southern sources) at any epoch during the period 1994–2003.

¹<http://www.physics.purdue.edu/MOJAVE/>

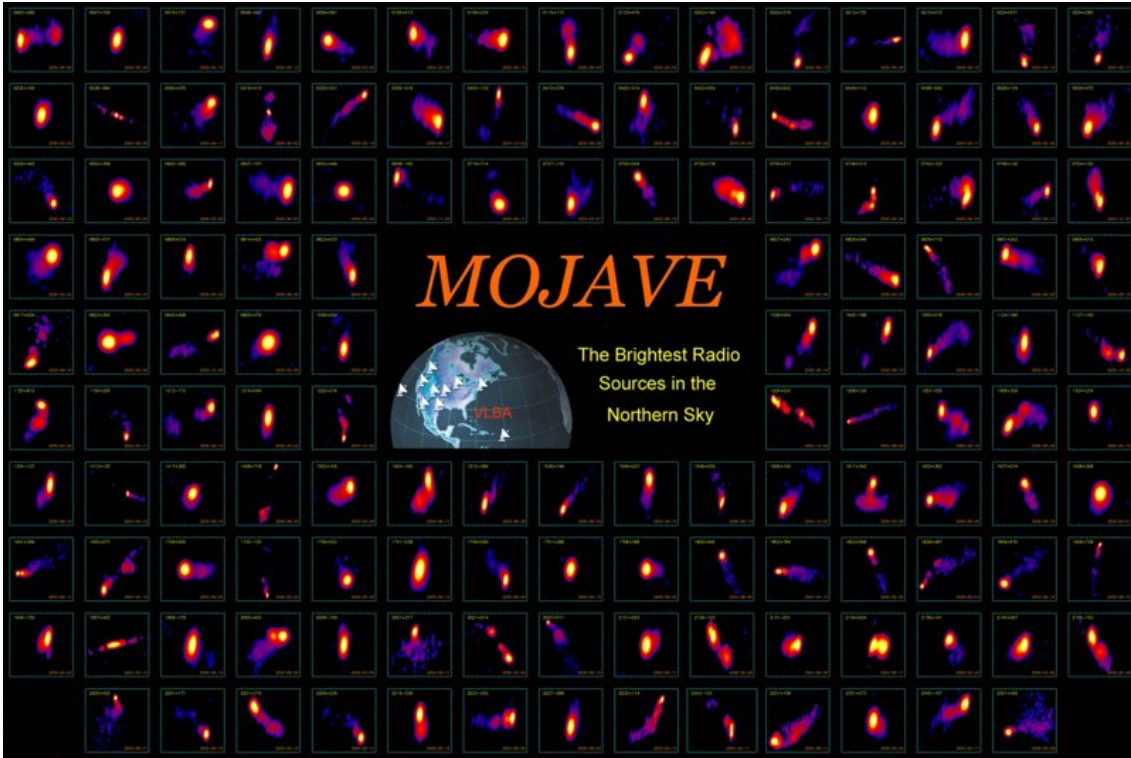


Figure 4.1: Stacked images of 135 MOJAVE I sources (image credit: the MOJAVE collaboration).

Table 4.1: Different phases of the MOJAVE project.

Project	Duration	Frequency	Sample	Reference
VLBA 2 cm Survey	1994–2002	15 GHz	170 AGNs	Zensus et al. (2002)
MOJAVE I ¹	2002–2005	15 GHz	135 AGNs	Lister et al. (2009a)
MOJAVE II	2005–2009	15 GHz ²	191 AGNs	
MOJAVE III ³	2009~ present	15 GHz	~300 AGNs	Lister (2010)

¹ The statistically complete sample.

² One epoch of observations also includes 8 and 12 GHz

³ Including 1 *Fermi*-MOJAVE sample.

Since the 1990s, the VLBA 2 cm Survey and the MOJAVE program have provided a long-term study of the physical parameters of parsec-scale jets at 15 GHz, such as apparent speed, brightness temperature, Lorentz factor, etc. The MOJAVE I sample consists of 135 bright AGNs (see Figure 4.1), which are mostly blazars, and are very active across the electromagnetic spectrum. With their jets being highly Doppler-boosted, blazars are good candidates for studying outflows, because their emission is jet-dominated with less contamination from other sources (e.g., the accretion disk). The MOJAVE program is currently observing ~300 AGN in the northern sky. Apart from continuously monitoring the MOJAVE I sample, the source list also includes: (1) all previously known EGRET γ -ray AGN with $\text{DEC} > -20^\circ$; (2) 33 low-luminosity AGN (15 GHz luminosity $< 10^{33} \text{ erg s}^{-1}$); (3) six GHz-peaked spectrum sources; (4) 11 AGN of the 2 cm Survey with unusual kine-

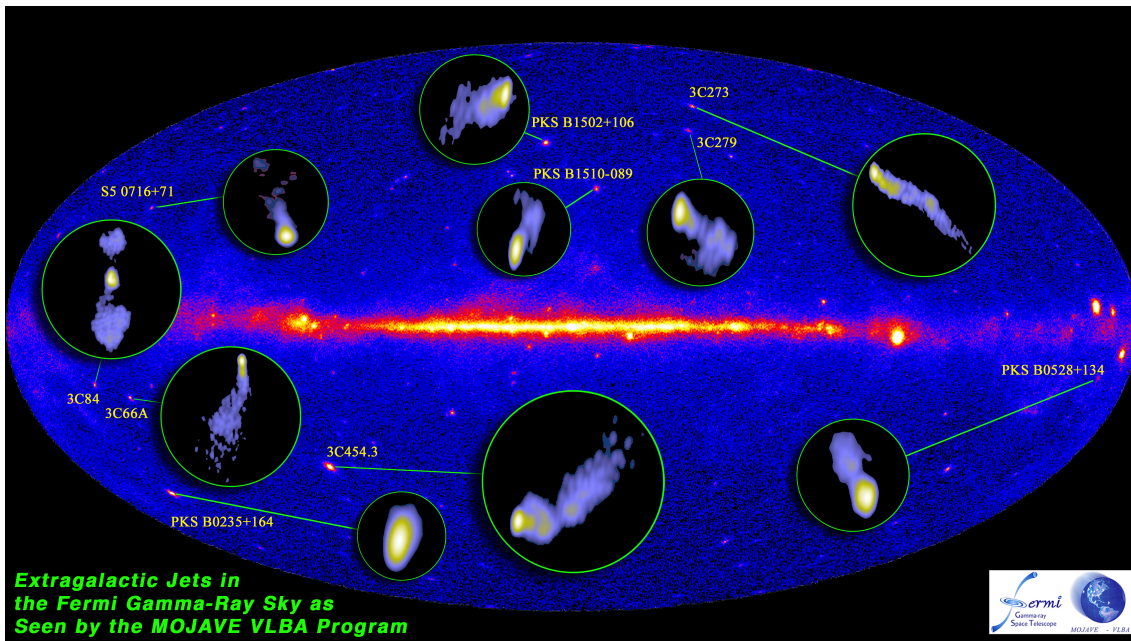


Figure 4.2: *Fermi*/LAT whole-sky map after three-month in orbit, overlaid with MOJAVE VLBI images (image credit: M. Kadler).

matics; (5) the brightest *Fermi*/LAT AGN with a flux density $S_{15\text{GHz}} > 200$ mJy. After one year of *Fermi*'s operation, the radio- γ -selected sample has finalized to 99 sources based on the *Fermi*/LAT first AGN catalog (1FGL; Abdo et al. 2010c), and is called 1 *Fermi*-MOJAVE (1FM) sample (Lister 2010). Figure 4.2 illustrates γ -bright AGNs in the *Fermi* whole-sky map as seen by VLBI.

4.1.1 Parsec-scale Jet Properties and High Energy Emission

The results from the MOJAVE team indicate that blazars usually show apparent superluminal motions in their inner radio-jets (e.g., Kellermann et al. 2004 and Lister et al. 2009b). This might be related to variability at higher energies, such as X-rays and gamma-rays. All of the MOJAVE sources are X-ray emitters (Kadler 2005), and recent results also show that the gamma-ray brightness of AGN is correlated with VLBI jet properties. Kovalev et al. (2009) studied the MOJAVE sources which are detected by *Fermi*/LAT at its first 3-month operation (*Fermi* LAT 3-month bright AGN source list (LBAS); see Abdo et al. 2009b). They found that the γ -ray photon flux correlates with compact radio flux density, and the *Fermi*/LAT-detected MOJAVE sources have higher brightness temperature compared with the non-LAT MOJAVE sources. Lister et al. (2009c) showed that the MOJAVE sources in the LBAS sample have higher apparent jet speeds than the non-LBAS sources with a median of $15c$ and a value up to $34c$. Pushkarev et al. (2009) investigated the apparent opening angles of the γ -bright MOJAVE sources, and found that the jet opening angles are preferentially larger for the γ -bright sources. Savolainen et al. (2010) found that the LAT-detected blazars have higher Doppler factors than non-LAT ones, additionally, γ -bright blazars have a narrower viewing angle in the comoving frame as well. Pushkarev et al. (2010b) investigated the time delays between the radio and the

γ -ray band using the observations by the VLBA at 15.4 GHz and the *Fermi*/LAT. They found a ~ 1.2 months time delay leaded by γ -ray emission. By studying the correlation between the γ -ray emission and the radio emission from different parts of AGN, they suggest that the γ -ray photons are produced within the compact opaque parsec-scale core of AGN.

4.2 The Project

Based on current models, high-energy emission could be generated from collimated jets composed of relativistic charged particles. To investigate the emission mechanisms and to pin down the emitting regions, we constructed the broadband SED catalog for the MOJAVE I sources. The 135 MOJAVE AGN are bright enough to provide high-quality SEDs, and the completeness of the sample allows us to study statistical properties with confidence. In this Chapter, we present the MOJAVE SED catalog. We modeled the two humps of the SED by two 2nd- or 4th- degree polynomial fits to the data in a $\log \nu$ - $\log \nu F_\nu$ plane. In a near future, we plan to apply physical SED models to all sources, in order to derive the physical parameters related to the emission (e.g., electron and photon distribution, accretion rate, magnetic field) of the jet and to understand the physical conditions in AGN.

The *Fermi*/LAT launched in August 2008 opens a new window to study the high-energy emission of extragalactic jets, and it has been collecting data with its whole-sky survey capability. In the mean time, the *Swift* also serves as a great complement with the *Fermi* observatory to study the spectra of AGN in optical, X-ray, and gamma-ray band. To study the X-ray properties of the MOJAVE sample, a dedicated *Swift* fill-in survey has been conducted since 2007 for the MOJAVE sample (P. I.: M. Kadler), and it provides simultaneous optical and X-ray observations. *Fermi*/LAT has detected two thirds of the MOJAVE sources (Abdo et al. 2010c, see Figure 4.2 for the whole-sky map), and *Fermi*/LAT upper-limit values have been determined for all remaining objects (M. Böck, priv. comm.). Furthermore, all MOJAVE sources have very good flux-density sampling in the radio spectrum.

4.3 Data Acquisition

Based on the available observations that *Swift* provides, we choose one epoch after *Fermi* entered operations (August 2008) for each source, and collect (quasi-)simultaneous multiwavelength data. The UMRAO monitoring program (see Section 4.3.1) has a good time sampling to all MOJAVE sources, and for most of the sources we have UMRAO and *Swift* datasets within 1 month, which is fairly good considering that the variability in the radio band is usually not dramatic in a monthly scale. The data from the F-GAMMA monitoring program (see Section 4.3.2), although are less densely sampled in time, have a 3-month scale of simultaneity with the *Swift* data. We include the γ -ray data from the first *Fermi*/LAT catalog (1 FGL; Abdo et al. 2010b, see Section 4.3.4), as for the hard X-ray, we include the *Swift*/BAT 22-month catalog result (see Section 4.3.3). We also include

Table 4.2: Facilities from radio to gamma-rays and bands used in this project.

Facility	Bands	Observing band
VLBA ^a	Radio	15 GHz
UMRAO	Radio	4.8, 8, 14.5 GHz
Effelsberg ^b	Radio	2.64, 4.85, 8.35, 10.45, 14.6, 23.05, 32 GHz
IRAM/Pico Veleta ^b	Millimeter	3, 2, 1 mm
APEX ^b	Millimeter	0.8 mm
<i>Swift</i> /UVOT	UV-Optical	170–650 nm
<i>Swift</i> /XRT	X-ray	0.2–10 keV
<i>Swift</i> /BAT	X-ray	15–150 keV
<i>Fermi</i> /LAT	gamma-ray	20 MeV to >300 GeV

^a The MOJAVE program.

^b The F-GAMMA project.

the historical data from the NASA/IPAC Extragalactic Database (NED)², which would help us to see whether the source is variable. If the NED data points don't deviate much from our simultaneous dataset, we keep the NED points in the broadband SED fitting, in order to increase the frequency coverage. If the source is highly variable, we exclude old measurement and only include the most recent ones.

In this section, I will introduce the facilities that we used when collecting data for the MOJAVE SED catalog. Table 4.2 lists the facilities that contributed data to this project.

4.3.1 University of Michigan Radio Astronomy Observatory

Since August 1984, the 26-meter UMRAO radio telescope³ is monitoring systematically the flux- and position-limited Pearson-Readhead sample (Pearson and Readhead 1981, 1988) at 14.5, 8.0, and 4.8 GHz (Aller et al. 1985, 2003). And from that time, the UMRAO dish has provided the community two decades of total flux density monitoring on bright AGNs. All of the MOJAVE I sources have UMRAO monitoring data until now, and the linearly polarized flux measured by the UMRAO typically has a high signal-to-noise ratio on the order of a few percent (Aller et al. 1996).

The telescope was constructed in 1958, and at that time, the Michigan dish was one of the largest radio telescopes in the world. Since 1977, the telescope was placed under full control of a computer system, and this allows to obtain data automatically. The dish surface was constructed from doubly curved panels of aluminum sheeting, and it deviates by less than 0.125 inches from a true paraboloid. The polar and declination axes are aligned to within an accuracy of 20 arcsec.

²<http://nedwww.ipac.caltech.edu/>

³<http://www.astro.lsa.umich.edu/obs/radiotel/>



Figure 4.3: The radio telescopes used in the F-GAMMA project. Left: the Effelsberg 100 m telescope; upper-right: the IRAM 30 m telescope; bottom-right: the APEX 12 m telescope.

4.3.2 *Fermi*-GST AGN Multi-frequency Monitoring Alliance

The F-GAMMA project⁴ (Fuhrmann et al. 2007, Angelakis et al. 2010) is a monthly-monitoring program which samples the radio continuum spectra of *Fermi*/LAT AGNs. Initially, the project was started in January 2007 to observe ~ 60 AGNs, which were predicted to be detected by *Fermi*/LAT using the Effelsberg 100 m telescope. Since January 2010, roughly 60 sources have been monitored monthly with Effelsberg 100 m telescope, the IRAM 30 m telescope, and the APEX 12 m telescope. Among the F-GAMMA sources, there are about 46 objects present in the MOJAVE sample, and the sources in the F-GAMMA sample change slightly based on the findings with the *Fermi*/LAT. The frequency range includes centimeter, millimeter, infrared and optical bands (see Table 4.2).

The Effelsberg 100 m Telescope The Effelsberg telescope, operated by the Max-Planck-Institut für Radioastronomie, is one of the largest fully steerable telescopes on earth since its operations started in 1972. Since construction, it has been continuously improved on antenna surface, receivers, and electronics. The Effelsberg telescope provides high-sensitivity, fast frequency-switching, polarization capabilities, and broad frequency coverage. Since January 2007, an initial sample of ~ 50 blazars were monitored by the Effelsberg telescope prior to the *Fermi*'s launch. Currently, the sample has increased to 61 sources to follow the brightest *Fermi* blazars (Angelakis et al. 2010), and 46 of the sources

⁴<http://www.mpifr-bonn.mpg.de/div/vlbi/fgamma/>

are in the MOJAVE I sample. The Effelsberg team members in the monitoring program are L. Fuhrmann (P. I.), E. Angelakis, J. A. Zensus, T. P. Krichbaum, N. Marchili, and I. Nestoras.

IRAM The IRAM 30 m telescope⁵ is located on Pico Veleta near Granada in Spain. Constructed by the MPIfR in the 1980s, it is operated by the Institut de Radioastronomie Millimétrique, with a 40% participation of Germany, and it is a sensitive millimeter telescope equipped to observe at 3, 2, 1, and 0.8 mm wavelengths, and it has joined the F-GAMMA project.

The APEX Telescope The Atacama Pathfinder Experiment (APEX) is a 12 m sub-millimeter telescope located in Chile⁶, and it serves as a pathfinder for the Atacama Large Millimeter Array. Constructed by the MPIfR, it was officially inaugurated in September 2005, and is operated by the MPIfR (50%) European Southern Observatory (27%), and Onsala Space Observatory (23%); 10% of the observing time is granted to the host country, Chile. The team members involved in the FGAMMA-APEX project are L. Fuhrmann (P.I.), S. Larsson (Onsala Observatory), E. Angelakis, J. A. Zensus, T. P. Krichbaum, N. Marchili, and I. Nestoras.

4.3.3 The *Swift* Gamma-Ray Burst Mission

NASA's *Swift* satellite is a mission dedicated to the study of gamma-ray burst science, and it carries three instruments onboard to observe gamma-ray bursts and afterglows in the gamma-ray, X-ray, UV, and optical bands (Figure 4.4). It is designed to obtain the spectra from optical to hard X-ray band immediately after gamma-ray bursts are detected. In this way, the ability of simultaneous multi-band measurements serves as an ideal instrument for AGN SED studies as well. The *Swift* spacecraft was launched on 20 November 2004, and its operation started on December 8. Since then, it provides the community a unique chance to follow active sources promptly with multiband observations. In the following paragraphs, I will introduce the three main instruments on board *Swift*.

Burst Alert Telescope The *Swift* Burst Alert Telescope (BAT; Gehrels et al. 2004) covers the energy band of 15–150 keV (see Figure 4.4). It was designed to provide critical GRB triggers and positions for instant follow-up observations, and it has a large field-of-view to detect burst events. In the first 22-month all-sky survey of *Swift*/BAT, 266 out of 461 sources were associated with Seyfert galaxies or blazars (Tueller et al. 2010), among which, 18 are MOJAVE sources (see Figure 4.5). We take the 22-month spectra of the BAT-detected sources and include them in the MOJAVE SED study as a first approach. To obtain simultaneous observations for all the MOJAVE I sources, we have contacted the *Swift*/BAT team, who agreed to collaborate and extract the BAT data for the 135 sources. These results are not included in this thesis, but will be presented in Chang et al., in preparation.

⁵<http://iram.fr/IRAMES/>

⁶<http://www.mpifr-bonn.mpg.de/div/mm/apex.html>

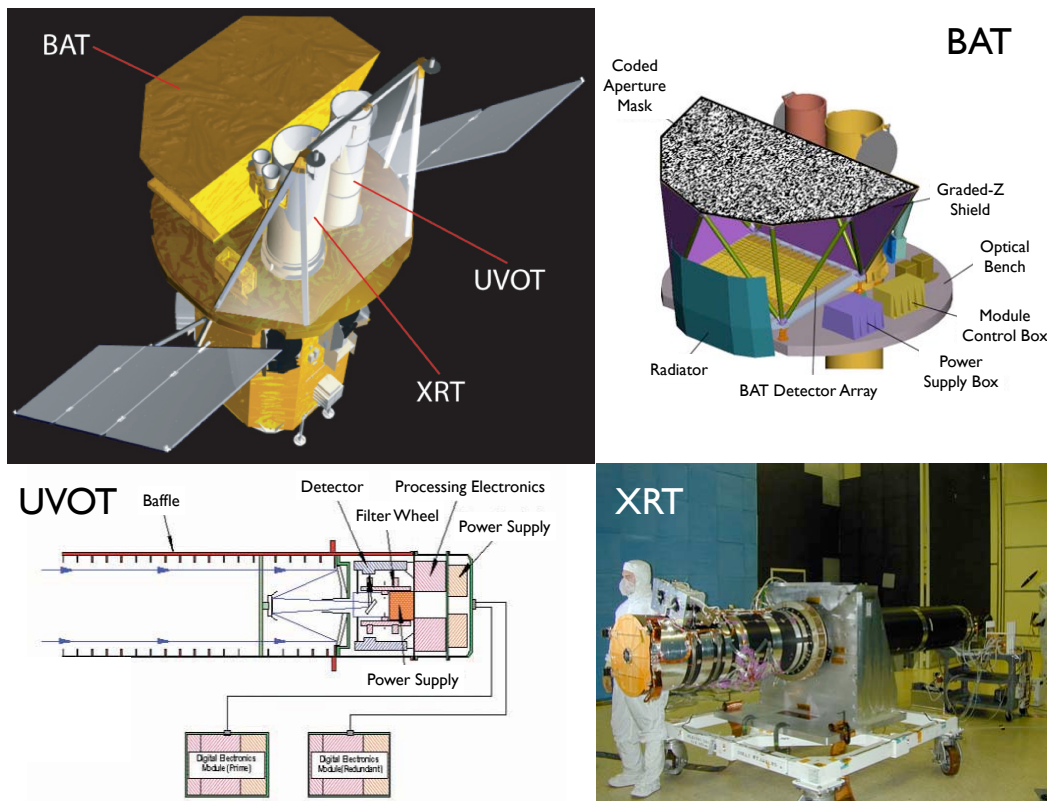


Figure 4.4: The *Swift* satellite (upper-left) and the three instruments on board: the burst alert telescope (upper-right), the X-ray telescope (bottom-right), and the UV-optical telescope (bottom-right).

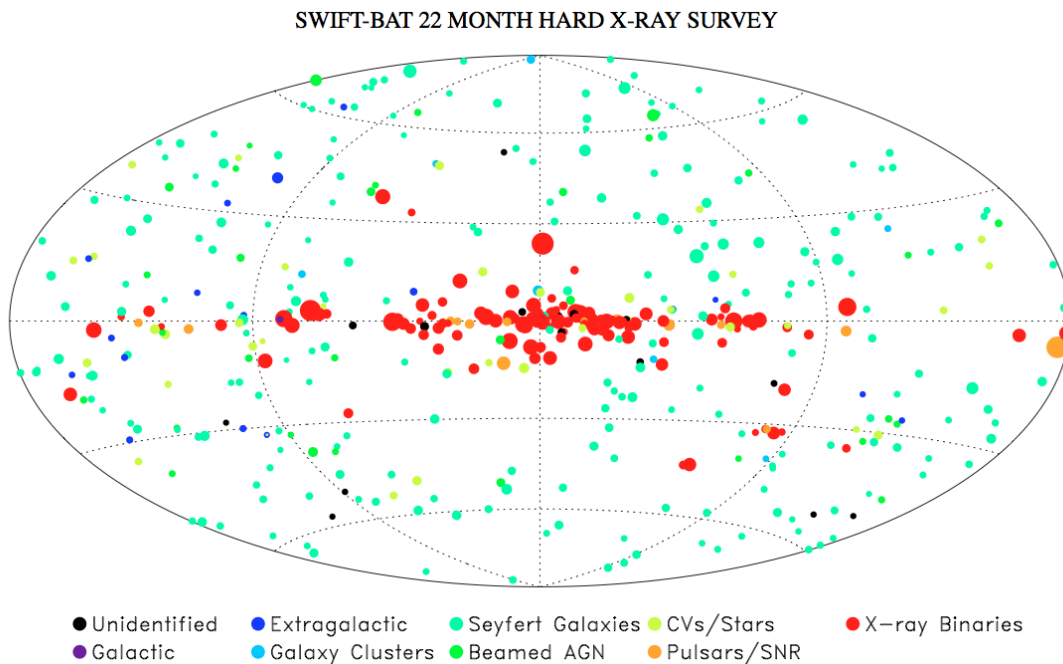


Figure 4.5: All-sky map of the *Swift*/BAT 22-month survey sources. There are 229 Seyfert Galaxies, 32 beamed AGNs, and 17 extragalactic sources in the map (Tueller et al. 2010).

Table 4.3: *Swift*/UVOT sensitivity limits. For an A0 star having the apparent magnitude $m_B=22.3$ with an integration time of 1000 s, the counts measured by each filter of UVOT are listed below.

UVOT filter	Wavelength (Å)	counts
V	5468	143
B	4392	441
U	3465	217
UVW1	2600	99
UVM2	2246	53
UVW2	1928	87
White	-	1306

http://heasarc.gsfc.nasa.gov/docs/swift/about_swift/uvot_desc.html

X-Ray Telescope The *Swift*/XRT (see Figure 4.4) is a focusing X-ray telescope with a 110 cm^2 effective area, 23.6×23.6 arcsec field of view (FOV), 18-arcsec resolution, and 0.2–10 keV energy range. The XRT has several readout modes:

1. Photodiode mode: this is a fast timing mode to produce accurate timing information for very bright sources, and it is suitable for fluxes below $1.44\times 10^{-6}\text{ erg s}^{-1}\text{ cm}^{-2}$.
2. Imaging mode: this is similar to photon-counting mode. The charged-coupled device (CCD) is operated like an optical CCD; photon pileup⁷ (Davis 2001a) is allowed, and there is no on-board processing on photon event recognition.
3. Window timing (WT) mode: WT mode a high-gain mode to achieve high resolution timing (2.2 ms) with one-dimensional position information and spectroscopy. This mode is restricted to a 200-column window covering the central 8 arcminutes of the field of view (FOV). Window timing mode is useful for fluxes below $1.2\times 10^{-6}\text{ erg s}^{-1}\text{ cm}^{-2}$ and has no pileup for fluxes below $1.44\times 10^{-8}\text{ erg s}^{-1}\text{ cm}^{-2}$ (Mineo et al. 2006).
4. Photon-counting (PC) mode: PC mode uses traditional frame transfer operation of an X-ray CCD. It retains full imaging and spectroscopic resolution, but the time resolution is only 2.5 seconds. This mode is operated only when sources are at very low fluxes (below $2.4\times 10^{-11}\text{ erg s}^{-1}\text{ cm}^{-2}$).

For almost all of the MOJAVE sources, PC mode is used for *Swift*/XRT observations, mostly because the sources are weak X-ray emitters, radio-selected, and extragalactic.

UV-Optical Telescope The UVOT is a 30-cm modified Ritchey-Chrétien telescope (see Figure 4.4) equipped with a grism filter, and its FOV is 17×17 arcmin with 2048×2048 CCD pixels. The seven filters on board UVOT cover the wavelength range of 170–650 nm in UV and optical band (see Figure 4.6), therefore it is capable of spectroscopic observations.

⁷Pileup in CCD is produced by the detection of two or more photons within the same region at the same gate time interval, and the detector is unable to resolve individual signals. The resultant effect is a lowering of the source flux and a hardening of the observed spectrum.

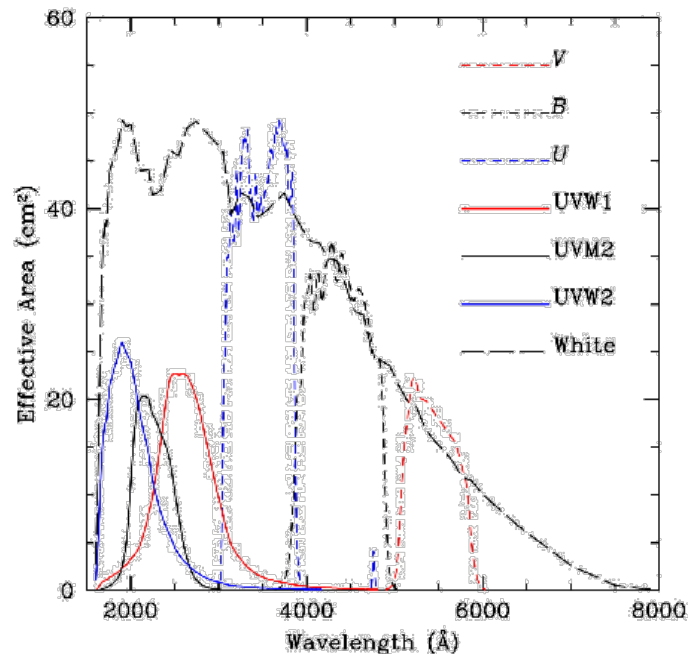


Figure 4.6: Effective area for the seven UVOT filters. Image credit: NASA *Swift* team.

4.3.4 *Fermi* Gamma-ray Space Telescope

NASA's *Fermi* Gamma-ray Space Telescope was launched on 11 June 2008, and there are two instruments on board: Gamma-ray Burst Monitor (GBM) and Large Area Telescope (LAT). The main instrument is LAT, and the GBM is used for gamma-ray burst detections. For more details of the LAT and the GBM, please see Atwood et al. (2009) and Meegan et al. (2009).

Large Area Telescope The LAT on board *Fermi* is an imaging high-energy telescope covering the energy range from 20 MeV to >300 GeV. The field of view of the *Fermi*/LAT covers $\sim 20\%$ of the sky, and the whole sky is scanned every three hours.

The LAT is a pair-conversion telescope. It detects gamma-ray photons by tracking the trajectories of the produced electron-positron pairs, and reconstructs the path of the incident photons (see Figure 4.7). Incident radiation first passes through an anticoincidence shield, which is sensitive to charged particles, then through thin layers of high atomic-number material called conversion foils, which would cause photon conversions to happen. After a conversion, the trajectories of the resulting electron and positron are measured by particle tracking detectors, and their energies are then measured by a calorimeter. The characteristic gamma-ray signature in the LAT is therefore (1) no signal in the anticoincidence shield, (2) more than one track starting from the same location within the volume of the tracker, and (3) an electromagnetic shower in the calorimeter.

The LAT consists of a 4×4 array of identical towers, and each 40×40 cm² tower comprises a tracker, calorimeter and data acquisition module. The tracking detector consists of 18 layers of silicon strip detectors. The calorimeter in each tower consists of eight layers of 12 CsI bars which are read out by photodiodes, and the total thickness is 10 radiation

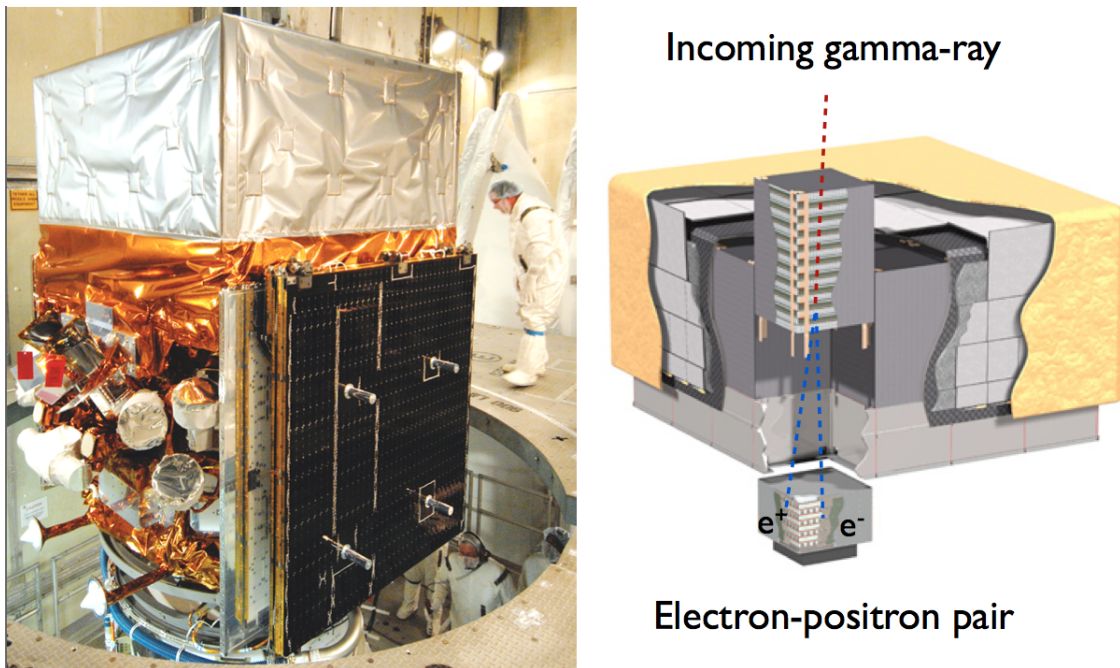


Figure 4.7: *Fermi* Gamma-ray Space Telescope (left) and the illustration of the Large Area Telescope on board (right).

lengths. The calorimeter measures three-dimensional profiles of showers, which permits corrections for energy leakage and enhances the capability to discriminate hadronic cosmic rays. The anticoincidence shield covers the array of towers, and is used to detect and eliminate cosmic rays.

Gamma-ray Burst Monitor The GBM includes two sets of detectors: twelve sodium iodide (NaI) scintillators, each 12.7 cm in diameter by 1.27 cm thick, and two cylindrical bismuth germanate (BGO) scintillators, each 12.7 cm in diameter and 12.7 cm in height. The NaI detectors are sensitive in the lower end of the energy range, from a few keV to about 1 MeV and provide burst triggers and locations. The BGO detectors cover the energy range 150 keV to 30 MeV, providing a good overlap with the NaI at the lower end and with the LAT at the high end.

Gamma-ray bursts will be detected by a significant change in count rate in at least two of the NaI scintillators; the trigger algorithm will be programmable. Time-tagged event data (with 5 μ s resolution) will be recorded continuously to provide ~ 50 s of pre-trigger information for gamma-ray bursts. After a trigger, the GBM processor will calculate preliminary position and spectral information for telemetry to the ground and possible autonomous repointing of *Fermi*. The GBM is expected to detect ~ 200 gamma-ray bursts per year.

After the first 11-month survey, *Fermi*/LAT has detected 709 AGNs (Abdo et al. 2010c), in which 85 of the MOJAVE sources are included (see Figure 4.8). In this study, we use the results of the 11-month catalog of *Fermi*/LAT to construct the MOJAVE SED catalog. Table 4.4 shows a list of MOJAVE sources together with the corresponding associations

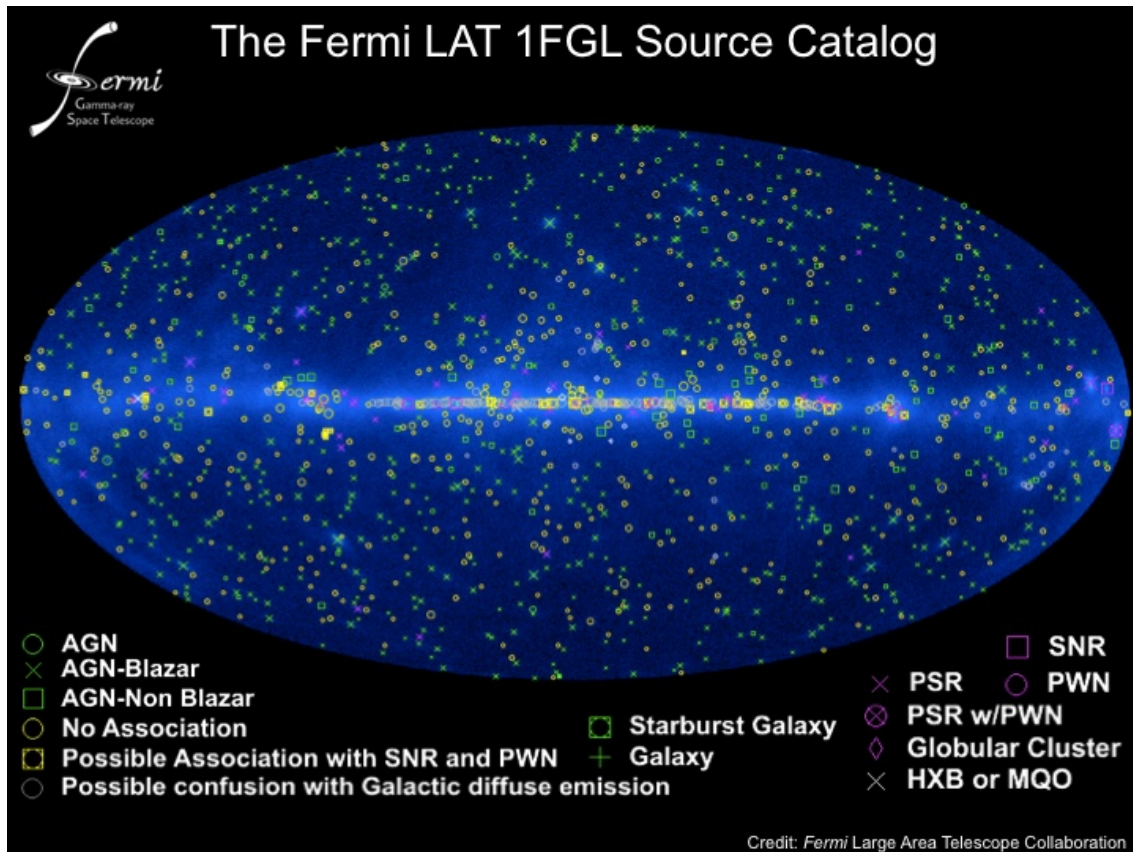


Figure 4.8: The *Fermi*/LAT all-sky map after 1-year of operation (Credit: *Fermi* LAT Collaboration).

of the 1FGL catalog. The redshift z , the apparent velocity $\beta_{\text{app,max}}$ as published by the MOJAVE team (Lister et al. 2009b), and the optical class are listed in the same table as well.

4.4 Data Analysis

As mentioned in the beginning of this Chapter, we chose one epoch of *Swift* observations for each source, and construct a simultaneous broadband SED according to the time of the chosen epoch. Here I summarize the procedures that we used to construct a SED:

1. Check the available archival *Swift* data from the HEASARC website⁸. Examine observation log, and if available, download the data with the longest integration time after August 2008. If there were no observations after August 2008, submit a request of *Swift* Target of Opportunity (ToO⁹; see Table 4.5 for a list of ToO sources).
2. The data of UVOT and XRT were analyzed with HEASOFT version 6.8¹⁰ following

⁸<http://heasarc.gsfc.nasa.gov/docs/archive.html>

⁹<http://www.swift.psu.edu/too.html>

¹⁰<http://heasarc.nasa.gov/lheasoft/>

the procedures described in Section 4.4.1 and 4.4.2. The *Swift* X-ray spectra were fitted with XSPEC version 12.5.1.

3. If the source inspected is in the *Swift*/BAT 22-month catalog, we downloaded the data from the BAT 22-month source catalog website¹¹.
4. We include the UMRAO data from the internal MOJAVE database. All of the MOJAVE sources have recent observations from the UMRAO monitoring program.
5. We include the F-GAMMA data points compiled by the F-GAMMA team (I. Nestoras, priv. comm.).
6. We include the historical data points from the NED website. We use the error bars provided by the database. According to differences of data qualities and the variability of the source, we exclude very old measurements.

Table 4.4: MOJAVE source list with 1FGL association.

IAU Name (1)	Alias (2)	<i>Fermi</i> 1FGL (3)	z (4)	$\beta_{\text{app,max}}$ (5)	Optical Class (6)
0003–066	NRAO 005		0.347	2.89±0.24	B
0007+106	III Zw 2		0.0893	0.971±0.094	G
0016+731			1.781	6.74±0.39	Q
0048–097*		J0050.6–0928	–	–	B
0059+581		J0102.8+5827	0.644	11.09±0.85	Q ^d
0106+013	4C +01.02	J0108.6+0135	2.099	26.5±3.9	Q
0109+224		J0112.0+2247	0.265	–	B
0119+115			0.570	17.10±0.67	Q
0133+476*	DA 55	J0137.0+4751	0.859	13.0±2.5	Q
0202+149	4C +15.05	J0204.5+1516	0.405	6.4±1.3	Q ^c
0202+319		J0205.3+3217	1.466	8.30±0.75	Q
0212+735		J0217.8+7353	2.367	7.64±0.27	Q
0215+015	OD 026	J0217.9+0144	1.715	34.2±2.1	Q
0224+671	4C +67.05		0.523	11.64±0.46	Q ^d
0234+285*	CTD 20	J0237.9+2848	1.207	12.27±0.84	Q
0235+164*		J0238.6+1637	0.940	–	B ^a
0238–084	NGC 1052		0.005037	0.347±0.010	G
0300+470	4C +47.08	J0303.1+4711		–	B
0316+413	3C 84	J0319.7+4130	0.0176	0.311±0.059	G
0333+321	NRAO 140		1.259	12.76±0.19	Q
0336–019	CTA 26	J0339.2–0143	0.852	22.4 ±3.7	Q
0403–132		J0405.6–1309	0.571	19.70±0.87	Q
0415+379	3C 111	J0419.0+3811	0.0491	5.865±0.094	G
0420–014*		J0423.2–0118	0.914	7.35±0.98	Q
0422+004		J0424.8+0036		–	B

¹¹<http://heasarc.gsfc.nasa.gov/docs/swift/results/bs22mon/>

Table 4.4 – *continued*

IAU Name (1)	Alias (2)	<i>Fermi</i> 1FGL (3)	z (4)	$\beta_{\text{app,max}}$ (5)	Optical Class (6)
0430+052	3C 120		0.033	5.38 ± 0.16	G
0446+112		J0448.6+1118		–	U ^b
0458–020		J0501.0–0200	2.286	16.52 ± 0.80	Q
0528+134*		J0531.0+1331	2.070	19.20 ± 0.42	Q
0529+075	OG 050	J0532.9+0733	1.254	12.7 ± 1.5	Q ^d
0529+483		J0533.0+4825	1.162	19.8 ± 3.0	Q
0552+398	DA 193		2.363	0.363 ± 0.091	Q
0605–085	OC –010	J0608.2–0837	0.872	19.79 ± 0.61	Q
0607–157			0.324	3.9 ± 1.1	Q
0642+449	OH 471		3.396	0.76 ± 0.11	Q
0648–165		J0650.6–1635		–	U ^d
0716+714*		J0721.9+7120	0.310	10.07 ± 0.35	B
0727–115*		J0730.3–1141	1.591	–	Q
0730+504			0.720	14.1 ± 4.2	Q
0735+178	OI 158	J0738.2+1741		–	B
0736+017	OI 061	J0739.1+0138	0.191	14.44 ± 0.94	Q
0738+313	OI 363		0.631	10.8 ± 1.1	Q
0742+103			2.624	–	Q ^d
0748+126		J0750.6+1235	0.889	18.37 ± 0.82	Q
0754+100		J0757.2+0956	0.266	14.4 ± 1.2	B
0804+499			1.436	1.83 ± 0.34	Q
0805–077		J0808.2–0750	1.837	$59.1\pm 27.$	Q
0808+019		J0811.2+0148	1.148	13.00 ± 0.81	B
0814+425	OJ 425	J0818.2+4222	0.245	1.71 ± 0.29	B
0823+033		J0825.9+0309	0.506	17.80 ± 0.81	B
0827+243	OJ 248	J0830.5+2407	0.940	22.0 ± 1.9	Q
0829+046	OJ 049	J0831.6+0429	0.174	10.11 ± 0.38	B
0836+710	4C 71.07	J0842.2+7054	2.218	25.38 ± 0.97	Q
0838+133	3C 207	J0840.8+1310	0.681	12.9 ± 1.2	Q
0851+202*	OJ 287	J0854.8+2006	0.306	15.18 ± 0.38	B
0906+015	4C +01.24	J0909.0+0126	1.024	20.66 ± 0.85	Q
0917+624		J0919.6+6216	1.446	15.6 ± 1.2	Q
0923+392	4C +39.25		0.695	4.29 ± 0.43	Q
0945+408	4C +40.24		1.249	18.60 ± 0.86	Q
0955+476			1.882	2.48 ± 0.24	Q
1036+054			0.473	6.15 ± 0.62	Q ^d
1038+064	4C +06.41		1.265	11.87 ± 0.99	Q
1045–188			0.595	8.57 ± 0.69	Q
1055+018*	4C +01.28	J1058.4+0134	0.890	11.0 ± 1.0	Q
1124–186		J1126.8–1854	1.048	–	Q
1127–145		J1130.2–1447	1.184	14.18 ± 0.59	Q
1150+812			1.250	7.09 ± 0.31	Q

Table 4.4 – *continued*

IAU Name (1)	Alias (2)	<i>Fermi</i> 1FGL (3)	z (4)	$\beta_{\text{app,max}}$ (5)	Optical Class (6)
1156+295*	4C +29.45	J1159.4+2914	0.729	24.9±1.8	Q
1213–172				–	U ^d
1219+044	4C +04.42	J1222.5+0415	0.965	2.35±0.41	Q
1222+216	4C +21.35	J1224.7+2121	0.432	21.0±1.9	Q
1226+023*	3C 273	J1229.1+0203	0.158	13.44±0.43	Q
1228+126	M87	J1230.8+1223	0.00436	0.056±0.023	G
1253–055*	3C 279	J1256.2–0547	0.536	20.58±0.79	Q
1308+326*		J1310.6+3222	0.997	27.2±1.2	Q
1324+224		J1326.6+2213	1.400	–	Q
1334–127	PKS 1335–127	J1337.7–1255	0.539	10.26±0.95	Q
1413+135			0.247	1.80±0.17	B
1417+385			1.831	15.4±3.0	Q
1458+718	3C 309.1		0.904	7.0±2.0	Q
1502+106*	4C +10.39	J1504.4+1029	1.839	14.8±1.2	Q
1504–166			0.876	4.31±0.47	Q
1510–089*		J1512.8–0906	0.360	20.2±1.2	Q
1538+149	4C +14.60		0.605	8.73±0.95	B ^a
1546+027		J1549.3+0235	0.414	12.1±1.3	Q
1548+056	4C +05.64	J1550.7+0527	1.422	11.6±1.7	Q
1606+106	4C +10.45	J1609.0+1031	1.226	18.9±1.3	Q
1611+343	DA 406	J1613.5+3411	1.397	14.09±0.60	Q
1633+382	4C +38.41	J1635.0+3808	1.814	29.5±1.6	Q
1637+574	OS 562		0.751	10.6±1.3	Q
1638+398	NRAO 512		1.666	12.3±1.6	Q
1641+399	3C 345	J1642.5+3947	0.593	19.27±0.52	Q
1655+077			0.621	14.4±1.1	Q
1726+455		J1727.3+4525	0.717	2.10±0.77	Q
1730–130	NRAO 530	J1733.0–1308	0.902	35.7±2.1	Q
1739+522	4C +51.37	J1740.0+5209	1.379	–	Q
1741–038			1.054	–	Q
1749+096*	4C +09.57	J1751.5+0937	0.322	6.84±0.78	B ^a
1751+288			1.118	3.07±0.74	Q ^d
1758+388			2.092	2.38±0.34	Q
1800+440			0.663	15.41±0.49	Q
1803+784		J1800.4+7827	0.680	9.0±2.5	B ^a
1807+698	3C 371	J1807.0+6945	0.051	0.104±0.017	B
1823+568	4C +56.27	J1824.0+5651	0.664	20.86±0.49	B ^a
1828+487	3C 380	J1829.8+4845	0.692	13.66±0.39	Q
1849+670*		J1849.3+6705	0.657	30.6±1.5	Q
1928+738	4C +73.18		0.302	8.43±0.34	Q
1936–155			1.657	2.60±0.74	Q
1957+405	Cygnus A		0.0561	0.215±0.059	G

Table 4.4 – *continued*

IAU Name (1)	Alias (2)	<i>Fermi</i> 1FGL (3)	z (4)	$\beta_{\text{app,max}}$ (5)	Optical Class (6)
1958–179		J2000.9–1749	0.650	1.90±0.19	Q
2005+403			1.736	12.2±1.7	Q
2008–159			1.180	7.99±0.95	Q
2021+317	4C +31.56		–	–	U ^d
2021+614	OW 637		0.227	0.159±0.043	G
2037+511	3C 418		1.686	3.30±0.15	Q
2121+053			1.941	13.29±0.57	Q
2128–123			0.501	6.94±0.45	Q
2131–021	4C –02.81	J2134.0–0203	1.285	20.0±1.4	B ^a
2134+004			1.932	5.94±0.41	Q
2136+141	OX 161		2.427	5.43±0.18	Q
2145+067	4C +06.69	J2148.5+0654	0.990	2.50±0.10	Q
2155–152		J2157.9–1503	0.672	18.1±1.8	Q
2200+420*	BL Lac	J2202.8+4216	0.0686	10.57±0.74	B
2201+171		J2203.5+1726	1.076	3.9±4.2	Q
2201+315	4C +31.63		0.295	7.88±0.41	Q
2209+236		J2212.1+2358	1.125	3.43±0.51	Q
2216–038			0.901	5.62±0.53	Q
2223–052	3C 446	J2225.8–0457	1.404	17.34±0.47	Q
2227–088	PHL 5225	J2229.7–0832	1.560	8.1±2.1	Q
2230+114	CTA 102	J2232.5+1144	1.037	15.41±0.65	Q
2243–123			0.632	5.49±0.33	Q
2251+158*	3C 454.3	J2253.9+1608	0.859	14.19±0.79	Q
2331+073		J2334.3+0735	0.401	4.47±0.46	Q ^d
2345–167		J2348.0–1629	0.576	–	Q
2351+456	4C +45.51		1.986	27.1±1.3	Q

Column note: (1) IAU J2000 name; (2) alias name; (3) 1FGL association; (4) redshift; (5) maximum apparent projected speed measured by the MOJAVE program (Lister et al. 2009b); (6) optical class.

* Broadband SED presented in Abdo et al. (2010a)

^a Source classified as a quasar in the Véron-Cetty and Véron (2006) catalog

^b Source classified as a possible BL Lac in the Véron-Cetty and Véron (2006) catalog

^c Source classified as a galaxy in the Véron-Cetty and Véron (2006) catalog

^d Source not listed in the Véron-Cetty and Véron (2006) catalog

4.4.1 *Swift*/XRT Data Reduction

There are several steps from raw X-ray data to obtaining spectral properties such as flux F_X and photon index Γ . In the following paragraphs, the procedures that we use to analyze *Swift*/XRT data will be described.

Table 4.5: Requests of *Swift* target of opportunity (approved and pending, as of August 2010).

IAU Name	<i>Swift</i> Obs. ID	Obs. dates	XRT Exp. Time [sec]	Status
0109+224	-	-	-	ToO required (2010-08-24)*
0202+319	-	-	-	ToO required (2010-09-08)*
0212+735	-	-	-	ToO required (2010-09-11)*
0215+015	-	-	-	ToO required (2010-09-11)*
0552+398	-	-	-	ToO required (2010-11-09)*
0754+100	00036195002	2010-02-27	9546	Observed
0906+015	00036200005	2010-03-10	4388	Observed
	00036200002	2010-03-04	1805	Observed
	00036200006	2010-03-09	1609	Observed
	00036200007	2010-03-10	878	Observed
	00036200003	2010-03-06	116	Observed
	00036200004	2010-03-05	10	Observed
0923+392	00036377005	2010-03-20	5401	Observed
	00036377004	2010-03-17	2034	Observed
	00036377003	2010-03-10	725	Observed
1036+054	00036242004	2010-04-26	3543	Observed
	00036242006	2010-04-28	3432	Observed
	00036242005	2010-04-27	1644	Observed
1213-172	00035036002	2010-03-24	10559	Observed
1219+044	00036330003	2010-04-28	4096	Observed
	00036330002	2010-04-24	3372	Observed
1324+224	00036205004	2010-03-29	7225	Observed
	00036205003	2010-03-28	2149	Observed
1413+135	00036386004	2010-04-03	9941	Observed
1726+455	00036214004	2010-05-03	3784	Observed
	00036214006	2010-05-11	2965	Observed
	00036214003	2010-05-04	2076	Observed
1741-038	00036216003	2010-05-09	6359	Observed
	00036216002	2010-05-09	2146	Observed
2216-038	00036227003	2010-01-06	3991	Observed
	00036227002	2010-01-06	1988	Observed
2351+456	-	-	-	ToO required (2010-08-03)*

* Planned *Swift* ToO submission date, which is the time when the source starts to have 11h right ascension difference w.r.t. the Sun.

Data and Calibration Files The XRT data are in the format of Flexible Image Transport System (FITS), and there are several kinds of files involved in the data calibration processes. The **event file** records the data from the XRT observation. In the event file, it contains the time, position, and intensity of photon incidence. The **response matrix file**¹² (RMF) contains information about the response of the XRT detector to be used during data calibration process. The **ancillary response file** (ARF) contains information of the effective area. Photon counts that are detected can be expressed as (see Davis 2001b):

¹²http://www.swift.ac.uk/XRT-LUX-CAL-108-RMF_v7.pdf

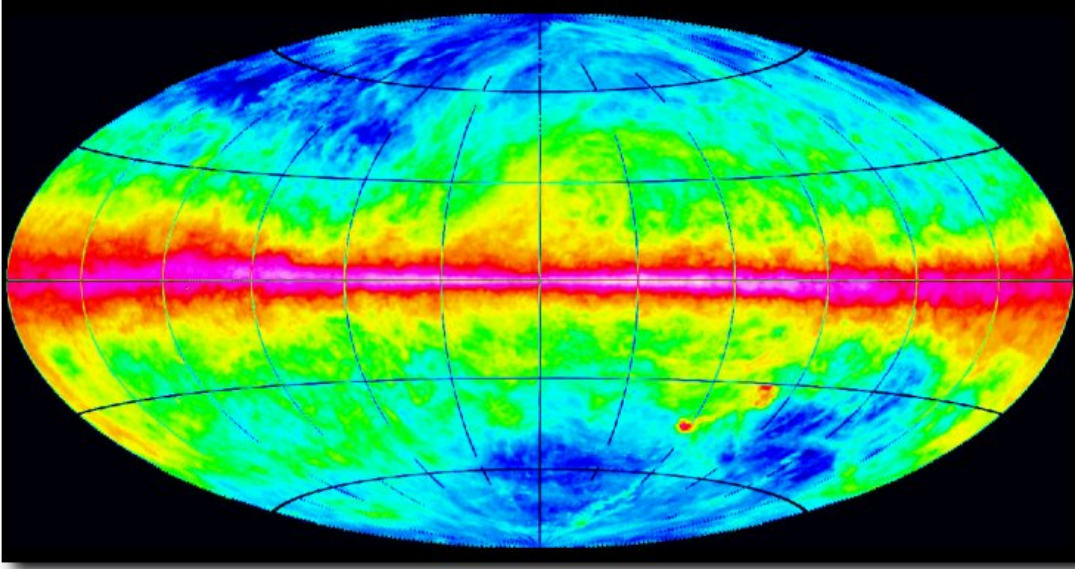


Figure 4.9: HI emission integrated over the velocity range $-400 < v < +400 \text{ km s}^{-1}$ in the LAB dataset, shown in Aitoff projection. The Galactic center is in the middle. The integrated emission ($0 < N_H < 2 \times 10^{22} \text{ cm}^{-2}$, logarithmic scale) yields column densities under the assumption of optical transparency; this assumption may be violated at latitudes within about 10° of the Galactic equator (Image credit: the LAB Survey website).

$$C(h) = \int_0^\infty \sum_i R_i(h, E) A_i(E) S_i(E) dE dT + B(h),$$

where $R(h, E)$ is the response matrix, $A(E)$ is the effective area (ancillary response), $S(E)$ is the source SED, $C(h)$ and $B(h)$ are the source and background counts (event), E is the photon energy, T is the integration time, and h is the pulse height analysis (PHA). When a photon is detected by a solid state detector, the pulse height is proportional to the incoming photon energy. The pulse height analysis aims to sort out the detected electronic pulses and heights from photons, digitize the signal, and store the information to channels for further spectral analysis. A PHA file stores the measured pulse height in channels, which are sort by energy, and it is used for spectral analysis.

Extracting the X-ray Spectrum First, we generate an image from XRT event file using `xselect` in FTOOLS. Based on the image, we select and save the source and background regions which we want to use to extract the spectrum. We extract the source and background spectrum using the command `filter region` in `xselect`. This would generate two spectral PHA files for the source and the background. For later spectral analysis, we need to generate the ARF file using the command `xrtmkarf` in FTOOLS. `xrtmkarf` connects to the HEASARC's calibration database¹³ (CALDB), and use the newest calibration files in the database to generate the ARF file based on the input source spectrum and source position.

¹³<http://heasarc.gsfc.nasa.gov/docs/heasarc/caldb/caldb.intro.html>

Binning the PHA File The PHA file records photon events in channels which are leveled by energy. To perform spectral analysis, it is necessary to bin data and make sure that each energy bin contains sufficient amount of events. To do this, we use the command `grppha` in `FTOOLS`, and we bin the data with the constrain that the minimum raw counts per energy bin should be greater than 20^{14} . Binning (grouping) PHA file is needed before performing spectral analysis in order to obtain a sufficient signal-to-noise value, because we will use χ^2 statistics to evaluate the goodness of fit and error in the next steps.

X-ray Spectral Analysis We perform the spectral analysis in `XSPEC12`. We load the binned data in `XSPEC` and fit the spectrum with an absorbed power-law model $F(E) = K M(E) E^{-\Gamma}$, where E is the energy bin, F is the flux, K is the normalization constant, $M(E)$ is the photoelectric absorption, and Γ is the photon index. The photoelectric absorption $M(E)$ can be described as

$$M(E) = e^{-N_{\text{H}}\sigma(E)},$$

where N_{H} is the equivalent hydrogen column density, $\sigma(E)$ is the cross-section as a function of photon energy. We set a lower limit of N_{H} using the result of the Leiden/Argentine/Bonn (LAB) Galactic HI Survey¹⁵ (Kalberla et al. 2005; see Figure 4.9), in which they measured the Galactic neutral hydrogen by observing λ 21 cm emission of the whole sky. For the abundances of the interstellar medium, we use the `wilm` abundance in `XSPEC` (Wilms et al. 2000), see Balucinska-Church and McCammon (1992) for a detailed discussion about computing the cross section of the interstellar medium.

We applied an absorbed power-law model to fit the X-ray spectra. In Table 4.6, we present a summary of the results of our XRT analysis, such as the observing date (column 3), epochs (column 4), and integration time (column 5) for each MOJAVE source; the galactic (column 6), the intrinsic (column 7), and the uncertainty of the N_{H} values; the photon index Γ_{X} (column 9), the flux F_{X} (column 10), the reduced χ^2 (χ_{red}^2 ; column 11), and the degree of freedom of fit (column 12). The model we applied to fit the X-ray spectrum in `XSPEC` is `phabs(1) × phabs(2) × powerlaw`, where `phabs(1)` is fixed to the Galactic N_{H} value of each source (column 6 in Table 4.6); `phabs2` is let free to be fitted, and the obtained value is the source intrinsic N_{H} value (column 7 in Table 4.6).

¹⁴In our X-ray spectral analysis of this thesis, we only use the threshold of 20 and 25 raw counts per energy bin to group the data, depending on data quality.

¹⁵http://www.astro.uni-bonn.de/~webaiub/english/tools_labsurvey.php

Table 4.6: Results of our *Swift* data analysis of the MOJAVE sources.

B1950 Name (1)	Alias (2)	Obs. Date (3)	Obs. ID (4)	T_{XRT} [s] (5)	Galactic Intrinsic Uncertainty (6) (7) (8)	Γ_X (9)	F_X [10^{-12} erg cm^{-2} s^{-1}] (10)	χ^2_{red} (11)	d.o.f. (12)	
0003-066	NRAO 005	2009-12-27	00036186005	3482	0.0467	0	1.97±0.54	0.975	1.18	3
0007+106	III Zw 2	2010-02-07	00036363005	5702	0.0572	0	1.75±0.09	6.834	1.23	44
0016+731		2009-09-11	00036187005	7403	0.191	0.4	1.96±0.63	0.668	1.02	2
0048-097		2009-05-25	00036364002	9917	0.0322	0.05	2.40±0.05	4.969	1.02	119
0059+581		2008-11-17	00036232006	11060	0.366	0.30	1.90±0.16	1.802	1.01	16
0106+013		2008-02-16	00036757002	5076	0.0232	0.07	2.14±0.47	0.523	1.03	2
0109+224		2006-05-31	00035001003	19492	0.0402	0	1.96±0.11	1.148	1.00	34
0119+115		2009-06-01	00036302003	11019	0.0374	0	1.93±0.33	4.932	1.13	5
0133+476	DA 55	2008-11-18	00036188004	6520	0.0971	0	1.41±0.21	2.052	1.03	8
0202+149	4C +15.05	2010-03-06	00036304004	9051	0.0480	0	1.20±0.44	1.226	0.31	3
0202+319		2006-06-24	00035394001	12793	0.0582	0	1.64±0.19	0.704	1.50	8
0212+735		2006-07-18	00035241002	6574	0.261	0.38	1.12±0.14	6.807	1.15	20
0215+015	OD 026	2005-06-28	00035032001	9414	0.0316	0.11	1.65±0.13	1.928	0.48	16
0224+671	4C +67.05	2008-09-14	00036234004	8094	0.398	0	1.33±0.30	1.786	0.87	6
0234+285	CTD 20	2007-07-16	00036189002	7270	0.0757	0	1.51±0.24	1.316	0.69	6
0235+164		2008-09-02	00030880024	6945	0.0681	0.16	1.72±0.14	3.256	0.68	20
0238-084	NGC 1052	2009-06-08	00036365002	10300	0.0295	16	2.11±0.88	3.698	0.88	11
0300+470	4C +47.08	2008-09-05	00036235005	7067	0.164	0.61	1.78±0.80	0.685	0.03	1
0316+413	3C 84	2009-12-30	00030354003	4344	0.132	0.127	1.88±0.04	303.0	1.16	518
0333+321	NRAO 140	2008-08-25	00036366003	19147	0.121	0.224	1.63±0.04	8.137	0.84	122
0336-019	CTA 26	2009-03-27	00036190005	7658	0.0413	0.11	1.80±0.28	0.735	1.33	4
0403-132		2009-03-29	00036191005	4928	0.0413	0	1.44±0.14	3.827	0.76	14
0415+379	3C 111	2010-01-09	00036367005	8976	0.293	0.81	1.60±0.04	47.88	1.04	222
0420-014		2009-07-10	00036368005	6170	0.0811	0.16	2.05±0.15	2.290	0.52	17
0422+004		2009-07-11	00036192008	6101	0.0705	0.05	2.34±0.32	0.591	0.26	5
0430+052	3C 120	2008-08-10	00036369003	20222	0.102	0.091	1.72±0.02	42.53	1.13	409
0446+112		2008-08-07	00036313006	7818	0.125	1.2	2.11±0.63	0.678	0.44	1
0458-020		2009-04-22	00036370004	4808	0.0597	0.3	1.95±0.32	1.497	0.704	5
0528+134		2009-09-24	00035384041	5926	0.239	0.7	1.82±0.41	1.440	1.01	3
0529+075	0G 050	2008-08-04	00036236004	3945	0.168	2.2	1.92±0.98	1.134	0.06	0

Table 4.6 – *continued*

B1950 Name (1)	Alias (2)	Obs. Date (3)	Swift Obs. ID (4)	T_{XRT} [s] (5)	Galactic Intrinsic (6)	N_{H} [10^{22} cm^{-2}] (7)	Uncertainty (8)	Γ_{X} (9)	F_{X} [$10^{-12} \text{ erg cm}^{-2} \text{ s}^{-1}$] (10)	χ^2_{red} (11)	d.o.f. (12)
0529+483 ^a		2009-01-18	00038383002	7265	0.248	-	-	1.8 ^b	0.317	-	-
0552+398	DA 193	2007-04-10	00036315002	7225	0.272	0	1.1	1.27±0.45	1.997	0.60	4
0605-085	OC -010	2008-08-08	00036371008	14955	0.185	0.13	0.08	1.58±0.13	2.267	1.31	25
0607-157		2008-08-14	00036193007	11556	0.117	0.06	0.04	1.90±0.11	2.054	0.74	28
0642+449	OH 471	2007-04-03	00036238001	7695	0.11	0	0.44	1.48±0.30	0.711	1.26	3
0648-165		2008-08-12	00036239005	6345	0.278	0.04	3.29	1.50±1.61	0.863	0.002	0
0716+714		2009-10-16	00035009041	5574	0.0306	0	0.04	2.37±0.11	161.6	1.38	32
0727-115		2008-12-06	00036240009	6234	0.339	0.3	0.4	1.92±0.50	1.425	0.12	4
0730+504		2008-02-15	00036319005	6639	0.0525	0	0.6	1.79±0.45	0.690	1.18	2
0735+178	OI 158	2010-01-31	00090099001	6509	0.0386	0.5	0.6	1.54±0.58	0.935	0.96	1
0736+017	OI 061	2008-12-12	00036373004	4037	0.0759	0.10	0.07	1.94±0.18	2.751	0.97	12
0738+313	OI 363	2009-08-31	00036374002	5210	0.0431	0	0.16	1.67±0.28	1.137	2.99	4
0742+103		2007-04-28	00036320003	7042	0.0288	1.0	1.3	0.98±0.55	1.828	1.48	3
0748+126		2008-09-06	00036194002	2382	0.0321	0.14	0.10	1.80±0.24	3.212	1.34	6
0754+100		2010-02-27	00036195002	9546	0.0211	0.04	0.02	1.81±0.08	2.975	0.83	38
0804+499		2009-02-27	00036196004	9451	0.046	0.12	0.17	1.89±0.27	1.052	0.43	8
0805-077		2009-05-18	00031413001	1994	0.103	0.39	0.83	2.29±0.98	1.577	0.06	1
0808+019		2009-09-19	00036197004	10885	0.0384	0	0.68	1.68±0.62	0.307	2.46	2
0814+425	OI 425	2009-03-03	00036321004	10087	0.0539	0	0.43	1.44±0.28	0.790	1.90	4
0823+033		2008-06-12	00036198002	5168	0.0387	0	0.21	1.57±0.25	2.251	1.47	8
0827+243	OI 248	2009-04-10	00036375014	8632	0.0264	0.03	0.06	1.67±0.17	1.355	0.33	11
0829+046	OI 049	2010-01-11	00090096001	5599	0.0241	0	0.24	1.54±0.21	1.545	0.85	6
0836+710	4C 71.07	2009-01-18	00036376005	9121	0.0276	0.05	0.02	1.55±0.05	11.03	1.35	91
0838+133 ^a	3C 207	2010-02-02	00039146001	1753	0.0528	-	-	1.8 ^b	1.07	-	-
0851+202	OI 287	2009-10-25	00030901053	5052	0.0239	0.09	0.04	1.87±0.09	8.257	0.91	49
0906+015	4C +01.24	2010-03-10	00036200005	4388	0.0283	0	0.45	1.77±0.38	1.040	1.84	4
0917+624		2009-03-17	00036201005	3951	0.0259	0	1.7	1.61±0.74	0.713	0.05	0
0923+392	4C +39.25	2010-03-20	00036377005	5401	0.0133	0.20	0.08	2.08±0.15	2.883	0.58	19
0945+408	4C +40.24	2007-05-03	00036202001	9381	0.013	0.036	0.065	1.73±0.21	0.816	0.21	7
0955+476		2008-01-12	00036241002	7466	0.0112	0.09	0.76	1.31±0.90	0.552	0	0
1036+054		2007-11-22	00036242001	10413	0.0243	0.10	0.12	1.70±0.29	0.698	0.57	5

Table 4.6 – *continued*

B1950 Name (1)	Alias (2)	Obs. Date (3)	Swift Obs. ID (4)	T_{XRT} [s] (5)	Galactic Intrinsic Uncertainty (6) (7) (8)	Γ_X (9)	F_X [10^{-12} erg cm^{-2} s^{-1}] (10)	χ^2_{red} (11)	d.o.f. (12)
1038+064	4C +06.41	2008-07-12	00036378003	5952	0.0235	0	1.52±0.22	0.79	6
1045-188		2006-12-31	00036203001	6673	0.0326	0.31	2.37±0.27	0.06	4
1055+018	4C +01.28	2009-07-18	00036379004	10227	0.0303	0	1.78±0.11	1.15	31
1124-186		2009-01-25	00036243002	8352	0.0354	0.15	2.85±0.18	1.06	24
1127-145		2010-02-24	00090095001	4766	0.0338	0.13	1.67±0.11	0.58	25
1150+812		2009-02-12	00036204005	7554	0.0474	0	1.00±0.64	1.57	2
1156+295	4C +29.45	2008-11-21	00036381004	6969	0.015	0.30	2.01±0.25	0.57	7
1213-172		2010-03-24	00035036002	10559	0.0387	0	1.87±0.70	1.74	2
1219+044		2010-04-28	00036330003	4096	0.0155	0	1.21±0.33	1.54	4
1222+216		2009-05-08	00090084002	2115	0.0197	0.10	1.52±0.38	1.02	3
1226+023	3C 273	2010-01-16	00035017052	2399	0.0162	0	1.64±0.03	1.37	254
1228+126	M87	2010-04-10	00031105021	1993	0.0161	0.13	2.28±0.05	1.44	225
1253-055	3C 279	2008-11-26	00035019009	22665	0.0212	0.063	1.79±0.04	0.93	157
1308+326		2008-08-20	00036384007	4774	0.0127	0.13	1.74±0.19	0.43	8
1324+224		2010-03-29	00036205004	7225	0.0149	0	1.32±0.23	0.97	5
1334-127		2010-01-26	00036385008	1489	0.0539	0.35	2.65±0.46	1.13	3
1413+135		2010-04-03	00036386004	9941	0.0157	8	2.64±1.69	0	0
1417+385		2007-01-24	00036206004	7068	0.0945	0	2.07±0.73	0.53	1
1458+718	3C 309.1	2009-06-07	00036387003	6872	0.0226	0.03	1.62±0.14	0.86	12
1502+106	4C +10.39	2008-08-08	00036388004	12467	0.0219	0	1.40±0.15	1.10	17
1504-166 ^a		2009-01-07	00036207004	4426	0.0658	-	1.8 ^b	0.182	-
1510-089		2009-01-16	00031173008	7227	0.0715	0	1.36±0.09	4.980	29
1538+149	4C +14.60	2009-12-15	00036208004	5876	0.0317	0.20	2.31±0.39	1.06	3
1546+027		2009-01-11	00036209002	2767	0.0688	0.20	1.93±0.34	0.38	4
1548+056	4C +05.64	2009-12-30	00039724002	5957	0.0407	0	1.97±0.40	2.10	5
1606+106	4C +10.45	2010-01-09	00036210004	13063	0.0418	0.15	1.52±0.17	0.70	11
1611+343	DA 406	2009-06-13	00090098002	6463	0.0134	0.048	1.91±0.33	1.19	5
1633+382	4C +38.41	2009-06-25	00036389018	12078	0.0111	0.02	1.73±0.12	0.49	17
1637+574	OS 562	2009-07-10	00036212006	6707	0.0131	0.0	2.13±0.20	1.86	9
1638+398	NRAO 512	2007-01-18	00036213001	8170	0.010	0.36	1.93±0.55	0.12	1
1641+399	3C 345	2009-09-11	00036390006	4262	0.0106	0.07	1.96±0.14	0.96	18

Table 4.6 – *continued*

B1950 Name (1)	Alias (2)	Obs. Date (3)	Swift Obs. ID (4)	T_{XRT} [s] (5)	Galactic Intrinsic Uncertainty (6) (7) (8)	Γ_X (9)	F_X [10^{-12} erg cm^{-2} s^{-1}] (10)	χ^2_{red} (11)	d.o.f. (12)	
1655+077		2010-01-18	00036391006	5574	0.0613	0.0	1.65±0.95	0.767	0.60	1
1726+455 ^a		2010-05-03	00036214004	3784	0.02	-	1.8 ^b	0.376	-	-
1730-130	NRAO 530	2009-06-24	00035387012	5129	0.182	0.0	1.64±0.45	1.480	1.10	3
1739+522	4C +51.37	2007-06-24	00036800001	8671	0.0295	0.0	1.25±0.22	1.458	2.00	7
1741-038		2010-05-09	00036216003	6359	0.184	0.0	1.25±0.29	1.955	2.42	7
1749+096	OT 081	2009-11-11	00036392009	2542	0.101	0.0	1.36±0.31	2.641	3.17	4
1751+288 ^a		2010-01-02	00036244011	7642	0.0498	-	1.8 ^b	0.306	-	-
1758+388 ^a		2006-11-05	00036245001	9789	0.0253	-	1.8 ^b	0.182	-	-
1800+440		2009-05-11	00036217003	4393	0.0323	0.13	1.91±0.60	0.600	0.25	1
1803+784		2009-06-07	00036393004	9374	0.034	0.06	1.70±0.10	2.427	1.13	26
1807+698	3C 371	2009-01-16	00036349003	15548	0.0411	0.057	1.84±0.11	1.724	0.86	31
1823+568	4C +56.27	2009-05-31	00036394006	4581	0.0468	0.049	1.72±0.17	2.753	0.70	12
1828+487	3C 380	2009-05-22	00036395004	3394	0.0603	0.24	2.13±0.18	2.789	0.94	11
1849+670		2009-05-30	00036218005	10828	0.0466	0.05	1.77±0.13	1.817	1.10	22
1928+738	4C +73.18	2008-08-22	00036396004	8249	0.071	0.0	1.69±0.12	3.135	1.32	27
1936-155		2006-11-01	00036219001	5677	0.0754	-	1.67±0.28	0.601	1.65	2
1957+405	Cygnus A	2008-08-23	00036397003	5653	0.236	0.19	1.49±0.04	44.24	1.26	164
1958-179		2009-04-07	00036220003	5018	0.0658	0.02	1.72±0.30	1.048	0.36	3
2005+403		2009-06-13	00036246005	8147	0.477	0.0	1.45±0.28	1.619	0.74	6
2008-159		2009-03-15	00036247003	8436	0.0558	0.15	1.53±0.11	3.540	0.82	24
2021+317	4C +31.56	2007-04-01	00036248003	17354	0.517	0.0	0.88±1.25	0.404	1.17	0
2021+614 ^a	OW 637	2009-07-17	00036352007	9653	0.135	-	1.8 ^b	0.076	-	-
2037+511 ^a	3C 418	2009-07-05	00036221007	8719	0.54	-	1.8 ^b	0.379	-	-
2121+053		2009-03-29	00036222003	4300	0.0599	0.0	1.98±0.28	0.831	0.65	4
2128-123		2008-11-20	00036357005	7964	0.0452	0.00	1.88±0.08	5.662	0.84	56
2131-021 ^a	4C -02.81	2009-08-25	00036223004	1527	0.0427	-	1.8 ^b	1.459	-	-
2134+004		2007-04-15	00036398001	7160	0.0472	0.18	2.07±0.19	1.109	0.29	9
2136+141	OX 161	2009-07-01	00036250004	4845	0.0568	0.0	1.45±0.35	1.091	1.07	3
2145+067	4C +06.69	2009-11-21	00036774003	5283	0.0454	0.0	1.68±0.14	3.466	1.11	19
2155-152		2009-04-06	00036224005	9856	0.0381	0.03	1.87±0.17	1.239	1.46	14
2200+420	BL Lac	2009-07-16	00035028027	16467	0.171	0.12	2.01±0.05	6.682	1.00	120

Table 4.6 – *continued*

B1950 Name (1)	Alias (2)	Obs. Date (3)	Swift Obs. ID (4)	T_{XRT} [s] (5)	Galactic N_{H} [10^{22} cm^{-2}] (6)	Intrinsic Uncertainty (7)	Γ_{X} (9)	F_{X} [$10^{-12} \text{ erg cm}^{-2} \text{ s}^{-1}$] (10)	χ_{red}^2 (11)	d.o.f. (12)
2201+171		2009-04-18	00036225005	7218	0.0456	0.07	1.93±0.29	0.679	0.86	4
2201+315	4C +31.63	2009-07-09	00036226008	7074	0.0862	0.06	1.99±0.11	3.155	0.76	29
2209+236		2009-04-15	00036359002	8999	0.0595	0.04	1.47±1.29	0.475	0.19	0
2216-038		2010-01-06	00036227003	3991	0.057	0.0	1.61±0.37	1.305	2.82	4
2223-052	3C 446	2009-07-24	00090089001	2951	0.0443	0.06	1.87±0.59	1.529	2.23	2
2227-088	PHL 5225	2009-11-19	00039788001	3961	0.0412	0.13	1.88±0.24	1.745	0.69	6
2230+114	CTA 102	2009-09-09	00090097003	6914	0.0467	0.086	1.53±0.13	3.274	1.88	19
2243-123		2007-04-21	00036402002	12539	0.044	0.0	1.99±0.13	1.271	0.58	23
2251+158	3C 454.3	2008-08-08	00031216021	4217	0.0724	0.00	1.49±0.06	28.40	0.89	96
2331+073		2009-12-20	00036251007	5149	0.0545	0.10	1.82±0.29	0.803	0.61	4
2345-167		2009-12-04	00036252005	3876	0.0166	0.18	2.19±0.40	0.917	0.24	4
2351+456 ^a	4C +45.51	2005-05-17	00035048001	8051	0.0918	-	1.8 ^b	0.216	-	-

Column note: (1) IAU B1950 name; (2) alias name; (3) *Swift* observation date; (4) *Swift* observation ID number; (5) the integration time of *Swift*/XRT observation;

(6) Galactic neutral hydrogen column density (the LAB Survey; Kalberla et al. 2005); (7) intrinsic neutral hydrogen column density obtained from the fitted X-ray spectrum; (8) the uncertainty of neutral hydrogen column density obtained from the fitted X-ray spectrum; (9) photon index; (10) X-ray flux in the energy range of 2–10 keV; (11) reduced χ^2 of the fitted X-ray spectrum; (12) degree of freedom of fit.

^a The X-ray spectrum has less than 3 bins. We assume an absorbed power law model, and estimate the flux by applying the galactic N_{H} value and fix $\Gamma=1.8$ to the model.

^b Average AGN photon index. Here we fix to this value when fitting the X-ray spectrum.

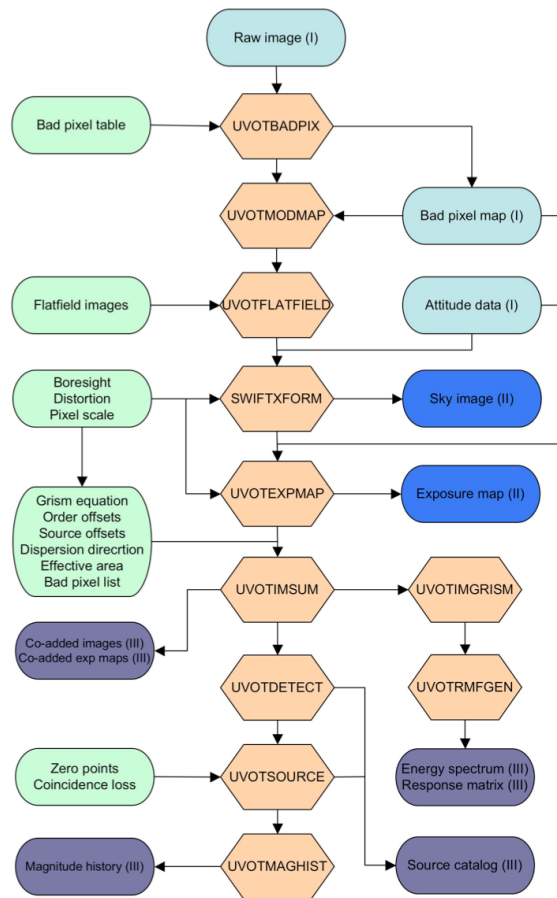


Figure 4.10: The UVOT imaging product chart. Orange denotes a software tool, green a calibration product, light-blue a Level I science product (raw data), medium-blue a Level II product (obtained by processing f Level I product), and dark blue a Level III product (obtained by processing Level II product). Image taken from the *Swift* UVOT User’s Guide.

4.4.2 *Swift*/UVOT Data Reduction

We performed the *Swift*/UVOT data analysis by following the UVOT User’s Guide¹⁶. Figure 4.10 illustrates the procedures of UVOT data reduction. The boxes marked in orange denote the task name in the HEASARC `FTOOLS`. We use Level II products from the HEASARC archive for flux extraction. We take the sky images, sum over multiple images extensions in a FITS file using `uvotimsum`, and extract the source flux using `uvotsource` with selected source and background regions. Depending on the AGN intensity and the filter used, we extract source fluxes with a circle of $5''$ to $10''$ radius. The background regions selected are between $12''$ and $18''$.

¹⁶<http://heasarc.gsfc.nasa.gov/docs/swift/analysis/UVOT-swguide-v2.2.pdf>

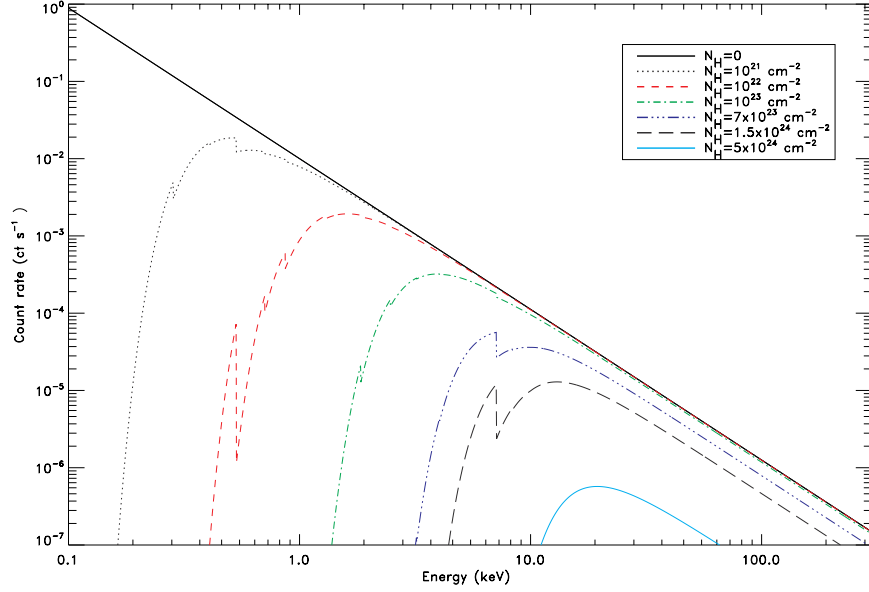


Figure 4.11: Effects of absorption on a power-law spectrum ($\Gamma=1.95$). As listed in the upper-right panel, the different curves indicate different values of N_{H} . The black solid line shows the condition when $N_{\text{H}}=0$. The spectra are calculated taking into account both photoelectric and Compton processes. Image credit: Ricci et al. (in prep.).

4.4.3 Extinction Correction

When the photons emitted by an extragalactic source travel to an observer on the Earth, additional effects of Galactic and extragalactic extinction deform the measured spectrum, since the dust and gas of the ISM absorb and scatter the radiation emitted by the source. Therefore, to obtain the original emitted spectrum of the source, we need to correct for this effect. The LAB Survey provides a good estimate of Galactic N_{H} value, and by the fitted result of X-ray spectrum between 0.2–10 keV (see Section 4.4.1 for details), we obtain the value of extragalactic N_{H} column density. Figure 4.11 shows the effect of absorption on a power-law spectrum. The absorption effect becomes significant at lower energies, especially between 0.1–10 keV. In the hard X-ray range (10–100 keV), the absorption becomes significant when the column density $N_{\text{H}} > 10^{23} \text{ cm}^{-2}$. Therefore, we performed corrections to the spectra of the optical/UV and the X-ray bands (0.2–10 keV) in our study.

X-ray Absorption Correction

We fitted an absorbed power law model to the X-ray spectrum using XSPEC (see Section 4.4.1), and we output the fluxes of X-ray data points (denote F_{data}) and the model (denote F_{model1}) by using the command `wdata` of `iplot` in XSPEC. To correct for the absorption, we set the fitted N_{H} value to 0, and output the model again (denote F_{model2}) without fitting the data. The corrected unabsorbed fluxes F_{unabsorb} can be obtained by this equation:

$$F_{\text{unabsorb}} = F_{\text{data}} \times \frac{F_{\text{model2}}}{F_{\text{model1}}}.$$

After applying the correction, most of the MOJAVE sources show obvious changes of SED shape. For some sources (e.g., 0528+134, 0607–157, 2155–152, 2243–123), the SED in the X-ray band becomes flat; some sources even show an inverted SED shape in the X-ray band (e.g., 0716+714, 1045–188, 1124–186, 2345+167). The individual broadband-SED plots are shown in Appendix B.

UV and Optical Extinction Correction

In the UV and optical bands, it is necessary to calculate the extinction coefficient A for different filters, and subtract it from the observed magnitude m in order to find the unabsorbed magnitude M^* :

$$M_{\lambda}^* = m_{\lambda} - A_{\lambda},$$

where λ indicates the wavelength of the filter. The extinction at a wavelength λ is related to the color excess of an object. The color excess E_{B-V} can be obtained by comparing the observed color index $M_{B-V}^{\text{Observed}}$ and the intrinsic color index $M_{B-V}^{\text{Intrinsic}}$,

$$E_{B-V} = M_{B-V}^{\text{Observed}} - M_{B-V}^{\text{Intrinsic}},$$

where the color index is defined by $M_{B-V} = M_B - M_V$, M_B denotes the magnitude of the optical B band, and M_V for the V band. The extinction coefficient can be determined by

$$A_{\lambda} = k(\lambda)E_{B-V}.$$

We define the extinction curve of our Galaxy as

$$R_V = \frac{A_V}{E_{B-V}},$$

and the extinction coefficient can be expressed as

$$A_{\lambda} = \frac{k(\lambda)}{R_V}A_V,$$

where a typical value of $R_V = 3.1$ in the Galaxy is used (Cardelli et al. 1989). Note that R_V can be found to be between 2.6 and 5.5 for different lines of sight (Clayton and Cardelli 1988). According to Predehl and Schmitt (1995), the extinction coefficient can be obtained by

$$A_V = \frac{N_H}{1.79 \times 10^{21} \text{ cm}^{-2}}.$$

In the optical band, the value of A_{λ} is given by Schlegel et al. (1998). As for the UV filters of *Swift*/UVOT, we estimated the extinction by using the reddening law by Allen (1976). The values are listed in Table 4.7.

The next step is to convert the corrected magnitudes to fluxes. First, one needs to convert the magnitude M into counts per second C (Poole et al. 2008):

$$M = M_{\text{zero}} - 2.5 \log(C),$$

Table 4.7: Parameters of *Swift*/UVOT filters for extinction correction.

UVOT filter	λ_c ^a [Å]	λ_{eff} ^b [Å]	$k(\lambda)/R_V$ ^c	M_{zero} ^d [mag]	A_{cf} ^e [$10^{-16} \text{ erg cm}^{-2} \text{ s}^{-1} \text{ Å}^{-1}$]
V	5468	5402	1	17.89 ± 0.01	2.614
B	4392	4329	1.321	19.11 ± 0.02	1.472
U	3465	3501	1.664	18.34 ± 0.02	1.63
UVW1	2600	2634	2.3	17.49 ± 0.03	4.0
UVM2	2246	2231	2.9	16.82 ± 0.03	8.5
UVW2	1928	2030	2.8	17.35 ± 0.03	6.2

^a The central wavelength of the filter.

^b The effective wavelengths of each filter for a Vega-like spectrum (see Poole et al. 2008 for derivation).

^c The values of $k(\lambda)/R_V$ are for deriving the extinction coefficient A_λ .

^d The zero-point magnitude.

^e The count rate to flux conversion factor.

where M_{zero} is the zero point magnitude (see the *Swift*/UVOT Calibration Documents¹⁷), which is defined as the magnitude when $C = 1 \text{ counts s}^{-1}$. The values of M_{zero} for the UVOT filters are listed in Table 4.7. To convert counts to flux density, we use the result of Poole et al. (2008), who calculated the count rate to flux conversion parameter A_{cf} for each filter (see Table 4.7). The flux density in the unit of Jansky S_ν is

$$S_\nu = 3.34 \times 10^4 F_\lambda \lambda^2,$$

where $F_\lambda = C \times A_{\text{cf}}$.

4.4.4 *Fermi*/LAT data

In the γ -ray band of the SED, we include the published *Fermi*/LAT first year catalog (*Fermi* 1 FGL catalog; Abdo et al. 2010b). There are 85 of the MOJAVE sources in the *Fermi* 1 FGL catalog, and Table 4.4 lists the associations between the MOJAVE and the 1 FGL sources. The public *Fermi*/LAT γ -ray spectra¹⁸ are available in six energy bins: 30 – 100 MeV, 100 – 300 MeV, 300 MeV – 1 GeV, 1 – 3 GeV, 3 – 10 GeV, and 10 – 100 GeV. Not all of the 1 FGL sources have fluxes available in all bins, and this depends on the source brightness, spectral shape, and data quality. We calculate the effective frequency of each energy bins from the γ -ray photon index, and add the γ -ray data to the SED.

For the non-1 FGL MOJAVE sources, their LAT upper limits are estimated by M. Boeck, who follows the same procedure as described in Boeck et al. (2010). The LAT upper limits that we used in this thesis are preliminary estimations, and the final results will be included in a future publication of this work.

¹⁷<http://heasarc.gsfc.nasa.gov/docs/heasarc/caldb/swift/docs/uvot/index.html>

¹⁸<http://fermi.gsfc.nasa.gov/ssc/data/access/lat/1yr-catalog/>

4.5 The Broadband SED of the MOJAVE sources

As described in the previous sections, we completed the optical and X-ray spectral analysis of all MOJAVE sources, and we collected the broadband data from the radio to the γ -rays. In this section, we will present our results. The X-ray spectra of the MOJAVE sources can be found in Appendix A; the broadband SED of the 135 sources with two polynomial fits to the data are shown in Appendix B. In Section 4.5, we will give a brief literature review of each source, and most importantly, to check if the broadband SED of each source has been studied earlier by others and has been presented in the literature. We include previously published broadband SED in Appendix C, and we compare our results with the literature ones.

Typically, the SED of the MOJAVE sources display a double-hump profile, which is caused by non-thermal processes (see Section 1.4.2 for details). The lower-energy hump is due to synchrotron emission from the radio jet, and the higher-energy hump is believed to be caused by one- or multi- component IC up-scattering of internal or external photon sources. We performed a mathematical polynomial fit to the synchrotron hump and the IC hump for each source. By this method, we could estimate the peak positions of synchrotron and IC components.

In this section, I will briefly summarize our findings and compare them with previously published results, especially focusing on the broadband SED study of each MOJAVE source. There are references which are quite relevant to our sample, and I will not go through them for each source in the next paragraphs. Abdo et al. (2010a) studied the broadband SED of 48 blazars in the *Fermi* LAT bright AGN sample (LBAS), which includes the AGNs detected by LAT after 3-month operations. Among the 48 sources studied by Abdo et al. (2010a), 20 are overlapped with the MOJAVE sample. Lee et al. (2008) performed a global 86 GHz VLBI survey of compact radio sources, in which many of the MOJAVE sources were included. The papers published by the MOJAVE team include: the first-epoch of 15 GHz linear polarization images of the MOJAVE sources (Lister and Homan 2005); the first-epoch 15 GHz circular polarization results of the MOJAVE sample (Homan and Lister 2006); the VLA images of the MOJAVE sources at 1.4 GHz (Cooper et al. 2007); the study of the MOJAVE sample about the parent luminosity function (Cara and Lister 2008); the multi-epoch VLBA images of the MOJAVE sample (Lister et al. 2009a); the kinematic results of the MOJAVE sample (Lister et al. 2009b); and the jet acceleration results of the MOJAVE sources (Homan et al. 2009a). The papers of the 2 cm Survey include: the VLBA images at 15 GHz during 1994 and 1997 (Kellermann et al. 1998); additional 39 sources of single-epoch VLBA observations at 15 GHz from 1997 to 2000 (Zensus et al. 2002); the kinematics of parsec-scale jet in the 2 cm Survey (Kellermann et al. 2004); the fine-scale structure of 250 flat spectrum radio sources in the 2 cm Survey (Kovalev et al. 2005). Additionally, the radio spectra of the MOJAVE sources are available in the MOJAVE website¹⁹. In the following paragraphs, we will present the discussion for each individual source ordered by RA.

¹⁹<http://www.physics.purdue.edu/MOJAVE/>

0003–066 NRAO 005 is a flat spectrum BL Lac object, and it is not detected by *CGRO/EGRET* and *Fermi/LAT*. Figure A.1 shows the X-ray spectrum of NRAO 005, and Figure B.1 shows the broadband SED of this source. The X-ray SED displays a flat profile, and we use the upper limit value for the *Fermi/LAT* flux estimated by Böck et al. (in preparation) in the polynomial fit (see Section 4.4.4 for details). The peak of the IC hump is lower than of the synchrotron hump, and the frequency location of the IC peak couldn't be found. Nieppola et al. (2006) studied the synchrotron part of the SED of NRAO 005 (Figure C.1), and they classified the source as LBL ($10^{13} \text{ Hz} < \nu_{\text{peak}} < 10^{14} \text{ Hz}$). The synchrotron peak we derived is $\nu_{\text{peak}} = 7.05 \times 10^{12} \text{ Hz}$, which is below the LBL limit that Nieppola et al. (2006) defined, and our result is consistent with their findings.

0007+106 III Zw 2 is a flat spectrum radio galaxy classified by Véron-Cetty and Véron (2006). However, Corbin and Boroson (1996) classified the source as a low-redshift quasar, and they studied its UV and optical spectra. Hughes et al. (2000) classified the source as a radio-quiet quasar, and presented the off-nuclear optical spectra of III Zw 2. This source is not detected in the γ -ray band, but it is active in the X-ray band and is in the *Swift/BAT* 22-month catalog (Tueller et al. 2010). Falcke et al. (1999) studied a radio outburst of III Zw 2, during the flaring period, it displayed an inverted radio spectrum. Shinozaki et al. (2006) have measured the X-ray spectral properties of this source with *XMM-Newton*, and they derived its photon index $\Gamma = 1.75_{-0.017}^{+0.018}$, the intrinsic $N_{\text{H}} = 0 \text{ cm}^{-2}$, and the flux $F = 7 \times 10^{-12} \text{ ergs cm}^{-2} \text{ s}^{-1}$. Our results derived from *Swift* observations are consistent with their findings (see Table 4.6), and Figure A.1 shows the X-ray spectrum of III Zw 2. Figure B.1 shows the broadband SED of this source. The SED of this source has a good frequency sampling in the synchrotron and the IC humps, and both humps have comparable energy peaks.

0016+731 0016+731 is a low polarization radio quasar. Bloom et al. (1994) presented the spectrum from the radio to the infrared band of this source, and Bloom et al. (1999) presented a multiband study of 0016+731 using the observations between 1991 to 1992 from the radio to the γ -ray bands. Sambruna (1997) studied the soft X-ray spectrum of this source at 0.1–2.4 keV using *ROSAT* observations in March 1992. They reported an X-ray photon index of $\Gamma = 1.43_{-1.19}^{+1.01}$ in the soft X-ray band, and we derived the photon index $\Gamma = 1.96 \pm 0.63$ at 0.3–10 keV from *Swift* 2009 observations (see Figure A.1 for the X-ray spectrum). Both results are compatible. Figure B.1 shows the broadband SED of 0016+731. The SED of the X-ray band locates at the tail of the synchrotron hump, and we do not fit a polynomial model to the IC hump due to the lack of high energy data. Previous studies on the SED of 0016+731 in the radio, optical, and X-ray bands show that the peak frequency of the synchrotron hump is $\nu_{\text{peak}}^{\text{sync}} \sim 10^{14} \text{ Hz}$ (from Brunner et al. 1994 and Sambruna et al. 1996; see Figure C.2), which is one order of magnitude lower than our findings ($\nu_{\text{peak}}^{\text{sync}} \sim 10^{15} \text{ Hz}$).

0048–097 0048–097 is a flat-spectrum BL Lac object. This source was not detected by *CGRO/EGRET*, but it is in the *Fermi* 1FGL catalog (Abdo et al. 2010b). Figure A.1 shows the X-ray spectrum of 0048–097, and Figure B.1 shows our broadband SED of 0048–097 from radio to γ -ray band. The synchrotron hump extends until the X-ray

range. We found a value of $\nu_{\text{peak}}^{\text{sync}} \sim 10^{15}$ Hz, and that the synchrotron and IC humps have comparable energy peak values. The broadband SED of this source has been studied by Giommi et al. (1995), Sambruna et al. (1996), Nieppola et al. (2006), and Abdo et al. (2010a), where the first three presented the synchrotron hump of the SED, and the last one presented the broadband SED from the radio to the γ -ray band including *Fermi*/LAT results (Figure C.3). Our results are consistent with previous findings.

0059+581 0059+581 is a flat spectrum radio quasar. This source was not detected by *CGRO*/EGRET, but it is in the *Fermi* 1 FGL catalog. Pyatunina et al. (2006) studied the multi-frequency light curves from 1994 to 2005, and suggested that the source has an activity cycle of four years. Figure A.1 illustrates the X-ray spectrum obtained by the *Swift*/XRT, and Figure B.1 shows the broadband SED of 0059+581. The humps of synchrotron and IC display comparable energy peak. Marecki et al. (1999) presented the radio spectrum of 0059+581 (see Figure C.4). To our knowledge, our broadband SED is the first one to be published for this source.

0106+013 4C +01.02 is a high polarization, flat spectrum radio quasar. It was not detected by *CGRO*/EGRET, but it is in the *Fermi* 1 FGL catalog. Ledden and Odell (1985) and Maraschi et al. (1986) presented the radio, optical, and X-ray data of 4C +01.02, and they reported values for the spectral indices α_{ro} (radio to optical), α_{rx} (radio to X-ray), and α_{ox} (optical to X-ray). The X-ray properties of the source were also reported by Siebert et al. (1998), who found a value of $\Gamma=2.05_{-1.77}^{+3.93}$, which is consistent with our result $\Gamma=2.14\pm 0.47$. Figure A.1 shows the X-ray spectrum of 4C +01.02, and Figure B.1 presents our broadband SED results of this source. As presented, the synchrotron hump of this source extends until the X-ray band. To our knowledge, our broadband SED is the first one to be published for this source.

0109+224 0109+224 is a flat spectrum BL Lac object. This source was not detected by *CGRO*/EGRET, but it is presented in the *Fermi* 1 FGL catalog. Figure A.2 shows the X-ray spectrum of this source, and Figure B.1 shows its broadband SED. We find that the X-ray band in the SED has a flat profile, which indicates a transition from the synchrotron to the IC hump in this range, and one can see it in our polynomial fit. There were several SED studies of this source. Antón et al. (2004) found that the broadband SED of 0109+224 has a broken power-law profile. Ciprini et al. (2004) presented the broadband SED as well as the SED models (see Figure C.5); they also studied its radio and optical flux variability with a possible characteristic time scale of 3 to 4 years.

0119+115 0119+115 is a flat spectrum radio quasar. This source was not detected by *CGRO*/EGRET and *Fermi*/LAT. Lee et al. (2008) used the 86 GHz VLBI image of this source to derive a lower-limit of the brightness temperature of $T_{\text{b}} > 5.9 \times 10^{10}$ K. This source has a high apparent projected speed $\beta_{\text{app}} = 17.10 \pm 0.67$ measured at 15 GHz (Lister et al. 2009b). Figure A.2 shows the X-ray spectrum of 0119+115, and Figure B.1 shows its broadband SED. The SED in the X-ray band has a flat profile, and the peak of the IC hump cannot be derived due to the lack of higher energy data. To our knowledge, our broadband SED is the first one to be published for this source.

0133+476 DA 55 is a flat spectrum, highly polarized radio quasar. It was not detected by *CGRO/EGRET*, but it is present in the *Fermi* 1 FGL catalog (Abdo et al. 2010b). The polarization properties of this source have been studied in the past. For instance, Lister (2001) and Pollack et al. (2003) studied the VLBI polarization properties of this high optical polarization radio quasar. Figure A.2 shows the X-ray spectrum of DA 55, and Figure B.2 shows its broadband SED. We find that the synchrotron peak lies at $\nu_{\text{peak}}^{\text{sync}} < 10^{14}$ Hz. The source can be classified as a low synchrotron peaked blazar, following the classification criteria of Abdo et al. (2010a), who presented the broadband SED of this source, as shown in Figure C.6.

0202+149 4C +15.05 is a flat spectrum, high polarization radio quasar. It is detected by *CGRO/EGRET* (Mattox et al. 2001) and *Fermi/LAT* (Abdo et al. 2010b). Figure A.2 shows the X-ray spectrum of this source. In our analysis, the *Swift/UVOT* observations on this source (Obs. ID: 00036304004) have data from two available filters in the UV band (UM2 and UW1), however, we could not detect the source with a 9 ks integration time. We used the background flux of the image to derive a flux upper-limit in the optical band, and included the two points in the broadband SED polynomial fit, as shown in Figure B.2. From our polynomial fit, we find that the IC hump has a higher energy peak than the synchrotron hump with a difference of two orders of magnitude. An earlier SED study on this source was performed by Celotti and Ghisellini (2008), who presented a broadband SED of 4C +15.05 using archival data, and they applied a physical model to the SED to estimate the power of the jet, as shown in Figure C.7; they also found a more dominant energy output in the IC hump than in the synchrotron hump.

0202+319 0202+319 is a flat spectrum, low polarization radio quasar. It was not detected by *CGRO/EGRET*, but it is present in the *Fermi* 1 FGL catalog. Figure A.2 shows the X-ray spectrum, and Figure B.2 shows the broadband SED of this source. In our analysis, we used the *Swift* observation obtained in June 2006 (Obs. ID 00035394001), because the source has not been observed by *Swift* since then. From the polynomial fit, we find comparable energy peak values of the synchrotron and the IC humps. The same dataset has also been used for the broadband SED study by Giommi et al. (2007), as shown in Figure C.8. In their study, they did not perform model fitting to the SED. 0202+319 becomes observable by *Swift* in September 2010, and a ToO observation is planned by then (see Table 4.5).

0212+735 0212+735 is a flat spectrum, high polarization radio quasar. It was not detected by *CGRO/EGRET*, but it is present in the *Fermi* 1 FGL catalog. This source has also been detected in the *Swift/BAT* 9-month and 22-month observations (Tueller et al. 2008, 2010). Figure A.2 shows the X-ray spectrum, and Figure B.2 shows the broadband SED of 0212+735. From our polynomial fit, we find that the IC hump has a slightly higher energy peak than the synchrotron hump. Sambruna et al. (2007b) presented the *Swift* observations during 2005 and 2006 of this source, and they constructed the broadband SED of 0212+735 (see Figure C.9). They modeled the SED using a simple one-zone SSC model by Ghisellini et al. (2002), and they found that the $\nu_{\text{peak}}^{\text{sync}} \sim 10^{13}$ Hz, which is consistent with our findings. However, we obtained a higher value for the peak frequency

of the IC hump, $\nu_{\text{peak}}^{\text{IC}} \sim 10^{23}$ Hz.

0215+015 OD 026 is a flat spectrum, high polarization radio quasar. It was not detected by *CGRO/EGRET*, but it is present in the *Fermi* 1 FGL catalog. This source has showed inter-night variability in the optical and the infrared bands during its outburst phase, as reported by Brindle (1996). In our X-ray analysis of OD 026, we used the *Swift* observation obtained in June 2005 (Obs. ID 00035032001; see Figure A.3 for its spectrum), and a *Swift* ToO is being requested in September 2010, when the source becomes observable for *Swift* (see Table 4.5). Figure B.2 shows our broadband SED results. We derived comparable energy peak values of the synchrotron hump and the IC hump. Giommi et al. (2007) has presented the radio-to-X-ray SED of OD 026 using the same observation epoch of *Swift* (see Figure C.10), but they did not include SED model fitting results.

0224+671 4C +67.05 is a flat spectrum radio quasar. This source was not detected by *CGRO/EGRET* and *Fermi/LAT*, and it is not very active in the high energy band (see Figure A.3 for its X-ray spectrum). *Swift* observed the source 4C +67.05 for 4 epochs in 2006 and 2008, but none of them had UVOT data. In the NED database of this source, no optical data are available. Figure B.2 shows the broadband SED of this source; we let the polynomial curve of the synchrotron hump passing through the lower-end of the X-ray data, in order to constrain the hump and to estimate the peak position. To our knowledge, our broadband SED is the first one to be published for this source.

0234+285 CTD 20 is a flat spectrum, high polarization radio quasar. It has a possible association with the EGRET source 3EG J0239+2815 (Mattox et al. 2001, Sowards-Emmerd et al. 2003), and it is present in the *Fermi* 1FGL catalog (Abdo et al. 2010b). Marscher et al. (2002b) studied its VLBA total and polarized intensity at 22 GHz. Figure A.3 shows the X-ray spectrum of CTD 20, and its broadband SED is shown in Figure B.2. We find the energy peak of the IC hump is one order of magnitude higher than the synchrotron hump. Our SED has a similar profile comparing to previously published SED results by Celotti and Ghisellini (2008) and Abdo et al. (2010a), see Figure C.11 for the latter work.

0235+164 The BL Lac object 0235+164 is famous for its rapid variability across the spectrum from the radio (Senkbeil et al. 2008, Frey et al. 2006), the optical (Hagen-Thorn et al. 2008, Raiteri et al. 2008), and the X-ray (Raiteri et al. 2006) bands. This source is detected by the *CGRO/EGRET* (Mattox et al. 2001) and the *Fermi/LAT* (Abdo et al. 2010b). The spectral variability during its active phase has been studied by Chen and Jiang (2001). Figure A.3 shows the X-ray spectrum of 0235+164, and In Figure B.2 one can find its broadband SED, which shows high variability in the optical band. Previous studies on the SED of this source include: Sambruna et al. (1996), Lin et al. (1999), Bach et al. (2007), Nieppola et al. (2006) and Abdo et al. (2010a). The high energy spectrum of this source was studied using *BeppoSAX* by Donato et al. (2005). Figure C.12 displays the SED presented by Bach et al. (2007) (synchrotron hump only) and Abdo et al. (2010a). Our results are consistent with their findings.

0238–084 NGC 1052 is a flat spectrum radio galaxy. This source is not active in the γ -ray band, and it is not detected by the *CGRO/EGRET* and the *Fermi/LAT*. NGC 1052 hosts a double-sided jet, and is a LINER galaxy (Kadler et al. 2004b). It has strong radio jet emission, and is bright in multiband observations (Kadler et al. 2004a). Tornainen et al. (2007) studied the radio continuum spectrum of NGC 1052 (see Figure C.13). A broad Fe $K\alpha$ line is detected in this galaxy, and it may be produced in dense plasma near the base of the jet (Kadler 2005, Brenneman et al. 2009). The X-ray spectrum of NGC 1052 is shown in Figure A.3; we used the XSPEC model `phabs (1) × (mekal20 + phabs (2) × powerlaw)` to fit the spectrum. Figure B.3 shows the broadband SED of NGC 1052; the SED in the optical band is highly variable, and our polynomial fit to the data displays a reasonable quality.

0300+470 4C +47.08 is a flat spectrum BL Lac object, which shows a compact asymmetric morphology in VLBI observations (Lister et al. 2009a). It displays a one-sided halo at kilo-parsec scales. This source is variable on a monthly timescale at centimeter wavelengths (Aller et al. 1985) in total flux and linear polarization, and the source is core-dominated (Nan et al. 1999). Jones et al. (1981) studied the radio spectrum of the source. Figure A.3 shows the X-ray spectrum, and Figure B.3 shows the broadband SED of 4C +47.08; we derived comparable values of the energy peaks for the synchrotron and the IC humps. Nieppola et al. (2006) presented the synchrotron part of the SED (see Figure C.14), and they obtained a frequency peak of $\nu_{\text{peak}}^{\text{sync}} \sim 10^{14}$ Hz, which is consistent with our results.

0316+413 3C 84 (also named NGC 1275) is a radio galaxy. It was not detected by the *CGRO/EGRET*, but it is detected by *Fermi/LAT* (Abdo et al. 2009a). The SED of this source were studied at low and high energy range. Its very-high-energy emission mechanism was studied by Roustazadeh and Böttcher (2010), and the spectral evolution in γ -ray observed by *Fermi/LAT* was studied by Kataoka et al. (2010). The SED from the infrared to the UV bands of 3C 84 were studied by Edelson and Malkan (1986), and the synchrotron hump of the SED was studied by Antón et al. (2004) (see Figure C.15). In our *Swift/XRT* observation of 3C 84, we see an iron line and a possible evidence of a warm absorber. Therefore, we use a power law absorbed model together with a gaussian component to model the line emission, and additionally we add a warm absorber model²¹ (see Figure A.4). Figure B.3 shows the broadband SED of 3C 84; the SED does not have a typical double-hump structure, and the polynomial model could barely fit the data well.

0333+321 NRAO 140 is a flat spectrum, low polarization radio quasar. and it has a maximum apparent jet speed of $\beta_{\text{app}} = 12.76 \pm 0.19$ at 15 GHz (Lister et al. 2009b). Asada et al. (2008b) studied the polarimetric properties of NRAO 140 using the VLBA at 5 and 8 GHz, and they suggested a possible detection of a helical magnetic field in the jet of this source. The X-ray spectrum of NRAO 140 was studied using the X-ray satellite *ASCA* (Reeves and Turner 2000). Figure A.4 displays the X-ray spectrum obtained by *Swift/XRT* from our analysis, and Figure B.3 shows our broadband SED of NRAO 140. We obtained

²⁰mekal is a warm absorber model for hot diffuse gas (Mewe et al. 1985).

²¹phabs (1) × phabs (2) × (powerlaw+gauss+mekal)

comparable energy peaks of the synchrotron and IC humps; the source is in the *Swift*/BAT 22-month catalog (Tueller et al. 2010), and it has a good frequency coverage in the high energy band. Ghosh and Soundararajaperumal (1995) presented part of the broadband spectrum using the *EXOSAT* observation in 1985 together with simultaneously measured radio data points; they also included historical far-infrared and optical data, and they fitted the spectrum with two parabolic components (see Figure C.16).

0336–019 CTA 26 is a flat spectrum, high polarization radio quasar, which has a high apparent jet speed $\beta_{\text{app}}=22.4\pm 3.7$ at 15 GHz (Lister et al. 2009b). The source was associated with the 3EG catalog source J0340–020 (Nolan et al. 2003), and it is detected by the *Fermi*/LAT (Abdo et al. 2010b). Figure A.4 shows the X-ray spectrum, and Figure B.3 shows our broadband SED plot of CTA 26, from which we obtained comparable energy peaks of the synchrotron and the IC hump. Celotti and Ghisellini (2008) studied the broadband SED of CTA 26, and they applied a physical jet model to the SED (see Figure C.17). They obtained a higher energy peak of IC hump than of the synchrotron hump, which is different from our results. Further investigation on the high energy emission of this source is need in order to understand the origin of the SED profile change.

0403–132 0403–132 is a flat spectrum, high polarization radio quasar, which has maximum apparent jet speed of $\beta_{\text{app}}=19.7\pm 0.9$ from 15 GHz VLBI observations (Lister et al. 2009b). It was not detected by *CGRO*/EGRET, but it is present in the *Fermi* 1 FGL catalog (Abdo et al. 2010b). The soft X-ray properties of this source were studied by Sambruna (1997) using the *ROSAT* observations in March 1991. Figure A.4 displays the X-ray spectrum obtained by the *Swift*/XRT from our analysis, and Figure B.3 shows our broadband SED of 0403–132. The simultaneous optical SED has a special inverted profile, which cannot be fit well by our polynomial model. To our knowledge, our broadband SED is the first one to be published for this source.

0415+379 3C 111 is a well-studied broad-line radio galaxy which shows a classical Fanaroff and Riley Class II morphology on kiloparsec scales (Linfield and Perley 1984). It hosts a highly collimated one-sided jet emitting from the central core to the northeastern lobe (see e.g., Kadler et al. 2008). 3C 111 is associated with the EGRET source 3EG J0416+3650, and the broadband SED study of the historical data suggests that its profile is similar to the ones of EGRET flat spectrum radio quasars (Hartman et al. 2008). The hard X-ray spectrum of 3C 111 was studied by Molina et al. (2008) (see Figure C.18). The X-ray spectrum obtained by *Swift*/XRT is presented in Figure A.4, and the broadband SED of 3C 111 is shown in Figure B.3, in which the SED has good frequency coverage, including the *Swift*/BAT 22-month data. To our knowledge, our broadband SED is the first one to be published for this source.

0420–014 0420–014 is a flat spectrum, high polarization radio quasar, which has been detected by the *CGRO*/EGRET (Mattox et al. 2001) and the *Fermi*/LAT (Mattox et al. 2001). This source is an OVV quasar, and it is also a variable γ -ray source. Wagner et al. (1995) found that the optical and γ -ray flares happened simultaneously. Stevens et al.

(1995) used multiband monitoring data between 375 and 22 GHz to investigate the spectral evolution of the radio outbursts in 0420–014. Figure A.4 shows the X-ray spectrum from our XRT analysis results, and Figure B.3 shows the broadband SED of 0420–014. Our SED profile is very similar to the recently published SED of this source by Abdo et al. (2010a) (shown in the right panel of Figure C.19). Radecke et al. (1995) also studied the SED of 0420–014 including the *EGRET* data (left panel in Figure C.19), however, the X-ray band seemed to locate in the tail of the synchrotron hump, which was different from our results; they did not perform SED model fit in their study.

0422+004 0422+004 is a flat spectrum BL Lac object. This source was not detected by *CGRO/EGRET*, but it is in the *Fermi* 1 FGL catalog (Abdo et al. 2010b). This source is variable in optical polarization (Angel et al. 1978), and it has been intensively studied in the optical band. For example, Massaro et al. (1996) performed optical monitoring on this source in 1994 and 1995. Figure A.5 shows the X-ray spectrum from our analysis, and Figure B.4 shows the broadband SED of 0422+004, which shows that the synchrotron hump is extended to the X-ray band. Nieppola et al. (2006) presented the synchrotron part of the SED of this source from the radio to the optical band, and they classified 0422+004 as an IBL ($10^{15} \text{ Hz} < \nu_{\text{peak}}^{\text{sync}} < 10^{16} \text{ Hz}$; see Figure C.20). Our results, which include the X-ray band, deviate from their finding, and we obtained a peak frequency of $\nu_{\text{peak}}^{\text{sync}} \sim 10^{14} \text{ Hz}$, which suggested that this source is a LBL.

0430+052 3C 120 is a close-by Seyfert 1 radio galaxy ($z=0.033$), and it has been intensively studied at different wavelengths. This source is not detected by the *CGRO/EGRET* and the *Fermi/LAT*. The proximity of 3C 120 allows us to resolve its jet by the VLBI technique, and to study its dynamic structure in total and polarized flux (e.g., Walker et al. 2001, Marscher et al. 2002a, 2007, Gómez et al. 2008). The X-ray properties of this galaxy have also been studied, e.g., the jet emission (Harris et al. 2004), the disk-jet connection (Kataoka et al. 2007), and combining with multiwavelength approach (Ogle et al. 2005). Figure A.5 shows the X-ray spectrum from our analysis, and Figure B.4 shows our broadband SED of 3C 120. In the *Fermi/LAT* result, there is a γ -ray source very close to 3C 120, however, it is still not clear if they are associated. Therefore, in our SED plot, we only include a lower-limit estimated by M. Böck instead a γ -ray spectrum. The X-ray band is well-sampled in frequency, since *Swift* XRT and BAT data are available. Previous SED studies of this source are shown in Figure C.21 by Ogle et al. (2005) and Kataoka et al. (2007).

0446+112 0446+112 is an unidentified AGN, according to the optical classification by Véron-Cetty and Véron (2006), and they noted it as an ‘uncertain BL-Lac-like AGN’. This source has an uncertain redshift. In our analysis, we use the *Swift/UVOT* observation in August 2008 (Obs. ID 00036313006), and there was no detection on this source after 7.8 ks of exposure time with the UVW2 filter. We used the observation and estimated a lower limit of 21.53 magnitude in the optical band. Figure A.5 shows the X-ray spectrum from our analysis, and Figure B.4 shows our broadband SED plot of 0446+112. In the literature, Celotti and Ghisellini (2008) presented the broadband SED of this source (see Figure C.22). Comparing our results with the SED model by Celotti and Ghisellini (2008),

the SED energy peaks of the two humps we derived has less than one order of magnitude in difference, whereas Celotti and Ghisellini (2008) obtained a more than two order of magnitude difference in the two energy peaks.

0458–020 0458–020 is a flat spectrum, high polarization radio quasar, and it is a distant AGN located at the redshift $z=2.286$. This source was detected by *CGRO/EGRET* (Mattox et al. 2001) and *Fermi/LAT* (Abdo et al. 2010b), and it is one of the γ -bright sources. Vercellone et al. (2004) studied the *EGRET* properties of this source. Fan (2005) studied the γ -ray variability timescale of this source, which is about 144 days, and derived the basic parameters of this AGN, such as the black hole mass. Figure A.5 shows the X-ray spectrum from our analysis, and Figure B.4 shows the broadband SED of 0458–020. Based on our results, the intersection of the synchrotron and the IC humps locates in the X-ray band, and we derived comparable energy peaks for the two humps. To our knowledge, our broadband SED is the first one to be published for this source.

0528+134 0528+134 is a flat spectrum, high polarization radio quasar. This source has been intensively studied at the radio (Pohl et al. 1995, Britzen et al. 1999, Cai et al. 2006), X-ray (Sambruna et al. 1997, Ghisellini et al. 1999), and γ -ray (Mukherjee et al. 1996, Bottcher and Collmar 1998) bands. 0528+134 is detected by the *CGRO/EGRET* (Mattox et al. 2001) and the *Fermi/LAT* (Abdo et al. 2010b). Figure A.5 shows the X-ray spectrum from our analysis, and Figure B.4 shows the broadband SED of 0528+134. The energy peak of the IC hump is 1.5 orders of magnitude higher than that of the synchrotron hump. Previous studies on the broadband SED of this source include: Sambruna et al. (1997), Bottcher and Collmar (1998), Ghisellini et al. (1999), Mukherjee et al. (1999), and Abdo et al. (2010a). Figure C.23 displays two published SED plots by Ghisellini et al. (1999) and Abdo et al. (2010a). As shown, our results are quite similar to previously published results, in which the IC hump has a larger energy output than the synchrotron hump.

0529+075 OG 050 is a flat spectrum radio quasar. This source is not detected by the *CGRO/EGRET*, but it is present in the *Fermi* 1FGL catalog (Abdo et al. 2010b). Most of the studies on this source were performed in the radio band. Edelson (1987) studied the millimeter spectrum and variability of 0529+075 at 2.7 mm and 1.5 cm wavelengths. Robson et al. (2001) reported the observations at a wavelength of $850\ \mu\text{m}$ on this source obtained by the James-Clerk-Maxwell telescope during 1997 and 2000. In our X-ray analysis, we used the *Swift* data obtained in August 2008 (Obs. ID 00036236004), which has an integration time of 4 ks. After data binning, there are only 3 energy bins available (see Figure A.5), and the derived intrinsic N_{H} value has a large uncertainty, therefore, we only used the Galactic N_{H} value for absorption correction. Figure B.4 shows the broadband SED of 0529+075; the IC hump has a higher energy peak than the synchrotron hump. To our knowledge, our broadband SED is the first one to be published for this source.

0529+483 0529+483 is a flat spectrum radio quasar; it has a possible association with the EGRET source 3EG 0533+4751 (Mattox et al. 2001), and it is detected by *Fermi/LAT* (Abdo et al. 2010b). In the work of Sowards-Emmerd et al. (2003), one can find the

observational parameters, optical classification, as well as the optical spectrum of this source. 0529+483 is very weak in the X-ray band; in our *Swift*/XRT observation of 7 ks integration time, we have a weak detection on this source. There are only two energy bins after data grouping, therefore, we assumed a photon index of 1.8 and estimated the source flux (see Figure A.6). Figure B.4 shows the broadband SED of 0529+483. Although the SED in the X-ray band is dimmer than in the optical band, we derived a higher energy peak of the IC hump due to the higher value of SED in the γ -ray band. To our knowledge, our broadband SED is the first one to be published for this source.

0552+398 DA 193 is a flat spectrum radio quasar with a compact structure, and it has a high redshift of $z = 2.363$. This source is not detected by the *CGRO*/EGRET and *Fermi*/LAT. It has been studied in the radio band using the VLBI technique (MacDonell and Bridle 1971, Schilizzi and Shaver 1981, Spangler et al. 1983, Fey et al. 1985, Wang et al. 2001). DA 193 was classified as a GHz-peaked spectrum (GPS) source by O’Dea et al. (1991), and has a synchrotron self-absorbed spectrum with a turnover at 5 GHz (see Figure C.24 by Fey et al. 1985). Figure A.6 shows the X-ray spectrum from our analysis, and Figure B.4 shows the broadband SED of DA 193. The SED in the optical band has higher value than in the X-ray band, and we obtained a half-order higher energy peak of the IC hump than the synchrotron hump by including the LAT upper limit estimated by M. Böck. To our knowledge, our broadband SED is the first one to be published for this source.

0605–085 OC –010 is a flat spectrum radio quasar, and it has high jet apparent speeds up to $\beta_{\text{app}}=19.79\pm 0.61$ at 15 GHz (Lister et al. 2009b). This source was not detected by the *CGRO*/EGRET, but it is present in the *Fermi* 1FGL catalog (Abdo et al. 2010b). Gambill et al. (2003) investigated the X-ray core emission of this source, and Sambruna et al. (2004) studied the X-ray properties of its radio jet by *Chandra* (see Figure C.25). Figure A.6 shows the X-ray spectrum from our analysis, and Figure B.5 displays the broadband SED of OC –010. The energy peak of the IC hump is slightly higher than the synchrotron hump. To our knowledge, our broadband SED is the first one to be published for this source.

0607–157 0607–157 is a flat spectrum radio quasar. This source is not detected by the *CGRO*/EGRET and the *Fermi*/LAT. Bondi et al. (1996) reported results from VLBI 18 cm observations on this source. The circular polarization of this source was studied by Homan et al. (2001), and Li et al. (2008) applied a simple jet model to derive the parameters like black hole mass and jet power. Figure A.6 shows the X-ray spectrum from our analysis, and Figure B.5 shows the broadband SED of 0607–157. The SED in the X-ray band displays a flat profile, and together with the estimated LAT upper-limit (Böck et al., in preparation), we derived a much lower energy peak of the IC hump than of the synchrotron hump with a difference of one order of magnitude. To our knowledge, our broadband SED is the first one to be published for this source.

0642+449 OH 471 is a flat spectrum radio quasar, and it has a redshift of $z = 3.396$, which is the highest in the MOJAVE I sample. It is not detected by the *CGRO*/EGRET

and the *Fermi*/LAT. Gurvits et al. (1992) and Marscher and Shaffer (1980) studied the compact structure of this source using the VLBI technique. Volvach and Kovalev (2006) have present its radio spectra since 1970. Figure A.6 shows the X-ray spectrum from our analysis, and Figure B.5 shows our broadband SED of OH 471. The energy peak of the synchrotron hump is higher than the IC hump for one order of magnitude. To our knowledge, our broadband SED is the first one to be published for this source.

0648–165 0648–165 is an unidentified AGN in the Véron-Cetty and Véron (2006) catalog, and it has a flat radio spectrum. This source was not detected by *CGRO*/EGRET, but it is present in the *Fermi* 1FGL catalog (Abdo et al. 2010b). The *Swift*/XRT observations we used had a 6.3 ks exposure time, however, the X-ray emission of this source was weak, and there were only three bins after data grouping (see Figure A.6). In the same epoch of the *Swift* observations, six UVOT filters were used, yet all of them had no detections on the source. Therefore, we only estimated the upper limits and included them in the broadband SED plot, which is shown in Figure B.5. To our knowledge, our broadband SED is the first one to be published for this source.

0716+714 0716+714 is a flat spectrum BL Lac object, and it is very active in the high energy band. This source has been detected by the *CGRO*/EGRET (Mattox et al. 2001) and the *Fermi*/LAT (Abdo et al. 2010b), and it is a TeV source (Teshima and The MAGIC Collaboration 2008). 0716+714 has been intensively studied in the radio (e.g., Bach et al. 2006a), optical (Montagni et al. 2006, Stalin et al. 2006, Wu et al. 2007, Pollock et al. 2007), X-ray bands (Giommi et al. 1999, Pian et al. 2005), as well as in multiband efforts (Raiteri et al. 2003, Foschini et al. 2006b, Villata et al. 2008). Figure A.7 shows the X-ray spectrum from our analysis, and Figure B.5 shows our broadband SED result of 0716+714, where the X-ray and the γ -ray data are similar to the results of Abdo et al. (2010a) (see Figure C.26). The X-ray measurements are located at the tail of the synchrotron hump. However, we do not have good data coverage in the optical band for the simultaneous SED, and the polynomial fit of the synchrotron hump is not satisfactory. The broadband SED of 0716+714 was previously studied by Giommi et al. (1995), Sambruna et al. (1996), Nieppola et al. (2006), and Abdo et al. (2010a). As shown in Figure C.26, Foschini et al. (2006b) presented their results of the simultaneous SED of 0716+714, and they applied an SED model of synchrotron radiation and Compton scattering from an emitting region of a cylinder-shaped jet (Ghisellini et al. 2002).

0727–115 0727–115 is a flat spectrum radio quasar. This source was not detected by the *CGRO*/EGRET, but it is present in the *Fermi* 1FGL catalog (Abdo et al. 2010b). Most of the studies on this source were mainly performed in the radio band. Aller et al. (1981) discovered that the quasar had rotations in its polarization position angles by the observations at 4.8, 8.0, and 14.5 GHz of the UMRAO 26-m telescope. Figure A.7 shows the X-ray spectrum from our analysis, and Figure B.5 shows the broadband SED of this source. We find a flat profile of the SED in the X-ray band, which implies that the transition between the synchrotron hump and the IC hump might happen in the X-ray band. Recently, Abdo et al. (2010a) presented the study of the broadband SED of 0727–115 (see Figure C.27). Comparing with the results of Abdo et al. (2010a), we obtained a

higher peak frequency of the synchrotron hump ($\nu_{\text{peak}}^{\text{sync}} \sim 10^{13}$ Hz), but the frequency peaks of both IC humps are consistent.

0730+504 0730+504 is a flat spectrum radio quasar. This source was not detected by the *CGRO/EGRET* and the *Fermi/LAT*, and the past studies of the source were mainly focusing on the radio band. Apart from this, the soft X-ray property of this source observed by *ROSAT* was reported by Britzen et al. (2007), and the object is also included in the CGRaBS catalog, which was an all-sky survey of bright blazars searching for the likely γ -ray AGN (Healey et al. 2008). Figure A.7 shows the X-ray spectrum from our analysis, and Figure B.5 shows the broadband SED of 0730+504. As presented, the value of the high energy hump is quite low compared with the other MOJAVE sources, implying that the source is relatively quiet in the high energy band, which is consistent with the previous studies on this source. To our knowledge, our broadband SED is the first one to be published for this source.

0735+178 OI 158 is a flat spectrum BL Lac object which has been studied in the radio, optical, and X-ray bands. This source is detected by the *CGRO/EGRET* (Mattox et al. 2001) and the *Fermi/LAT* (Abdo et al. 2010b). Ciprini et al. (2007) studied the optical variability in a ten-year monitoring on this source. Agudo et al. (2006) presented the milliarcsecond jet morphology of OI 158 using the VLBI technique at 5 to 43 GHz. A change of the parsec-scale jet trajectory was suggested by Gómez et al. (1999, 2001), and the radio polarization of the jet was studied by Gabuzda et al. (1994). Figure A.7 shows the X-ray spectrum from our analysis, and in Figure B.5 we present the broadband SED of the object, which appears to be highly variable, especially in the synchrotron hump where there were more observations in the past. The broadband SED in the synchrotron part were also presented by Nieppola et al. (2006) (see Figure C.28).

0736+017 OI 061 is a flat spectrum, high polarization radio quasar. It was not detected by the *CGRO/EGRET*, but it is present in the *Fermi* 1FGL catalog (Abdo et al. 2010b). This source has been intensively studied in the optical band (e.g., Baldwin 1975, Wright et al. 1998, Clements et al. 2003, Ramírez et al. 2004). This source was detected by the global 86 GHz VLBI survey (Lee et al. 2008), and it was also included in the multifrequency monitoring program of γ -ray loud blazars (Bach et al. 2007). Figure A.7 shows the X-ray spectrum from our analysis. We present the broadband SED of 0736+017 in Figure B.6, in which one can find that the SED in the X-ray band appears to be flat, which might indicate that the transition between the synchrotron and the IC hump locates close to the X-ray band. To our knowledge, our broadband SED is the first one to be published for this source.

0738+313 OI 363 is a flat spectrum radio quasar, and this source is not detected by the *CGRO/EGRET* and the *Fermi/LAT*. There were many studies in the X-ray band on this source. The extended jet structure in the X-ray band of OI 363 was discovered by Siemiginowska et al. (2003) using *Chandra*'s observations, and new X-ray studies were followed by Kataoka and Stawarz (2005), Kim et al. (2007), and Siemiginowska et al. (2008). Figure A.7 shows the X-ray spectrum from our analysis, and Figure B.6 shows

our broadband SED of OI 363. We obtained a higher energy peak of the synchrotron hump than the value of the IC hump. Haro-Corzo et al. (2007) studied the SED from the far-UV to the X-ray band on this source, and they reported that the source presented evidence of jet emission. To our knowledge, our broadband SED is the first one to be published for this source.

0742+103 0742+103 is a GPS radio quasar (see e.g., Stanghellini et al. 1998). This source is not detected by the *CGRO/EGRET* and the *Fermi/LAT*. Multifrequency radio observations of 0742+103 were performed by Ojha et al. (2006) using VLBA, and they presented the VLBI images at 1.6, 2.3, 8.4, and 15 GHz. Labiano et al. (2007) performed optical observations on GPS sources including 0742+103, and they found the optical counterpart of this source. Torniiainen et al. (2005) constructed the radio continuum spectrum on this source (see Figure C.29). Figure A.8 shows the X-ray spectrum from our analysis, and Figure B.6 shows the broadband SED of this object, from which one can see that the fitted IC hump is higher than the synchrotron hump, implying that the energy output could be larger in the IC hump. However, in the γ -ray band we only have the estimated LAT upper limit (Böck et al., in prep.), and the polynomial fit is determined by the slope in the X-ray band. Further investigation is needed to confirm our findings.

0748+126 0748+126 is a flat spectrum, low polarization radio quasar (Wills et al. 1992). It was not detected by the *CGRO/EGRET*, but it is present in the *Fermi* 1FGL catalog (Abdo et al. 2010b). Torniiainen et al. (2005) studied its radio spectrum, and suggested that the source was a flat-spectrum source, and he found that during outbursts the source showed an inverted spectrum (see Figure C.30). Marshall et al. (2005) performed a *Chandra* survey of quasar jets on 20 sources including 0748+126, yet this source was not detected. Figure A.8 shows the X-ray spectrum from our analysis, and Figure B.6 shows the broadband SED of this object. The energy peaks of the synchrotron and the IC hump are comparable. To our knowledge, our broadband SED is the first one to be published for this source.

0754+100 0754+100 is a flat spectrum BL Lac object, and it is cataloged as a low-frequency peaked BL Lac (LBL) by Fiorucci et al. (2004). It was not detected by the *CGRO/EGRET*, but it is present in the *Fermi* 1FGL catalog (Abdo et al. 2010b). VLA observations showed that there is a diffuse halo around the core at 1.5 and 5 GHz up to scales of >120 kpc (Antonucci and Ulvestad 1985, Kollgaard et al. 1992). Recently, B0754+100 was reported to be flaring in the near-infrared band (Carrasco et al. 2010). Figure A.8 shows the X-ray spectrum from our analysis, and Figure B.6 shows the broadband SED of 0754+100. Based on our polynomial fit, the energy peak of the synchrotron hump is slightly higher than the one of the IC hump. According to the blazar classification defined by Abdo et al. (2010a), 0754+100 would be a low synchrotron peaked blazar ($\nu_{\text{peak}}^{\text{sync}} \leq 10^{14}$ Hz) based on our polynomial fit. Previously, Giommi et al. (1995) presented the broadband SED from radio to X-rays using archival data (see Figure C.31).

0804+499 0804+499 is a flat spectrum, high polarization radio quasar. This source has a possible association with the EGRET source 3EG J0808+4844 (Mattox et al. 2001),

but it is not present in the *Fermi* 1FGL catalog. The parsec-scale circular polarization at 15–43 GHz has been studied by Vitriřchak et al. (2008). Bloom et al. (1999) studied the multifrequency observations in the radio band, and Celotti and Ghisellini (2008) presented the broadband SED on this source (see Figure C.32). In our study, we use the *Swift*/XRT observation (Obs. ID: 00036196004) obtained in February 2009, however, the UVOT observation was not available in this epoch. Therefore, we use the *Swift*/UVOT data obtained in October 2009 (Obs. ID: 00036196006). Figure A.8 shows the X-ray spectrum from our analysis, and Figure B.6 shows the broadband SED of 0804+499, in which one can see that the X-ray data has a flat profile, and in the γ -ray band, the *Fermi*/LAT upper limit is shown (Böck et al. in preparation). We derived a lower energy peak of the IC hump than the synchrotron hump. Our result is different from the previously published results by Celotti and Ghisellini (2008). They derived a higher value of IC energy peak from their model (Figure C.32).

0805–077 0805–077 is a flat spectrum radio quasar, and following the projected apparent speeds in its jet of up to $\beta_{\text{app}} = 59.1 \pm 27.0$, which is the highest in the MOJAVE I sample (Lister et al. 2009b). It should have a high Lorentz factor. This source has a possible association with the EGRET source 3EG J0812–0646 (Tornikoski et al. 2002), and it is present in the *Fermi* 1FGL catalog (Abdo et al. 2010b). In our analysis, we used *Swift* data collected in May 2009. Figure A.8 shows the X-ray spectrum from our analysis, and Figure B.6 shows the broadband SED of 0805–077, from which we find that the X-ray band is located at the end of the synchrotron hump in the SED. Previously, Giommi et al. (2007) studied the broadband SED of this source using *Swift* data taken in 2005 (see Figure C.33). They found that the optical/UV data showed significant variability, and the X-ray band was at the beginning of the IC hump in the SED. Similar result was shown in Celotti and Ghisellini (2008) (see Figure C.33). Further investigation is needed to confirm the dramatic change in the broadband SED profile of 0805–077 from 2005 to 2009.

0808+019 0808+019 is a flat spectrum BL Lac object. It was not detected by the *CGRO*/EGRET, but it is present in the *Fermi* 1FGL catalog (Abdo et al. 2010b). For a short review on this source, see the work by Veron-Cetty and Veron (1993). Figure A.8 shows the X-ray spectrum from our analysis, and Figure B.6 shows our broadband SED of this source. The intersection between the synchrotron and IC hump is taken place in the X-ray band that transforms in the observed SED break. Our polynomial fit describes the data quite well. Previously, Nieppola et al. (2006) published the synchrotron part of the SED on this source, and they found that the peak frequency was around 10^{13} Hz (see Figure C.34). We find a higher peak frequency of $\nu_{\text{peak}}^{\text{sync}} \sim 10^{14}$ Hz.

0814+425 OJ 425 is a flat spectrum BL Lac object. This source was not detected by the *CGRO*/EGRET, but it is present in the *Fermi* 1FGL catalog (Abdo et al. 2010b). OJ 425 has been studied in the radio (e.g., Rector and Stocke 2003, Lee et al. 2008), optical (e.g., Lawrence et al. 1996, Pursimo et al. 2002), and X-ray bands (e.g., Britzen et al. 2007). Figure A.9 shows the X-ray spectrum from our analysis, and Figure B.7 shows the broadband SED of OJ 425. The energy peak of the IC hump is 1.5-order higher than the synchrotron hump. There were previous studies on the SED of this source by Sambruna

et al. (1996) and Nieppola et al. (2006), including only the synchrotron hump. As shown in Figure C.35, they derived the peak frequency $\nu_{\text{peak}}^{\text{sync}} \sim 10^{13-14}$ Hz, which is consistent with our results.

0823+033 0823+033 is a flat spectrum BL Lac object. This source was not detected by the *CGRO/EGRET*, but it is present in the *Fermi* 1FGL catalog (Abdo et al. 2010b). Its VLBI properties have been studied in various aspects. For example, Vitriřchak et al. (2008) studied its parsec-scale circular polarization properties at 15–43 GHz, and Lee et al. (2008) presented 86 GHz global VLBI results on this source. Figure A.9 shows the X-ray spectrum from our analysis, and Figure B.7 shows the broadband SED of 0823+033. We derived comparable energy peaks of the synchrotron and the IC hump. The synchrotron part of the SED was previously studied by Giommi et al. (1995) and Nieppola et al. (2006) (see Figure C.36). Nieppola et al. (2006) obtained a peak frequency of $\nu_{\text{peak}}^{\text{sync}} \sim 10^{13}$ Hz, which is consistent with our results.

0827+243 OJ 248 is a flat spectrum, low-polarization radio quasar. This γ -ray bright quasar has been detected by the *CGRO/EGRET* (Mattox et al. 2001) and the *Fermi/LAT* (Abdo et al. 2010b). There were a lot of studies on this source in the radio band (Marscher and Broderick 1983). Jorstad and Marscher (2004) presented imaging results of this source in the radio (VLA 5 and 15 GHz), optical (*HST*) and X-ray (*Chandra* 0.2–8 keV) bands (see Figure C.37 for an overlaid image of radio and X-ray). For our analysis of the *Swift* observations on this source, we use the XRT data obtained in April 2009 (Obs.ID 00036375014), which has the longest exposure time of XRT. However, the UVOT observations were not available in the same epoch. We use the UVOT observation obtained in March 2008 (Obs. ID 00036375002) in our analysis. Figure A.9 shows the X-ray spectrum from our analysis, and Figure B.7 shows the broadband SED of OJ 248, in which we derived a higher energy peak of the IC hump than in the synchrotron hump. Celotti and Ghisellini (2008) previously studied the broadband SED of OJ 248, and they applied a model of SSC jet to fit the SED (see Figure C.37); their results are consistent with ours.

0829+046 OJ 049 is a flat spectrum BL Lac object. It is a γ -ray loud source detected by the *CGRO/EGRET* (Mattox et al. 2001) and the *Fermi/LAT* (Abdo et al. 2010b), and Dondi and Ghisellini (1995) classified it as a LBL. OJ 049 shows rapid and large optical variability (Liller and Liller 1975), and it has rich polarization features in the parsec-scale jet (Kharb et al. 2008, Vitriřchak et al. 2008). Andruchow et al. (2005) studied the variability of optical polarization on this source, and Giroletti et al. (2004) reported a two-sided structure with a south-eastern extended emission in the VLA observation at 1.4 GHz. Figure A.9 shows the X-ray spectrum from our analysis, and Figure B.7 shows the broadband SED of OJ 049, and we derived comparable energy peaks of the synchrotron and IC hump. The synchrotron hump of the SED was previously presented by Nieppola et al. (2006), as shown in Figure C.38; they derived a peak frequency of $\nu_{\text{peak}}^{\text{sync}} \sim 10^{13-14}$ Hz, which is consistent with our results.

0836+710 4C+71.07 is a flat spectrum, low polarization radio quasar which hosts a radio jet extending up to kiloparsec scales. This source has been detected by the

CGRO/EGRET (Mattox et al. 2001) and the *Fermi/LAT* (Abdo et al. 2010b). Broadband variability was observed in this source (Otterbein et al. 1998), and space VLBI observations have revealed detailed jet structures (Lobanov et al. 1998, Perucho and Lobanov 2007). Bloom et al. (1999) studied the multiband observations in the radio, infrared, X-ray, and γ -ray bands. Here we included the *Swift* data of 4C +71.07 observed in February 2009 with an integration time of 9 ks (obsid 00036376005). Figure A.9 shows the X-ray spectrum from our analysis, and Figure B.7 shows the broadband SED of 4C +71.07. The frequency coverage is quite good because the FGAMMA and *Swift/BAT* 22-month data are available. We derived a higher energy peak of the IC hump than of the synchrotron hump with a difference of one order of magnitude. The peak frequencies of the two humps that we obtained are $\nu_{\text{peak}}^{\text{sync}} \sim 10^{14}$ Hz and $\nu_{\text{peak}}^{\text{IC}} \sim 10^{22}$ Hz. Sambruna et al. (2007b) previously published the broadband SED of 4C +71.07 (see Figure C.39); from their SED model, the synchrotron peak was not clearly shown. The frequency peak of the IC hump they derived is $\nu_{\text{peak}}^{\text{IC}} \sim 10^{20}$ Hz, which is lower than ours.

0838+133 3C 207 is a flat spectrum radio quasar. This source was not detected by the *CGRO/EGRET*, but it is present in the *Fermi* 1FGL catalog (Abdo et al. 2010b). The *Chandra* observations revealed that the source has diffuse X-ray emission from its radio lobes (Brunetti et al. 2002), and further studies on the magnetic field and particle content in the lobes were performed by Croston et al. (2005). Tavecchio et al. (2005) presented the result of the survey with *Chandra* and *HST* about the X-ray and optical emission from radio hot spots and lobes of 3C 207, as well as the SED of one hot spot of the source. Figure A.9 shows the X-ray spectrum from our analysis, and Figure B.7 shows the broadband SED of 3C 207. The synchrotron hump has a flatter profile comparing with the other MOJAVE sources, and the energy peak of the IC hump is one-order of magnitude higher than the synchrotron hump. To our knowledge, our broadband SED is the first one to be published for this source.

0851+202 OJ 287 is a flat spectrum BL Lac object. This source has been detected by the *CGRO/EGRET* (Mattox et al. 2001) and the *Fermi/LAT* (Abdo et al. 2010b). This source has been studied in the optical band for more than 100 years, and its light curve showed that the source has a quasi-periodicity of ~ 12 years, suggested by Sillanpaa et al. (1988), who also proposed a binary black hole model to explain the periodicity of this source. Massaro et al. (2003) studied the optical and X-ray variability of OJ 287, and they also presented the SED in this range (see Figure C.40). Figure A.10 shows the X-ray spectrum from our analysis, and Figure B.7 displays the broadband SED of OJ 287. From the polynomial fit, we obtained a higher energy peak of the synchrotron hump than the IC hump. The broadband SED from the radio to the γ -ray band of this source was recently presented by Abdo et al. (2010a) (see Figure C.40), and they obtained a quite similar SED profile to ours.

0906+015 4C +01.24 is a flat spectrum, high polarization radio quasar, and it has projected apparent speeds up to $\beta_{\text{app}} = 20.66 \pm 0.85$ at 15 GHz (Lister et al. 2009b). This source was not detected by the *CGRO/EGRET* (Mattox et al. 2001), but it is present in the *Fermi* 1FGL catalog (Abdo et al. 2010b). Siebert et al. (1998) studied the X-ray prop-

erties of this source, and Liu et al. (2006) investigated the relation of the jet power and the black hole mass of this source. 4C +01.24 was successfully detected and imaged using global VLBI at 86 GHz (Lee et al. 2008). Figure B.7 shows the broadband SED of this source; the SED in the X-ray band appears to have a turn-over, therefore, we set the transition of the synchrotron and IC hump in the X-ray band while applying polynomial fit. The energy peak of the IC hump is more than one order of magnitude higher than the synchrotron hump. To our knowledge, our broadband SED is the first one to be published for this source.

0917+624 0917+624 is a flat spectrum radio quasar. This source was not detected by the *CGRO/EGRET*, but it is present in the *Fermi* 1FGL catalog (Abdo et al. 2010b). 0917+624 is famous for its intra-day variability (IDV) since its discovery by Heeschen et al. (1987). There are studies on whether the variability is intrinsically from the source (e.g., Wagner and Witzel 1995), or is caused by interstellar scintillation (e.g., Rickett et al. 1995, 2001). Gabuzda et al. (2000b) studied the IDV in the polarization properties of 0917+624, and Standke et al. (1996) presented the study using VLBI and X-ray observations. Figure A.10 shows the X-ray spectrum from our analysis, and Figure B.8 shows the broadband SED of 0917+624. The SED in the X-ray band displays a flat profile, and we derived a slightly higher energy peak of the IC hump than the synchrotron hump. To our knowledge, our broadband SED is the first one to be published for this source.

0923+392 4C +39.25 is a flat spectrum, low polarization radio quasar. This source was not detected by the *CGRO/EGRET* and the *Fermi/LAT*. There are many studies related to its VLBI properties (e.g., Alberdi et al. 1997, Fey et al. 1997, Alberdi et al. 2000). Figure A.10 shows the X-ray spectrum from our analysis, and Figure B.8 shows the broadband SED of 4C +39.25. As presented, the SED in the optical band displays an inverted profile, suggesting a third hump in the SED. However, further observations are needed to confirm the SED profile of this source, and here we still use a double-hump polynomial model to fit the data. Figure C.41 shows the radio spectrum of 4C 39.25 by Marscher et al. (1991). To our knowledge, our broadband SED is the first one to be published for this source.

0945+408 4C +40.24 is a flat spectrum, low polarization radio quasar, which was not detected by the *CGRO/EGRET* and *Fermi/LAT*. The radio variability of this source in different frequencies was studied by Ciaramella et al. (2004), and the multiband properties in the submillimeter, infrared, and X-ray were investigated by Bloom et al. (1999). Sambruna (1997) studied the soft X-ray properties of this source, and they found the photon index of 4C +40.24 is 1.96 ± 0.23 from 0.1 keV to 2.4 keV. Figure A.10 shows the X-ray spectrum from our analysis, and Figure B.8 shows the broadband SED of 4C +40.24, and we found that the SED in the optical band has a slightly inverted profile, in which the energy intensity increases with frequency. To our knowledge, our broadband SED is the first one to be published for this source.

0955+476 0955+476 is a flat spectrum radio quasar, which was neither detected by the *CGRO/EGRET* nor the *Fermi/LAT*. Bloom et al. (1999) studied the multiband properties from radio to infrared, and X-ray to γ -ray band by using the VLBI observations at 8.4

and 22 GHz, together with *ROSAT* observations. Britzen et al. (2007) presented the soft X-ray properties of this source using *ROSAT*'s observations. In our analysis, we used the *Swift*/XRT observation in January 2008 (Obs. ID 00036241002) with an exposure time of 7.5 ks, however, there were only three energy bins after data grouping. Figure A.10 shows the X-ray spectrum from our analysis, and Figure B.8 shows the broadband SED of 0955+476. From the polynomial fit, we derived a higher energy peak of the synchrotron hump than the IC hump with a difference of one-order of magnitude. To our knowledge, our broadband SED is the first one to be published for this source.

1036+054 1036+054 is a flat spectrum radio quasar, which was not detected by the *CGRO*/EGRET and the *Fermi*/LAT. This source has been mainly studied in the radio band, and with less published works in the X-ray band, due to its low brightness in this band. Although there are *Swift* observations available after the *Fermi*'s launch, the exposure time was too short to obtain a sensible spectrum (1–3 ks). Therefore, we use the *Swift* observations in 2007 with an exposure time of 10 ks (Obs. ID 00036242001) in the analysis. Figure A.11 shows the X-ray spectrum from our analysis, and Figure B.8 shows the broadband SED of 1036+054. From the polynomial fit, we obtained comparable energy peaks of the synchrotron and IC humps. To our knowledge, our broadband SED is the first one to be published for this source.

1038+064 4C+06.41 is a flat spectrum radio quasar. This source was not detected by the *CGRO*/EGRET and *Fermi*/LAT. Siebert et al. (1998) presented its X-ray properties using the *ROSAT* survey data, and Evans and Koratkar (2004) studied the spectrum in the UV and optical bands using *HST*. Figure A.11 shows the X-ray spectrum from our analysis, and Figure B.8 shows the broadband SED of 4C+06.41. There are no data available in the γ -ray band, therefore we cannot obtain a satisfactory polynomial fit and estimate $\nu_{\text{peak}}^{\text{IC}}$ value. To our knowledge, our broadband SED is the first one to be published for this source.

1045–188 1045–188 is a flat spectrum radio quasar. This source was neither detected by the *CGRO*/EGRET nor by the *Fermi*/LAT. There are studies in the radio band on this quasar (e.g., at 20 GHz by Massardi et al. 2008, and at 22 GHz by Moellenbrock et al. 1996). The black hole mass of this source is estimated to be $6.83 M_{\odot}$ (Woo and Urry 2002) based on properties of the host galaxy bulges. Figure A.11 shows the X-ray spectrum from our analysis, and Figure B.8 shows the broadband SED of 1045–188. The SED in the X-ray band has a negative slope, which appears to belong to the end of the synchrotron hump. We fit the polynomial model and obtained a peak frequency of $\nu_{\text{peak}}^{\text{sync}} \sim 10^{14-15}$ Hz. However, the fit in the optical band is not satisfactory. We are not able to constrain the IC hump profile because of the lack of data. To our knowledge, our broadband SED is the first one to be published for this source.

1055+018 4C+01.28 is a flat spectrum, high polarization radio quasar. This source was not detected by the *CGRO*/EGRET, but it is present in the *Fermi* 1FGL catalog (Abdo et al. 2010b). Attridge et al. (1999) reported the discovery of the polarization structure in the jet of 4C+01.28, which consists of an inner spine with a transverse magnetic field and

a distinct boundary layer with a longitudinal magnetic field, and Pushkarev et al. (2005) studied the polarization structure using the VLBI Space Observatory Program (VSOP) at 1.6 and 5 GHz. Sambruna et al. (2004) studied the extended jet structure of this quasar using *Chandra* and *HST* observations. Figure A.11 shows the X-ray spectrum from our analysis, and Figure B.8 shows the broadband SED of 4C +01.28. We derived a higher energy peak value of IC hump than those of the synchrotron with a difference of less than an order of magnitude. The broadband SED that we obtained for (see) is quite similar with the previously published broadband SED by Abdo et al. (2010a) (see Figure C.42).

1124–186 1124–186 is a flat spectrum, high polarization radio quasar. This source was not detected by the *CGRO/EGRET*, but it is present in the *Fermi* 1FGL catalog (Abdo et al. 2010b). Siebert et al. (1998) presented the power law photon index of this source in the 0.1–2.4 keV energy band. Moellenbrock et al. (1996) studied 1124–186 using VLBI at 22 GHz, and they derived its brightness temperature to be $> 3.71 \times 10^{11}$ K. Figure A.11 shows the X-ray spectrum from our analysis, and Figure B.9 shows the broadband SED of 1124–186. From our result, we see that the X-ray emission of 1124–186 locates at the tail of the synchrotron hump in the broadband SED. We derived comparable energy peak values of the two humps from the polynomial fit. To our knowledge, our broadband SED is the first one to be published for this source.

1127–145 1127–145 is a flat spectrum radio quasar. This source is possibly associated with the EGRET source 3EG J1134–1530 (Mattox et al. 2001, Tornikoski et al. 2002), and it is detected by the *Fermi/LAT*. The observations by *Chandra* revealed that the X-ray jet of 1127–145 has a projected scale of 300 kpc (Siemiginowska et al. 2002). Further observations by *Chandra* and VLA at 1.4, 5, and 8.5 GHz on the strong X-ray jet of this source suggest that the one-zone emission model fail to explain the X-ray part of the SED, and that at least a two-component model is needed to explain the broadband emission of the jet (Siemiginowska et al. 2007). Figure A.11 shows the X-ray spectrum from our analysis, and in Figure B.9, one can find the broadband SED of 1127–145. From the polynomial fit, we derived a higher energy peak of the IC hump than the synchrotron hump with a one order of magnitude difference. Błażejowski et al. (2004) modeled the broadband SED of the parsec-scale jet of 1127–145 (see Figure C.43), and they proposed that the thermal infrared photons from the relativistic jet are up-scattered through IC mechanism, producing high energy emission.

1150+812 1150+812 is a flat spectrum radio quasar. This source is not detected by the *CGRO/EGRET* and *Fermi/LAT*. The VLBI properties and morphology of 1150+812 were described by Ros et al. (2001), and this source was included by the Effelsberg 100 m telescope flux density monitoring (Peng et al. 2000). Figure A.12 shows the X-ray spectrum from our analysis, and Figure B.9 shows the broadband SED of 1150+812. We derived a comparable energy peak of the synchrotron and the IC hump. Previously published broadband SED include the work by Sambruna et al. (1996) (see Figure C.44), who obtained a peak frequency of $\nu_{\text{peak}}^{\text{sync}} \sim 10^{13-14}$ Hz, which is consistent with our result.

1156+295 4C+29.45 is a flat spectrum, high polarization radio quasar. This source is possibly associated with the EGRET source 3EG J1200+2847 (Hartman et al. 1999, Mattox et al. 2001), and it is detected by the *Fermi*/LAT (Abdo et al. 2010b). The source has a bent jet (McHardy et al. 1990), and it shows rapid changes in the optical linear polarization. Piner and Kingham (1997a) studied the jet speed of 4C+29.45 using VLBI observations at 2 and 8 GHz during 1988 and 1996. Hong et al. (2004) suggest a jet model of a helical trajectory along a cone surface, in order to explain the phenomena observed by the long-term multifrequency VLBI observations. Figure A.12 shows the X-ray spectrum from our analysis, and Figure B.9 shows the broadband SED of 4C+29.45, in which one can find that the SED in the X-ray band is flat, indicating that the intersection of the synchrotron and the IC hump locates in the X-ray band. From the polynomial fit, we obtained comparable energy peak values of the two humps. Previous broadband SED studies in literature include: Glassgold et al. (1983), Celotti and Ghisellini (2008), and Abdo et al. (2010a). Figure C.45 shows the SED of the latter two. We obtained a value of $\nu_{\text{peak}}^{\text{sync}} \sim 10^{15}$ Hz, higher than the previous results of $\nu_{\text{peak}}^{\text{sync}} \sim 10^{13}$ Hz.

1213–172 1213–172 is a flat spectrum radio galaxy which has no known optical counterpart, and is not listed in the Véron-Cetty and Véron (2006) catalog. This source was not detected by the *CGRO*/EGRET and the *Fermi*/LAT, and the redshift of this source is unknown. The projected apparent speed of 1213–172 is $118 \pm 12 \mu\text{as yr}^{-1}$ (Lister et al. 2009b). The *Swift*/UVOT data of this source are not available because there is a 2.8 mag star in the field of view. Figure A.12 shows the X-ray spectrum from our analysis, and Figure B.9 shows the broadband SED of 1213–172. As presented, the available data are limited, and in order to constrain the SED humps, we locate the intersection of the synchrotron and IC hump at the X-ray band, and estimate the peak positions. Previously, Giommi et al. (2007) published the broadband SED of this source using *Swift* data obtained on 17 December 2005 (see Figure C.46), however, no attempt was made to model fit the observed SED data. From the results by Giommi et al. (2007), the SED in the X-ray band has a positive slope, indicating that the X-ray band is located at the beginning of the IC hump. Their results deviate from ours, and further observations are needed to confirm the broadband SED behavior of 1213–172.

1219+044 1219+044 is a flat spectrum, high polarization radio quasar. It was not detected by the *CGRO*/EGRET, but it is present in the *Fermi* 1FGL catalog (Abdo et al. 2010b). This source was also detected by *INTEGRAL* above 20 keV in the soft γ -ray band (Bassani et al. 2006, Bodaghee et al. 2007, Bird et al. 2007). Piner et al. (2007) presented the projected apparent speed of the jet in 1219+044 using the data from VLBI observations at 2 and 8 GHz to be $\beta_{\text{app}} = 3.3 \pm 2.0$, which is consistent with the results obtained by Lister et al. (2009b). Tschöke et al. (2000) studied the *ROSAT* observations of 1219+044 in the soft X-ray band (0.1–2.4 keV). Figure A.12 shows the X-ray spectrum from our analysis, and Figure B.9 shows the broadband SED of this source. We derived a higher energy peak of the IC hump than the synchrotron hump with a difference of 1.5 orders of magnitude. Previously, de Rosa et al. (2008) presented the spectrum in the energy range of 0.2–200 keV observed by *XMM-Newton* and *INTEGRAL*, and they studied the non-simultaneous broadband SED of 1219+044 (see Figure C.47).

1222+216 4C+21.35 is a flat spectrum radio quasar. Hooimeyer et al. (1992) firstly reported its possible VLBI property of superluminal motion. This quasar is active in the γ -ray band. It is one of the EGRET blazars (Nolan et al. 2003), and the *Fermi*/LAT has detected two GeV flares from 4C+21.35 (Ciprini 2009, Donato 2010). The VLBI properties of this γ -ray bright blazar were studied using the VLBA observations (e.g., Homan and Wardle 1999, Jorstad et al. 2001, Marscher et al. 2002b). Figure A.12 shows the X-ray spectrum from our analysis, and Figure B.9 shows the broadband SED of 4C+21.35. We see that the SED in the optical band is rising and has a high energy value. Previous works on broadband SED of 4C+21.35 were published by Ghisellini et al. (1998) and Celotti and Ghisellini (2008) (see Figure C.48).

1226+023 3C 273 is a well-studied flat spectrum, low polarization radio quasar, and it was detected by *CGRO*/EGRET. This source is bright in the radio, optical, X-ray and γ -ray bands, and the low redshift this source has makes it a ideal target to be studied in different bands. The *Fermi*/LAT has detected multiple luminous γ -ray outbursts from 3C 273 (Abdo et al. 2010e), and the γ -ray spectral properties were studied during its active phase. Paltani et al. (2008) reported the hard X-ray results observed by *INTEGRAL*/IBIS in the 20–60 keV band. Asada et al. (2008a) presented the rotation measure gradient in the jet of 3C 273. Figure A.12 shows the X-ray spectrum from our analysis, and Figure B.9 shows the broadband SED of 3C 273. As presented, one can see that the source is very variable in all bands. We derived comparable energy peaks of the synchrotron and IC humps. There were many multiwavelength studies on this source. Pacciani et al. (2009) reported the results of the 3-week *AGILE* multiwavelength campaign, and they studied the simultaneous broadband SED of 3C 273 (see Figure C.49). Soldi et al. (2008) presented the variability multiband studies, and they showed the average broadband SED with the timescale spanning from 4 to 44 years of observations (see Figure C.50). Abdo et al. (2010a) also presented the broadband SED of 3C 273 (Figure C.51).

1228+126 M 87 is a well-studied steep spectrum radio galaxy (see Chapter 2 for a detailed introduction). There are plenty of multiwavelength studies on this source. Baes et al. (2010) presented the *Herschel* observations in the far-infrared band, and they found that the emission can be explained by synchrotron mechanism. M 87 was not detected by the *CGRO*/EGRET. In 2008 and 2009, M 87 was monitored by the VERITAS at the VHE band, and the results were reported in Acciari et al. (2010). In our analysis, we use the XSPEC model `phabs (1) × (mekal+phabs (2) ×powerlaw)` to fit the X-ray spectrum of M 87 (see Figure A.13). In Figure B.10 one can find the broadband SED of M 87, and we do not include the polynomial fit in the plot, because the source is highly variable. Abdo et al. (2009c) reported the detection of M 87 by the *Fermi*/LAT, and they studied its γ -ray spectrum, as well as the broadband SED (see Figure C.52).

1253–055 3C 279 is a well-studied high polarization radio quasar, and it is active from the radio to the VHE bands. It is a TeV source, and high energy emission is observed frequently (e.g., Ciprini and Chaty 2008, Iafrate et al. 2009, and Giuliani et al. 2009). The parsec-scale polarization properties of 3C 279 in the core region were studied by Homan et al. (2009b) using multifrequency VLBA observations. Possible correlations

of multiband variabilities of 3C 279 were reported by Chatterjee et al. (2008). As of the broadband SED study on 3C 279, Böttcher et al. (2009) discussed about the models to interpret the broadband SED of 3C 279, and they concluded that an one-zone homogeneous leptonic jet model cannot explain the broadband emission. They suggest that either a multi-zone model or a hadronic model is capable of reproducing the observed SED of 3C 279. The *AGILE* collaboration reported the detection of 3C 279, and they also presented its broadband SED (Giuliani et al. 2009). Figure A.13 shows the X-ray spectrum from our analysis, and Figure B.10 shows our broadband SED of 3C 279. This source is in the *Swift*/BAT 22-month catalog, and the X-ray band has a good frequency coverage. Other broadband SED studies of 3C 279 include the works by Abdo et al. (2010c) and Fermi-Lat Collaboration et al. (2010) (see Figure C.53).

1308+326 The source 1308+326 shows properties of both BL Lac objects and quasars. Stickel et al. (1991) classified 1308+326 as a BL Lac object because it lacks optical line emissions, and it has high polarization and strong variability in the optical band. However, this source also shows quasar-like polarization properties in VLBI observations (Gabuzda et al. 1993). 1308+326 is variable in different bands (Moore et al. 1980, Mufson et al. 1985). This source was not detected by the *CGRO*/EGRET, but it is detected by the *Fermi*/LAT (Abdo et al. 2010b). Figure A.13 shows the X-ray spectrum from our analysis, and our broadband SED is shown in Figure B.10. The optical part in the broadband SED of 1308+326 shows strong variability. Previous studies of the SED of 1308+326 include the works by Giommi et al. (1995), Sambruna et al. (1996), Watson et al. (2000), and Abdo et al. (2010a) (see Figure C.54). Comparing the peak frequency that we obtained ($\nu_{\text{peak}}^{\text{sync}} \sim 10^{14-15}$) with previous findings, we derived a slightly higher peak frequency for the synchrotron hump in the SED.

1324+224 1324+224 is a flat spectrum radio quasar, and it has a high redshift of $z = 1.4$. This source is possibly associated to an *EGRET* unidentified source 3EG J1323+2200 (Mattox et al. 2001, Fegan et al. 2005), and it is in the 1FGL catalog of *Fermi* (Abdo et al. 2010b). Figure A.13 shows the X-ray spectrum from our analysis, and Figure B.10 shows the broadband SED of 1324+224. As presented, we derived a higher energy peak of the IC hump than the synchrotron hump. To our knowledge, our broadband SED is the first one to be published for this source.

1334–127 PKS 1335–127 is a flat spectrum, high polarization radio quasar. This source is detected by the *CGRO*/EGRET (Mattox et al. 2001) and the *Fermi*/LAT (Abdo et al. 2010b). The VLBI circular polarization properties of PKS 1335–127 was studied by Vitriřchak et al. (2008). Figure A.13 shows the X-ray spectrum from our analysis, and Figure B.10 shows our broadband SED of PKS 1335–127. As presented, we obtained a slightly higher energy peak of the IC hump than the synchrotron hump. Previously, Maraschi et al. (1995) presented the results of *ROSAT* observations in the X-ray band, and from their non-simultaneous broadband SED study, they suggested that IC mechanism is the origin for the X-ray band emission. Figure C.55 shows the broadband SED studied by Maraschi et al. (1995) and Celotti and Ghisellini (2008); they found that the peak frequency $\nu_{\text{peak}}^{\text{sync}} \sim 10^{13}$ Hz, which is consistent with our results.

1413+135 1413+135 is a flat spectrum BL Lac object. It was not detected by the *CGRO/EGRET* and *Fermi/LAT*. This source is one of the few radio-loud AGNs with an apparent spiral host galaxy, and it is not clear that if the AGN is located in the background or in the spiral galaxy (Stoche et al. 1992, McHardy et al. 1994, Lamer et al. 1999, Perlman et al. 2002). Perlman et al. (1996) presented the multifrequency VLBI observations of PKS 1413+135, which showed a two-sided parsec-scale jet, and they suggested that the source is young radio source. Figure A.13 shows the X-ray spectrum from our analysis, and Figure B.10 shows the broadband SED of 1413+135. Note that the SED in the X-ray band have a negative slope. By applying polynomial fits to the data, we obtained a significantly higher energy peak of the IC hump than the synchrotron hump. Previously, Giommi et al. (1995) and Nieppola et al. (2006) studied the synchrotron hump of the SED of PKS 1413+135 (see Figure C.56); Nieppola et al. (2006) obtained the peak frequency $\nu_{\text{peak}}^{\text{sync}} \sim 10^{13}$ Hz, which is consistent with our findings.

1417+385 1417+385 is a flat spectrum radio quasar. It is possibly associated to the *EGRET* source 3EG J1424+3734 (Mattox et al. 2001), however, it is not present in the *Fermi* 1FGL catalog. The soft X-ray properties obtained by *ROSAT* of 1417+385 were presented by Britzen et al. (2007). Figure A.14 shows the X-ray spectrum from our analysis, and in Figure B.10, one can find the broadband SED of 1417+385. The SED in the X-ray band displays a negative slope, therefore, we extend the polynomial fit of the synchrotron hump until the X-ray band. We do not perform a polynomial fit to the IC hump due to the lack of data. To our knowledge, our broadband SED is the first one to be published for this source.

1458+718 3C 309.1 is a compact steep-spectrum, low polarization radio quasar. It is not detected by the *CGRO/EGRET* and the *Fermi/LAT*. The source shows a distorted one-sided jet observed by the VLBA and VSOP at multifrequencies (e.g., Ros and Lobanov 2001, Rossetti et al. 2005, Gawroński and Kus 2006). Siemiginowska et al. (2008) presented the X-ray properties of 3C 309.1 derived from *Chandra* observation of 17 ks; other X-ray studies on this source include Hardcastle and Worrall (1999), Belsole et al. (2007) and Salvati et al. (2008). The *Spitzer* observations reveal the mid-infrared properties of 3C 309.1, which is luminous in this band (Cleary et al. 2007). Figure A.14 shows the X-ray spectrum from our analysis. As shown in Figure B.10, the broadband SED of 3C 309.1 is quite variable in the synchrotron hump range, and we derived a slightly higher energy peak of the synchrotron hump than of the IC hump. To our knowledge, our broadband SED is the first one to be published for this source.

1502+106 4C +10.39 is a flat spectrum, high polarization radio quasar with a high redshift of $z = 1.839$. It was not detected by the *CGRO/EGRET*, but it is present in the *Fermi* 1FGL catalog (Abdo et al. 2010b). The multifrequency study using the EVN and the VLBA revealed its curved jet and superluminal motion (An et al. 2004). George et al. (1994) reported the X-ray properties and spectrum of 4C +10.39 using the data obtained by *ROSAT* and *ASKA* during 1990 and 1994. Figure A.14 shows the X-ray spectrum from our analysis, and Figure B.11 shows the broadband SED of 4C +10.39. As presented, we derived a 2-order of magnitude higher peak of the IC hump than the synchrotron hump.

Previously, George et al. (1994) and Abdo et al. (2010a) also presented the broadband SED of this source (see Figure C.57); the former derived a lower IC hump, whileas the latter derived a higher IC hump. Our results are consistent with the recent findings by Abdo et al. (2010a).

1504–166 1504–166 is a flat spectrum, high polarization radio quasar, which has a possible association with the *EGRET* source 3EG J1504–1537 (Mattox et al. 2001, Tornikoski et al. 2002), and it is not in the *Fermi* 1FGL catalog. The X-ray properties were obtained by the *Einstein* observatory (Henriksen et al. 1984, Wilkes et al. 1994). Tornikoski et al. (2000) presented the multifrequency radio properties of this source at 90 and 230 GHz. In our analysis, the X-ray spectrum of this source (*Swift* Obs. ID 00036207004) has poor quality (Figure A.14), and we are not able to derive the intrinsic neutral hydrogen column density N_{H} and photon index Γ . To estimate the flux, we assume a absorbed power law model to this source; we fix the value of N_{H} to the galactic column density measured by the LAB survey (Kalberla et al. 2005), and we assume a photon index of $\Gamma = 1.8$. Figure B.11 shows our broadband SED of 1504–166. We derived a low energy peak of the synchrotron hump, and we do not perform a polynomial fit to the IC hump due to the lack of data. To our knowledge, our broadband SED is the first one to be published for this source.

1510–089 1510–089 is a flat spectrum, high polarization radio quasar, and it is very active in the high energy band. The source has been detected by the *CGRO/EGRET* (Thompson et al. 1993) and *Fermi/LAT* (Fermi-LAT Collaboration 2010), moreover, it is a newly-discovered TeV source²². Homan et al. (2002) studied the relativistic jet of this source, as well as the radio polarization properties. Figure A.14 shows the X-ray spectrum from our analysis, and Figure B.11 shows the broadband SED of 1510–089, in which one can see that the high-energy hump has more energy output compare with the synchrotron hump. In recent years, there were many studies related to the broadband SED of 1510–089, such as works by Singh et al. (1990, 1997), Kataoka et al. (2008), Abdo et al. (2010a), and Fermi-LAT Collaboration (2010) (see Figure C.58). Previous studies also found that the IC hump has a higher energy peak than the synchrotron hump, and are consistent with our findings.

1538+149 4C +14.60 is a flat spectrum BL Lac object, and it is not detected by the *CGRO/EGRET* and the *Fermi/LAT*. Gear et al. (1994) presented the submillimeter spectrum of this source, and its X-ray properties were studied by Ciliegi et al. (1993, 1995). Falomo et al. (1993) studied the simultaneous UV, optical, and near-infrared data of 4C +14.60, and they found that the spectrum can be well-described by a single power law model. Gabuzda et al. (2006) investigated the polarization emission in the optical and radio band in this source. Vitriishchak et al. (2008) presented the circular polarization properties in the parsec-scale jet of 4C +14.60. Figure A.14 shows the X-ray spectrum from our analysis, and Figure B.11 shows the broadband SED of 4C +14.60. As presented, the SED in the X-ray band appears to be located in the tail of the synchrotron

²²<http://tevcat.uchicago.edu/>

hump. We applied the polynomial fit to the synchrotron hump and skipped the high-energy region one due to the lack of data. Previous published SED results include the studies of the synchrotron hump by Sambruna et al. (1996) and Nieppola et al. (2006) (see Figure C.59), and they found a peak frequency of $\nu_{\text{peak}}^{\text{sync}} \sim 10^{14-15}$ Hz, which is consistent with our findings.

1546+027 1546+027 is a flat spectrum, high polarization radio quasar. This source was not detected by the *CGRO/EGRET*, but it is present in the *Fermi* 1FGL catalog (Abdo et al. 2010b). The optical properties of this source were studied by Smith et al. (1994), including its spectrum and polarization. Mosoni et al. (2002) presented results on 5 GHz space VLBI observations of 1546+027. Worrall and Wilkes (1990) studied the soft X-ray spectrum of this source at the energy range of 0.1–3.5 keV obtained by the *Einstein* observatory, and Siebert et al. (1998) presented the results obtained by *ROSAT* in the 0.1–2.4 keV energy band. Tornainen et al. (2005) studied the long term radio variability and the radio spectrum of 1546+027 (see Figure C.60). Figure A.15 shows the X-ray spectrum from our analysis, and Figure B.11 shows the broadband SED of 1546+027. As presented, the energy peak of the IC hump is slightly higher than the synchrotron hump. To our knowledge, our broadband SED is the first one to be published for this source.

1548+056 4C+05.64 is a flat spectrum, high polarization radio quasar. This source was not detected by the *CGRO/EGRET*, but it is present in the *Fermi* 1FGL catalog (Abdo et al. 2010b). The X-ray properties of this source obtained by *ROSAT* were studied by (Siebert et al. 1998), and the Faraday rotation measure properties of the parsec-scale jet were obtained from VLBA images (Zavala and Taylor 2004). Figure A.15 shows the X-ray spectrum from our analysis, and Figure B.11 shows the broadband SED of 4C+05.64. We found that the IC hump has a slightly higher energy peak than the synchrotron hump. Previously, Giommi et al. (2007) presented the unmodeled data of broadband SED of this source (see Figure C.61).

1606+106 4C+10.45 is a flat spectrum radio quasar. It is a known γ -ray bright source, and it is detected by both the *CGRO/EGRET* (Schoenfelder 1994, McLaughlin et al. 1996) and the *Fermi/LAT* (Abdo et al. 2010b). Comastri et al. (1997) studied the soft X-ray spectra of this source using *ROSAT* observations at 0.1–2.0 keV. Figure A.15 shows the X-ray spectrum from our analysis, and Figure B.11 shows our broadband SED of 4C+10.45. The fitted polynomial models show that the IC hump has a significantly higher energy output than the synchrotron hump. The previously published SED by Celotti and Ghisellini (2008) also shows the same result (see Figure C.62).

1611+343 DA 406 is a flat spectrum, low polarization radio quasar, and it was detected by the *CGRO/EGRET* (Hartman et al. 1999) and the *Fermi/LAT* (Abdo et al. 2010b). Cotton and Spangler (1979) carried out multifrequency radio observations at 0.325–15.5 GHz during an outburst of DA 406, and they found that the outburst appeared to be simultaneous at all frequencies. Piner and Kingham (1997b) studied the VLBI properties of DA 406 at 2 and 8 GHz, and they found it to have apparent superluminal motions (see

also Piner and Kingham 1997b for previous observations of DA 406). Figure A.15 shows the X-ray spectrum from our analysis, and Figure B.11 shows our broadband SED of this source. We derive an energy peak of the IC hump slightly higher than that of the synchrotron hump. Celotti and Ghisellini (2008) presented the SED of this source previously. They obtained a much higher peak of the IC hump comparing to the synchrotron hump based on their jet model (see Figure C.63); the synchrotron peak frequency they obtained ($\nu_{\text{peak}}^{\text{sync}} \sim 10^{13-14}$ Hz) is consistent with our findings.

1633+382 4C +38.41 is a flat spectrum, high polarization radio quasar, and it is highly variable in the radio and optical bands. Besides, it is a γ -ray bright source detected by *CGRO/EGRET* (Hartman et al. 1999) and *Fermi/LAT* (Abdo et al. 2010b). Barthel et al. (1995) reported superluminal motion at 5 GHz of 4C +38.41, which was one of the few γ -ray AGN having this property at that time. This source was found to have a power law γ -ray spectrum with an energy spectral index of 0.9 at 30 MeV–30 GeV (Mattox et al. 1993). Peng et al. (2003) performed an optical monitoring of R and B bands from February to March 2002, and they reported amplitude variations of up to 0.78 magnitude in two months. A variability of 11.6% of 4C +38.41 was observed at 92 cm wavelength using the Westerbork Synthesis Radio Telescope (Peng 2002). Figure A.15 shows the X-ray spectrum from our analysis, and Figure B.12 shows our broadband SED of 4C +38.41. The peak of IC hump is one order of magnitude higher than the synchrotron hump. Our findings are consistent with previously published work by Mattox et al. (1993) and Celotti and Ghisellini (2008) (see Figure C.64).

1637+574 OS 562 is a flat spectrum, low polarization radio quasar, and it is not active in the high energy band. It was not detected by *CGRO/EGRET* and *Fermi/LAT*, and most of the studies of this source are performed in the radio and optical bands. Lawrence et al. (1996) presented the optical spectra of this source covering the wavelength range of 3800–9400 Å, and Wills et al. (1995) reported the optical spectrum obtained by the *HST*. 1637+574 is found to be fast-varying at 6 and 11 mm wavelength (Kraus et al. 2003), and it is a GPS source candidate, of which the long term variability at 37 GHz was studied by Tornaiainen et al. (2005). Vitriushchak et al. (2008) measured the upper limit of the circular polarization of this source to be 0.24% at 15 GHz, 0.48% at 22 GHz, and 0.8% at 43 GHz. Figure A.15 shows the X-ray spectrum from our analysis, and Figure B.12 shows the broadband SED of 1637+574. We find that the SED in the X-ray band appears to be located in the tail of the synchrotron hump. We do not apply polynomial fit to the IC hump due to the lack of data. To our knowledge, our broadband SED is the first one to be published for this source.

1638+398 NRAO 512 is a flat spectrum radio quasar, and it is not active in the high energy bands. It is not present in the *Fermi/LAT* 1FGL catalog. A possible association with the EGRET source 2EG J1635+3813 (Iler et al. 1997) was suggested. Bloom et al. (1999) presented the multiband observations of NRAO 512, and the data were obtained by the VLBI observations at 8.4 and 22 GHz, as well as by *ROSAT* in the X-ray band. Figure A.16 shows the X-ray spectrum from our analysis, and Figure B.12 shows the broadband SED of NRAO 512. The peak of the high energy hump is one order of magnitude lower

than of the synchrotron hump. To our knowledge, our broadband SED is the first one to be published for this source.

1641+399 3C 345 is a flat spectrum, high polarization radio quasar, and it has been intensively studied in the radio and optical band. Ros et al. (2000) studied the parsec-scale structure of 3C 345 at 1.3, 2, 3.6, and 6 cm wavelengths of VLBA total intensity and linear polarization observations. Hirotani et al. (2000) investigated if the parsec-scale jet of this source is dominated by a normal plasma or an electron-positron plasma, and they concluded it is likely to be the latter case. Sambruna et al. (2004) presented the overlaid images of radio (VLA at 5 GHz) and X-ray (*Chandra* at 0.5–8 keV) band (see Figure C.65). Lobanov and Roland (2005) proposed a supermassive binary black hole model to 3C 345, in order to explain the quasi-periodic flaring activities of this source. 3C 345 is not detected by *CGRO/EGRET*, and it is possibly associated to the *Fermi/LAT* source 1FGL J1642.5+3947, yet still need further confirmation (Schinzel et al. 2010). Figure A.16 shows the X-ray spectrum from our analysis, and Figure B.12 shows the broadband SED of 3C 345. The frequency coverage is quite good by including the *Swift/BAT* 22-month data. The division of the synchrotron and IC humps appears to be located between the XRT and BAT sampling range (10–15 keV), as seen in Figure B.12. Tavecchio et al. (2002) studied the broadband SED model and applied a model of SSC plus IC from external radiation field (see Figure C.65).

1655+077 1655+077 is a flat spectrum, high polarization radio quasar, which is not active in the high energy range. This source is not detected by *CGRO/EGRET* and *Fermi/LAT*. There were a few studies in the X-ray band. For example, Siebert et al. (1998) presented the X-ray properties using the *ROSAT* observations at 0.1–2.4 keV, and they obtained a flux upper-limit of $3.28 \times 10^{-13} \text{ erg cm}^{-2} \text{ s}^{-1}$. Wilkes et al. (1994) presented the results of *Einstein Observatory* observations at 0.16–3.5 keV. Figure A.16 shows the X-ray spectrum from our analysis, and Figure B.12 shows the broadband SED of 1655+077. As presented, we derived a higher energy peak in the IC hump than in the synchrotron hump. Note that this result is due to the X-ray archival data position. To our knowledge, our broadband SED is the first one to be published for this source.

1726+455 1726+455 is a flat spectrum radio quasar. This source is not detected by *CGRO/EGRET*, but it is present in the *Fermi/LAT* 1FGL list (Abdo et al. 2010b). Britzen et al. (2007) presented the soft X-ray properties obtained by *ROSAT* at 0.1–2.4 keV. In our analysis, we used the *Swift* observation which has ~ 4 ks exposure time (Obs. ID 00036214004), and the source appears to be quite weak. There were only one bin after grouping the X-ray spectrum (see Figure A.16), and we were not able to perform spectral fitting to the X-ray data. Therefore, we estimated the flux of the source by assuming a photon index of $\Gamma = 1.8$ and N_{H} value of $2 \times 10^{20} \text{ cm}^{-2}$ (the LAB survey; Kalberla et al. 2005) with an absorbed power law model. Figure B.12 shows the broadband SED of 1726+455, and the energy peak of the synchrotron hump is slightly lower than the IC humps. To our knowledge, our broadband SED is the first one to be published for this source.

1730–130 NRAO 530 is a flat spectrum, high polarization radio quasar which hosts a double-sided kilo-parsec scale jet. This source is actively variable in the radio (Marscher and Broderick 1981, Feng et al. 2006), optical (Pollock et al. 1979), X-ray (Foschini et al. 2006a), and γ -ray (Hartman et al. 1999, Abdo et al. 2010b) wavebands. Bower and Backer (1998) presented space VLBI observations (VSOP) on this source at 1.6 and 5 GHz. Figure A.16 shows the X-ray spectrum from our analysis, and Figure B.12 shows our broadband SED results of NRAO 530. As presented, we derived comparable energy peaks in the synchrotron and IC hump. Previously published broadband SED include the works by Ghisellini et al. (1998) and Foschini et al. (2006a) (see Figure C.66). Comparing our results with previously published works, the peak frequencies of the synchrotron and the IC peak have similar values.

1739+522 4C+51.37 is a high polarization radio quasar. This source is detected by *CGRO/EGRET* (Hartman et al. 1999), and it is present in the *Fermi* 1FGL catalog (Abdo et al. 2010b). Ghisellini et al. (1998) constructed the broadband SED of 4C+51.37 from archival data, and they applied the emission model of SSC and external Compton (EC) mechanism to fit the data (see Figure C.67). Celotti and Ghisellini (2008) presented the broadband SED of archival data and applied a slightly different SED model (SSC+EC) to derive the power output of the jet (see Figure C.67). Figure A.16 shows the X-ray spectrum from our analysis, and Figure B.12 shows our broadband SED result. By examining the peak frequencies of the synchrotron and the IC humps, our results are consistent with the previous findings.

1741–038 1741–038 is a γ -ray bright, high polarization radio quasar. This source was detected by *CGRO/EGRET* (Hartman et al. 1999), and was found to be variable in the γ -ray band (Nolan et al. 2003); however, it is not present in the *Fermi* 1FGL catalog. The source experienced dramatic changes²³ in flux densities at 2.3 and 8.1 GHz during June to August, 1992 (Clegg et al. 1996, Lazio et al. 2000). Figure A.17 shows the X-ray spectrum from our analysis, and Figure B.13 shows the broadband SED of 1741–038. The *Fermi/LAT* upper limit (M. Böck et al., in prep.) is not available for this source, therefore, we are not able to estimate the IC peak. The broadband SED of this source were studied by Ghisellini et al. (1998) and Celotti and Ghisellini (2008), and their results are shown in Figure C.68.

1749+096 4C+09.57 is a flat spectrum BL Lac object. This source is not detected by *CGRO/EGRET*, but it is present in the *Fermi* 1FGL catalog (Abdo et al. 2010b). Iguchi et al. (2000) performed VSOP and VLBA observations at 4.8, 8.4, 15, and 22 GHz after its radio outburst in May 1998, and they suggested that the rapid variability of 4C+09.57 was due to the variation of the viewing angle. Figure A.17 shows the X-ray spectrum from our analysis, and Figure B.13 shows our broadband SED of this source. The broadband SED of 4C+09.57 has been studied by Giommi et al. (1995), Sambruna et al. (1996, 1999), Nieppola et al. (2006), and Abdo et al. (2010a). Figure C.69 shows the results of Sambruna et al. (1999) and Abdo et al. (2010a). By examining the peak frequency of

²³The event was so-called extreme scattering events (see Fiedler et al. 1987 for definition), which is due to the variation in the interstellar medium.

the two humps in the SED, our results are consistent with the previous findings by (Abdo et al. 2010a).

1751+288 1751+288 is a flat spectrum radio quasar, and it is not active in the high energy band. This source is mainly studied in the radio band, and it lacks the study in the X-ray and the γ -ray bands. The source was not detected by *CGRO/EGRET* and *Fermi/LAT*. In our analysis, we used *Swift* observations in January 2010 with an integration time of 7.6 ks, yet the source was too weak in the X-ray band to allow us to study its spectral properties (two spectral bins after grouping; see Figure A.17). To estimate the flux, we assumed a photon index of $\Gamma = 1.8$ and a N_{H} value of $4.98 \times 10^{20} \text{ cm}^{-2}$ with an absorbed power-law model. Figure B.13 shows the broadband SED of 1751+288. The peaks of the synchrotron and the IC hump have comparable values, according to our SED fitting results. To our knowledge, our broadband SED is the first one to be published for this source.

1758+388 1758+388 is a flat spectrum radio quasar at a redshift of $z = 2.092$. This quasar is not detected by the *CGRO/EGRET* and the *Fermi/LAT*. Britzen et al. (2007) presented the soft X-ray properties of 1758+388 obtained by *ROSAT*. In our analysis, we used the *Swift* observation obtained in November 2006 with an integration time of 9.8 ks, yet the source was too weak in the X-ray band to study its spectral properties (two bins after grouping; see Figure A.17). To estimate the flux, we assumed a photon index of $\Gamma = 1.8$ and a N_{H} value of $2.53 \times 10^{20} \text{ cm}^{-2}$ with an absorbed power-law model. A more recent observation taken in May 2009 is available, however, the integration time was too short (1 ks) to provide a reasonable X-ray spectrum. We plan to request for *Swift* ToO observations later. Figure B.13 shows the broadband SED of 1758+388. The X-ray band appears to be at the tail of the synchrotron hump. We omitted the polynomial fit to the IC hump due to the lack of data. To our knowledge, our broadband SED is the first one to be published for this source.

1800+440 1800+440 is a flat spectrum radio quasar, and it displays projected jet apparent speeds up to $\beta_{\text{app}} = 15.41 \pm 0.49$ (Lister et al. 2009b). This source was not detected by the *CGRO/EGRET* and *Fermi/LAT*. 1800+440 has been studied in the radio (Zhang and Fan 2003, Lee et al. 2008), optical (Caccianiga et al. 2002), and X-ray (Britzen et al. 2007) bands. Figure A.17 shows the X-ray spectrum from our analysis, and Figure B.13 shows our broadband SED of 1800+440. The X-ray SED locates in the tail of the synchrotron hump, and in the γ -ray band, we included the *Fermi/LAT* upper limit (Böck et al., in prep.). We cannot apply a polynomial fit to the IC hump due to the lack of data points. To our knowledge, our broadband SED is the first one to be published for this source.

1803+784 1803+784 is a flat spectrum BL Lac object, and it has been studied from the radio to the high-energy bands. This source is not detected by the *CGRO/EGRET*, but it is present in the *Fermi* 1FGL catalog (Abdo et al. 2010b). Britzen et al. (2005) reported the VLBI monitoring on this source at 3.6 cm wavelength between 1986 and 1993, and they found that the jet ridge line is significantly curved and discussed the possibility of a

helical path in its jet. Gabuzda and Chernetskii (2003) presented the VLBI polarization properties of 1803+784 at 5, 8, 15, and 22 GHz, and they found that the region with polarized emission extends up to 150 pc away from the core. The optical light curve of this source showed an overall variation greater than 3 magnitude including flares (Nesci et al. 2002). Figure A.17 shows the X-ray spectrum from our analysis, and Figure B.13 shows the broadband SED of 1803+784, in which the frequency sampling is quite good in the synchrotron hump. We derived comparable energy peaks for the synchrotron and the IC hump. Previous studies in the literature on the SED of this source include Giommi et al. (1995), Sambruna et al. (1996), Nesci et al. (2002), Nieppola et al. (2006). Figure C.70 displays the SED by Nesci et al. (2002) and Nieppola et al. (2006). As shown, our results are consistent with previous findings.

1807+698 3C 371 is a flat spectrum BL Lac object, and it has a redshift of $z = 0.051$. This source is not detected by *CGRO/EGRET*, but it is present in the *Fermi* 1FGL catalog (Abdo et al. 2010b). The jet of this source was discovered in the radio (Wrobel and Lind 1990), optical (Nilsson et al. 1997, Scarpa et al. 1999), and X-rays (Pesce et al. 2001, Sambruna et al. 2007a) bands. Carini et al. (1998) reported on optical variability of this source from photometric measurements. Gómez and Marscher (2000) presented the first space VLBI observations of 3C 371 at 4.8 GHz, and they found the inner jet had a size of 7 mas. Figure A.18 shows the X-ray spectrum from our analysis, and Figure B.13 shows the broadband SED of 3C 371. The source is quite variable in the optical band. The frequency sampling in the synchrotron hump is good, and we see comparable energy peaks of the synchrotron and the IC humps. Previous SED studies of this source include Giommi et al. (1995), Sambruna et al. (1996), and Nieppola et al. (2006) (see Figure C.71). Our results are consistent with previous findings in the synchrotron part of the SED.

1823+568 4C +56.27 is a flat spectrum BL Lac object which has high apparent projected speeds up to $\beta_{\text{app}} = 20.86 \pm 0.49$ in its jet (Lister et al. 2009b). This source is not detected by the *CGRO/EGRET*, but it is in the *Fermi* 1FGL catalog (Abdo et al. 2010b). Jorstad et al. (2007) presented the results of multifrequency linear polarization monitoring of this source obtained at optical and with VLBA (1, 3, and 7 mm wavelengths). Figure B.13 shows our broadband SED of 4C +56.27, as presented, we obtained a slightly higher energy peak in the IC hump than in the synchrotron hump. Previous SED studies of this source include the works of Giommi et al. (1995), Sambruna et al. (1996), and Nieppola et al. (2006) (see Figure C.72). The peak frequency of the synchrotron hump is located at $\nu_{\text{peak}}^{\text{sync}} \sim 10^{13}$ Hz from our results, which are consistent with previous findings.

1828+487 3C 380 is a low polarization, compact steep spectrum radio quasar. This source was not detected by the *CGRO/EGRET*, but it is in the *Fermi* 1FGL catalog. Two knots in the jet of 3C 380 were detected in the optical band by *HST* and in the radio band by the VLA at 15, 22, and 43 GHz (de Vries et al. 1999, O’Dea et al. 1999). Marshall et al. (2005) presented the X-ray imaging and spectroscopy results of this source obtained by *Chandra*, and a knot in the jet 1.8'' from the core was detected in the X-rays. Papa-georgiou et al. (2006) performed a rotation measure (RM) study on 3C 380 using space

VLBI observations at 1.6 GHz and ground-based VLBI at 5 GHz, and they found variations in RM around a bright knot in the source. Figure A.18 shows the X-ray spectrum from our analysis, and Figure B.14 shows our broadband SED results of 3C 380. To our knowledge, our broadband SED is the first one to be published for this source.

1849+670 1849+670 is a flat spectrum radio quasar. This source is not detected by the *CGRO/EGRET*, but it is in the *Fermi/LAT* 1FGL catalog (Abdo et al. 2010b). This source was mainly studied in the radio and optical bands. In the X-ray band, Britzen et al. (2007) presented the soft X-ray properties of this source. Figure A.18 shows the X-ray spectrum from our analysis, and Figure B.14 shows our broadband SED of 1849+670. We find a higher energy output in the IC hump than in the synchrotron hump. Abdo et al. (2010a) published a broadband SED of this source (see Figure C.73), and their results are consistent with our SED findings.

1928+738 4C +73.18 is a flat spectrum, low polarization radio quasar, and it was not detected by the *CGRO/EGRET* and *Fermi/LAT*. There were many studies about its superluminal jet (e.g, Johnston et al. 1987, Hummel et al. 1992, Guirado et al. 1995, and Guirado et al. 1998). Ghosh and Soundararajaperumal (1992) and Yuan et al. (2000) studied the X-ray properties of this source using *EXOSAT* and *ASCA* observations at 0.5–10 keV. Figure A.18 shows the X-ray spectrum from our analysis, and Figure B.14 shows the broadband SED of 4C +73.18. The polynomial fits provide a higher peak in the synchrotron hump than in the IC hump. Sambruna et al. (1996) and Yuan et al. (2000) presented the broadband SED of this source, as shown in Figure C.74. The results for the synchrotron hump peak from Sambruna et al. (1996) and ours are consistent.

1936–155 1936–155 is a high polarization, flat spectrum radio quasar. It was possibly associated to the EGRET source 3EG J1937–1529 (Mattox et al. 2001, Tornikoski et al. 2002), but it is not present in the *Fermi* 1FGL catalog. This source was classified as a high-peaking GPS source (Tornikoski et al. 2001), and Tornainen et al. (2005) presented the radio spectrum of this source (see Figure C.75). In our X-ray analysis of this source, we fix the N_{H} to the Galactic value (Kalberla et al. 2005) in order to obtain a reasonable fit due to the poor quality of the X-ray spectrum (see Figure A.18). Figure B.14 shows the broadband SED of 1936–155, and it does not have a typical double-hump profile as most of the blazars have. The slopes of the optical and the X-ray bands are both negative. As shown, we applied the polynomial fit to the synchrotron hump extended to the X-ray band, in order to estimate the peak position. It is not clear if the double-hump model is the best to describe the SED of 1936–155 as long as we don't have γ -ray data available. To our knowledge, our broadband SED is the first one to be published for this source.

1957+405 Cygnus A is a radio galaxy which has a steep spectrum. It host a two-sided jet with two giant radio lobes in the end, in which one can find hot spots forming due to the jets colliding with interstellar medium (Stawarz et al. 2007). There are many multi-wavelength studies on the hot spots of this strong radio source (e.g., Bałucińska-Church et al. 2005, Lazio et al. 2006, and Stawarz et al. 2007). Cygnus A was not detected by the *CGRO/EGRET* and the *Fermi/LAT*. However, the giant lobe of Cygnus A might generate

γ -ray emission from external source, e.g., cosmic rays and extragalactic background light (Atoyan and Dermer 2008). Figure A.19 shows the X-ray spectrum from our analysis, and Figure B.14 shows the broadband SED of Cygnus A. The SED is quite variable from the radio to X-ray band. We omit the polynomial fit of the SED, and only data points are shown in the plot. Previously, Stawarz et al. (2007) studied the broadband SED of the hot spots in Cygnus A.

1958–179 1958–179 is a flat spectrum, high polarization radio quasar. It is not detected by the *CGRO/EGRET*, but it is in the *Fermi* 1FGL catalog (Abdo et al. 2010b). The polarization properties in the radio band of 1958–179 were studied by Homan et al. (2001) at 5 GHz, and Ricci et al. (2004) at 18.5 GHz. Siebert et al. (1998) studied the X-ray properties of this source using *ROSAT* observations in the 0.1–2.4 keV energy band. Figure A.19 shows the X-ray spectrum from our analysis, and Figure B.14 shows the broadband SED of 1958–179 from radio to γ -ray band. We obtained comparable energy peaks of the synchrotron and the IC hump. To our knowledge, our broadband SED is the first one to be published for this source.

2005+403 2005+403 is a flat spectrum radio quasar. This source is not active in the high energy band, and it was not detected by the *CGRO/EGRET* and the *Fermi/LAT*. There were more studies in the radio band of this source. Gabányi et al. (2006) studied the variability and source structure of 2005+403 during 1992 and 2003 using VLBI observations at 1.6, 5, 8, 15, 22, and 43 GHz. Figure A.19 shows the X-ray spectrum from our analysis, and Figure B.14 shows the broadband SED of 2005+403. As presented, the optical data are not available. To constrain the synchrotron hump, we set the intersection of the two humps at the of the XRT spectrum. This assumption gives us an estimate of the upper limit of the synchrotron peak. To our knowledge, our broadband SED is the first one to be published for this source.

2008–159 2008–159 is a flat spectrum radio quasar. This source is not detected by the *CGRO/EGRET* and the *Fermi/LAT*. 2008–159 was identified as an extreme-GPS source by Tornikoski et al. (2000); Tornainen et al. (2005) presented the radio spectrum of this source (see Figure C.76). Siebert et al. (1998) presented the X-ray properties of this source using the *ROSAT* in the 0.1–2.4 keV energy band. Figure A.19 shows the X-ray spectrum from our analysis, and Figure B.14 shows the broadband SED of 2008–159. The energy peak of the synchrotron hump is slightly higher than of the IC hump. To our knowledge, our broadband SED is the first one to be published for this source.

2021+317 4C +31.56 is an extragalactic source which is not included in the Véron-Cetty and Véron (2006) catalog, and the optical class and redshift are unknown. This source is not detected by the *CGRO/EGRET* and *Fermi/LAT*, and there were not many X-ray studies on this source. In our analysis, we used the *Swift* observation obtained in April 2007 with the longest integration time of 18 ks (Obs. ID 00036248003). We cannot use the *Swift* observations in August 2008 due to the poor quality of the X-ray spectrum. Figure A.19 shows the X-ray spectrum from our analysis, and Figure B.15 shows the broadband SED of 4C +31.56. The optical data are not available, therefore, we

are not able to estimate the peak position of the synchrotron hump. To our knowledge, our broadband SED is the first one to be published for this source.

2021+614 OW 637 is a flat spectrum GPS radio galaxy. This source is not detected by the *CGRO/EGRET* and *Fermi/LAT*. Tschager et al. (2000) performed VSOP observations at 5 GHz to study this source, and they found a slow motion in its jet; see their paper for a review on this source. The radio spectrum of this source was studied by Tornainen et al. (2005) (see Figure C.77). Giommi et al. (2007) presented the first X-ray studies of OW 637 obtained by *Swift/XRT* in February 2006 with an integration time of 2.3 ks. Here we analyzed the *Swift* data obtained in July 2009 with an integration time of 9.6 ks (Obs. ID 00036352007). However, the obtained X-ray emission was too weak to have a reasonable spectral analysis (one bin after grouping; see Figure A.19). To estimate the flux, we assumed a photon index of $\Gamma = 1.8$ and a N_{H} value of $1.35 \times 10^{21} \text{ cm}^{-2}$ with an absorbed power-law model. Figure A.19 shows the X-ray spectrum from our analysis, and Figure B.15 shows the broadband SED of OW 637. As shown, we omit the polynomial fit of the IC hump due to the lack of data. To our knowledge, our broadband SED is the first one to be published for this source.

2037+511 3C 418 is a flat spectrum radio quasar. This source is not detected by the *CGRO/EGRET* and *Fermi/LAT*. It is proposed that 3C 418 has a precessing jet based on the jet structure (Muxlow et al. 1984, Lu and Zhou 2005). The X-ray properties were reported by Worrall et al. (1987) and Wilkes et al. (1994). In our analysis, the *Swift/XRT* observation has an integration time of 8.7 ks (Obs. ID 00036221007), and the X-ray spectrum has only 3 energy bins after data grouping (see Figure A.20). To estimate the flux, we assumed a photon index of $\Gamma = 1.8$ and a N_{H} value of $5.4 \times 10^{21} \text{ cm}^{-2}$ with an absorbed power-law model. Figure B.15 shows the broadband SED of 3C 418, and as shown, the peaks of the synchrotron and the IC hump have comparable values. To our knowledge, our broadband SED is the first one to be published for this source.

2121+053 2121+053 is a flat spectrum, high polarization radio quasar. This source is not detected by the *CGRO/EGRET* and *Fermi/LAT*. 2121+053 was classified as a high frequency peaker by Dallacasa et al. (2000). Tornainen et al. (2005) studied the radio spectrum of this source, and reported its extremely high variability (see Figure C.78). Figure A.20 shows the X-ray spectrum from our analysis, and Figure B.15 shows the broadband SED of 2121+053. The optical SED has a positive slope, and the X-ray SED has a negative one; this might suggest a narrow hump from the optical to the X-ray band to be further investigated. To estimate the peak position, we applied a polynomial fit from the radio to the X-ray band to the synchrotron hump in the SED. To our knowledge, our broadband SED is the first one to be published for this source.

2128–123 2128–123 is a flat spectrum, low polarization radio quasar, and it was identified as a GPS source by Tornikoski et al. (2001). Tornainen et al. (2008) presented the radio spectrum of this source, and they found a mild variability on this source (see Figure C.79). 2128–123 is not detected by the *CGRO/EGRET* and the *Fermi/LAT*. Its X-ray properties were studied by Worrall and Marshall (1984) and Shastri et al. (1993)

using the *Einstein* observatory. Moles et al. (1985) presented optical observations of this source, and they suggested a compact structure based on its 1-day variability in the optical band. Lanzetta et al. (1993) presented the ultraviolet spectrum of this source. Figure A.20 shows the X-ray spectrum from our analysis, and Figure B.15 shows the broadband SED of 2128–123, in which we find that the variability in the optical band is high. To obtain a reasonable fit, we give the simultaneous optical *Swift* measurement more weighting while fitting, and we derive a higher synchrotron peak than IC peak. To our knowledge, our broadband SED is the first one to be published for this source.

2131–021 4C –02.81 is a flat spectrum BL Lac object, and it has projected apparent speeds up to $\beta_{\text{app}} = 20.0 \pm 1.4$. It is not detected by the *CGRO/EGRET*, but it is in the *Fermi* 1FGL catalog (Abdo et al. 2010b). Urry et al. (1996) presented the X-ray properties of this source using *ROSAT* observations. Vitriřchak et al. (2008) studied the parsec-scale polarization properties at 15, 22, and 43 GHz on this source, and detected polarization at all three frequencies. In our analysis, the *Swift/XRT* observation of this source has an integration time of 1.5 ks (Obs. ID 00036223004), and the X-ray spectrum has only one energy bin after grouping (see Figure A.20). To estimate the flux, we assumed a photon index of $\Gamma = 1.8$ and a N_{H} value of $4.27 \times 10^{20} \text{ cm}^{-2}$ with an absorbed power-law model. Figure B.15 shows the broadband SED of 4C –02.81, and the optical data display a high variability. We obtained comparable energy peaks of the two humps. Previously published broadband SED studies include the works by Giommi et al. (1995), Sambruna et al. (1996), and Nieppola et al. (2006) (see Figure C.80). By examining the peak frequency of the synchrotron hump, our results are consistent with those.

2134+004 2134+004 is a flat spectrum, low polarization radio quasar. This source is not detected by the *CGRO/EGRET* and *Fermi/LAT*. 2134+004 was classified as a GPS source by O’Dea (1998), and a high frequency peaker (HFP) by Dallacasa et al. (2000). Orienti et al. (2006) performed a study on the parsec-scale morphology of HFP sources including this source using VLBA observations at 8.4, 15.3, 22.2, and 43.2 GHz. Orienti et al. (2007) investigated the spectral variability of this source as a HFP source. Figure C.81 displays the radio spectrum presented by Torniainen et al. (2005). Sambruna (1997) reports the soft X-ray properties of this source using *ROSAT* observations in the 0.1–2.4 keV energy range. Figure A.20 shows the X-ray spectrum from our analysis, and Figure B.15 shows the broadband SED of 2134+004. As presented, the energy peak of the synchrotron hump is about 1.5 orders of magnitude higher than the IC hump. To our knowledge, our broadband SED is the first one to be published for this source.

2136+141 OX 161 is a flat spectrum radio quasar, and it has a redshift of $z = 2.427$. This source is not detected by *CGRO/EGRET* and *Fermi/LAT*. OX 161 was identified as a GPS source by Tornikoski et al. (2001), and Torniainen et al. (2005) presented its radio spectrum (see Figure C.82). Savolainen et al. (2006) reported that the jet of OX 161 is extremely curved based on multifrequency VLBA observations from 2.3 to 43 GHz. Figure A.20 shows the X-ray spectrum from our analysis, and Figure B.15 shows the broadband SED of OX 161. The optical data are not available, and we are not able to estimate the peak position of the synchrotron hump. To our knowledge, our broadband

SED is the first one to be published for this source.

2145+067 4C+06.69 is a low polarization, flat spectrum radio quasar. This source is not detected by the *CGRO/EGRET*, but it is in the *Fermi* 1FGL catalog (Abdo et al. 2010b). Yamasaki et al. (2000) reported the results of X-ray observations using *ASCA*. This source was found to be very variable and have a flat radio spectrum until 5 GHz; the spectrum was then inverted up to 20 GHz (Tornikoski et al. 2001). Tornainen et al. (2005) found that the radio spectrum of this source is convex only during outbursts (see Figure C.83). Evans and Koratkar (2004) presented the UV spectrum of 4C+06.69 at 1200–3300 Å using the *HST* observations. Figure A.21 shows the X-ray spectrum from our analysis, and Figure B.16 shows the broadband SED of this source. Notice that the SED in the optical band is inverted, which might imply a third hump is needed when fitting the SED. At present stage, we still apply a double-hump polynomial model to the SED to estimate the peak positions. We obtained similar values for the energy peaks of the synchrotron and the IC hump. To our knowledge, our broadband SED is the first one to be published for this source.

2155–152 2155–152 is a flat spectrum, high polarization radio quasar (Véron-Cetty and Véron 2006), however, Kuehr and Schmidt (1990) and Gabuzda et al. (2000a) classified this source as a BL Lac object. Sambruna (1997) studied the soft X-ray spectrum of 2155–152 using *ROSAT* observations, and they found that 2155–152 has a steep, HBL-like soft X-ray spectrum. This source is not detected by the *CGRO/EGRET*, but it is in the *Fermi* 1FGL source list (Abdo et al. 2010b). Figure A.21 shows the X-ray spectrum from our analysis, and Figure B.16 shows the broadband SED of 2155–152. The SED in the X-ray band has a flat profile, which might imply the intersection of the synchrotron and the IC hump is in the X-ray band. We obtained similar values for the energy peaks of the two humps. To our knowledge, our broadband SED is the first one to be published for this source.

2200+420 BL Lac is a flat spectrum BL Lac object. This famous source is well-studied and is very active across the electromagnetic spectrum. BL Lac is associated with the EGRET source 3EG J2202+4217 (Mattox et al. 2001), and it is also detected by *Fermi/LAT* (Abdo et al. 2010b); it is also a TeV emitter (Albert et al. 2007). Papadakis et al. (2007) reported the long term optical spectral variability of this source, and Villata et al. (2009) studied its optical and radio long term variability. Bach et al. (2006b) studied the structural evolution of BL Lac using VLBI observations. Figure A.21 shows the X-ray spectrum from our analysis, and Figure B.16 shows the broadband SED of BL Lac. As presented, we obtained a slightly higher energy peak for the synchrotron hump than the IC hump. We derived a synchrotron peak frequency of $\sim 10^{14}$ Hz, and it is in the range of low synchrotron peaked BL Lac object, according to the threshold set by Abdo et al. (2010a). Previous broadband SED study of BL Lac include the works by Giommi et al. (1995), Sambruna et al. (1996), Nieppola et al. (2006), Albert et al. (2007), Celotti and Ghisellini (2008), and Abdo et al. (2010a) (see Figure C.84 for two of the SED plots). Compare our results with previous findings, we see that the SED profile obtained by Abdo et al. (2010a) is very similar to ours, and the peak frequencies of the two humps are consistent

with earlier results.

2201+171 2201+171 is a flat spectrum radio quasar. This source is not detected by the *CGRO/EGRET*, however, it is present in the *Fermi* 1FGL catalog (Abdo et al. 2010b). Homan et al. (2001) investigated the parsec-scale circular polarization properties of this source, and they found that the source has a fractional core linear polarization of 2.3%, and a fractional core circular polarization of +0.24%. Figure A.21 shows the X-ray spectrum from our analysis, and Figure B.16 shows the broadband SED of 2201+171. As presented, we obtained a higher energy peak of the IC hump than the synchrotron hump with one-order of magnitude difference. To our knowledge, our broadband SED is the first one to be published for this source.

2201+315 4C+31.63 is a flat spectrum, low polarization radio quasar. This source is not detected by the *CGRO/EGRET* and the *Fermi/LAT*. Corbin and Boroson (1996) studied the spectrum in the UV and the optical band of 4C+31.63, and Netzer et al. (2007) presented the SED of this source in the optical, near IR, and far IR band with the *Spitzer* measurements. Figure A.21 shows the X-ray spectrum from our analysis, Figure B.16 shows the broadband SED of 4C+31.63. From our results, one can see that the source is quite variable in the optical band. The SED in the X-ray band is flat, and in the γ -ray band there is only one upper-limit point estimated by M. Böck (priv. comm.). We obtained a higher energy peak of the synchrotron hump than the IC hump. To our knowledge, our broadband SED is the first one to be published for this source.

2209+236 2209+236 is a core-dominated flat-spectrum radio quasar. The radio turn-over frequency of this source is above 5 GHz (Dallacasa et al. 2000), which indicates that the source is very compact and is possibly young. This source was identified as a HFP source (Dallacasa et al. 2002), and Orienti et al. (2007) studied its spectral variability in the radio band. 2209+236 is detected by the *CGRO/EGRET* (Mattox et al. 2001) and the *Fermi/LAT* (Abdo et al. 2010b). Giommi et al. (2007) presented the *Swift/XRT* results obtained in April 2005. Here we used the *Swift* observation obtained in April 2009 with an integration time of 9 ks in the SED study (Obs. ID 00036359002). Figure A.21 shows the X-ray spectrum from our analysis, and Figure B.16 shows the broadband SED of 2209+236. The source has a typical blazar SED profile, where the peaks of the low- and high-energy part have a comparable value. To our knowledge, our broadband SED is the first one to be published for this source.

2216–038 2216–038 is a flat spectrum radio quasar, and it is not detected by the *CGRO/EGRET* and the *Fermi/LAT*. Tornikoski et al. (2001) studied the radio spectra and variability of this source, and they found that it has an inverted spectrum between 1 and 8 GHz; Tornainen et al. (2005) presented the radio spectrum of 2216–038, and reported a turnover frequency of 7.4 GHz (see Figure C.85). Figure A.22 shows the X-ray spectrum from our analysis, and Figure B.16 shows the broadband SED of 2216–038. As presented, we obtained a higher energy peak for the synchrotron hump than the IC hump with a difference of one order of magnitude. To our knowledge, our broadband SED is the first one to be published for this source.

2223–052 3C 446 is a flat spectrum, low polarization radio quasar. It is not detected by the *CGRO/EGRET*, but it is in the *Fermi* 1FGL catalog (Abdo et al. 2010b). Figure A.22 shows the X-ray spectrum from our analysis, and Figure B.16 shows the broadband SED of 3C 446. As presented, the synchrotron hump of the SED is well-sampled in frequency. We obtained comparable values for the synchrotron and the IC hump of the SED. Previously, Giommi et al. (1995) and Nieppola et al. (2006) presented the synchrotron part of the broadband SED (see Figure C.86 for the result of Nieppola et al. 2006). We derived a peak frequency of 10^{13} Hz for the synchrotron hump, and our result is consistent with previous findings.

2227–088 PHL 5225 is a flat spectrum, high polarization radio quasar. It is not detected by the *CGRO/EGRET*, but it is in the *Fermi* 1FGL catalog (Abdo et al. 2010b). Tornikoski et al. (2000) studied the millimeter spectrum from 90 GHz to 230 GHz of PHL 5225; Siebert et al. (1998) reported the X-ray properties of this source. Figure A.22 shows the X-ray spectrum from our analysis, and Figure B.17 shows the broadband SED of PHL 5225. As presented, we obtained a much higher energy peak for the IC hump than the synchrotron hump with almost two-order of magnitude difference. Previously, Giommi et al. (2007) presented the broadband SED of this source using the *Swift* observation and archival data (see Figure C.87), however, they did not apply models to the SED.

2230+114 CTA 102 is a flat spectrum, high polarization radio quasar. This source is possibly associated to the EGRET source 3EG J2232+1147 (Mattox et al. 2001), and it is detected by *Fermi/LAT* (Abdo et al. 2010b). Gabuzda et al. (2008) studied the radio circular polarization of CTA 102, and they suggested a helical magnetic field in its jet. Figure A.22 shows the X-ray spectrum from our analysis, and Figure B.17 shows the broadband SED of CTA 102. As shown, we derived a higher IC energy peak than the synchrotron hump with one-order of magnitude difference. Celotti and Ghisellini (2008) studied the broadband SED of CTA 102, and they applied a jet model with SSC and EC photon source to the data points (see Figure C.88). They obtained a higher IC hump than the synchrotron hump, which is consistent with our results, and the values of the peak frequencies they derived are similar to ours.

2243–123 2243–123 is a flat spectrum, high polarization radio quasar. This source is not detected by the *CGRO/EGRET* and the *Fermi/LAT*. Figure A.22 shows the X-ray spectrum from our analysis, and Figure B.17 shows the broadband SED of 2243–123. As presented, we obtained a very low energy peak of the IC hump, which is more than one order of magnitude lower than the synchrotron hump. Tavecchio et al. (2002) studied the broadband SED of 2243–123, and they applied an SED model using SSC plus EC radiation field (see Figure C.89). They obtained a higher energy peak of the synchrotron hump than the IC hump, which is consistent with our result.

2251+158 3C 454.3 is a flat spectrum, high polarization radio quasar. This source is detected by the *CGRO/EGRET* (Mattox et al. 2001) and the *Fermi/LAT* (Abdo et al. 2010b), and it is well-studied from the radio to the γ -ray band. There are many broadband SED studies of this source (e.g., Giommi et al. 2006, Ghisellini et al. 2007, Tavecchio et al.

2007, Celotti and Ghisellini 2008, and Sikora et al. 2008). Figure A.22 shows the X-ray spectrum from our analysis, and Figure B.17 shows the broadband SED of 3C 454.3. As presented, the SED has a very good frequency coverage. We derived a higher energy peak of the IC hump than the synchrotron hump with a difference of two orders of magnitudes. Figure C.90 displays two broadband SED studies by Ghisellini et al. (2007) and Abdo et al. (2010a), and one can find that the variations of the SED are quite significant during its flaring phase. To understand the physical mechanism of this source, simultaneous observations in all bands are needed in order to constrain the SED models better.

2331+073 2331+073 is a flat spectrum radio quasar. This source is not detected by the *CGRO/EGRET*, but it is in the *Fermi* 1FGL catalog (Abdo et al. 2010a). Figure A.23 shows the X-ray spectrum from our analysis, and Figure B.17 shows the broadband SED of this source. The SED in the optical band shows an inverted profile compare with a typical blazar SED, and this might imply a third hump is needed in the SED fit. However, we keep the double hump profile and derive the peak positions in our study. We obtained comparable values of the energy peaks for the synchrotron and the IC hump of the SED. To our knowledge, our broadband SED is the first one to be published for this source.

2345–167 2345–167 is a flat spectrum, high polarization radio quasar. This source is not detected by the *CGRO/EGRET*, but it is in the *Fermi* 1FGL catalog (Abdo et al. 2010a). Siebert et al. (1998) presented the X-ray properties of 2345–167. Figure A.23 shows the X-ray spectrum from our analysis, and Figure B.17 shows the broadband SED of this source. We find that the SED in the optical and the X-ray band have different slopes compared to typical blazar SED profiles, and it appears that there is a third hump from the optical to the X-ray band. Further investigation is needed to confirm this possible hump. At current stage, we still keep the double-hump polynomial models and derive the peak positions of the SED. We obtained a slightly higher energy peak of the IC hump than the synchrotron hump. To our knowledge, our broadband SED is the first one to be published for this source.

2351+456 4C +45.51 is a flat spectrum radio quasar. This source is possibly associated to the EGRET source 3EG J2358+4604 (Mattox et al. 2001), and it is not detected by the *Fermi/LAT*. In our analysis, the *Swift/XRT* observation of this source has an integration time of 8 ks (Obs. ID 00035048001), and the X-ray spectrum has only one energy bin after grouping (see Figure A.23). To estimate the flux, we assumed a photon index of $\Gamma = 1.8$ and a N_{H} value of $9.18 \times 10^{20} \text{ cm}^{-2}$ with an absorbed power-law model. The *Swift/UVOT* observation of the same epoch has no detections of this source in the optical band, and we used the available data obtained by the six filters to estimate the upper-limit of the source. Figure A.23 shows the X-ray spectrum from our analysis, and Figure B.17 shows the broadband SED of 2351+456. As noted, the data in the optical bands are upper-limits. We obtained comparable values of the synchrotron peak and the IC peak. To our knowledge, our broadband SED is the first one to be published for this source.

4.6 Statistical Properties of the MOJAVE Sample

In the previous section, we presented the broadband SED of each MOJAVE source, and we compared our results with earlier SED studies, if any. As mentioned, the MOJAVE I sample consists of 135 radio-selected bright blazars which constitute a statistically complete sample of 101 quasars, 22 BL Lac Objects, 8 radio galaxies, and 4 unidentified AGN. In this section, we will investigate the relationships between different parameters derived from the VLBI, X-ray, and broadband SED properties. By distinguishing different types of AGN in our sample, we are able to study the behaviors of each group. In the previous sections, we derived the flux and the photon index (Γ_X) in the X-ray band of the MOJAVE sources (see Table 4.6). By using the flux and luminosity distance, we can derive the luminosity of each source (L_X). From the polynomial fit of broadband SED, we derived the peak positions of the synchrotron and the IC hump ($\nu_{\text{peak}}^{\text{sync}}$, $\nu_{\text{peak}}^{\text{IC}}$, $\nu F_{\nu_{\text{peak}}^{\text{sync}}}$, and $\nu F_{\nu_{\text{peak}}^{\text{IC}}}$; see Appendix B). In Section 4.6.1, we will present the histograms of the derived parameters, and we want to see if there is any difference between quasars, BL Lac objects, and radio galaxies. In Section 4.6.2, we investigate possible relations between the derived parameters of our results and VLBI properties: the maximum apparent jet speed (β_{app} ; Lister et al. 2009b). We show the dispersion plots of those parameters and discuss possible correlations.

4.6.1 Histograms

X-ray Properties

Figure 4.12 and 4.13 show the distributions of the X-ray photon index and luminosity of the MOJAVE sample. Figure 4.12 shows the distributions of quasars and BL Lac objects

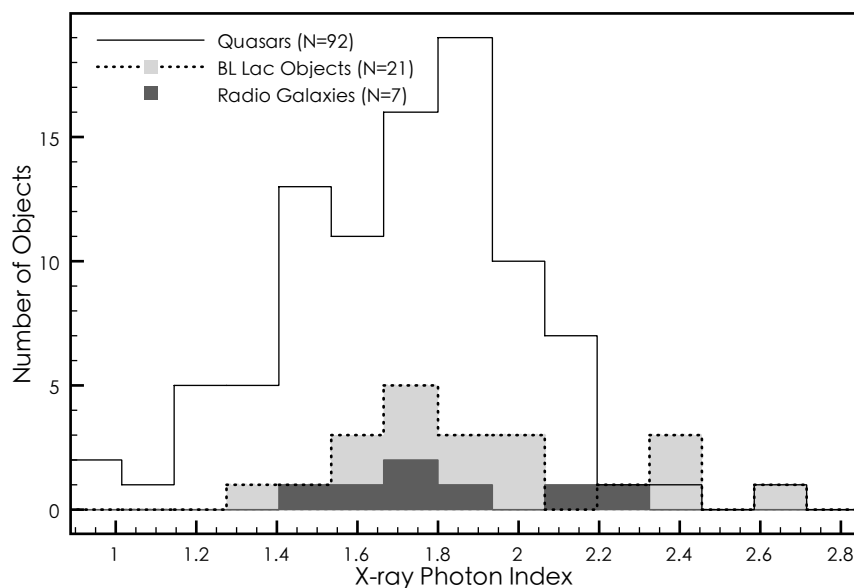


Figure 4.12: X-ray photon index distribution of the MOJAVE sample.

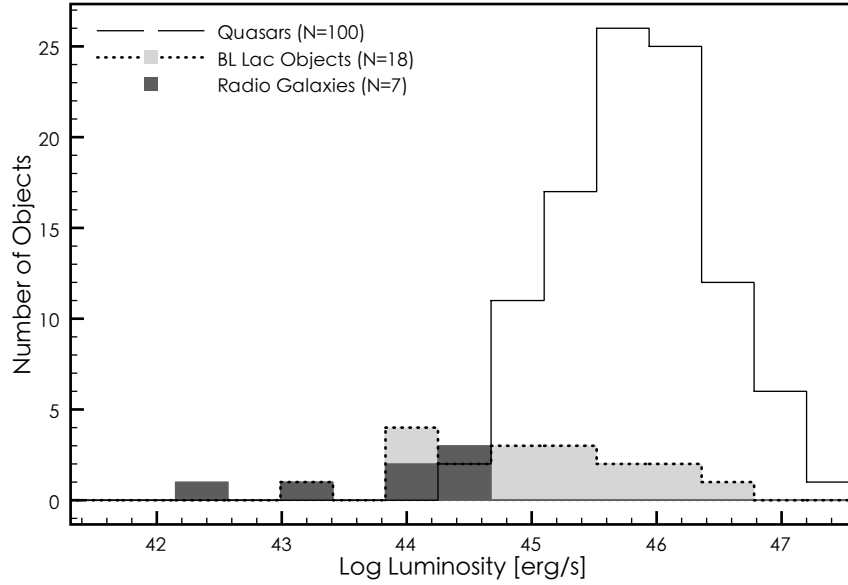


Figure 4.13: X-ray luminosity distribution of the MOJAVE sample.

share the same tendency, that both groups have a maximum number of objects with the photon indices in the range of $1.6 < \Gamma_X < 1.9$. As for the radio galaxies, most of the objects locate in the range of $1.5 < \Gamma_X < 1.8$. Note that we excluded 10 sources (see Table 4.8 for the list) in the analysis of the photon index, since we could not obtain reliable values for them from the poor quality of the spectra. To estimate their fluxes, we assumed a value for the photon index of 1.8 (see Appendix A for details). Figure 4.13 shows the distribution of the X-ray luminosity of the MOJAVE sample. We see that quasars have the maximum number of objects located at $\sim 10^{45.8} \text{ erg s}^{-1}$, whereas BL Lac objects distribute more evenly in the range of $10^{44-47} \text{ erg s}^{-1}$. The X-ray luminosity distribution of the radio galaxies is at a lower energy range, which is between $10^{42} \text{ erg s}^{-1}$ and $10^{45} \text{ erg s}^{-1}$. Four BL Lac objects were excluded in the luminosity analysis since their redshifts are unknown (see Table 4.8 for a list of the four sources).

Table 4.8: Sources excluded from the parameter study.

L_X ^(a)	Γ_X ^(b)		SED_{sync} ^(c)	SED^{IC} ^(d)		
0048-097	0529+483	1758+388	0316+413	0003-066	1228+126	1758+388
0300+470	0838+133	2021+614	0716+714	0016+731	1417+385	1800+440
0422+004	1504-166	2037+511	1228+126	0119+115	1504-166	1936-155
0735+178	1726+455	2131-021	1957+405	0316+413	1538+149	2021+614
	1751+288	2351+456	2136+141	1038+064	1637+574	2121+053
				1045-188	1741-038	

^(a) Sources excluded for the X-ray luminosity study due to unknown redshift.

^(b) Sources excluded for the X-ray photon index study due to poor quality of X-ray spectrum.

^(c) Sources excluded for the synchrotron hump study due to poor data sampling in the SED.

^(d) Sources excluded for the IC hump study due to poor data sampling in the SED.

Kadler (2005) studied the X-ray luminosity and photon index distribution of quasars, BL Lac objects, and radio galaxies in the 2cm-X-Sample, which is a subsample of the MOJAVE sample, and he presented the distribution of the two parameters in his work as well. He found that quasars have a higher range of luminosity ($10^{44} < L_X < 10^{48} \text{ erg s}^{-1}$), while as BL Lac objects distribute in the range of $10^{43.5-46.5} \text{ erg s}^{-1}$, and radio galaxies locate at the range of $10^{41-44} \text{ erg s}^{-1}$. For the X-ray photon indices, Kadler (2005) found that quasars tend to have flatter spectra with their distribution centered at $\Gamma_X \sim 1.7$ and spanning from 1.1 to 2; BL Lac objects distribute evenly in a range of $1.4 < \Gamma_X < 2$, and radio galaxies have the steepest distribution in the range of $1.6 < \Gamma_X < 2.4$. Our results on the X-ray properties derived from the MOJAVE sample are consistent with the previous findings by Kadler (2005) using the 2cm-X-Sample.

Broadband SED Properties

As shown in Appendix B, we derived the peak positions of the SED for most of the objects. For the synchrotron hump, we have estimated all peak positions except for five sources (see Table 4.8). For example, we do not include the result of the synchrotron peak of the radio galaxy 0316+413 due to the high variability of the data (see Figure B.3). For the IC hump, there are 16 sources that have no peak value estimated due to the lack of high energy data. Among them, there are 12 quasars, 2 BL Lac objects, and 2 radio galaxies (see Table 4.8 for a list of the 16 sources).

Figure 4.14 and 4.15 show the distribution of the peak frequencies of the low energy (synchrotron) and high energy (IC) hump, $\nu_{\text{peak}}^{\text{sync}}$ and $\nu_{\text{peak}}^{\text{IC}}$. In Figure 4.14, we see that most of the MOJAVE quasars have the synchrotron peak frequency below 10^{14} Hz , which can be classified as low synchrotron peaked blazars by the definition of Abdo et al.

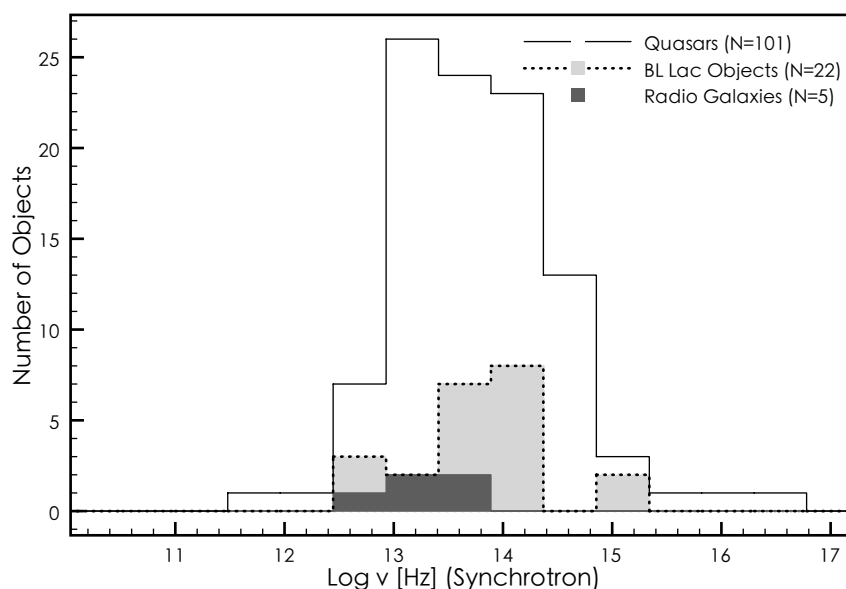


Figure 4.14: Distribution of $\nu_{\text{peak}}^{\text{sync}}$, which is the peak frequency of the synchrotron hump in the SED, of the MOJAVE sample.

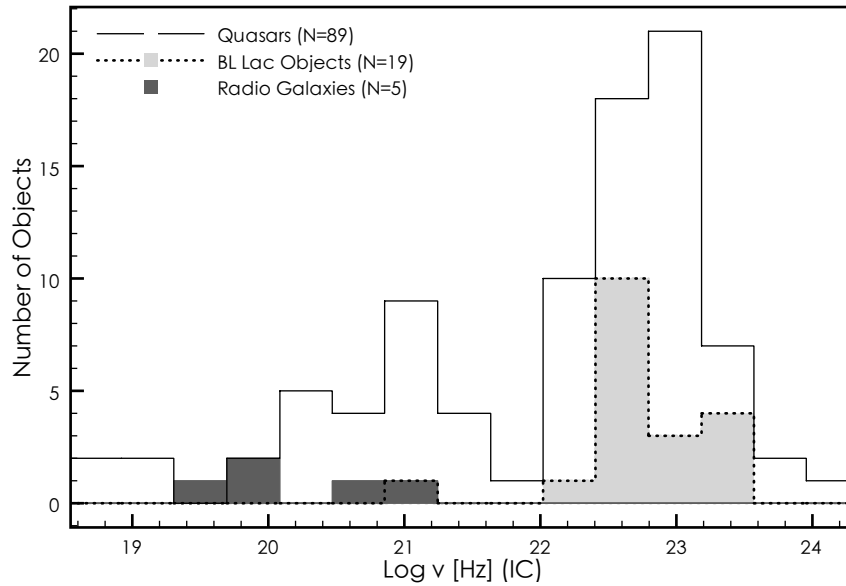


Figure 4.15: Distribution of $\nu_{\text{peak}}^{\text{IC}}$, which is the peak frequency of the IC hump in the SED, of the MOJAVE sample.

(2010a). Also, the majority of the MOJAVE blazars have the peak frequency in the range of 10^{13-15} Hz. The synchrotron peak frequencies of BL Lac objects are mostly in the range of $10^{13.5-14.5}$ Hz, and the radio galaxies have a lower value of $\nu_{\text{peak}}^{\text{sync}}$, which is in the range of $10^{12.5-14}$ Hz.

In Figure 4.15, we find that the peak frequencies of the IC hump have a wider range in their distribution. The first thing to be noticed is that the quasars seem to have two dominant peaks in the histogram, one centered at $\nu_{\text{peak}}^{\text{IC}} \sim 10^{21}$ Hz, and another centered at $\nu_{\text{peak}}^{\text{IC}} \sim 10^{23}$ Hz. The BL Lac objects have their peak frequencies distributed in a high energy range of $10^{22.5} \text{ Hz} < \nu_{\text{peak}}^{\text{IC}} < 10^{23.5} \text{ Hz}$, whereas the radio galaxies have a much lower value of $\nu_{\text{peak}}^{\text{IC}}$.

The energy peak histograms of the synchrotron and the IC hump also look a bit different. Figure 4.16 shows the histogram of the synchrotron energy peak $\nu F_{\nu}^{\text{sync}}$. From this plot, we find that the radio galaxies have the highest energy peak of the synchrotron hump among all sources. The BL Lac objects have their distribution centered at $\nu F_{\nu}^{\text{sync}} \sim 10^{12.2} \text{ Hz Jy}$, and the quasars have their highest distribution at $\nu F_{\nu}^{\text{sync}} \sim 10^{12} \text{ Hz Jy}$, which is the lowest among the three.

The energy peak histogram of the IC hump is shown in Figure 4.17, in which we excluded 17 sources for IC peak analysis due to the lack of high energy data (see Table 4.8 for the list). Again, the IC energy peaks of quasars appear to have two dominant distribution peaks, one centered at $\nu F_{\nu}^{\text{IC}} \sim 10^{11-11.5} \text{ Hz Jy}$, and another centered at $\nu F_{\nu}^{\text{IC}} \sim 10^{13} \text{ Hz Jy}$. This result is similar to the histogram of the IC peak frequency (see Figure 4.15). For the BL Lac objects, we find the dominant distribution peaks at $10^{12.5} \text{ Hz Jy}$. The radio galaxies have a peak distribution around $\nu F_{\nu}^{\text{IC}} \sim 10^{13} \text{ Hz Jy}$.

Abdo et al. (2010a) studied the broadband SED of the γ -ray selected *Fermi* LBAS sample (see Abdo et al. 2009b for the LBAS sample). They found that the synchrotron

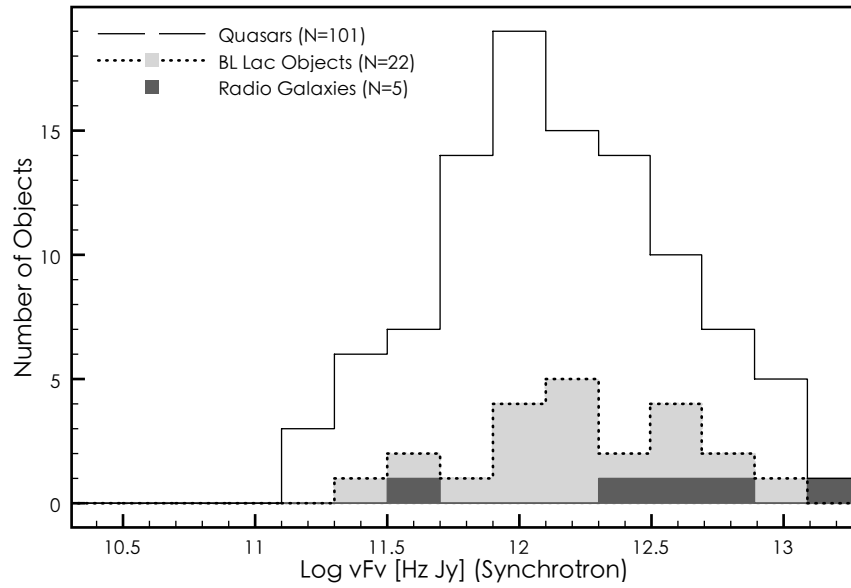


Figure 4.16: Distribution of νF_ν^{sync} , which is the energy peak of the synchrotron hump in the SED, of the MOJAVE sample.

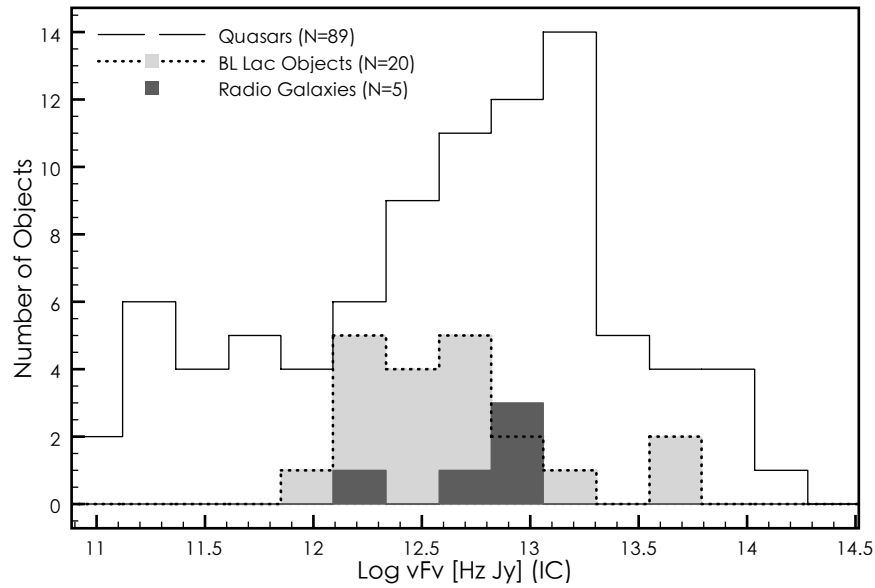


Figure 4.17: Distribution of νF_ν^{IC} , which is the energy peak of the IC hump in the SED, of the MOJAVE sample.

peak frequencies of the SED for the flat spectrum radio quasars (FSRQ) in the LBAS sample locate in a range of $10^{12.5} \text{ Hz} < \nu_{\text{peak}}^{\text{sync}} < 10^{14} \text{ Hz}$, and for the BL Lac objects, they span in a broader range of $10^{12.5-16.5} \text{ Hz}$ (see Figure 4.18). We obtain similar results for the quasars in the MOJAVE sample, however, the BL Lac objects in our sample share the same distribution range as the quasars. This is due to a selection effect: the high

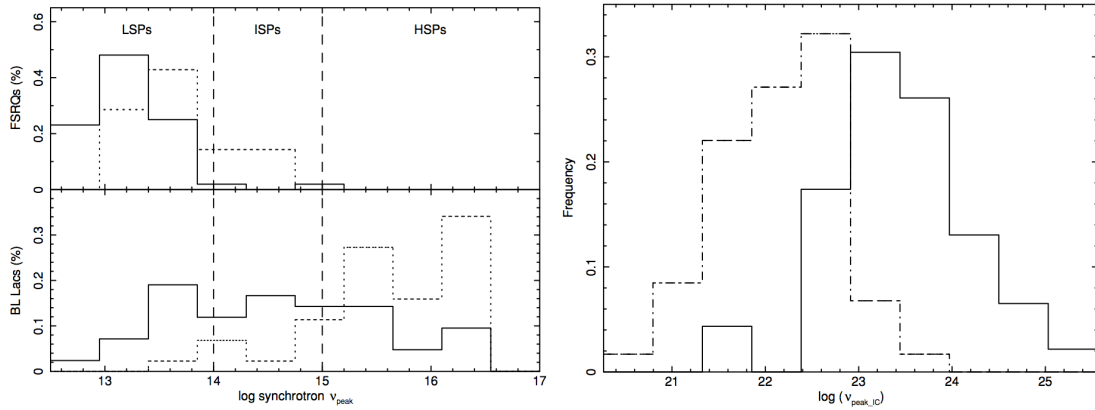


Figure 4.18: The distributions of $\nu_{\text{peak}}^{\text{sync}}$ (left) and $\nu_{\text{peak}}^{\text{IC}}$ (right) by Abdo et al. (2010a). The upper panel of the left-hand-side figure shows the $\nu_{\text{peak}}^{\text{sync}}$ distribution of the flat spectrum radio quasars (FSRQ) in the *Fermi* LBAS sample (Abdo et al. 2009b), and the lower panel shows the distribution of the BL Lac objects. The dot-dashed line in the right-hand-side figure represents the $\nu_{\text{peak}}^{\text{IC}}$ distribution of the LBAS FSRQ, and the solid line represents the BL Lac objects in the LBAS sample.

synchrotron peaked blazars have lower radio flux densities, and those objects are not included in the radio-selected MOJAVE sample.

The distributions of the IC peak frequency ($\nu_{\text{peak}}^{\text{IC}}$) for FSRQ and BL Lac objects by Abdo et al. (2010a) are shown in Figure 4.18. They found that LBAS FSRQ have a lower IC peak frequency distribution with the majority of sources located in $10^{21.5}\text{Hz} < \nu_{\text{peak}}^{\text{IC}} < 10^{23}\text{Hz}$, whileas BL Lac objects have a higher value of frequency distribution with most of the sources located in $10^{22.5}\text{Hz} < \nu_{\text{peak}}^{\text{IC}} < 10^{24}\text{Hz}$. Compare to our results shown in Figure 4.15, we obtain two peaks for the quasar distribution, and the distribution of BL Lac objects overlaps with the quasar distribution at higher frequencies. We need to investigate further to understand the double-peaked distribution of the IC peak frequency.

4.6.2 Dispersion Relation

In this section, we present the dispersion plots of the seven parameters: the apparent jet speed β_{app} , the luminosity L_X , the photon index Γ_X , and the SED peaks: $\nu_{\text{peak}}^{\text{sync}}$, $\nu_{\text{peak}}^{\text{IC}}$, $\nu F_{\nu}^{\text{sync}}$, and νF_{ν}^{IC} . Except β_{app} , taken from the results by Lister et al. (2009b), the other six parameters are the results of this thesis. We plot two of the parameters in each plot, and from Figure 4.19 to 4.39, we show all combinations of the seven parameters. We want to search for possible relations between the six parameters, and for quick indexing, Table 4.9 lists the corresponding number of the figures of each pair-parameter. Further correlations with other parameters collected by the MOJAVE collaboration and related works are outside of the scope of this work.

Apparent Jet Speed

From Figure 4.19 to 4.24, we present six dispersion plots which show the relation between β_{app} and the other six parameters. From the plots, we see that the apparent jet speed has

Table 4.9: The number of figures which correspond to different pair-parameters.

	β_{app}	L_X	Γ_X	$\nu_{\text{peak}}^{\text{sync}}$	$\nu F_{\nu_{\text{peak}}}^{\text{sync}}$	$\nu_{\text{peak}}^{\text{IC}}$	$\nu F_{\nu_{\text{peak}}}^{\text{IC}}$
β_{app}	-	-	-	-	-	-	-
L_X	Figure 4.19	-	-	-	-	-	-
Γ_X	Figure 4.20	Figure 4.25	-	-	-	-	-
$\nu_{\text{peak}}^{\text{sync}}$	Figure 4.21	Figure 4.26	Figure 4.30	-	-	-	-
$\nu F_{\nu_{\text{peak}}}^{\text{sync}}$	Figure 4.22	Figure 4.27	Figure 4.31	Figure 4.34	-	-	-
$\nu_{\text{peak}}^{\text{IC}}$	Figure 4.23	Figure 4.28	Figure 4.32	Figure 4.35	Figure 4.37	-	-
$\nu F_{\nu_{\text{peak}}}^{\text{IC}}$	Figure 4.24	Figure 4.29	Figure 4.33	Figure 4.36	Figure 4.38	Figure 4.39	-

a possible relation with three parameters: X-ray luminosity, synchrotron energy peak ($\nu F_{\nu_{\text{peak}}}^{\text{sync}}$), and IC peak frequency ($\nu_{\text{peak}}^{\text{IC}}$).

β_{app} and L_X Figure 4.19 displays the relation of the apparent jet speed and the X-ray luminosity of the MOJAVE sources. As shown, there is no low luminosity sources with high apparent jet speeds. We found that the radio galaxies distribute at lower luminosity range and have lower apparent jet speed, and the quasars have the highest apparent jet speed and X-ray luminosity. Similar results are obtained in the radio band (Cohen et al. 2007) and in the γ -ray band (Kadler et al. in prep.) using the MOJAVE sample.

β_{app} and $\nu F_{\nu_{\text{peak}}}^{\text{sync}}$ Figure 4.22 shows the relation of the apparent jet speed and the synchrotron energy peak of the SED for the MOJAVE sources. We find that for quasars, there is no source with a low synchrotron energy peak displays a high apparent speed. However, this trend is not obvious for BL Lac objects and radio galaxies. This might imply that the energy output of the SED synchrotron hump is related to the apparent jet speed.

β_{app} and $\nu_{\text{peak}}^{\text{IC}}$ Figure 4.23 shows the relation of the apparent jet speed and the IC peak frequency of the SED for the MOJAVE sources. In this plot, we see a clear relation between the two parameters: no sources with low IC peak frequencies have high apparent speeds, and the sources with the highest IC peak frequency have the highest apparent speeds. From our current understanding of the broadband emission from blazar jet, the IC hump in the SED is produced by seed photons upscattered through leptonic and hadronic mechanisms. To obtain a higher value of IC peak frequency, highly-energetic photons and protons are needed to upscatter seed photons, and this is more likely to happen in blazar jets with high Lorentz factors, which would cause higher apparent speeds.

We do not see obvious relations between apparent jet speed and the three other parameters (Γ_X , $\nu_{\text{peak}}^{\text{sync}}$, and $\nu F_{\nu_{\text{peak}}}^{\text{IC}}$; see Figure 4.20, 4.21, and 4.24). Figure 4.24 shows the relation of the apparent jet speed and the IC energy peak of the SED for the MOJAVE sources. We see that for the sources with apparent jet speed $\beta_{\text{app}} < 22$, they distribute evenly in the $\nu F_{\nu_{\text{peak}}}^{\text{IC}}$ axis at the range of 10^{11-14} Hz Jy. For the sources with higher apparent jet speeds of $\beta_{\text{app}} > 22$, they are all quasars and occupy a higher range of $\nu F_{\nu_{\text{peak}}}^{\text{IC}}$ between 10^{13-14} Hz Jy.

X-ray and Broadband SED Properties

In this section, we will discuss about possible relations of X-ray and broadband SED properties for the MOJAVE sources. From Figure 4.25 to 4.33, we show the dispersion plots of X-ray and broadband SED parameters.

L_X and Γ_X Figure 4.25 shows the relation of X-ray luminosity and photon index of the MOJAVE sample. We find that the sources with flatter spectra tend to have higher X-ray luminosity, and note that there is no source with a low X-ray photon index and a low X-ray luminosity. This relation is more obvious for the quasars and the radio galaxies in the MOJAVE sample; BL Lac objects have a looser distribution and we do not see the trend.

L_X and $\nu F_{\nu_{\text{peak}}}^{\text{sync}}$ Figure 4.27 shows the relation between X-ray luminosity and synchrotron energy peak of the SED for the MOJAVE sources. We do not find a general trend for the three classes of AGN, however, we see a small trend for the quasars. The quasars which have a higher synchrotron energy peak tend to have a slightly higher X-ray luminosity. The radio galaxies locate at the bottom of the plot due to their low X-ray luminosity, and the BL Lac objects distribute loosely without any trend.

L_X and $\nu_{\text{peak}}^{\text{IC}}$ Figure 4.28 shows the relation between X-ray luminosity and IC peak frequency of the SED for the MOJAVE sources. We see that the three classes of AGN have a tendency to cluster together with its own kind: the quasars distribute at the upper part of the plot due to their high X-ray luminosity; the BL Lac objects distribute on the right-hand-side of the plot for their higher value of $\nu_{\text{peak}}^{\text{IC}}$; the radio galaxies distribute at the lower-left of the plot for their low X-ray luminosity and IC peak frequency. However, we do not observe a clear relation between X-ray luminosity and IC peak frequency.

Γ_X and $\nu_{\text{peak}}^{\text{sync}}$ Figure 4.30 shows the relation between X-ray photon index and synchrotron peak frequency of the SED for the MOJAVE sources. We see a possible positive trend between the two parameters, that the sources with steeper X-ray spectrum tend to have a slightly higher synchrotron peak frequency. However, there are a few sources disperse from the cluster of sources, and we need further examination to verify this relation.

We do not see obvious trends for the following pair-parameters: $L_X - \nu_{\text{peak}}^{\text{sync}}$ (Figure 4.26), $L_X - \nu F_{\nu_{\text{peak}}}^{\text{IC}}$ (Figure 4.29), $\nu F_{\nu_{\text{peak}}}^{\text{sync}} - \Gamma_X$ (Figure 4.31), $\Gamma_X - \nu_{\text{peak}}^{\text{IC}}$ (Figure 4.32), and $\nu F_{\nu_{\text{peak}}}^{\text{IC}} - \Gamma_X$ (Figure 4.33).

The Relation between Broadband SED Peaks

In this section, we investigate possible relations between the peak positions of the synchrotron and the IC hump in the broadband SED of the MOJAVE sources. From Figure 4.34 to 4.39, we show the dispersion plots between the four parameters: $\nu_{\text{peak}}^{\text{sync}}$, $\nu F_{\nu_{\text{peak}}}^{\text{sync}}$, $\nu_{\text{peak}}^{\text{IC}}$, and $\nu F_{\nu_{\text{peak}}}^{\text{IC}}$.

$\nu_{\text{peak}}^{\text{IC}}$ and νF_{ν}^{IC} Figure 4.39 shows the relation between IC peak frequency and energy peak value in the SED of the MOJAVE sample. We see a positive trend in the dispersion plot: the sources which have a higher IC peak frequency tend to have a higher value of IC energy peak. This trend is very obvious for the MOJAVE quasars, for which no low-IC frequency peak sources have a high IC energy peak in the broadband SED. The BL Lac objects and the radio galaxies occupy the two ends of the quasar distribution, and the relation in the two classes of AGN is less prominent.

We do not find obvious trends for the following pair-parameters: $\nu F_{\nu}^{\text{sync}} - \nu_{\text{peak}}^{\text{sync}}$ (Figure 4.34), $\nu_{\text{peak}}^{\text{IC}} - \nu_{\text{peak}}^{\text{sync}}$ (Figure 4.35), $\nu F_{\nu}^{\text{IC}} - \nu_{\text{peak}}^{\text{sync}}$ (Figure 4.36), $\nu F_{\nu}^{\text{sync}} - \nu_{\text{peak}}^{\text{IC}}$ (Figure 4.37), and $\nu F_{\nu}^{\text{IC}} - \nu F_{\nu}^{\text{sync}}$ (Figure 4.38).

4.7 Summary

In this chapter, we constructed the (quasi-)simultaneous broadband SED for the 135 MOJAVE sources. We analyzed *Swift* UVOT and XRT data, and we derived the X-ray parameter for each source by fitting X-ray spectrum. We performed polynomial fits to the double-hump profile of the blazar SED, and we derived the peak positions of the synchrotron and the IC hump in the SED for all sources. In the last section, we presented the preliminary distribution study of the derived parameters from the X-ray and broadband SED analysis. The complete statistical analysis for searching correlations between parameters will be presented in a forthcoming publication (Chang et al. in prep.).

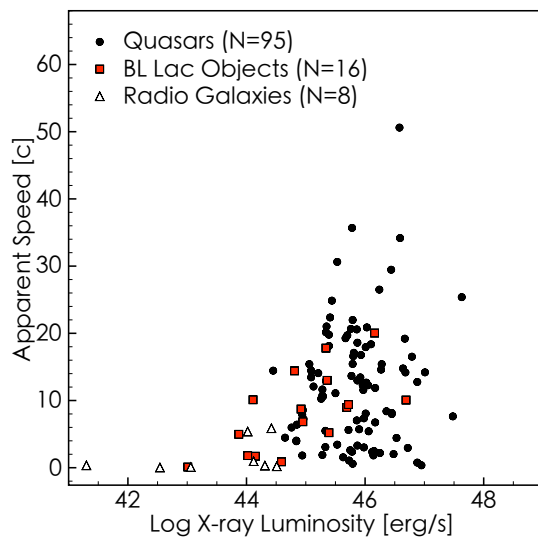


Figure 4.19: Maximum apparent speed (Lister et al. 2009b) as a function of the X-ray luminosity for the sources in the MOJAVE sample. See text for discussion.

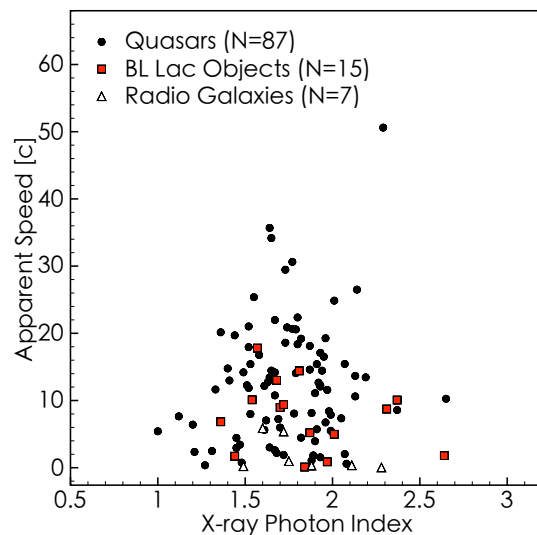


Figure 4.20: Maximum apparent speed (Lister et al. 2009b) as a function of the X-ray photon index for the sources in the MOJAVE sample.

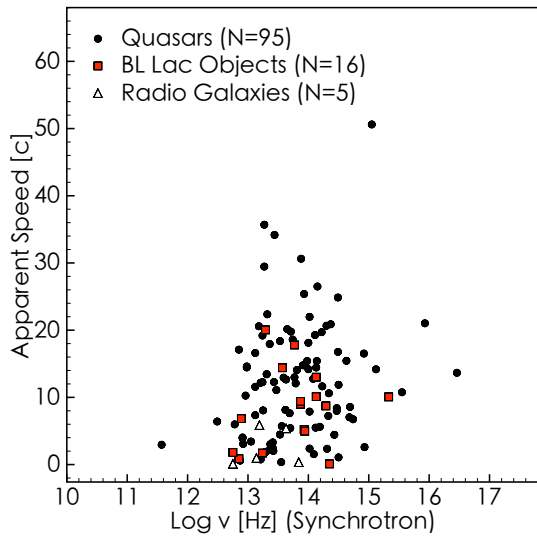


Figure 4.21: Maximum apparent speed (Lister et al. 2009b) as a function of the synchrotron peak frequency ($\nu_{\text{peak}}^{\text{sync}}$) for the sources in the MOJAVE sample.

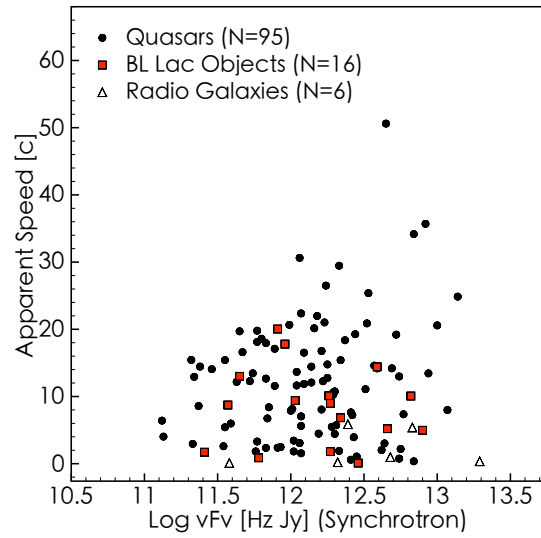


Figure 4.22: Maximum apparent speed (Lister et al. 2009b) as a function of the synchrotron energy peak ($\nu F_{\nu}^{\text{sync}}$) for the sources in the MOJAVE sample. See text for discussion.

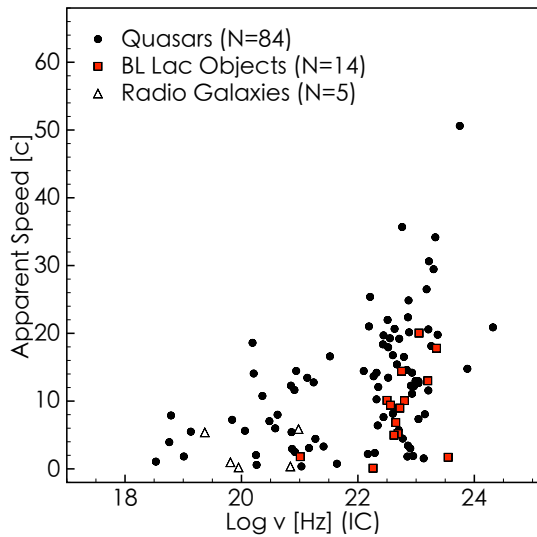


Figure 4.23: Maximum apparent speed (Lister et al. 2009b) as a function of the IC peak frequency ($\nu_{\text{peak}}^{\text{IC}}$) for the sources in the MOJAVE sample. See text for discussion.

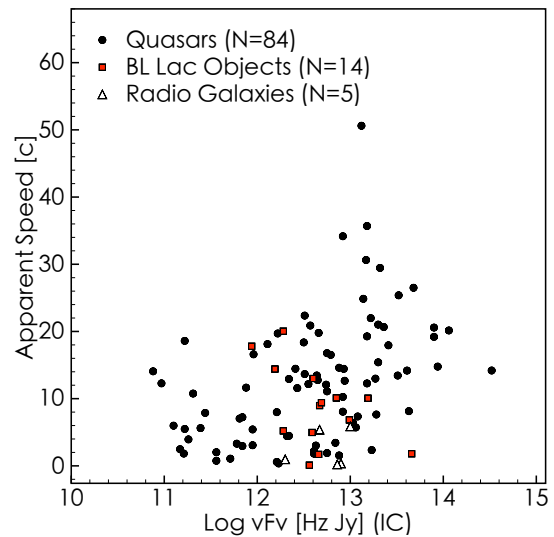


Figure 4.24: Maximum apparent speed (Lister et al. 2009b) as a function of the IC energy peak (νF_{ν}^{IC}) for the sources in the MOJAVE sample.

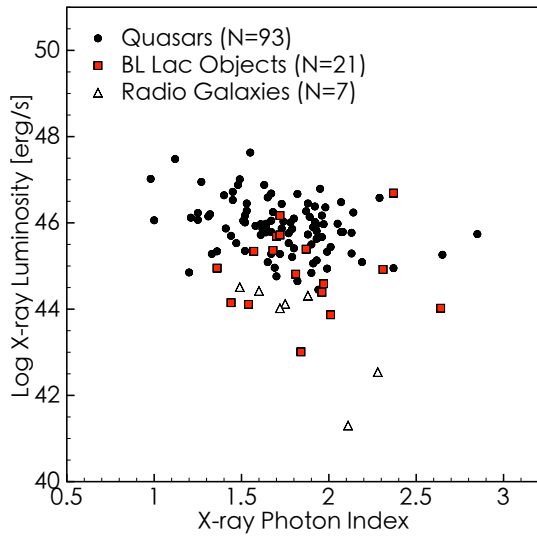


Figure 4.25: X-ray luminosity as a function of X-ray photon index for the sources in the MOJAVE sample. See text for discussion.

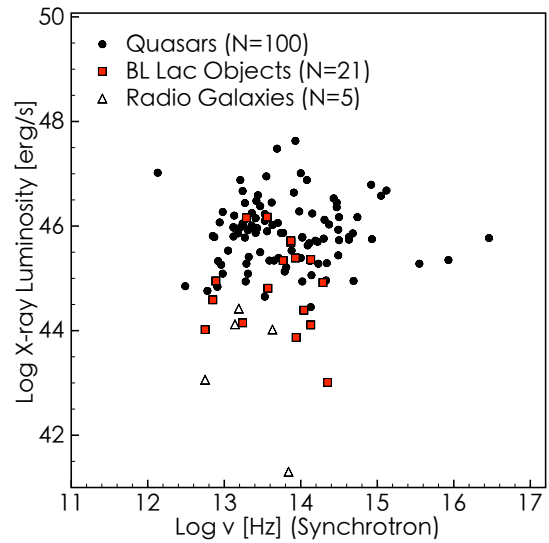


Figure 4.26: X-ray luminosity as a function of synchrotron peak frequency ($\nu_{\text{peak}}^{\text{sync}}$) for the sources in the MOJAVE sample.

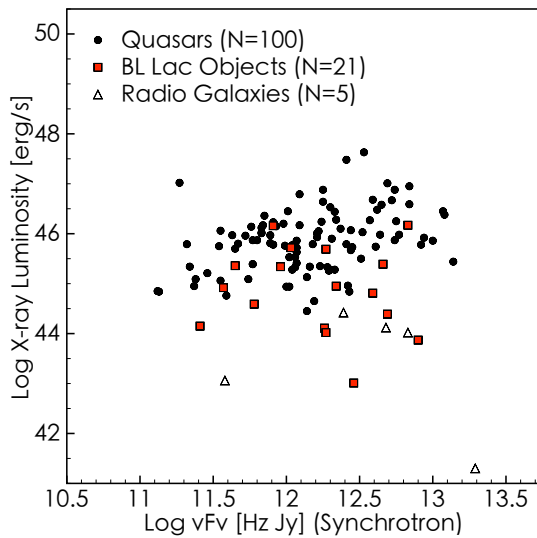


Figure 4.27: X-ray luminosity as a function of synchrotron energy peak of the SED ($\nu F_{\nu}^{\text{sync}}$) for the sources in the MOJAVE sample. See text for discussion.

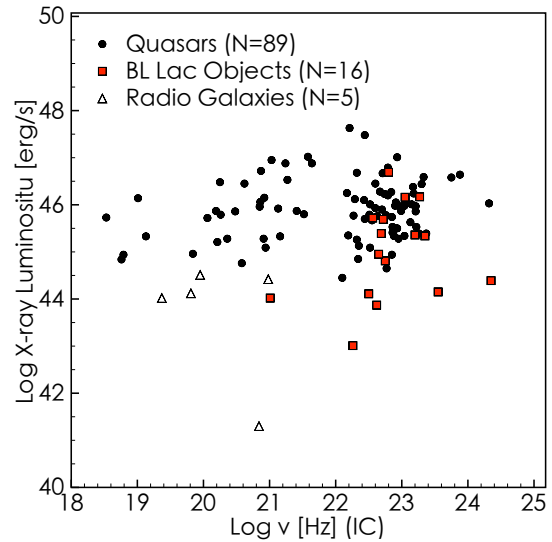


Figure 4.28: X-ray luminosity as a function of IC peak frequency of the SED ($\nu_{\text{peak}}^{\text{IC}}$) for the sources in the MOJAVE sample. See text for discussion.

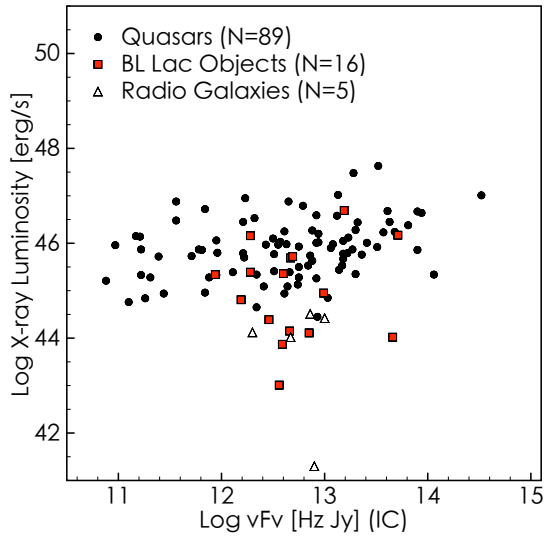


Figure 4.29: X-ray luminosity as a function of IC energy peak of the SED (νF_{ν}^{IC}) for the sources in the MOJAVE sample.

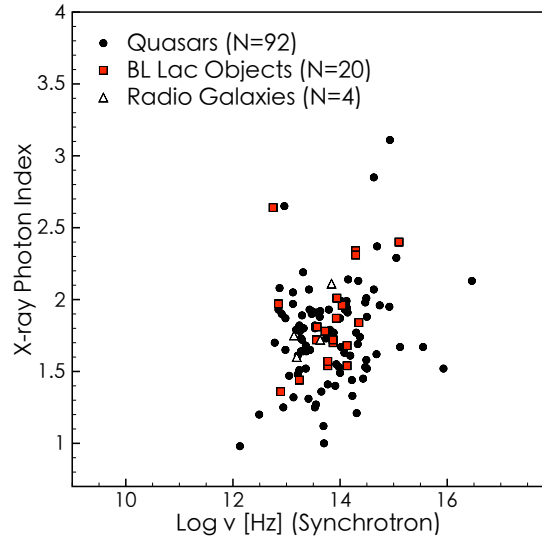


Figure 4.30: X-ray photon index as a function of synchrotron peak frequency of the SED ($\nu_{\text{peak}}^{\text{sync}}$) for the sources in the MOJAVE sample. See text for discussion.

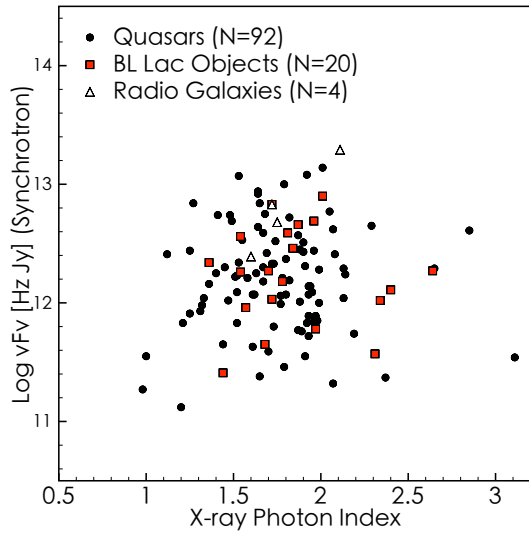


Figure 4.31: Synchrotron energy peak of the SED ($\nu F_{\nu}^{\text{sync}}$) as a function of X-ray photon index for the sources in the MOJAVE sample.

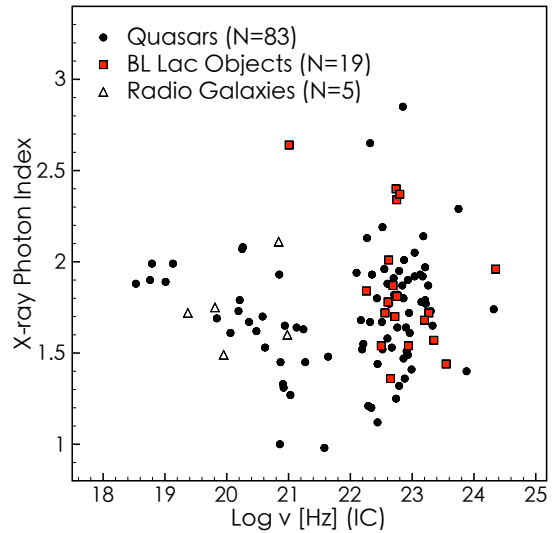


Figure 4.32: X-ray photon index as a function of IC peak frequency of the SED ($\nu_{\text{peak}}^{\text{IC}}$) for the sources in the MOJAVE sample.

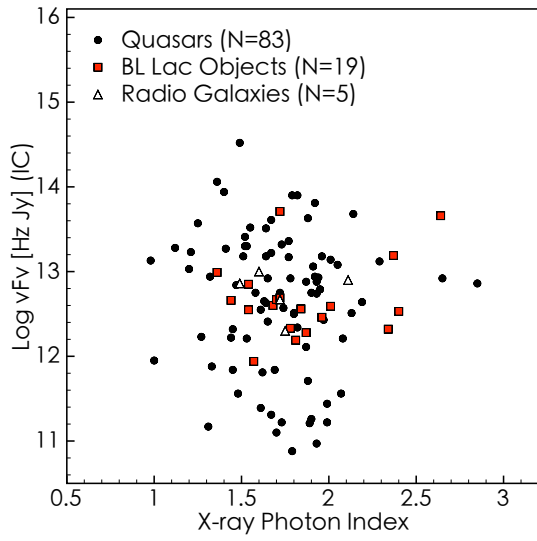


Figure 4.33: IC energy peak of the SED (νF_{ν}^{IC}) as a function of X-ray photon index for the sources in the MOJAVE sample.

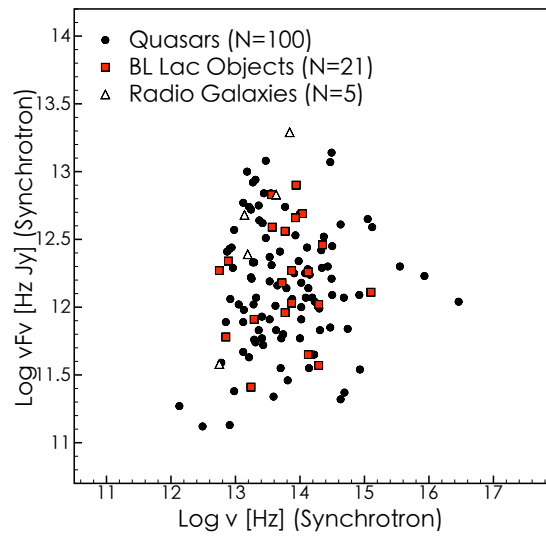


Figure 4.34: Synchrotron energy peak ($\nu F_{\nu}^{\text{sync}}$) as a function of synchrotron peak frequency (ν^{sync}) of the SED for the sources in the MOJAVE sample.

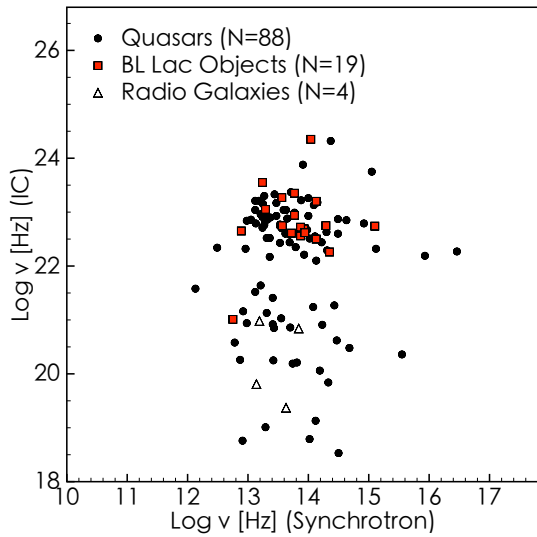


Figure 4.35: IC peak frequency (ν^{IC}) as a function of synchrotron peak frequency (ν^{sync}) of the SED for the sources in the MOJAVE sample.

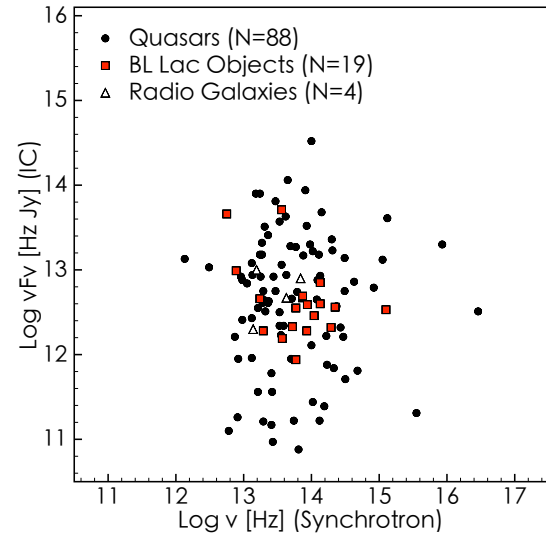


Figure 4.36: IC energy peak (νF_{ν}^{IC}) as a function of synchrotron peak frequency (ν^{sync}) of the SED for the sources in the MOJAVE sample.

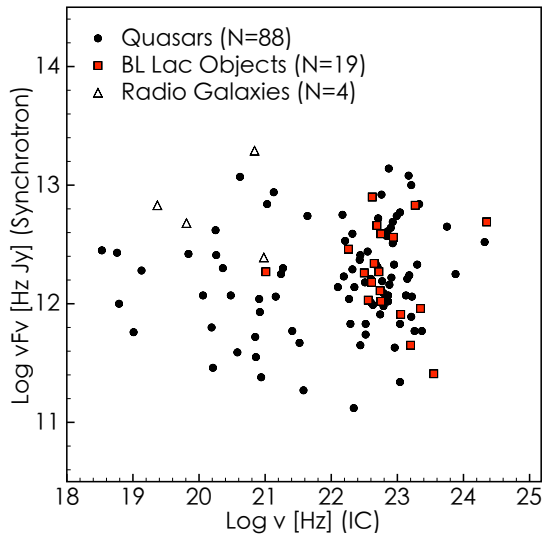


Figure 4.37: Synchrotron energy peak ($\nu F_{\nu}^{\text{sync}}$) as a function of IC peak frequency ($\nu_{\text{peak}}^{\text{IC}}$) of the SED for the sources in the MOJAVE sample.

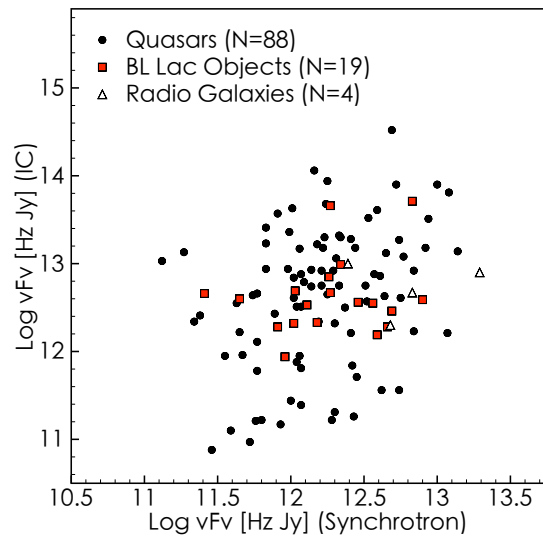


Figure 4.38: IC energy peak (νF_{ν}^{IC}) as a function of synchrotron energy peak ($\nu F_{\nu}^{\text{sync}}$) of the SED for the sources in the MOJAVE sample.

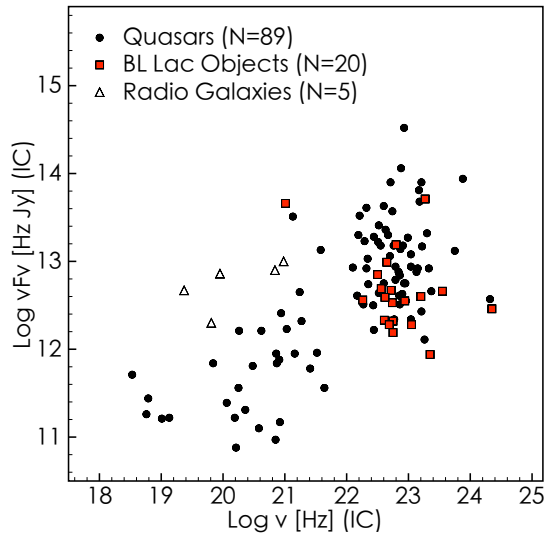


Figure 4.39: IC energy peak (νF_{ν}^{IC}) as a function of IC peak frequency ($\nu_{\text{peak}}^{\text{IC}}$) of the SED for the sources in the MOJAVE sample. See text for discussion.

A The X-ray Spectra of the MOJAVE Sample

We analyzed the X-ray spectra of all the MOJAVE sources observed by the *Swift*/XRT. In this Appendix, we present the X-ray spectra of the 135 sources together with a fit to the data. As described in Section 4.4.1, we applied an absorbed power law model to each source (see Table A.1 for exceptional cases). The fitting results are reasonably good for most of the sources. However, there are a few exceptional cases in which the absorbed power law model does not give a satisfactory fit. For those sources, we applied different models to them (see Table A.1). Nine of the sources have less than three energy bins after data grouping, which is less than the free parameters in the absorbed power law model. For those sources, we fix the N_{H} value to the Galactic measurement (Kalberla et al. 2005), and we assume the photon index to be $\Gamma_{\text{X}} = 1.8$, in order to estimate the source flux (see Table 4.6 for those sources). In Table 4.6, we presented the derived parameters from the spectral fitting results: intrinsic N_{H} value, photon index (Γ_{X}), flux (F_{X}), reduced χ^2 (χ_{red}^2), and degree of freedom (d.o.f.), which is simply the number of energy bins subtracted by the free parameters of fit.

Table A.1: The different models used to fit the spectra of the MOJAVE sources.

Name	XSPEC model
0238–084	phabs (1) \times (mekal+phabs (2) \times powerlaw)
0316+413	phabs (1) \times phabs (2) \times (powerlaw+gauss+mekal)
1228+126	phabs (1) \times (mekal+phabs (2) \times powerlaw)
Other sources	phabs (1) \times phabs (2) \times powerlaw

Note: phabs – photoelectric absorption model;

mekal – warm absorber model for hot diffuse gas (Mewe et al. 1985);

powerlaw – a simple photon power law model;

gauss – Gaussian component to model line emission.

A The X-ray Spectra of the MOJAVE Sample

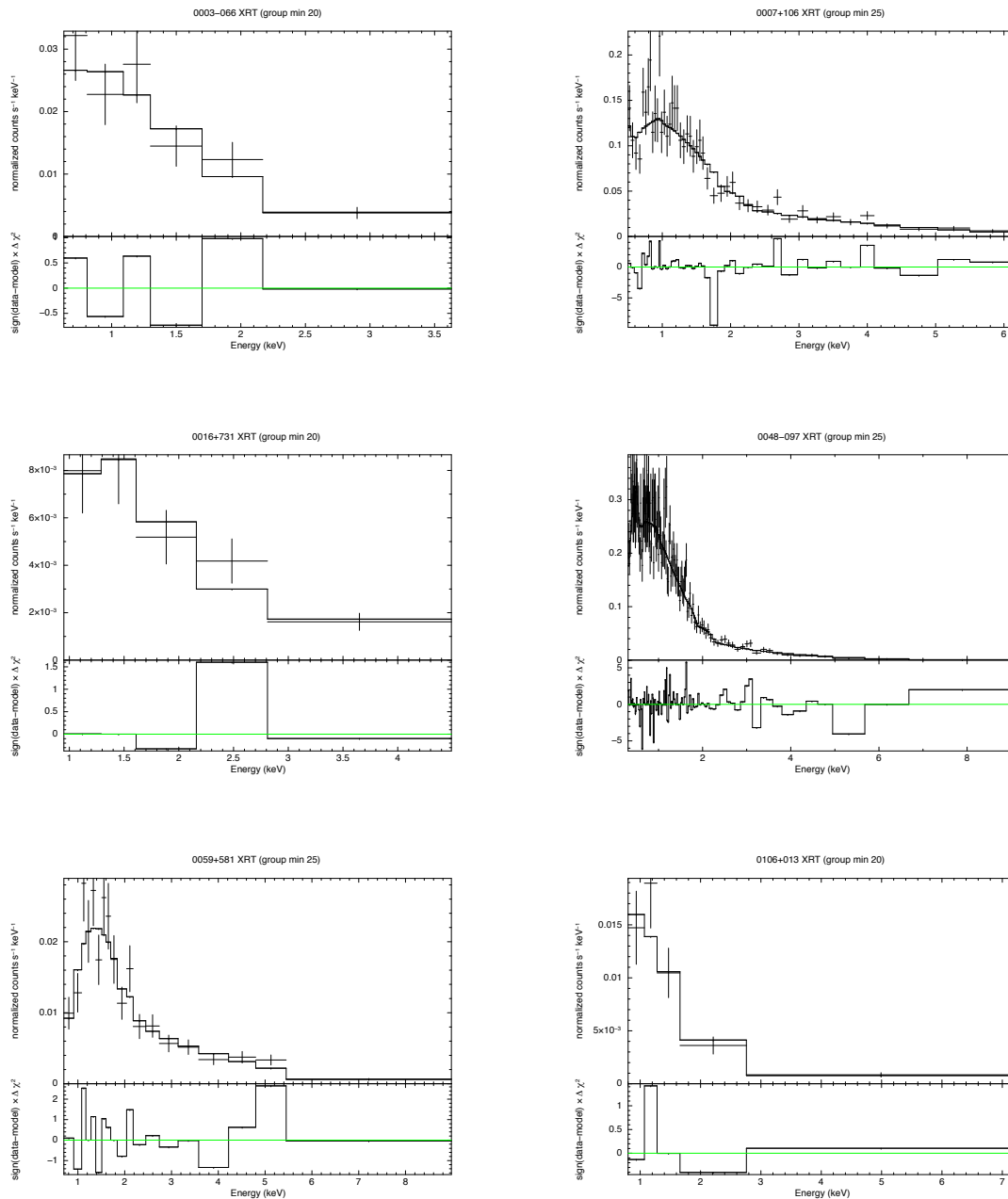


Figure A.1: The X-ray spectra of the MOJAVE sources measured by *Swift*/XRT ordered by RA. The B1950 source name is shown in the title of each plot, together with data grouping criteria: the minimum raw counts in each energy bin. The x-axis is the energy of emission in the unit of keV, and the y-axis is the normalized counts in the unit of $\text{counts s}^{-1} \text{keV}^{-1}$. The upper panel shows the spectral data (cross) and the fitted model (solid line); the lower panel shows the goodness of fit: $(\text{data}-\text{model}) \times \Delta\chi^2$. From upper-left to bottom-right: 0003-066, 0007+106, 0016+731, 0048-097, 0059+581, and 0106+013.

A The X-ray Spectra of the MOJAVE Sample

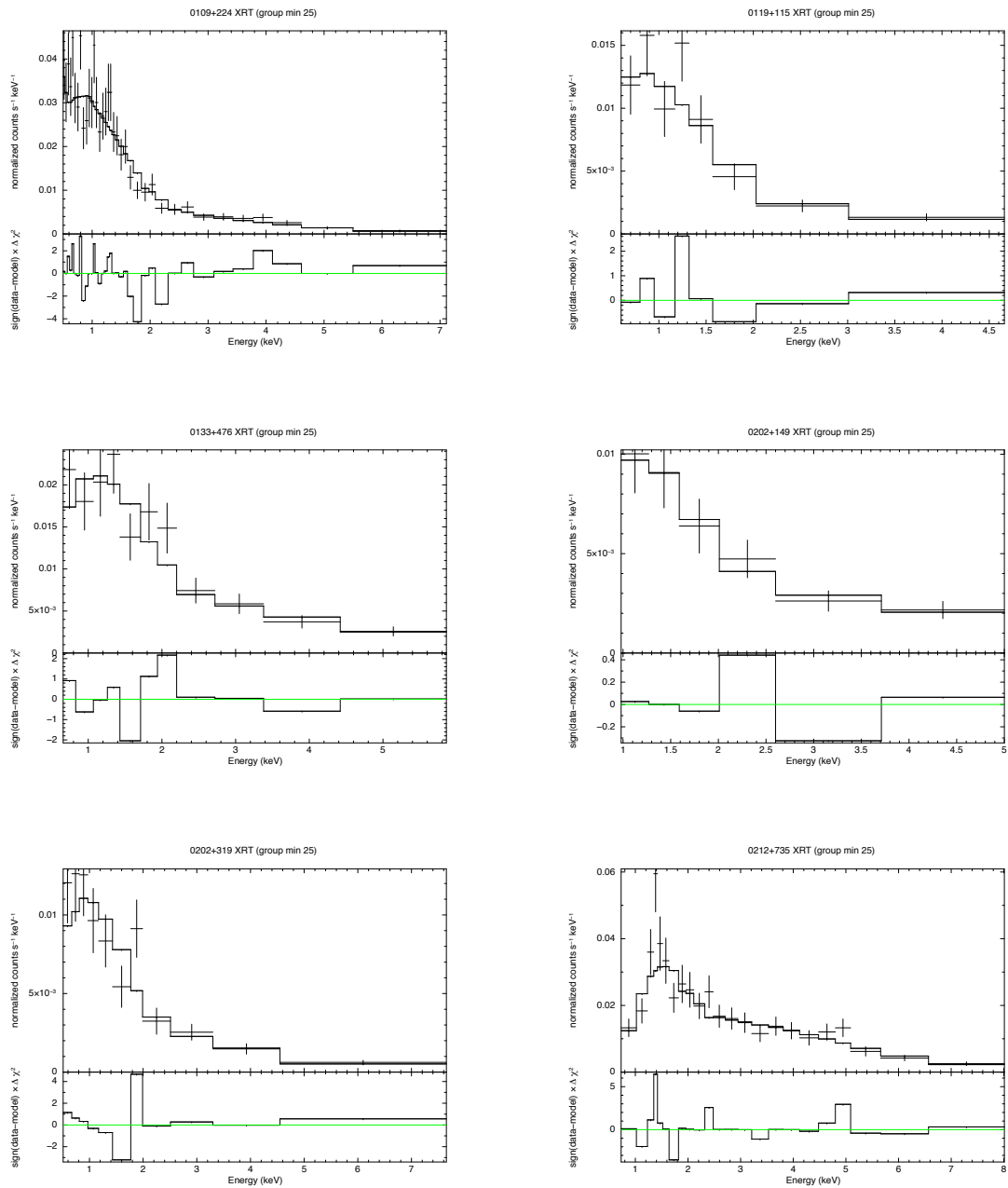


Figure A.2: The X-ray spectrum of the MOJAVE sources measured by *Swift*/XRT ordered by RA (continuation). From upper-left to bottom-right: 0109+224, 0119+115, 0133+476, 0202+149, 0202+319, and 0212+735.

A The X-ray Spectra of the MOJAVE Sample

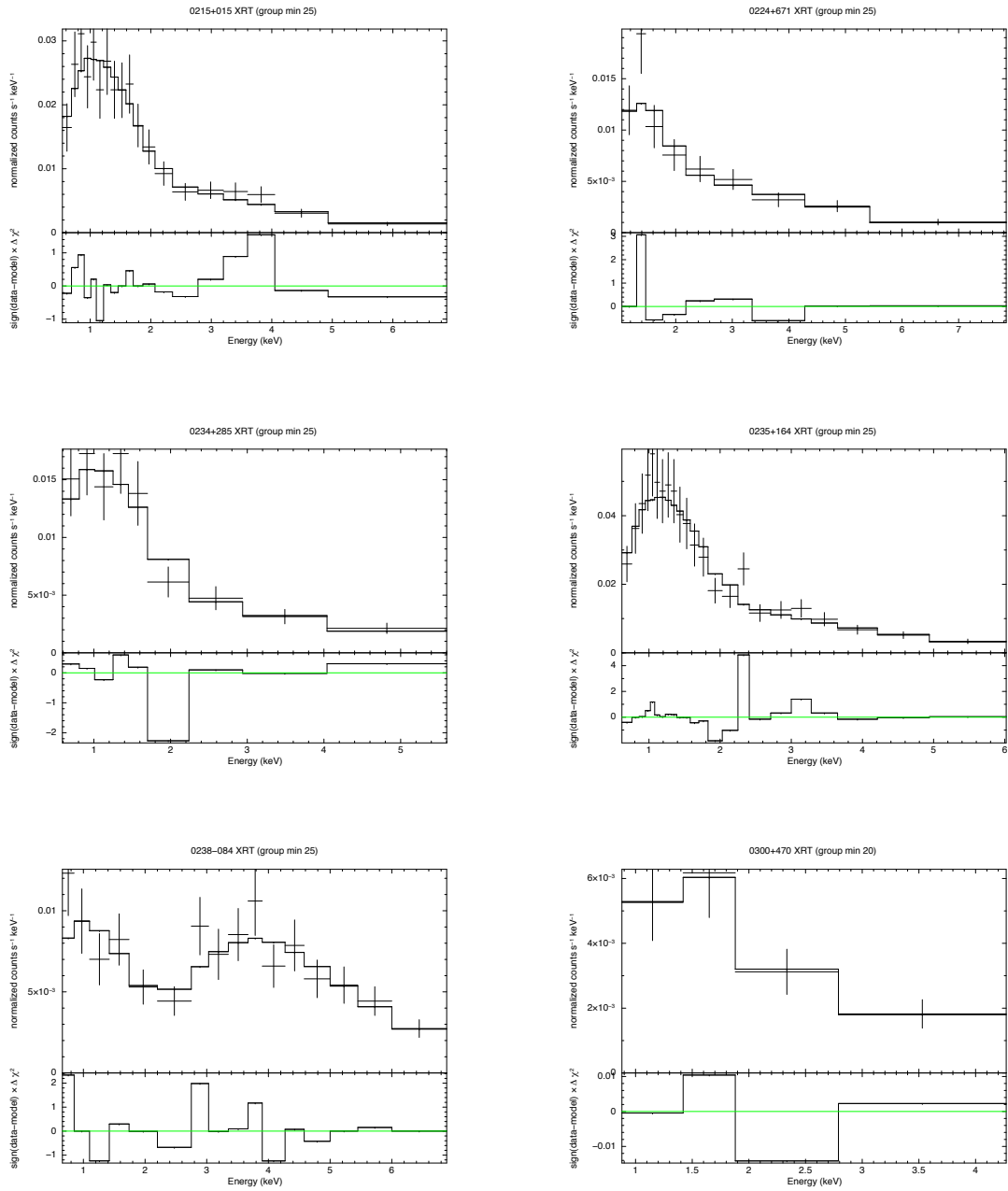


Figure A.3: The X-ray spectrum of the MOJAVE sources measured by *Swift*/XRT ordered by RA (continuation). From upper-left to bottom-right: 0215+015, 0224+671, 0234+285, 0235+164, 0238-084, and 0300+470.

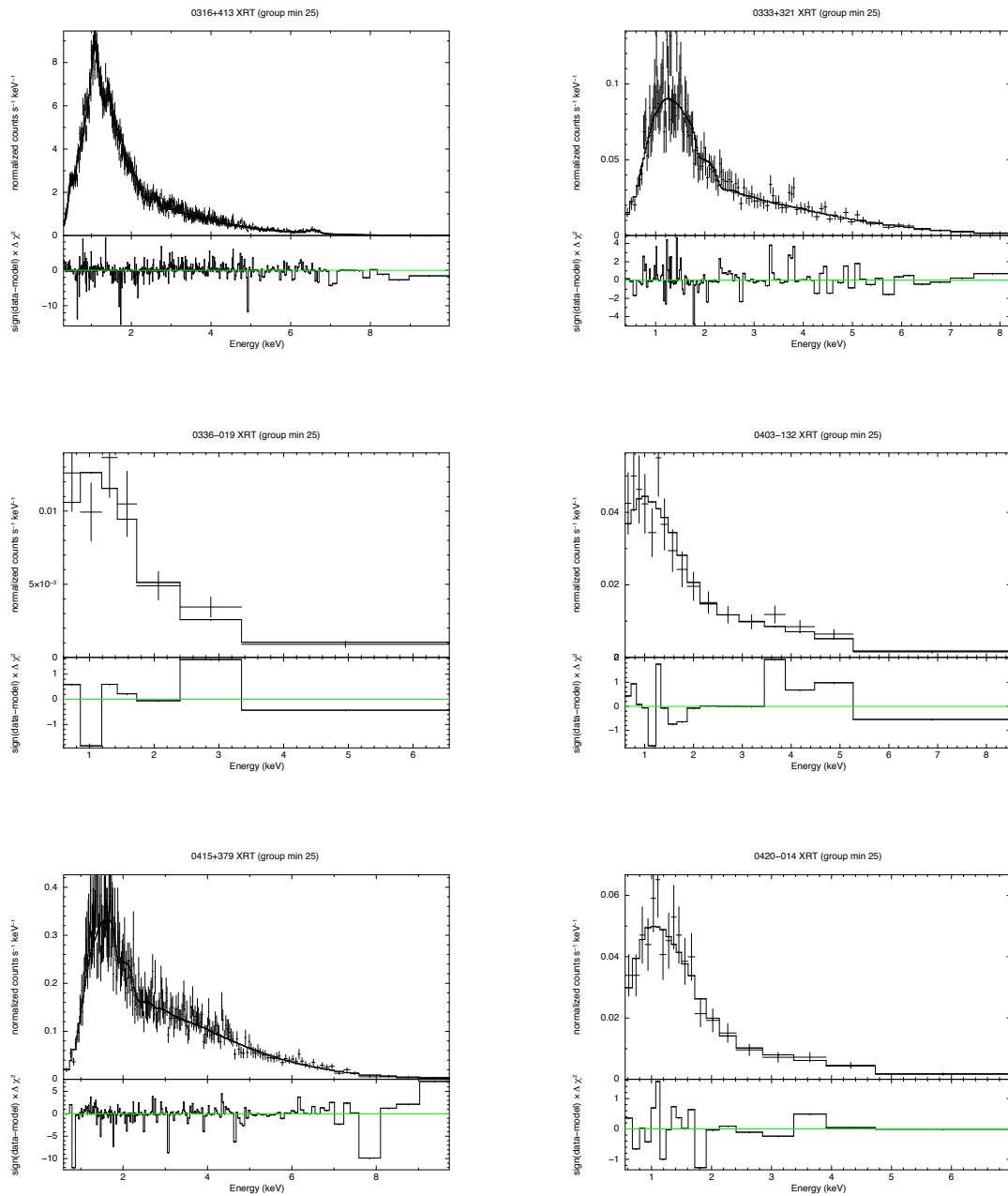


Figure A.4: The X-ray spectrum of the MOJAVE sources measured by *Swift*/XRT ordered by RA (continuation). From upper-left to bottom-right: 0316+413, 0333+321, 0336-019, 0403-132, 0415+379, and 0420-014.

A The X-ray Spectra of the MOJAVE Sample

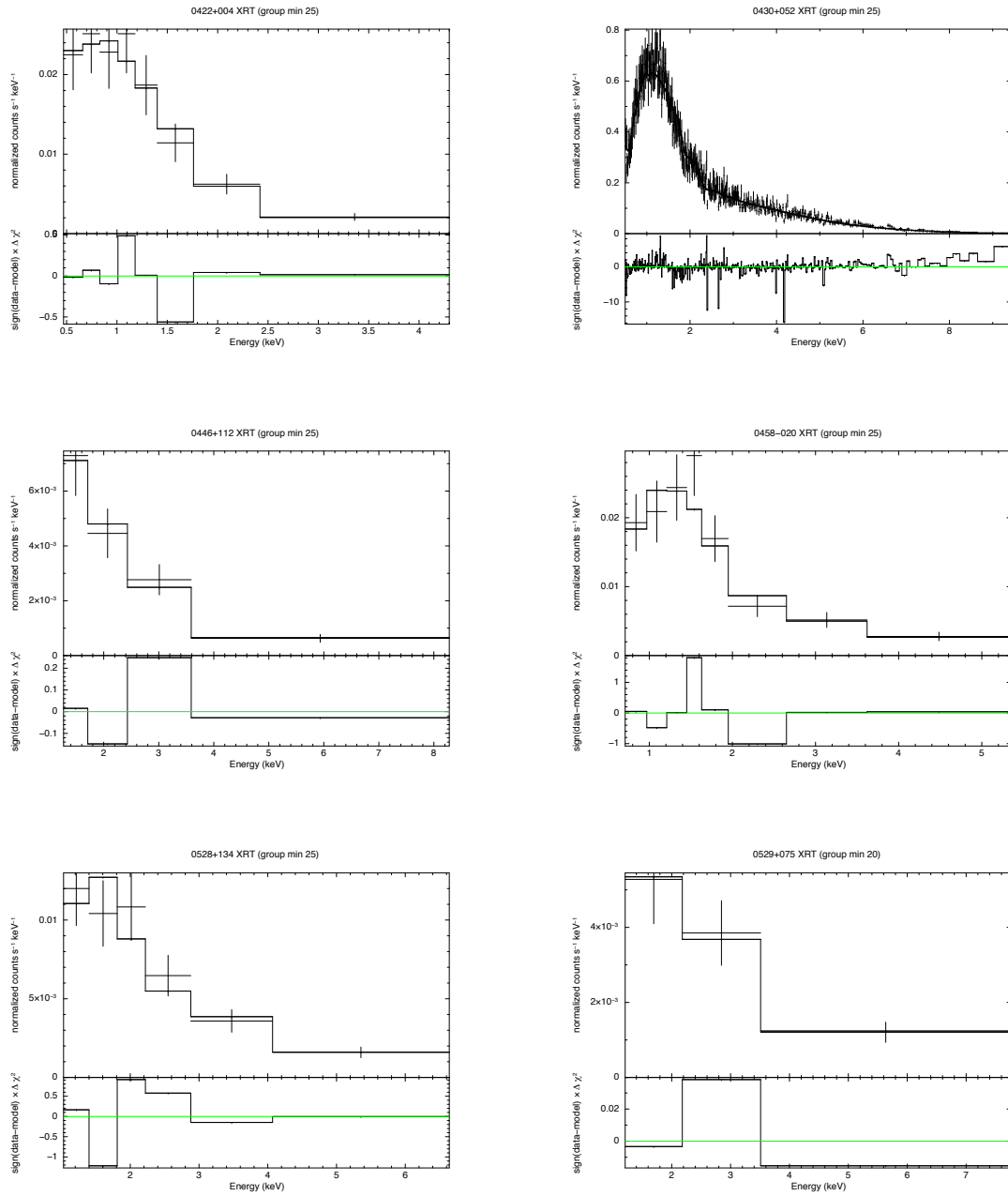


Figure A.5: The X-ray spectrum of the MOJAVE sources measured by *Swift*/XRT ordered by RA (continuation). From upper-left to bottom-right: 0422+004, 0430+052, 0446+112, 0458-020, 0528+134, and 0529+075.

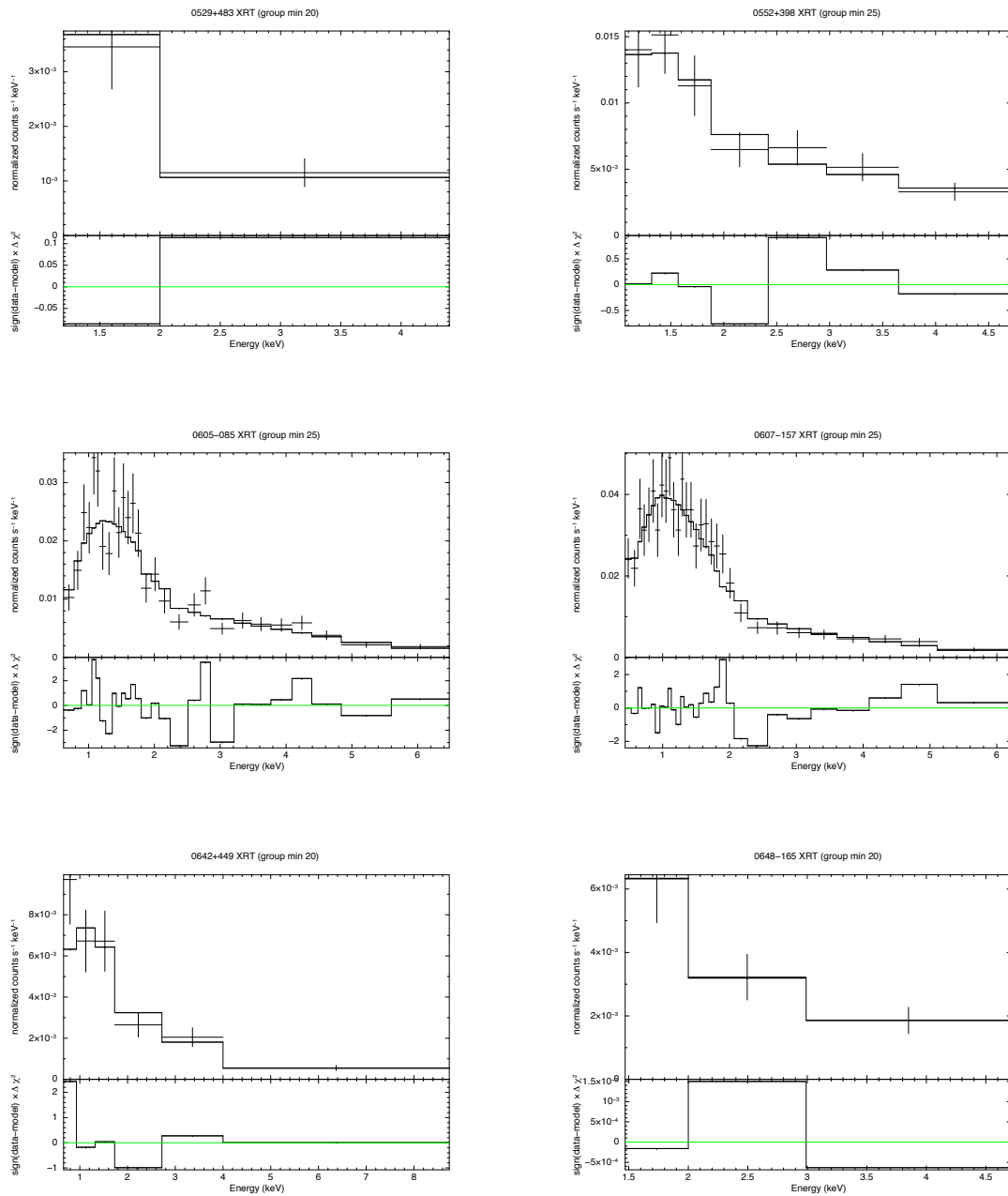


Figure A.6: The X-ray spectrum of the MOJAVE sources measured by *Swift*/XRT ordered by RA (continuation). From upper-left to bottom-right: 0529+483, 0552+398, 0605-085, 0607-157, 0642+449, and 0648-165.

A The X-ray Spectra of the MOJAVE Sample

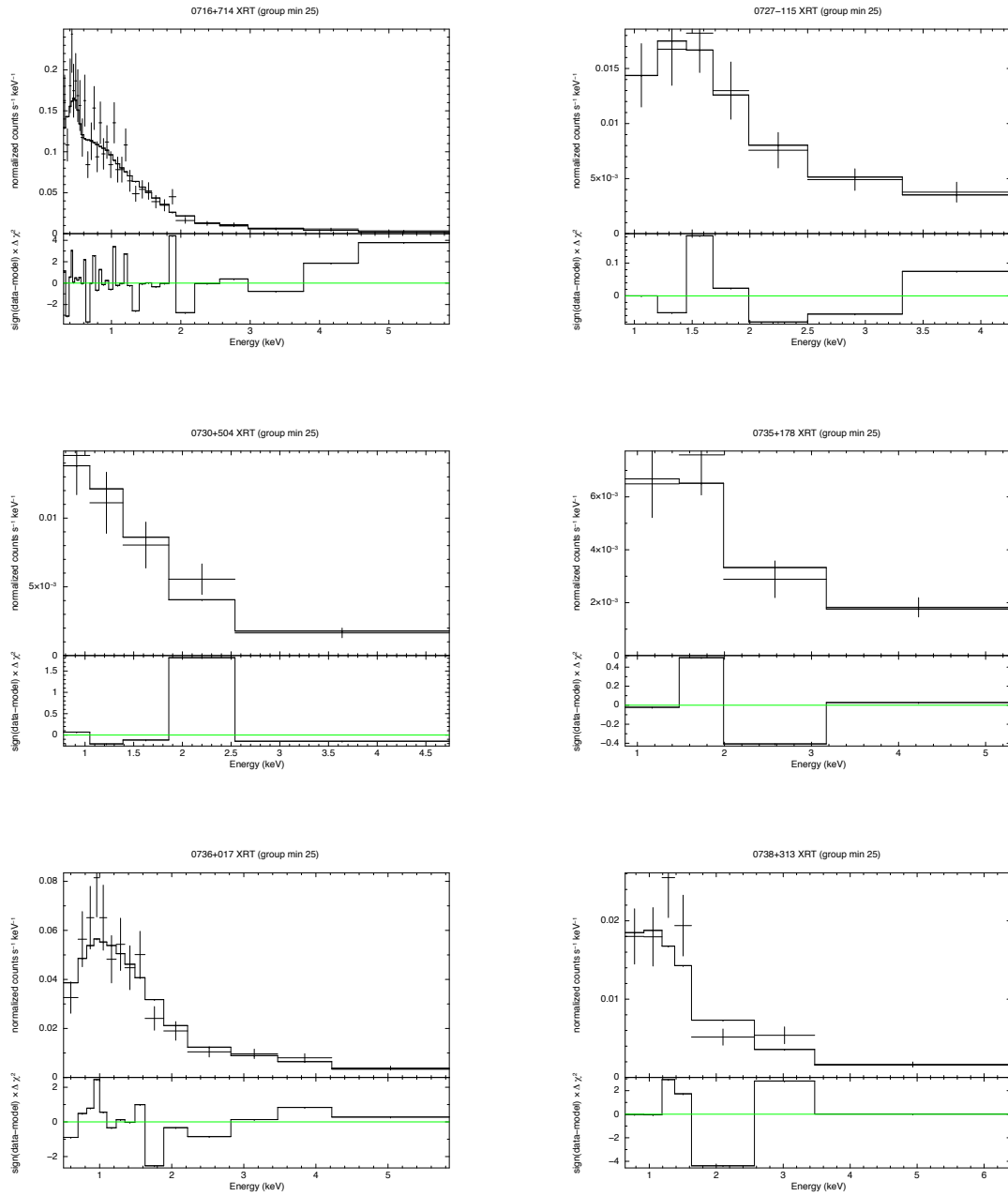


Figure A.7: The X-ray spectrum of the MOJAVE sources measured by *Swift*/XRT ordered by RA (continuation). From upper-left to bottom-right: 0716+714, 0727-115, 0730+504, 0735+178, 0736+017, and 0738+313.

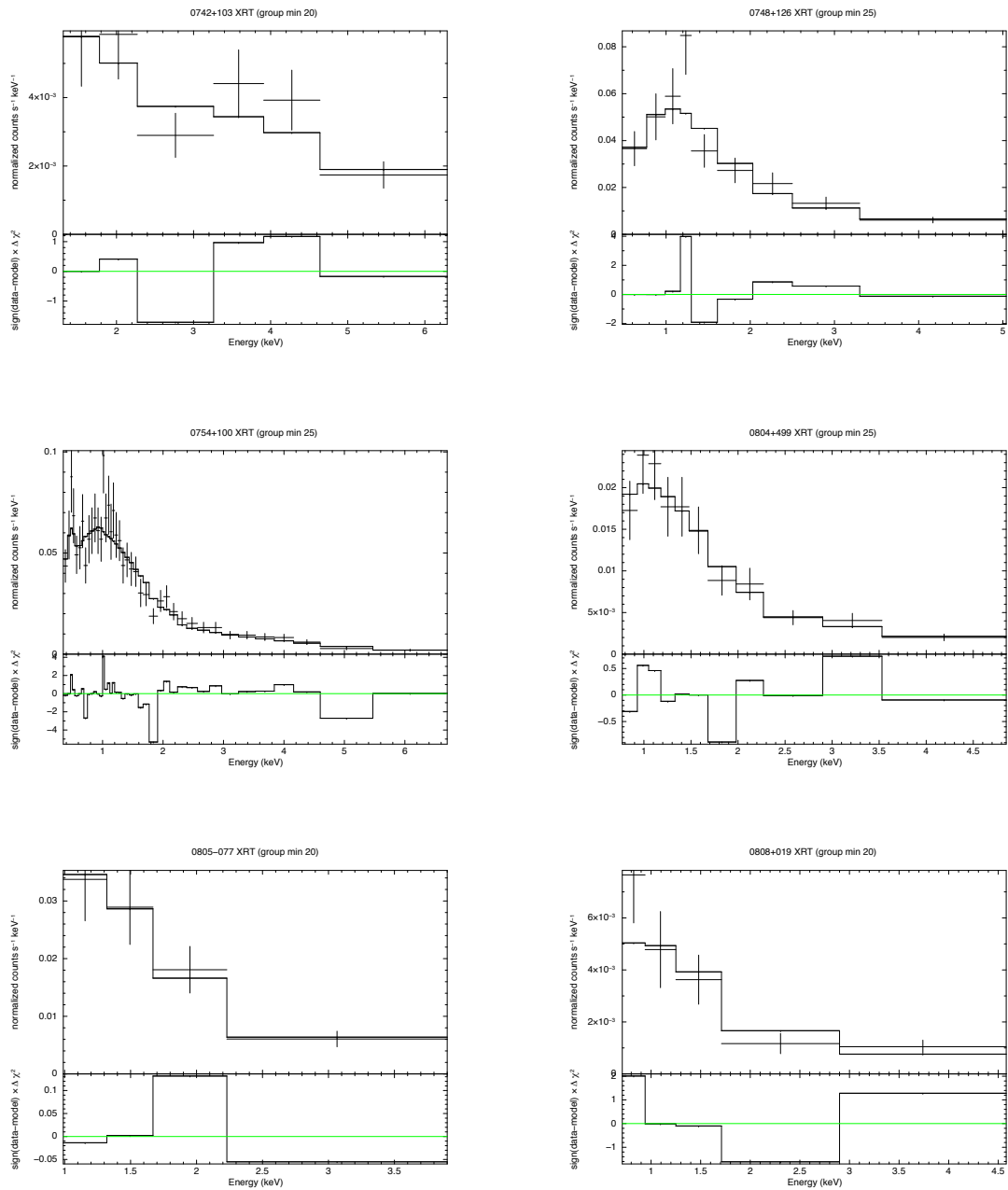


Figure A.8: The X-ray spectrum of the MOJAVE sources measured by *Swift*/XRT ordered by RA (continuation). From upper-left to bottom-right: 0742+103, 0748+126, 0754+100, 0804+499, 0805-077, and 0808+019.

A The X-ray Spectra of the MOJAVE Sample

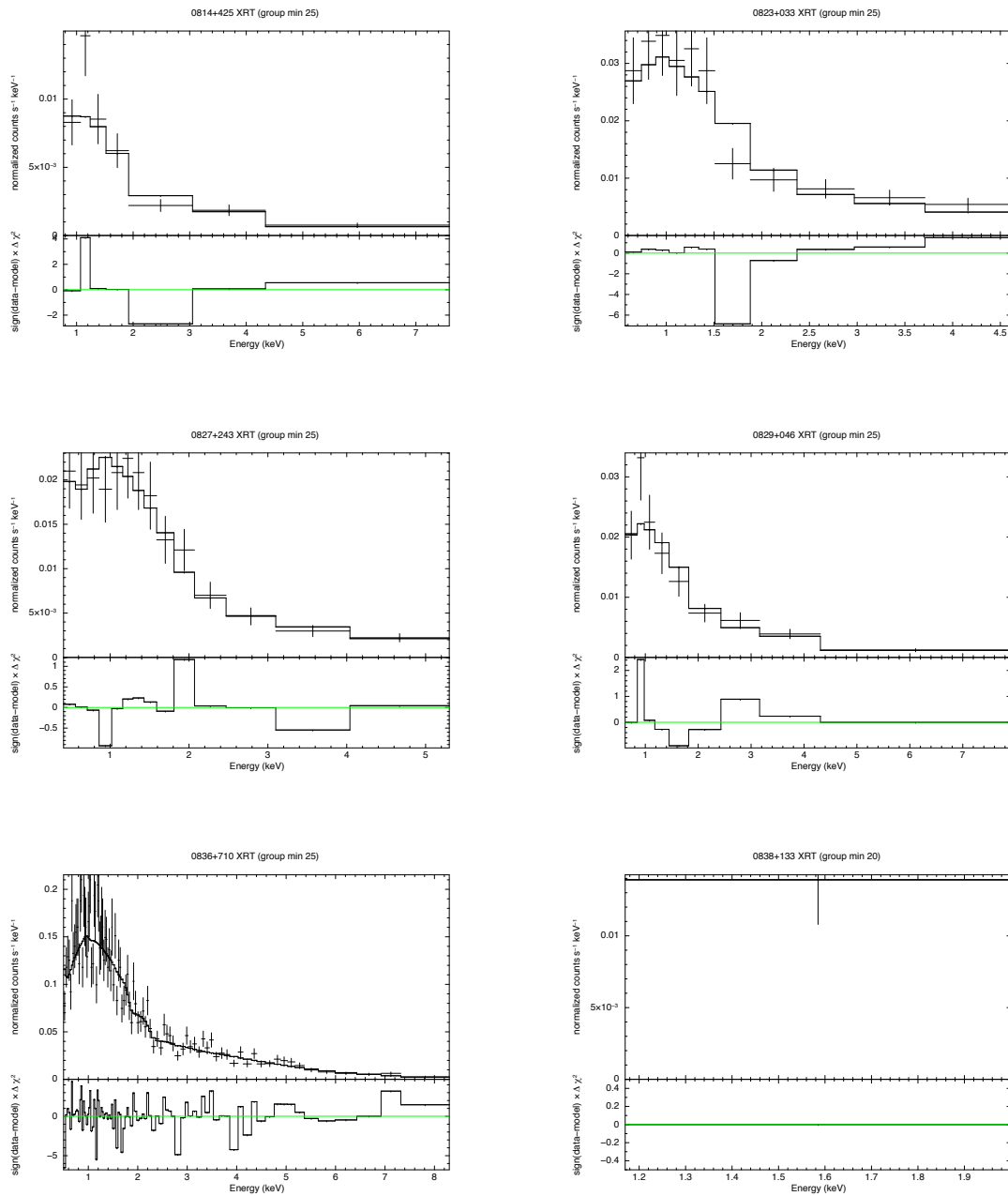


Figure A.9: The X-ray spectrum of the MOJAVE sources measured by *Swift*/XRT ordered by RA (continuation). From upper-left to bottom-right: 0814+425, 0823+033, 0827+243, 0829+046, 0836+710, and 0838+133.

A The X-ray Spectra of the MOJAVE Sample

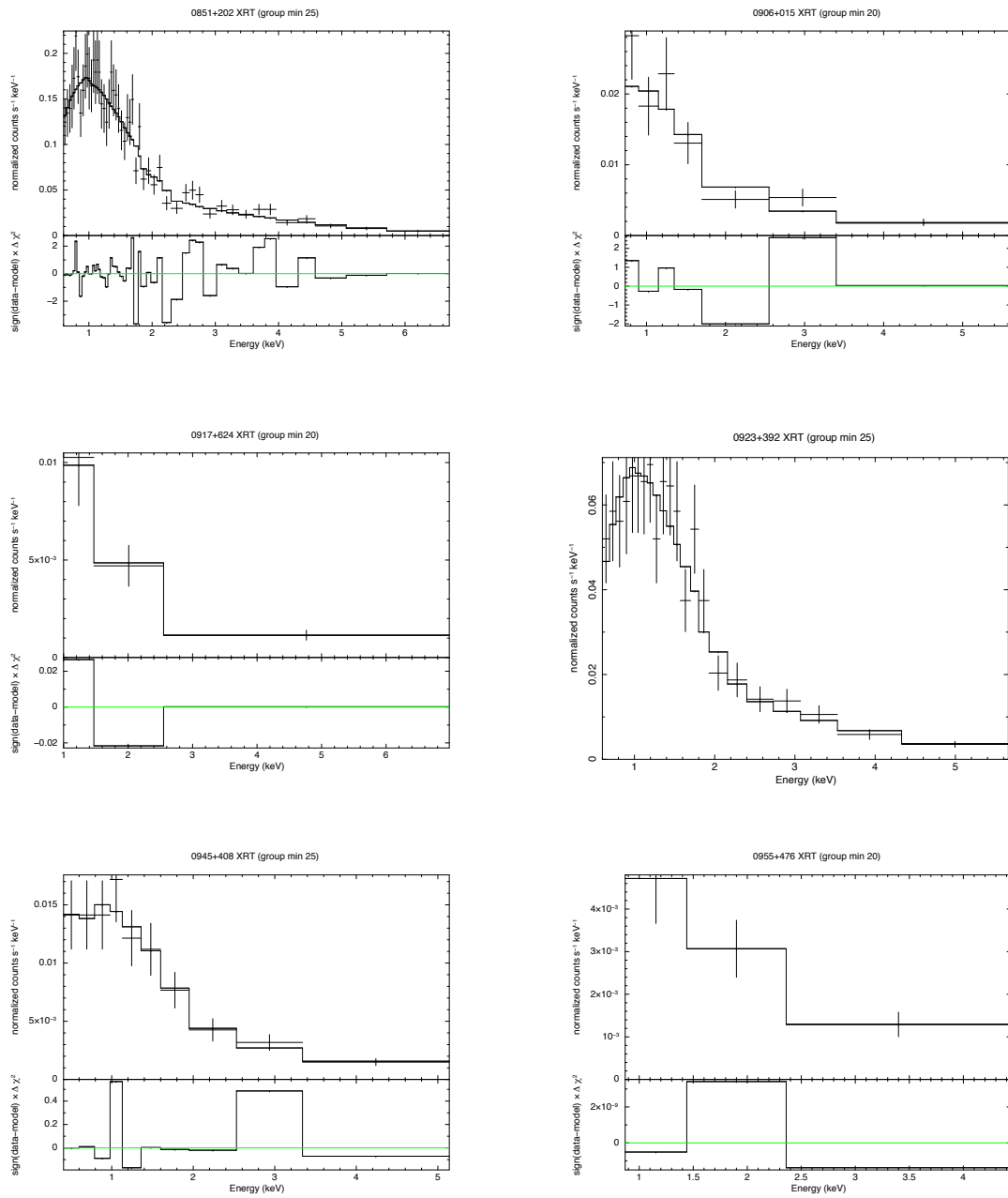


Figure A.10: The X-ray spectrum of the MOJAVE sources measured by *Swift*/XRT ordered by RA (continuation). From upper-left to bottom-right: 0851+202, 0906+015, 0917+624, 0923+392, 0945+408, and 0955+476.

A The X-ray Spectra of the MOJAVE Sample

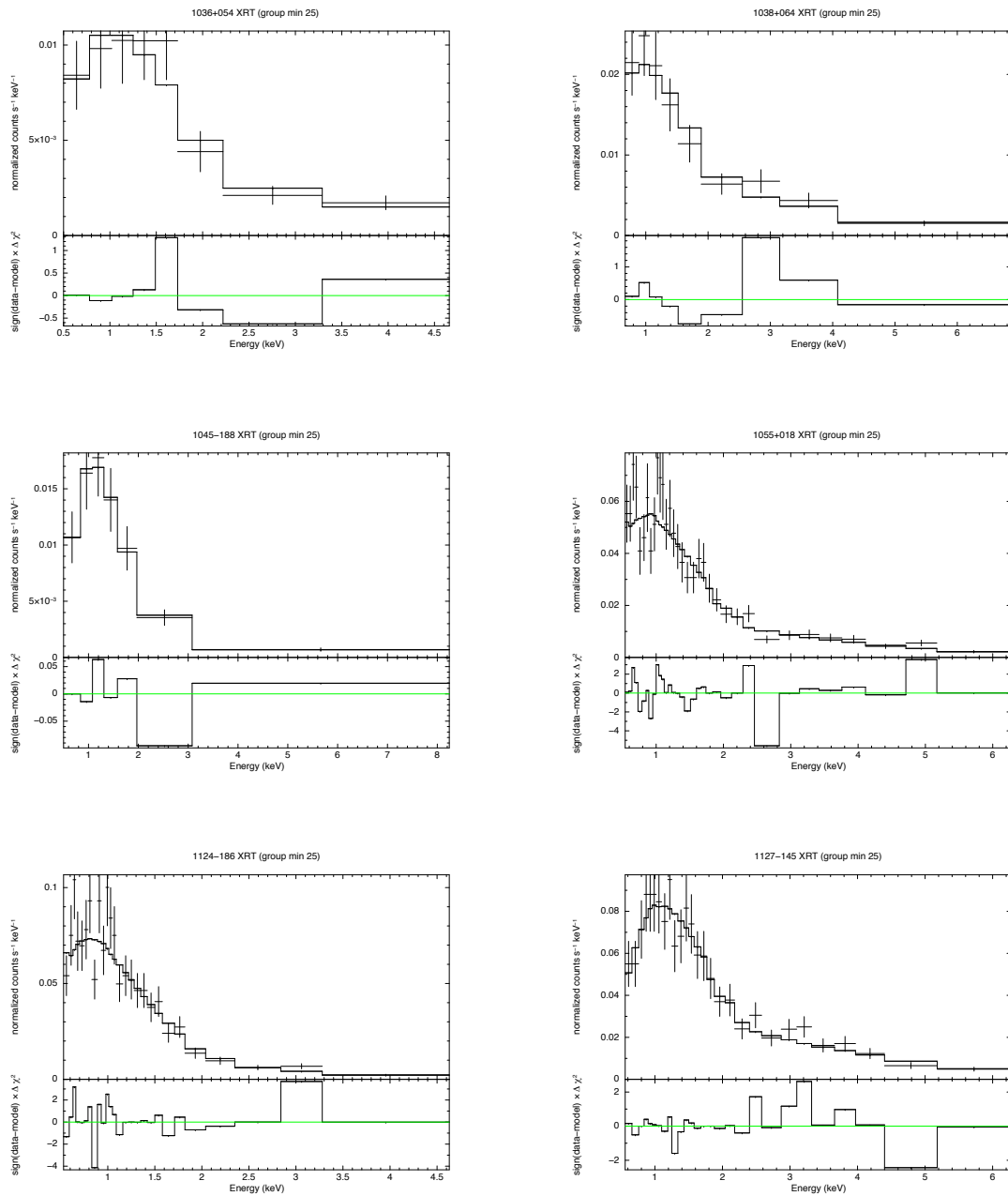


Figure A.11: The X-ray spectrum of the MOJAVE sources measured by *Swift*/XRT ordered by RA (continuation). From upper-left to bottom-right: 1036+054, 1038+064, 1045-188, 1055+018, 1124-186, and 1127-145.

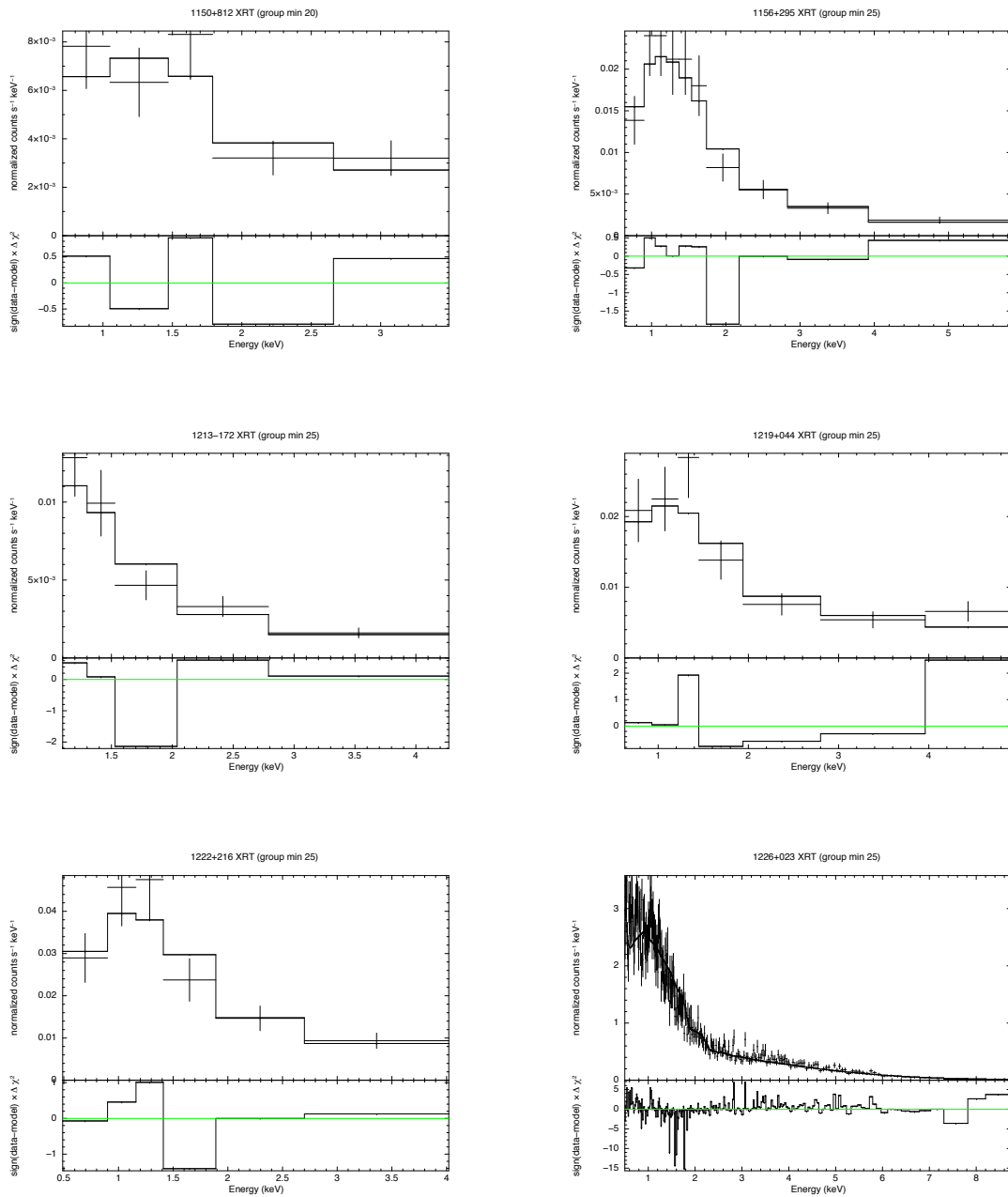


Figure A.12: The X-ray spectrum of the MOJAVE sources measured by *Swift*/XRT ordered by RA (continuation). From upper-left to bottom-right: 1150+812, 1156+295, 1213-172, 1219+044, 1222+216, and 1226+023.

A The X-ray Spectra of the MOJAVE Sample

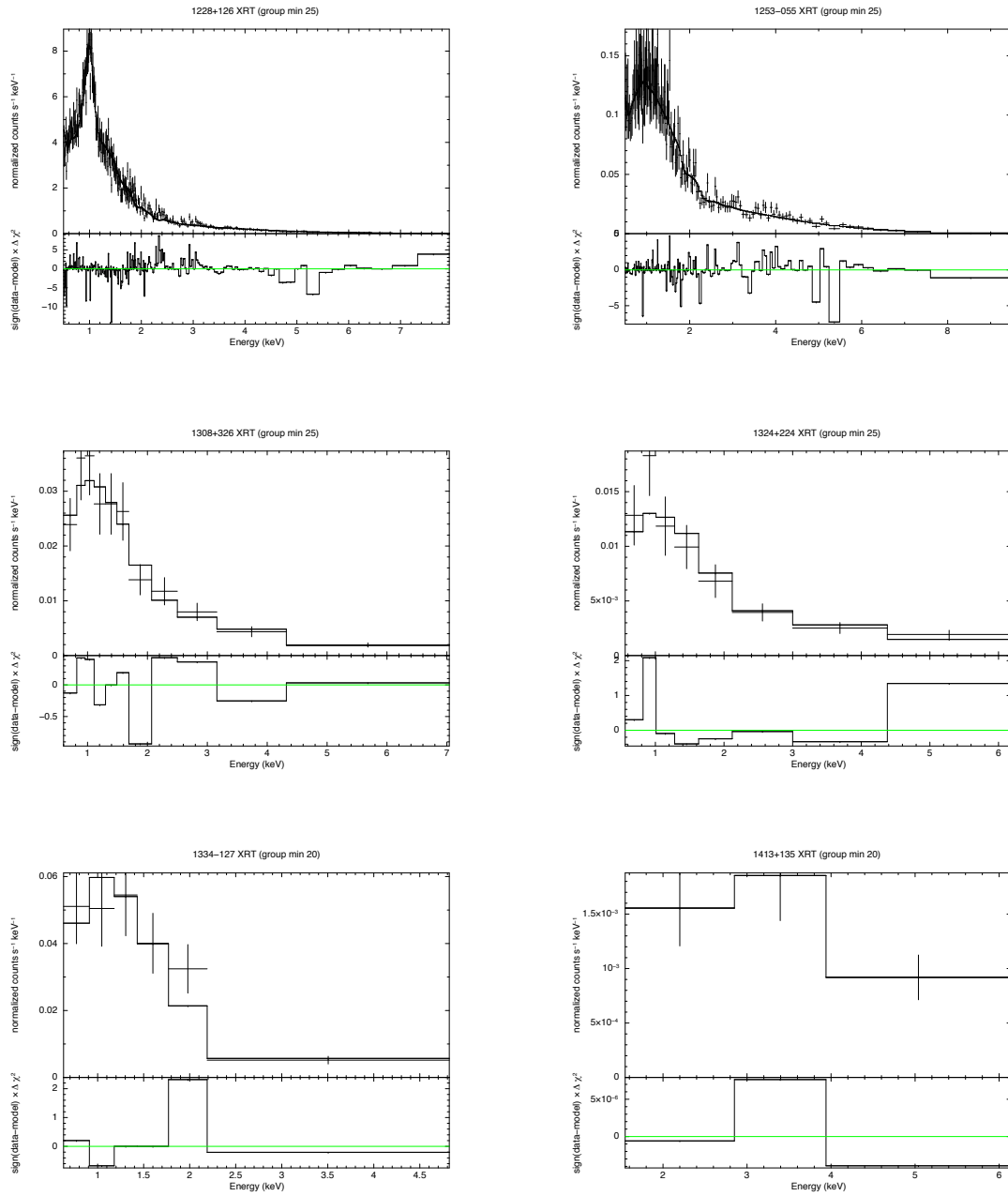


Figure A.13: The X-ray spectrum of the MOJAVE sources measured by *Swift*/XRT ordered by RA (continuation). From upper-left to bottom-right: 1228+126, 1253-055, 1308+326, 1324+224, 1334-127, and 1413+135.

A The X-ray Spectra of the MOJAVE Sample

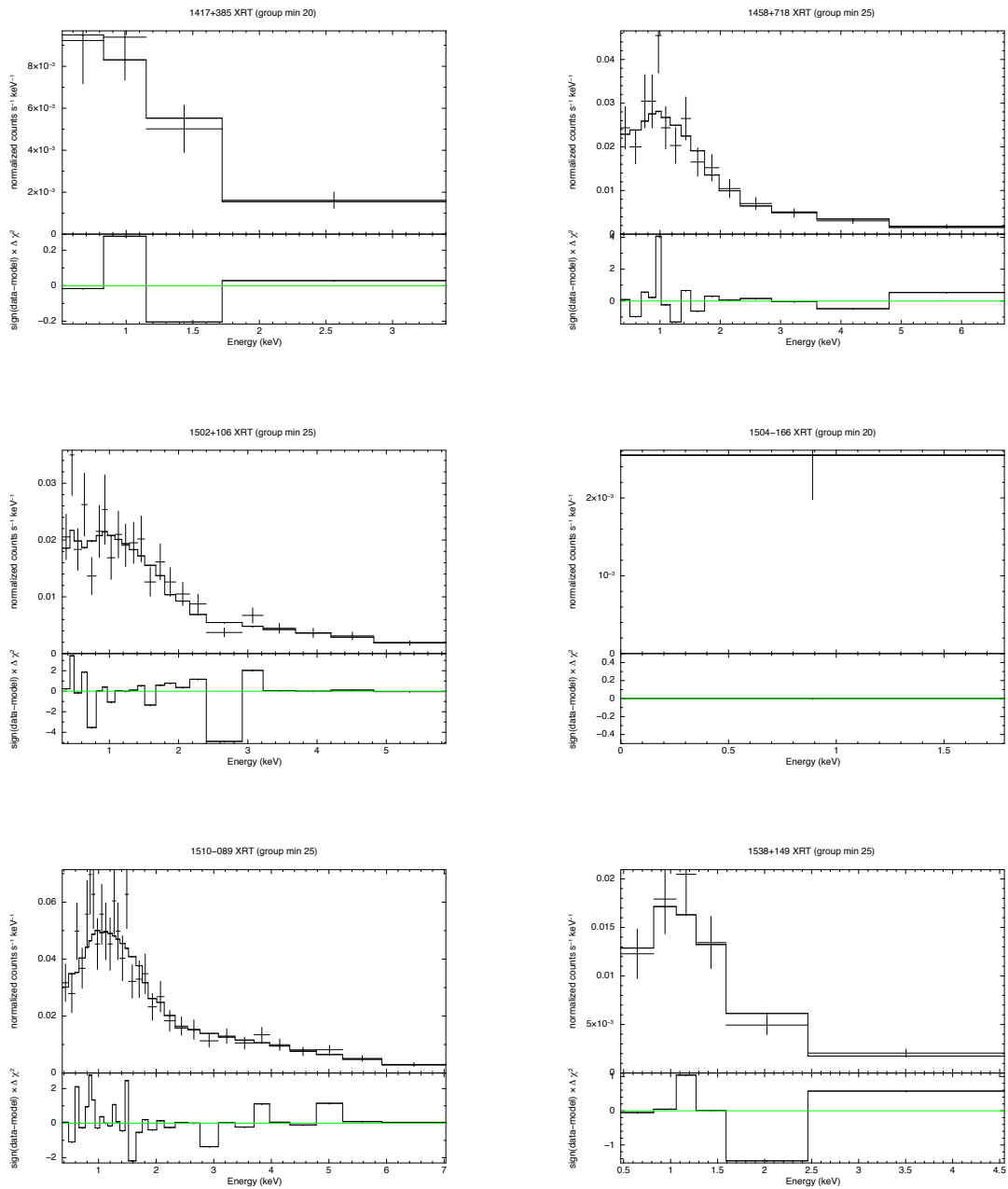


Figure A.14: The X-ray spectrum of the MOJAVE sources measured by *Swift*/XRT ordered by RA (continuation). From upper-left to bottom-right: 1417+385, 1458+718, 1502+106, 1504-166, 1510-089, and 1538+149.

A The X-ray Spectra of the MOJAVE Sample

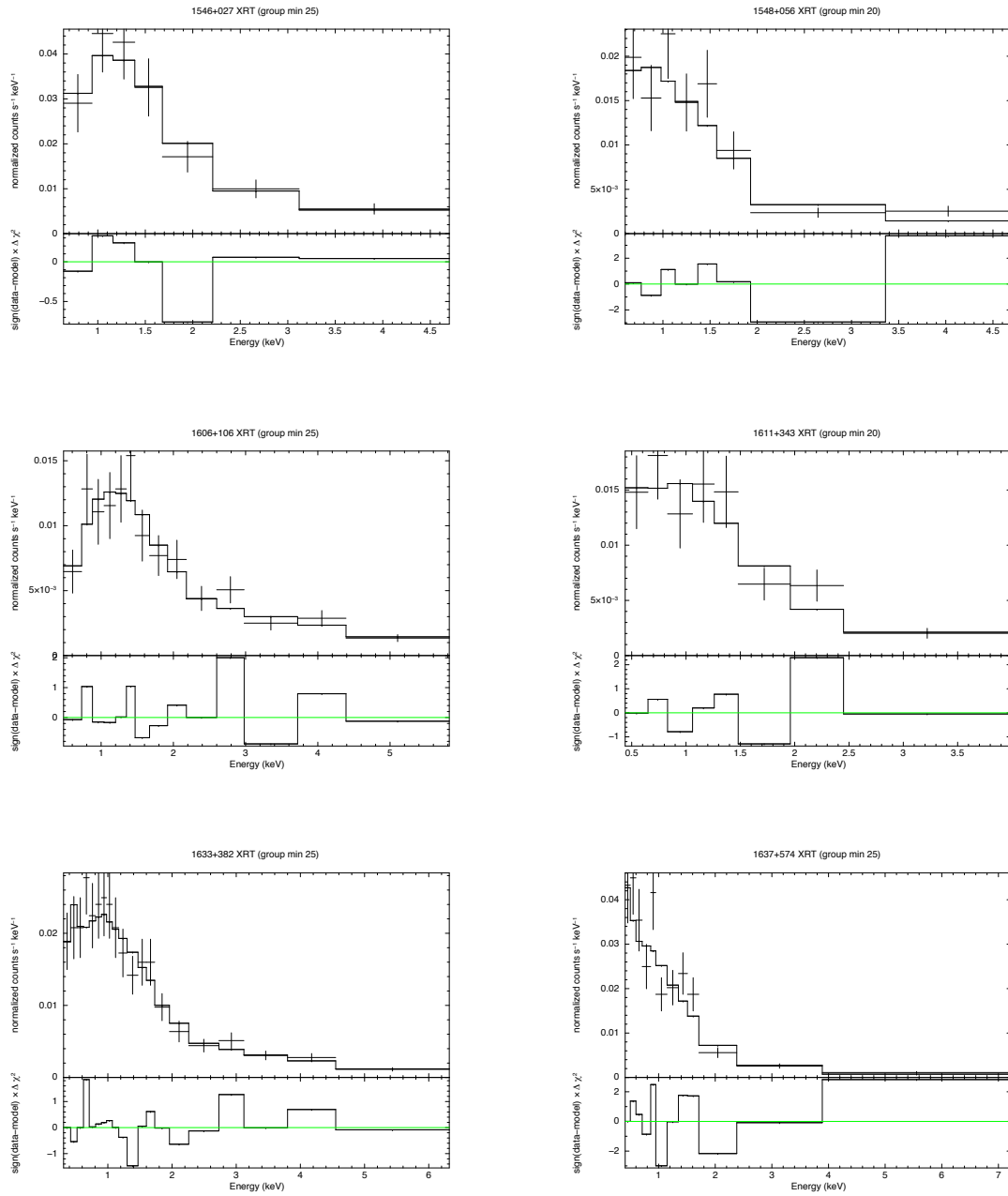


Figure A.15: The X-ray spectrum of the MOJAVE sources measured by *Swift*/XRT ordered by RA (continuation). From upper-left to bottom-right: 1546+027, 1548+056, 1606+106, 1611+343, 1633+382, and 1637+574.

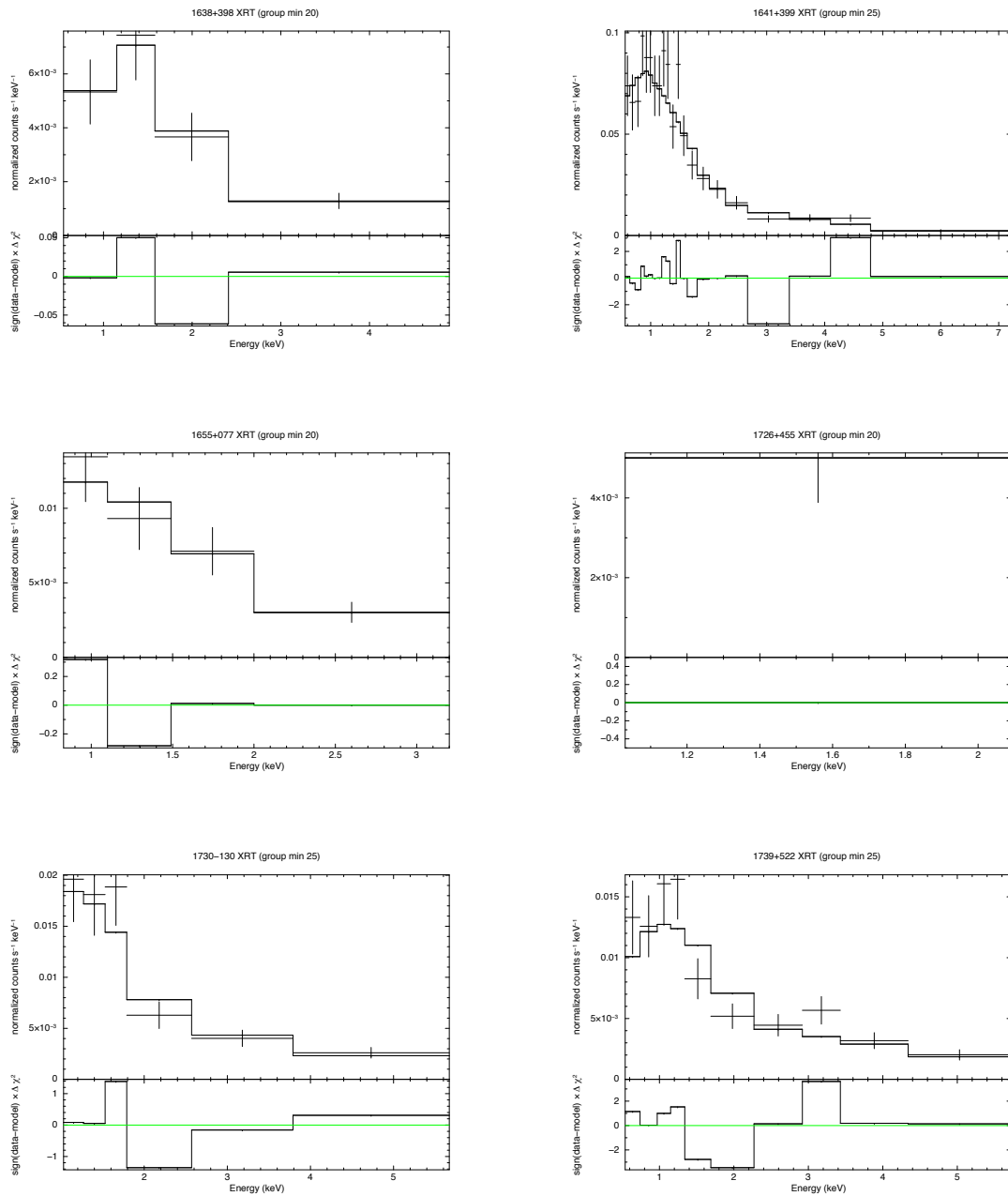


Figure A.16: The X-ray spectrum of the MOJAVE sources measured by *Swift*/XRT ordered by RA (continuation). From upper-left to bottom-right: 1638+398, 1641+399, 1655+077, 1726+455, 1730-130, and 1739+522.

A The X-ray Spectra of the MOJAVE Sample

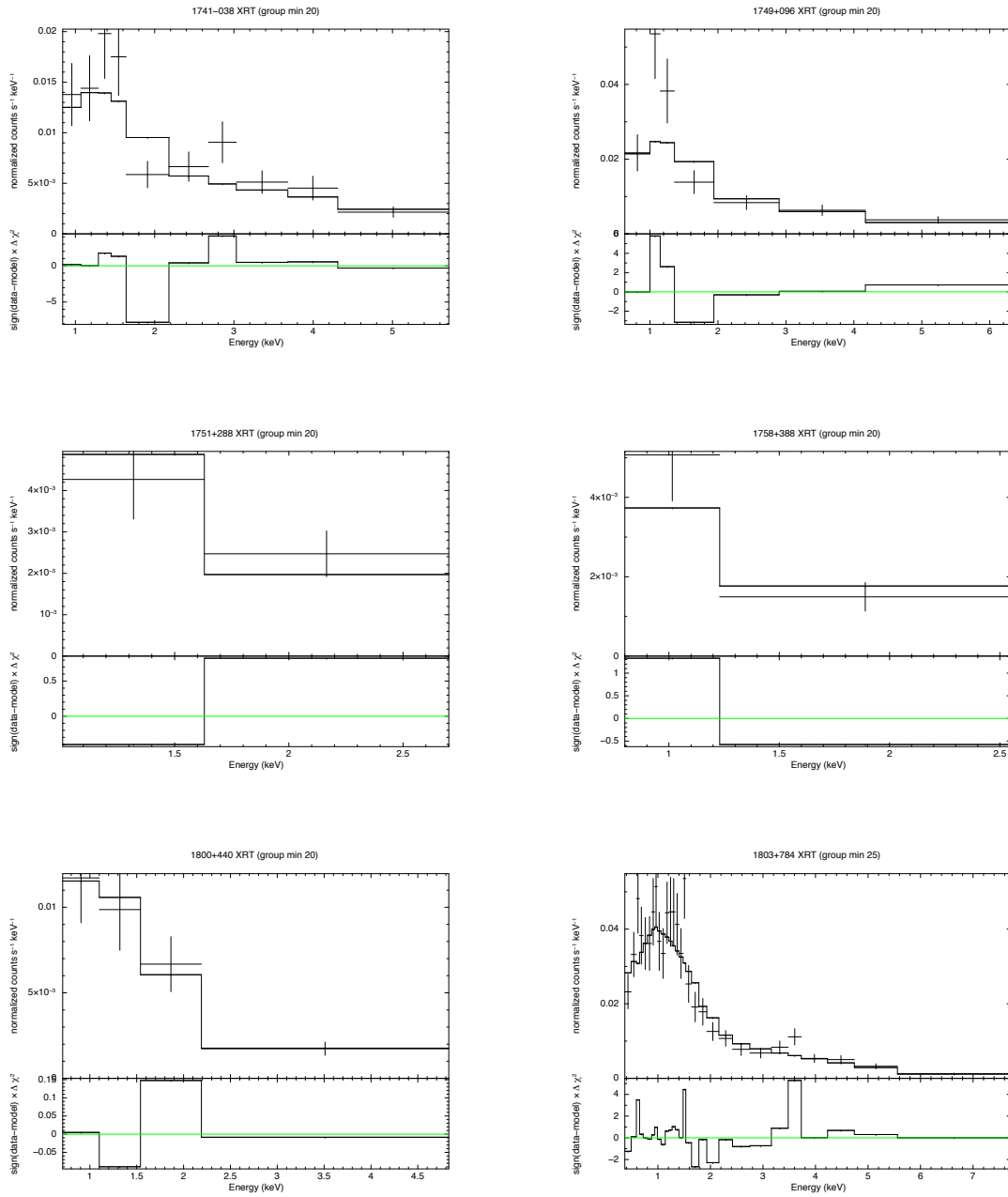


Figure A.17: The X-ray spectrum of the MOJAVE sources measured by *Swift*/XRT ordered by RA (continuation). From upper-left to bottom-right: 1741-038, 1749+096, 1751+288, 1758+388, 1800+440, and 1803+784.

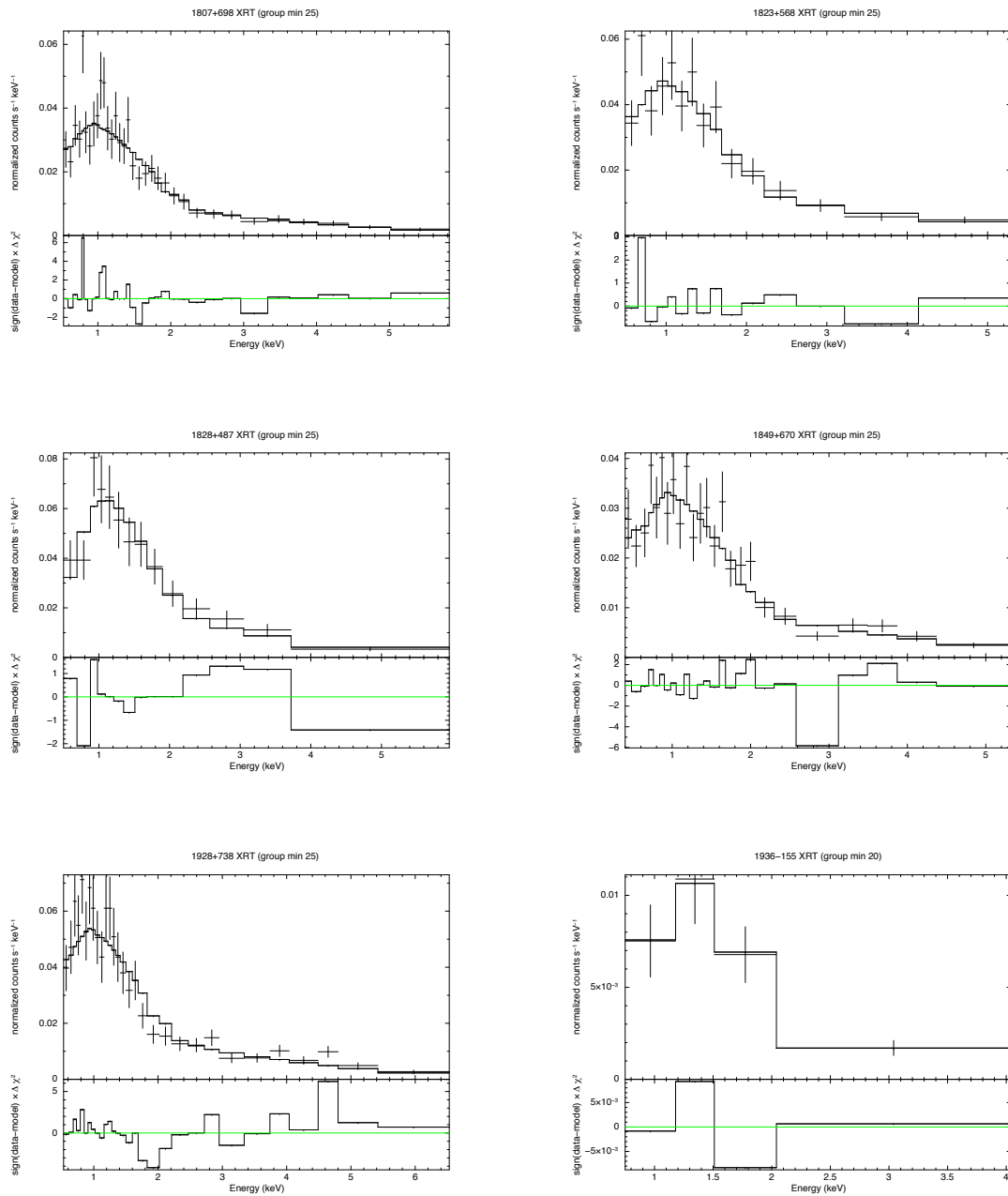


Figure A.18: The X-ray spectrum of the MOJAVE sources measured by *Swift*/XRT ordered by RA (continuation). From upper-left to bottom-right: 1807+698, 1823+568, 1828+487, 1849+670, 1928+738, and 1936-155.

A The X-ray Spectra of the MOJAVE Sample

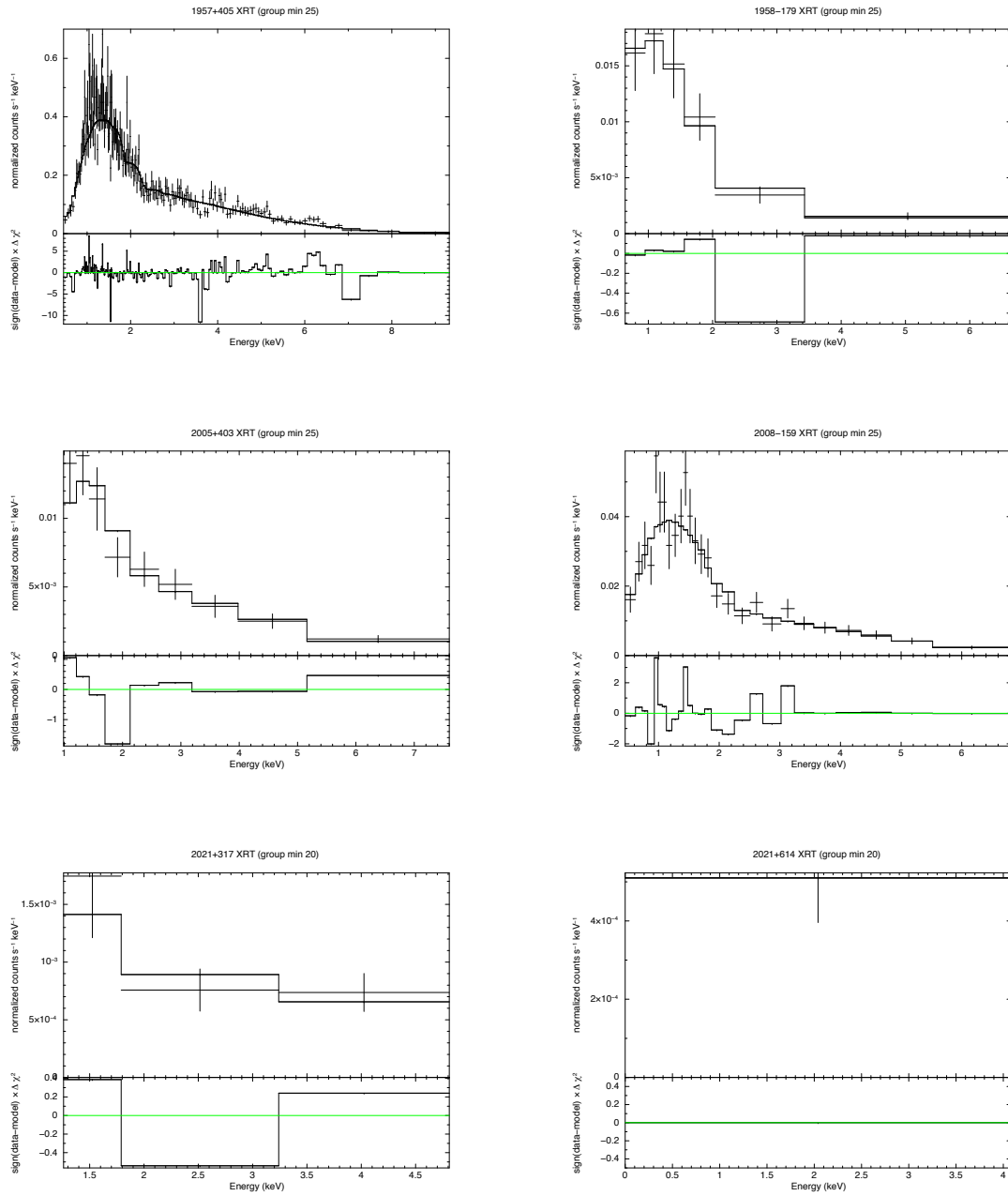


Figure A.19: The X-ray spectrum of the MOJAVE sources measured by *Swift*/XRT ordered by RA (continuation). From upper-left to bottom-right: 1957+405, 1958-179, 2005+403, 2008-159, 2021+317, and 2021+614.

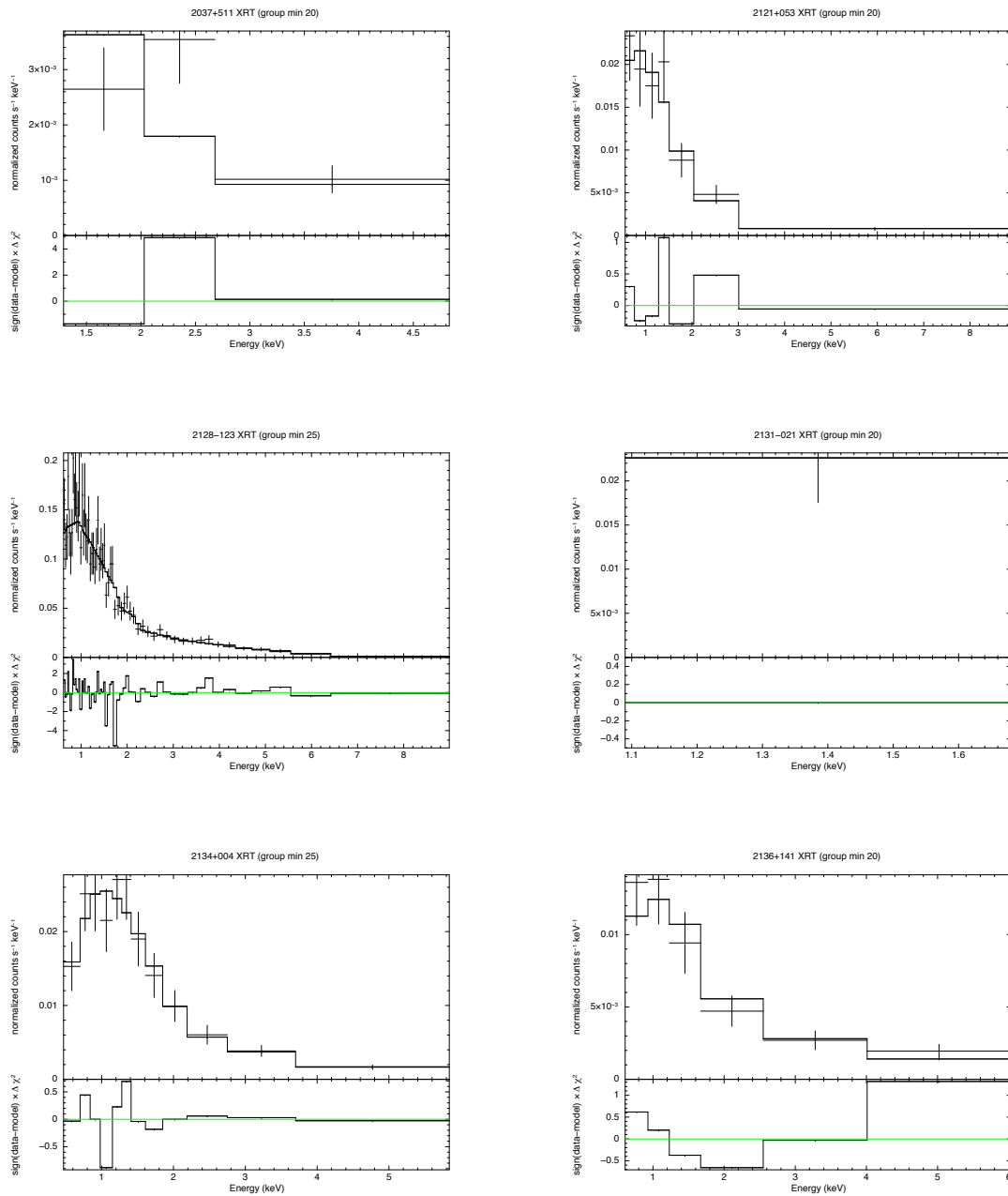


Figure A.20: The X-ray spectrum of the MOJAVE sources measured by *Swift*/XRT ordered by RA (continuation). From upper-left to bottom-right: 2037+511, 2121+053, 2128-123, 2131-021, 2134+004, and 2136+141.

A The X-ray Spectra of the MOJAVE Sample

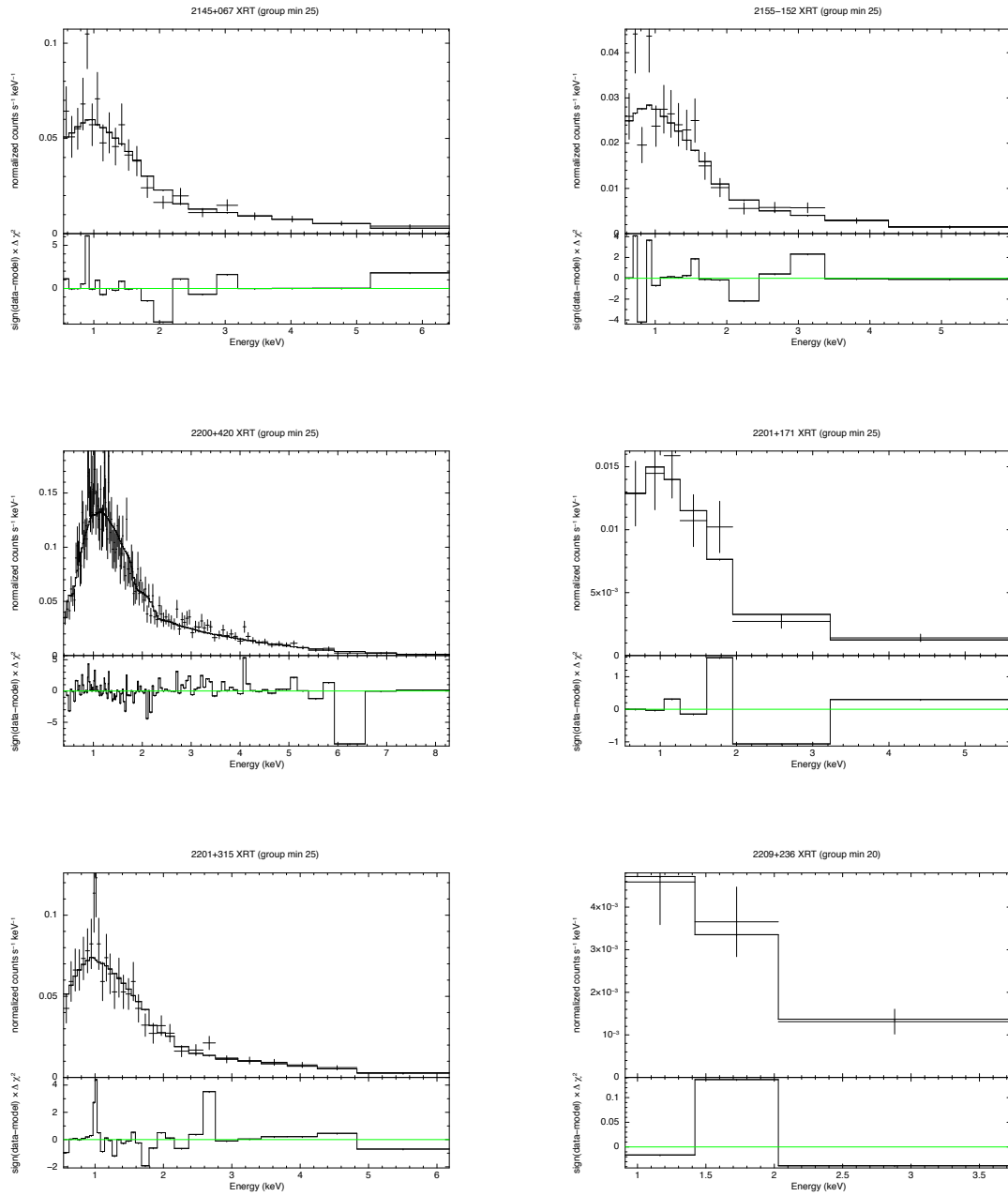


Figure A.21: The X-ray spectrum of the MOJAVE sources measured by *Swift*/XRT ordered by RA (continuation). From upper-left to bottom-right: 2145+067, 2155-152, 2200+420, 2201+171, 2201+315, and 2209+236.

A The X-ray Spectra of the MOJAVE Sample

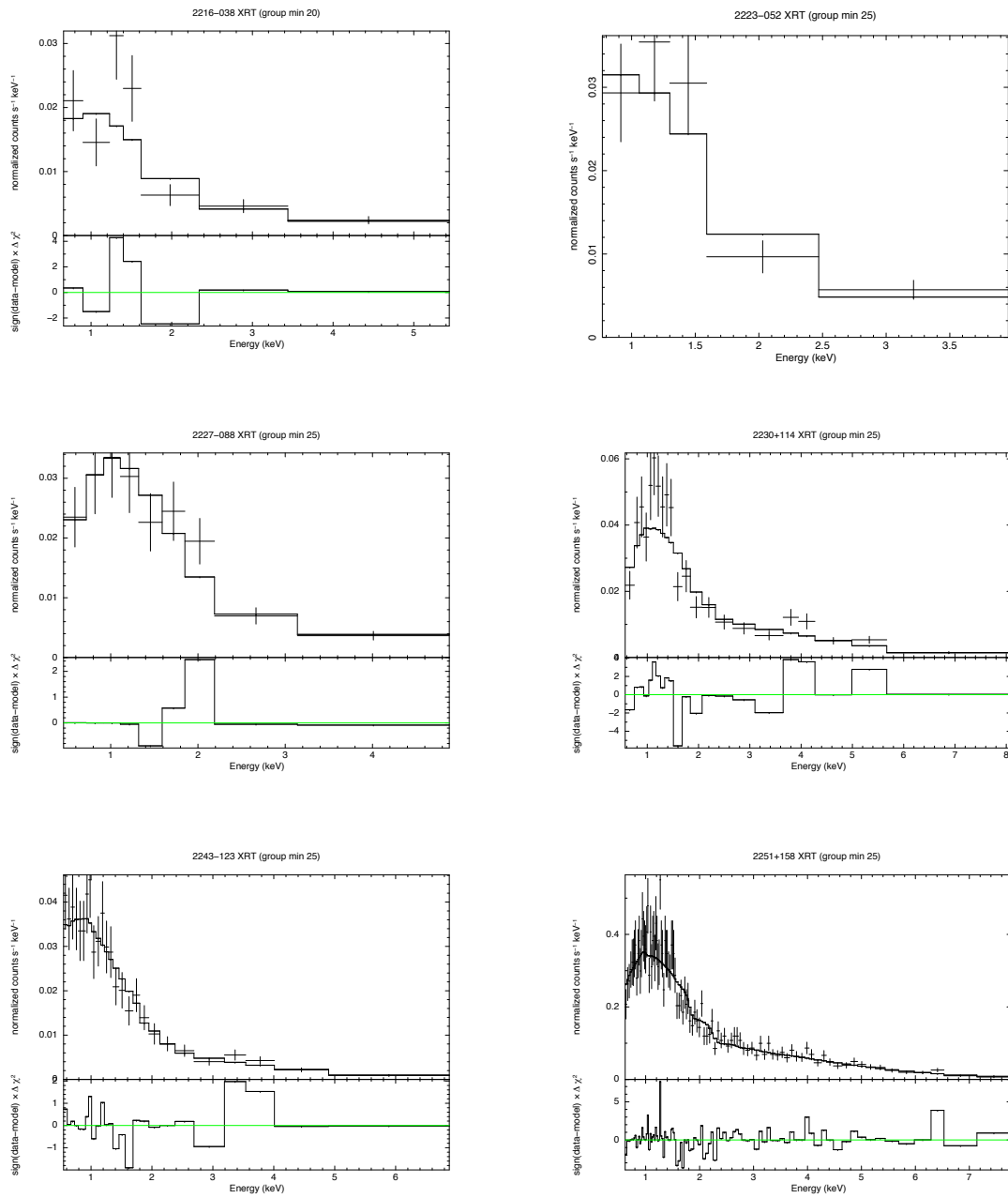


Figure A.22: The X-ray spectrum of the MOJAVE sources measured by *Swift*/XRT ordered by RA (continuation). From upper-left to bottom-right: 2216-038, 2223-052, 2227-088, 2230+114, 2243-123, and 2251+158.

A The X-ray Spectra of the MOJAVE Sample

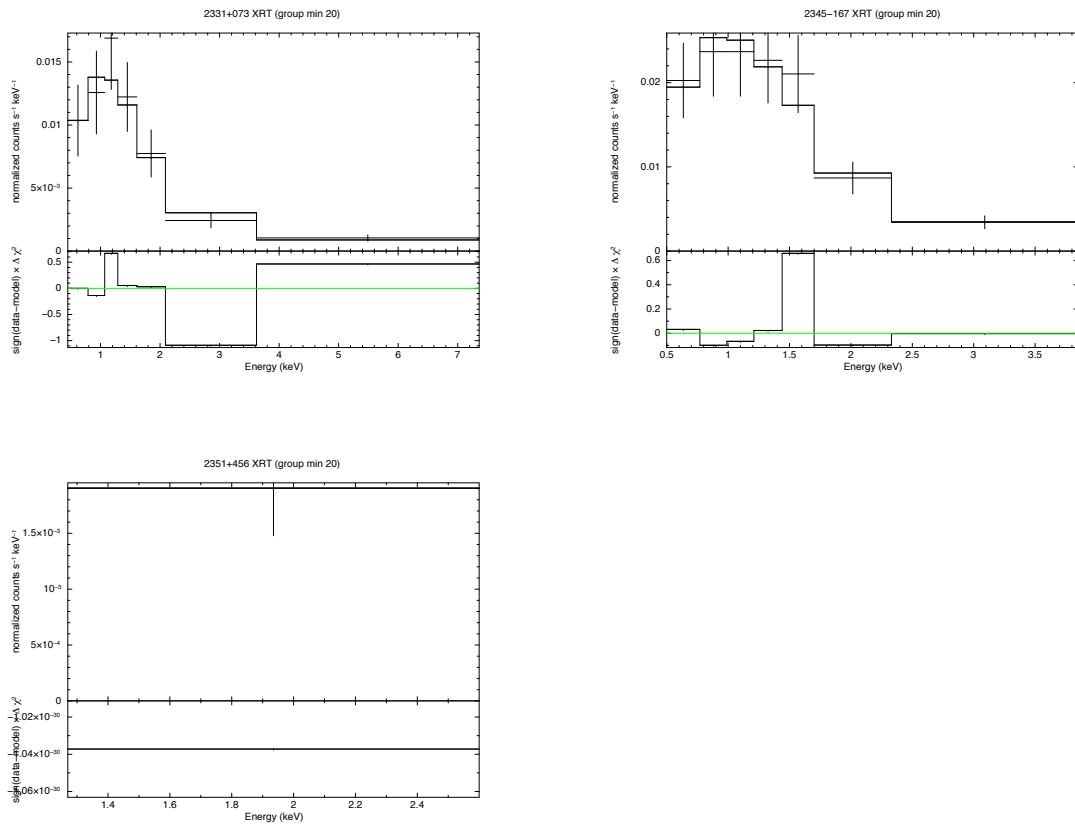


Figure A.23: The X-ray spectrum of the MOJAVE sources measured by *Swift*/XRT ordered by RA (continuation). From upper-left to bottom-right: 2331+073, 2345-167, and 2351+456.

B The Broadband SED of the MOJAVE Sample

B The Broadband SED of the MOJAVE Sample

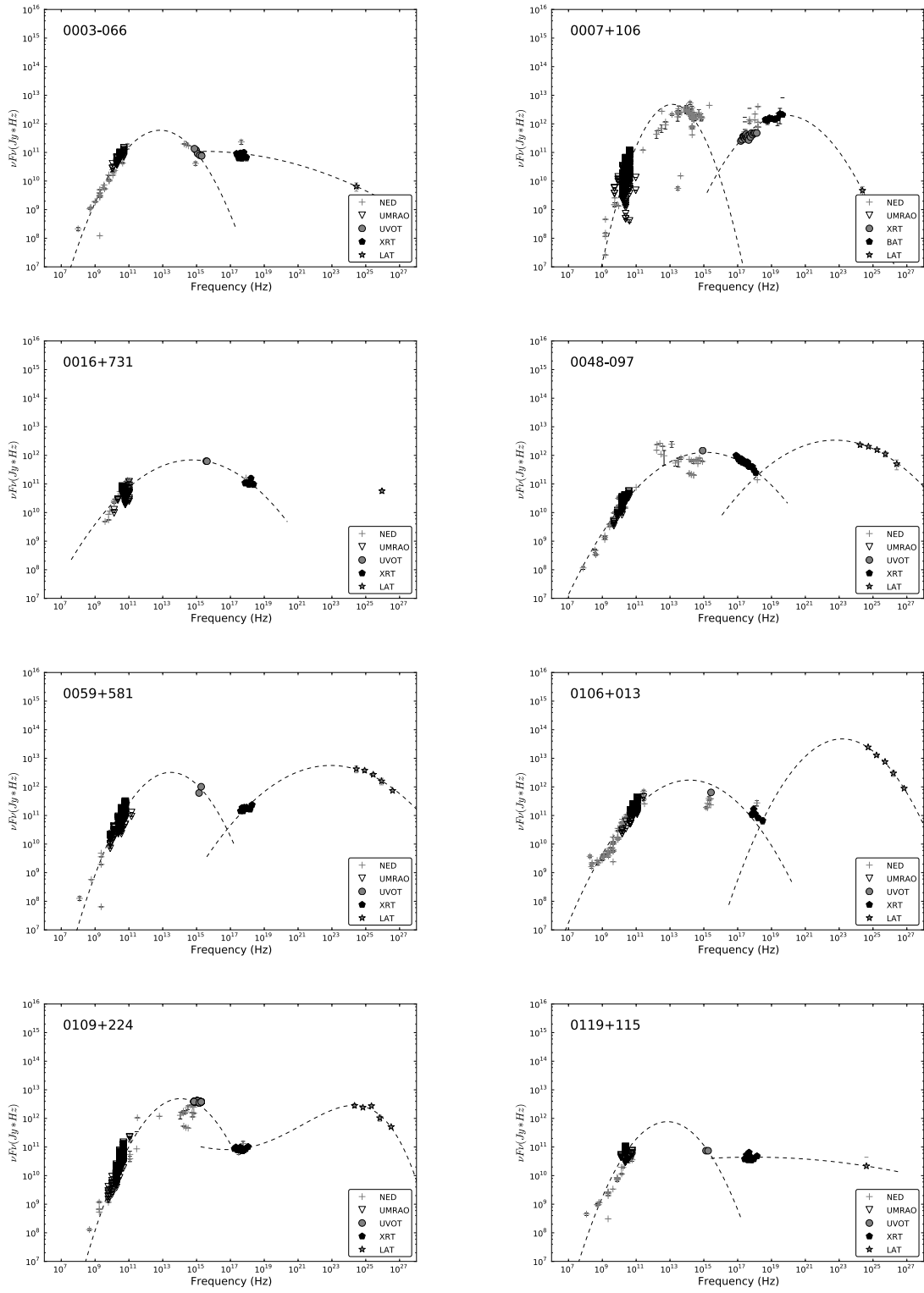


Figure B.1: The broadband SEDs of the MOJAVE sources.

B The Broadband SED of the MOJAVE Sample

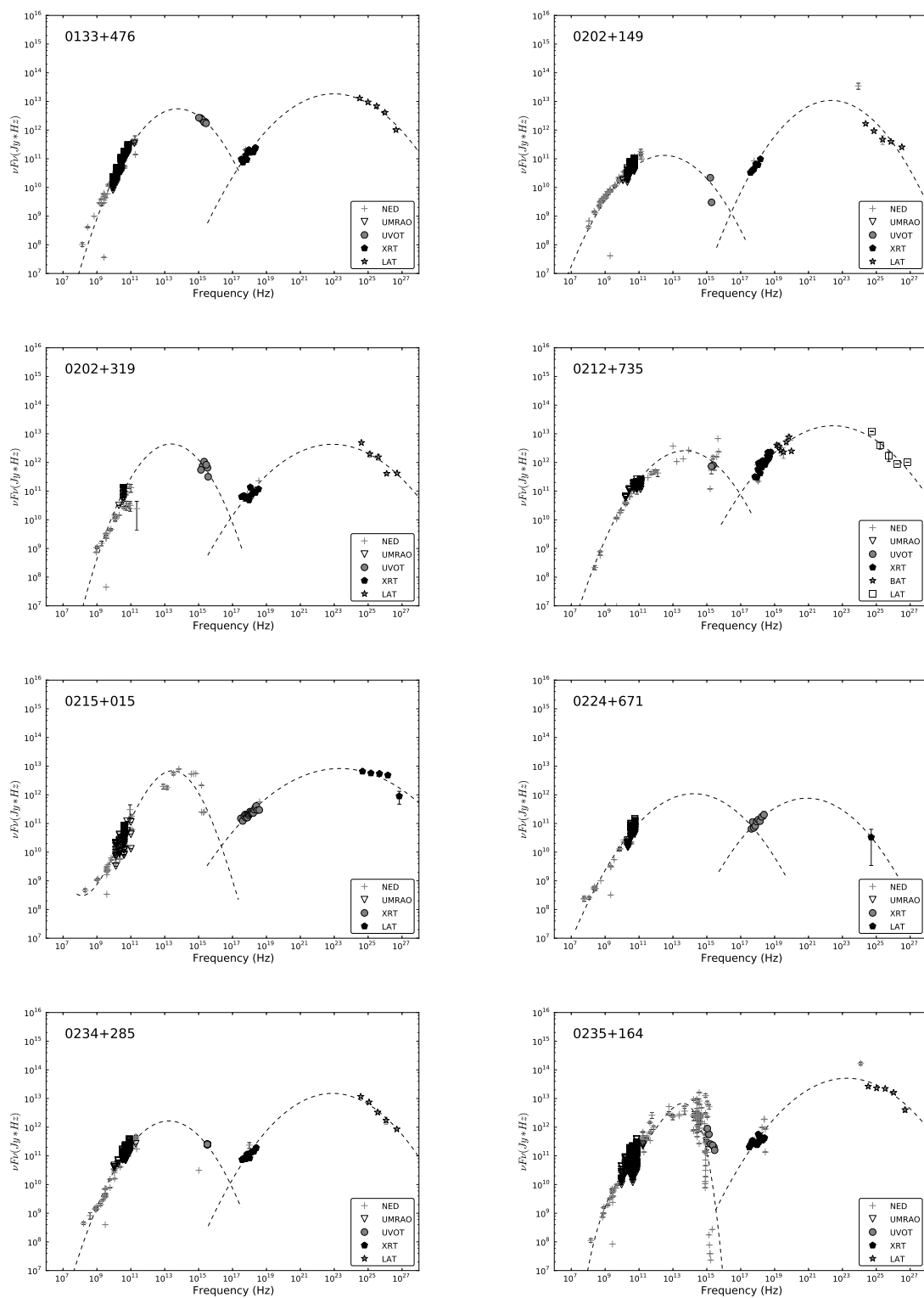


Figure B.2: The broadband SEDs of the MOJAVE sources.

B The Broadband SED of the MOJAVE Sample

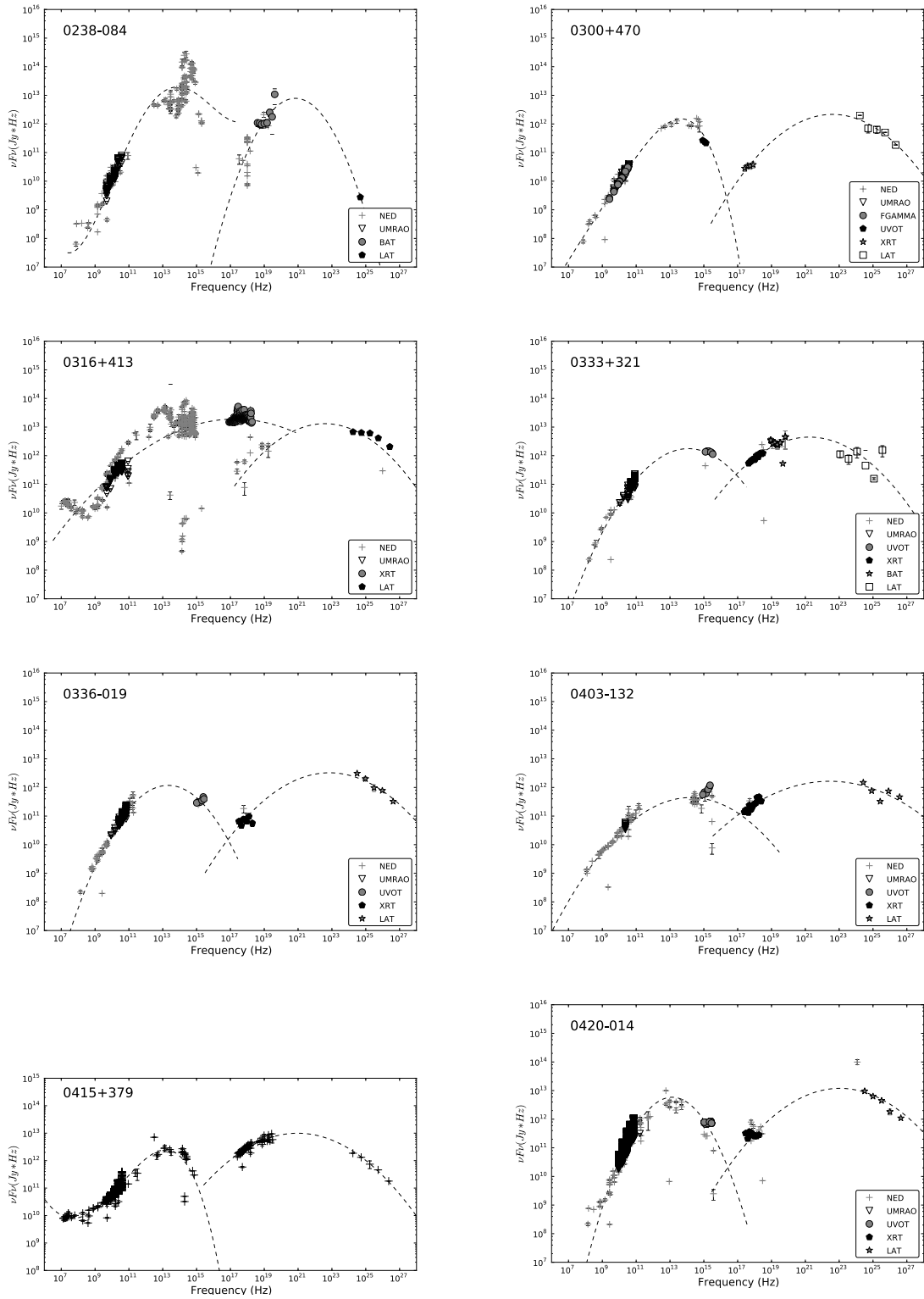


Figure B.3: The broadband SEDs of the MOJAVE sources.

B The Broadband SED of the MOJAVE Sample

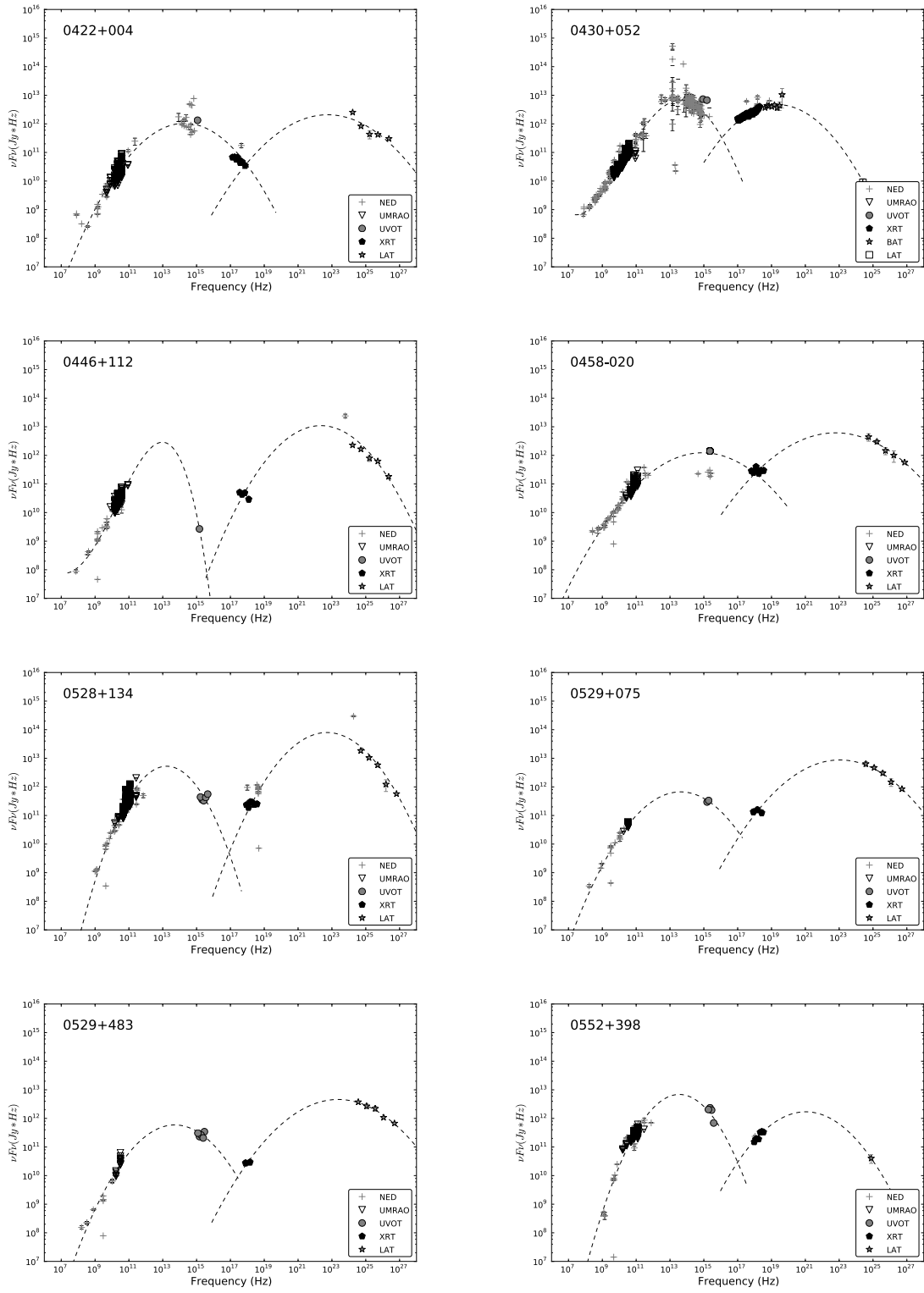


Figure B.4: The broadband SEDs of the MOJAVE sources.

B The Broadband SED of the MOJAVE Sample

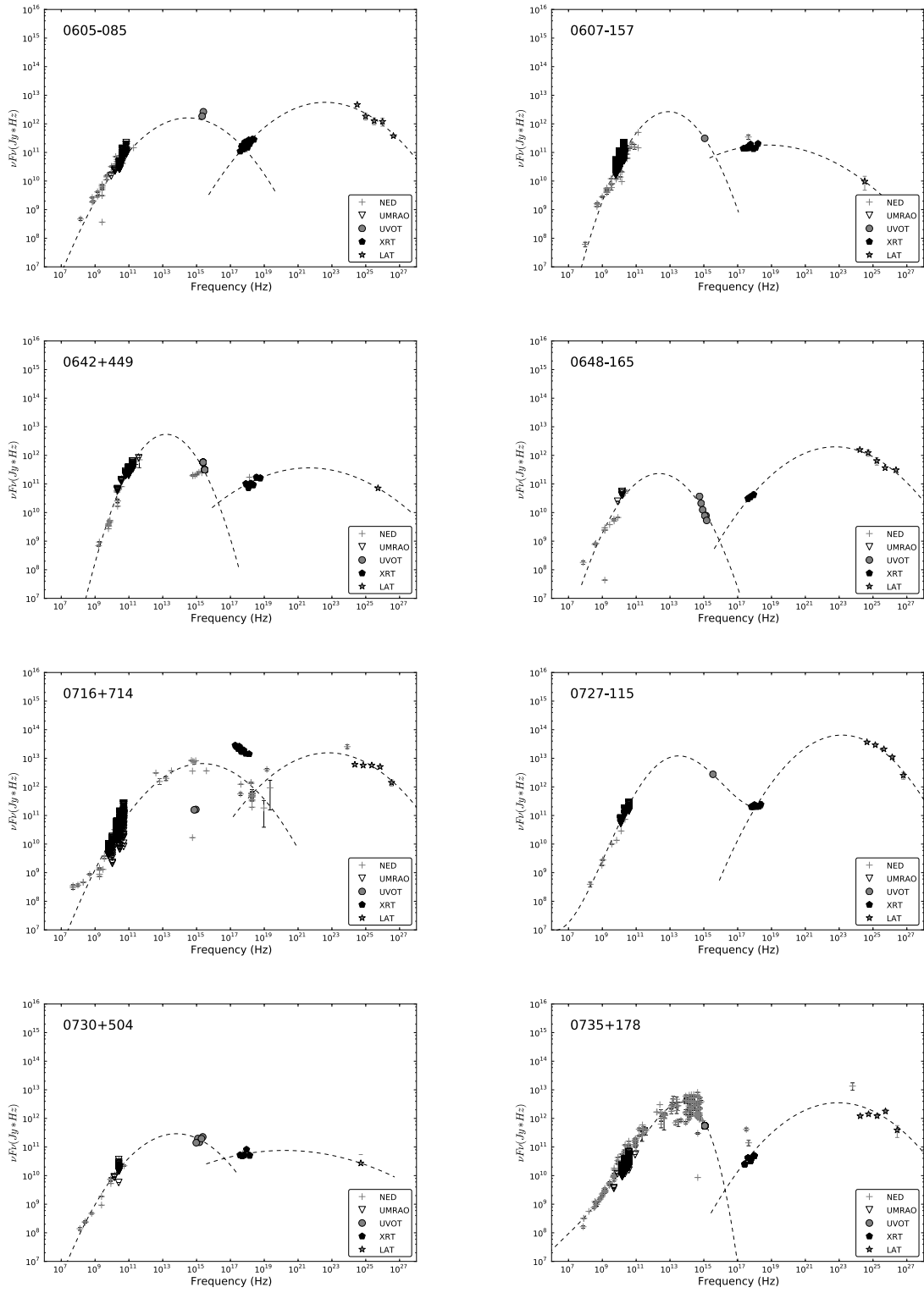


Figure B.5: The broadband SEDs of the MOJAVE sources.

B The Broadband SED of the MOJAVE Sample

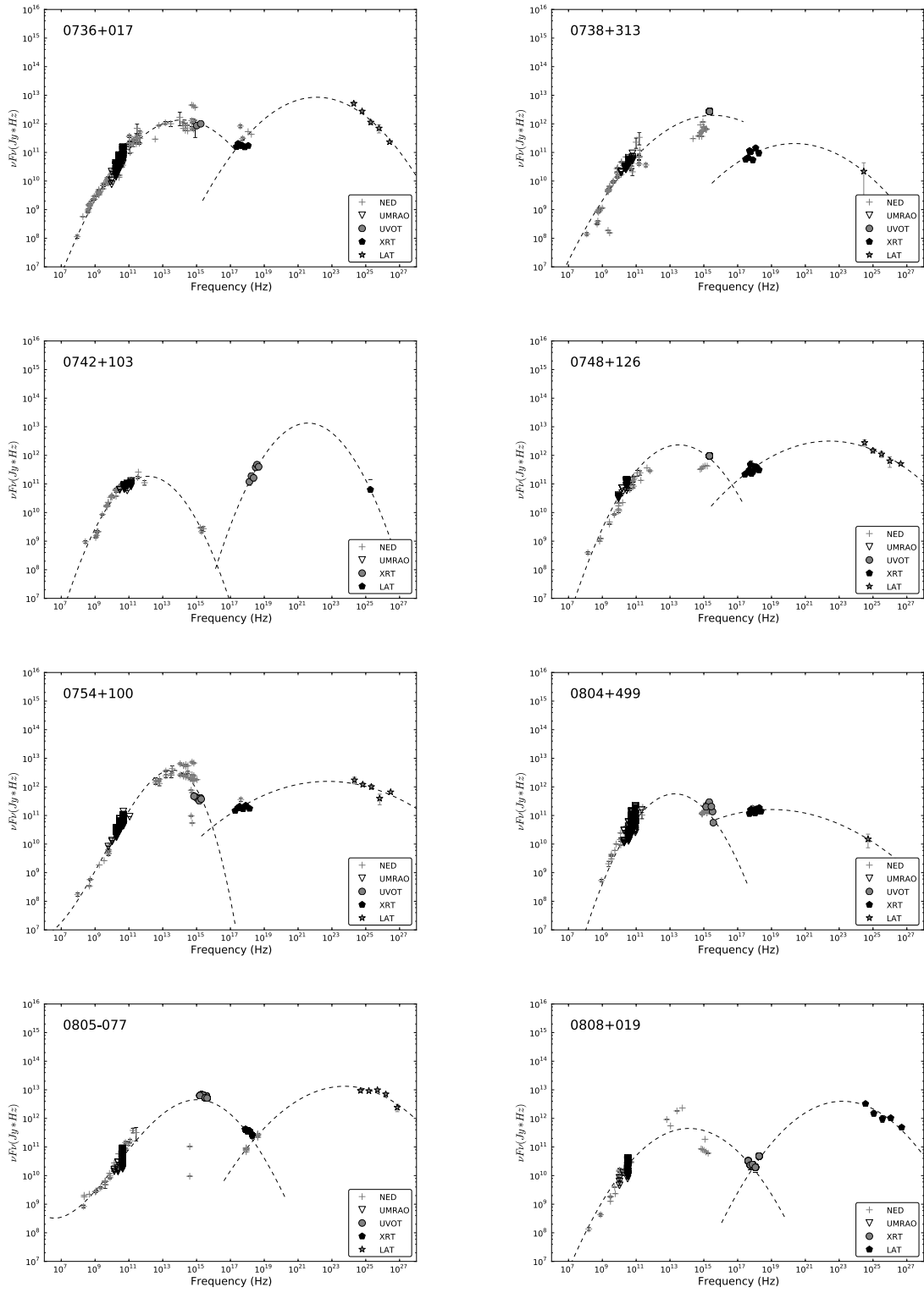


Figure B.6: The broadband SEDs of the MOJAVE sources.

B The Broadband SED of the MOJAVE Sample

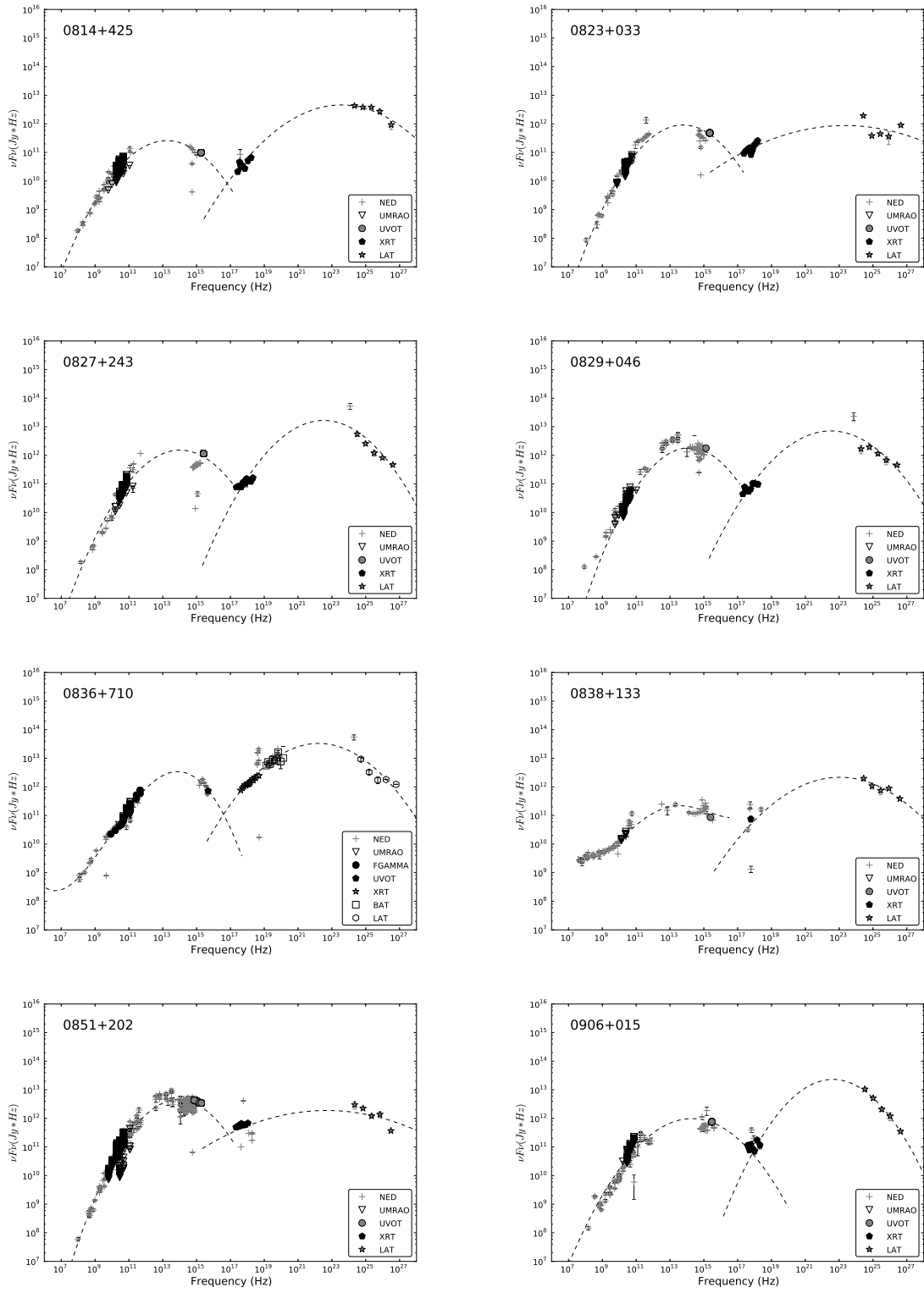


Figure B.7: The broadband SEDs of the MOJAVE sources.

B The Broadband SED of the MOJAVE Sample

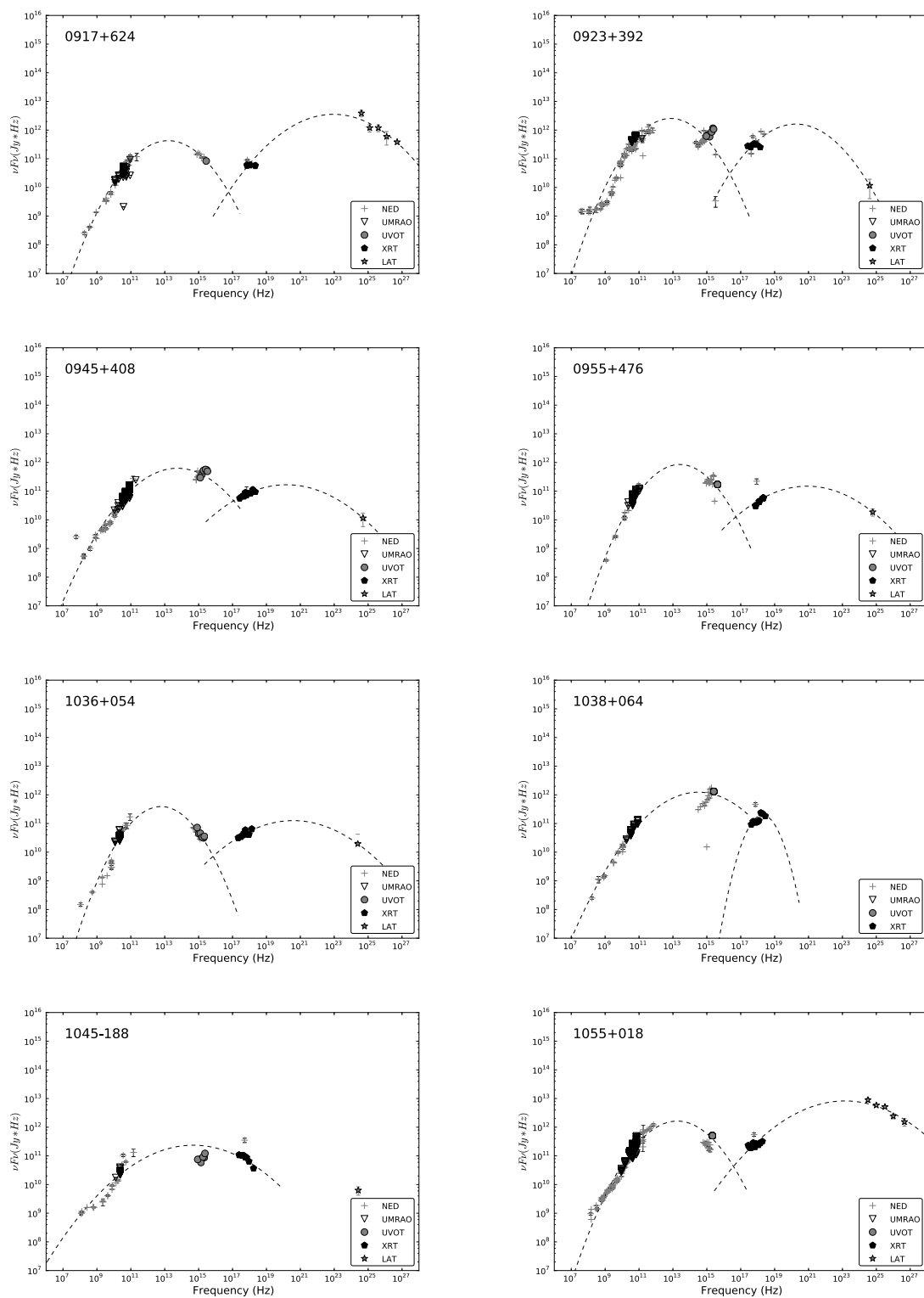


Figure B.8: The broadband SEDs of the MOJAVE sources.

B The Broadband SED of the MOJAVE Sample

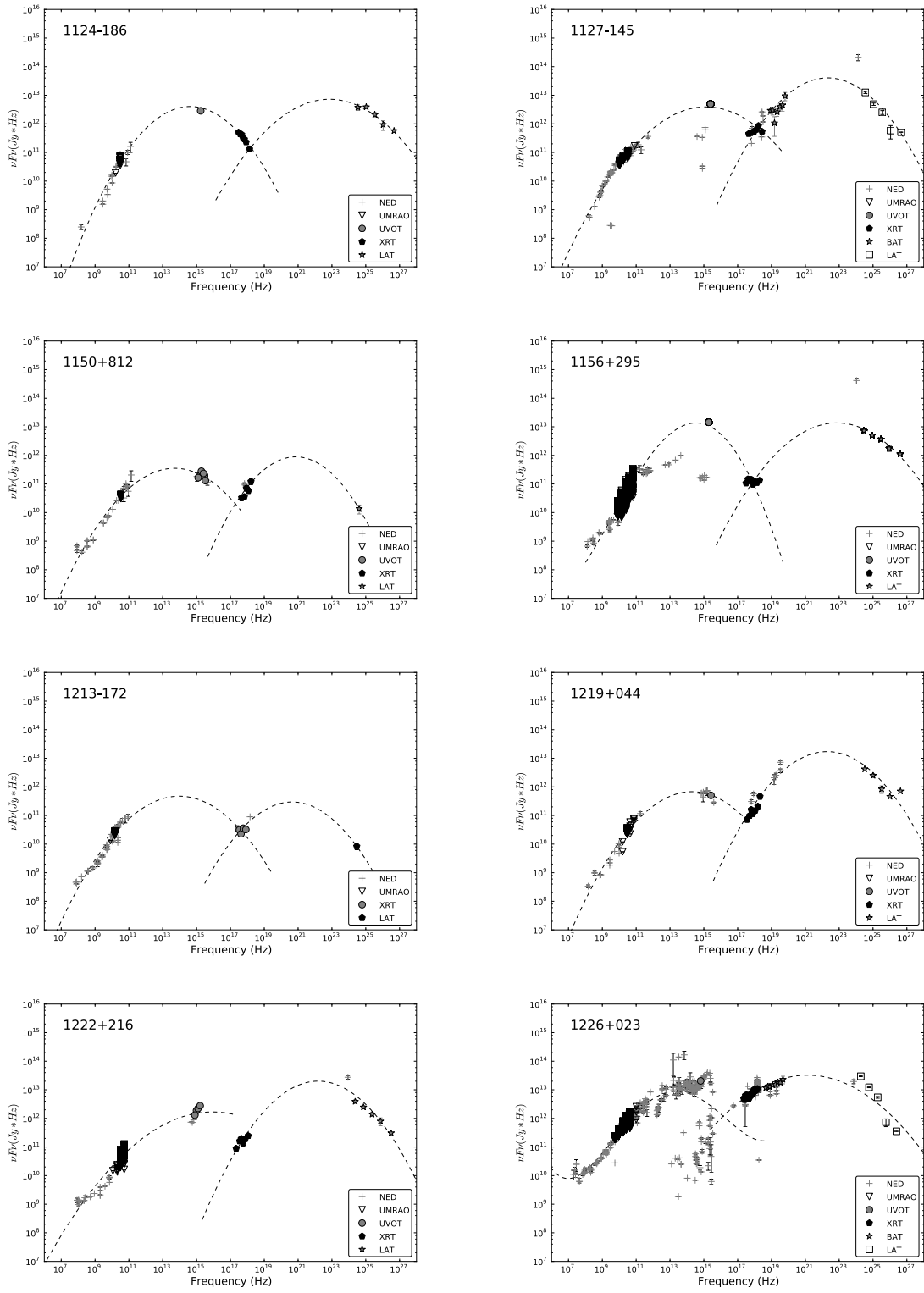


Figure B.9: The broadband SEDs of the MOJAVE sources.

B The Broadband SED of the MOJAVE Sample

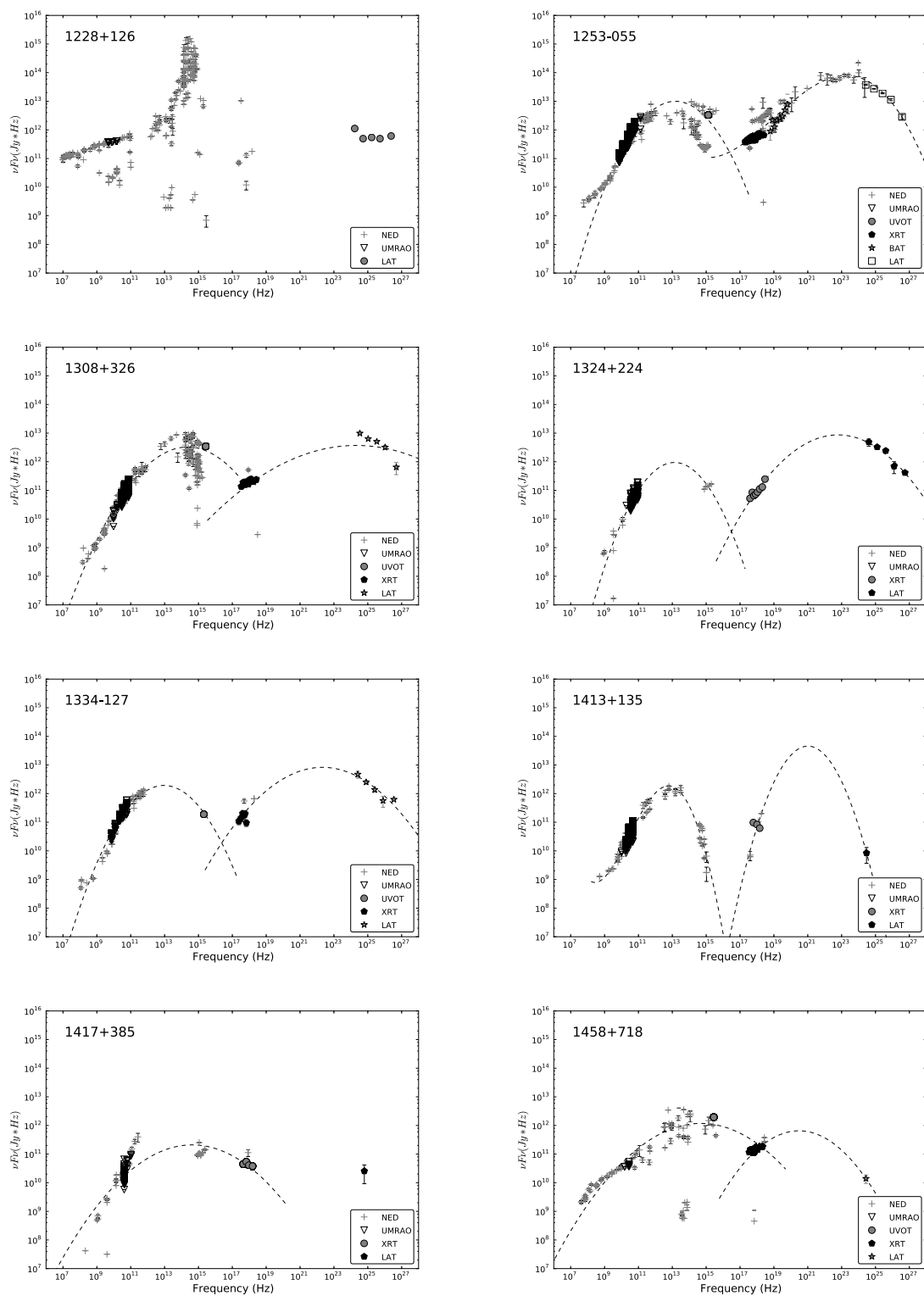


Figure B.10: The broadband SEDs of the MOJAVE sources.

B The Broadband SED of the MOJAVE Sample

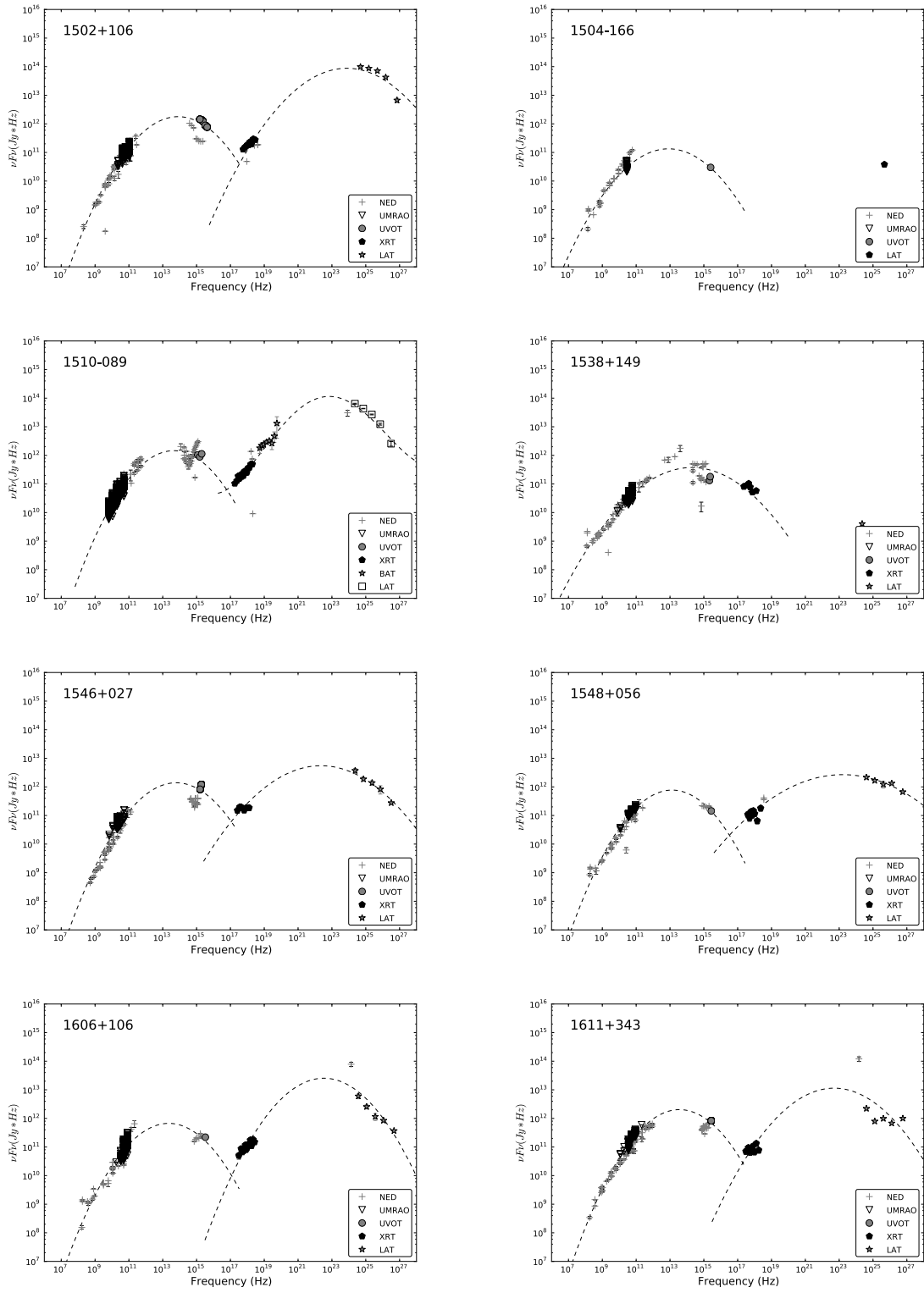


Figure B.11: The broadband SEDs of the MOJAVE sources.

B The Broadband SED of the MOJAVE Sample

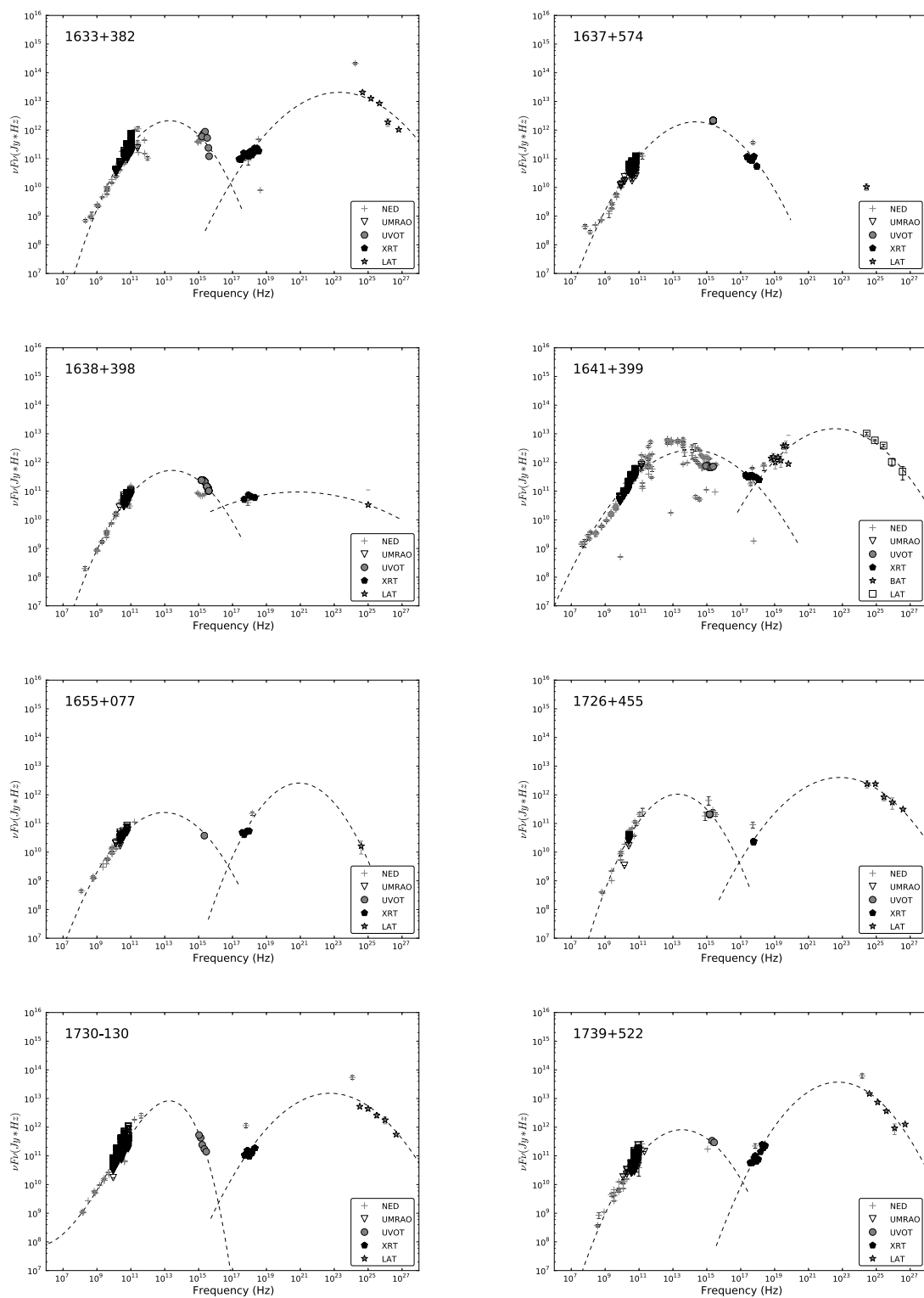


Figure B.12: The broadband SEDs of the MOJAVE sources.

B The Broadband SED of the MOJAVE Sample

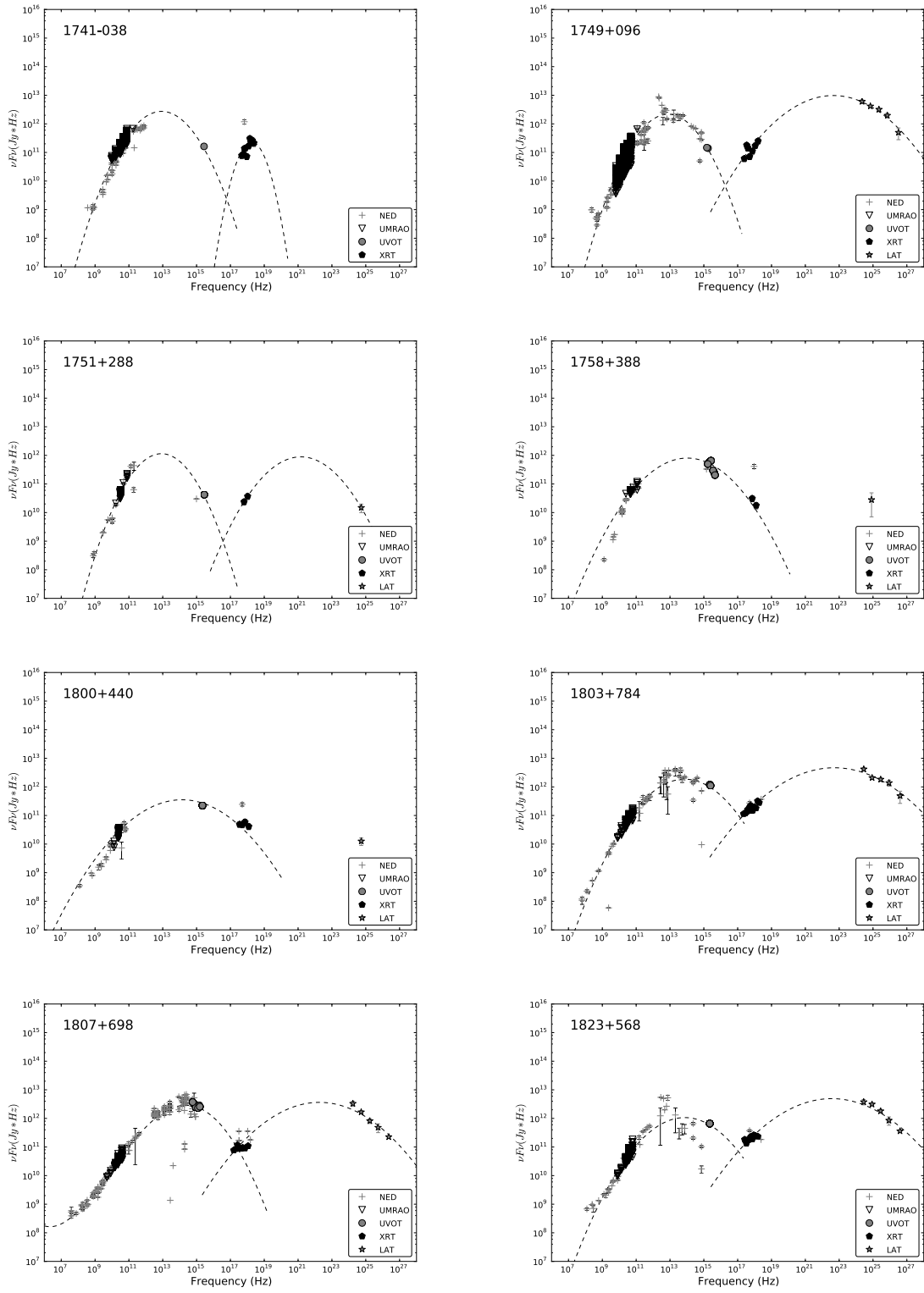


Figure B.13: The broadband SEDs of the MOJAVE sources.

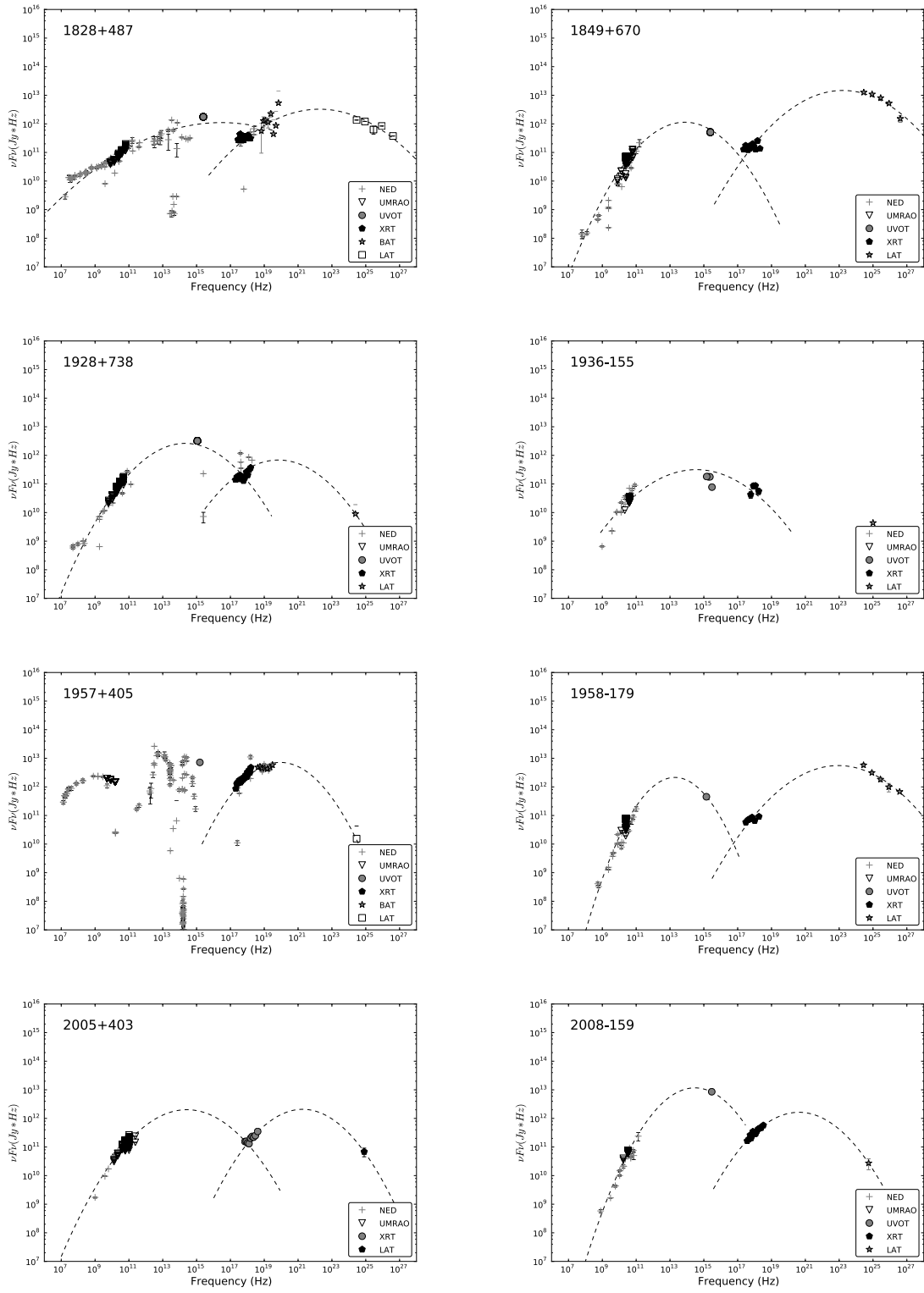


Figure B.14: The broadband SEDs of the MOJAVE sources.

B The Broadband SED of the MOJAVE Sample

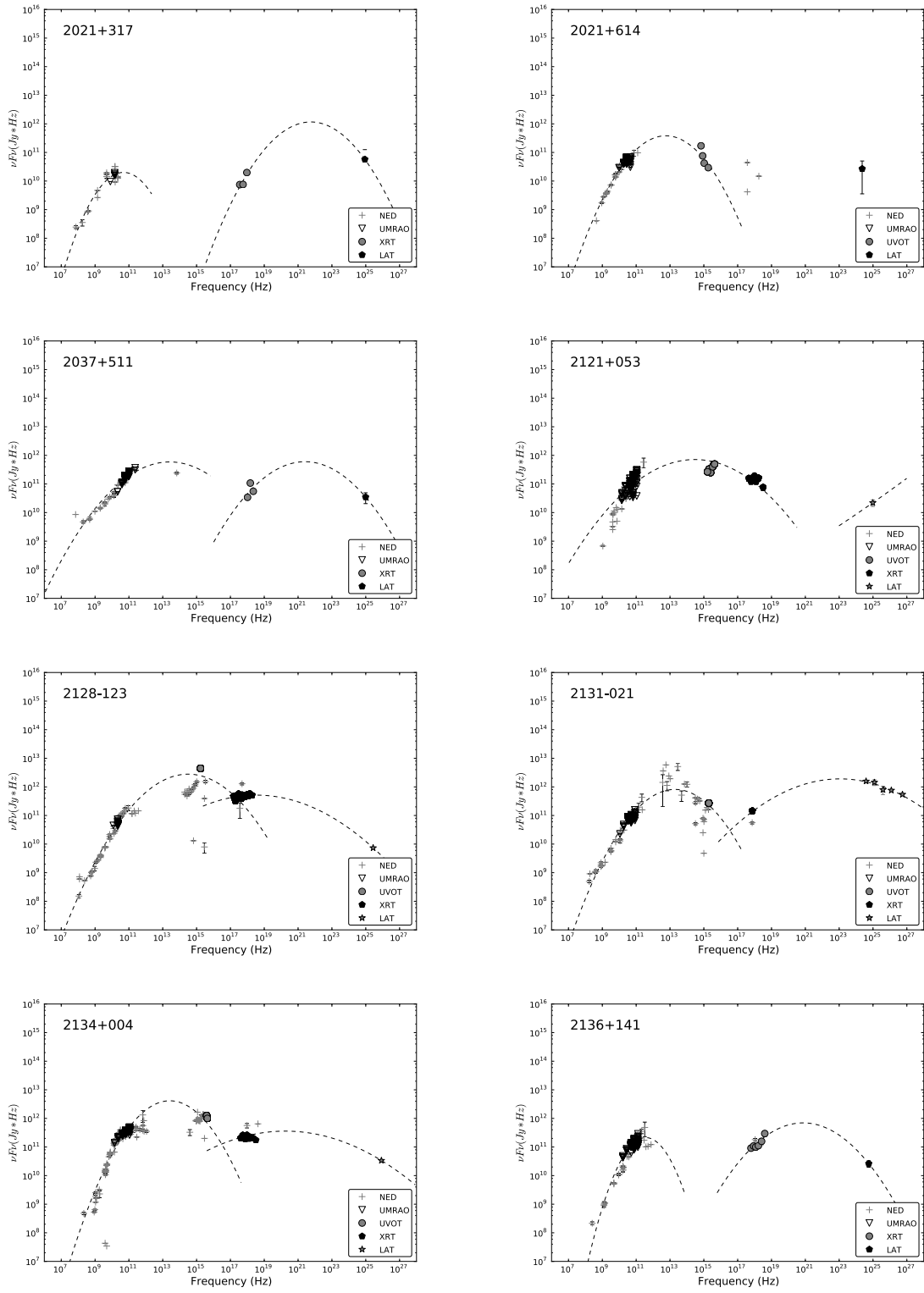


Figure B.15: The broadband SEDs of the MOJAVE sources.

B The Broadband SED of the MOJAVE Sample

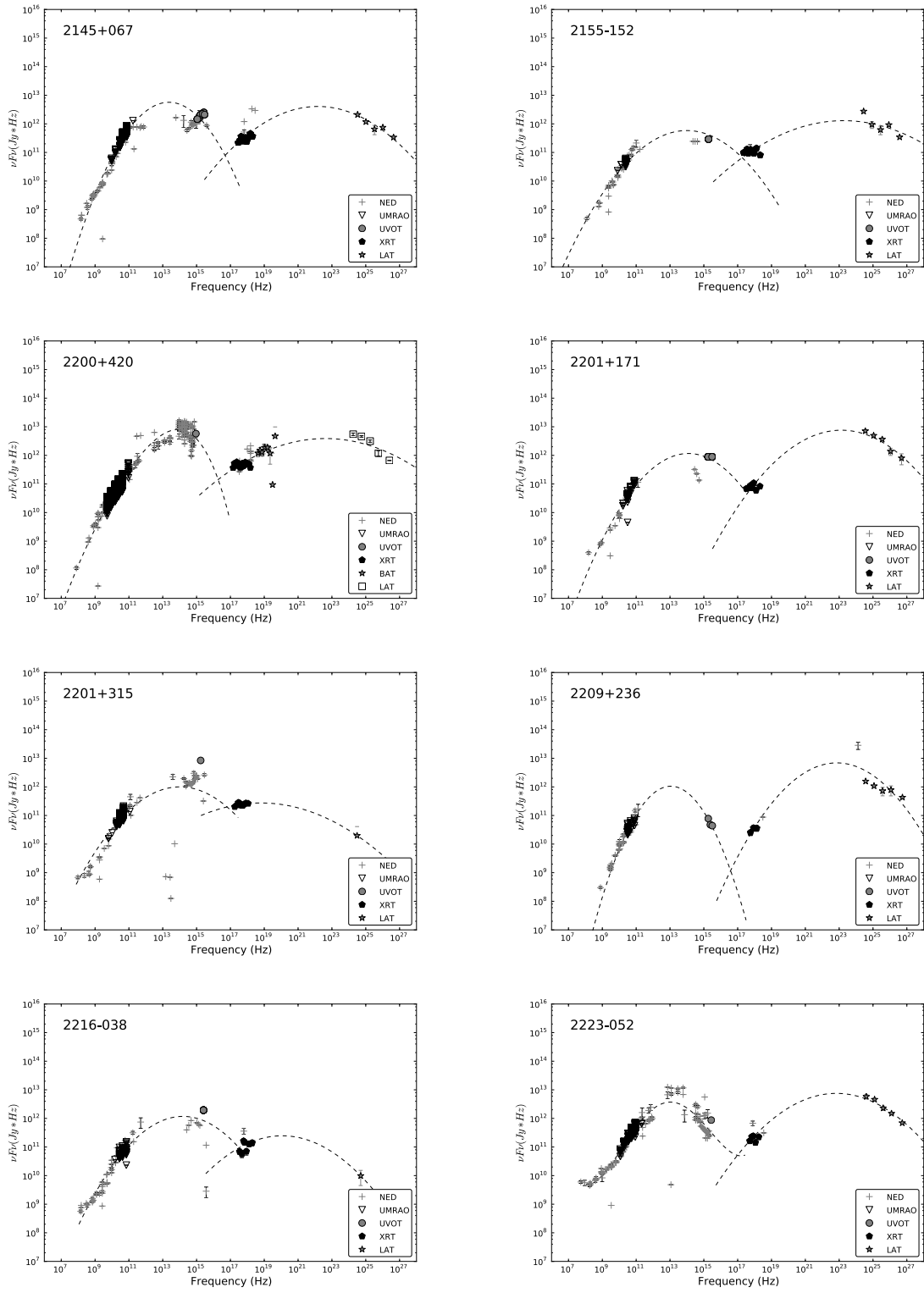


Figure B.16: The broadband SEDs of the MOJAVE sources.

B The Broadband SED of the MOJAVE Sample

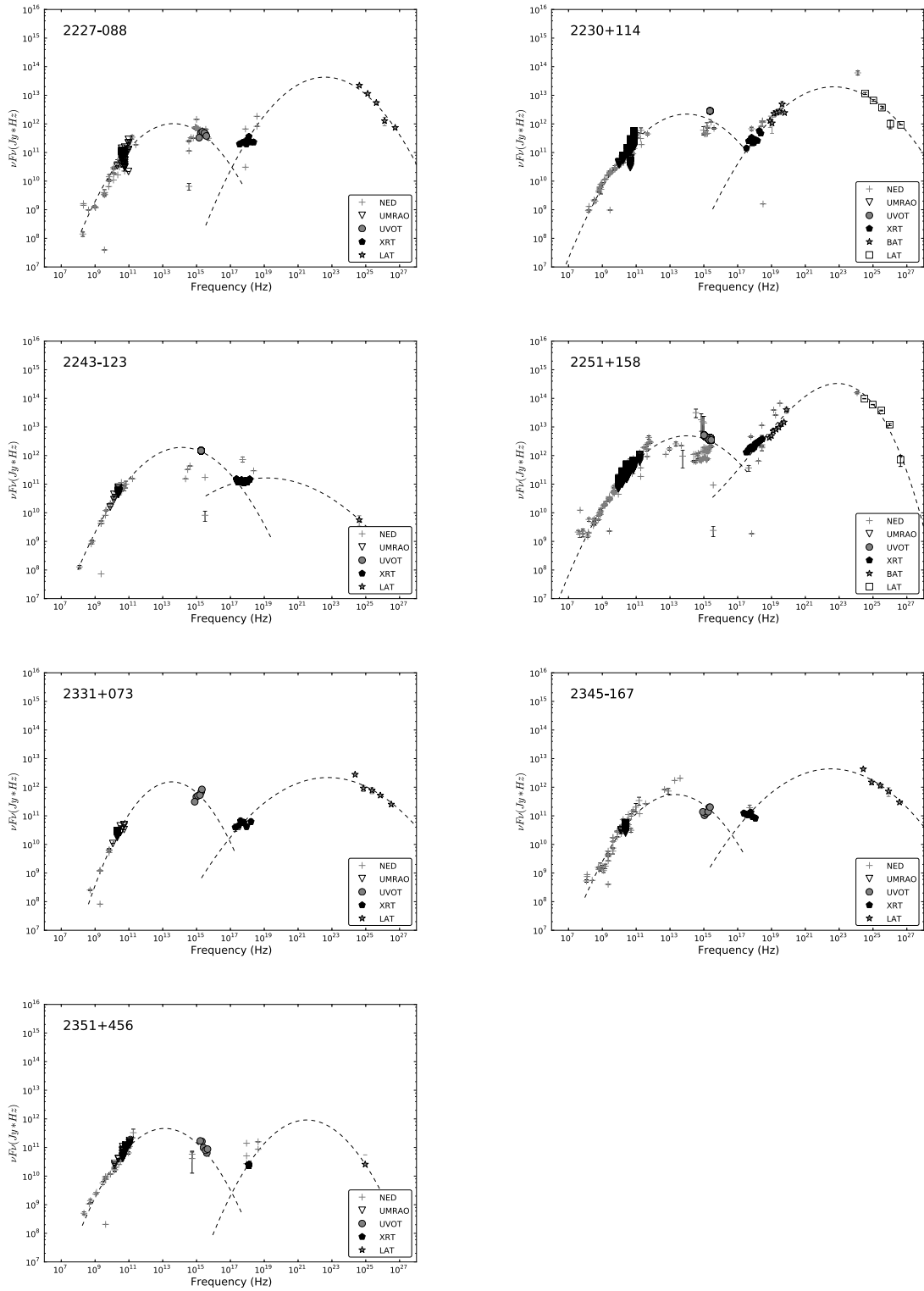


Figure B.17: The broadband SEDs of the MOJAVE sources.

C Previously Published Broadband SED of the MOJAVE Sources

In this Appendix, we collected the published spectrum and broadband SED related to our study of the MOJAVE sources. References, a detailed discussion, and the relationship to our findings can be found in Section 4.5. Our SED results are shown in Appendix B.

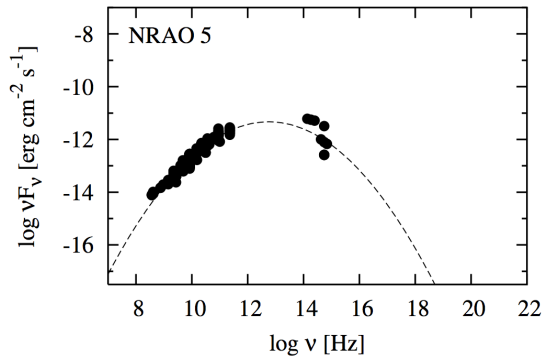


Figure C.1: The SED of 0003–066 at the synchrotron hump by Nieppola et al. (2006). The data are non-simultaneous, and were collected from databases and the literature. The dashed line denotes a parabolic fit to the synchrotron component of the SED.

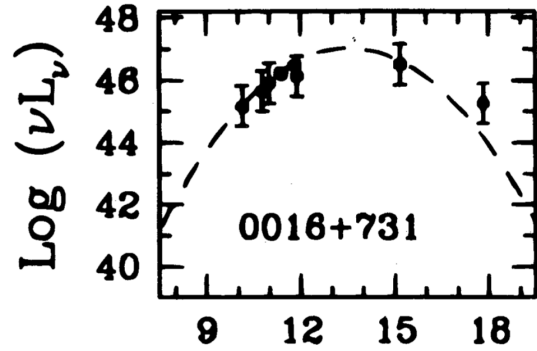


Figure C.2: The SED of 0016+731 of the synchrotron hump by Sambruna et al. (1996). The x-axis is the frequency in the unit of Hz.

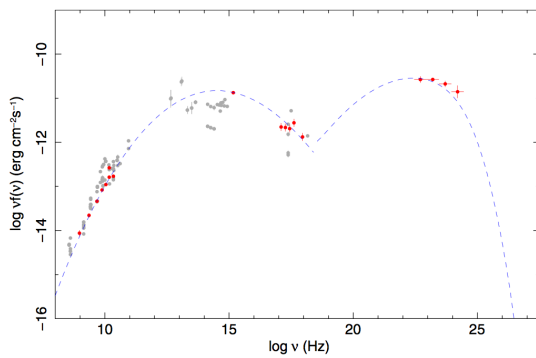


Figure C.3: The broadband SED of 0048–097 presented by Abdo et al. (2010a). The quasi-simultaneous data are represented as large filled red symbols, and the non-simultaneous archival measurements are shown as small open grey points. The dashed lines represent the best fit of a third degree polynomial to the quasi-simultaneous data.

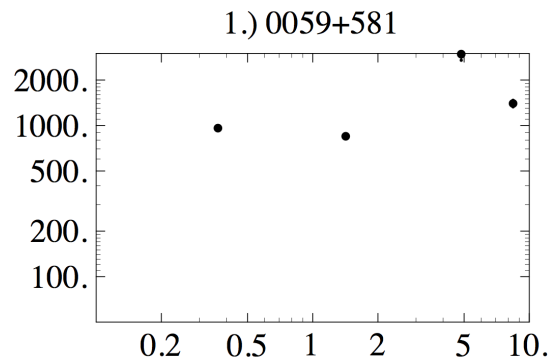


Figure C.4: The radio spectrum of the flat spectrum radio quasar 0059+581 (Marecki et al. 1999). The x-axis denotes frequency (GHz), and the y-axis is the flux density (mJy).

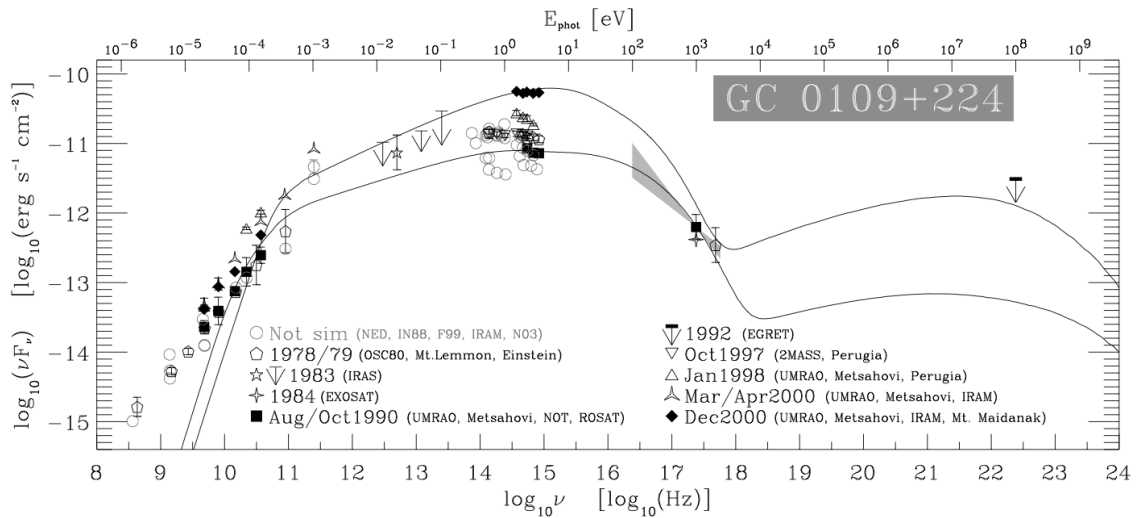


Figure C.5: The broadband SED of 0109+224 by Ciprini et al. (2004). The open and filled symbols are the multiwavelength data source (noted in the plot); the arrows denote upper limits; the bow-tie area is the slope obtained by *ROSAT*. The solid lines are the SSC fits to the SED at the flaring state in December 2000 and low state in 1990.

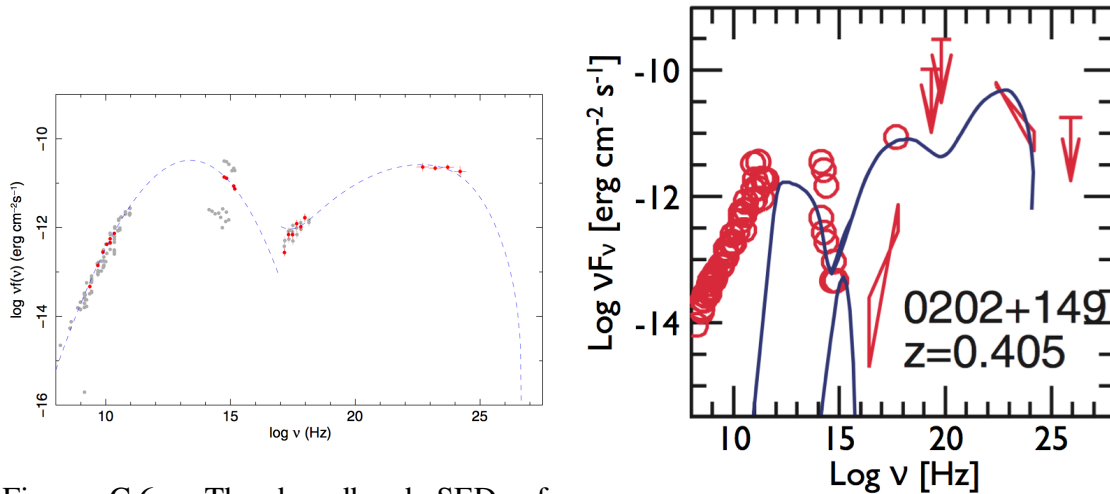


Figure C.6: The broadband SED of 0133+476 by Abdo et al. (2010a). The quasi-simultaneous data are represented as large filled red symbols, and the non-simultaneous archival measurements are shown as small open grey points. The dashed lines represent the best fit of a third degree polynomial to the quasi-simultaneous data.

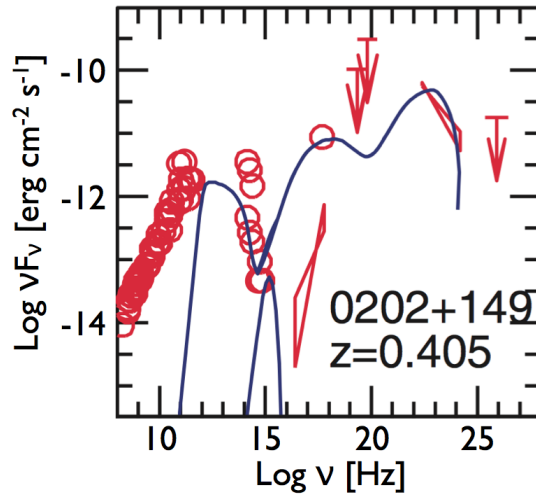


Figure C.7: The broadband SED of 0202+149 by Celotti and Ghisellini (2008). The model shown here was based on a one-zone leptonic synchrotron and IC mechanism, taking into account of the seed photons originated both in the jet and from external emission.

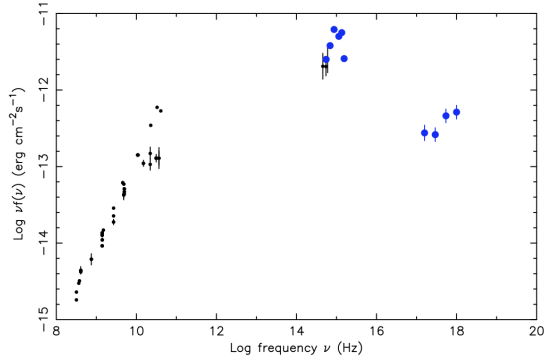


Figure C.8: The broadband SED of 0202+319 by Giommi et al. (2007). The blue points denote *Swift* UVOT and XRT observations obtained in June 2006.

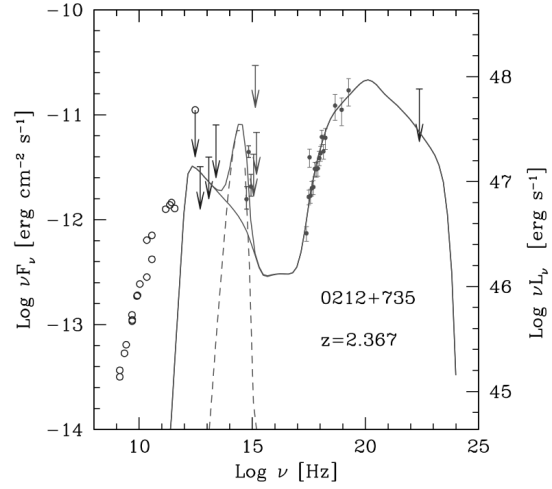


Figure C.9: The broadband SED of 0212+735 by Sambruna et al. (2007b). The filled circles denote *Swift* UVOT, XRT, and BAT 9-month data. The open circles represent archival data. The solid line represents the best fit with a synchrotron and IC model, and the dashed line represents the contribution of the disk.

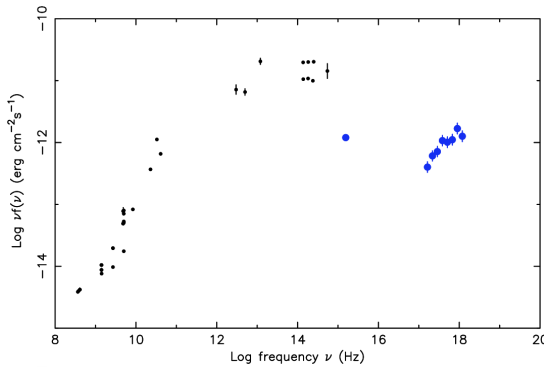


Figure C.10: The broadband SED of 0215+015 by Giommi et al. (2007). The blue filled circles denotes the *Swift* UVOT/XRT data observed in June 2005. No physical or mathematical model was fitted to the data.

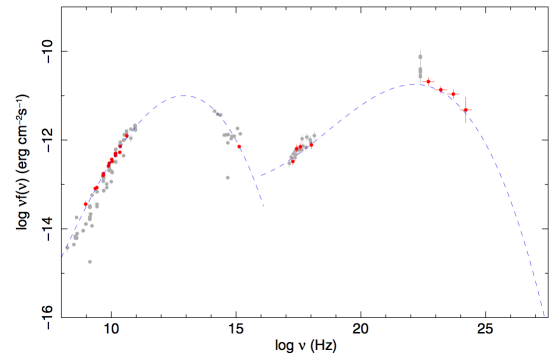


Figure C.11: The broadband SED of 0234+285 by Abdo et al. (2010a). The quasi-simultaneous data are represented as large filled red symbols, and the non-simultaneous archival measurements are shown as small open grey points. The dashed lines represent the best fit of a third degree polynomial to the quasi-simultaneous data.

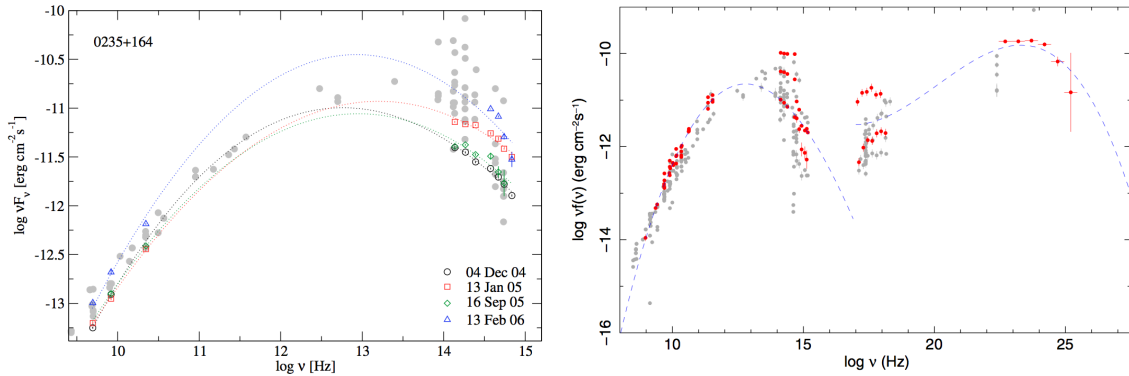


Figure C.12: The published broadband SED of 0235+164. Left: the SED variability study by Bach et al. (2007). Different colors of points denote different epochs of observation. Right: the SED study by Abdo et al. (2010a). The quasi-simultaneous data are represented as large filled red symbols, and the non-simultaneous archival measurements are shown as small open grey points. The dashed lines represent the best fit of a third degree polynomial to the quasi-simultaneous data.

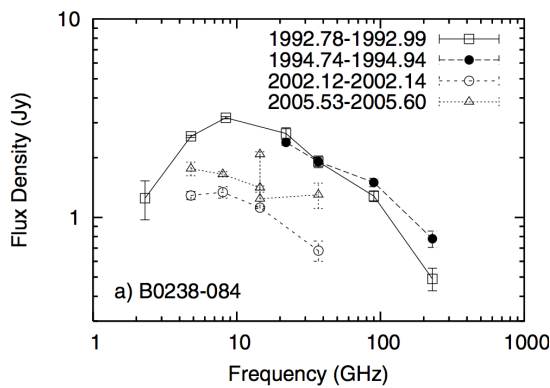


Figure C.13: Radio spectra of 0238-084 by Toriainen et al. (2007).

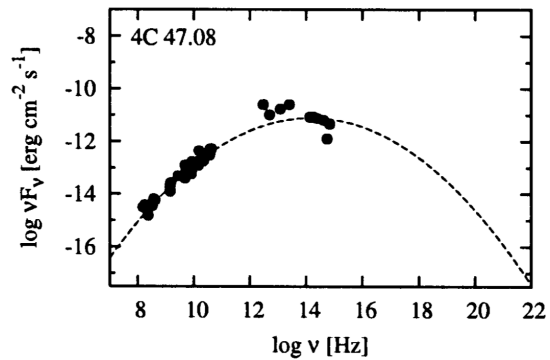


Figure C.14: The simultaneous broadband SED of 0300+470 by Nieppola et al. (2006). The data are non-simultaneous, and were collected from databases and the literature. The dashed line denotes the parabolic fit to the synchrotron component of the SED.

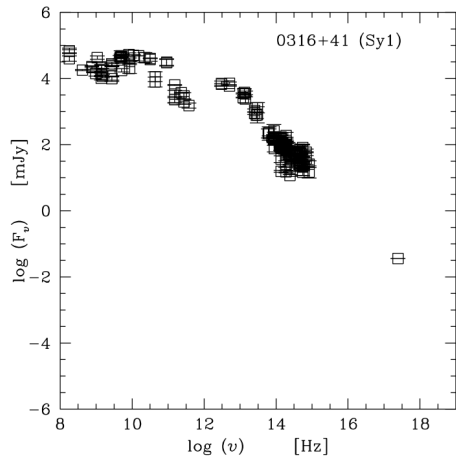


Figure C.15: The synchrotron part of the broadband spectrum of 0316+413 by Ant3n et al. (2004)

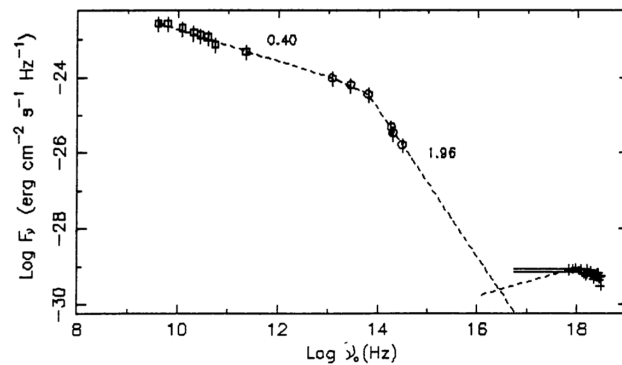


Figure C.16: The radio to X-ray spectrum of 0333+321 by Ghosh and Soundararajaperumal (1995). The X-ray data ($\sim 10^{18}$ GHz) were obtained by *EXOSAT* in January 1985, and the other points denote archival data. The numbers denote the two-point spectral indices derived from the dashed line.

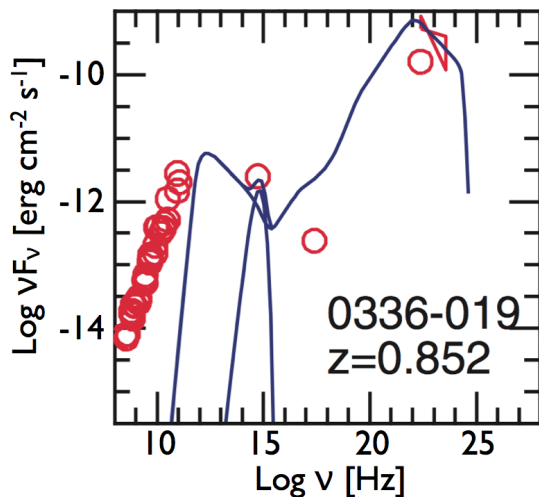


Figure C.17: The broadband SED of 0336-019 (Celotti and Ghisellini 2008). The model shown here was based on an one-zone leptonic synchrotron and the IC mechanism, taking into account the seed photons originated both in the jet and from external emission.

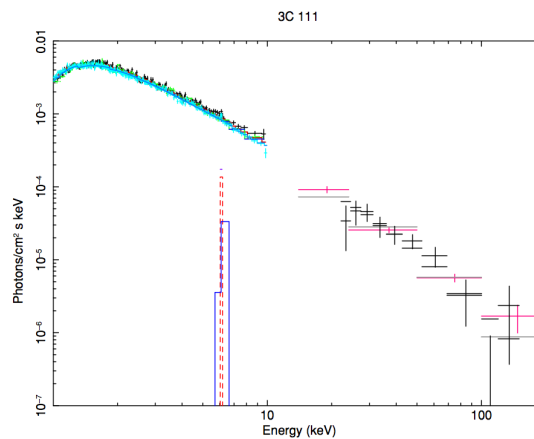


Figure C.18: The hard X-ray spectrum of 0415+379 obtained by *INTEGRAL* (Molina et al. 2008). The model is a cut-off power law absorbed by Galactic and intrinsic N_{H} column density, reflected by neutral material plus a narrow Gaussian component of the iron line.

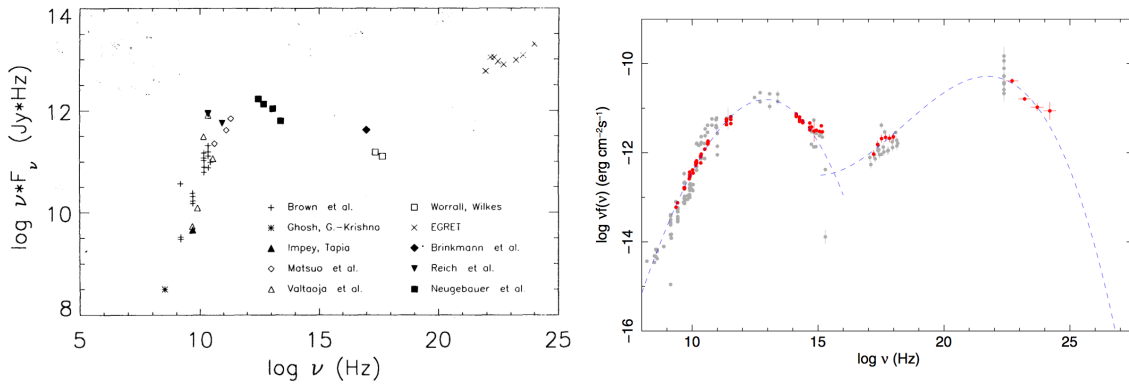


Figure C.19: The published broadband SED of 0420–014. Left: the archival SED collected by Radecke et al. (1995). Right: the SED study by Abdo et al. (2010a). The quasi-simultaneous data are represented as large filled red symbols, and the non-simultaneous archival measurements are shown as small open grey points. The dashed lines represent the best fit of a third degree polynomial to the quasi-simultaneous data.

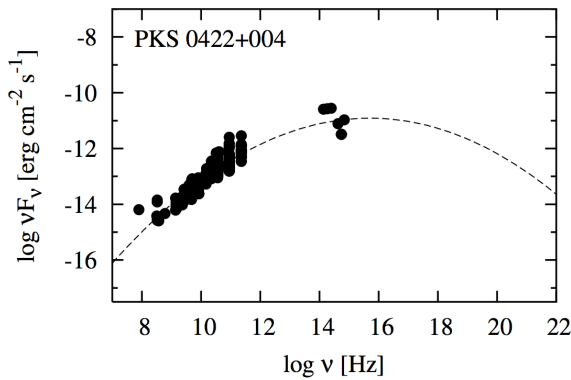


Figure C.20: The synchrotron hump of the SED on 0422+004 (Nieppola et al. 2006). The data are non-simultaneous, and were collected from databases and the literature. The dashed line denotes the parabolic fit to the synchrotron component of the SED.

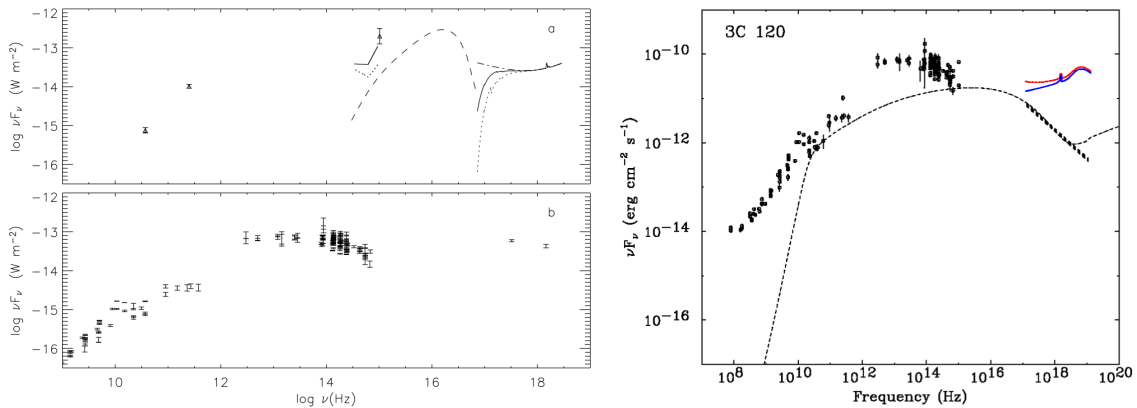


Figure C.21: The published broadband SED of 0430+052. Left: the SED constructed by Ogle et al. (2005). Panel a displays the observation of *XMM-NEWTON* in August 2003, and panel b shows the flux points from the NED from 1967 to 2003. Right: the SED study by Kataoka et al. (2007). The X-ray data were observed by *Suzaku* in March 2006, and the other data are taken from the NED. The dashed line is the SED fit of an one-zone homogeneous SSC model.

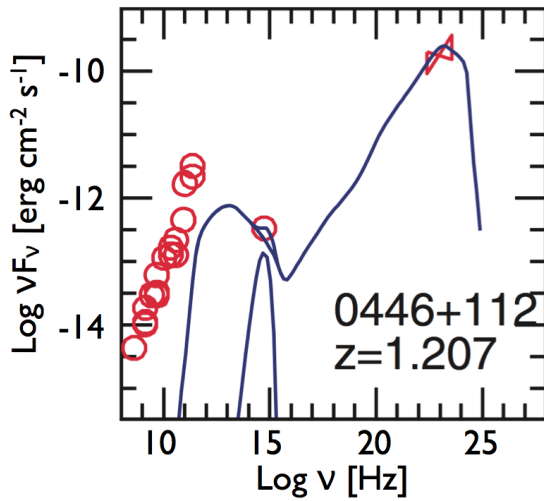


Figure C.22: The SED of 0446+112 by Celotti and Ghisellini (2008). The model shown here was based on an one-zone leptonic synchrotron and IC mechanism, taking into account of the seed photons originated both in the jet and from external emission.

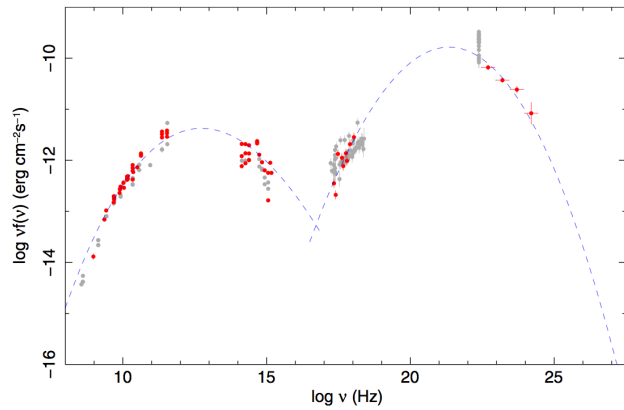
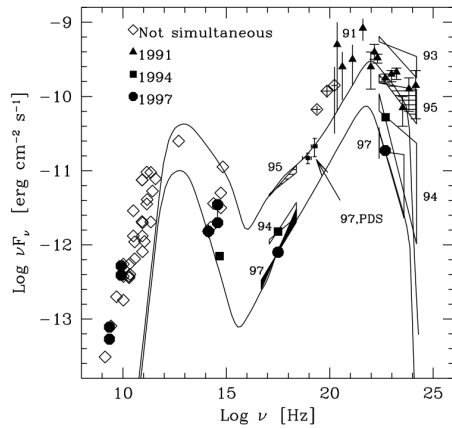
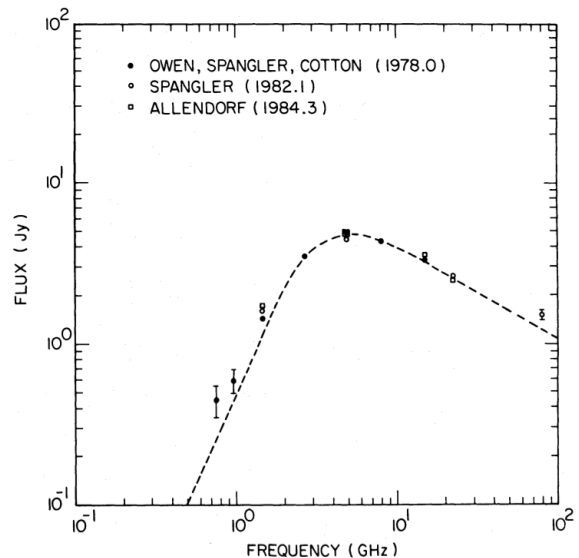


Figure C.23: The published broadband SED of PKS 0528+134. Left: the SED constructed by Ghisellini et al. (1999). Simultaneous observations are indicated by different marks as labeled, and the solid lines are best fits to the 1995 and the 1997 spectra of a homogeneous one-zone model. Right: the SED study by Abdo et al. (2010a). The quasi-simultaneous data are represented as large filled red symbols, and the non-simultaneous archival measurements are shown as small open grey points. The dashed lines represent the best fit of a third degree polynomial to the quasi-simultaneous data.

Figure C.24: The radio spectrum of 0552+398 (Fey et al. 1985).



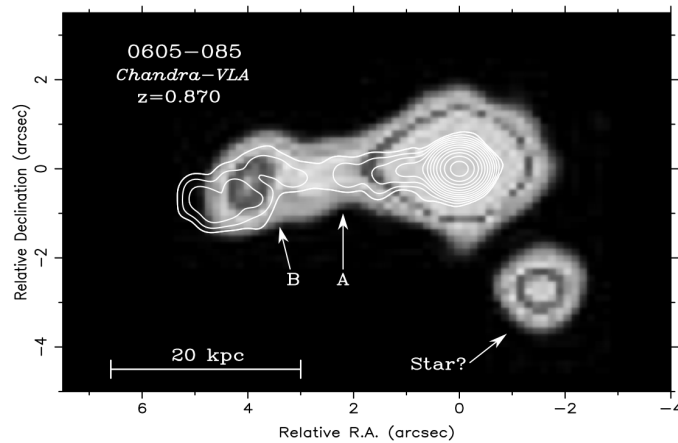


Figure C.25: The radio and X-ray overlaid image of 0605–085 by Sambruna et al. (2004). The white contour is the VLA 5 GHz observation, and the grey-scale represents the *Chandra* image in the 0.5–8 keV energy range.

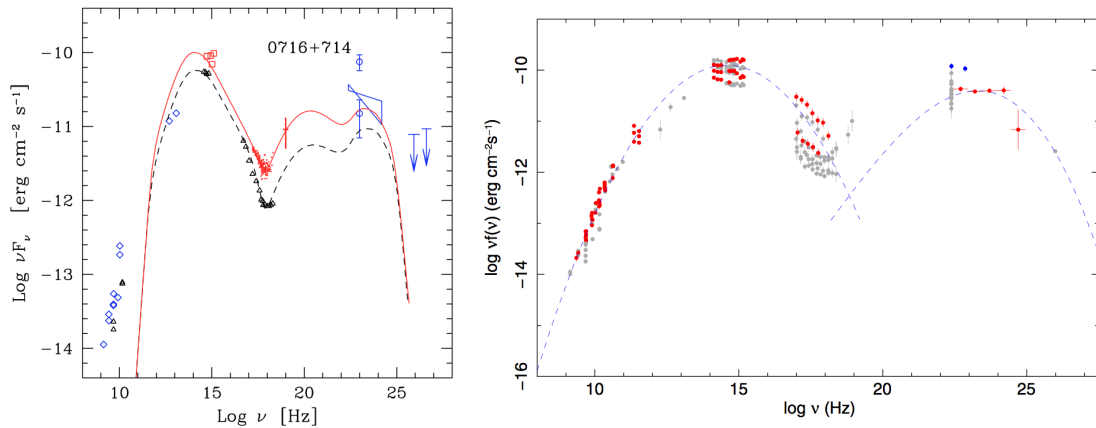


Figure C.26: Selected published broadband SED of 0716+714. Left: the SED constructed by Foschini et al. (2006a). The cross, points, and open squares represent simultaneous *INTEGRAL* data (Pian et al. 2005), *XMM-Newton* EPIC and OM data. The triangles represent the radio to the X-ray observations in 1996 (Giommi et al. 1999). Right: the SED study by Abdo et al. (2010a). The quasi-simultaneous data are represented as large filled red symbols, and the non-simultaneous archival measurements are shown as small open grey points. The dashed lines represent the best fit of a third degree polynomial to the quasi-simultaneous data.

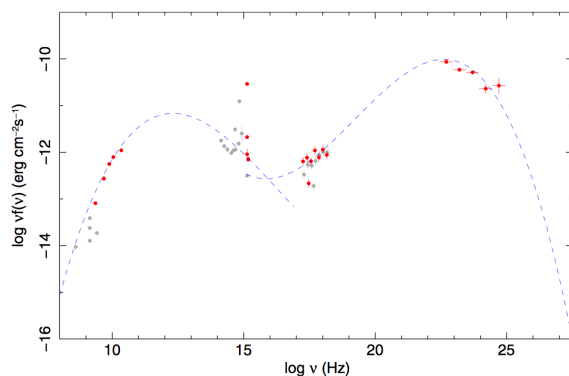


Figure C.27: The broadband SED of 0727–115 published by Abdo et al. (2010a). The quasi-simultaneous data are represented as large filled red symbols, and the non-simultaneous archival measurements are shown as small open grey points. The dashed lines represent the best fit of a third degree polynomial to the quasi-simultaneous data.

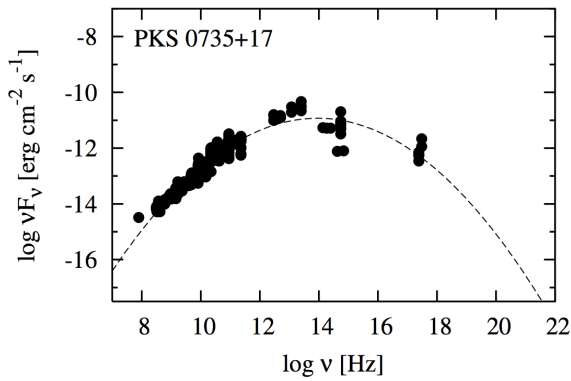


Figure C.28: The broadband SED of 0735+178 published by Nieppola et al. (2006). The data are non-simultaneous, and were collected from databases and the literature. The dashed line denotes the parabolic fit to the synchrotron component of the SED.

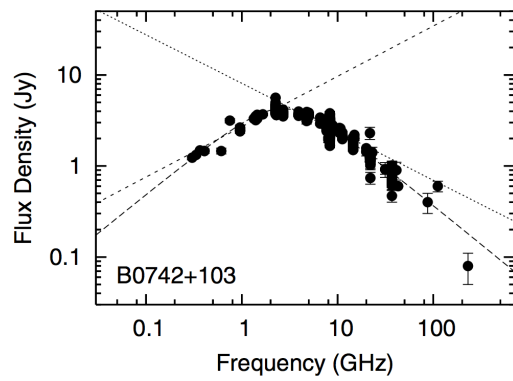


Figure C.29: The SED in the radio band of 0742+103 presented by Torniiainen et al. (2005). The dashed lines represent the linear fit performed to derive different spectral indices separated by the turn-over frequency.

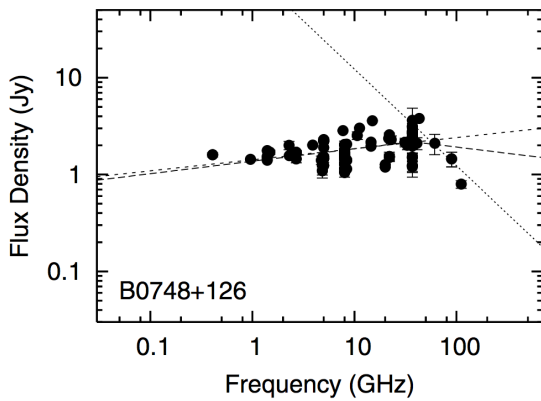


Figure C.30: The SED in the radio band of 0748+126 presented by Torniiainen et al. (2005). The dashed lines represent the linear fit performed to derive different spectral indices separated by the turn-over frequency, which is 37 GHz in this case.

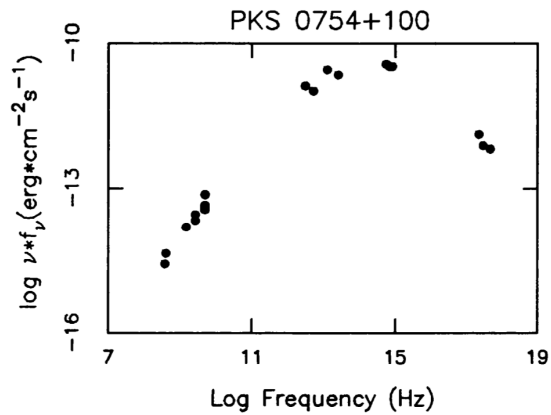
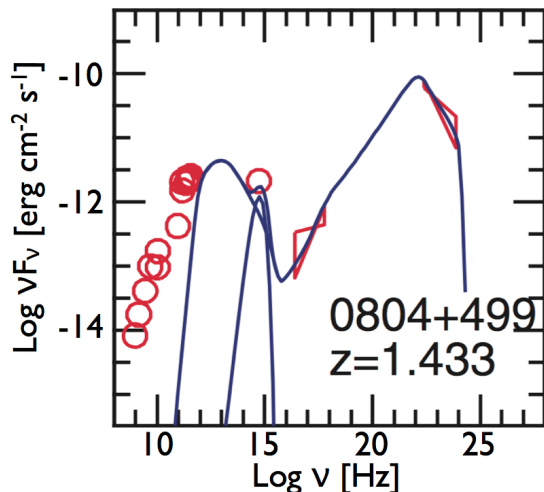


Figure C.31: The synchrotron hump of the broadband SED of 0754+100 presented by Giommi et al. (1995). The data presented are taken from non-simultaneous archival data.

Figure C.32: The broadband SED of 0804+499 presented by Celotti and Ghisellini (2008). The model shown here was based on an one-zone leptonic synchrotron and IC mechanism, taking into account of the seed photons originated both in the jet and from external emission.



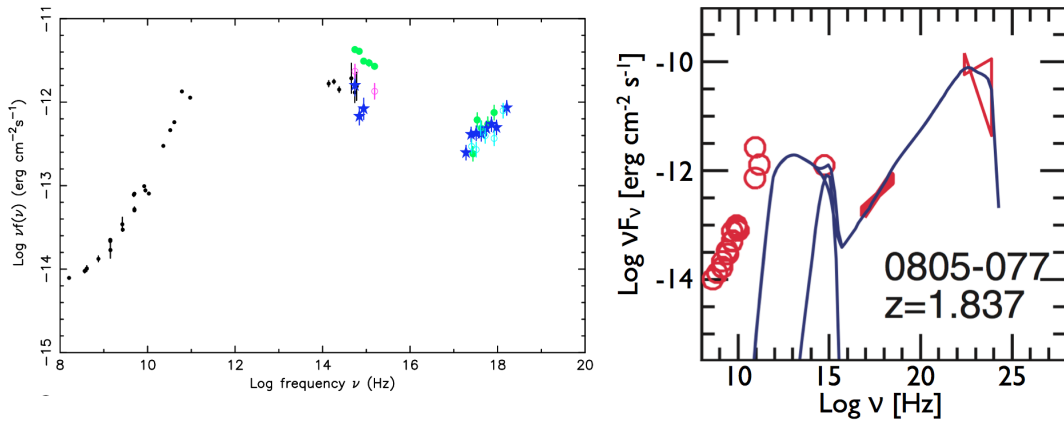


Figure C.33: The published broadband SEDs of 0805–077. Left: the SED constructed by Giommi et al. (2007). The *Swift* data taken at different dates are shown as filled stars (22 May 2005), open circles (4 June 2005), and filled circles (25 September/October 1, 2005). Right: the SED study by Celotti and Ghisellini (2008). The model shown here was based on an one-zone leptonic synchrotron and IC mechanism, taking into account of the seed photons originated both in the jet and from external emission.

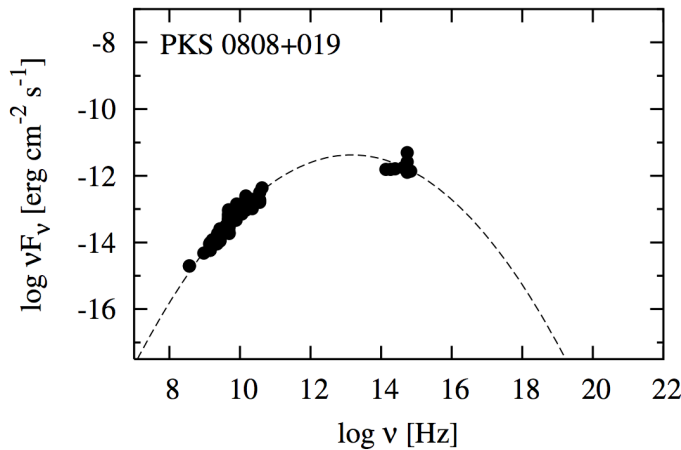


Figure C.34: The synchrotron hump of the broadband SED of 0808+019 by Nieppola et al. (2006). The data are non-simultaneous, and were collected from databases and the literature. The dashed line denotes the parabolic fit to the synchrotron component of the SED.

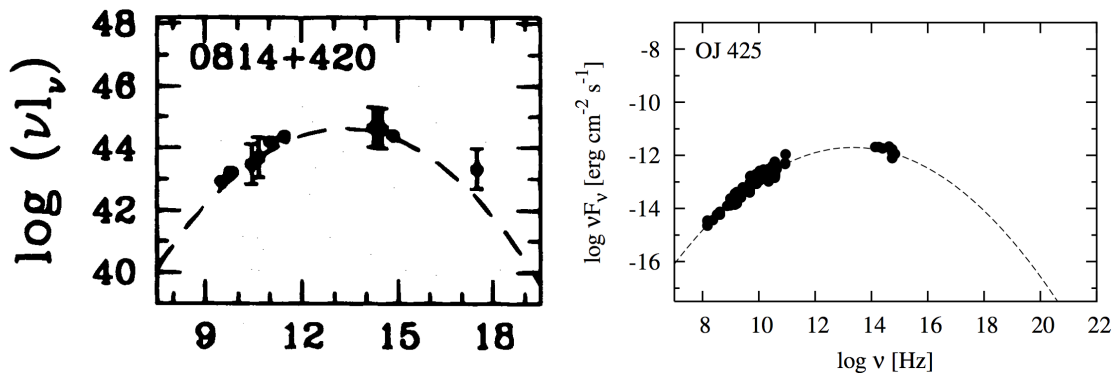


Figure C.35: The published synchrotron part of the broadband SEDs on 0814+425. Left: the SED constructed by Sambruna et al. (1996). The dashed line denotes the parabolic fit to the synchrotron component of the SED. Right: the SED study by Nieppola et al. (2006). The data are non-simultaneous, and were collected from databases and the literature. The dashed line denotes the parabolic fit to the synchrotron component of the SED.

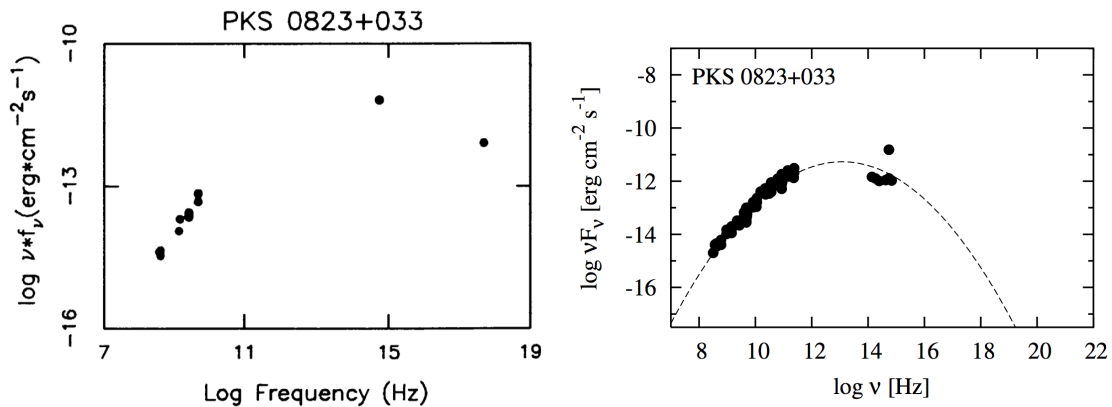


Figure C.36: The published synchrotron part of the broadband SEDs on 0823+033. Left: the SED constructed by Giommi et al. (1995). The data were compiled from non-simultaneous archival data. Right: the SED study by Nieppola et al. (2006). The data are non-simultaneous, and were collected from databases and the literature. The dashed line denotes the parabolic fit to the synchrotron component of the SED.

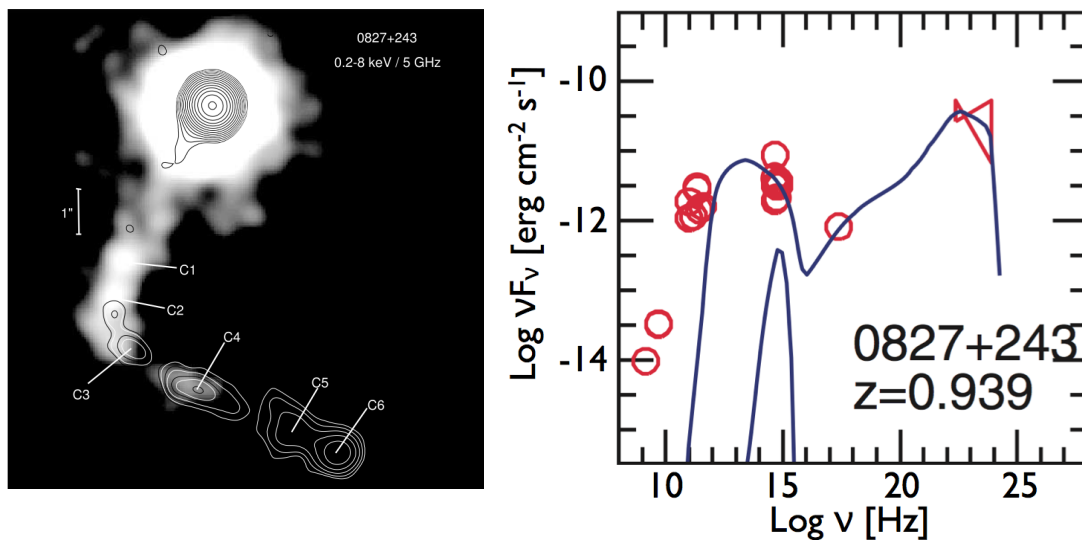


Figure C.37: Left: the radio (contours, VLA image at 4.9 GHz) and X-ray (gray scale, *Chandra* image at 0.2–8 keV) overlaid image of 0827+243 by Jorstad and Marscher (2004). The images are convolved with the same Gaussian beam of FWHM 0.5'' \times 0.5''. Right: the broadband SED of 0827+243 by Celotti and Ghisellini (2008). The model shown here was based on an one-zone leptonic synchrotron and IC mechanism, taking into account of the seed photons originated both in the jet and from external emission.

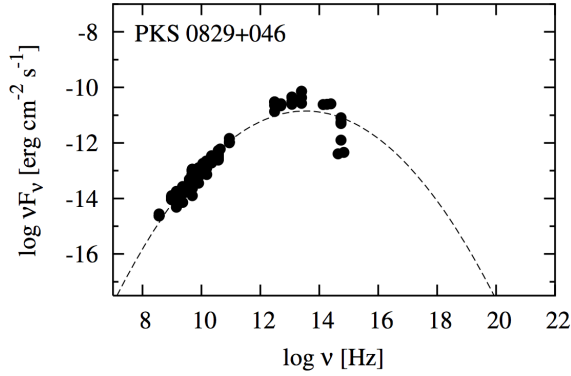


Figure C.38: The broadband SED of 0829+046 by Nieppola et al. (2006). The data are non-simultaneous, and were collected from databases and the literature. The dashed line denotes the parabolic fit to the synchrotron component of the SED.

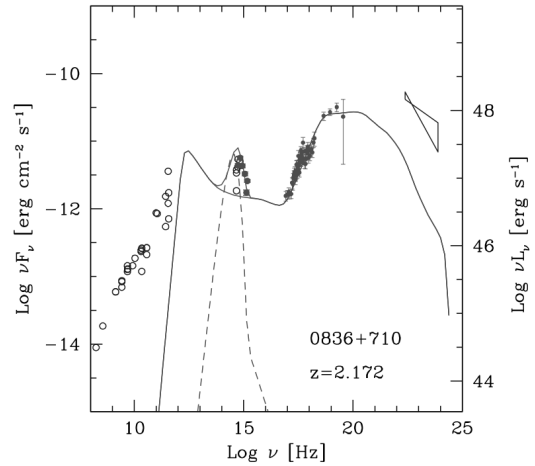


Figure C.39: The broadband SED of 0836+710 by Sambruna et al. (2007b). The filled circles denote *Swift* UVOT, XRT, and BAT 9-month data. The open circles represent archival data. The solid line represents the best fit with a synchrotron and IC model, and the dashed line represents the contribution of the disk.

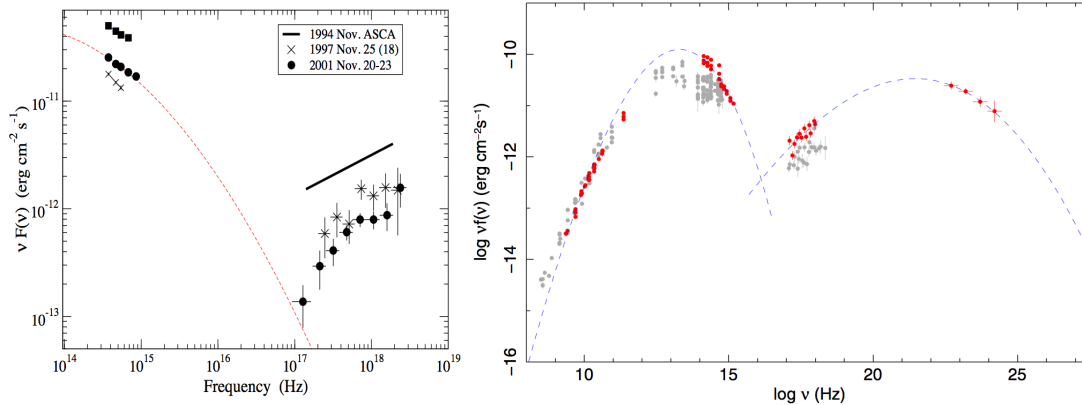


Figure C.40: The published broadband SED of 0851+202. Left: the SED in the optical and the X-ray band (*BeppoSAX* observations in 1997 and 2001; *ASCA* observations in 1994 and 1997) by Massaro et al. (2003). Right: the broadband SED by Abdo et al. (2010a). The quasi-simultaneous data are represented as large filled red symbols, and the non-simultaneous archival measurements are shown as small open grey points. The dashed lines represent the best fits of third degree polynomials to the quasi-simultaneous data.

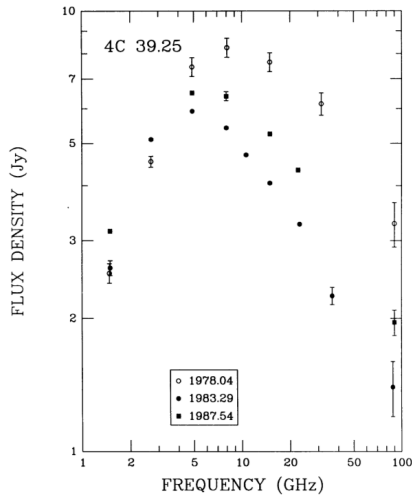


Figure C.41: The radio spectrum of 0923+392 (Marscher et al. 1991).

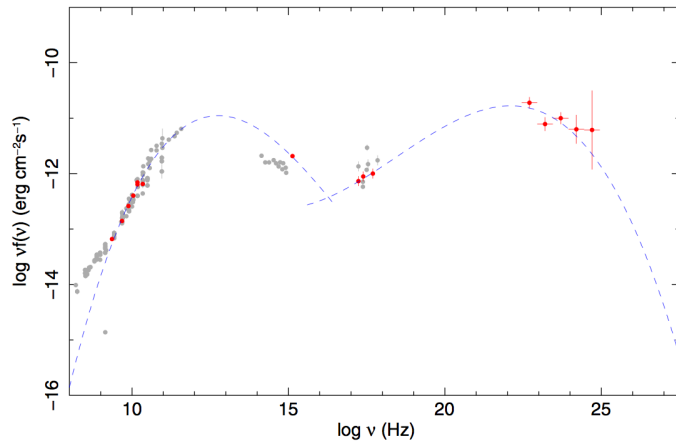


Figure C.42: The broadband SED of 1055+018 (Abdo et al. 2010a). The quasi-simultaneous data are represented as large filled red symbols, and the non-simultaneous archival measurements are shown as small open grey points. The dashed lines represent the best fit of a third degree polynomial to the quasi-simultaneous data.

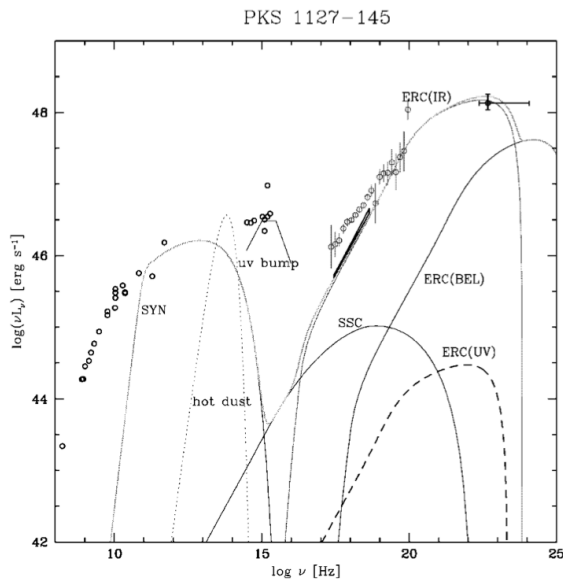


Figure C.43: The broadband SED of 1127-145 (Błażejowski et al. 2004). The curves are the applied model components: SYN - synchrotron radiation, SSC - SSC radiation, ERC - external radiation Compton emission.

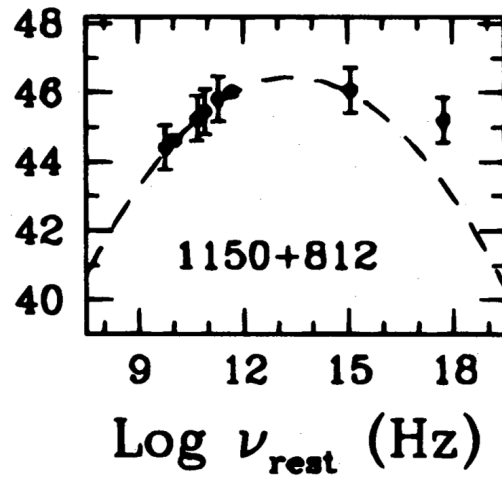


Figure C.44: The broadband SED of 1150+812 (Sambruna et al. 1996).

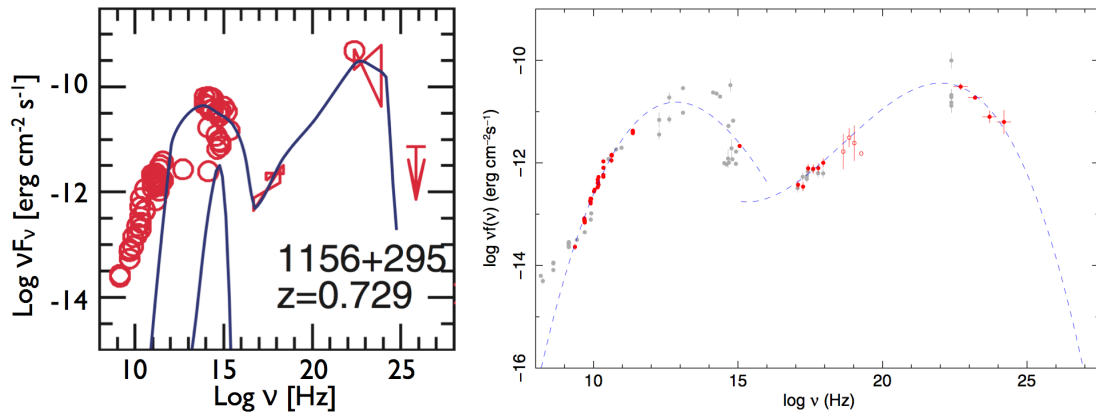


Figure C.45: Left: The broadband SED of 1156+295 by Celotti and Ghisellini (2008). The model shown here was based on an one-zone leptonic synchrotron and IC mechanism, taking into account of the seed photons originated both in the jet and from external emission. Right: The broadband SED of 1156+295 by Abdo et al. (2010a). The quasi-simultaneous data are represented as large filled red symbols, and the non-simultaneous archival measurements are shown as small open grey points. The dashed lines represent the best fits of third degree polynomials to the quasi-simultaneous data.

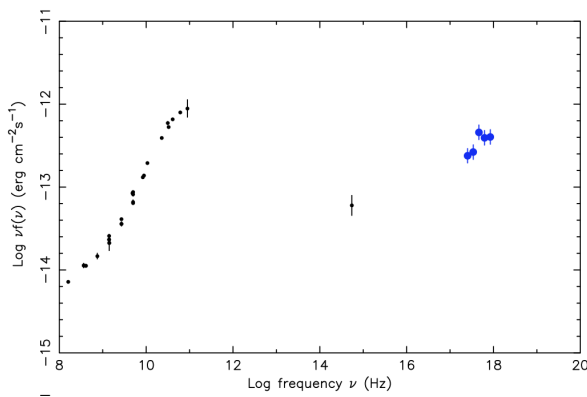


Figure C.46: The broadband SED of 1213-172 by Giommi et al. (2007). The blue points denote the *Swift*/XRT data obtained on 17 December 2005, and the black points are archival data.

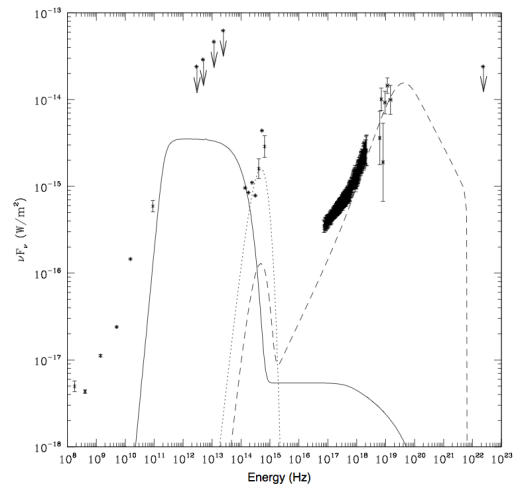


Figure C.47: The broadband SED of 1219+044 by de Rosa et al. (2008). The data in the X-ray band were obtained by *XMM-Newton* and *INTEGRAL*, and the other data were taken from the NED archive.

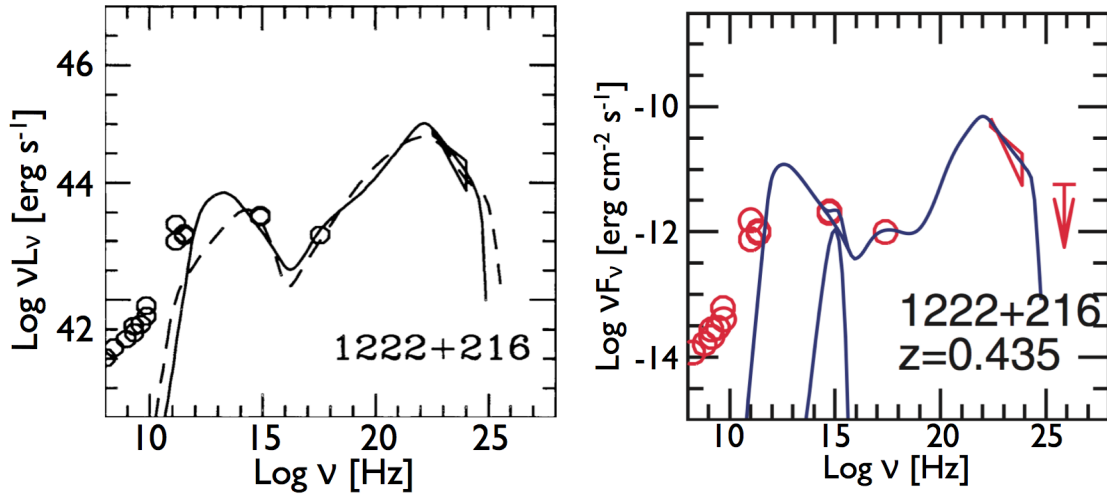


Figure C.48: The broadband SED of 1222+216 published by Ghisellini et al. (1998) and Celotti and Ghisellini (2008).

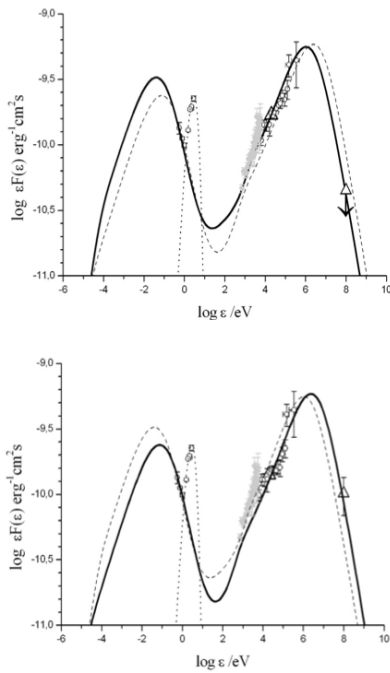


Figure C.49: The simultaneous broadband SED of 1226+023 (3C 273) published by Pacciani et al. (2009). These are the results from the *AGILE* multiwavelength campaign spanning for 3 weeks in December 2007–January 2008. Upper panel: SED for the first week. Lower panel: SED for the second week. Triangles denote *AGILE* data, gray symbols refer to the XRT observations performed in the third week. The model is composed of an one-zone SSC and an external IC from the accretion disk.

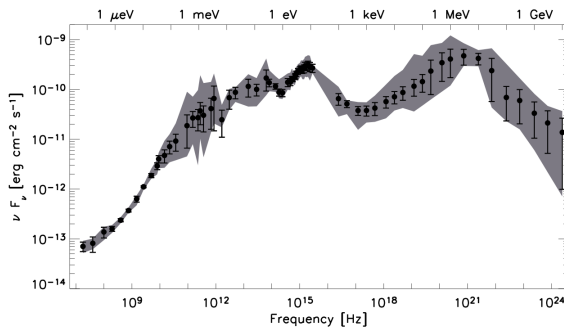


Figure C.50: The average broadband SED of 1226+023 (3C 273) spanning from 4 to 44 years of observations (Soldi et al. 2008). The grey area represents the observed range of variations.

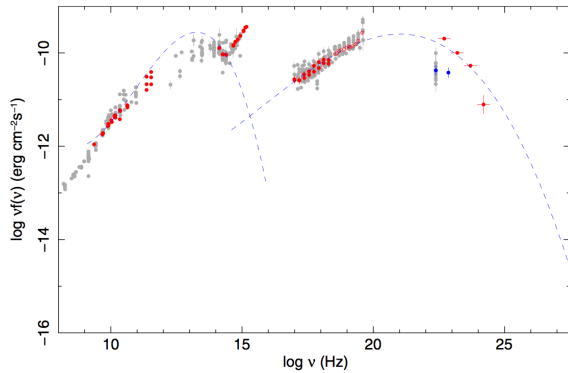


Figure C.51: The broadband SED of 1226+023 (3C 273) published by the *Fermi*/LAT team (Abdo et al. 2010a). The quasi-simultaneous data are represented as large filled red symbols, and the non-simultaneous archival measurements are shown as small open grey points. The dashed lines represent the best fit of a third degree polynomial to the quasi-simultaneous data.

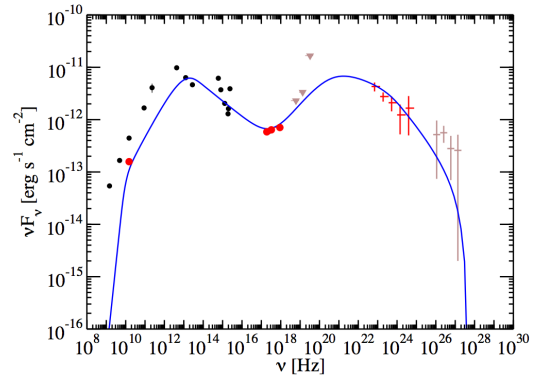


Figure C.52: The broadband SED of 1228+126 (M 87) published by the *Fermi*/LAT team (Abdo et al. 2009c). The simultaneous observations on 7 January 2009 are marked in red, the non-simultaneous data are marked in light brown, and historical measurements are marked in black. The blue curve represents the one-zone SSC emission model.

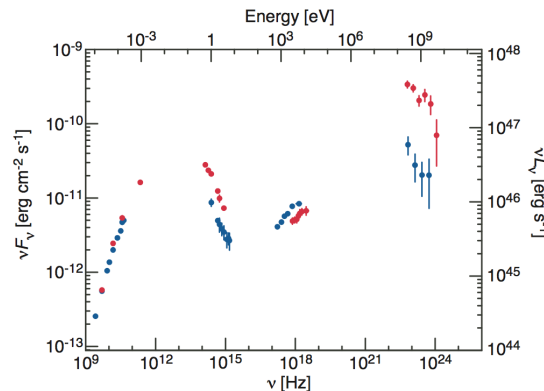
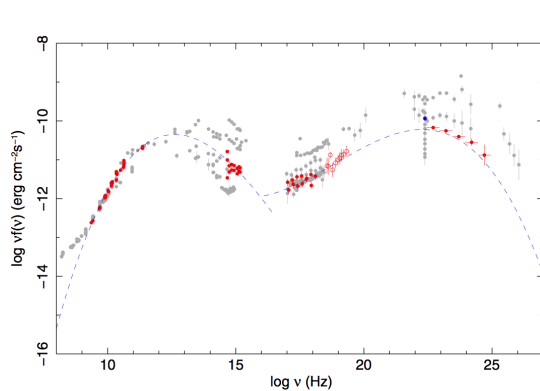


Figure C.53: Selected broadband SED of 1253–055 (3C 279). Left: The broadband SED presented by Abdo et al. (2010a). The quasi-simultaneous data are represented as large filled red symbols, and the non-simultaneous archival measurements are shown as small open grey points. The dashed lines represent the best fit of a third degree polynomial to the quasi-simultaneous data. Right: The broadband SED at two different epochs presented by Fermi-Lat Collaboration et al. (2010). The red points denote the epoch obtained during a sharp γ -ray flare, and the blue points denote the epoch obtained around an isolated X-ray flare.

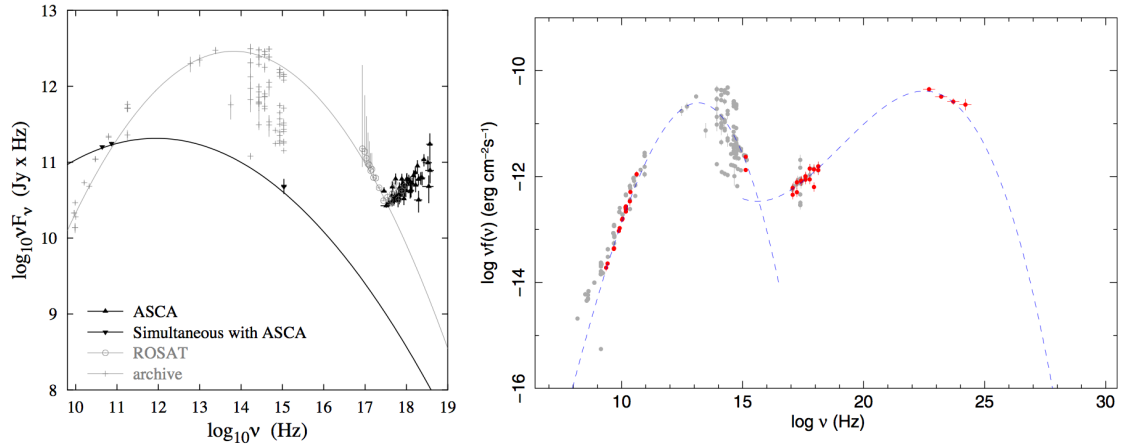


Figure C.54: The published broadband SED of 1308+326. Left: The broadband SED presented by Watson et al. (2000). Right: The broadband SED presented by Abdo et al. (2010a). The quasi-simultaneous data are represented as large filled red symbols, and the non-simultaneous archival measurements are shown as small open grey points. The dashed lines represent the best fit of a third degree polynomial to the quasi-simultaneous data.

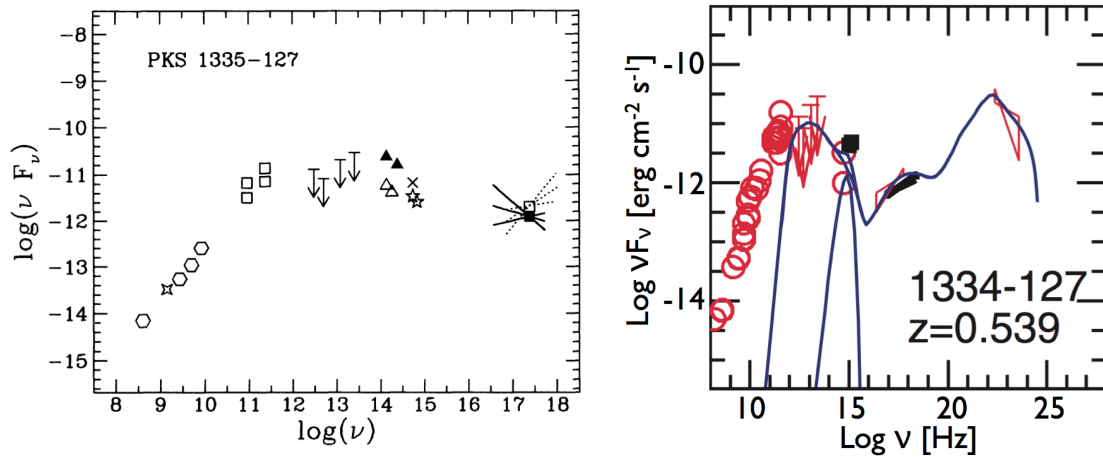


Figure C.55: The published broadband SED of 1334-127. Left: The non-simultaneous broadband SED presented by Maraschi et al. (1995). Right: The broadband SED presented by Celotti and Ghisellini (2008). The model shown here was based on an one-zone leptonic synchrotron and IC mechanism, taking into account of the seed photons originated both in the jet and from external emission.

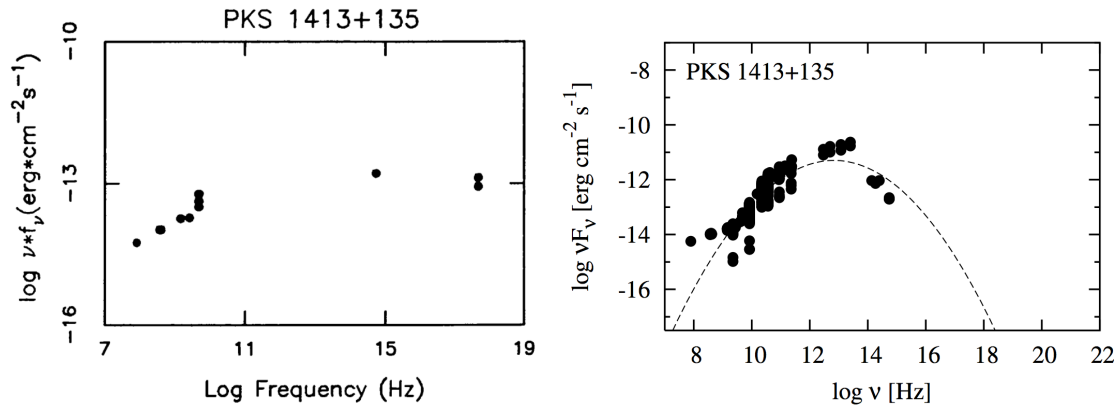


Figure C.56: The synchrotron hump of the broadband SED of 1413+135. Left: The broadband SED presented by Giommi et al. (1995). The data were from non-simultaneous archival data. Right: The broadband SED presented by Nieppola et al. (2006). The data are non-simultaneous, and were collected from databases and the literature. The dashed line denotes the parabolic fit to the synchrotron component of the SED.

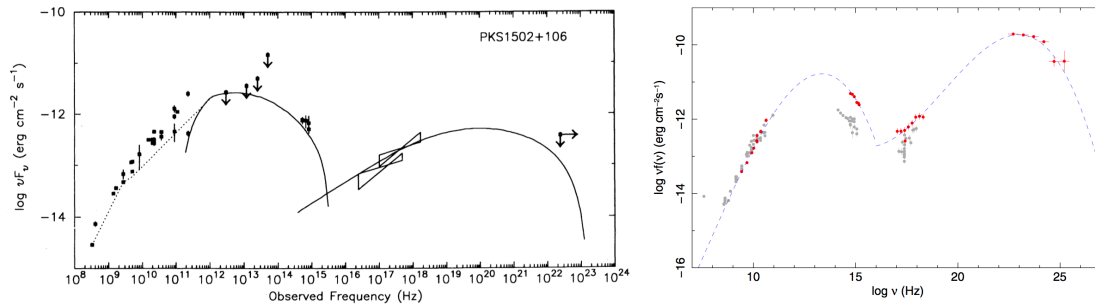


Figure C.57: The broadband SED of 1502+106. Left: The broadband SED presented by George et al. (1994); the X-ray spectra were obtained by *ROSAT* and *ASCA*, and the data of other bands were compiled from the literature. The SED model is an inhomogeneous SSC jet model. Right: The broadband SED presented by Abdo et al. (2010a). The quasi-simultaneous data are represented as large filled red symbols, and the non-simultaneous archival measurements are shown as small open grey points. The dashed lines represent the best fit of a third degree polynomial to the quasi-simultaneous data.

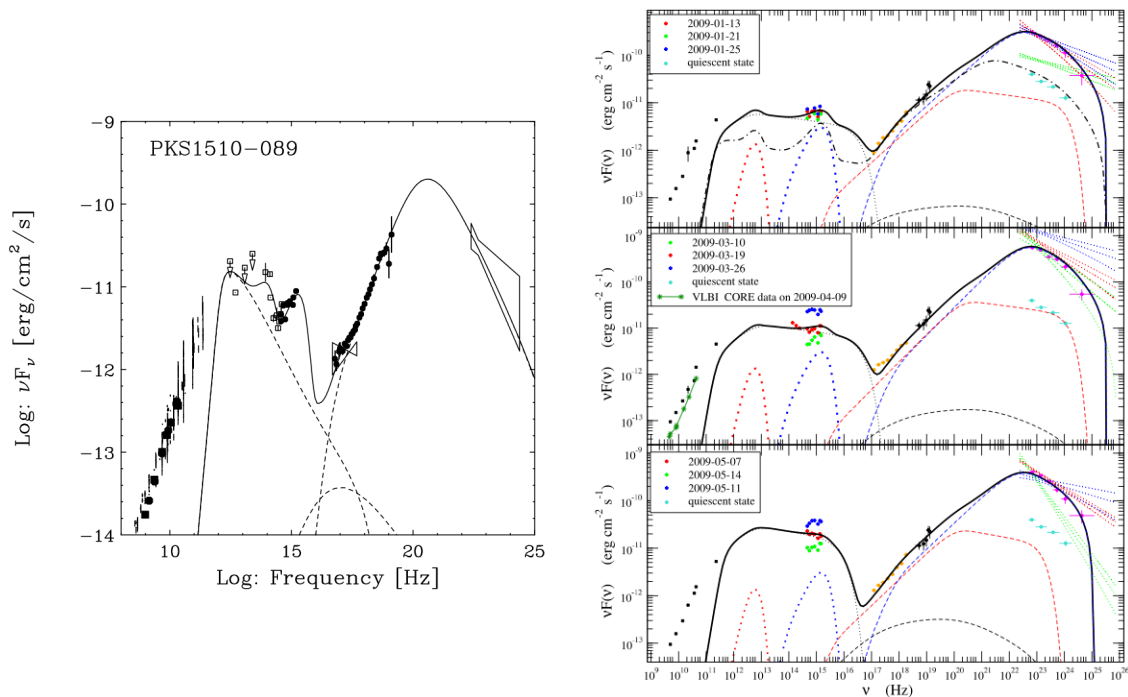


Figure C.58: The broadband SED of 1510–089. Left: The broadband SED presented by Kataoka et al. (2008); the data obtained from a multiwavelength campaign are marked as filled circles. Right: The broadband SED presented by Fermi-LAT Collaboration (2010). The SED in the three panels show the multiwavelength campaign taken place in January 2009, March 2009, and May 2009. In each panel, data obtained in different time range are marked in different colors, as denoted in upper-left corner of the plot.

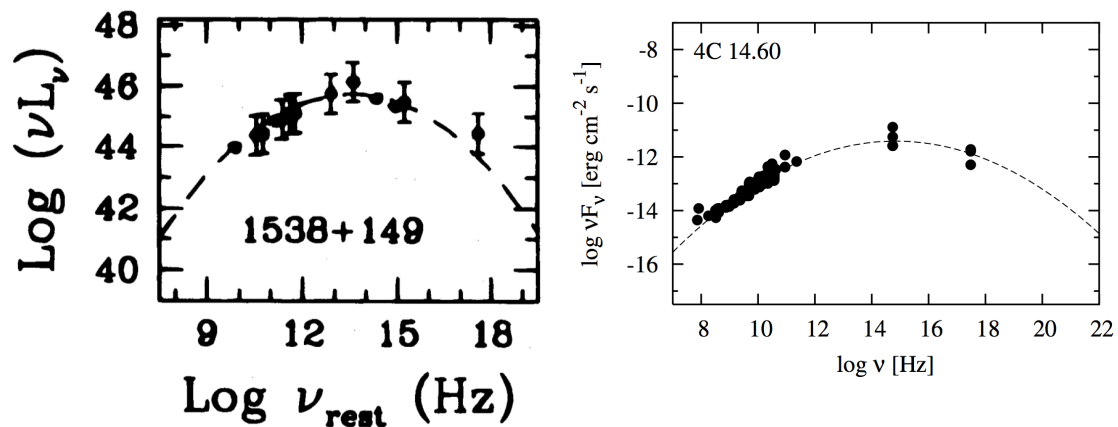


Figure C.59: The synchrotron hump of the broadband SED of 1538+149. Left: The synchrotron hump of the SED presented by Sambruna et al. (1996). Right: The synchrotron hump of the SED presented by Nieppola et al. (2006). The data are non-simultaneous, and were collected from databases and the literature. The dashed line denotes the parabolic fit to the synchrotron component of the SED.

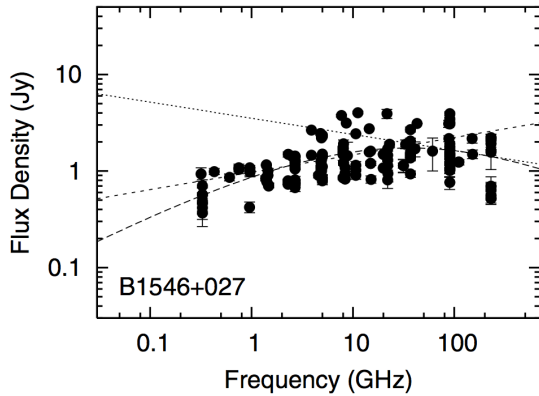


Figure C.60: The radio spectrum of 1546+027 by Tornaiainen et al. (2005). The dashed lines represent the linear fit performed to derive different spectral indices separated by the turn-over frequency.

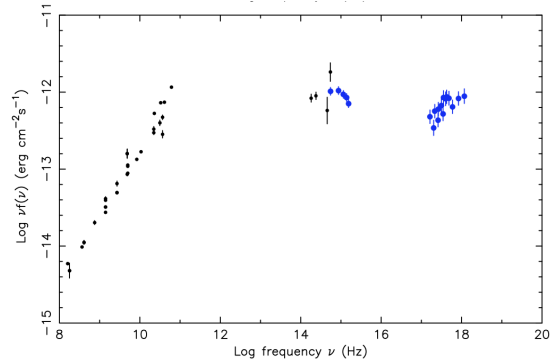


Figure C.61: The broadband SED of 1548+056 by Giommi et al. (2007). The blue data points denote *Swift* UVOT and XRT observations obtained on 15 September 2005.

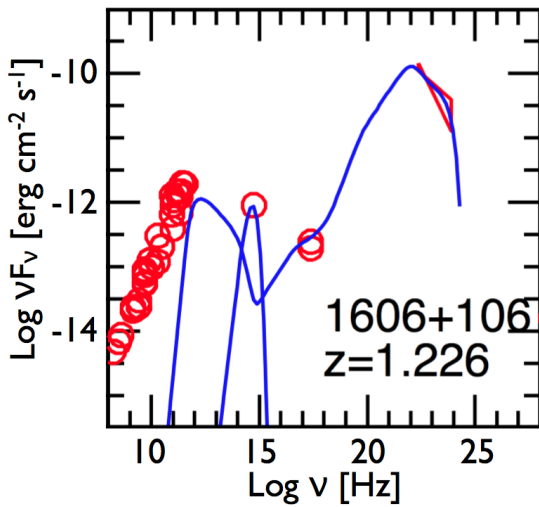


Figure C.62: The broadband SED of 1606+106 by Celotti and Ghisellini (2008). The model shown here was based on an one-zone leptonic synchrotron and IC mechanism, taking into account of the seed photons originated both in the jet and from external emission.

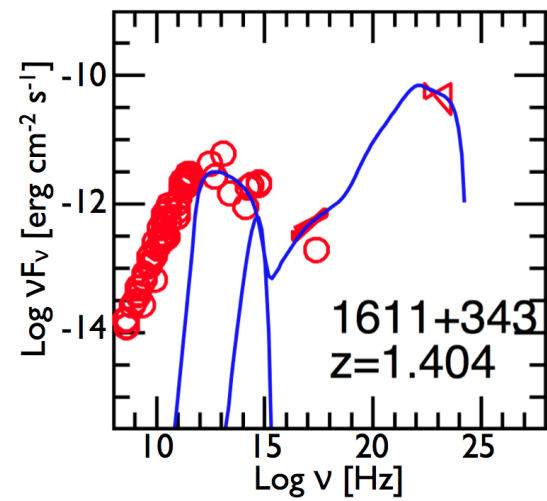


Figure C.63: The broadband SED of 1611+343 by Celotti and Ghisellini (2008). The model shown here was based on an one-zone leptonic synchrotron and IC mechanism, taking into account of the seed photons originated both in the jet and from external emission.

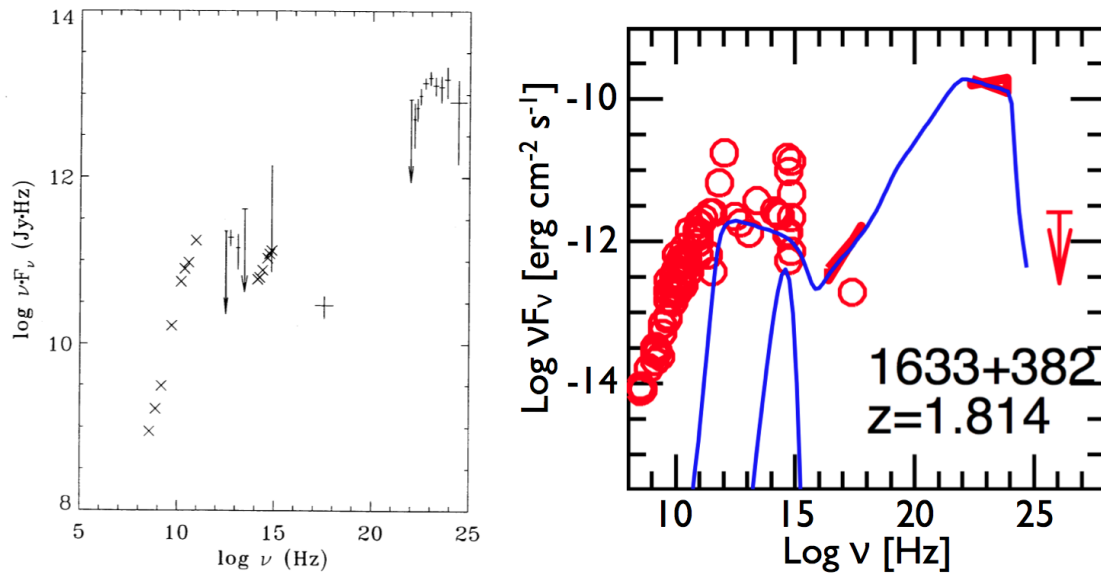


Figure C.64: The broadband SED of 1633+382. Left: the SED presented by Mattox et al. (1993). The γ -ray data were obtained by *CGRO/EGRET*, the X-ray data were obtained by the *Einstein Observatory*, and the rest were archival data. Right: the SED presented by Celotti and Ghisellini (2008). The model shown here was based on an one-zone leptonic synchrotron and IC mechanism, taking into account of the seed photons originated both in the jet and from external emission.

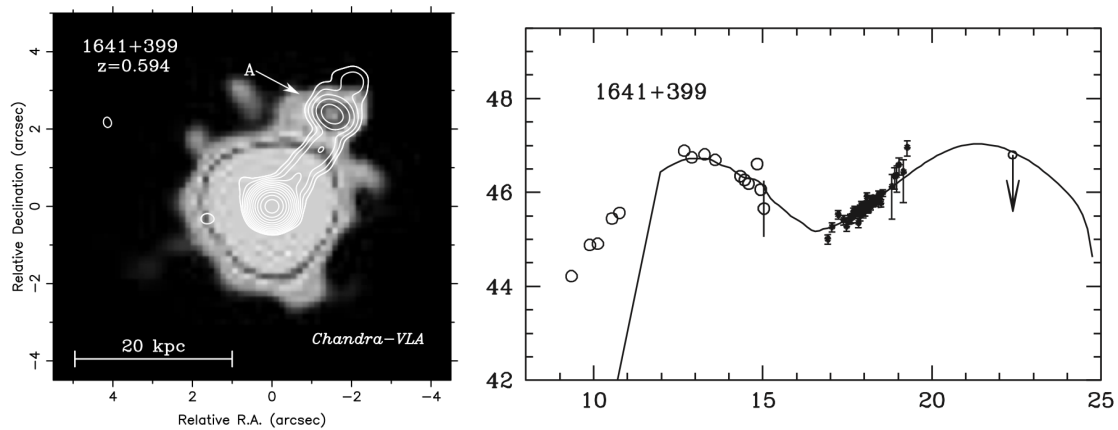


Figure C.65: Left: the overlaid plot of 1641+399 with *Chandra* (0.5–8 keV; grey scale) and VLA (5 GHz; white contour) images (Sambruna et al. 2004). Right: the broadband SED of 1641+399 presented by Tavecchio et al. (2002). The data in the plot include the X-ray data obtained by *BeppoSAX* (0.1–200 keV; filled circles), together with archival data (open circles). The solid line represents the best fit of the SED using a model of SSC plus IC from external radiation field.

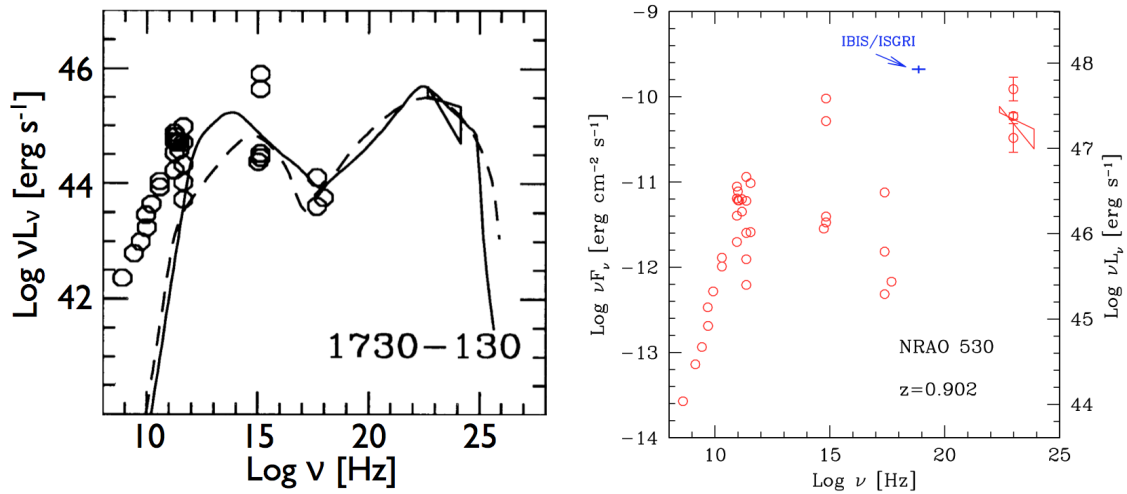


Figure C.66: The broadband SED of 1730–130. Left: the SED published by (Ghisellini et al. 1998). The data points (open circles) were collected from the literature. The solid line represents the best-fit SED model of SSC and EC mechanism. Right: the broadband SED presented by Foschini et al. (2006a). The X-ray data were obtained by *ROSAT*, *Einstein*, and *HEAO-I*; the γ -ray data were obtained by *CGRO/EGRET*; the blue cross represents the *INTEGRAL* IBIS/ISGRI data; the rest of the data were from the literature.

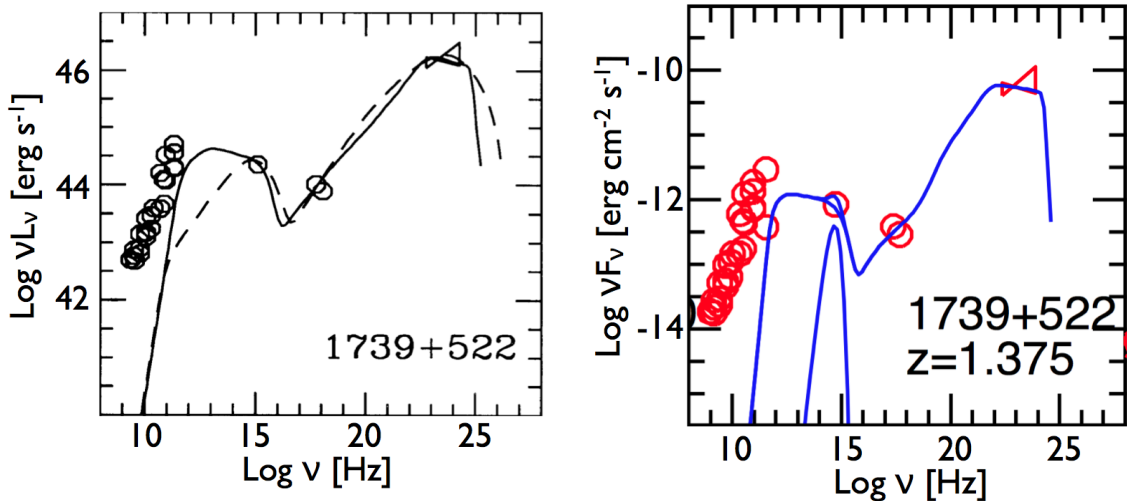


Figure C.67: The broadband SED of 1739+522. Left: the SED presented by Ghisellini et al. (1998). The open circles denote the archival data, and the solid line represents the SED model of SSC and EC. Right: the SED presented by Celotti and Ghisellini (2008). The open circles denote the archival data, and the solid line represents the SED model of SSC and EC.

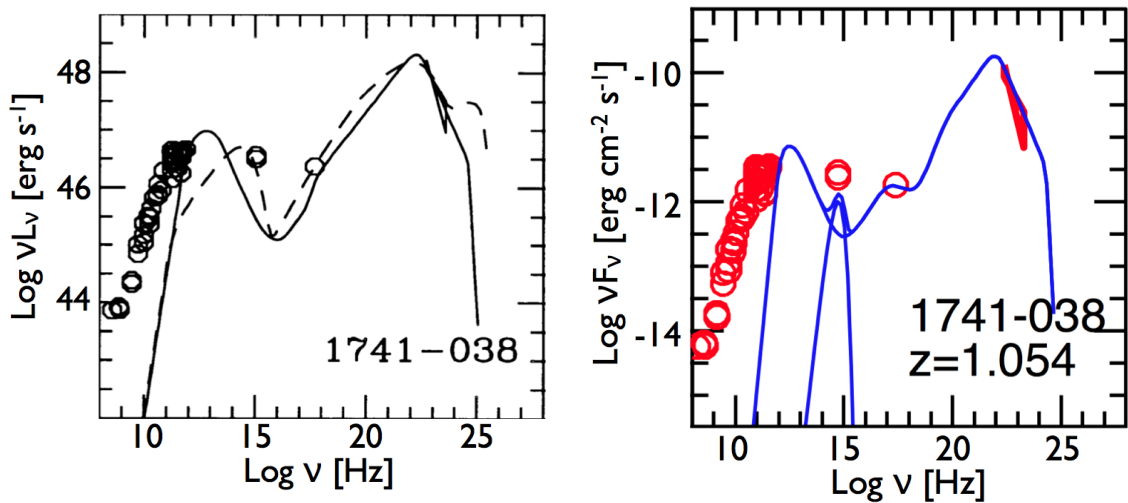


Figure C.68: The broadband SED of 1741–038. Left: the SED presented by Ghisellini et al. (1998). The open circles denote the archival data, and the solid line represents the SED model of SSC and EC. Right: the SED presented by Celotti and Ghisellini (2008). The open circles denote the archival data, and the solid line represents the SED model of SSC and EC.

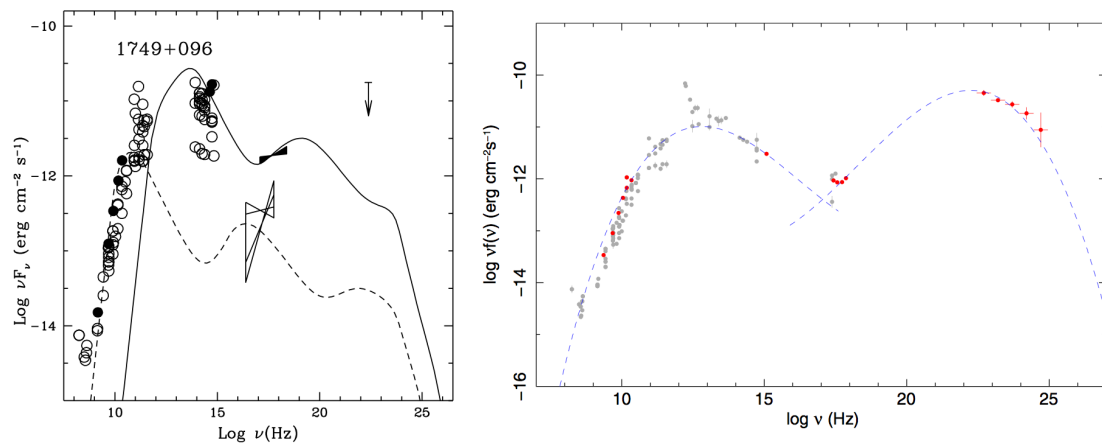


Figure C.69: The broadband SED of 1749+096. Left: the SED presented by Sambruna et al. (1999). The filled symbols denote the quasi-simultaneous data obtained by the authors in September 1995, while the open symbols are literature data. The solid line is the best fit to the data with a homogeneous one-zone SSC model; the dashed line is the contribution to the radio spectrum from a more extended region. Right: the SED presented by Abdo et al. (2010a). The quasi-simultaneous data are represented as large filled red symbols, and the non-simultaneous archival measurements are shown as small open grey points. The dashed lines represent the best fit of a third degree polynomial to the quasi-simultaneous data.

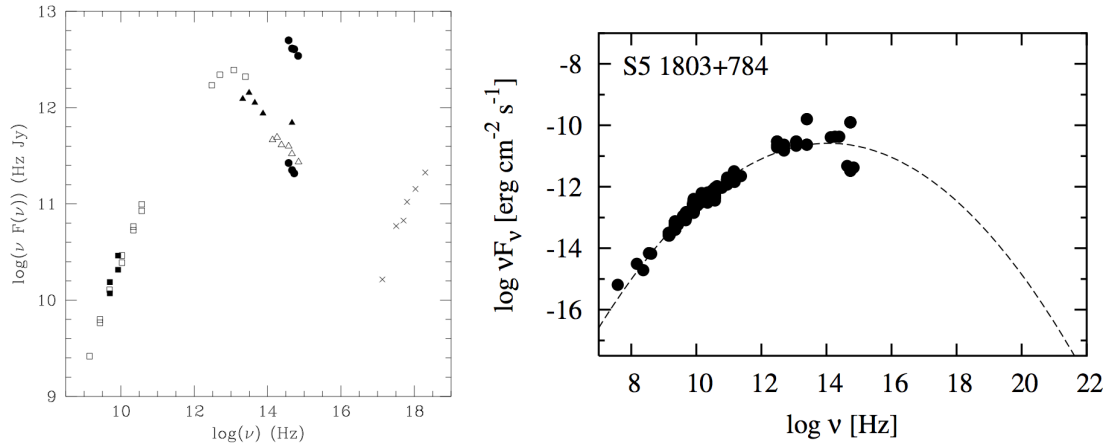


Figure C.70: Published SED of 1803+784. Left: the SED presented by Nesci et al. (2002). Open squares: the NED data; filled squares: radio monitoring obtained by the antennas in Medicina and Noto; filled triangles: simultaneous optical data; open triangles: simultaneous near infrared/optical data; filled circles: maximum and minimum value measured from the optical monitoring of 1803+784; crosses: *BeppoSAX* X-ray data. Right: the synchrotron hump of SED presented by Nieppola et al. (2006). The data are non-simultaneous, and were collected from databases and the literature. The dashed line denotes the parabolic fit to the synchrotron component of the SED.

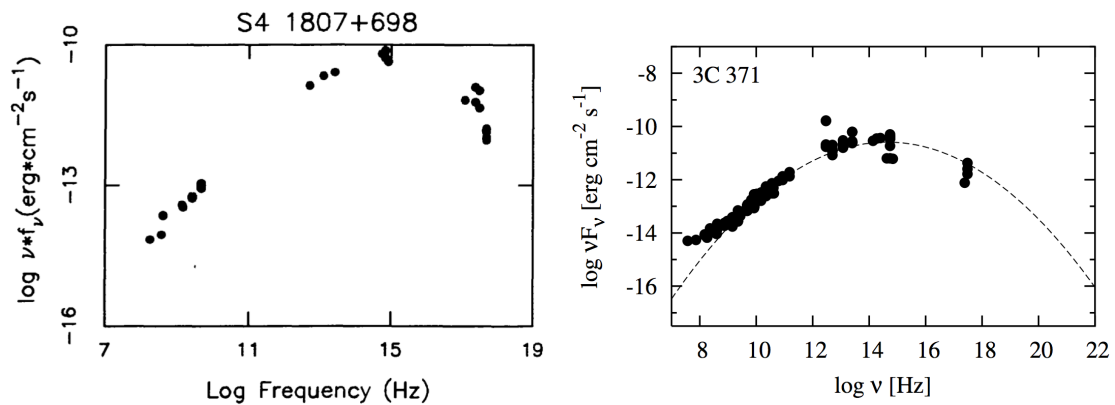


Figure C.71: The synchrotron hump of the broadband SED of 1807+698. Left: SED presented by Giommi et al. (1995). The data were from non-simultaneous archival data. Right: the SED presented by Nieppola et al. (2006). Shown data include non-simultaneous archival measurements. The dashed line denotes the parabolic fit to the synchrotron component of the SED.

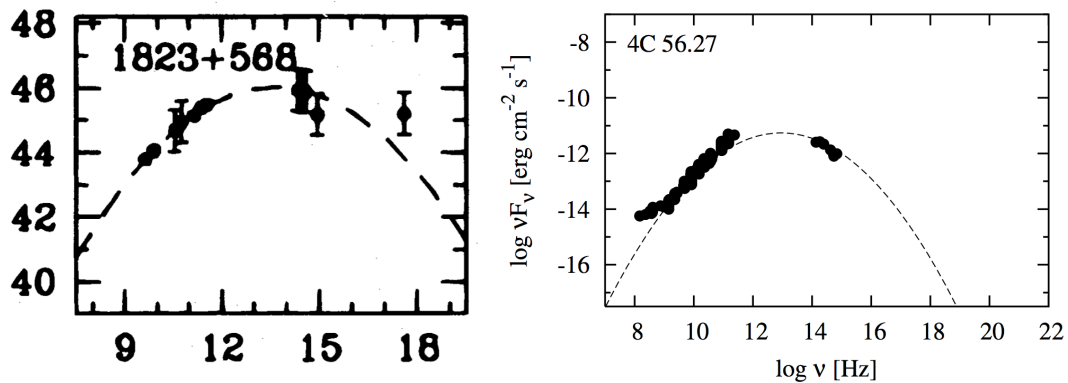


Figure C.72: The synchrotron hump of the broadband SED of 1823+568. Left: the SED presented by Sambruna et al. (1996). The data were non-simultaneous archival data from the NED, and the dashed line denotes a parabolic fit. X-axis: $\log \nu$ (Hz); y-axis: $\log \nu L_\nu$ (erg s⁻¹). Right: the SED presented by Nieppola et al. (2006). The data are non-simultaneous, and were collected from databases and the literature. The dashed line denotes the parabolic fit to the synchrotron component of the SED.

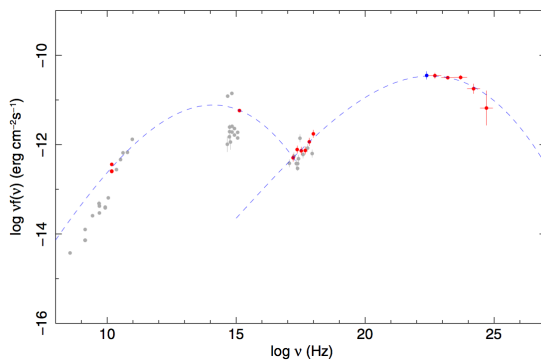


Figure C.73: The broadband SED of 1849+670 presented by Abdo et al. (2010a). The quasi-simultaneous data are represented as large filled red symbols, and the non-simultaneous archival measurements are shown as small open grey points. The dashed lines represent the best fit of a third degree polynomial to the quasi-simultaneous data.

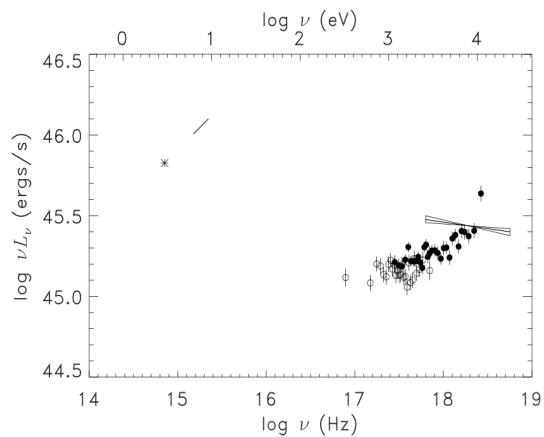
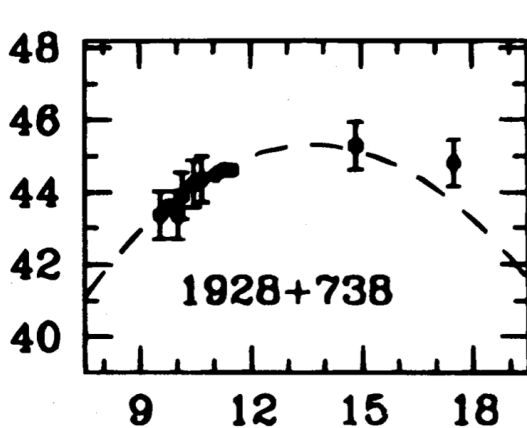


Figure C.74: The broadband SED of 1928+738. Left: the synchrotron hump of the SED presented by Sambruna et al. (1996). The data were non-simultaneous archival data from the NED, and the dashed line denotes a second-degree parabolic fit. X-axis: $\log \nu$ (Hz); y-axis: $\log \nu L_\nu$ (erg s⁻¹). Right: the optical to X-ray SED presented by Yuan et al. (2000). The optical data were obtained by *HST*, the open circles are the *ROSAT* data, and the filled circles are the *ASCA* data.

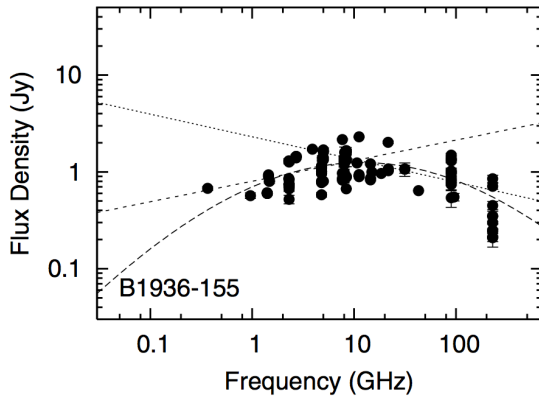


Figure C.75: The radio spectrum of 1936–155 published by Tornainen et al. (2005). The dashed lines represent the linear fit performed to derive different spectral indices separated by the turn-over frequency.

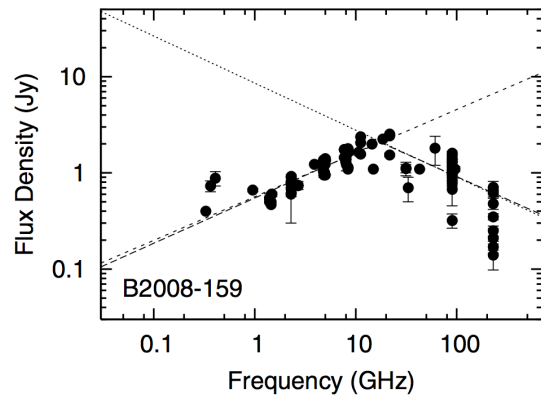


Figure C.76: The radio spectrum of 2008–159 published by Tornainen et al. (2005). The dashed lines represent the linear fit performed to derive different spectral indices separated by the turn-over frequency.

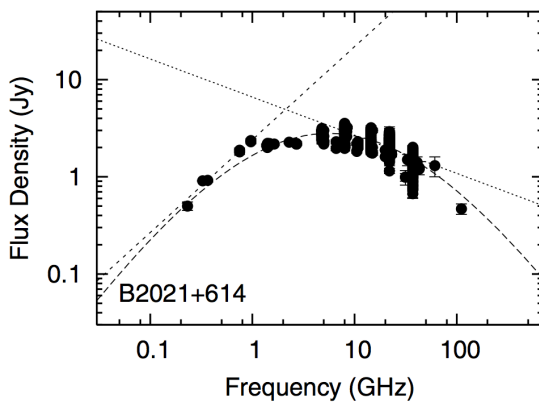


Figure C.77: The radio spectrum of 2021+614 published by Tornainen et al. (2005). The dashed lines represent the linear fit performed to derive different spectral indices separated by the turn-over frequency.

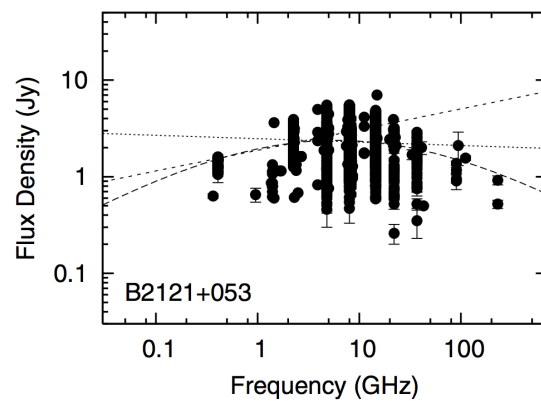


Figure C.78: The radio spectrum of 2121+053 published by Tornainen et al. (2005). The dashed lines represent the linear fit performed to derive different spectral indices separated by the turn-over frequency.

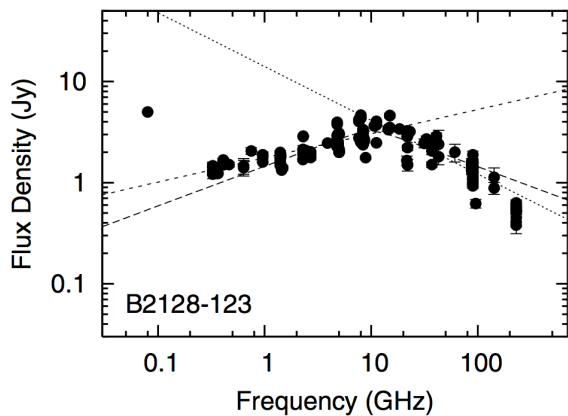


Figure C.79: The radio spectrum of 2128–123 published by Tornaiainen et al. (2005). The dashed lines represent the linear fit performed to derive different spectral indices separated by the turn-over frequency.

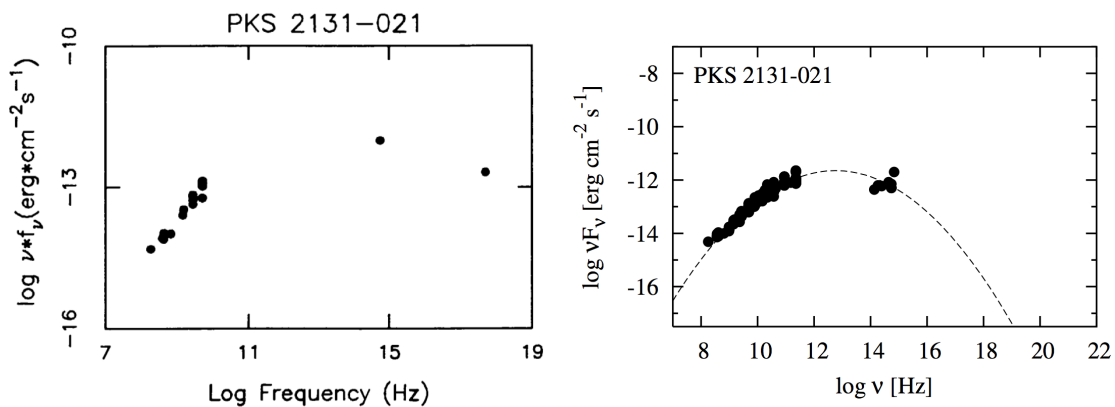


Figure C.80: The broadband SED of 2131–021. Left: the synchrotron hump of the SED presented by Giommi et al. (1995). The data are from non-simultaneous archival data. Right: the synchrotron hump of the SED presented by Nieppola et al. (2006). The data are non-simultaneous, and were collected from databases and the literature. The dashed line denotes the parabolic fit to the synchrotron component of the SED.

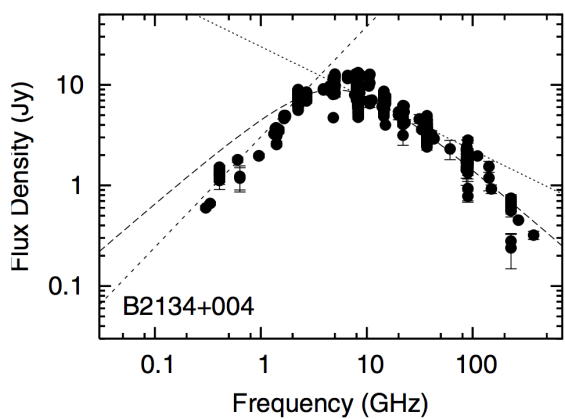


Figure C.81: The radio spectrum of 2134+004 published by Tornaiainen et al. (2005). The dashed lines represent the linear fit performed to derive different spectral indices separated by the turn-over frequency.

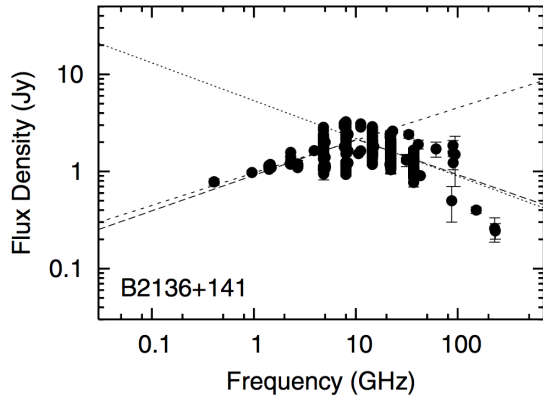


Figure C.82: The radio spectrum of 2136+141 published by Tornainen et al. (2005). The dashed lines represent the linear fit performed to derive different spectral indices separated by the turn-over frequency.

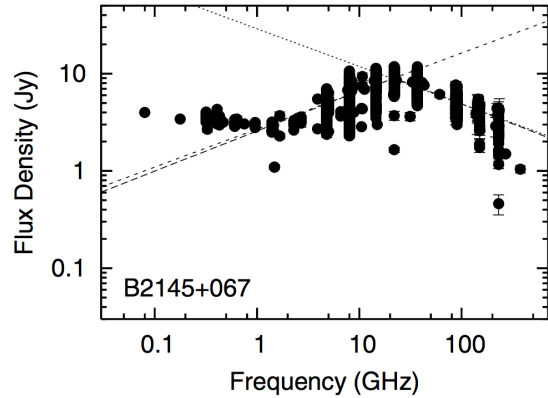


Figure C.83: The radio spectrum of 2145+067 published by Tornainen et al. (2005). The dashed lines represent the linear fit performed to derive different spectral indices separated by the turn-over frequency.

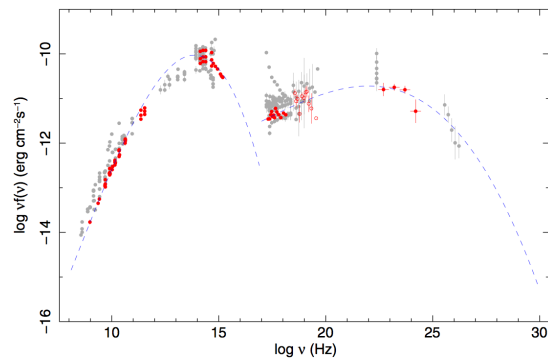
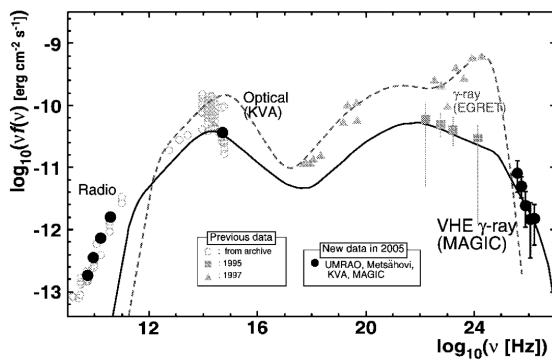


Figure C.84: The broadband SED of 2200+420. Left: the results presented by Albert et al. (2007). The black filled circles represent simultaneous 2005 data of KVA, MAGIC and UMRAD; the gray symbols denote old measurements. The solid line represents a one-zone SSC model for the 1994 data; the dashed line is produced with SSC and EC components for the data of the 1997 flare. Right: the SED presented by Abdo et al. (2010a). The quasi-simultaneous data are represented as large filled red symbols, and the non-simultaneous archival measurements are shown as small open grey points. The dashed lines represent the best fit of a third degree polynomial to the quasi-simultaneous data.

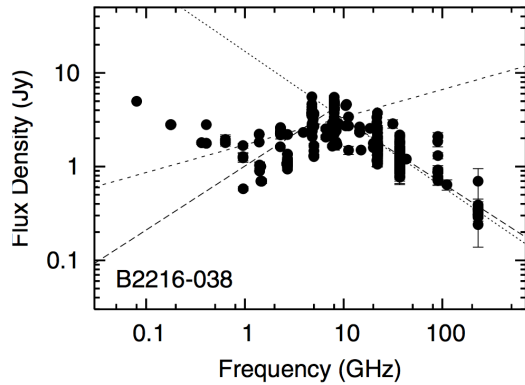


Figure C.85: The radio spectrum of 2216–038 published by Tornaiainen et al. (2005). The dashed lines represent the linear fit performed to derive different spectral indices separated by the turn-over frequency.

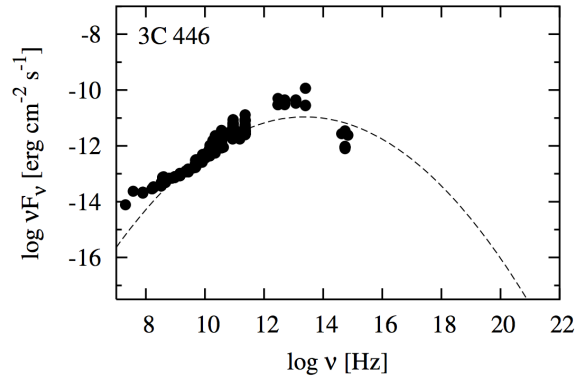


Figure C.86: The SED of 2223–052 at the synchrotron hump by Nieppola et al. (2006). The data are non-simultaneous, and were collected from databases and the literature. The dashed line denotes the parabolic fit to the synchrotron component of the SED.

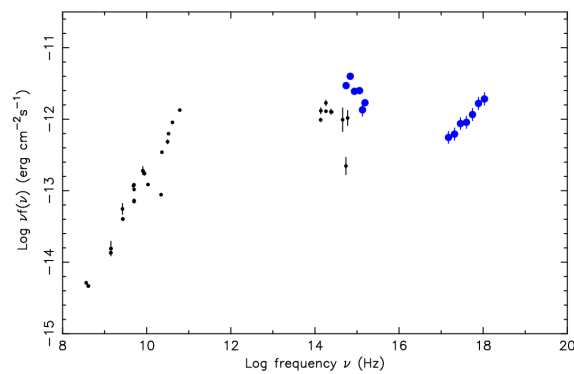


Figure C.87: The broadband SED of 2227–088 by Giommi et al. (2007). The blue points denote *Swift* UVOT and XRT observations obtained in June 2006.

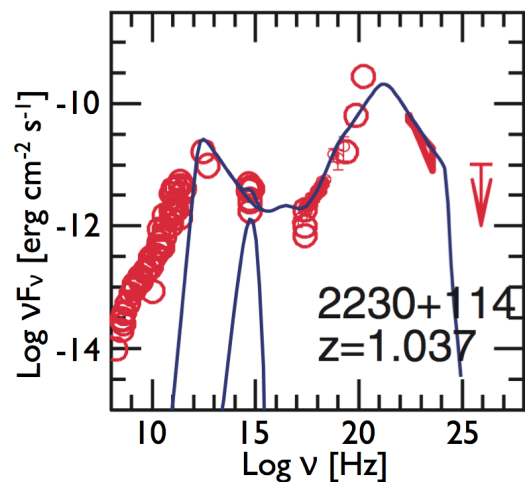


Figure C.88: The broadband SED of 2230+114 by Celotti and Ghisellini (2008). The model shown here was based on an one-zone leptonic synchrotron and IC mechanism, taking into account of the seed photons originated both in the jet and from external emission.

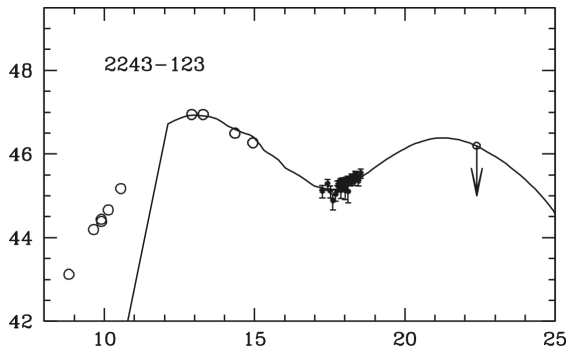


Figure C.89: The broadband SED of 2243–123 presented by Tavecchio et al. (2002). The X-axis is frequency in Hz, and the Y-axis is luminosity in erg s^{-1} . The data in the plot include the X-ray data obtained by *BeppoSAX* (0.1–200 keV; filled circles), together with archival data (open circles). The solid line represents the best fit of the SED using a model of SSC plus IC from external radiation field.

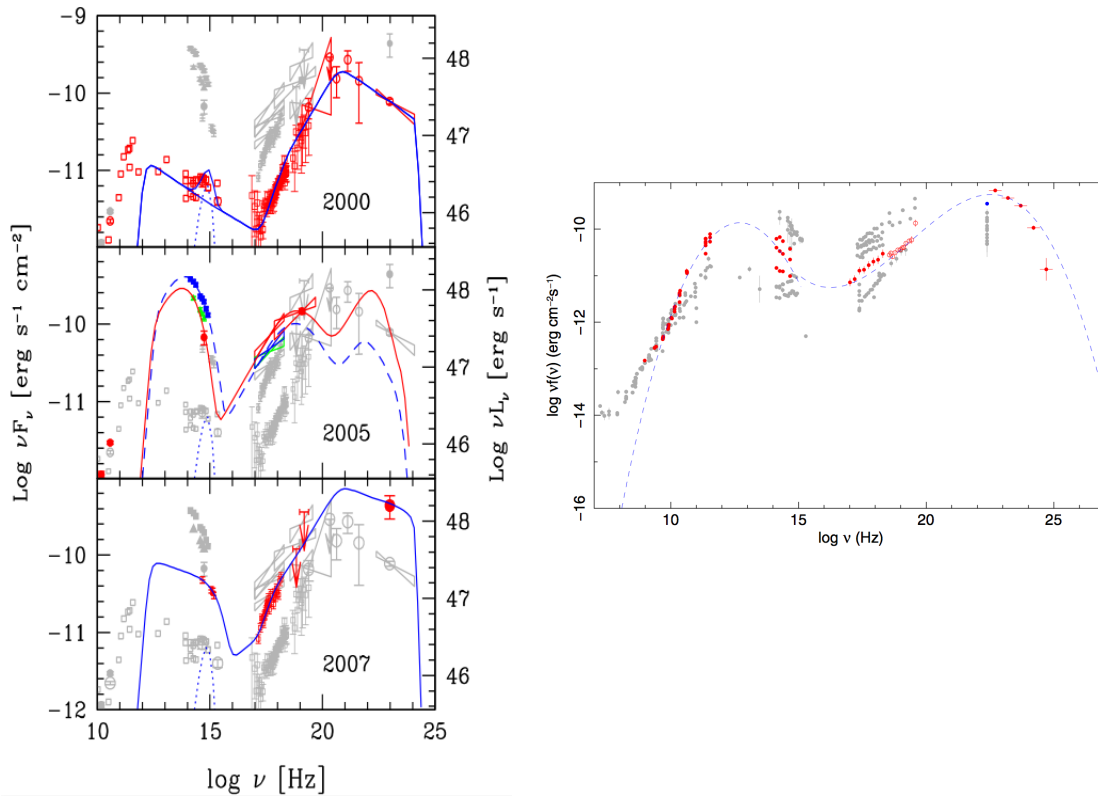


Figure C.90: The broadband SED of 2251+158. Left: the results presented by Ghisellini et al. (2007). Top panel: the SED in 2000 obtained by *BeppoSAX* (Tavecchio et al. 2002), and the other points are not simultaneous; mid panel: the SED during an optical flare in 2005 (Pian et al. 2006, Giommi et al. 2006), and different colors denote different sets of simultaneous data; bottom panel: the SED obtained by Ghisellini et al. (2007) using *AGILE* and *Swift*. The solid line is the best-fit model, and the dotted line denotes the contribution from the accretion disk. Right: the SED presented by Abdo et al. (2010a). The quasi-simultaneous data are represented as large filled red symbols, and the non-simultaneous archival measurements are shown as small open grey points. The dashed lines represent the best fit of a third degree polynomial to the quasi-simultaneous data.

D Glossary of Acronyms

- **ALMA** – The Atacama Large Millimeter/submillimeter Array.
- **APEX** – The Atacama Pathfinder **EX**periment (APEX)
- **ASCA** – The Advanced Satellite for Cosmology and Astrophysics. Japan’s cosmic X-ray astronomy mission (Tanaka et al. 1994).
- **ATCA** – Australia Telescope Compact Array
- **AGN** – Active Galactic Nuclei
- **BAT** – Burst Alert Telescope onboard *Swift*.
- **BeppoSAX** – Italian/Dutch X-ray astronomy mission.
- **Chandra** – NASA space X-ray observatory
- **CGRO** – Compton Gamma Ray Observatory
- **DEC** – Declination.
- **EC** – External Compton.
- **EGRET** – The Energetic Gamma Ray Experiment Telescope onboard *CGRO*.
- **Einstein** – NASA space X-ray observatory.
- **ERC** – External Radiation Compton, see Section 1.2.3.
- **EVN** – European VLBI Network
- **FGAMMA** – *Fermi*-GST AGN Multi-frequency Monitoring Alliance.
- **FITS** – Flexible Image Transport System
- **GPS** – Gigahertz Peaked Spectrum
- **HBL** – High-frequency peaked **BL** Lac object
- **HEASARC** – High Energy Astrophysics Science Archive Research Center
- **HESS** – High Energy Stereoscopic System
- **HFP** – High Frequency Peaker
- **HST** – Hubble Space Telescope
- **IBL** – Intermediate-frequency peaked **BL** Lac object
- **IC** – Inverse Compton
- **IRAM** – Institut de RadioAstronomie Millimétrique
- **LAT** – Large Area Telescope onboard *Fermi*.
- **LBA** – Australian Long Baseline Array

- **LBAS** – *Fermi* LAT Bright AGN Sample
- **LBL** – Low-frequency peaked BL Lac object
- **LINER** – Low-Ionization Nuclear Emission-line Region
- **MERLIN** – Multi-Element Radio Linked Interferometer Network
- **MOJAVE** – Monitoring Of Jets in Active galactic nuclei with VLBA Experiments
- **NED** – NASA/IPAC Extragalactic Database
- **OVV** – Optically Violent Variable
- **RA** – Right Ascension.
- **ROSAT** – From the German word *Röntgensatellit*. German/British/US X-ray observatory.
- **RXTE** – Rossi X-ray Timing Explorer
- **SED** – Spectral Energy Distribution.
- **SMBH** – Super Massive Black Hole
- **SSC** – Synchrotron Self-Compton, see Section 1.2.3.
- **TANAMI** – Tracking Active Galactic Nuclei with Austral Milliarcsecond Interferometry
- **ToO** – Target of Opportunity
- **UMRAO** – University of Michigan Radio Astronomy Observatory
- **UVOT** – UV/Optical Telescope
- **VHE** – Very High Energy
- **VLA** – Very Large Array
- **VLBA** – Very Long Baseline Array
- **VLBI** – Very Long Baseline Interferometry
- **VSOP** – VLBI Space Observatory Program
- **XMM-Newton** – X-ray Multi-Mirror Mission. ESA X-ray observatory.

Bibliography

Abdo, A. A., Ackermann, M., Agudo, I., Ajello, M., Aller, H. D., Aller, M. F., Angelakis, E., Arkharov, A. A., Axelsson, M., Bach, U., Baldini, L., Ballet, J., Barbiellini, G., Bastieri, D., Baughman, B. M., Bechtol, K., Bellazzini, R., Benitez, E., Berdyugin, A., Berenji, B., Blandford, R. D., Bloom, E. D., Boettcher, M., Bonamente, E., Borgland, A. W., Bregeon, J., Brez, A., Brigida, M., Bruel, P., Burnett, T. H., Burrows, D., Buson, S., Caliandro, G. A., Calzoletti, L., Cameron, R. A., Capalbi, M., Caraveo, P. A., Carosati, D., Casandjian, J. M., Cavazzuti, E., Cecchi, C., Çelik, Ö., Charles, E., Chaty, S., Chekhtman, A., Chen, W. P., Chiang, J., Chincarini, G., Ciprini, S., Claus, R., Cohen-Tanugi, J., Colafrancesco, S., Cominsky, L. R., Conrad, J., Costamante, L., Cutini, S., D'ammadio, F., Deitrick, R., D'Elia, V., Dermer, C. D., de Angelis, A., de Palma, F., Digel, S. W., Donnarumma, I., Silva, E. d. C. e., Drell, P. S., Dubois, R., Dultzin, D., Dumora, D., Falcone, A., Farnier, C., Favuzzi, C., Fegan, S. J., Focke, W. B., Forné, E., Fortin, P., Frailis, M., Fuhrmann, L., Fukazawa, Y., Funk, S., Fusco, P., Gómez, J. L., Gargano, F., Gasparrini, D., Gehrels, N., Germani, S., Giebels, B., Giglietto, N., Giommi, P., Giordano, F., Giuliani, A., Glanzman, T., Godfrey, G., Grenier, I. A., Gronwall, C., Grove, J. E., Guillemot, L., Guiriec, S., Gurwell, M. A., Hadasch, D., Hanabata, Y., Harding, A. K., Hayashida, M., Hays, E., Healey, S. E., Heidt, J., Hiriart, D., Horan, D., Hoversten, E. A., Hughes, R. E., Itoh, R., Jackson, M. S., Jóhannesson, G., Johnson, A. S., Johnson, W. N., Jorstad, S. G., Kadler, M., Kamae, T., Katagiri, H., Kataoka, J., Kawai, N., Kennea, J., Kerr, M., Kimeridze, G., Knödseder, J., Kocian, M. L., Kopatskaya, E. N., Koptelova, E., Konstantinova, T. S., Kovalev, Y. Y., Kovalev, Y. A., Kurtanidze, O. M., Kuss, M., Lande, J., Larionov, V. M., Latronico, L., Leto, P., Lindfors, E., Longo, F., Loparco, F., Lott, B., Lovellette, M. N., Lubrano, P., Madejski, G. M., Makeev, A., Marchegiani, P., Marscher, A. P., Marshall, F., Max-Moerbeck, W., Mazziotta, M. N., McConville, W., McEnery, J. E., Meurer, C., Michelson, P. F., Mitthumsiri, W., Mizuno, T., Moiseev, A. A., Monte, C., Monzani, M. E., Morselli, A., Moskalenko, I. V., Murgia, S., Nestoras, I., Nilsson, K., Nizhelsky, N. A., Nolan, P. L., Norris, J. P., Nuss, E., Ohsugi, T., Ojha, R., Omodei, N., Orlando, E., Ormes, J. F., Osborne, J., Ozaki, M., Pacciani, L., Padovani, P., Pagani, C., Page, K., Paneque, D., Panetta, J. H., Parent, D., Pasanen, M., Pavlidou, V., Pelassa, V., Pepe, M., Perri, M., Pesce-Rollins, M., Piranomonte, S., Piron, F., Pittori, C., Porter, T. A., Puccetti, S., Rahoui, F., Rainò, S., Raiteri, C., Rando, R., Razzano, M., Reimer, A., Reimer, O., Reposeur, T., Richards, J. L., Ritz, S., Rochester, L. S., Rodriguez, A. Y., Romani, R. W., Ros, J. A., Roth, M., Roustazadeh, P., Ryde, F., Sadrozinski, H., Sadun, A., Sanchez, D., Sander, A., Saz Parkinson, P. M., Scargle, J. D., Sellerholm, A., Sgrò, C., Shaw, M. S., Sigua, L. A., Siskind, E. J., Smith, D. A., Smith, P. D., Spandre, G., Spinelli, P., Starck, J., Stevenson, M., Stratta, G., Strickman, M. S., Su-

son, D. J., Tajima, H., Takahashi, H., Takahashi, T., Takalo, L. O., Tanaka, T., Thayer, J. B., Thayer, J. G., Thompson, D. J., Tibaldo, L., Torres, D. F., Tosti, G., Tramacere, A., Uchiyama, Y., Usher, T. L., Vasileiou, V., Verrecchia, F., Vilchez, N., Villata, M., Vitale, V., Waite, A. P., Wang, P., Winer, B. L., Wood, K. S., Ylinen, T., Zensus, J. A., Zhekanis, G. V., and Ziegler, M. (2010a). The Spectral Energy Distribution of Fermi Bright Blazars. *The Astrophysical Journal*, 716:30–70.

Abdo, A. A., Ackermann, M., Ajello, M., Allafort, A., Antolini, E., Atwood, W. B., Axelsson, M., Baldini, L., Ballet, J., Barbiellini, G., Bastieri, D., Baughman, B. M., Bechtol, K., Bellazzini, R., Belli, F., Berenji, B., Bisello, D., Blandford, R. D., Bloom, E. D., Bonamente, E., Bonnell, J., Borgland, A. W., Bouvier, A., Bregeon, J., Brez, A., Brigida, M., Bruel, P., Burnett, T. H., Busetto, G., Buson, S., Caliendo, G. A., Cameron, R. A., Campana, R., Canadas, B., Caraveo, P. A., Carrigan, S., Casandjian, J. M., Cavazzuti, E., Ceccanti, M., Cecchi, C., Çelik, Ö., Charles, E., Chekhtman, A., Cheung, C. C., Chiang, J., Cillis, A. N., Ciprini, S., Claus, R., Cohen-Tanugi, J., Conrad, J., Corbet, R., Davis, D. S., DeKlotz, M., den Hartog, P. R., Dermer, C. D., de Angelis, A., de Luca, A., de Palma, F., Digel, S. W., Dormody, M., Silva, E. d. C. e., Drell, P. S., Dubois, R., Dumora, D., Fabiani, D., Farnier, C., Favuzzi, C., Fegan, S. J., Ferrara, E. C., Focke, W. B., Fortin, P., Frailis, M., Fukazawa, Y., Funk, S., Fusco, P., Gargano, F., Gasparrini, D., Gehrels, N., Germani, S., Giavitto, G., Giebels, B., Giglietto, N., Giommi, P., Giordano, F., Giroletti, M., Glanzman, T., Godfrey, G., Grenier, I. A., Grondin, M., Grove, J. E., Guillemot, L., Guiriec, S., Gustafsson, M., Hadasch, D., Hanabata, Y., Harding, A. K., Hayashida, M., Hays, E., Healey, S. E., Hill, A. B., Horan, D., Hughes, R. E., Iafate, G., Jóhannesson, G., Johnson, A. S., Johnson, R. P., Johnson, T. J., Johnson, W. N., Kamae, T., Katagiri, H., Kataoka, J., Kawai, N., Kerr, M., Knödlseeder, J., Kocevski, D., Kuss, M., Lande, J., Landriu, D., Latronico, L., Lee, S., Lemoine-Goumard, M., Lionetto, A. M., Llana Garde, M., Longo, F., Loparco, F., Lott, B., Lovellette, M. N., Lubrano, P., Madejski, G. M., Makeev, A., Marangelli, B., Marelli, M., Massaro, E., Mazziotta, M. N., McConville, W., McEnery, J. E., Michelson, P. F., Minuti, M., Mitthumsiri, W., Mizuno, T., Moiseev, A. A., Mongelli, M., Monte, C., Monzani, M. E., Moretti, E., Morselli, A., Moskalenko, I. V., Murgia, S., Nakajima, H., Nakamori, T., Naumann-Godo, M., Nolan, P. L., Norris, J. P., Nuss, E., Ohno, M., Ohsugi, T., Omodei, N., Orlando, E., Ormes, J. F., Ozaki, M., Paccagnella, A., Paneque, D., Panetta, J. H., Parent, D., Pelassa, V., Pepe, M., Pesce-Rollins, M., Pinchera, M., Piron, F., Porter, T. A., Poupard, L., Rainò, S., Rando, R., Ray, P. S., Razzano, M., Razzaque, S., Rea, N., Reimer, A., Reimer, O., Reposeur, T., Ripken, J., Ritz, S., Rochester, L. S., Rodriguez, A. Y., Romani, R. W., Roth, M., Sadrozinski, H., Salvetti, D., Sanchez, D., Sander, A., Saz Parkinson, P. M., Scargle, J. D., Schalk, T. L., Scolieri, G., Sgrò, C., Shaw, M. S., Siskind, E. J., Smith, D. A., Smith, P. D., Spandre, G., Spinelli, P., Starck, J., Stephens, T. E., Striani, E., Strickman, M. S., Strong, A. W., Suson, D. J., Tajima, H., Takahashi, H., Takahashi, T., Tanaka, T., Thayer, J. B., Thayer, J. G., Thompson, D. J., Tibaldo, L., Tibolla, O., Tinebra, F., Torres, D. F., Tosti, G., Tramacere, A., Uchiyama, Y., Usher, T. L., Van Etten, A., Vasileiou, V., Vilchez, N., Vitale, V., Waite, A. P., Wallace, E., Wang, P., Watters, K., Winer, B. L., Wood, K. S., Yang, Z., Ylinen, T., and Ziegler, M. (2010b). Fermi Large Area Telescope First Source Catalog. *Astrophysical Journal Supplement Series*, 188:405–436.

Abdo, A. A., Ackermann, M., Ajello, M., Allafort, A., Antolini, E., Atwood, W. B., Axelsson, M., Baldini, L., Ballet, J., Barbiellini, G., Bastieri, D., Baughman, B. M., Bechtol, K., Bellazzini, R., Berenji, B., Blandford, R. D., Bloom, E. D., Bogart, J. R., Bonamente, E., Borgland, A. W., Bouvier, A., Bregeon, J., Brez, A., Brigida, M., Bruel, P., Buehler, R., Burnett, T. H., Buson, S., Caliandro, G. A., Cameron, R. A., Cannon, A., Caraveo, P. A., Carrigan, S., Casandjian, J. M., Cavazzuti, E., Cecchi, C., Çelik, Ö., Celotti, A., Charles, E., Chekhtman, A., Chen, A. W., Cheung, C. C., Chiang, J., Ciprini, S., Claus, R., Cohen-Tanugi, J., Conrad, J., Costamante, L., Cotter, G., Cutini, S., D'Elia, V., Dermer, C. D., de Angelis, A., de Palma, F., De Rosa, A., Digel, S. W., Silva, E. d. C. e., Drell, P. S., Dubois, R., Dumora, D., Escande, L., Farnier, C., Favuzzi, C., Fegan, S. J., Ferrara, E. C., Focke, W. B., Fortin, P., Frailis, M., Fukazawa, Y., Funk, S., Fusco, P., Gargano, F., Gasparrini, D., Gehrels, N., Germani, S., Giebels, B., Giglietto, N., Giommi, P., Giordano, F., Giroletti, M., Glanzman, T., Godfrey, G., Grandi, P., Grenier, I. A., Grondin, M., Grove, J. E., Guiriec, S., Hadasch, D., Harding, A. K., Hayashida, M., Hays, E., Healey, S. E., Hill, A. B., Horan, D., Hughes, R. E., Iafrate, G., Itoh, R., Jóhannesson, G., Johnson, A. S., Johnson, R. P., Johnson, T. J., Johnson, W. N., Kamae, T., Katagiri, H., Kataoka, J., Kawai, N., Kerr, M., Knödlseeder, J., Kuss, M., Lande, J., Latronico, L., Lavalley, C., Lemoine-Goumard, M., Llena Garde, M., Longo, F., Loparco, F., Lott, B., Lovellette, M. N., Lubrano, P., Madejski, G. M., Makeev, A., Malaguti, G., Massaro, E., Mazziotta, M. N., McConville, W., McEnery, J. E., McGlynn, S., Michelson, P. F., Mitthumsiri, W., Mizuno, T., Moiseev, A. A., Monte, C., Monzani, M. E., Morselli, A., Moskalenko, I. V., Murgia, S., Nolan, P. L., Norris, J. P., Nuss, E., Ohno, M., Ohsugi, T., Omodei, N., Orlando, E., Ormes, J. F., Ozaki, M., Paneque, D., Panetta, J. H., Parent, D., Pelassa, V., Pepe, M., Pesce-Rollins, M., Piranomonte, S., Piron, F., Porter, T. A., Rainò, S., Rando, R., Razzano, M., Reimer, A., Reimer, O., Reposeur, T., Ripken, J., Ritz, S., Rodriguez, A. Y., Romani, R. W., Roth, M., Ryde, F., Sadrozinski, H., Sanchez, D., Sander, A., Saz Parkinson, P. M., Scargle, J. D., Sgrò, C., Shaw, M. S., Siskind, E. J., Smith, P. D., Spandre, G., Spinelli, P., Starck, J., Stawarz, Ł., Strickman, M. S., Suson, D. J., Tajima, H., Takahashi, H., Takahashi, T., Tanaka, T., Taylor, G. B., Thayer, J. B., Thayer, J. G., Thompson, D. J., Tibaldo, L., Torres, D. F., Tosti, G., Tramacere, A., Ubertini, P., Uchiyama, Y., Usher, T. L., Vasileiou, V., Vilchez, N., Villata, M., Vitale, V., Waite, A. P., Wallace, E., Wang, P., Winer, B. L., Wood, K. S., Yang, Z., Ylinen, T., and Ziegler, M. (2010c). The First Catalog of Active Galactic Nuclei Detected by the Fermi Large Area Telescope. *Astrophysical Journal*, 715:429–457.

Abdo, A. A., Ackermann, M., Ajello, M., Asano, K., Baldini, L., Ballet, J., Barbiellini, G., Bastieri, D., Baughman, B. M., Bechtol, K., Bellazzini, R., Blandford, R. D., Bloom, E. D., Bonamente, E., Borgland, A. W., Bregeon, J., Brez, A., Brigida, M., Bruel, P., Burnett, T. H., Caliandro, G. A., Cameron, R. A., Caraveo, P. A., Casandjian, J. M., Cavazzuti, E., Cecchi, C., Celotti, A., Chekhtman, A., Cheung, C. C., Chiang, J., Ciprini, S., Claus, R., Cohen-Tanugi, J., Colafrancesco, S., Cominsky, L. R., Conrad, J., Costamante, L., Dermer, C. D., de Angelis, A., de Palma, F., Digel, S. W., Donato, D., do Couto e Silva, E., Drell, P. S., Dubois, R., Dumora, D., Farnier, C., Favuzzi, C., Finke, J., Focke, W. B., Frailis, M., Fukazawa, Y., Funk, S., Fusco, P., Gargano, F., Georganopoulos, M., Germani, S., Giebels, B., Giglietto, N., Giordano, F., Glanzman,

T., Grenier, I. A., Grondin, M., Grove, J. E., Guillemot, L., Guiriec, S., Hanabata, Y., Harding, A. K., Hartman, R. C., Hayashida, M., Hays, E., Hughes, R. E., Jóhannesson, G., Johnson, A. S., Johnson, R. P., Johnson, W. N., Kadler, M., Kamae, T., Kanai, Y., Katagiri, H., Kataoka, J., Kawai, N., Kerr, M., Knödlseeder, J., Kuehn, F., Kuss, M., Latronico, L., Lemoine-Goumard, M., Longo, F., Loparco, F., Lott, B., Lovellette, M. N., Lubrano, P., Madejski, G. M., Makeev, A., Mazziotta, M. N., McEnery, J. E., Meurer, C., Michelson, P. F., Mitthumsiri, W., Mizuno, T., Moiseev, A. A., Monte, C., Monzani, M. E., Morselli, A., Moskalenko, I. V., Murgia, S., Nakamori, T., Nolan, P. L., Norris, J. P., Nuss, E., Ohsugi, T., Omodei, N., Orlando, E., Ormes, J. F., Paneque, D., Panetta, J. H., Parent, D., Pepe, M., Pesce-Rollins, M., Piron, F., Porter, T. A., Rainò, S., Razzano, M., Reimer, A., Reimer, O., Reposeur, T., Ritz, S., Rodriguez, A. Y., Romani, R. W., Ryde, F., Sadrozinski, H., Sambruna, R., Sanchez, D., Sander, A., Sato, R., Parkinson, P. M. S., Sgrò, C., Smith, D. A., Smith, P. D., Spandre, G., Spinelli, P., Starck, J., Strickman, M. S., Strong, A. W., Suson, D. J., Tajima, H., Takahashi, H., Takahashi, T., Tanaka, T., Taylor, G. B., Thayer, J. G., Thompson, D. J., Torres, D. F., Tosti, G., Uchiyama, Y., Usher, T. L., Vilchez, N., Vitale, V., Waite, A. P., Wood, K. S., Ylinen, T., Ziegler, M., Aller, H. D., Aller, M. F., Kellermann, K. I., Kovalev, Y. Y., Kovalev, Y. A., Lister, M. L., and Pushkarev, A. B. (2009a). Fermi Discovery of Gamma-ray Emission from NGC 1275. *Astrophysical Journal*, 699:31–39.

Abdo, A. A., Ackermann, M., Ajello, M., Atwood, W. B., Axelsson, M., Baldini, L., Ballet, J., Barbiellini, G., Bastieri, D., Baughman, B. M., Bechtol, K., Bellazzini, R., Berenji, B., Bloom, E. D., Bogaert, G., Bonamente, E., Borgland, A. W., Bregeon, J., Brez, A., Brigida, M., Bruel, P., Burnett, T. H., Caliandro, G. A., Cameron, R. A., Caraveo, P. A., Casandjian, J. M., Cavazzuti, E., Cecchi, C., Çelik, Ö., Chekhtman, A., Cheung, C. C., Chiang, J., Ciprini, S., Claus, R., Cohen-Tanugi, J., Conrad, J., Cutini, S., Dermer, C. D., de Angelis, A., de Palma, F., Digel, S. W., Silva, E. d. C. e., Drell, P. S., Dubois, R., Dumora, D., Farnier, C., Favuzzi, C., Fegan, S. J., Ferrara, E. C., Focke, W. B., Frailis, M., Fuhrmann, L., Fukazawa, Y., Funk, S., Fusco, P., Gargano, F., Gasparrini, D., Gehrels, N., Germani, S., Giebels, B., Giglietto, N., Giordano, F., Giroletti, M., Glanzman, T., Godfrey, G., Grenier, I. A., Grondin, M., Grove, J. E., Guillemot, L., Guiriec, S., Hanabata, Y., Harding, A. K., Hayashida, M., Hays, E., Hughes, R. E., Jóhannesson, G., Johnson, A. S., Johnson, R. P., Johnson, W. N., Kadler, M., Kamae, T., Katagiri, H., Kataoka, J., Kerr, M., Knödlseeder, J., Kocian, M. L., Kuehn, F., Kuss, M., Lande, J., Latronico, L., Lemoine-Goumard, M., Longo, F., Loparco, F., Lott, B., Lovellette, M. N., Lubrano, P., Madejski, G. M., Makeev, A., Marelli, M., Massaro, E., Max-Moerbeck, W., Mazziotta, M. N., McConville, W., McEnery, J. E., Meurer, C., Michelson, P. F., Mitthumsiri, W., Mizuno, T., Moiseev, A. A., Monte, C., Monzani, M. E., Morselli, A., Moskalenko, I. V., Murgia, S., Nolan, P. L., Norris, J. P., Nuss, E., Ohsugi, T., Omodei, N., Orlando, E., Ormes, J. F., Ozaki, M., Paneque, D., Panetta, J. H., Parent, D., Pavlidou, V., Pearson, T. J., Pelassa, V., Pepe, M., Pesce-Rollins, M., Piron, F., Porter, T. A., Rainò, S., Rando, R., Razzano, M., Razzaque, S., Readhead, A., Reimer, A., Reimer, O., Reposeur, T., Richards, J. L., Ritz, S., Rochester, L. S., Rodriguez, A. Y., Romani, R. W., Roth, M., Ryde, F., Sadrozinski, H., Sanchez, D., Sander, A., Saz Parkinson, P. M., Scargle, J. D., Sgrò, C., Shaw, M. S., Siskind, E. J., Smith, D. A., Smith, P. D., Spandre, G., Spinelli, P., Stevenson, M., Strickman,

- M. S., Suson, D. J., Tajima, H., Takahashi, H., Tanaka, T., Thayer, J. B., Thayer, J. G., Thompson, D. J., Tibaldo, L., Tibolla, O., Torres, D. F., Tosti, G., Tramacere, A., Ubertini, P., Uchiyama, Y., Usher, T. L., Vasileiou, V., Vilchez, N., Vitale, V., Waite, A. P., Wang, P., Winer, B. L., Wood, K. S., Yasuda, H., Ylinen, T., Zensus, J. A., Ziegler, M., The FERMI LAT Collaboration, Angelakis, E., Hovatta, T., Hoversten, E., Ikejiri, Y., Kawabata, K. S., Kovalev, Y. Y., Kovalev, Y. A., Krichbaum, T. P., Lister, M. L., Lähteenmäki, A., Marchili, N., Ogle, P., Pagani, C., Pushkarev, A. B., Sakimoto, K., Sasada, M., Tornikoski, M., Uemura, M., Yamanaka, M., and Yamashita, T. (2010d). PKS 1502+106: A New and Distant Gamma-ray Blazar in Outburst Discovered by the Fermi Large Area Telescope. *Astrophysical Journal*, 710:810–827.
- Abdo, A. A., Ackermann, M., Ajello, M., Atwood, W. B., Axelsson, M., Baldini, L., Ballet, J., Barbiellini, G., Bastieri, D., Baughman, B. M., Bechtol, K., Bellazzini, R., Blandford, R. D., Bloom, E. D., Bonamente, E., Borgland, A. W., Bouvier, A., Bregeon, J., Brez, A., Brigida, M., Bruel, P., Burnett, T. H., Caliendo, G. A., Cameron, R. A., Caraveo, P. A., Casandjian, J. M., Cavazzuti, E., Cecchi, C., Charles, E., Chekhtman, A., Chen, A. W., Cheung, C. C., Chiang, J., Ciprini, S., Claus, R., Cohen-Tanugi, J., Colafrancesco, S., Collmar, W., Cominsky, L. R., Conrad, J., Costamante, L., Cutini, S., Dermer, C. D., de Angelis, A., de Palma, F., Digel, S. W., do Couto e Silva, E., Drell, P. S., Dubois, R., Dumora, D., Farnier, C., Favuzzi, C., Fegan, S. J., Ferrara, E. C., Finke, J., Focke, W. B., Foschini, L., Frailis, M., Fuhrmann, L., Fukazawa, Y., Funk, S., Fusco, P., Gargano, F., Gasparrini, D., Gehrels, N., Germani, S., Giebels, B., Giglietto, N., Giommi, P., Giordano, F., Giroletti, M., Glanzman, T., Godfrey, G., Grenier, I. A., Grondin, M., Grove, J. E., Guillemot, L., Guiriec, S., Hanabata, Y., Harding, A. K., Hartman, R. C., Hayashida, M., Hays, E., Healey, S. E., Horan, D., Hughes, R. E., Jóhannesson, G., Johnson, A. S., Johnson, R. P., Johnson, T. J., Johnson, W. N., Kadler, M., Kamae, T., Katagiri, H., Kataoka, J., Kerr, M., Knödseder, J., Kocian, M. L., Kuehn, F., Kuss, M., Lande, J., Latronico, L., Lemoine-Goumard, M., Longo, F., Loparco, F., Lott, B., Lovellette, M. N., Lubrano, P., Madejski, G. M., Makeev, A., Massaro, E., Mazziotta, M. N., McConville, W., McEnery, J. E., McGlynn, S., Meurer, C., Michelson, P. F., Mitthumsiri, W., Mizuno, T., Moiseev, A. A., Monte, C., Monzani, M. E., Moretti, E., Morselli, A., Moskalenko, I. V., Murgia, S., Nolan, P. L., Norris, J. P., Nuss, E., Ohsugi, T., Omodei, N., Orlando, E., Ormes, J. F., Ozaki, M., Paneque, D., Panetta, J. H., Parent, D., Pelassa, V., Pepe, M., Pesce-Rollins, M., Piron, F., Porter, T. A., Rainò, S., Rando, R., Razzano, M., Razzaque, S., Reimer, A., Reimer, O., Reposeur, T., Reyes, L. C., Ritz, S., Rochester, L. S., Rodriguez, A. Y., Romani, R. W., Ryde, F., Sadrozinski, H., Sanchez, D., Sander, A., Saz Parkinson, P. M., Scargle, J. D., Schalk, T. L., Sellerholm, A., Sgrò, C., Shaw, M. S., Smith, D. A., Smith, P. D., Spandre, G., Spinelli, P., Starck, J., Strickman, M. S., Suson, D. J., Tajima, H., Takahashi, H., Takahashi, T., Tanaka, T., Taylor, G. B., Thayer, J. B., Thayer, J. G., Thompson, D. J., Tibaldo, L., Torres, D. F., Tosti, G., Tramacere, A., Uchiyama, Y., Usher, T. L., Vilchez, N., Villata, M., Vitale, V., Waite, A. P., Winer, B. L., Wood, K. S., Ylinen, T., and Ziegler, M. (2009b). Bright Active Galactic Nuclei Source List from the First Three Months of the Fermi Large Area Telescope All-Sky Survey. *The Astrophysical Journal*, 700:597–622.
- Abdo, A. A., Ackermann, M., Ajello, M., Atwood, W. B., Axelsson, M., Baldini, L., Bal-

let, J., Barbiellini, G., Bastieri, D., Bechtol, K., Bellazzini, R., Berenji, B., Blandford, R. D., Bloom, E. D., Bonamente, E., Borgland, A. W., Bregeon, J., Brez, A., Brigida, M., Bruel, P., Burnett, T. H., Caliendo, G. A., Cameron, R. A., Cannon, A., Caraveo, P. A., Casandjian, J. M., Cavazzuti, E., Cecchi, C., Çelik, Ö., Charles, E., Cheung, C. C., Chiang, J., Ciprini, S., Claus, R., Cohen-Tanugi, J., Colafrancesco, S., Conrad, J., Costamante, L., Cutini, S., Davis, D. S., Dermer, C. D., de Angelis, A., de Palma, F., Digel, S. W., Donato, D., Silva, E. d. C. e., Drell, P. S., Dubois, R., Dumora, D., Edmonds, Y., Farnier, C., Favuzzi, C., Fegan, S. J., Finke, J., Focke, W. B., Fortin, P., Frailis, M., Fukazawa, Y., Funk, S., Fusco, P., Gargano, F., Gasparrini, D., Gehrels, N., Georganopoulos, M., Germani, S., Giebels, B., Giglietto, N., Giommi, P., Giordano, F., Giroletti, M., Glanzman, T., Godfrey, G., Grenier, I. A., Grondin, M., Grove, J. E., Guillemot, L., Guiriec, S., Hanabata, Y., Harding, A. K., Hayashida, M., Hays, E., Horan, D., Jóhannesson, G., Johnson, A. S., Johnson, R. P., Johnson, T. J., Johnson, W. N., Kamae, T., Katagiri, H., Kataoka, J., Kawai, N., Kerr, M., Knödseder, J., Kocian, M. L., Kuss, M., Lande, J., Latronico, L., Lemoine-Goumard, M., Longo, F., Loparco, F., Lott, B., Lovellette, M. N., Lubrano, P., Madejski, G. M., Makeev, A., Mazziotta, M. N., Mc Conville, W., Mc Enery, J. E., Meurer, C., Michelson, P. F., Mitthumsiri, W., Mizuno, T., Moiseev, A. A., Monte, C., Monzani, M. E., Morselli, A., Moskalenko, I. V., Murgia, S., Nolan, P. L., Norris, J. P., Nuss, E., Ohsugi, T., Omodei, N., Orlando, E., Ormes, J. F., Ozaki, M., Paneque, D., Panetta, J. H., Parent, D., Pelassa, V., Pepe, M., Pesce-Rollins, M., Piron, F., Porter, T. A., Rainò, S., Rando, R., Razzano, M., Reimer, A., Reimer, O., Reposeur, T., Ritz, S., Rochester, L. S., Rodriguez, A. Y., Romani, R. W., Roth, M., Ryde, F., Sadrozinski, H., Sambruna, R., Sanchez, D., Sander, A., Saz Parkinson, P. M., Scargle, J. D., Sgrò, C., Shaw, M. S., Smith, D. A., Smith, P. D., Spandre, G., Spinelli, P., Strickman, M. S., Suson, D. J., Tajima, H., Takahashi, H., Tanaka, T., Taylor, G. B., Thayer, J. B., Thompson, D. J., Tibaldo, L., Torres, D. F., Tosti, G., Tramacere, A., Uchiyama, Y., Usher, T. L., Vasileiou, V., Vilchez, N., Waite, A. P., Wang, P., Winer, B. L., Wood, K. S., Ylinen, T., Ziegler, M., Harris, D. E., Marsaro, F., and Stawarz, Ł. (2009c). Fermi Large Area Telescope Gamma-Ray Detection of the Radio Galaxy M87. *Astrophysical Journal*, 707:55–60.

Abdo, A. A., Ackermann, M., Ajello, M., Baldini, L., Ballet, J., Barbiellini, G., Bastieri, D., Bechtol, K., Bellazzini, R., Berenji, B., Blandford, R. D., Bloom, E. D., Bonamente, E., Borgland, A. W., Bouvier, A., Bregeon, J., Brez, A., Brigida, M., Bruel, P., Burnett, T. H., Buson, S., Caliendo, G. A., Cameron, R. A., Cannon, A., Caraveo, P. A., Carrigan, S., Casandjian, J. M., Cavazzuti, E., Cecchi, C., Çelik, Ö., Charles, E., Chekhtman, A., Cheung, C. C., Chiang, J., Ciprini, S., Claus, R., Cohen-Tanugi, J., Conrad, J., Costamante, L., Dermer, C. D., de Angelis, A., de Palma, F., Silva, E. d. C. e., Drell, P. S., Dubois, R., Dumora, D., Farnier, C., Favuzzi, C., Fegan, S. J., Focke, W. B., Frailis, M., Fukazawa, Y., Funk, S., Fusco, P., Gargano, F., Gasparrini, D., Gehrels, N., Germani, S., Giglietto, N., Giommi, P., Giordano, F., Glanzman, T., Godfrey, G., Grenier, I. A., Grondin, M., Guiriec, S., Hayashida, M., Hays, E., Hill, A. B., Horan, D., Hughes, R. E., Jóhannesson, G., Johnson, A. S., Johnson, W. N., Kamae, T., Katagiri, H., Kataoka, J., Kawai, N., Knödseder, J., Kuss, M., Lande, J., Larsson, S., Latronico, L., Lemoine-Goumard, M., Lena Garde, M., Longo, F., Loparco, F., Lott, B., Lovellette, M. N., Lubrano, P., Madejski, G. M., Makeev, A.,

- Mansutti, O., Massaro, E., Mazziotta, M. N., McConville, W., McEnery, J. E., Meurer, C., Michelson, P. F., Mitthumsiri, W., Mizuno, T., Moiseev, A. A., Monte, C., Monzani, M. E., Morselli, A., Moskalenko, I. V., Murgia, S., Nolan, P. L., Norris, J. P., Nuss, E., Ohsugi, T., Omodei, N., Orlando, E., Ormes, J. F., Paneque, D., Panetta, J. H., Pelassa, V., Pepe, M., Pesce-Rollins, M., Piron, F., Porter, T. A., Rainò, S., Rando, R., Razzano, M., Reimer, A., Reimer, O., Ritz, S., Rodriguez, A. Y., Romani, R. W., Roth, M., Ryde, F., Sadrozinski, H., Sander, A., Scargle, J. D., Schalk, T. L., Sgrò, C., Siskind, E. J., Smith, P. D., Spandre, G., Spinelli, P., Starck, J., Strickman, M. S., Suson, D. J., Tajima, H., Takahashi, H., Takahashi, T., Tanaka, T., Thayer, J. B., Thayer, J. G., Thompson, D. J., Tibaldo, L., Torres, D. F., Tosti, G., Tramacere, A., Uchiyama, Y., Usher, T. L., Vasileiou, V., Vilchez, N., Vitale, V., Waite, A. P., Wang, P., Wehrle, A. E., Winer, B. L., Wood, K. S., Yang, Z., Ylinen, T., and Ziegler, M. (2010e). Fermi-Large Area Telescope Observations of the Exceptional Gamma-ray Outbursts of 3C 273 in 2009 September. *Astrophysical Journal, Letters*, 714:L73–L78.
- Acciari, V. A., Aliu, E., Arlen, T., Aune, T., Beilicke, M., Benbow, W., Boltuch, D., Bradbury, S. M., Buckley, J. H., Bugaev, V., Byrum, K., Cannon, A., Cesarini, A., Chow, Y. C., Ciupik, L., Cogan, P., Cui, W., Dickherber, R., Duke, C., Finley, J. P., Finnegan, G., Fortin, P., Fortson, L., Furniss, A., Galante, N., Gall, D., Gillanders, G. H., Godambe, S., Grube, J., Guenette, R., Gyuk, G., Hanna, D., Holder, J., Hui, C. M., Humensky, T. B., Imran, A., Kaaret, P., Karlsson, N., Kertzman, M., Kieda, D., Konopelko, A., Krawczynski, H., Krennrich, F., Lang, M. J., LeBohec, S., Maier, G., McArthur, S., McCann, A., McCutcheon, M., Millis, J., Moriarty, P., Ong, R. A., Otte, A. N., Pandel, D., Perkins, J. S., Pichel, A., Pohl, M., Quinn, J., Ragan, K., Reyes, L. C., Reynolds, P. T., Roache, E., Rose, H. J., Rovero, A. C., Schroedter, M., Sembroski, G. H., Senturk, G. D., Smith, A. W., Steele, D., Swordy, S. P., Theiling, M., Thibadeau, S., Varlotta, A., Vincent, S., Wagner, R. G., Wakely, S. P., Ward, J. E., Weekes, T. C., Weinstein, A., Weisgarber, T., Williams, D. A., Wissel, S., Wood, M., Zitzer, B., Harris, D. E., and Massaro, F. (2010). Veritas 2008-2009 Monitoring of the Variable Gamma-ray Source M87. *The Astrophysical Journal*, 716:819–824.
- Acciari, V. A., Aliu, E., Arlen, T., Bautista, M., Beilicke, M., Benbow, W., Bradbury, S. M., Buckley, J. H., Bugaev, V., Butt, Y., Byrum, K., Cannon, A., Celik, O., Cesarini, A., Chow, Y. C., Ciupik, L., Cogan, P., Cui, W., Dickherber, R., Fegan, S. J., Finley, J. P., Fortin, P., Fortson, L., Furniss, A., Gall, D., Gillanders, G. H., Grube, J., Guenette, R., Gyuk, G., Hanna, D., Holder, J., Horan, D., Hui, C. M., Humensky, T. B., Imran, A., Kaaret, P., Karlsson, N., Kieda, D., Kildea, J., Konopelko, A., Krawczynski, H., Krennrich, F., Lang, M. J., LeBohec, S., Maier, G., McCann, A., McCutcheon, M., Millis, J., Moriarty, P., Ong, R. A., Otte, A. N., Pandel, D., Perkins, J. S., Petry, D., Pohl, M., Quinn, J., Ragan, K., Reyes, L. C., Reynolds, P. T., Roache, E., Roache, E., Rose, H. J., Schroedter, M., Sembroski, G. H., Smith, A. W., Swordy, S. P., Theiling, M., Toner, J. A., Varlotta, A., Vincent, S., Wakely, S. P., Ward, J. E., Weekes, T. C., Weinstein, A., Williams, D. A., Wissel, S., Wood, M., Walker, R. C., Davies, F., Hardee, P. E., Junor, W., Ly, C., Aharonian, F., Akhperjanian, A. G., Anton, G., Barres de Almeida, U., Bazer-Bachi, A. R., Becherini, Y., Behera, B., Bernlöhr, K., Bochow, A., Boisson, C., Bolmont, J., Borrel, V., Brucker, J., Brun, F., Brun, P., Bühler, R., Bulik, T., Büsching, I., Boutelier, T., Chadwick, P. M., Charbonnier, A., Chaves, R. C. G., Cheesebrough,

- A., Chounet, L., Clapson, A. C., Coignet, G., Dalton, M., Daniel, M. K., Davids, I. D., Degrange, B., Deil, C., Dickinson, H. J., Djannati-Ataï, A., Domainko, W., Drury, L. O. ., Dubois, F., Dubus, G., Dyks, J., Dyrda, M., Egberts, K., Emmanoulopoulos, D., Espigat, P., Farnier, C., Feinstein, F., Fiasson, A., Förster, A., Fontaine, G., Füßling, M., Gabici, S., Gallant, Y. A., Gérard, L., Gerbig, D., Giebels, B., Glicenstein, J. F., Glück, B., Goret, P., Göhring, D., Hauser, D., Hauser, M., Heinz, S., Heinzelmann, G., Henri, G., Hermann, G., Hinton, J. A., Hoffmann, A., Hofmann, W., Holleran, M., Hoppe, S., Horns, D., Jacholkowska, A., de Jager, O. C., Jahn, C., Jung, I., Katarzyński, K., Katz, U., Kaufmann, S., Kendziorra, E., Kerschhaggl, M., Khangulyan, D., Khélifi, B., Keogh, D., Kluźniak, W., Kneiske, T., Komin, N., Kosack, K., Lamanna, G., Lenain, J., Lohse, T., Marandon, V., Martin, J. M., Martineau-Huynh, O., Marcowith, A., Maurin, D., McComb, T. J. L., Medina, M. C., Moderski, R., Moulin, E., Naumann-Godo, M., de Naurois, M., Nedbal, D., Nekrassov, D., Nicholas, B., Niemiec, J., Nolan, S. J., Ohm, S., Olive, J., Wilhelmi, E. d. O., Orford, K. J., Ostrowski, M., Panter, M., Arribas, M. P., Pedalletti, G., Pelletier, G., Petrucci, P., Pita, S., Pühlhofer, G., Punch, M., Quirrenbach, A., Raubenheimer, B. C., Raue, M., Rayner, S. M., Renaud, M., Rieger, F., Ripken, J., Rob, L., Rosier-Lees, S., Rowell, G., Rudak, B., Rulten, C. B., Ruppel, J., Sahakian, V., Santangelo, A., Schlickeiser, R., Schöck, F. M., Schröder, R., Schwanke, U., Schwarzburg, S., Schwemmer, S., Shalchi, A., Sikora, M., Skilton, J. L., Sol, H., Spangler, D., Stawarz, Ł., Steenkamp, R., Stegmann, C., Stinzing, F., Superina, G., Szostek, A., Tam, P. H., Tavernet, J., Terrier, R., Tibolla, O., Tluczykont, M., van Eldik, C., Vasileiadis, G., Venter, C., Venter, L., Vialle, J. P., Vincent, P., Vivier, M., Völk, H. J., Volpe, F., Wagner, S. J., Ward, M., Zdziarski, A. A., Zech, A., Anderhub, H., Antonelli, L. A., Antoranz, P., Backes, M., Baixeras, C., Balestra, S., Barrio, J. A., Bastieri, D., González, J. B., Becker, J. K., Bednarek, W., Berger, K., Bernardini, E., Biland, A., Bock, R. K., Bonnoli, G., Bordas, P., Tridon, D. B., Bosch-Ramon, V., Bose, D., Braun, I., Bretz, T., Britvitch, I., Camara, M., Carmona, E., Commichau, S., Contreras, J. L., Cortina, J., Costado, M. T., Covino, S., Curtef, V., Dazzi, F., De Angelis, A., Cea del Pozo, E. D., Mendez, C. D., De los Reyes, R., De Lotto, B., De Maria, M., De Sabata, F., Dominguez, A., Dorner, D., Doro, M., Elsaesser, D., Errando, M., Ferenc, D., Fernández, E., Firpo, R., Fonseca, M. V., Font, L., Galante, N., López, R. J. G., Garczarczyk, M., Gaug, M., Goebel, F., Hadasch, D., Hayashida, M., Herrero, A., Hildebrand, D., Höhne-Mönch, D., Hose, J., Hsu, C. C., Jogler, T., Kranich, D., La Barbera, A., Laille (2009). Radio Imaging of the Very-High-Energy γ -Ray Emission Region in the Central Engine of a Radio Galaxy. *Science*, 325:444.
- Agudo, I., Gómez, J. L., Gabuzda, D. C., Marscher, A. P., Jorstad, S. G., and Alberdi, A. (2006). The milliarcsecond-scale jet of PKS 0735+178 during quiescence. *Astronomy and Astrophysics*, 453:477–486.
- Aharonian, F., Akhperjanian, A. G., Bazer-Bachi, A. R., Beilicke, M., Benbow, W., Berge, D., Bernlöhr, K., Boisson, C., Bolz, O., Borrel, V., Braun, I., Brown, A. M., Bühler, R., Büsching, I., Carrigan, S., Chadwick, P. M., Chounet, L., Coignet, G., Cornils, R., Costamante, L., Degrange, B., Dickinson, H. J., Djannati-Ataï, A., Drury, L. O., Dubus, G., Egberts, K., Emmanoulopoulos, D., Espigat, P., Feinstein, F., Ferrero, E., Fiasson, A., Fontaine, G., Funk, S., Funk, S., Füßling, M., Gallant, Y. A., Giebels, B., Glicenstein, J. F., Goret, P., Hadjichristidis, C., Hauser, D., Hauser, M., Heinzelmann,

- G., Henri, G., Hermann, G., Hinton, J. A., Hoffmann, A., Hofmann, W., Holleran, M., Hoppe, S., Horns, D., Jacholkowska, A., de Jager, O. C., Kendziorra, E., Kerschhaggl, M., Khélifi, B., Komin, N., Konopelko, A., Kosack, K., Lamanna, G., Latham, I. J., Le Gallou, R., Lemièrre, A., Lemoine-Goumard, M., Lenain, J., Lohse, T., Martin, J. M., Martineau-Huynh, O., Marcowith, A., Masterson, C., Maurin, G., McComb, T. J. L., Moulin, E., de Naurois, M., Nedbal, D., Nolan, S. J., Noutsos, A., Orford, K. J., Osborne, J. L., Ouchrif, M., Panter, M., Pelletier, G., Pita, S., Pühlhofer, G., Punch, M., Ranchon, S., Raubenheimer, B. C., Raue, M., Rayner, S. M., Reimer, A., Ripken, J., Rob, L., Rolland, L., Rosier-Lees, S., Rowell, G., Sahakian, V., Santangelo, A., Saugé, L., Schlenker, S., Schlickeiser, R., Schröder, R., Schwanke, U., Schwarzburg, S., Schwemmer, S., Shalchi, A., Sol, H., Spangler, D., Spanier, F., Steenkamp, R., Stegmann, C., Superina, G., Tam, P. H., Tavernet, J., Terrier, R., Tluczykont, M., van Eldik, C., Vasileiadis, G., Venter, C., Vialle, J. P., Vincent, P., Völk, H. J., Wagner, S. J., and Ward, M. (2006). Fast Variability of Tera-Electron Volt γ Rays from the Radio Galaxy M87. *Science*, 314:1424–1427.
- Alberdi, A., Gómez, J. L., Marcaide, J. M., Marscher, A. P., and Pérez-Torres, M. A. (2000). 4C 39.25: Witnessing the interaction between a moving and a stationary component. *Astronomy and Astrophysics*, 361:529–534.
- Alberdi, A., Krichbaum, T. P., Graham, D. A., Greve, A., Grewing, M., Marcaide, J. M., Witzel, A., Booth, R. S., Baath, L. B., Colomer, F., Doeleman, S., Marscher, A. P., Rogers, A. E. E., Schalinski, C. J., and Standke, K. (1997). The high-frequency compact radio structure of the peculiar quasar 4C 39.25. *Astronomy and Astrophysics*, 327:513–521.
- Albert, J., Aliu, E., Anderhub, H., Antoranz, P., Armada, A., Baixeras, C., Barrio, J. A., Bartko, H., Bastieri, D., Becker, J. K., Bednarek, W., Berger, K., Bigongiari, C., Biland, A., Bock, R. K., Bordas, P., Bosch-Ramon, V., Bretz, T., Britvitch, I., Camara, M., Carmona, E., Chilingarian, A., Coarasa, J. A., Commichau, S., Contreras, J. L., Cortina, J., Costado, M. T., Curtef, V., Danielyan, V., Dazzi, F., De Angelis, A., Delgado, C., de los Reyes, R., De Lotto, B., Domingo-Santamaría, E., Dorner, D., Doro, M., Errando, M., Fagiolini, M., Ferenc, D., Fernández, E., Firpo, R., Flix, J., Fonseca, M. V., Font, L., Fuchs, M., Galante, N., García-López, R., Garczarczyk, M., Gaug, M., Giller, M., Goebel, F., Hakobyan, D., Hayashida, M., Hengstebeck, T., Herrero, A., Höhne, D., Hose, J., Hsu, C. C., Jacon, P., Jogler, T., Kosyra, R., Kranich, D., Kritzer, R., Laille, A., Lindfors, E., Lombardi, S., Longo, F., López, J., López, M., Lorenz, E., Majumdar, P., Maneva, G., Mannheim, K., Mansutti, O., Mariotti, M., Martínez, M., Mazin, D., Merck, C., Meucci, M., Meyer, M., Miranda, J. M., Mirzoyan, R., Mizobuchi, S., Moralejo, A., Nilsson, K., Ninkovic, J., Oña-Wilhelmi, E., Otte, N., Oya, I., Paneque, D., Panniello, M., Paoletti, R., Paredes, J. M., Pasanen, M., Pascoli, D., Pauss, F., Pegna, R., Persic, M., Peruzzo, L., Piccioli, A., Poller, M., Prandini, E., Puchades, N., Raymers, A., Rhode, W., Ribó, M., Rico, J., Rissi, M., Robert, A., Rügamer, S., Saggion, A., Sánchez, A., Sartori, P., Scalzotto, V., Scapin, V., Schmitt, R., Schweizer, T., Shayduk, M., Shinozaki, K., Shore, S. N., Sidro, N., Sillanpää, A., Sobczynska, D., Stamerra, A., Stark, L. S., Takalo, L., Temnikov, P., Tesaro, D., Teshima, M., Tonello, N., Torres, D. F., Turini, N., Vankov, H., Vitale, V., Wagner, R. M., Wibig, T., Wittek,

- W., Zandanel, F., Zanin, R., and Zapatero, J. (2007). Discovery of Very High Energy γ -Ray Emission from the Low-Frequency-peaked BL Lacertae Object BL Lacertae. *Astrophysical Journal*, 666:L17–L20.
- Allen, D. A. (1976). An attempt to determine the circumstellar reddening law. *Monthly Notices of the Royal Astronomical Society*, 174:29P–33P.
- Aller, H. D., Aller, M. F., Latimer, G. E., and Hodge, P. E. (1985). Spectra and linear polarizations of extragalactic variable sources at centimeter wavelengths. *Astrophysical Journal Supplement Series*, 59:513–768.
- Aller, H. D., Hodge, P. E., and Aller, M. F. (1981). Radio polarization rotators - BL Lacertae and 0727-115. *Astrophysical Journal, Letters*, 248:L5–L8.
- Aller, M. F., Aller, H. D., and Hughes, P. A. (1996). Centimeter-wavelength Flux and Polarization Variability as a Probe of the Physical Conditions in AGN (I). In H. R. Miller, J. R. Webb, & J. C. Noble, editor, *Blazar Continuum Variability*, volume 110 of *Astronomical Society of the Pacific Conference Series*, page 193.
- Aller, M. F., Aller, H. D., and Hughes, P. A. (2003). Pearson-Readhead Survey Sources. II. The Long-Term Centimeter-Band Total Flux and Linear Polarization Properties of a Complete Radio Sample. *The Astrophysical Journal*, 586:33–51.
- An, T., Hong, X. Y., Venturi, T., Jiang, D. R., and Wang, W. H. (2004). Extreme superluminal motion in the curved Jet of γ ASTROBJ γ PKS 1502+106 γ ASTROBJ γ . *Astronomy and Astrophysics*, 421:839–846.
- Andruchow, I., Romero, G. E., and Cellone, S. A. (2005). Polarization microvariability of BL Lacertae objects. *Astronomy and Astrophysics*, 442:97–107.
- Angel, J. R. P., Boroson, T. A., Adams, M. T., Duerr, R. E., Glampapa, M. S., Cresham, M. S., Gural, P. S., Hubbard, E. N., Kopriva, D. A., and Moore, R. L. (1978). On the polarization and mass of BL Lac objects. In A. M. Wolfe, editor, *BL Lac Objects*, pages 117–146.
- Angelakis, E., Fuhrmann, L., Nestoras, I., Zensus, J. A., Marchili, N., Pavlidou, V., and Krichbaum, T. P. (2010). The F-GAMMA program: multi-wavelength AGN studies in the Fermi-GST era. *Proceedings of the Workshop "Fermi meets Jansky - AGN in Radio and Gamma-Rays"*, Savolainen, T., Ros, E., Porcas, R.W. and Zensus, J.A. (eds.), *MPIfR, Bonn, June 21-23 2010*, page 81.
- Antón, S., Browne, I. W. A., Marchã, M. J. M., Bondi, M., and Polatidis, A. (2004). The spectral energy distributions of the revised 200-mJy sample. *Monthly Notices of the Royal Astronomical Society*, 352:673–688.
- Antonucci, R. (1993). Unified models for active galactic nuclei and quasars. *Annual review of astronomy and astrophysics*, 31:473–521.
- Antonucci, R. R. J. and Miller, J. S. (1985). Spectropolarimetry and the nature of NGC 1068. *Astrophysical Journal*, 297:621–632.

- Antonucci, R. R. J. and Ulvestad, J. S. (1985). Extended radio emission and the nature of blazars. *Astrophysical Journal*, 294:158–182.
- Asada, K., Inoue, M., Kamenno, S., and Nagai, H. (2008a). Time Variation of the Rotation Measure Gradient in the 3C 273 Jet. *Astrophysical Journal*, 675:79–82.
- Asada, K., Inoue, M., Nakamura, M., Kamenno, S., and Nagai, H. (2008b). Multifrequency Polarimetry of the NRAO 140 Jet: Possible Detection of a Helical Magnetic Field and Constraints on Its Pitch Angle. *Astrophysical Journal*, 682:798–802.
- Atoyan, A. and Dermer, C. D. (2008). Gamma Rays from Ultra-High-Energy Cosmic Rays in Cygnus A. *Astrophysical Journal Supplement Series*, 687:L75–L78.
- Attridge, J. M., Roberts, D. H., and Wardle, J. F. C. (1999). Radio Jet-Ambient Medium Interactions on Parsec Scales in the Blazar 1055+018. *Astrophysical Journal*, 518:L87–L90.
- Atwood, W. B., Abdo, A. A., Ackermann, M., Althouse, W., Anderson, B., Axelsson, M., Baldini, L., Ballet, J., Band, D. L., Barbiellini, G., Bartelt, J., Bastieri, D., Baughman, B. M., Bechtol, K., Bédérède, D., Bellardi, F., Bellazzini, R., Berenji, B., Bignami, G. F., Bisello, D., Bissaldi, E., Blandford, R. D., Bloom, E. D., Bogart, J. R., Bonamente, E., Bonnell, J., Borgland, A. W., Bouvier, A., Bregeon, J., Brez, A., Brigida, M., Bruel, P., Burnett, T. H., Busetto, G., Caliandro, G. A., Cameron, R. A., Caraveo, P. A., Carius, S., Carlson, P., Casandjian, J. M., Cavazzuti, E., Ceccanti, M., Cecchi, C., Charles, E., Chekhtman, A., Cheung, C. C., Chiang, J., Chipaux, R., Cillis, A. N., Ciprini, S., Claus, R., Cohen-Tanugi, J., Condamore, S., Conrad, J., Corbet, R., Corucci, L., Costamante, L., Cutini, S., Davis, D. S., Decotigny, D., DeKlotz, M., Dermer, C. D., de Angelis, A., Digel, S. W., do Couto e Silva, E., Drell, P. S., Dubois, R., Dumora, D., Edmonds, Y., Fabiani, D., Farnier, C., Favuzzi, C., Flath, D. L., Fleury, P., Focke, W. B., Funk, S., Fusco, P., Gargano, F., Gasparrini, D., Gehrels, N., Gentit, F., Germani, S., Giebels, B., Giglietto, N., Giommi, P., Giordano, F., Glanzman, T., Godfrey, G., Grenier, I. A., Grondin, M., Grove, J. E., Guillemot, L., Guiriec, S., Haller, G., Harding, A. K., Hart, P. A., Hays, E., Healey, S. E., Hirayama, M., Hjalmarsdotter, L., Horn, R., Hughes, R. E., Jóhannesson, G., Johansson, G., Johnson, A. S., Johnson, R. P., Johnson, T. J., Johnson, W. N., Kamae, T., Katagiri, H., Kataoka, J., Kavelaars, A., Kawai, N., Kelly, H., Kerr, M., Klamra, W., Knödlseeder, J., Kocian, M. L., Komin, N., Kuehn, F., Kuss, M., Landriu, D., Latronico, L., Lee, B., Lee, S., Lemoine-Goumard, M., Lionetto, A. M., Longo, F., Loparco, F., Lott, B., Lovellette, M. N., Lubrano, P., Madejski, G. M., Makeev, A., Marangelli, B., Massai, M. M., Mazziotta, M. N., McEnery, J. E., Menon, N., Meurer, C., Michelson, P. F., Minuti, M., Mirizzi, N., Mitthumsiri, W., Mizuno, T., Moiseev, A. A., Monte, C., Monzani, M. E., Moretti, E., Morselli, A., Moskalenko, I. V., Murgia, S., Nakamori, T., Nishino, S., Nolan, P. L., Norris, J. P., Nuss, E., Ohno, M., Ohsugi, T., Omodei, N., Orlando, E., Ormes, J. F., Paccagnella, A., Paneque, D., Panetta, J. H., Parent, D., Pearce, M., Pepe, M., Perazzo, A., Pesce-Rollins, M., Picozza, P., Pieri, L., Pinchera, M., Piron, F., Porter, T. A., Poupard, L., Rainò, S., Rando, R., Rapposelli, E., Razzano, M., Reimer, A., Reimer, O., Reposeur, T., Reyes, L. C., Ritz, S., Rochester, L. S., Rodriguez, A. Y., Romani, R. W., Roth, M., Russell, J. J., Ryde, F., Sabatini, S., Sadrozinski, H., Sanchez, D.,

- Sander, A., Sapozhnikov, L., Parkinson, P. M. S., Scargle, J. D., Schalk, T. L., Scolieri, G., Sgrò, C., Share, G. H., Shaw, M., Shimokawabe, T., Shrader, C., Sierpowska-Bartosik, A., Siskind, E. J., Smith, D. A., Smith, P. D., Spandre, G., Spinelli, P., Starck, J., Stephens, T. E., Strickman, M. S., Strong, A. W., Suson, D. J., Tajima, H., Takahashi, H., Takahashi, T., Tanaka, T., Tenze, A., Tether, S., Thayer, J. B., Thayer, J. G., Thompson, D. J., Tibaldo, L., Tibolla, O., Torres, D. F., Tosti, G., Tramacere, A., Turri, M., Usher, T. L., Vilchez, N., Vitale, V., Wang, P., Watters, K., Winer, B. L., Wood, K. S., Ylinen, T., and Ziegler, M. (2009). The Large Area Telescope on the Fermi Gamma-Ray Space Telescope Mission. *Astrophysical Journal*, 697:1071–1102.
- Baade, W. (1956). Polarization in the Jet of Messier 87. *Astrophysical Journal*, 123:550–551.
- Bach, U., Krichbaum, T. P., Kraus, A., Witzel, A., and Zensus, J. A. (2006a). Space-VLBI polarimetry of the BL Lacertae object S5 0716+714: rapid polarization variability in the VLBI core. *Astronomy and Astrophysics*, 452:83–95.
- Bach, U., Raiteri, C. M., Villata, M., Fuhrmann, L., Buemi, C. S., Larionov, V. M., Letog, P., Arkharov, A. A., Coloma, J. M., di Paola, A., Dolci, M., Efimova, N., Forné, E., Ibrahimov, M. A., Hagen-Thorn, V., Konstantinova, T., Kopatskaya, E., Lanteri, L., Kurtanidze, O. M., Maccaferri, G., Nikolashvili, M. G., Orlati, A., Ros, J. A., Tosti, G., Trigilio, C., and Umama, G. (2007). Multi-frequency monitoring of γ -ray loud blazars. I. Light curves and spectral energy distributions. *Astronomy and Astrophysics*, 464:175–186.
- Bach, U., Villata, M., Raiteri, C. M., Agudo, I., Aller, H. D., Aller, M. F., Denn, G., Gómez, J. L., Jorstad, S., Marscher, A., Mutel, R. L., and Teräsranta, H. (2006b). Structure and flux variability in the VLBI jet of BL Lacertae during the WEBT campaigns (1995-2004). *Astronomy and Astrophysics*, 456:105–115.
- Baes, M., Clemens, M., Xilouris, E. M., Fritz, J., Cotton, W. D., Davies, J. I., Bendo, G. J., Bianchi, S., Cortese, L., de Looze, I., Pohlen, M., Verstappen, J., Böhringer, H., Bomans, D. J., Boselli, A., Corbelli, E., Dariush, A., di Serego Alighieri, S., Fadda, D., Garcia-Appadoo, D. A., Gavazzi, G., Giovanardi, C., Grossi, M., Hughes, T. M., Hunt, L. K., Jones, A. P., Madden, S., Pierini, D., Sabatini, S., Smith, M. W. L., Vlahakis, C., and Zibetti, S. (2010). The Herschel Virgo Cluster Survey . VI. The far-infrared view of M 87. *Astronomy and Astrophysics*, 518:L53.
- Bailyn, C. and Muir, G. (2009). Continued Optical Activity in PKS 2052-474. *The Astronomer's Telegram*, 2162:1.
- Baldwin, J. A. (1975). The Spectra of 3c 273 and PKS 0736+01. *Astrophysical Journal Letters*, 196:L91.
- Balucinska-Church, M. and McCammon, D. (1992). Photoelectric absorption cross sections with variable abundances. *Astrophysical Journal*, 400:699.
- Bałucińska-Church, M., Ostrowski, M., Stawarz, ł., and Church, M. J. (2005). Discovery of hard X-ray features around the hotspots of Cygnus A. *Monthly Notices of the Royal Astronomical Society*, 357:L6–L10.

- Barthel, P. D., Conway, J. E., Myers, S. T., Pearson, T. J., and Readhead, A. C. S. (1995). New superluminal quasar 1633 + 382 and the blazar-gamma-ray connection. *Astrophysical Journal*, 444:L21–L24.
- Bassani, L., Molina, M., Malizia, A., Stephen, J. B., Bird, A. J., Bazzano, A., Bélanger, G., Dean, A. J., De Rosa, A., Laurent, P., Lebrun, F., Ubertini, P., and Walter, R. (2006). INTEGRAL IBIS Extragalactic Survey: Active Galactic Nuclei Selected at 20-100 keV. *Astrophysical Journal*, 636:L65–L68.
- Beasley, A. J., Conway, J. E., Booth, R. S., Nyman, L., and Holdaway, M. (1997). SEST observations of southern flat-spectrum radio sources. *Astronomy and Astrophysics Supplement Series*, 124:469–474.
- Belsole, E., Worrall, D. M., Hardcastle, M. J., and Croston, J. H. (2007). High-redshift Fanaroff-Riley type II radio sources: large-scale X-ray environment. *Monthly Notices of the Royal Astronomical Society*, 381:1109–1126.
- Billings, D. E. (1966). A Guide to the Solar Corona. *Academic Press, New York*.
- Bird, A. J., Malizia, A., Bazzano, A., Barlow, E. J., Bassani, L., Hill, A. B., Bélanger, G., Capitanio, F., Clark, D. J., Dean, A. J., Fiocchi, M., Götz, D., Lebrun, F., Molina, M., Produit, N., Renaud, M., Sguera, V., Stephen, J. B., Terrier, R., Ubertini, P., Walter, R., Winkler, C., and Zurita, J. (2007). The Third IBIS/ISGRI Soft Gamma-Ray Survey Catalog. *Astrophysical Journal Supplement Series*, 170:175–186.
- Biretta, J. A., Sparks, W. B., and Macchetto, F. (1999). Hubble Space Telescope Observations of Superluminal Motion in the M87 Jet. *Astrophysical Journal*, 520:621–626.
- Błażejowski, M., Siemiginowska, A., Sikora, M., Moderski, R., and Bechtold, J. (2004). X-Ray Emission from the Quasar PKS 1127-145: Comptonized Infrared Photons on Parsec Scales. *Astrophysical Journal*, 600:L27–L30.
- Błażejowski, M., Sikora, M., Moderski, R., and Madejski, G. M. (2000). Comptonization of Infrared Radiation from Hot Dust by Relativistic Jets in Quasars. *The Astrophysical Journal*, 545:107–116.
- Bloom, S. D., Marscher, A. P., Gear, W. K., Terasranta, H., Valtaoja, E., Aller, H. D., and Aller, M. F. (1994). Radio, millimeter-submillimeter, and infrared spectra of flat-spectrum extragalactic radio sources. *Astronomical Journal*, 108:398–404.
- Bloom, S. D., Marscher, A. P., Moore, E. M., Gear, W., Teräsanta, H., Valtaoja, E., Aller, H. D., and Aller, M. F. (1999). Multiwaveband Observations of Quasars with Flat Radio Spectra and Strong Millimeter-Wave Emission. *Astrophysical Journal Supplement Series*, 122:1–27.
- Bodaghee, A., Courvoisier, T., Rodriguez, J., Beckmann, V., Produit, N., Hannikainen, D., Kuulkers, E., Willis, D. R., and Wendt, G. (2007). A description of sources detected by INTEGRAL during the first 4 years of observations. *Astronomy and Astrophysics*, 467:585–596.

- Boeck, M., Kadler, M., Tosti, G., Burnett, T. H., Mueller, C., Ojha, R., and Wilms, J. (2010). The gamma-ray properties of radio-selected extragalactic jets. *Proceedings of the Workshop "Fermi meets Jansky - AGN in Radio and Gamma-Rays"*, Savolainen, T., Ros, E., Porcas, R. W. and Zensus, J. A. (eds.), MPIfR, Bonn, June 21-23 2010.
- Bondi, M., Padrielli, L., Fanti, R., Ficarra, A., Gregorini, L., Mantovani, F., Bartel, N., Romney, J. D., Nicolson, G. D., and Weiler, K. W. (1996). Three epoch VLBI observations at 18cm of low frequency variable sources. *Astronomy and Astrophysics*, 308:415–427.
- Böttcher, M. and Collmar, W. (1998). Spectral variability in PKS 0528+134 at gamma-ray energies. *Astronomy and Astrophysics*, 329:L57–L60.
- Böttcher, M., Reimer, A., and Marscher, A. P. (2009). Implications of the very High Energy Gamma-Ray Detection of the Quasar 3C279. *Astrophysical Journal*, 703:1168–1175.
- Bower, G. C. and Backer, D. C. (1998). Space VLBI Observations Show $T_b \sim 10^{12}$ K in the Quasar NRAO 530. *Astrophysical Journal*, 507:L117–L120.
- Brenneman, L. W., Weaver, K. A., Kadler, M., Tueller, J., Marscher, A., Ros, E., Zensus, A., Kovalev, Y. Y., Aller, M., Aller, H., Irwin, J., Kerp, J., and Kaufmann, S. (2009). Spectral Analysis of the Accretion Flow in NGC 1052 with Suzaku. *Astrophysical Journal*, 698:528–540.
- Briggs, D. S., Schwab, F. R., and Sramek, R. A. (1999). Imaging. In G. B. Taylor, C. L. Carilli, & R. A. Perley, editor, *Synthesis Imaging in Radio Astronomy II*, volume 180 of *Astronomical Society of the Pacific Conference Series*, page 127.
- Brindle, C. (1996). The internight variability of the optical to near-infrared flux density and polarization of the blazars 0215+015 and 0851+202 during outbursts. *Monthly Notices of the Royal Astronomical Society*, 282:788–796.
- Britzen, S., Brinkmann, W., Campbell, R. M., Gliozzi, M., Readhead, A. C. S., Browne, I. W. A., and Wilkinson, P. (2007). The soft X-ray properties of AGN from the CJF sample. A correlation analysis between soft X-ray and VLBI properties. *Astronomy and Astrophysics*, 476:759–777.
- Britzen, S., Witzel, A., Krichbaum, T. P., Beckert, T., Campbell, R. M., Schalinski, C., and Campbell, J. (2005). The radio structure of S5 1803+784. *Monthly Notices of the Royal Astronomical Society*, 362:966–974.
- Britzen, S., Witzel, A., Krichbaum, T. P., Qian, S. J., and Campbell, R. M. (1999). 8.4 GHz VLBI monitoring of the gamma-bright blazar PKS 0528+134. *Astronomy and Astrophysics*, 341:418–426.
- Brunetti, G., Bondi, M., Comastri, A., and Setti, G. (2002). Chandra discovery of extended non-thermal emission in 3C 207 and the spectrum of the relativistic electrons. *Astronomy and Astrophysics*, 381:795–809.

- Brunner, H., Lamer, G., Worrall, D. M., and Staubert, R. (1994). X-ray spectra of a complete sample of extragalactic core-dominated radio sources. *Astronomy and Astrophysics*, 287:436–452.
- Burbidge, G. R., Jones, T. W., and Odell, S. L. (1974). Physics of compact nonthermal sources. III - Energetic considerations. *Astrophysical Journal*, 193:43–54.
- Caccianiga, A., Marchã, M. J., Antón, S., Mack, K., and Neeser, M. J. (2002). The CLASS blazar survey - II. Optical properties. *Monthly Notices of the Royal Astronomical Society*, 329:877–889.
- Cai, H., Shen, Z., Chen, X., and Shang, L. (2006). Quasi-simultaneous five-frequency VLBA observations of PKS 0528+134. *Astronomy and Astrophysics*, 458:753–760.
- Cara, M. and Lister, M. L. (2008). MOJAVE: Monitoring of Jets in AGN with VLBA Experiments. IV. The Parent Luminosity Function of Radio-Loud Blazars. *Astrophysical Journal*, 674:111–121.
- Cardelli, J. A., Clayton, G. C., and Mathis, J. S. (1989). The relationship between infrared, optical, and ultraviolet extinction. *Astrophysical Journal*, 345:245–256.
- Carini, M. T., Noble, J. C., and Miller, H. R. (1998). The Timescales of the Optical Variability of Blazars. V. 3C 371. *Astronomical Journal*, 116:2667–2671.
- Carrasco, L., Mayya, D., Y., Carramiñana, A., Recillas, E., Porras, and A. (2010). NIR flaring of the Gamma ray source [HB89] 0754+100. *The Astronomer's Telegram*, 2516:1.
- Celotti, A. and Ghisellini, G. (2008). The power of blazar jets. *Monthly Notices of the Royal Astronomical Society*, 385:283–300.
- Chang, C. S. (2009). Fermi LAT detection of increasing gamma-ray activity of blazar PKS 2052-474. *The Astronomer's Telegram*, 2160:1.
- Chang, C. S., Ros, E., Kadler, M., Ojha, R., the Fermi Lat Collaboration, the Tanami Team, and the F-Gamma Team (2009). Multiwavelength campaign of the gamma-ray flaring source PKS 2052-47. *2009 Fermi Symposium, eConf Proceedings C091122*.
- Chatterjee, R., Jorstad, S. G., Marscher, A. P., Oh, H., McHardy, I. M., Aller, M. F., Aller, H. D., Balonek, T. J., Miller, H. R., Ryle, W. T., Tosti, G., Kurtanidze, O., Nikolashvili, M., Larionov, V. M., and Hagen-Thorn, V. A. (2008). Correlated Multi-Wave Band Variability in the Blazar 3C 279 from 1996 to 2007. *Astrophysical Journal*, 689:79–94.
- Chen, Y. J. and Jiang, D. R. (2001). The spectral energy distribution of AO 0235+164 during two active optical phases. *Astronomy and Astrophysics*, 376:69–76.
- Cheung, C. C., Harris, D. E., and Stawarz, Ł. (2007). Superluminal Radio Features in the M87 Jet and the Site of Flaring TeV Gamma-Ray Emission. *Astrophysical Journal, Letters*, 663:L65–L68.

- Ciaramella, A., Bongardo, C., Aller, H. D., Aller, M. F., De Zotti, G., Lähteenmaki, A., Longo, G., Milano, L., Tagliaferri, R., Teräsranta, H., Tornikoski, M., and Urpo, S. (2004). A multifrequency analysis of radio variability of blazars. *Astronomy and Astrophysics*, 419:485–500.
- Ciliegi, P., Bassani, L., and Caroli, E. (1993). A catalog of X-ray spectra of BL Lacertae objects. *Astrophysical Journal Supplement Series*, 85:111–118.
- Ciliegi, P., Bassani, L., and Caroli, E. (1995). On the X-ray spectra of BL Lacertae objects. *Astrophysical Journal*, 439:80–89.
- Ciprini, S. (2009). Fermi LAT confirmation of a strong GeV flare from 4C 21.35 (PKS 1222+21). *The Astronomer's Telegram*, 2349:1.
- Ciprini, S. and Chaty, S. (2008). Fermi LAT detections of increasing gamma ray activity of blazar 3C 279. *The Astronomer's Telegram*, 1864:1.
- Ciprini, S., Takalo, L. O., Tosti, G., Raiteri, C. M., Fiorucci, M., Villata, M., Nucciarelli, G., Lanteri, L., Nilsson, K., and Ros, J. A. (2007). Ten-year optical monitoring of PKS 0735+178: historical comparison, multiband behavior, and variability timescales. *Astronomy and Astrophysics*, 467:465–483.
- Ciprini, S., Tosti, G., Teräsranta, H., and Aller, H. D. (2004). Radio-optical flux behaviour and spectral energy distribution of the intermediate blazar GC 0109+224. *Monthly Notices of the Royal Astronomical Society*, 348:1379–1387.
- Clayton, G. C. and Cardelli, J. A. (1988). Polarization and the ratio of total-to-selective extinction. *Astronomical Journal*, 96:695–700.
- Cleary, K., Lawrence, C. R., Marshall, J. A., Hao, L., and Meier, D. (2007). Spitzer Observations of 3C Quasars and Radio Galaxies: Mid-Infrared Properties of Powerful Radio Sources. *Astrophysical Journal*, 660:117–145.
- Clegg, A. W., Fey, A. L., and Fiedler, R. L. (1996). VLA Polarization Observations of the Extragalactic Source 1741-038 During an Extreme Scattering Event. *Astrophysical Journal*, 457:L23.
- Clements, S. D., Jenks, A., and Torres, Y. (2003). PKS 0736+017: A Striking Optical Flare and Intriguing Microvariability. *Astronomical Journal*, 126:37–46.
- Cohen, M. H., Lister, M. L., Homan, D. C., Kadler, M., Kellermann, K. I., Kovalev, Y. Y., and Vermeulen, R. C. (2007). Relativistic Beaming and the Intrinsic Properties of Extragalactic Radio Jets. *Astrophysical Journal*, 658:232–244.
- Comastri, A., Fossati, G., Ghisellini, G., and Molendi, S. (1997). On the Soft X-Ray Spectra of gamma -loud Blazars. *Astrophysical Journal*, 480:534.
- Cooper, N. J., Lister, M. L., and Kochanzyk, M. D. (2007). MOJAVE: Monitoring of Jets in Active Galactic Nuclei with VLBA Experiments. III. Deep VLA Images at 1.4 GHz. *Astrophysical Journal Supplement Series*, 171:376–388.

- Corbin, M. R. and Boroson, T. A. (1996). Combined Ultraviolet and Optical Spectra of 48 Low-Redshift QSOs and the Relation of the Continuum and Emission-Line Properties. *Astrophysical Journal Supplement Series*, 107:69.
- Cotton, W. D. and Spangler, S. R. (1979). Broad-band flux density variations of the extragalactic radio source 1611+343. *Astrophysical Journal*, 228:L63–L66.
- Croston, J. H., Hardcastle, M. J., Harris, D. E., Belsole, E., Birkinshaw, M., and Worrall, D. M. (2005). An X-Ray Study of Magnetic Field Strengths and Particle Content in the Lobes of FR II Radio Sources. *Astrophysical Journal*, 626:733–747.
- Curtis, H. D. (1918). The planetary nebulae. *Publications of Lick Observatory*, 13:31.
- Dallacasa, D., Falomo, R., and Stanghellini, C. (2002). Optical identifications of High Frequency Peakers. *Astronomy and Astrophysics*, 382:53–59.
- Dallacasa, D., Stanghellini, C., Centonza, M., and Fanti, R. (2000). High frequency peakers. I. The bright sample. *Astronomy and Astrophysics*, 363:887–900.
- Davis, J. E. (2001a). Event Pileup in Charge-coupled Devices. *The Astrophysical Journal*, 562:575–582.
- Davis, J. E. (2001b). The Formal Underpinnings of the Response Functions Used in X-Ray Spectral Analysis. *Astrophysical Journal*, 548:1010–1019.
- de Rosa, A., Bassani, L., Ubertini, P., Malizia, A., and Dean, A. J. (2008). Bulk Compton motion in the luminous quasar 4C04.42? *Monthly Notices of the Royal Astronomical Society*, 388:L54–L58.
- de Vries, W. H., O’Dea, C. P., Baum, S. A., and Barthel, P. D. (1999). Optical-Radio Alignment in Compact Steep-Spectrum Radio Sources. *Astrophysical Journal*, 526:27–39.
- Dermer, C. D. and Gehrels, N. (1995). Two Classes of Gamma-Ray-emitting Active Galactic Nuclei. *Astrophysical Journal*, 447:103.
- Dermer, C. D. and Schlickeiser, R. (1993). Model for the High-Energy Emission from Blazars. *Astrophysical Journal*, 416:458.
- Dermer, C. D. and Schlickeiser, R. (1994). On the location of the acceleration and emission sites in gamma-ray blazars. *Astrophysical Journal Supplement Series*, 90:945–948.
- Dermer, C. D. and Schlickeiser, R. (2002). Transformation Properties of External Radiation Fields, Energy-Loss Rates and Scattered Spectra, and a Model for Blazar Variability. *The Astrophysical Journal*, 575:667–686.
- Donato, D. (2010). Fermi LAT observed another strong GeV flare from 4C 21.35 (PKS 1222+21). *The Astronomer’s Telegram*, 2584:1.
- Donato, D., Sambruna, R. M., and Gliozzi, M. (2005). Six years of BeppoSAX observations of blazars: A spectral catalog. *Astronomy and Astrophysics*, 433:1163–1169.

- Dondi, L. and Ghisellini, G. (1995). Gamma-ray-loud blazars and beaming. *Monthly Notices of the Royal Astronomical Society*, 273:583–595.
- Edelson, R. A. (1987). Millimeter-wave spectra and variability of bright, compact radio sources. *Astronomical Journal*, 94:1150–1155.
- Edelson, R. A. and Malkan, M. A. (1986). Spectral energy distributions of active galactic nuclei between 0.1 and 100 microns. *Astrophysical Journal*, 308:59–77.
- Evans, I. N. and Koratkar, A. P. (2004). A Complete Atlas of Recalibrated Hubble Space Telescope Faint Object Spectrograph Spectra of Active Galactic Nuclei and Quasars. I. Pre-COSTAR Spectra. *Astrophysical Journal Supplement Series*, 150:73–164.
- Falcke, H., Bower, G. C., Lobanov, A. P., Krichbaum, T. P., Patnaik, A. R., Aller, M. F., Aller, H. D., Teräsranta, H., Wright, M. C. H., and Sandell, G. (1999). A Major Radio Outburst in III ZW 2 with an Extremely Inverted, Millimeter-peaked Spectrum. *Astrophysical Journal*, 514:L17–L20.
- Falomo, R., Treves, A., Chiappetti, L., Maraschi, L., Pian, E., and Tanzi, E. G. (1993). The ultraviolet-to-near-infrared spectral flux distribution of four BL Lacertae. *Astrophysical Journal Supplement Series*, 402:532–536.
- Fan, J. H. (2005). The basic parameters of γ -ray-loud blazars. *Astronomy and Astrophysics*, 436:799–804.
- Fanaroff, B. L. and Riley, J. M. (1974). The morphology of extragalactic radio sources of high and low luminosity. *Monthly Notices of the Royal Astronomical Society*, 167:31P–36P.
- Fegan, S. J., Badran, H. M., Bond, I. H., Boyle, P. J., Bradbury, S. M., Buckley, J. H., Carter-Lewis, D. A., Catanese, M., Celik, O., Cui, W., Daniel, M., D’Vali, M., de la Calle Perez, I., Duke, C., Falcone, A., Fegan, D. J., Finley, J. P., Fortson, L. F., Gaidos, J. A., Gammell, S., Gibbs, K., Gillanders, G. H., Grube, J., Hall, J., Hall, T. A., Hanna, D., Hillas, A. M., Holder, J., Horan, D., Jarvis, A., Jordan, M., Kenny, G. E., Kertzman, M., Kieda, D., Kildea, J., Knapp, J., Kosack, K., Krawczynski, H., Krennrich, F., Lang, M. J., Le Bohec, S., Lessard, R. W., Linton, E., Lloyd-Evans, J., Milovanovic, A., McEnery, J., Moriarty, P., Mukherjee, R., Muller, D., Nagai, T., Nolan, S., Ong, R. A., Palladini, R., Petry, D., Power-Mooney, B., Quinn, J., Quinn, M., Ragan, K., Rebillot, P., Reynolds, P. T., Rose, H. J., Schroedter, M., Sembroski, G. H., Swordy, S. P., Syson, A., Vassiliev, V. V., Wakely, S. P., Walker, G., Weekes, T. C., and Zweerink, J. (2005). A Survey of Unidentified EGRET Sources at Very High Energies. *Astrophysical Journal*, 624:638–655.
- Feng, S., Shen, Z., Cai, H., Chen, X., Lu, R., and Huang, L. (2006). Multi-frequency VLBI observations of NRAO 530. *Astronomy and Astrophysics*, 456:97–104.
- Fermi-LAT Collaboration (2010). Fermi Large Area Telescope and multi-wavelength observations of the flaring activity of PKS 1510-089 between 2008 September and 2009 June. *ArXiv e-prints*.

Fermi-Lat Collaboration, Members Of The 3C 279 Multi-Band Campaign, Abdo, A. A., Ackermann, M., Ajello, M., Axelsson, M., Baldini, L., Ballet, J., Barbiellini, G., Bastieri, D., Baughman, B. M., Bechtol, K., Bellazzini, R., Berenji, B., Blandford, R. D., Bloom, E. D., Bock, D., Bogart, J. R., Bonamente, E., Borgland, A. W., Bouvier, A., Bregeon, J., Brez, A., Brigida, M., Bruel, P., Burnett, T. H., Buson, S., Caliandro, G. A., Cameron, R. A., Caraveo, P. A., Casandjian, J. M., Cavazzuti, E., Cecchi, C., Çelik, Ö., Chekhtman, A., Cheung, C. C., Chiang, J., Ciprini, S., Claus, R., Cohen-Tanugi, J., Collmar, W., Cominsky, L. R., Conrad, J., Corbel, S., Corbet, R., Costamante, L., Cutini, S., Dermer, C. D., de Angelis, A., de Palma, F., Digel, S. W., Do Couto E Silva, E., Drell, P. S., Dubois, R., Dumora, D., Farnier, C., Favuzzi, C., Fegan, S. J., Ferrara, E. C., Focke, W. B., Fortin, P., Frailis, M., Fuhrmann, L., Fukazawa, Y., Funk, S., Fusco, P., Gargano, F., Gasparrini, D., Gehrels, N., Germani, S., Giebels, B., Giglietto, N., Giommi, P., Giordano, F., Giroletti, M., Glanzman, T., Godfrey, G., Grenier, I. A., Grove, J. E., Guillemot, L., Guiriec, S., Hanabata, Y., Harding, A. K., Hayashida, M., Hays, E., Horan, D., Hughes, R. E., Iafrate, G., Itoh, R., Jackson, M. S., Jóhannesson, G., Johnson, A. S., Johnson, W. N., Kadler, M., Kamae, T., Katagiri, H., Kataoka, J., Kawai, N., Kerr, M., Knödlseeder, J., Kocian, M. L., Kuss, M., Lande, J., Larsson, S., Latronico, L., Lemoine-Goumard, M., Longo, F., Loparco, F., Lott, B., Lovellette, M. N., Lubrano, P., Macquart, J., Madejski, G. M., Makeev, A., Max-Moerbeck, W., Mazziotta, M. N., McConville, W., McEnery, J. E., McGlynn, S., Meurer, C., Michelson, P. F., Mitthumsiri, W., Mizuno, T., Moiseev, A. A., Monte, C., Monzani, M. E., Morselli, A., Moskalenko, I. V., Murgia, S., Nestoras, I., Nolan, P. L., Norris, J. P., Nuss, E., Ohsugi, T., Okumura, A., Omodei, N., Orlando, E., Ormes, J. F., Paneque, D., Panetta, J. H., Parent, D., Pavlidou, V., Pearson, T. J., Pelassa, V., Pepe, M., Pesce-Rollins, M., Piron, F., Porter, T. A., Rainò, S., Rando, R., Razzano, M., Readhead, A., Reimer, A., Reimer, O., Reposeur, T., Reyes, L. C., Richards, J. L., Rochester, L. S., Rodriguez, A. Y., Roth, M., Ryde, F., Sadrozinski, H., Sanchez, D., Sander, A., Saz Parkinson, P. M., Scargle, J. D., Sgrò, C., Shaw, M. S., Shrader, C., Siskind, E. J., Smith, D. A., Smith, P. D., Spandre, G., Spinelli, P., Stawarz, L., Stevenson, M., Strickman, M. S., Suson, D. J., Tajima, H., Takahashi, H., Takahashi, T., Tanaka, T., Taylor, G. B., Thayer, J. B., Thayer, J. G., Thompson, D. J., Tibaldo, L., Torres, D. F., Tosti, G., Tramacere, A., Uchiyama, Y., Usher, T. L., Vasileiou, V., Vilchez, N., Vitale, V., Waite, A. P., Wang, P., Wehrle, A. E., Winer, B. L., Wood, K. S., Ylinen, T., Zensus, J. A., Uemura, M., Ikejiri, Y., Kawabata, K. S., Kino, M., Sakimoto, K., Sasada, M., Sato, S., Yamanaka, M., Villata, M., Raiteri, C. M., Agudo, I., Aller, H. D., Aller, M. F., Angelakis, E., Arkharov, A. A., Bach, U., Benítez, E., Berdyugin, A., Blinov, D. A., Boettcher, M., Buemi, C. S., Chen, W. P., Dolci, M., Dultzin, D., Efimova, N. V., Gurwell, M. A., Gusbar, C., Gómez, J. L., Heidt, J., Hiriart, D., Hovatta, T., Jorstad, S. G., Konstantinova, T. S., Kopatskaya, E. N., Koptelova, E., Kurtanidze, O. M., Lahteenmaki, A., Larionov, V. M., Larionova, E. G., Leto, P., Lin, H. C., Lindfors, E., Marscher, A. P., McHardy, I. M., Melnichuk, D. A., Mommert, M., Nilsson, K., di Paola, A., Reinthal, R., Richter, G. M., Roca-Sogorb, M., Roustazadeh, P., Sigua, L. A., Takalo, L. O., Tornikoski, M., Trigilio, C., Troitsky, I. S., Umana, G., Villforth, C., Grainge, K., Moderski, R., Nalewajko, K., and Sikora, M. (2010). A change in the optical polarization associated with a γ -ray flare in the blazar 3C279. *Nature*, 463:919–923.

- Fey, A. L., Eubanks, M., and Kingham, K. A. (1997). The Proper Motion of 4C 39.25. *Astronomy and Astrophysics*, 114:2284.
- Fey, A. L., Spangler, S. R., Mutel, R. L., and Benson, J. M. (1985). VLBI observations at 22.2 gigahertz of the radio source 0552 + 398 (DA 193). *Astrophysical Journal*, 295:134–138.
- Fiedler, R. L., Dennison, B., Johnston, K. J., and Hewish, A. (1987). Extreme scattering events caused by compact structures in the interstellar medium. *Nature*, 326:675–678.
- Finke, J. D. and Dermer, C. D. (2010). On the Break in the Fermi-Large Area Telescope Spectrum of 3C 454.3. *Astrophysical Journal*, 714:L303–L307.
- Fiorucci, M., Ciprini, S., and Tosti, G. (2004). The continuum spectral features of blazars in the optical region. *Astronomy and Astrophysics*, 419:25–34.
- Foschini, L., Pian, E., Maraschi, L., Raiteri, C. M., Tavecchio, F., Ghisellini, G., Tosti, G., Malaguti, G., and Di Cocco, G. (2006a). A short hard X-ray flare from the blazar NRAO 530 observed by INTEGRAL. *Astronomy and Astrophysics*, 450:77–81.
- Foschini, L., Tagliaferri, G., Pian, E., Ghisellini, G., Treves, A., Maraschi, L., Tavecchio, F., Di Cocco, G., and Rosen, S. R. (2006b). Simultaneous X-ray and optical observations of S5 0716+714 after the outburst of March 2004. *Astronomy and Astrophysics*, 455:871–877.
- Frey, S., Gurvits, L. I., Gabuzda, D. C., Salter, C. J., Alschuler, D. R., Perillat, P., Aller, M. F., Aller, H. D., Hirabayashi, H., and Davis, M. M. (2006). VSOP Monitoring of the Compact BL Lac Object AO 0235+164. *Publ. of the Astronomical Society of Japan*, 58:217–222.
- Fuhrmann, L., Zensus, J. A., Krichbaum, T. P., Angelakis, E., and Readhead, A. C. S. (2007). Simultaneous Radio to (Sub-) mm-Monitoring of Variability and Spectral Shape Evolution of potential GLAST Blazars. In S. Ritz, P. Michelson, & C. A. Meegan, editor, *The First GLAST Symposium*, volume 921 of *American Institute of Physics Conference Series*, pages 249–251.
- Gabányi, K. É., Krichbaum, T. P., Britzen, S., Bach, U., Ros, E., Witzel, A., and Zensus, J. A. (2006). High frequency VLBI observations of the scatter-broadened quasar B 2005+403. *Astronomy and Astrophysics*, 451:85–98.
- Gabuzda, D. C. and Chernetskii, V. A. (2003). Parsec-scale Faraday rotation distribution in the BL Lac object 1803+784. *Monthly Notices of the Royal Astronomical Society*, 339:669–679.
- Gabuzda, D. C., Kochenov, P. Y., and Cawthorne, T. V. (2000a). Serendipitous VLBI observations of polarization intraday variability in three BL Lacertae objects. 319:1125–1135.
- Gabuzda, D. C., Kochenov, P. Y., Kollgaard, R. I., and Cawthorne, T. V. (2000b). VLBI and VLA observations of intraday polarization variability in 0917+624 and 0954+658. *Monthly Notices of the Royal Astronomical Society*, 315:229–240.

- Gabuzda, D. C., Kollgaard, R. I., Roberts, D. H., and Wardle, J. F. C. (1993). Is 1308+326 A BL Lacertae object or a quasar? *Astrophysical Journal*, 410:39–43.
- Gabuzda, D. C., Rastorgueva, E. A., Smith, P. S., and O’Sullivan, S. P. (2006). Evidence for cospatial optical and radio polarized emission in active galactic nuclei. *Monthly Notices of the Royal Astronomical Society*, 369:1596–1602.
- Gabuzda, D. C., Vitrishchak, V. M., Mahmud, M., and O’Sullivan, S. P. (2008). Radio circular polarization produced in helical magnetic fields in eight active galactic nuclei. *Monthly Notices of the Royal Astronomical Society*, 384:1003–1014.
- Gabuzda, D. C., Wardle, J. F. C., Roberts, D. H., Aller, M. F., and Aller, H. D. (1994). Unusual evolution in the VLBI structure of 0735+178. *Astrophysical Journal*, 435:128–139.
- Gambill, J. K., Sambruna, R. M., Chartas, G., Cheung, C. C., Maraschi, L., Tavecchio, F., Urry, C. M., and Pesce, J. E. (2003). Chandra observations of nuclear X-ray emission from a sample of radio sources. *Astronomy and Astrophysics*, 401:505–517.
- Gawroński, M. P. and Kus, A. J. (2006). Multi-frequency VSOP and VLBI observations of the quasar 3C309.1. In *Proceedings of the 8th European VLBI Network Symposium*.
- Gear, W. K., Stevens, J. A., Hughes, D. H., Litchfield, S. J., Robson, E. I., Terasranta, H., Valtaoja, E., Steppe, H., Aller, M. F., and Aller, H. D. (1994). A Comparison of the Radio / Submillimetre Spectra of BL-Lacertae Objects and Flat Spectrum Radio Quasars. *Monthly Notices of the Royal Astronomical Society*, 267:167.
- Gehrels, N., Chincarini, G., Giommi, P., Mason, K. O., Nousek, J. A., Wells, A. A., White, N. E., Barthelmy, S. D., Burrows, D. N., Cominsky, L. R., Hurley, K. C., Marshall, F. E., Mészáros, P., Roming, P. W. A., Angelini, L., Barbier, L. M., Belloni, T., Campana, S., Caraveo, P. A., Chester, M. M., Citterio, O., Cline, T. L., Cropper, M. S., Cummings, J. R., Dean, A. J., Feigelson, E. D., Fenimore, E. E., Frail, D. A., Fruchter, A. S., Garmire, G. P., Gendreau, K., Ghisellini, G., Greiner, J., Hill, J. E., Hunsberger, S. D., Krimm, H. A., Kulkarni, S. R., Kumar, P., Lebrun, F., Lloyd-Ronning, N. M., Markwardt, C. B., Mattson, B. J., Mushotzky, R. F., Norris, J. P., Osborne, J., Paczynski, B., Palmer, D. M., Park, H., Parsons, A. M., Paul, J., Rees, M. J., Reynolds, C. S., Rhoads, J. E., Sasseen, T. P., Schaefer, B. E., Short, A. T., Smale, A. P., Smith, I. A., Stella, L., Tagliaferri, G., Takahashi, T., Tashiro, M., Townsley, L. K., Tueller, J., Turner, M. J. L., Vietri, M., Voges, W., Ward, M. J., Willingale, R., Zerbi, F. M., and Zhang, W. W. (2004). The Swift Gamma-Ray Burst Mission. *The Astrophysical Journal*, 611:1005–1020.
- George, I. M., Nandra, K., Turner, T. J., and Celotti, A. (1994). The X-ray spectrum of the highly polarized quasar PKS 1502+106. *Astrophysical Journal*, 436:L59–L62.
- Ghisellini, G., Celotti, A., and Costamante, L. (2002). Low power BL Lacertae objects and the blazar sequence. Clues on the particle acceleration process. *Astronomy and Astrophysics*, 386:833–842.

- Ghisellini, G., Celotti, A., Fossati, G., Maraschi, L., and Comastri, A. (1998). A theoretical unifying scheme for gamma-ray bright blazars. *Monthly Notices of the Royal Astronomical Society*, 301:451–468.
- Ghisellini, G., Costamante, L., Tagliaferri, G., Maraschi, L., Celotti, A., Fossati, G., Pian, E., Comastri, A., de Francesco, G., Lanteri, L., Raiteri, C. M., Sobrito, G., Villata, M., Glass, I. S., Grandi, P., Perola, C., and Treves, A. (1999). The blazar PKS 0528+134: new results from BeppoSAX observations. *Astronomy and Astrophysics*, 348:63–70.
- Ghisellini, G., Foschini, L., Tavecchio, F., and Pian, E. (2007). On the 2007 July flare of the blazar 3C 454.3. *Monthly Notices of the Royal Astronomical Society*, 382:L82–L86.
- Ghisellini, G. and Madau, P. (1996). On the origin of the gamma-ray emission in blazars. *Monthly Notices of the RAS*, 280:67–76.
- Ghisellini, G. and Maraschi, L. (1989). Bulk acceleration in relativistic jets and the spectral properties of blazars. *Astrophysical Journal*, 340:181–189.
- Ghosh, K. K. and Soundararajaperumal, S. (1992). The X-ray spectrum of the superluminal quasar 1928 + 73. *Monthly Notices of the Royal Astronomical Society*, 254:563–567.
- Ghosh, K. K. and Soundararajaperumal, S. (1995). Multifrequency Spectra of EXOSAT Blazars. *Astrophysical Journal Supplement Series*, 100:37.
- Giommi, P., Ansari, S. G., and Micol, A. (1995). Radio to X-ray energy distribution of BL Lacertae objects. *Astron. Astrophys. Suppl.*, 109:267–291.
- Giommi, P., Blustin, A. J., Capalbi, M., Colafrancesco, S., Cucchiara, A., Fuhrmann, L., Krimm, H. A., Marchili, N., Massaro, E., Perri, M., Tagliaferri, G., Tosti, G., Tramacere, A., Burrows, D. N., Chincarini, G., Falcone, A., Gehrels, N., Kennea, J., and Sambruna, R. (2006). Swift and infra-red observations of the blazar 3C 454.3 during the giant X-ray flare of May 2005. *Astronomy and Astrophysics*, 456:911–916.
- Giommi, P., Capalbi, M., Cavazzuti, E., Colafrancesco, S., Cucchiara, A., Falcone, A., Kennea, J., Nesci, R., Perri, M., Tagliaferri, G., Tramacere, A., Tosti, G., Blustin, A. J., Branduardi-Raymont, G., Burrows, D. N., Chincarini, G., Dean, A. J., Gehrels, N., Krimm, H., Marshall, F., Parsons, A. M., and Zhang, B. (2007). Swift detection of all previously undetected blazars in a micro-wave flux-limited sample of WMAP foreground sources. *Astronomy and Astrophysics*, 468:571–579.
- Giommi, P., Massaro, E., Chiappetti, L., Ferrara, E. C., Ghisellini, G., Jang, M., Maesano, M., Miller, H. R., Montagni, F., Nesci, R., Padovani, P., Perlman, E., Raiteri, C. M., Sclavi, S., Tagliaferri, G., Tosti, G., and Villata, M. (1999). Synchrotron and inverse Compton variability in the BL Lacertae object S5 0716+714. *Astronomy and Astrophysics*, 351:59–64.
- Giroletti, M., Giovannini, G., Taylor, G. B., and Falomo, R. (2004). A Sample of Low-Redshift BL Lacertae Objects. I. The Radio Data. *Astrophysical Journal*, 613:752–769.

- Giuliani, A., D'Ammando, F., Vercellone, S., Vittorini, V., Chen, A. W., Donnarumma, I., Pacciani, L., Pucella, G., Trois, A., Bulgarelli, A., Longo, F., Tavani, M., Tosti, G., Impiombato, D., Argan, A., Barbiellini, G., Boffelli, F., Caraveo, P. A., Cattaneo, P. W., Cocco, V., Costa, E., Del Monte, E., de Paris, G., Di Cocco, G., Evangelista, Y., Feroci, M., Fiorini, M., Fornari, F., Froyland, T., Fuschino, F., Galli, M., Gianotti, F., Labanti, C., Lapshov, Y., Lazzarotto, F., Lipari, P., Marisaldi, M., Mereghetti, S., Morselli, A., Pellizzoni, A., Perotti, F., Picozza, P., Prest, M., Rapisarda, M., Rappoldi, A., Soffitta, P., Trifoglio, M., Vallazza, E., Zambra, A., Zanello, D., Cutini, S., Gasparrini, D., Pittori, C., Preger, B., Santolamazza, P., Verrecchia, F., Giommi, P., Colafrancesco, S., and Salotti, L. (2009). AGILE observation of a gamma-ray flare from the blazar 3C 279. *Astronomy and Astrophysics*, 494:509–513.
- Glassgold, A. E., Bregman, J. N., Huggins, P. J., Kinney, A. L., Pica, A. J., Pollock, J. T., Leacock, R. J., Smith, A. G., Webb, J. R., Wisniewski, W. Z., Jeske, N., Spinrad, H., Henry, R. B. C., Miller, J. S., Impey, C., Neugebauer, G., Aller, M. F., Aller, H. D., Hodge, P. E., Balonek, T. J., Dent, W. A., and O'Dea, C. P. (1983). Multifrequency observations of the flaring quasar 1156+295. *Astrophysical Journal*, 274:101–112.
- Gómez, J. and Marscher, A. P. (2000). Space VLBI Observations of 3C 371. *Astrophysical Journal*, 530:245–250.
- Gómez, J., Marscher, A. P., Alberdi, A., and Gabuzda, D. C. (1999). The Twisted Parsec-Scale Structure of 0735+178. *Astrophysical Journal*, 519:642–646.
- Gómez, J. L., Guirado, J. C., Agudo, I., Marscher, A. P., Alberdi, A., Marcaide, J. M., and Gabuzda, D. C. (2001). Changes in the trajectory of the radio jet in 0735+178? *Monthly Notices of the Royal Astronomical Society*, 328:873–881.
- Gómez, J. L., Marscher, A. P., Jorstad, S. G., Agudo, I., and Roca-Sogorb, M. (2008). Faraday Rotation and Polarization Gradients in the Jet of 3C 120: Interaction with the External Medium and a Helical Magnetic Field? *Astrophysical Journal, Letters*, 681:L69–L72.
- Gopal-Krishna and Wiita, P. J. (2000). Extragalactic radio sources with hybrid morphology: implications for the Fanaroff-Riley dichotomy. *Astronomy and Astrophysics*, 363:507–516.
- Gracia, J., Vlahakis, N., Agudo, I., Tsinganos, K., and Bogovalov, S. V. (2009). Synthetic Synchrotron Emission Maps from MHD Models for the Jet of M87. *Astrophysical Journal*, 695:503–510.
- Greenhill, L. J., Booth, R. S., Ellingsen, S. P., Herrnstein, J. R., Jauncey, D. L., McCulloch, P. M., Moran, J. M., Norris, R. P., Reynolds, J. E., and Tzioumis, A. K. (2003). A Warped Accretion Disk and Wide-Angle Outflow in the Inner Parsec of the Circinus Galaxy. *The Astrophysical Journal*, 590:162–173.
- Greisen, E. W. (1998). Recent Developments in Experimental AIPS. In R. Albrecht, R. N. Hook, & H. A. Bushouse, editor, *Astronomical Data Analysis Software and Systems VII*, volume 145 of *Astronomical Society of the Pacific Conference Series*, pages 204–+.

- Groves, B. (2007). The Narrow-line Region: Current Models and Future Questions. In L. C. Ho & J.-W. Wang, editor, *The Central Engine of Active Galactic Nuclei*, volume 373 of *Astronomical Society of the Pacific Conference Series*, page 511.
- Guirado, J. C., Marcaide, J. M., Elosegui, P., Ratner, M. I., Shapiro, I. I., Eckart, A., Quirrenbach, A., Schalinski, C. J., and Witzel, A. (1995). VLBI differential astrometry of the radio sources 1928+738 and 2007+777 at 5 GHz. *Astronomy and Astrophysics*, 293:613–625.
- Guirado, J. C., Marcaide, J. M., Ros, E., Ratner, M. I., Shapiro, I. I., Quirrenbach, A., and Witzel, A. (1998). Submilliarcsecond shift of the brightness peak of the radio sources 1928+738 and 2007+777. *Astronomy and Astrophysics*, 336:385–392.
- Gurvits, L. I., Kardashev, N. S., Popov, M. V., Schilizzi, R. T., Barthel, P. D., Pauliny-Toth, I. I. K., and Kellermann, K. I. (1992). The compact radio structure of the high redshift quasars 0642 + 449, 1402 + 044, 1614 + 051. *Astronomy and Astrophysics*, 260:82–88.
- Hagen-Thorn, V. A., Larionov, V. M., Jorstad, S. G., Arkharov, A. A., Hagen-Thorn, E. I., Efimova, N. V., Larionova, L. V., and Marscher, A. P. (2008). The Outburst of the Blazar AO 0235+164 in 2006 December: Shock-in-Jet Interpretation. *Astrophysical Journal*, 672:40–47.
- Hardcastle, M. J. and Worrall, D. M. (1999). ROSAT X-ray observations of 3CRR radio sources. *Monthly Notices of the Royal Astronomical Society*, 309:969–990.
- Harms, R. J., Ford, H. C., Tsvetanov, Z. I., Hartig, G. F., Dressel, L. L., Kriss, G. A., Bohlin, R., Davidsen, A. F., Margon, B., and Kochhar, A. K. (1994). HST FOS spectroscopy of M87: Evidence for a disk of ionized gas around a massive black hole. *Astrophysical Journal, Letters*, 435:L35–L38.
- Haro-Corzo, S. A. R., Binette, L., Krongold, Y., Benitez, E., Humphrey, A., Nicastro, F., and Rodríguez-Martínez, M. (2007). Energy Distribution of Individual Quasars from Far-Ultraviolet to X-Rays. I. Intrinsic Ultraviolet Hardness and Dust Opacities. *Astrophysical Journal*, 662:145–165.
- Harris, D. E., Biretta, J. A., Junor, W., Perlman, E. S., Sparks, W. B., and Wilson, A. S. (2003). Flaring X-Ray Emission from HST-1, a Knot in the M87 Jet. *Astrophysical Journal, Letters*, 586:L41–L44.
- Harris, D. E., Cheung, C. C., Biretta, J. A., Sparks, W. B., Junor, W., Perlman, E. S., and Wilson, A. S. (2006). The Outburst of HST-1 in the M87 Jet. *Astrophysical Journal*, 640:211–218.
- Harris, D. E., Cheung, C. C., Stawarz, Ł., Biretta, J. A., and Perlman, E. S. (2009). Variability Timescales in the M87 Jet: Signatures of E^2 Losses, Discovery of a Quasi Period in HST-1, and the Site of TeV Flaring. *Astrophysical Journal*, 699:305–314.

- Harris, D. E., Cheung, C. C., Stawarz, L., Biretta, J. A., Sparks, W., Perlman, E. S., and Wilson, A. S. (2008). The Continuing Saga of the Explosive Event(s) in the M87 Jet: Is M87 a Blazar? In Rector, T. A. and De Young, D. S., editors, *Extragalactic Jets: Theory and Observation from Radio to Gamma Ray*, volume 386 of *Astronomical Society of the Pacific Conference Series*, page 80.
- Harris, D. E., Mossman, A. E., and Walker, R. C. (2004). The X-Ray Jet of 3C 120: Evidence for a Nonstandard Synchrotron Spectrum. *Astrophysical Journal*, 615:161–172.
- Hartman, R. C., Bertsch, D. L., Bloom, S. D., Chen, A. W., Deines-Jones, P., Esposito, J. A., Fichtel, C. E., Friedlander, D. P., Hunter, S. D., McDonald, L. M., Sreekumar, P., Thompson, D. J., Jones, B. B., Lin, Y. C., Michelson, P. F., Nolan, P. L., Tompkins, W. F., Kanbach, G., Mayer-Hasselwander, H. A., Mücke, A., Pohl, M., Reimer, O., Kniffen, D. A., Schneid, E. J., von Montigny, C., Mukherjee, R., and Dingus, B. L. (1999). The Third EGRET Catalog of High-Energy Gamma-Ray Sources. *The Astrophysical Journal Supplement Series*, 123:79–202.
- Hartman, R. C., Kadler, M., and Tueller, J. (2008). Gamma-Ray Emission from the Broad-Line Radio Galaxy 3C 111. *The Astrophysical Journal*, 688:852–858.
- Hauser, M., Behera, B., Hagen, H., and Wagner, S. (2009). Detection of an optical flare from PKS 2052-474. *The Astronomer's Telegram*, 2158:1.
- Hazard, C., Mackey, M. B., and Shimmins, A. J. (1963). Investigation of the Radio Source 3C 273 By The Method of Lunar Occultations. *Nature*, 197:1037–1039.
- Healey, S. E., Romani, R. W., Cotter, G., Michelson, P. F., Schlafly, E. F., Readhead, A. C. S., Giommi, P., Chaty, S., Grenier, I. A., and Weintraub, L. C. (2008). CGRaBS: An All-Sky Survey of Gamma-Ray Blazar Candidates. *The Astrophysical Journal Supplement Series*, 175:97–104.
- Heeschen, D. S., Krichbaum, T., Schalinski, C. J., and Witzel, A. (1987). Rapid variability of extragalactic radio sources. *Astronomical Journal*, 94:1493–1507.
- Henriksen, M. J., Marshall, F. E., and Mushotzky, R. F. (1984). An X-ray survey of variable radio bright quasars. *Astrophysical Journal*, 284:491–496.
- Hirovani, K., Iguchi, S., Kimura, M., and Wajima, K. (2000). Pair Plasma Dominance in the Parsec-Scale Relativistic Jet of 3C 345. *Astrophysical Journal*, 545:100–106.
- Homan, D. C., Attridge, J. M., and Wardle, J. F. C. (2001). Parsec-Scale Circular Polarization Observations of 40 Blazars. *Astrophysical Journal*, 556:113–120.
- Homan, D. C., Kadler, M., Kellermann, K. I., Kovalev, Y. Y., Lister, M. L., Ros, E., Savolainen, T., and Zensus, J. A. (2009a). MOJAVE: Monitoring of Jets in Active Galactic Nuclei with VLBA Experiments. VII. Blazar Jet Acceleration. *Astrophysical Journal*, 706:1253–1268.

- Homan, D. C. and Lister, M. L. (2006). MOJAVE: Monitoring of Jets in Active Galactic Nuclei with VLBA Experiments. II. First-Epoch 15 GHz Circular Polarization Results. *Astronomical Journal*, 131:1262–1279.
- Homan, D. C., Lister, M. L., Aller, H. D., Aller, M. F., and Wardle, J. F. C. (2009b). Full Polarization Spectra of 3C 279. *Astrophysical Journal*, 696:328–347.
- Homan, D. C. and Wardle, J. F. C. (1999). Detection and Measurement of Parsec-Scale Circular Polarization in Four AGNS. *Astronomical Journal*, 118:1942–1962.
- Homan, D. C., Wardle, J. F. C., Cheung, C. C., Roberts, D. H., and Attridge, J. M. (2002). PKS 1510-089: A Head-on View of a Relativistic Jet. *Astrophysical Journal*, 580:742–748.
- Hong, X. Y., Jiang, D. R., Gurvits, L. I., Garrett, M. A., Garrington, S. T., Schilizzi, R. T., Nan, R. D., Hirabayashi, H., Wang, W. H., and Nicolson, G. D. (2004). A relativistic helical jet in the γ -ray AGN 1156+295. *Astronomy and Astrophysics*, 417:887–904.
- Hooimeyer, J. R. A., Schilizzi, R. T., Miley, G. K., and Barthel, P. D. (1992). Two new candidate superluminal quasars - 4C 28.45 and 4C 21.35. *Astronomy and Astrophysics*, 261:5–8.
- Hughes, D. H., Kukula, M. J., Dunlop, J. S., and Boroson, T. (2000). Optical off-nuclear spectra of quasar hosts and radio galaxies. *Monthly Notices of the Royal Astronomical Society*, 316:204–224.
- Hummel, C. A., Schalinski, C. J., Krichbaum, T. P., Rioja, M. J., Quirrenbach, A., Witzel, A., Muxlow, T. W. B., Johnston, K. J., Matveenko, L. I., and Shevchenko, A. (1992). The jets of quasar 1928+738 - Superluminal motion and large-scale structure. *Astronomy and Astrophysics*, 257:489–500.
- Iafrate, G., Longo, F., and Collmar, W. (2009). Fermi LAT and INTEGRAL detection of increasing high-energy activity of blazar 3C279. *The Astronomer's Telegram*, 2154:1.
- Iguchi, S., Fujisawa, K., Kamenno, S., Inoue, M., Shen, Z., Hirotsu, K., and Miyoshi, M. (2000). Multi-Frequency VLBI Observations of OT 081. *Publ. of the Astronomical Society of Japan*, 52:1037.
- Iler, A. L., Schachter, J. F., and Birkinshaw, M. (1997). Radio Polarization in EGRET Blazars. *Astrophysical Journal*, 486:117.
- Jauncey, D. L., Batty, M. J., Wright, A. E., Peterson, B. A., and Savage, A. (1984). Redshifts of southern radio sources. VI. *Astrophysical Journal*, 286:498–502.
- Johnston, K. J., Simon, R. S., Eckart, A., Biermann, P., Schalinski, C., Witzel, A., and Strom, R. G. (1987). 1928 + 738 - A superluminal source with large-scale structure. *Astrophysical Journal*, 313:L85–L90.
- Jones, T. W., O'dell, S. L., and Stein, W. A. (1974). Physics of Compact Nonthermal Sources. Theory of Radiation Processes. *Astrophysical Journal*, 188:353–368.

- Jones, T. W., Rudnick, L., Owen, F. N., Puschell, J. J., Ennis, D. J., and Werner, M. W. (1981). The broad-band spectra and variability of compact nonthermal sources. *Astrophysical Journal*, 243:97–107.
- Jordán, A., Côté, P., Blakeslee, J. P., Ferrarese, L., McLaughlin, D. E., Mei, S., Peng, E. W., Tonry, J. L., Merritt, D., Milosavljević, M., Sarazin, C. L., Sivakoff, G. R., and West, M. J. (2005). The ACS Virgo Cluster Survey. X. Half-Light Radii of Globular Clusters in Early-Type Galaxies: Environmental Dependencies and a Standard Ruler for Distance Estimation. *Astrophysical Journal*, 634:1002–1019.
- Jorstad, S. G. and Marscher, A. P. (2004). The Highly Relativistic Kiloparsec-Scale Jet of the Gamma-Ray Quasar 0827+243. *Astrophysical Journal*, 614:615–625.
- Jorstad, S. G., Marscher, A. P., Mattox, J. R., Wehrle, A. E., Bloom, S. D., and Yurchenko, A. V. (2001). Multiepoch Very Long Baseline Array Observations of EGRET-detected Quasars and BL Lacertae Objects: Superluminal Motion of Gamma-Ray Bright Blazars. *Astrophysical Journal Supplement Series*, 134:181–240.
- Jorstad, S. G., Marscher, A. P., Stevens, J. A., Smith, P. S., Forster, J. R., Gear, W. K., Cawthorne, T. V., Lister, M. L., Stirling, A. M., Gómez, J. L., Greaves, J. S., and Robson, E. I. (2007). Multiwaveband Polarimetric Observations of 15 Active Galactic Nuclei at High Frequencies: Correlated Polarization Behavior. *Astronomical Journal*, 134:799–824.
- Kadler, M. (2005). Compact radio cores in agn: The x-ray connection. *PhD Thesis at Rheinische Friedrich-Wilhelms-Universität Bonn*.
- Kadler, M., Kerp, J., Ros, E., Falcke, H., Pogge, R. W., and Zensus, J. A. (2004a). Jet emission in γ ASTROBJ γ NGC 1052 γ ASTROBJ γ at radio, optical, and X-ray frequencies. *Astronomy and Astrophysics*, 420:467–474.
- Kadler, M., Ros, E., Lobanov, A. P., Falcke, H., and Zensus, J. A. (2004b). The twin-jet system in NGC 1052: VLBI-scrutiny of the obscuring torus. *Astronomy and Astrophysics*, 426:481–493.
- Kadler, M., Ros, E., Perucho, M., Kovalev, Y. Y., Homan, D. C., Agudo, I., Kellermann, K. I., Aller, M. F., Aller, H. D., Lister, M. L., and Zensus, J. A. (2008). The Trails of Superluminal Jet Components in 3C 111. *The Astrophysical Journal*, 680:867–884.
- Kalberla, P. M. W., Burton, W. B., Hartmann, D., Arnal, E. M., Bajaja, E., Morras, R., and Pöppel, W. G. L. (2005). The Leiden/Argentine/Bonn (LAB) Survey of Galactic HI. Final data release of the combined LDS and IAR surveys with improved stray-radiation corrections. *Astronomy and Astrophysics*, 440:775–782.
- Kataoka, J., Madejski, G., Sikora, M., Roming, P., Chester, M. M., Grupe, D., Tsubuku, Y., Sato, R., Kawai, N., Tosti, G., Impiombato, D., Kovalev, Y. Y., Kovalev, Y. A., Edwards, P. G., Wagner, S. J., Moderski, R., Stawarz, Ł., Takahashi, T., and Watanabe, S. (2008). Multiwavelength Observations of the Powerful Gamma-Ray Quasar PKS 1510-089: Clues on the Jet Composition. *Astrophysical Journal*, 672:787–799.

- Kataoka, J., Reeves, J. N., Iwasawa, K., Markowitz, A. G., Mushotzky, R. F., Arimoto, M., Takahashi, T., Tsubuku, Y., Ushio, M., Watanabe, S., Gallo, L. C., Madejski, G. M., Terashima, Y., Isobe, N., Tashiro, M. S., and Kohmura, T. (2007). Probing the Disk-Jet Connection of the Radio Galaxy 3C 120 Observed with Suzaku. *Publ. of the Astronomical Society of Japan*, 59:279–297.
- Kataoka, J. and Stawarz, Ł. (2005). X-Ray Emission Properties of Large-Scale Jets, Hot Spots, and Lobes in Active Galactic Nuclei. *Astrophysical Journal*, 622:797–810.
- Kataoka, J., Stawarz, Ł., Cheung, C. C., Tosti, G., Cavazzuti, E., Celotti, A., Nishino, S., Fukazawa, Y., Thompson, D. J., and McConville, W. F. (2010). γ -ray Spectral Evolution of NGC 1275 Observed with Fermi Large Area Telescope. *Astrophysical Journal*, 715:554–560.
- Kedziora-Chudczer, L. L., Jauncey, D. L., Wieringa, M. H., Tzioumis, A. K., and Reynolds, J. E. (2001). The ATCA intraday variability survey of extragalactic radio sources. *Monthly Notices of the Royal Astronomical Society*, 325:1411–1430.
- Kellermann, K. I., Lister, M. L., Homan, D. C., Vermeulen, R. C., Cohen, M. H., Ros, E., Kadler, M., Zensus, J. A., and Kovalev, Y. Y. (2004). Sub-Milliarcsecond Imaging of Quasars and Active Galactic Nuclei. III. Kinematics of Parsec-scale Radio Jets. *Astrophysical Journal*, 609:539–563.
- Kellermann, K. I., Vermeulen, R. C., Zensus, J. A., and Cohen, M. H. (1998). Sub-Milliarcsecond Imaging of Quasars and Active Galactic Nuclei. *The Astronomical Journal*, 115:1295–1318.
- Kharb, P., Gabuzda, D., and Shastri, P. (2008). Parsec-scale magnetic field structures in HEAO-1 BL Lacs. *Monthly Notices of the Royal Astronomical Society*, 384:230–250.
- Kim, M., Kim, D., Wilkes, B. J., Green, P. J., Kim, E., Anderson, C. S., Barkhouse, W. A., Evans, N. R., Ivezić, Ž., Karovska, M., Kashyap, V. L., Lee, M. G., Maksym, P., Mossman, A. E., Silverman, J. D., and Tananbaum, H. D. (2007). Chandra Multiwavelength Project X-Ray Point Source Catalog. *Astrophysical Journal Supplement Series*, 169:401–429.
- Klöckner, H., Baan, W. A., and Garrett, M. A. (2003). Investigation of the obscuring circumnuclear torus in the active galaxy Mrk231. *Nature*, 421:821–823.
- Kollgaard, R. I., Wardle, J. F. C., Roberts, D. H., and Gabuzda, D. C. (1992). Radio constraints on the nature of BL Lacertae objects and their parent population. *Astronomical Journal*, 104:1687–1705.
- Komatsu, E., Dunkley, J., Nolte, M. R., Bennett, C. L., Gold, B., Hinshaw, G., Jarosik, N., Larson, D., Limon, M., Page, L., Spergel, D. N., Halpern, M., Hill, R. S., Kogut, A., Meyer, S. S., Tucker, G. S., Weiland, J. L., Wollack, E., and Wright, E. L. (2009). Five-Year Wilkinson Microwave Anisotropy Probe Observations: Cosmological Interpretation. *Astrophysical Journal, Supplement*, 180:330–376.

- Kovalev, Y. Y., Aller, H. D., Aller, M. F., Homan, D. C., Kadler, M., Kellermann, K. I., Kovalev, Y. A., Lister, M. L., McCormick, M. J., Pushkarev, A. B., Ros, E., and Zensus, J. A. (2009). The Relation Between AGN Gamma-Ray Emission and Parsec-Scale Radio Jets. *The Astrophysical Journal Letters*, 696:L17–L21.
- Kovalev, Y. Y., Kellermann, K. I., Lister, M. L., Homan, D. C., Vermeulen, R. C., Cohen, M. H., Ros, E., Kadler, M., Lobanov, A. P., Zensus, J. A., Kardashev, N. S., Gurvits, L. I., Aller, M. F., and Aller, H. D. (2005). Sub-Milliarcsecond Imaging of Quasars and Active Galactic Nuclei. IV. Fine-Scale Structure. *Astronomical Journal*, 130:2473–2505.
- Kovalev, Y. Y., Lister, M. L., Homan, D. C., and Kellermann, K. I. (2007). The Inner Jet of the Radio Galaxy M87. *Astrophysical Journal, Letters*, 668:L27–L30.
- Kraus, A., Krichbaum, T. P., Wegner, R., Witzel, A., Cimò, G., Quirrenbach, A., Britzen, S., Fuhrmann, L., Lobanov, A. P., Naundorf, C. E., Otterbein, K., Peng, B., Risse, M., Ros, E., and Zensus, J. A. (2003). Intraday variability in compact extragalactic radio sources. II. Observations with the Effelsberg 100 m radio telescope. *Astronomy and Astrophysics*, 401:161–172.
- Krolik, J. H. (1999). *Active galactic nuclei : from the central black hole to the galactic environment*.
- Kuehr, H. and Schmidt, G. D. (1990). Complete samples of radio-selected BL Lac objects. *Astronomical Journal*, 99:1–6.
- Labiano, A., Barthel, P. D., O’Dea, C. P., de Vries, W. H., Pérez, I., and Baum, S. A. (2007). GPS radio sources: new optical observations and an updated master list. *Astronomy and Astrophysics*, 463:97–104.
- Lamer, G., Newsam, A. M., and McHardy, I. M. (1999). The unusual host galaxy of the BL Lac object PKS 1413+135. *Monthly Notices of the Royal Astronomical Society*, 309:1085–1088.
- Lanzetta, K. M., Turnshek, D. A., and Sandoval, J. (1993). Ultraviolet spectra of QSOs, BL Lacertae objects, and Seyfert galaxies. *Astrophysical Journal Supplement Series*, 84:109–184.
- Lawrence, C. R., Zucker, J. R., Readhead, A. C. S., Unwin, S. C., Pearson, T. J., and Xu, W. (1996). Optical Spectra of a Complete Sample of Radio Sources. I. The Spectra. *Astrophysical Journal Supplement Series*, 107:541.
- Lazio, T. J. W., Cohen, A. S., Kassim, N. E., Perley, R. A., Erickson, W. C., Carilli, C. L., and Crane, P. C. (2006). Cygnus A: A Long-Wavelength Resolution of the Hot Spots. *Astrophysical Journal*, 642:L33–L36.
- Lazio, T. J. W., Fey, A. L., Dennison, B., Mantovani, F., Simonetti, J. H., Alberdi, A., Foley, A. R., Fiedler, R., Garrett, M. A., Hirabayashi, H., Jauncey, D. L., Johnston,

- K. J., Marcaide, J., Migenes, V., Nicolson, G. D., and Venturi, T. (2000). The Extreme Scattering Event toward PKS 1741-038: VLBI Images. *Astrophysical Journal*, 534:706–717.
- Ledden, J. E. and Odell, S. L. (1985). The radio-optical-X-ray spectral flux distributions of blazars. *Astrophysical Journal*, 298:630–643.
- Lee, S., Lobanov, A. P., Krichbaum, T. P., Witzel, A., Zensus, A., Bremer, M., Greve, A., and Grewing, M. (2008). a Global 86 GHz VLBI Survey of Compact Radio Sources. *Astronomical Journal*, 136:159–180.
- Li, Y., Wang, D., and Gan, Z. (2008). A simplified model of jet power from active galactic nuclei. *Astronomy and Astrophysics*, 482:1–8.
- Liang, E. W. and Liu, H. T. (2003). The masses of central supermassive black holes and the variability time-scales in gamma-ray loud blazars. *Monthly Notices of the Royal Astronomical Society*, 340:632–638.
- Liller, M. H. and Liller, W. (1975). Photometric histories of QSOs - Two QSOs with large light amplitude. *Astrophysical Journal, Letters*, 199:L133–L135.
- Lin, Y. C., Bertsch, D. L., Bloom, S. D., Esposito, J. A., Hartman, R. C., Hunter, S. D., Kanbach, G., Kniffen, D. A., Mayer-Hasselwander, H. A., Michelson, P. F., Mukherjee, R., Mücke, A., Nolan, P. L., Pohl, M., Reimer, O., Schneid, E. J., Thompson, D. J., and Tompkins, W. F. (1999). EGRET Spectral Index and the Low-Energy Peak Position in the Spectral Energy Distribution of EGRET-detected Blazars. *Astrophysical Journal*, 525:191–194.
- Linfield, R. and Perley, R. (1984). 3C 111 - A luminous radio galaxy with a highly collimated jet. *Astrophysical Journal*, 279:60–73.
- Lister, M. L. (2001). Parsec-Scale Jet Polarization Properties of a Complete Sample of Active Galactic Nuclei at 43 GHz. *Astrophysical Journal*, 562:208–232.
- Lister, M. L. (2010). Parsec-scale jet properties of Fermi-detected AGN. *Proceedings of the Workshop "Fermi meets Jansky - AGN in Radio and Gamma-Rays"*, Savolainen, T., Ros, E., Porcas, R.W. and Zensus, J.A. (eds.), MPIfR, Bonn, June 21-23 2010, page 159.
- Lister, M. L., Aller, H. D., Aller, M. F., Cohen, M. H., Homan, D. C., Kadler, M., Kellermann, K. I., Kovalev, Y. Y., Ros, E., Savolainen, T., Zensus, J. A., and Vermeulen, R. C. (2009a). MOJAVE: Monitoring of Jets in Active Galactic Nuclei with VLBA Experiments. V. Multi-Epoch VLBA Images. *Astronomical Journal*, 137:3718–3729.
- Lister, M. L., Cohen, M. H., Homan, D. C., Kadler, M., Kellermann, K. I., Kovalev, Y. Y., Ros, E., Savolainen, T., and Zensus, J. A. (2009b). MOJAVE: Monitoring of Jets in Active Galactic Nuclei with VLBA Experiments. VI. Kinematics Analysis of a Complete Sample of Blazar Jets. *Astronomical Journal*, 138:1874–1892.

- Lister, M. L. and Homan, D. C. (2005). MOJAVE: Monitoring of Jets in Active Galactic Nuclei with VLBA Experiments. I. First-Epoch 15 GHz Linear Polarization Images. *Astronomical Journal*, 130:1389–1417.
- Lister, M. L., Homan, D. C., Kadler, M., Kellermann, K. I., Kovalev, Y. Y., Ros, E., Savolainen, T., and Zensus, J. A. (2009c). A Connection Between Apparent VLBA Jet Speeds and Initial Active Galactic Nucleus Detections Made by the Fermi Gamma-Ray Observatory. *The Astrophysical Journal Letters*, 696:L22–L26.
- Liu, Y., Jiang, D. R., and Gu, M. F. (2006). The Jet Power, Radio Loudness, and Black Hole Mass in Radio-loud Active Galactic Nuclei. *Astrophysical Journal*, 637:669–681.
- Lobanov, A. P. (1998). Ultracompact jets in active galactic nuclei. *Astronomy and Astrophysics*, 330:79–89.
- Lobanov, A. P., Krichbaum, T. P., Witzel, A., Kraus, A., Zensus, J. A., Britzen, S., Otterbein, K., Hummel, C. A., and Johnston, K. (1998). VSOP imaging of S5 0836+710: a close-up on plasma instabilities in the jet. *Astronomy and Astrophysics*, 340:L60–L64.
- Lobanov, A. P. and Roland, J. (2005). A supermassive binary black hole in the quasar 3C 345. , 431:831–846.
- Lu, J. and Zhou, B. (2005). Observational Evidence of Jet Precession in Galactic Nuclei Caused by Accretion Disks. *Astrophysical Journal*, 635:L17–L20.
- Ly, C., Walker, R. C., and Junor, W. (2007). High-Frequency VLBI Imaging of the Jet Base of M87. *Astrophysical Journal*, 660:200–205.
- MacDonell, D. G. and Bridle, A. H. (1971). Variable radio sources-Studies of DW 0224+67, DA 193 and DW 0727-11. *Nature*, 234:88.
- Madrid, J. P. (2009). Hubble Space Telescope Observations of an Extraordinary Flare in the M87 Jet. *Astronomical Journal*, 137:3864–3868.
- Maraschi, L., Ciapi, A., Fossati, G., Tagliafferi, G., and Treves, A. (1995). ROSAT observations of the two radio-selected blazars PKS 1034-293 and PKS 1335-127. *Astrophysical Journal*, 443:29–34.
- Maraschi, L., Ghisellini, G., Tanzi, E. G., and Treves, A. (1986). Spectral Properties of Blazars. II. an X-Ray Observed Sample. *Astrophysical Journal*, 310:325.
- Marecki, A., Falcke, H., Niezgod, J., Garrington, S. T., and Patnaik, A. R. (1999). Gigahertz Peaked Spectrum sources from the Jodrell Bank-VLA Astrometric Survey. I. Sources in the region $35\text{deg} < \delta < 75\text{deg}$. *Astrophysical Journal Supplement Series*, 135:273–289.
- Marscher, A. P. (2008). The Core of a Blazar Jet. In Rector, T. A. and De Young, D. S., editors, *Extragalactic Jets: Theory and Observation from Radio to Gamma Ray*, volume 386 of *Astronomical Society of the Pacific Conference Series*, pages 437–443.

- Marscher, A. P. and Broderick, J. J. (1981). X-ray and VLBI radio observations of the quasars NRAO 140 and NRAO 530. *Astrophysical Journal*, 249:406–414.
- Marscher, A. P. and Broderick, J. J. (1983). VLBI observations of the quasars CTD20 (0234+285), OJ248 (0827+243), and 4C19.44 (1354+195), and the millimeter-X-ray connection. *Astronomical Journal*, 88:759–763.
- Marscher, A. P., Jorstad, S. G., Aller, M. F., McHardy, I., Balonek, T. J., Teräsranta, H., and Tosti, G. (2004). Relative Timing of Variability of Blazars at X-Ray and Lower Frequencies. In P. Kaaret, F. K. Lamb, & J. H. Swank, editor, *X-ray Timing 2003: Rossi and Beyond*, volume 714 of *American Institute of Physics Conference Series*, pages 167–173.
- Marscher, A. P., Jorstad, S. G., Gómez, J., Aller, M. F., Teräsranta, H., Lister, M. L., and Stirling, A. M. (2002a). Observational evidence for the accretion-disk origin for a radio jet in an active galaxy. *Nature*, 417:625–627.
- Marscher, A. P., Jorstad, S. G., Gómez, J. L., McHardy, I. M., Krichbaum, T. P., and Agudo, I. (2007). Search for Electron-Positron Annihilation Radiation from the Jet in 3C 120. *Astrophysical Journal*, 665:232–236.
- Marscher, A. P., Jorstad, S. G., Mattox, J. R., and Wehrle, A. E. (2002b). High-Frequency VLBA Total and Polarized Intensity Images of Gamma-Ray Bright Blazars. *Astrophysical Journal*, 577:85–97.
- Marscher, A. P., Marshall, F. E., Mushotzky, R. F., Dent, W. A., Balonek, T. J., and Hartman, M. F. (1979). Search for X-ray emission from bursting radio sources. *Astrophysical Journal*, 233:498–503.
- Marscher, A. P. and Shaffer, D. B. (1980). VLBI observations at 18 and 2.8 CM - 0133 + 47, 0735 + 178, OH 471, OQ 172, 1633 + 38, and NRAO 667 /2147 + 145/. *Astronomical Journal*, 85:668–672.
- Marscher, A. P., Zhang, Y. F., Shaffer, D. B., Aller, H. D., and Aller, M. F. (1991). Multifrequency VLA, VLBI, and single-dish observations of the quasar 4C 39.25. *Astrophysical Journal*, 371:491–500.
- Marshall, H. L., Schwartz, D. A., Lovell, J. E. J., Murphy, D. W., Worrall, D. M., Birkinshaw, M., Gelbord, J. M., Perlman, E. S., and Jauncey, D. L. (2005). A Chandra Survey of Quasar Jets: First Results. *The Astrophysical Journal Supplement Series*, 156:13–33.
- Massardi, M., Ekers, R. D., Murphy, T., Ricci, R., Sadler, E. M., Burke, S., de Zotti, G., Edwards, P. G., Hancock, P. J., Jackson, C. A., Kesteven, M. J., Mahony, E., Phillips, C. J., Staveley-Smith, L., Subrahmanyan, R., Walker, M. A., and Wilson, W. E. (2008). The Australia Telescope 20-GHz (AT20G) Survey: the Bright Source Sample. *Monthly Notices of the Royal Astronomical Society*, 384:775–802.
- Massaro, E., Giommi, P., Perri, M., Tagliaferri, G., Nesci, R., Tosti, G., Ciprini, S., Montagnani, F., Ravasio, M., Ghisellini, G., Frasca, A., Marilli, E., Valentini, G., Kurtanidze,

- O. M., and Nikolashvili, M. G. (2003). Optical and X-ray observations of the two BL Lac objects OJ 287 and MS 1458+22. *Astronomy and Astrophysics*, 399:33–38.
- Massaro, E., Nesci, R., Maesano, M., Montagni, F., Trevese, D., Fiorucci, M., Tosti, G., Ghisellini, G., Raiteri, C. M., Villata, M., de Francesco, G., Bosio, S., and Latini, G. (1996). Optical monitoring of the BL Lacertae object PKS 0422+004 in the 1994/95 autumn-winter. *Astronomy and Astrophysics*, 314:87–93.
- Mattox, J. R., Bertsch, D. L., Chiang, J., Dingus, B. L., Fichtel, C. E., Hartman, R. C., Hunter, S. D., Kanbach, G., Kniffen, D. A., Kwok, P. W., Lin, Y. C., Mayer-Hasselwander, H. A., Michelson, P. F., von Montigny, C., Nolan, P. L., Pinkau, K., Schneid, E., Sreekumar, P., and Thompson, D. J. (1993). The EGRET detection of quasar 1633 + 382. *Astrophysical Journal*, 410:609–614.
- Mattox, J. R., Hartman, R. C., and Reimer, O. (2001). A Quantitative Evaluation of Potential Radio Identifications for 3EG EGRET Sources. *Astrophysical Journal Supplement Series*, 135:155–175.
- McHardy, I., Lawson, A., Newsam, A., Marscher, A., Robson, I., and Stevens, J. (1999). Simultaneous X-ray and IR variability in the quasar 3C 273. *Monthly Notices of the RAS*, 310:571–576.
- McHardy, I. M., Marscher, A. P., Gear, W. K., Muxlow, T., Lehto, H. J., and Abraham, R. G. (1990). VLBI MERLIN and VLA Observations of the Blazar 1156+295 - a Bending Relativistic Jet. *Monthly Notices of the Royal Astronomical Society*, 246:305.
- McHardy, I. M., Merrifield, M. R., Abraham, R. G., and Crawford, C. S. (1994). Hubble Space Telescope Observations of the BL Lac Object PKS:1413+135: The Host Galaxy Revealed. *Monthly Notices of the Royal Astronomical Society*, 268:681.
- McLaughlin, M. A., Mattox, J. R., Cordes, J. M., and Thompson, D. J. (1996). Variability of CGRO/EGRET Gamma-Ray Sources. *Astrophysical Journal*, 473:763.
- Meegan, C., Lichti, G., Bhat, P. N., Bissaldi, E., Briggs, M. S., Connaughton, V., Diehl, R., Fishman, G., Greiner, J., Hoover, A. S., van der Horst, A. J., von Kienlin, A., Kippen, R. M., Kouveliotou, C., McBreen, S., Paciesas, W. S., Preece, R., Steinle, H., Wallace, M. S., Wilson, R. B., and Wilson-Hodge, C. (2009). The Fermi Gamma-ray Burst Monitor. *Astrophysical Journal*, 702:791–804.
- Mewe, R., Gronenschild, E. H. B. M., and van den Oord, G. H. J. (1985). Calculated X-radiation from optically thin plasmas. V. *Astronomy and Astrophysics Supplement Series*, 62:197–254.
- Miller, J. S. and Goodrich, R. W. (1990). Spectropolarimetry of high-polarization Seyfert 2 galaxies and unified Seyfert theories. *Astrophysical Journal*, 355:456–467.
- Mineo, T., Romano, P., Mangano, V., Moretti, A., Cusumano, G., La Parola, V., Troja, E., Campana, S., Chincarini, G., Tagliaferri, G., Capalbi, M., Perri, M., Giommi, P., and Burrows, D. (2006). Pile-up correction for the Swift-XRT observations in WT mode. *Nuovo Cimento B Serie*, 121:1521–1522.

- Moellenbrock, G. A., Fujisawa, K., Preston, R. A., Gurvits, L. I., Dewey, R. J., Hirabayashi, H., Inoue, M., Kamenno, S., Kawaguchi, M., Iwata, T., Jauncey, D. L., Migenes, V., Roberts, D. H., Schilizzi, R. T., and Tingay, S. J. (1996). A 22 GHz VLBI Survey of 140 Compact Extragalactic Radio Sources. *Astronomical Journal*, 111:2174.
- Moles, M., Garcia-Pelayo, J., Masegosa, J., and Aparicio, A. (1985). On the optical variability of the QSO PKS 2128-123. *Astronomical Journal*, 90:39–42.
- Molina, M., Bassani, L., Malizia, A., Bird, A. J., Dean, A. J., Fiocchi, M., Panessa, F., de Rosa, A., and Landi, R. (2008). A broad-band spectral analysis of eight radio-loud type 1 active galactic nuclei selected in the hard X-ray band. *Monthly Notices of the Royal Astronomical Society*, 390:1217–1228.
- Montagni, F., Maselli, A., Massaro, E., Nesci, R., Sclavi, S., and Maesano, M. (2006). The intra-night optical variability of the bright BL Lacertae object S5 0716+714. *Astronomy and Astrophysics*, 451:435–442.
- Moore, R. L., Angel, J. R. P., Lebofsky, M. J., Wisniewski, W. Z., Mufson, S. L., Vrba, F. J., McGimsey, B. Q., Williamon, R. M., Rieke, G. H., and Miller, H. R. (1980). Optical and infrared variability of B2 1308+326. *Astrophysical Journal*, 235:717–723.
- Mosoni, L., Frey, S., Paragi, Z., Fejes, I., Edwards, P. G., Fomalont, E. B., Gurvits, L. I., and Scott, W. K. (2002). 1546+027: Space VLBI observations of a compact quasar. In E. Ros, R. W. Porcas, A. P. Lobanov, & J. A. Zensus, editor, *Proceedings of the 6th EVN Symposium*, page 97.
- Mufson, S. L., Stein, W. A., Wisniewski, W. Z., Pollock, J. T., Aller, H. D., and Aller, M. F. (1985). The bursting behavior of the BL Lacertae object B2 1308 + 326. *Astrophysical Journal*, 288:718–724.
- Mukherjee, R., Böttcher, M., Hartman, R. C., Sreekumar, P., Thompson, D. J., Mahoney, W. A., Pursimo, T., Sillanpää, A., and Takalo, L. O. (1999). Broadband Spectral Analysis of PKS 0528+134: A Report on Six Years of EGRET Observations. *Astrophysical Journal*, 527:132–142.
- Mukherjee, R., Dingus, B. L., Gear, W. K., Hartman, R. C., Hunter, S. D., Marscher, A. P., Moore, E. M., Pohl, M., Robson, E. I., Sreekumar, P., Stevens, J. A., Teraesranta, H., Tornikoski, M., Travis, J. P., Wagner, S. J., and Zhang, Y. F. (1996). EGRET Observations of the 1993 March Gamma-Ray Flare from PKS 0528+134. *Astrophysical Journal*, 470:831.
- Müller, A. and Camenzind, M. (2004). Relativistic emission lines from accreting black holes. The effect of disk truncation on line profiles. *Astronomy and Astrophysics*, 413:861–878.
- Muxlow, T. W. B., Jullian, M., and Linfield, R. (1984). The Radio Jet in 3C418. In R. Fanti, K. I. Kellermann, & G. Setti, editor, *VLBI and Compact Radio Sources*, volume 110 of *IAU Symposium*, page 141.

- Nan, R. D., Zhang, H. Y., Gabuzda, D. C., and Inoue, M. (1999). VLBA Polarimetry Observation of the BL Lacertae Object 0300+470. *Publ. of the Astronomical Society of Japan*, 51:955–959.
- Nandikotkur, G., Jahoda, K. M., Hartman, R. C., Mukherjee, R., Sreekumar, P., Böttcher, M., Sambruna, R. M., and Swank, J. H. (2007). Does the Blazar Gamma-Ray Spectrum Harden with Increasing Flux? Analysis of 9 Years of EGRET Data. *Astrophysical Journal*, 657:706–724.
- Nesci, R., Massaro, E., Maesano, M., Montagni, F., Sclavi, S., Venturi, T., Dallacasa, D., and D’Alessio, F. (2002). Optical and Radio Monitoring of S5 1803+784. *Astronomical Journal*, 124:53–64.
- Netzer, H., Lutz, D., Schweitzer, M., Contursi, A., Sturm, E., Tacconi, L. J., Veilleux, S., Kim, D., Rupke, D., Baker, A. J., Dasyra, K., Mazzarella, J., and Lord, S. (2007). Spitzer Quasar and ULIRG Evolution Study (QUEST). II. The Spectral Energy Distributions of Palomar-Green Quasars. *Astrophysical Journal*, 666:806–816.
- Nieppola, E., Tornikoski, M., and Valtaoja, E. (2006). Spectral energy distributions of a large sample of BL Lacertae objects. *Astronomy and Astrophysics*, 445:441–450.
- Nilsson, K., Heidt, J., Pursimo, T., Sillanpää, A., Takalo, L. O., and Jaeger, K. (1997). Discovery of an Optical Jet in the BL Lacertae Object 3C 371. *Astrophysical Journal*, 484:L107.
- Nolan, P. L., Tompkins, W. F., Grenier, I. A., and Michelson, P. F. (2003). Variability of EGRET Gamma-Ray Sources. *Astrophysical Journal*, 597:615–627.
- O’Dea, C. P. (1998). The Compact Steep-Spectrum and Gigahertz Peaked-Spectrum Radio Sources. *The Publications of the Astronomical Society of the Pacific*, 110:493–532.
- O’Dea, C. P., Baum, S. A., and Stanghellini, C. (1991). What are the gigahertz peaked-spectrum radio sources? *Astrophysical Journal*, 380:66–77.
- O’Dea, C. P., de Vries, W., Biretta, J. A., and Baum, S. A. (1999). Hubble Space Telescope and VLA Observations of Two Optical Continuum Knots in the Jet of 3C 380. *Astronomical Journal*, 117:1143–1150.
- Ogle, P. M., Davis, S. W., Antonucci, R. R. J., Colbert, J. W., Malkan, M. A., Page, M. J., Sasseen, T. P., and Tornikoski, M. (2005). Multiwavelength Observations of Radio Galaxy 3C 120 with XMM-Newton. *Astrophysical Journal*, 618:139–154.
- Ojha, R., Fey, A. L., Johnston, K. J., Jauncey, D. L., Reynolds, J. E., Tzioumis, A. K., Quick, J. F. H., Nicolson, G. D., Ellingsen, S. P., Dodson, R. G., and McCulloch, P. M. (2004). VLBI Observations of Southern Hemisphere ICRF Sources. I. *Astronomical Journal*, 127:3609–3621.
- Ojha, R., Fey, A. L., Lazio, T. J. W., Jauncey, D. L., Lovell, J. E. J., and Kedziora-Chudczer, L. (2006). Scatter Broadening of Scintillating and Nonscintillating AGNs. I. A Multifrequency VLBA Survey. *Astrophysical Journal Supplement Series*, 166:37–68.

- Ojha, R., Kadler, M., Böck, M., Booth, R., Dutka, M. S., Edwards, P. G., Fey, A. L., Fuhrmann, L., Gaume, R. A., Hase, H., Horiuchi, S., Jauncey, D. L., Johnston, K. J., Katz, U., Lister, M., Lovell, J. E. J., Müller, C., Plötz, C., Quick, J. F. H., Ros, E., Taylor, G. B., Thompson, D. J., Tingay, S. J., Tosti, G., Tzioumis, A. K., Wilms, J., and Zensus, J. A. (2010a). TANAMI: Tracking Active Galactic Nuclei with Austral Milliarcsecond Interferometry I. First-Epoch 8.4 GHz Images. *submitted to Astronomy and Astrophysics*.
- Ojha, R., Kadler, M., Böck, M., Hungwe, F., Müller, C., Wilms, J., and Ros, E. (2010b). The TANAMI Program. *Proceedings of the Workshop "Fermi meets Jansky - AGN in Radio and Gamma-Rays"*, Savolainen, T., Ros, E., Porcas, R.W. and Zensus, J.A. (eds.), *MPIfR, Bonn, June 21-23 2010*, page 179.
- Orienti, M., Dallacasa, D., and Stanghellini, C. (2007). Constraining the nature of high frequency peakers. The spectral variability. *Astronomy and Astrophysics*, 475:813–820.
- Orienti, M., Dallacasa, D., Tinti, S., and Stanghellini, C. (2006). VLBA images of high frequency peakers. *Astronomy and Astrophysics*, 450:959–970.
- Osterbrock, D. E. (1989). *Astrophysics of gaseous nebulae and active galactic nuclei*.
- Otterbein, K., Krichbaum, T. P., Kraus, A., Lobanov, A. P., Witzel, A., Wagner, S. J., and Zensus, J. A. (1998). Gamma-ray to radio activity and ejection of a VLBI component in the jet of the S5-quasar 0836+710. *Astronomy and Astrophysics*, 334:489–497.
- Pacciani, L., Donnarumma, I., Vittorini, V., D'Ammando, F., Fiacchi, M. T., Impiombato, D., Stratta, G., Verrecchia, F., Bulgarelli, A., Chen, A. W., Giuliani, A., Longo, F., Pucella, G., Vercellone, S., Tavani, M., Argan, A., Barbiellini, G., Boffelli, F., Caraveo, P. A., Cattaneo, P. W., Cocco, V., Costa, E., Del Monte, E., Di Cocco, G., Evangelista, Y., Feroci, M., Froyland, T., Fuschino, F., Galli, M., Gianotti, F., Labanti, C., Lapshov, I., Lazzarotto, F., Lipari, P., Marisaldi, M., Mereghetti, S., Morselli, A., Pellizzoni, A., Perotti, F., Picozza, P., Prest, M., Rapisarda, M., Soffitta, P., Trifoglio, M., Tosti, G., Trois, A., Vallazza, E., Zanello, D., Antonelli, L. A., Colafrancesco, S., Cutini, S., Gasparri, D., Giommi, P., Pittori, C., and Salotti, L. (2009). High energy variability of 3C 273 during the AGILE multiwavelength campaign of December 2007-January 2008. *Astronomy and Astrophysics*, 494:49–61.
- Padovani, P. and Giommi, P. (1995). The connection between x-ray- and radio-selected BL Lacertae objects. *Astrophysical Journal*, 444:567–581.
- Paltani, S., Walter, R., McHardy, I. M., Dwelly, T., Steiner, C., and Courvoisier, T. (2008). A deep INTEGRAL hard X-ray survey of the 3C 273/Coma region. *Astronomy and Astrophysics*, 485:707–718.
- Papadakis, I. E., Villata, M., and Raiteri, C. M. (2007). The long-term optical spectral variability of BL Lacertae. *Astronomy and Astrophysics*, 470:857–863.
- Papageorgiou, A., Cawthorne, T. V., Stirling, A., Gabuzda, D., and Polatidis, A. G. (2006). Space very long baseline interferometry observations of polarization in the jet of 3C380. *Monthly Notices of the Royal Astronomical Society*, 373:449–456.

- Pearson, T. J. and Readhead, A. C. S. (1981). The milli-arcsecond structure of a complete sample of radio sources. I - VLBI maps of seven sources. *Astrophysical Journal*, 248:61–81.
- Pearson, T. J. and Readhead, A. C. S. (1988). The milliarcsecond structure of a complete sample of radio sources. II - First-epoch maps at 5 GHz. *Astrophysical Journal*, 328:114–142.
- Peng, B. (2002). Variability investigation of quasars 4C38.41 and 3C345 at 92cm: additional 14 observations. *Monthly Notices of the Royal Astronomical Society*, 330:344–348.
- Peng, B., Kraus, A., Krichbaum, T. P., and Witzel, A. (2000). Long-term monitoring of selected radio sources. *Astronomy and Astrophysics Supplement Series*, 145:1–10.
- Peng, B., Wu, J., and Zhou, X. (2003). Optical monitoring of the quasar 4C 38.41. *Monthly Notices of the Royal Astronomical Society*, 346:483–488.
- Penzias, A. A. and Wilson, R. W. (1965). A Measurement of Excess Antenna Temperature at 4080 Mc/s. *Astrophysical Journal*, 142:419–421.
- Perlman, E. S., Carilli, C. L., Stocke, J. T., and Conway, J. (1996). Multifrequency VLBI Observations of PKS 1413+135: A Very Young Radio Galaxy. *Astronomical Journal*, 111:1839.
- Perlman, E. S., Stocke, J. T., Carilli, C. L., Sugihō, M., Tashiro, M., Madejski, G., Wang, Q. D., and Conway, J. (2002). The Apparent Host Galaxy of PKS 1413+135: Hubble Space Telescope, ASCA, and Very Long Baseline Array Observations. *Astronomical Journal*, 124:2401–2412.
- Perucho, M. and Lobanov, A. P. (2007). Physical properties of the jet in JAS-TROBJ₀₈₃₆₊₇₁₀/ASTROBJ₀₈₃₆₊₇₁₀ revealed by its transversal structure. *Astronomy and Astrophysics*, 469:L23–L26.
- Pesce, J. E., Sambruna, R. M., Tavecchio, F., Maraschi, L., Cheung, C. C., Urry, C. M., and Scarpa, R. (2001). Detection of an X-Ray Jet in 3C 371 with Chandra. *Astrophysical Journal*, 556:L79–L82.
- Petrov, L., Gordon, D., Gipson, J., MacMillan, D., Ma, C., Fomalont, E., Walker, R. C., and Carabajal, C. (2009). Precise geodesy with the Very Long Baseline Array. *Journal of Geodesy*, 83:859–876.
- Petrov, L., Kovalev, Y. Y., Fomalont, E. B., and Gordon, D. (2008). The Sixth VLBA Calibrator Survey: VCS6. *Astronomical Journal*, 136:580–585.
- Pian, E., Foschini, L., Beckmann, V., Sillanpää, A., Soldi, S., Tagliaferri, G., Takalo, L., Barr, P., Ghisellini, G., Malaguti, G., Maraschi, L., Palumbo, G. G. C., Treves, A., Courvoisier, T., Di Cocco, G., Gehrels, N., Giommi, P., Hudec, R., Lindfors, E., Marcowith, A., Nilsson, K., Pasanen, M., Pursimo, T., Raiteri, C. M., Savolainen, T., Sikora, M., Tornikoski, M., Tosti, G., Türler, M., Valtaoja, E., Villata, M., and

- Walter, R. (2005). INTEGRAL observations of the field of the BL Lacertae object S5 0716+714. *Astronomy and Astrophysics*, 429:427–431.
- Pian, E., Foschini, L., Beckmann, V., Soldi, S., Türler, M., Gehrels, N., Ghisellini, G., Giommi, P., Maraschi, L., Pursimo, T., Raiteri, C. M., Tagliaferri, G., Tornikoski, M., Tosti, G., Treves, A., Villata, M., Barr, P., Courvoisier, T., Di Cocco, G., Hudec, R., Fuhrmann, L., Malaguti, G., Persic, M., Tavecchio, F., and Walter, R. (2006). INTEGRAL observations of the blazar 3C 454.3 in outburst. *Astronomy and Astrophysics*, 449:L21–L25.
- Piner, B. G. and Kingham, K. A. (1997a). A Slower Superluminal Velocity for the Quasar 1156+295. *Astrophysical Journal*, 485:L61.
- Piner, B. G. and Kingham, K. A. (1997b). VLBI Observations of the Gamma-Ray Blazar 1611+343. *Astrophysical Journal*, 479:684.
- Piner, B. G., Mahmud, M., Fey, A. L., and Gospodinova, K. (2007). Relativistic Jets in the Radio Reference Frame Image Database. I. Apparent Speeds from the First 5 Years of Data. *Astronomical Journal*, 133:2357–2388.
- Pohl, M., Reich, W., Krichbaum, T. P., Standke, K., Britzen, S., Reuter, H. P., Reich, P., Schlickeiser, R., Fiedler, R. L., Waltman, E. B., Ghigo, F. D., and Johnston, K. J. (1995). Radio observations of the γ -ray quasar 0528+134. Superluminal motion and an extreme scattering event. *Astronomy and Astrophysics*, 303:383.
- Pollack, L. K., Taylor, G. B., and Zavala, R. T. (2003). VLBI Polarimetry of 177 Sources from the Caltech-Jodrell Bank Flat-Spectrum Survey. *Astrophysical Journal*, 589:733–751.
- Pollock, J. T., Pica, A. J., Smith, A. G., Leacock, R. J., Edwards, P. L., and Scott, R. L. (1979). Long-term optical variations of 20 violently variable extragalactic radio sources. *Astronomical Journal*, 84:1658–1676.
- Pollock, J. T., Webb, J. R., and Azarnia, G. (2007). Simultaneous Microvariability Observations of 0716+71. *Astronomical Journal*, 133:487–488.
- Poole, T. S., Breeveld, A. A., Page, M. J., Landsman, W., Holland, S. T., Roming, P., Kuin, N. P. M., Brown, P. J., Gronwall, C., Hunsberger, S., Koch, S., Mason, K. O., Schady, P., vanden Berk, D., Blustin, A. J., Boyd, P., Broos, P., Carter, M., Chester, M. M., Cucchiara, A., Hancock, B., Huckle, H., Immler, S., Ivanushkina, M., Kennedy, T., Marshall, F., Morgan, A., Pandey, S. B., de Pasquale, M., Smith, P. J., and Still, M. (2008). Photometric calibration of the Swift ultraviolet/optical telescope. *Monthly Notices of the Royal Astronomical Society*, 383:627–645.
- Popovic, L. C. (2006). The Broad Line Region of AGN: Kinematics and Physics. *Serbian Astronomical Journal*, 173:1.
- Predehl, P. and Schmitt, J. H. M. M. (1995). X-raying the interstellar medium: ROSAT observations of dust scattering halos. *Astronomy and Astrophysics*, 293:889–905.

- Pursimo, T., Nilsson, K., Takalo, L. O., Sillanpää, A., Heidt, J., and Pietilä, H. (2002). Deep optical imaging of radio selected BL Lacertae objects. *Astronomy and Astrophysics*, 381:810–824.
- Pushkarev, A. B., Gabuzda, D. C., Vetukhnovskaya, Y. N., and Yakimov, V. E. (2005). Spine-sheath polarization structures in four active galactic nuclei jets. *Monthly Notices of the Royal Astronomical Society*, 356:859–871.
- Pushkarev, A. B., Kovalev, Y. Y., and Lister, M. L. (2010a). Radio/gamma-ray time delay in the cores of AGN. *Proceedings of the Workshop "Fermi meets Jansky - AGN in Radio and Gamma-Rays"*, Savolainen, T., Ros, E., Porcas, R.W. and Zensus, J.A. (eds.), *MPIfR, Bonn, June 21-23 2010*, page 163.
- Pushkarev, A. B., Kovalev, Y. Y., and Lister, M. L. (2010b). Radio/gamma-ray time delay in the parsec-scale cores of active galactic nuclei. *submitted to the Astrophysical Journal Letters*.
- Pushkarev, A. B., Kovalev, Y. Y., Lister, M. L., and Savolainen, T. (2009). Jet opening angles and gamma-ray brightness of AGN. *Astronomy and Astrophysics*, 507:L33–L36.
- Pyatunina, T. B., Gabuzda, D. C., Jorstad, S. G., Kudryavtseva, N. A., Aller, M. F., Aller, H. D., and Teräsranta, H. (2006). The blazar 0059+581: Successful prognosis of activity. *Astronomy Reports*, 50:468–482.
- Radecke, H., Bertsch, D. L., Dingus, B. L., Fichtel, C. E., Hartman, R. C., Hunter, S. D., Kanbach, G., Kniffen, D. A., Lin, Y. C., Mattox, J. R., Mayer-Hasselwander, H. A., Michelson, P. F., von Montigny, C., Nolan, P. L., Schneid, E., and Thompson, D. J. (1995). EGRET detection of the blazar PKS 0420-014. *Astrophysical Journal*, 438:659–662.
- Raiteri, C. M., Villata, M., Kadler, M., Krichbaum, T. P., Böttcher, M., Fuhrmann, L., and Orio, M. (2006). X-ray emission from the blazar AO 0235+16: the XMM-Newton and Chandra point of view. *Astronomy and Astrophysics*, 452:845–856.
- Raiteri, C. M., Villata, M., Larionov, V. M., Aller, M. F., Bach, U., Gurwell, M., Kurtanidze, O. M., Lähteenmäki, A., Nilsson, K., Volvach, A., Aller, H. D., Arkharov, A. A., Bachev, R., Berdyugin, A., Böttcher, M., Buemi, C. S., Calcidese, P., Cozzi, E., di Paola, A., Dolci, M., Fan, J. H., Forné, E., Foschini, L., Gupta, A. C., Hagen-Thorn, V. A., Hooks, L., Hovatta, T., Joshi, M., Kadler, M., Kimeridze, G. N., Konstantinova, T. S., Kostov, A., Krichbaum, T. P., Lanteri, L., Larionova, L. V., Lee, C., Leto, P., Lindfors, E., Montagni, F., Nesci, R., Nieppola, E., Nikolashvili, M. G., Ohlert, J., Oksanen, A., Ovcharov, E., Pääkkönen, P., Pasanen, M., Pursimo, T., Ros, J. A., Semkov, E., Sigua, L. A., Smart, R. L., Strigachev, A., Takalo, L. O., Torii, K., Tornainen, I., Tornikoski, M., Tringilio, C., Tsunemi, H., Umana, G., and Valcheva, A. (2008). Radio-to-UV monitoring of AO 0235+164 by the WEBT and Swift during the 2006-2007 outburst. *Astronomy and Astrophysics*, 480:339–347.
- Raiteri, C. M., Villata, M., Tosti, G., Nesci, R., Massaro, E., Aller, M. F., Aller, H. D., Teräsranta, H., Kurtanidze, O. M., Nikolashvili, M. G., Ibrahimov, M. A., Papadakis,

- I. E., Krichbaum, T. P., Kraus, A., Witzel, A., Ungerechts, H., Lisenfeld, U., Bach, U., Cimò, G., Ciprini, S., Fuhrmann, L., Kimeridze, G. N., Lanteri, L., Maesano, M., Montagni, F., Nucciarelli, G., and Ostorero, L. (2003). Optical and radio behaviour of the BL Lacertae object 0716+714. *Astronomy and Astrophysics*, 402:151–169.
- Ramírez, A., de Diego, J. A., Dultzin-Hacyan, D., and González-Pérez, J. N. (2004). Optical variability of PKS 0736+017. *Astronomy and Astrophysics*, 421:83–89.
- Readhead, A. C. S. (1994). Equipartition brightness temperature and the inverse Compton catastrophe. *Astrophysical Journal*, 426:51–59.
- Rector, T. A. and Stocke, J. T. (2003). High-Resolution Radio Imaging of Gravitational Lensing Candidates in the 1 Jansky BL Lacertae Sample. *Astronomical Journal*, 125:2447–2454.
- Rees, M. J. (1966). Appearance of Relativistically Expanding Radio Sources. *Nature*, 211:468–470.
- Reeves, J. N. and Turner, M. J. L. (2000). X-ray spectra of a large sample of quasars with ASCA. *Monthly Notices of the Royal Astronomical Society*, 316:234–248.
- Ricci, R., Prandoni, I., Gruppioni, C., Sault, R. J., and De Zotti, G. (2004). High-frequency polarization properties of southern Kühn sources. *Astronomy and Astrophysics*, 415:549–558.
- Rickett, B. J., Quirrenbach, A., Wegner, R., Krichbaum, T. P., and Witzel, A. (1995). Interstellar scintillation of the radio source 0917+624. *Astronomy and Astrophysics*, 293:479–492.
- Rickett, B. J., Witzel, A., Kraus, A., Krichbaum, T. P., and Qian, S. J. (2001). Annual Modulation in the Intraday Variability of Quasar 0917+624 due to Interstellar Scintillation. *Astrophysical Journal*, 550:L11–L14.
- Robson, E. I., Stevens, J. A., and Jenness, T. (2001). Observations of flat-spectrum radio sources at $\lambda 850 \mu\text{m}$ from the James Clerk Maxwell Telescope - I. 1997 April to 2000 April. *Monthly Notices of the Royal Astronomical Society*, 327:751–770.
- Ros, E. and Lobanov, A. P. (2001). Opacity in the Jet of 3C 309.1. In D. Behrend & A. Rius, editor, *15th Workshop Meeting on European VLBI for Geodesy and Astrometry*, page 208.
- Ros, E., Marcaide, J. M., Guirado, J. C., and Pérez-Torres, M. A. (2001). Absolute kinematics of radio source components in the complete S5 polar cap sample. I. First and second epoch maps at 8.4 GHz. *Astronomy and Astrophysics*, 376:1090–1105.
- Ros, E., Zensus, J. A., and Lobanov, A. P. (2000). Total intensity and polarized emission of the parsec-scale jet in 3C 345. *Astronomy and Astrophysics*, 354:55–66.
- Rossetti, A., Mantovani, F., Dallacasa, D., Fanti, C., and Fanti, R. (2005). Multi-frequency VLBA observations of compact sources from the Peacock and Wall catalogue. *Astronomy and Astrophysics*, 434:449–458.

- Roustazadeh, P. and Böttcher, M. (2010). Very High Energy Gamma-ray-induced Pair Cascades in Blazars and Radio Galaxies: Application to NGC 1275. *Astrophysical Journal*, 717:468–473.
- Salvati, M., Risaliti, G., Véron, P., and Woltjer, L. (2008). The X-ray emission of the most luminous 3CR radio sources. *Astronomy and Astrophysics*, 478:121–126.
- Sambruna, R. M. (1997). Soft X-Ray Properties of Flat-Spectrum Radio Quasars. *Astrophysical Journal*, 487:536.
- Sambruna, R. M., Donato, D., Tavecchio, F., Maraschi, L., Cheung, C. C., and Urry, C. M. (2007a). Deep Chandra and Multicolor HST Observations of the Jets of 3C 371 and PKS 2201+044. *Astrophysical Journal*, 670:74–91.
- Sambruna, R. M., Gambill, J. K., Maraschi, L., Tavecchio, F., Cerutti, R., Cheung, C. C., Urry, C. M., and Chartas, G. (2004). A Survey of Extended Radio Jets with Chandra and the Hubble Space Telescope. *Astrophysical Journal*, 608:698–720.
- Sambruna, R. M., Ghisellini, G., Hooper, E., Kollgaard, R. I., Pesce, J. E., and Urry, C. M. (1999). ASCA and Contemporaneous Ground-based Observations of the BL Lacertae Objects 1749+096 and 2200+420 (BL Lac). *Astrophysical Journal*, 515:140–152.
- Sambruna, R. M., Maraschi, L., and Urry, C. M. (1996). On the Spectral Energy Distributions of Blazars. *Astrophysical Journal*, 463:444.
- Sambruna, R. M., Tavecchio, F., Ghisellini, G., Donato, D., Holland, S. T., Markwardt, C. B., Tueller, J., and Mushotzky, R. F. (2007b). Swift Observations of High-Redshift Radio-loud Quasars. *The Astrophysical Journal*, 669:884–892.
- Sambruna, R. M., Urry, C. M., Maraschi, L., Ghisellini, G., Mukherjee, R., Pesce, J. E., Wagner, S. J., Wehrle, A. E., Hartman, R. C., Lin, Y. C., and von Montigny, C. (1997). The High-Energy Continuum Emission of the Gamma-Ray Blazar PKS 0528+134. *Astrophysical Journal*, 474:639.
- Sanders, D. B. (1999). Infrared Emission from AGN. In Y. Terzian, E. Khachikian, & D. Weedman, editor, *Activity in Galaxies and Related Phenomena*, volume 194 of *IAU Symposium*, page 25.
- Sargent, W. L. W., Young, P. J., Lynds, C. R., Boksenberg, A., Shortridge, K., and Hartwick, F. D. A. (1978). Dynamical evidence for a central mass concentration in the galaxy M87. *Astrophysical Journal*, 221:731–744.
- Savolainen, T., Homan, D. C., Hovatta, T., Kadler, M., Kovalev, Y. Y., Lister, M. L., Ros, E., and Zensus, J. A. (2010). Relativistic beaming and gamma-ray brightness of blazars. *Astronomy and Astrophysics*, 512:A24.
- Savolainen, T., Wiik, K., Valtaoja, E., Kadler, M., Ros, E., Tornikoski, M., Aller, M. F., and Aller, H. D. (2006). An Extremely Curved Relativistic Jet in PKS 2136+141. *Astrophysical Journal*, 647:172–184.

- Scarpa, R., Urry, C. M., Falomo, R., and Treves, A. (1999). Hubble Space Telescope Observations of the Optical Jets of PKS 0521-365, 3C 371, and PKS 2201+044. *Astrophysical Journal*, 526:643–648.
- Schilizzi, R. T. and Shaver, P. A. (1981). VLBI observations of the quasar DA 193. *Astronomy and Astrophysics*, 96:365–368.
- Schinzel, F. K., Lobanov, A. P., Jorstad, S. G., Marscher, A. P., Taylor, G. B., and Zensus, J. A. (2010). Radio Flaring Activity of 3C 345 and its Connection to γ -ray Emission. *Proceedings of the Workshop "Fermi meets Jansky - AGN in Radio and Gamma-Rays"*, Savolainen, T., Ros, E., Porcas, R. W. and Zensus, J.A. (eds.), MPIfR, Bonn, June 21-23 2010.
- Schlegel, D. J., Finkbeiner, D. P., and Davis, M. (1998). Maps of Dust Infrared Emission for Use in Estimation of Reddening and Cosmic Microwave Background Radiation Foregrounds. *Astrophysical Journal*, 500:525.
- Schoenfelder, V. (1994). Gamma-ray properties of active galactic nuclei. *Astrophysical Journal Supplement Series*, 92:593–598.
- Senkbeil, C. E., Ellingsen, S. P., Lovell, J. E. J., Macquart, J., Cimò, G., and Jauncey, D. L. (2008). A Compact Extreme Scattering Event Cloud toward AO 0235+164. *The Astrophysical Journal*, 672:L95–L98.
- Seyfert, C. K. (1943). Nuclear Emission in Spiral Nebulae. *Astrophysical Journal*, 97:28.
- Shastri, P., Wilkes, B. J., Elvis, M., and McDowell, J. (1993). Quasar X-ray spectra revisited. *Astrophysical Journal*, 410:29–38.
- Shepherd, M. C. (1997). Difmap: an Interactive Program for Synthesis Imaging. In G. Hunt & H. Payne, editor, *Astronomical Data Analysis Software and Systems VI*, volume 125 of *Astronomical Society of the Pacific Conference Series*, page 77.
- Shinozaki, K., Miyaji, T., Ishisaki, Y., Ueda, Y., and Ogasaka, Y. (2006). Spectral Statistics and Local Luminosity Function of a Complete Hard X-Ray Sample of the Brightest Active Galactic Nuclei. *Astronomical Journal*, 131:2843–2858.
- Shklovsky, I. S. (1964). Nature of Jets in Radio Galaxies. *Soviet Astronomy*, 7:748–754.
- Siebert, J., Brinkmann, W., Drinkwater, M. J., Yuan, W., Francis, P. J., Peterson, B. A., and Webster, R. L. (1998). X-ray properties of the Parkes sample of flat-spectrum radio sources: dust in radio-loud quasars? *Monthly Notices of the Royal Astronomical Society*, 301:261–279.
- Siemiginowska, A., Bechtold, J., Aldcroft, T. L., Elvis, M., Harris, D. E., and Dobrzycki, A. (2002). Chandra Discovery of a 300 Kiloparsec X-Ray Jet in the Gigahertz-peaked Spectrum Quasar PKS 1127-145. *Astrophysical Journal*, 570:543–556.
- Siemiginowska, A., LaMassa, S., Aldcroft, T. L., Bechtold, J., and Elvis, M. (2008). X-Ray Properties of the Gigahertz Peaked and Compact Steep Spectrum Sources. *Astrophysical Journal*, 684:811–821.

- Siemiginowska, A., Stanghellini, C., Brunetti, G., Fiore, F., Aldcroft, T. L., Bechtold, J., Elvis, M., Murray, S. S., Antonelli, L. A., and Colafrancesco, S. (2003). Chandra Discovery of an X-Ray Jet and Extended X-Ray Structure in the $z = 0.63$ Quasar B2 0738+313. *Astrophysical Journal*, 595:643–655.
- Siemiginowska, A., Stawarz, Ł., Cheung, C. C., Harris, D. E., Sikora, M., Aldcroft, T. L., and Bechtold, J. (2007). The 300 kpc Long X-Ray Jet in PKS 1127-145, $z = 1.18$ Quasar: Constraining X-Ray Emission Models. *Astrophysical Journal*, 657:145–158.
- Sikora, M., Begelman, M. C., and Rees, M. J. (1994). Comptonization of diffuse ambient radiation by a relativistic jet: The source of gamma rays from blazars? *Astrophysical Journal*, 421:153–162.
- Sikora, M., Moderski, R., and Madejski, G. M. (2008). 3C 454.3 Reveals the Structure and Physics of Its “Blazar Zone”. *Astrophysical Journal*, 675:71–78.
- Sillanpaa, A., Haarala, S., and Korhonen, T. (1988). Optical monitoring of quasars and BL Lac objects. *Astronomy and Astrophysics Supplement Series*, 72:347–354.
- Singh, K. P., Rao, A. R., and Vahia, M. N. (1990). EXOSAT observations of the blazar PKS 1510 - 089. *Astrophysical Journal*, 365:455–459.
- Singh, K. P., Shrader, C. R., and George, I. M. (1997). X-Ray Spectrum of the High-Polarization Quasar PKS 1510-089. *Astrophysical Journal*, 491:515.
- Siringo, G., Kreysa, E., Kovács, A., Schuller, F., Weiß, A., Esch, W., Gemünd, H., Jethava, N., Lundershausen, G., Colin, A., Güsten, R., Menten, K. M., Beelen, A., Bertoldi, F., Beeman, J. W., and Haller, E. E. (2009). The Large APEX BOlometer CAmera LABOCA. *Astronomy and Astrophysics*, 497:945–962.
- Smith, P. S., Schmidt, G. D., Jannuzi, B. T., and Elston, R. (1994). The synchrotron continuum of the highly polarized quasar PKS 1546+027. *Astrophysical Journal*, 426:535–541.
- Sokolov, A. and Marscher, A. P. (2005). External Compton Radiation from Rapid Non-thermal Flares in Blazars. *The Astrophysical Journal*, 629:52–60.
- Sokolov, A., Marscher, A. P., and McHardy, I. M. (2004). Synchrotron Self-Compton Model for Rapid Nonthermal Flares in Blazars with Frequency-dependent Time Lags. *The Astrophysical Journal*, 613:725–746.
- Soldi, S., Türler, M., Paltani, S., Aller, H. D., Aller, M. F., Burki, G., Chernyakova, M., Lähteenmäki, A., McHardy, I. M., Robson, E. I., Staubert, R., Tornikoski, M., Walter, R., and Courvoisier, T. (2008). The multiwavelength variability of 3C 273. *Astronomy and Astrophysics*, 486:411–425.
- Sowards-Emmerd, D., Romani, R. W., and Michelson, P. F. (2003). The Gamma-Ray Blazar Content of the Northern Sky. *Astrophysical Journal*, 590:109–122.

- Spangler, S. R., Mutel, R. L., and Benson, J. M. (1983). VLBI observations of the radio sources 0552 + 398 and 1848 + 283 - Measurements of the departure from equipartition. *Astrophysical Journal*, 271:44–50.
- Stalin, C. S., Gopal-Krishna, Sagar, R., Wiita, P. J., Mohan, V., and Pandey, A. K. (2006). Multiband optical monitoring of the blazars S5 0716+714 and BL Lacertae. *Monthly Notices of the Royal Astronomical Society*, 366:1337–1345.
- Standke, K. J., Quirrenbach, A., Krichbaum, T. P., Witzel, A., Otterbein, K., Alef, W., Eckart, A., Alberdi, A., Marcaide, J. M., Ros, E., Lesch, H., Steffen, W., Kraus, A., and Zensus, J. A. (1996). The intraday variable quasar 0917+624: VLBI and X-ray observations. *Astronomy and Astrophysics*, 306:27.
- Stanghellini, C., O’Dea, C. P., Dallacasa, D., Baum, S. A., Fanti, R., and Fanti, C. (1998). A complete sample of GHz-peaked-spectrum radio sources and its radio properties. *Astron. Astrophys. Suppl.*, 131:303–315.
- Stawarz, Ł., Aharonian, F., Kataoka, J., Ostrowski, M., Siemiginowska, A., and Sikora, M. (2006). Dynamics and high-energy emission of the flaring HST-1 knot in the M 87 jet. *Monthly Notices of the RAS*, 370:981–992.
- Stawarz, Ł., Cheung, C. C., Harris, D. E., and Ostrowski, M. (2007). The Electron Energy Distribution in the Hotspots of Cygnus A: Filling the Gap with the Spitzer Space Telescope. *Astrophysical Journal*, 662:213–223.
- Stevens, J. A., Litchfield, S. J., Robson, E. I., Gear, W. K., Terasranta, H., and Valtaoja, E. (1995). The Spectral Evolution of High-Frequency Radio Outbursts in the Blazar PKS:0420-014. *Monthly Notices of the Royal Astronomical Society*, 275:1146.
- Stickel, M., Padovani, P., Urry, C. M., Fried, J. W., and Kuehr, H. (1991). The complete sample of 1 Jansky BL Lacertae objects. I - Summary properties. *Astrophysical Journal*, 374:431–439.
- Stocke, J. T., Wurtz, R., Wang, Q., Elston, R., and Jannuzi, B. T. (1992). The BL Lacertae object PKS 1413 + 135 - Is it within or behind a spiral galaxy? *Astrophysical Journal*, 400:L17–L20.
- Tanaka, Y., Inoue, H., and Holt, S. S. (1994). The X-ray astronomy satellite ASCA. *Publ. of the Astronomical Society of Japan*, 46:L37–L41.
- Tavecchio, F., Cerutti, R., Maraschi, L., Sambruna, R. M., Gambill, J. K., Cheung, C. C., and Urry, C. M. (2005). X-Ray and Optical Emission from Radio Hot Spots of Powerful Quasars. *Astrophysical Journal*, 630:721–728.
- Tavecchio, F., Maraschi, L., Ghisellini, G., Celotti, A., Chiappetti, L., Comastri, A., Fosfati, G., Grandi, P., Pian, E., Tagliaferri, G., Treves, A., and Sambruna, R. (2002). Spectral Energy Distributions of Flat-Spectrum Radio Quasars Observed with BeppoSAX. *Astrophysical Journal*, 575:137–144.

- Tavecchio, F., Maraschi, L., Wolter, A., Cheung, C. C., Sambruna, R. M., and Urry, C. M. (2007). Chandra and Hubble Space Telescope Observations of Gamma-Ray Blazars: Comparing Jet Emission at Small and Large Scales. *Astrophysical Journal*, 662:900–908.
- Teshima, M. and The MAGIC Collaboration (2008). MAGIC discovers VHE gamma ray emission from the blazar S50716+714. *The Astronomer's Telegram*, 1500:1.
- Thompson, A. R. (1999). Fundamentals of Radio Interferometry. In G. B. Taylor, C. L. Carilli, & R. A. Perley, editor, *Synthesis Imaging in Radio Astronomy II*, volume 180 of *Astronomical Society of the Pacific Conference Series*, page 11.
- Thompson, D. J., Bertsch, D. L., Dingus, B. L., Esposito, J. A., Etienne, A., Fichtel, C. E., Friedlander, D. P., Hartman, R. C., Hunter, S. D., Kendig, D. J., Mattox, J. R., McDonald, L. M., von Montigny, C., Mukherjee, R., Ramanamurthy, P. V., Sreekumar, P., Fierro, J. M., Lin, Y. C., Michelson, P. F., Nolan, P. L., Shriver, S. K., Willis, T. D., Kanbach, G., Mayer-Hasselwander, H. A., Merck, M., Radecke, H., Kniffen, D. A., and Schneid, E. J. (1995). The Second EGRET Catalog of High-Energy Gamma-Ray Sources. *Astrophysical Journal Supplement Series*, 101:259.
- Thompson, D. J., Bertsch, D. L., Dingus, B. L., Fichtel, C. E., Hartman, R. C., Hunter, S. D., Kanbach, G., Kniffen, D. A., Lin, Y. C., Mattox, J. R., Mayer-Hasselwander, H. A., Michelson, P. F., von Montigny, C., Nolan, P. L., Schneid, E. J., and Sreekumar, P. (1993). EGRET observations of active galactic nuclei - 0836 + 710, 0454 - 234, 0804 + 499, 0906 + 430, 1510-089, and 2356 + 196. *Astrophysical Journal, Letters*, 415:L13–L16.
- Torniaainen, I., Tornikoski, M., Lähteenmäki, A., Aller, M. F., Aller, H. D., and Mingaliev, M. G. (2007). Radio continuum spectra of gigahertz-peaked spectrum galaxies. *Astronomy and Astrophysics*, 469:451–457.
- Torniaainen, I., Tornikoski, M., Teräsranta, H., Aller, M. F., and Aller, H. D. (2005). Long term variability of gigahertz-peaked spectrum sources and candidates. *Astronomy and Astrophysics*, 435:839–856.
- Torniaainen, I., Tornikoski, M., Turunen, M., Lainela, M., Lähteenmäki, A., Hovatta, T., Mingaliev, M. G., Aller, M. F., and Aller, H. D. (2008). Cluster analyses of gigahertz-peaked spectrum sources with self-organising maps. *Astronomy and Astrophysics*, 482:483–498.
- Tornikoski, M., Jussila, I., Johansson, P., Lainela, M., and Valtaoja, E. (2001). Radio Spectra and Variability of Gigahertz-Peaked Spectrum Radio Sources and Candidates. *Astronomical Journal*, 121:1306–1318.
- Tornikoski, M., Lähteenmäki, A., Lainela, M., and Valtaoja, E. (2002). Possible Identifications for Southern EGRET Sources. *Astrophysical Journal*, 579:136–147.
- Tornikoski, M., Lainela, M., and Valtaoja, E. (2000). The High Radio Frequency Spectra and Variability of Southern Flat-Spectrum Radio Sources. *Astronomical Journal*, 120:2278–2283.

- Tschager, W., Schilizzi, R. T., Röttgering, H. J. A., Snellen, I. A. G., and Miley, G. K. (2000). The GHz-peaked spectrum radio galaxy 2021+614: detection of slow motion in a compact symmetric object. *Astronomy and Astrophysics*, 360:887–895.
- Tschöke, D., Hensler, G., and Junkes, N. (2000). X-rays from the barred galaxy NGC 4303. *Astronomy and Astrophysics*, 360:447–456.
- Tueller, J., Baumgartner, W. H., Markwardt, C. B., Skinner, G. K., Mushotzky, R. F., Ajello, M., Barthelmy, S., Beardmore, A., Brandt, W. N., Burrows, D., Chincarini, G., Campana, S., Cummings, J., Cusumano, G., Evans, P., Fenimore, E., Gehrels, N., Godet, O., Grupe, D., Holland, S., Kennea, J., Krimm, H. A., Koss, M., Moretti, A., Mukai, K., Osborne, J. P., Okajima, T., Pagani, C., Page, K., Palmer, D., Parsons, A., Schneider, D. P., Sakamoto, T., Sambruna, R., Sato, G., Stamatikos, M., Stroh, M., Ukwata, T., and Winter, L. (2010). The 22 Month Swift-BAT All-Sky Hard X-ray Survey. *The Astrophysical Journal Supplement*, 186:378–405.
- Tueller, J., Mushotzky, R. F., Barthelmy, S., Cannizzo, J. K., Gehrels, N., Markwardt, C. B., Skinner, G. K., and Winter, L. M. (2008). Swift BAT Survey of AGNs. *Astrophysical Journal*, 681:113–127.
- Ulvestad, J. S. and Wrobel, J. M. (2009). *VLBA status summary*, <http://www.vlba.nrao.edu/astro/obstatus/current/obssum.html>. NRAO.
- Urry, C. M. and Padovani, P. (1995). Unified Schemes for Radio-Loud Active Galactic Nuclei. *Publications of the ASP*, 107:803.
- Urry, C. M., Sambruna, R. M., Worrall, D. M., Kollgaard, R. I., Feigelson, E. D., Perlman, E. S., and Stocke, J. T. (1996). Soft X-Ray Properties of a Complete Sample of Radio-selected BL Lacertae Objects. *Astrophysical Journal*, 463:424.
- Vercellone, S., Soldi, S., Chen, A. W., and Tavani, M. (2004). On the duty-cycle of γ -ray blazars. *Monthly Notices of the Royal Astronomical Society*, 353:890–902.
- Veron-Cetty, M. and Veron, P. (1993). Spectroscopic observations of sixteen BL Lacertae candidates. *Astronomy and Astrophysics Supplement Series*, 100:521–529.
- Véron-Cetty, M. and Véron, P. (2006). A catalogue of quasars and active nuclei: 12th edition. *Astronomy and Astrophysics*, 455:773–777.
- Villata, M., Raiteri, C. M., Larionov, V. M., Kurtanidze, O. M., Nilsson, K., Aller, M. F., Tornikoski, M., Volvach, A., Aller, H. D., Arkharov, A. A., Bach, U., Beltrame, P., Bhatta, G., Buemi, C. S., Böttcher, M., Calcidese, P., Carosati, D., Castro-Tirado, A. J., da Rio, D., di Paola, A., Dolci, M., Forné, E., Frasca, A., Hagen-Thorn, V. A., Heidt, J., Hiriart, D., Jelínek, M., Kimeridze, G. N., Konstantinova, T. S., Kopatskaya, E. N., Lanteri, L., Leto, P., Ligustri, R., Lindfors, E., Lähteenmäki, A., Marilli, E., Nieppola, E., Nikolashvili, M. G., Pasanen, M., Ragozzine, B., Ros, J. A., Sigua, L. A., Smart, R. L., Sorcia, M., Takalo, L. O., Tavani, M., Tringilio, C., Turchetti, R., Uckert, K., Umana, G., Vercellone, S., and Webb, J. R. (2008). Multifrequency monitoring of the blazar $\text{J}0716+714$ during the GASP-WEBT-AGILE campaign of 2007. *Astronomy and Astrophysics*, 481:L79–L82.

- Villata, M., Raiteri, C. M., Larionov, V. M., Nikolashvili, M. G., Aller, M. F., Bach, U., Carosati, D., Hroch, F., Ibrahimov, M. A., Jorstad, S. G., Kovalev, Y. Y., Lähteenmäki, A., Nilsson, K., Teräsraanta, H., Tosti, G., Aller, H. D., Arkharov, A. A., Berdyugin, A., Boltwood, P., Buemi, C. S., Casas, R., Charlot, P., Coloma, J. M., di Paola, A., di Rico, G., Kimeridze, G. N., Konstantinova, T. S., Kopatskaya, E. N., Kovalev, Y. A., Kurtanidze, O. M., Lanteri, L., Larionova, E. G., Larionova, L. V., Le Campion, J., Leto, P., Lindfors, E., Marscher, A. P., Marshall, K., McFarland, J. P., McHardy, I. M., Miller, H. R., Nucciarelli, G., Osterman, M. P., Pasanen, M., Pursimo, T., Ros, J. A., Sadun, A. C., Sigua, L. A., Sixtova, L., Takalo, L. O., Tornikoski, M., Trigilio, C., Umana, G., Xie, G. Z., Zhang, X., and Zhou, S. B. (2009). The correlated optical and radio variability of γ -ray emitting BL Lacertae. WEBT data analysis 1994–2005. *Astronomy and Astrophysics*, 501:455–460.
- Vitrichchak, V. M., Gabuzda, D. C., Algaba, J. C., Rastorgueva, E. A., O’Sullivan, S. P., and O’Dowd, A. (2008). The 15–43 GHz parsec-scale circular polarization of 41 active galactic nuclei. *Monthly Notices of the Royal Astronomical Society*, 391:124–135.
- Volvach, A. E. and Kovalev, Y. Y. (2006). Multi-Frequency Long-Term Radio Variability and the Milliarcsecond Structure of the High-Redshift Quasar OH 471. In C. M. Gaskell, I. M. McHardy, B. M. Peterson, & S. G. Sergeev, editor, *Astronomical Society of the Pacific Conference Series*, volume 360 of *Astronomical Society of the Pacific Conference Series*, page 149.
- Wagner, S. J., Camenzind, M., Dreissigacker, O., Borgeest, U., Britzen, S., Brinkmann, W., Hopp, U., Schramm, K., and von Linde, J. (1995). Simultaneous optical and gamma-ray flaring in PKS 0420-014. Implications for emission processes and rotating jet models. *Astronomy and Astrophysics*, 298:688.
- Wagner, S. J. and Witzel, A. (1995). Intraday Variability In Quasars and BL Lac Objects. *Annual Review of Astronomy and Astrophysics*, 33:163–198.
- Walker, R. C., Benson, J. M., Unwin, S. C., Lystrup, M. B., Hunter, T. R., Pilbratt, G., and Hardee, P. E. (2001). The Structure and Motions of the 3C 120 Radio Jet on Scales of 0.6–300 Parsecs. *Astrophysical Journal*, 556:756–772.
- Walker, R. C., Ly, C., Junor, W., and Hardee, P. J. (2008). A VLBA movie of the jet launch region in M87. *Journal of Physics Conference Series*, 131(1):012053.
- Wang, C. and Zhou, H. (2009). Determination of the intrinsic velocity field in the M87 jet. *Monthly Notices of the RAS*, 395:301–310.
- Wang, W. H., Hong, X. Y., Jiang, D. R., Venturi, T., Chen, Y. J., and An, T. (2001). An accelerated jet in DA193? *Astronomy and Astrophysics*, 380:123–129.
- Watson, D., Smith, N., Hanlon, L., McBreen, B., Quilligan, F., Tashiro, M., Metcalfe, L., Doyle, P., Teräsraanta, H., Carramiñana, A., and Guichard, J. (2000). ASCA and other contemporaneous observations { } of the blazar B2 1308+326. *Astronomy and Astrophysics*, 364:43–52.

- Wilkes, B. J., Tananbaum, H., Worrall, D. M., Avni, Y., Oey, M. S., and Flanagan, J. (1994). The Einstein database of IPC x-ray observations of optically selected and radio-selected quasars, 1. *Astrophysical Journal Supplement Series*, 92:53–109.
- Wills, B. J., Thompson, K. L., Han, M., Netzer, H., Wills, D., Baldwin, J. A., Ferland, G. J., Browne, I. W. A., and Brotherton, M. S. (1995). Hubble Space Telescope Sample of Radio-loud Quasars: Ultraviolet Spectra of the First 31 Quasars. *Astrophysical Journal*, 447:139.
- Wills, B. J., Wills, D., Breger, M., Antonucci, R. R. J., and Barvainis, R. (1992). A survey for high optical polarization in quasars with core-dominant radio structure - Is there a beamed optical continuum? *Astrophysical Journal*, 398:454–475.
- Wilms, J., Allen, A., and McCray, R. (2000). On the Absorption of X-Rays in the Interstellar Medium. *The Astrophysical Journal*, 542:914–924.
- Woo, J. and Urry, C. M. (2002). Active Galactic Nucleus Black Hole Masses and Bolometric Luminosities. *Astrophysical Journal*, 579:530–544.
- Worrall, D. M. and Marshall, F. E. (1984). The broad-band X-ray spectrum of a QSO sample. *Astrophysical Journal*, 276:434–439.
- Worrall, D. M., Tananbaum, H., Giommi, P., and Zamorani, G. (1987). X-ray studies of quasars with the Einstein Observatory. IV - X-ray dependence on radio emission. *Astrophysical Journal*, 313:596–606.
- Worrall, D. M. and Wilkes, B. J. (1990). X-ray spectra of compact extragalactic radio sources. *Astrophysical Journal*, 360:396–407.
- Wright, S. C., McHardy, I. M., and Abraham, R. G. (1998). Host galaxies of the optically violently variable quasars PKS 0736+017, OJ 287 and LB 2136. *Monthly Notices of the Royal Astronomical Society*, 295:799–812.
- Wrobel, J. M. and Lind, K. R. (1990). The double-lobed blazar 3C 371. *Astrophysical Journal*, 348:135–140.
- Wu, J., Zhou, X., Ma, J., Wu, Z., Jiang, Z., and Chen, J. (2007). Optical Monitoring of BL Lacertae Object S5 0716+714 with a Novel Multipeak Interference Filter. *Astronomical Journal*, 133:1599–1608.
- Yamasaki, N. Y., Ishikawa, T., and Ohashi, T. (2000). ASCA Observation of the Lyman-Limit Quasar PKS 2145+067. *Publ. of the Astronomical Society of Japan*, 52:763–767.
- Young, P. J., Westphal, J. A., Kristian, J., Wilson, C. P., and Landauer, F. P. (1978). Evidence for a supermassive object in the nucleus of the galaxy M87 from SIT and CCD area photometry. *Astrophysical Journal*, 221:721–730.
- Yuan, W., Brinkmann, W., Gliozzi, M., Zhao, Y., and Matsuoka, M. (2000). X-ray observation of the super-luminal quasar 4C +73.18 (1928+738) by ASCA. *Astronomy and Astrophysics*, 362:19–26.

- Zavala, R. T. and Taylor, G. B. (2004). A View through Faraday's Fog. II. Parsec-Scale Rotation Measures in 40 Active Galactic Nuclei. *Astrophysical Journal*, 612:749–779.
- Zensus, J. A., Ros, E., Kellermann, K. I., Cohen, M. H., Vermeulen, R. C., and Kadler, M. (2002). Sub-milliarcsecond Imaging of Quasars and Active Galactic Nuclei. II. Additional Sources. *The Astronomical Journal*, 124:662–674.
- Zhang, J. and Fan, J. (2003). Spectral Indices of Core and Extended Components of Extragalactic Radio Sources. *Chinese Journal of Astronomy & Astrophysics*, 3:415–422.

Acknowledgements

It is a pleasure for me to thank all those who made this thesis possible. First of all, I would like to express my deep and sincere gratitude to my supervisor, Professor Eduardo Ros. Since the beginning of my PhD, he has been guiding me through each stage of the study, and provides me detailed and constructive comments on my work. His encouragement, guidance and support from the initial to the final step has enabled me to develop an understanding of the subject. I thank him for sharing his enthusiasm in science and knowledge with me, as well as his warmth and sympathy to people.

I am grateful for the support of the Marie Curie EU framework ESTRELA (Early-Stage TRaining site for European Long-wavelength Astronomy), without it, this work would have been impossible. Also, I would like to thank Prof. Anton Zensus, and the VLBI group in the Max-Planck-Institut für Radioastronomie (MPIfR), for providing an excellent environment for science research. I benefited from the International Max Planck Research School (IMPRS) for Astronomy and Astrophysics from seminars, soft skill training, and student meetings. I thank MPIfR for providing hardware and software support, as well as great facilities. I would like to thank the previous IMPRS secretary, Gabriele Breuer, for her help when I just arrived Bonn.

I would like to thank Matthias Kadler, who hosted me during my stay in the Goddard Space Flight Center, and provided his knowledge in X-ray data analysis. Thanks to Joern Wilms, Laura Barragán, Moritz Böck, and Sera Markoff, for providing their knowledge in high energy data analysis and broadband SED study. Thanks to Anupreeta Moré, Richard Porcas, Tuomas Savolainen, G. Cimò, S. Mühle, M. A. Garrett, R. C. Walker, Frank Schinzel, and Kirill Sokolovsky, for valuable comments and inspiring discussions. I also wish to thank the MOJAVE team, the FGAMMA team, and the *Fermi*/LAT team, for their assistance and support to make this work as it is. Thanks to Ioannis Nestoras for compiling the FGAMMA data in this thesis.

In my daily work, I was lucky to have a group of nice and cheerful friends who have supported me all the time. Marios Karouzos is definitely the best friend you can find, he is supportive, understandable and by your side. The last phase of our PhD will be a nice memory in my life. I always enjoyed the inspiring talks with Filomena Volino, who shared her philosophy of life with me. Mar Mezcua, always cheerful and bringing happiness to people, has been my good officemate in the last 1.5 years. Christian Fromm, my good officemate for the last three years, helped me a lot in python scripting and supermarket-shopping. There are many more friends to be mentioned: Luciano Cerrigone, Gabriele Surcis, Laura Gomez, Tzu-Chen Peng, Seungkyung Oh, Yoon,-Kyung Choi, Fang-Chun Liu, Xun Shi, and John Morgan. I owe them my gratitude for their support and help in various aspects.

I owe my loving thank to Claudio Ricci, who has been always with me in the last phase

Acknowledgements

of my PhD study, not only providing me his professional knowledge, but more importantly his loving support during my ups and downs, and especially at difficult moments.

Lastly, I wish to express my gratitude to my beloved family, for their understanding and love, throughout the duration of my study.

This research was supported by the EU Framework 6 Marie Curie Early Stage Training program under contract number MEST-CT-2005-19669 "ESTRELA" (Early-Stage TRaining site for European Long-wavelength Astronomy). C. S. Chang is a member of the International Max Planck Research School of Astronomy and Astrophysics. This research has made use of data from the MOJAVE database that is maintained by the MOJAVE team (Lister et al. 2009a). This research has made use of data from the University of Michigan Radio Astronomy Observatory which has been supported by the University of Michigan and by a series of grants from the National Science Foundation, most recently AST-0607523. Part of this work is based on archival data, software or on-line services provided by the ASI Science Data Center (ASDC). This research has made use of data obtained from the High Energy Astrophysics Science Archive Research Center (HEASARC), provided by NASA's Goddard Space Flight Center. The National Radio Astronomy Observatory is a facility of the National Science Foundation operated under cooperative agreement by Associated Universities, Inc.

致謝

能夠完成這篇論文，我受到了很多人的幫助。首先最想感謝的是我的指導教授 Prof. Dr. Eduardo Ros，沒有他的鼓勵跟指導，這篇論文是不可能完成的，在他身上我也學到很多，除了學術研究外，更多的是待人的溫暖及對工作的熱忱。

還要感謝歐盟的ESTRELA計畫，沒有這個計畫，我是不可能德國完成學業的。感謝Prof. Dr. Anton Zensus, Max Planck Institute for Radio Astronomy 的 VLBI團隊，以及International Max Planck Research School在我求學階段的幫忙。

我想謝謝身邊的朋友一路上情感的支持：楊晶安與我同時赴德求學，一東一西，不時加油打氣；羅慧芬亦與我同年赴歐，分別在巴黎與德國學習，她在我困難的時候情感上的支持，是我很感謝的；感謝常常關心我的老友吳美慧，從台灣給我溫暖的支持；感謝我的好友陳易馨，除了深厚的友誼之外，也提供了對於本論文中摘要的專業意見；還要感謝章學涵在我求學的頭兩年對我的支持，他是我在低潮時的浮木，情感人生的垃圾桶。很謝謝他。

我最想感謝的，是我最親愛的家人：父親張書偉、母親蔡玉仙、及妹妹張靖筠。在我離家求學的三年裡，他們在台灣安穩地生活，讓我能安心求學，堅強可靠的父親，溫柔解人的母親，及我可愛的妹妹。家人自始至終都是最支持我的，在我人生的每個階段，他們是我厚實永恆的支柱。

感謝是說不完的，對更多人的感謝，我放在心底。

Erklärung

Ich versichere, das ich die von mir vorgelegte Dissertation selbständig angefertigt, die benutzen Quellen und Hilfsmittel vollständig angegeben und die Stellen der Arbeit - einschließlich Tabellen, Karten und Abbildungen -, die anderen Werken im Wortlaut oder dem Sinn nach entnommen sind, in jedem Einzelfall als Entlehnung kenntlich gemacht habe; dass diese Dissertation noch keiner anderen Fakultät oder Universität zur Prüfung vorgelegen hat; dass sie - abgesehen von unten angegebenen Teilpublikationen - noch nicht veröffentlicht worden ist sowie, dass ich eine solche Veröffentlichung vor Abschluß des Promotionsverfahrens nicht vornehmen werde. Die Bestimmungen dieser Promotionsverfahrens sind mir bekannt. Die von mir vorgelegte Dissertation ist von Prof. Andreas Eckart und Prof. Eduardo Ros Ibarra betreut worden.

Köln, den 07.09.2010

Teilpublikationen:

- C. S. Chang, E. Ros, Y. Y. Kovalev, and M. L. Lister, *VLBI detection of the HST-1 feature in the M 87 jet at 2 cm*, *Astronomy & Astrophysics*, 515, A38 (2010)
- C. S. Chang, E. Ros, Y. Y. Kovalev, and M. L. Lister, *A Multi-band Flare in the M87 Jet 80 pc away from the Central Engine*, *Memorie della Società Astronomica Italiana*, in press
- C. S. Chang, E. Ros, M. Kadler, M. F. Aller, H. D. Aller, E. Angelakis, L. Fuhrmann, I. Nestoras, and H. Ungerechts, *The Broadband Spectral Energy Distribution of the MOJAVE Sample*, *Proceedings of the Workshop “Fermi meets Jansky - AGN in Radio and Gamma-rays”*, T. Savolainen, E. Ros, R. W. Porcas, and J. A. Zensus (eds.), 2010 [arXiv:1006.4777]
- C. S. Chang, E. Ros, M. Kadler, the Fermi-LAT collaboration, and the F-GAMMA team, *The spectral energy distribution of gamma-faint compact radio sources*, 2009 Fermi Symposium, eConf Proceedings C091122 [arXiv:1001.1566]
- C. S. Chang, E. Ros, M. Kadler, R. Ojha, the Fermi-LAT collaboration, the TANAMI Team, and the F-GAMMA Team, *Multiwavelength campaign of the gamma-ray flaring source PKS 2052–47*, 2009 Fermi Symposium, eConf Proceedings C091122 [arXiv:1001.1563]
- C. S. Chang, E. Ros, Y. Y. Kovalev, and M. L. Lister, *A closer look at the flaring feature in the M87 jet*, *ASP Conference Series*, “Accretion and Ejection in AGN: A Global View” [arXiv:0910.0135]

- C. S. Chang, E. Ros , Y. Y. Kovalev, and M. L. Lister, *15 GHz VLBI detections of the HST-1 feature in the M87 jet*, The 9th EVN Symposium, Proceedings of Science, 2008 [arXiv:0812.0126]

Curriculum Vitae

Persönliche Daten

Name: Chin-Shin Chang

Anschrift: Lutfridstrasse 5, 53121 Bonn, Deutschland

Geburtsdatum: 23. Mai 1982

Geburtsort: Taipeh, Taiwan

Staatsangehörigkeit: Taiwan

Wissenschaftlicher Werdegang

September 1997 – Juni 2000: National Experimental High School, Hsinchu, Taiwan

September 2000 – Juni 2004: Bachelor of Science in Physics, Department of Physics, National Tsing Hua University, Taiwan

September 2004 – Juli 2006: Master of Science in Astronomy, “Preliminary Data Reduction of Asteroseismic Data from EAST Network and Light Curves of GN And and BI CMi” Institute of Astronomy, National Tsing Hua University, Taiwan, betreut durch Prof. Dr. D. Y. Chou; Referenten: Prof. Dr. I. G. Jiang und Prof. Dr. W. P. Chen

01.08.2006 – 30.06.2007: Research assistant in the Astrophysics laboratory of Prof. Dr. D. Y. Chou

13.08.2007 – 12.08.2010: Doktorand in der Very Long Baseline Interferometry Gruppe des Max-Planck-Instituts für Radioastronomie. Mitglied des Marie Curie EU Netzwerkes ESTRELA (**E**arly-**S**tage **T**Raining site for **E**uropean **L**ong-wavelength **A**stronomy).

13.08.2010 – : Doktorand und Mitglied der Very Long Baseline Interferometry Gruppe des Max-Planck-Institut für Radioastronomie. Mitglied der the **I**nternational **M**ax **P**lanck **R**esearch **S**chool (IMPRS) for Astronomy and Astrophysics.

Bonn, den 7. September 2010

